A Quaternary history of ice sheet dynamics in the Transantarctic Mountains

Kurt Richard Joy

Department of Geological Sciences

University of Canterbury

A thesis submitted for the degree of

Doctor of Philosophy (PhD)

July 2013

Abstract

The Antarctic Ice Sheets responded significantly to climatic conditions during the Last Glacial Maximum (LGM) and the subsequent warming that followed. Therefore, an understanding of how Antarctica reacted to past climates is necessary to predict the response of its ice sheets to current and future climate change.

This thesis presents new evidence about the timing and magnitude of East and West Antarctic ice sheet (EAIS & WAIS) changes during the Quaternary Period, from the Darwin Hatherton glacial system (DHGS, 79.5°S, 158°E). The DHGS drains the EAIS through the Transantarctic Mountains into the Ross Ice Shelf and glacial deposits have been used to constrain ice sheet thicknesses in this sector of the Ross Sea Embayment. At four sites along the length of the system, glacial deposits were mapped and 73 erratic and bedrock samples collected for ^{10}Be and ^{26}Al surface exposure dating (SED). The exposure ages range from 0.01 to 2.2 Ma and generally show a trend of oldest ages at the highest elevations, thus suggesting an overall decrease of ice volume within the DHGS over the Quaternary. The older ages suggest that during the Plio-Pleistocene, DHGS ice was at least 800-1000 metres thicker than present, while in the mid to late-Holocene thickening was less than 50-80 metres.

Four glacial advance and retreat events were described and mapped previously from the DHGS by Bockheim et al. (1989). The Isca and Danum Drifts, are $\approx$1-2 and 0.6 Ma respectively. The Britannia-II Drift, previously assumed to mark the maximum extent of the Last Glacial Maximum advance is more complex, with clusters of ages at $\approx$6.5,

≈36 and ≈125 ka. The youngest drift, the Hatherton is mid to late-Holocene (<4.5 ka) and suggests that the DHGS has been near its equilibrium position during this period.

Throughout the DHGS no unequivocal evidence of the LGM was observed and therefore poses questions about the past thickness of the Antarctic ice sheets during the LGM. Exposure ages from sites near the head of the Hatherton Glacier (Dubris Valley & Lake Wellman) suggest that at the LGM, the East Antarctic Ice Sheet may have been of similar size, or slightly smaller, than present. In stark contrast, at the confluence of the Darwin Glacier and the Ross Ice Shelf, a WAIS ≈400-900 metres above the modern ice surface is tentatively suggested; A value in agreement with that proposed by modern glaciological models. Additionally, while the results from the Dubris and Bibra valleys show that the EAIS thins during glacial climates (*i.e.* the LGM), it also suggests thickening during interglacials. The Britannia-I and II drifts representing retreats at ≈6.5 and ≈125 ka from glacial highstands.

A number of key findings related to the application of SED in Antarctic settings are also presented. The use of dual-nuclides (^{10}Be & ^{26}Al) show that within the DHGS, the proportion of samples displaying a prior burial history increases with distance from the catchment. The spread of exposure ages observed in the dataset also show the complexity of the depositional processes occurring at cold-based glacial margins and therefore judicious sample selection is required to obtain exposure ages that are representative of the true deglaciation age.

Deputy Vice-Chancellor's Office
Postgraduate Office

UNIVERSITY OF CANTERBURY
Te Whare Wānanga o Waitaha
CHRISTCHURCH NEW ZEALAND

Co-Authorship Form

This form is to accompany the submission of any thesis that contains research reported in co-authored work that has been published, accepted for publication, or submitted for publication. A copy of this form should be included for each co-authored work that is included in the thesis. Completed forms should be included at the front (after the thesis abstract) of each copy of the thesis submitted for examination and library deposit.

Please indicate the chapter/section/pages of this thesis that are extracted from co-authored work and provide details of the publication or submission from the extract comes:

Chapter 5 summaries the surface exposure results from the paper:

A 2 million year glacial chronology of the Hatherton Glacier, Antarctica and implications for the size of the East Antarctic Ice Sheet at the Last Glacial Maximum. 10Be evidence for Quaternary East Antarctic Ice Sheet dynamics. Dubris Valley Area, Britannia Range, Antarctica.
Joy, K., Fink, D., Storey, B. C. & Atkins C.(2013). Journal of Quaternary Science (in review)

This paper is also included in appendix B1 of this thesis.

Please detail the nature and extent (%) of contribution by the candidate:

70%. Primary author of draft paper.

-Calculation, analysis and interpretation of surface exposure ages.

-All figures, plots, fieldwork, mapping and sample collection.

Certification by Co-authors:

If there is more than one co-author then a single co-author can sign on behalf of all
The undersigned certifys that:

- The above statement correctly reflects the nature and extent of the PhD candidate's contribution to this co-authored work
- In cases where the candidate was the lead author of the co-authored work he or she wrote the text

Name: *Bryan Storey* Date: *12/7/2013*

Deputy Vice-Chancellor's Office
Postgraduate Office

UNIVERSITY OF CANTERBURY
Te Whare Wānanga o Waitaha
CHRISTCHURCH NEW ZEALAND

Co-Authorship Form

This form is to accompany the submission of any thesis that contains research reported in co-authored work that has been published, accepted for publication, or submitted for publication. A copy of this form should be included for each co-authored work that is included in the thesis. Completed forms should be included at the front (after the thesis abstract) of each copy of the thesis submitted for examination and library deposit.

Please indicate the chapter/section/pages of this thesis that are extracted from co-authored work and provide details of the publication or submission from the extract comes:

Chapter 6 summaries the surface exposure results from the paper:

"Cosmogenic nuclide exposure age constraints on the glacial history of the Lake Wellman area, Darwin Mountains, Antarctica."
Storey, B. C., Fink, D., Hood, D., Joy, K., Shulmeister, J., Riger-Kusk, M., & Stevens, M. I. (2010). Antarctic Science, 22 (06), 603-618.

This paper is also included in appendix B2 of this thesis.

Please detail the nature and extent (%) of contribution by the candidate:

30%

-Calculation, analysis and interpretation of surface exposure ages.

-All figures and plots.

Certification by Co-authors:

If there is more than one co-author then a single co-author can sign on behalf of all
The undersigned certifys that:

- The above statement correctly reflects the nature and extent of the PhD candidate's contribution to this co-authored work
- In cases where the candidate was the lead author of the co-authored work he or she wrote the text

Name: *Bryan Storey* Date: *12/7/2013*

Acknowledgements

I have so many people to thank it's not funny. First up, the people who have stumped up the cash to allow me to do what I have loved for the last four and a half years.

- Antarctica New Zealand.
- Christchurch City Council.
- Helicopters New Zealand.
- University of Canterbury: Gateway Antarctica.
- The Australian Institute of Nuclear Science and Engineering.

Without the financial support of these organisations, there is no way I could have finished my thesis. Given the economic climate, it makes the idea of people handing over their hard earned cash to support my research even more humbling.

My supervisors: Bryan Storey, David Fink and Cliff Atkins. You guys have supported me a billion percent (actually make that a billion^2 percent!). From the day I sent my CV to Bryan to the last frantic emails before submission, I have received nothing but fantastic support from them, both at home and in the field.

A massive thanks to the staff of Antarctic New Zealand both in Christchurch and Scott Base (my second home).

On the technical side, a number of people have assisted in me in the arduous task of taking a pile of Antarctic rocks and reducing them to atoms. Rob Spiers, James Oram and Sacha Baldwin-Cunningham at the University of Canterbury. Charles Mifsud and Toshi Fujioka at ANSTO.

David Hood and Nita Smith for collecting samples for SED during their Antarctic fieldwork at the Darwin.

Anekant Wandres, Josh Blackstock, Jesse Dykstra and Tom Brookman at the University of Canterbury for 'emotional support', kasundi and chilli sauce in the times when my science went pear shaped.

Last and definitely not least! My family. Mum, Dad, Sue and my wife Katherine (possibly even the cats). They have believed in me since day one, when I got a foolhardy idea to pursue science and head to the ice. Words can't express how much I owe them for everything.

Especially Katherine, as I know she would love Antarctica as much as I do.

Contents

List of Figures

List of Tables

Glossary

AMS Accelerator mass spectrometry

ANSTO Australian Nuclear Science and Technology Organisation

DHGS Darwin Hatherton glacial system

DBV Dubris and Bibra valleys

EAIS East Antarctic Ice Sheet

EPICA European Project for Ice Coring in Antarctica

ESL Eustatic sea level

LGM Last Glacial Maximum

MIS Marine isotope stage

masl Metres above sea level

msle Metres sea level equivalent

RIS Ross Ice Shelf

SED Surface exposure dating

TAMs Transantarctic Mountains

TCN Terrestrial Cosmogenic Nuclide

UC University of Canterbury

WAIS West Antarctic Ice Sheet

Chapter 1

Introduction

The discovery by Louis Agassiz (1807-1873) of glacially striated bedrock throughout the Scottish highlands in 1840 provided evidence of the past glaciation of the British Isles. This discovery raised the question, what was the extent of glacial ice during the last ice age? In the years since, geologists and glaciologists have attempted to establish the size and geometry of the ice sheets that existed at the height of the last ice age. This period, referred to as the Last Glacial Maximum (LGM, ≈20-18 ka), is just one of many glaciations now recognised to have occurred in the past.

Terrestrial and marine paleo-climate records have been invaluable in showing the relationship between ice sheet formation (*i.e.* ice volume) and global sea levels. Lisiecki and Raymo (2005) published a oceanic stable isotope record from benthic foraminifera that suggested cyclic periods of ice sheet expansion and retreat over the last 5 Ma. This record clearly displayed glacial-interglacial cycles lasting 40 ka then 100 ka following the mid-Pleistocene climate transition (≈1 Ma, Mudelsee and Schulz 1997). Remarkably similar to the marine record of Lisiecki and Raymo (2005) were the ice-core records of Augustin et al. (2004) and Petit et al. (1999) that demonstrated the links between East Antarctic δ^{18}O values, glacial conditions and ice sheet expansion. But it was the seminal work of Fairbanks (1989) using a paleo-depth record from Barbados coral reefs that suggested an LGM sea level 116-126 metres lower than present, proving that even within relatively short time frames, ice volume and sea level changes were intrinsically linked. Although the relationship between the expansion of Northern Hemisphere ice sheets and falling sea levels are relatively well understood Carlson and Winsor (2012), the role that

Antarctica has played in global ice volume flux and sea level rise is far less constrained (Bentley, 2010).

Antarctica has not always been the ice covered continent that appears today (Figure 1.1). Global changes in climate, oceanic circulation and tectonics led to the first appearance of ice approximately 35 Ma ago and the development of short lived ice sheets in high elevation mountain ranges and plateaus (DeConto and Pollard, 2003). The continued thermal isolation of the continent allowed the expansion of the first permanent ice sheets around 15 Ma. The modern glaciological setting of the Antarctic is dominated by the presence of two major ice masses, estimated to contain an ice volume equivalent to 66 metres of sea level rise (Denton and Marchant, 2000): the larger East Antarctic Ice Sheet (EAIS) and smaller West Antarctic Ice Sheet (WAIS). The predominantly land based EAIS and the marine WAIS, the bulk of which is grounded beneath sea level, are separated by the 3500 km long Transantarctic Mountains (TAMs), running across the continent and acting as a geological barrier to ice flow (Faure and Mensing, 2011).

As the EAIS and WAIS play major roles in global climate, oceanic and atmospheric circulation, understanding how Antarctica reacted to a warming world at the end of Quaternary ice ages is key to predicting the effect modern climate change may have on global sea levels (IPCC, 2007). The ability to model EAIS and WAIS response to both atmospheric and oceanic warming has led to the development of a number of glaciological models (Denton and Hughes, 2002; Golledge et al., 2012; Huybrechts, 2002; Mackintosh et al., 2011). The models attempt to predict Antarctic ice sheet dynamics, paleo-ice volumes and contribution to the $\approx$120 metres of sea level rise since the last ice age. To calibrate and constrain Antarctic ice sheets models, physical evidence from a variety of geological records are used. Although much evidence of former ice sheet extent and dynamics can be found in the marine and offshore record (Anderson et al., 2013) , the onshore evidence is scarce, being limited to ice free mountainous and coastal areas (Denton and Marchant, 2000). Therefore, given the rarity of terrestrial evidence, any additional proxy records of past ice sheet behaviour are an important tool in aiding the calibrating of ice sheet models, both at the local and continental scale.

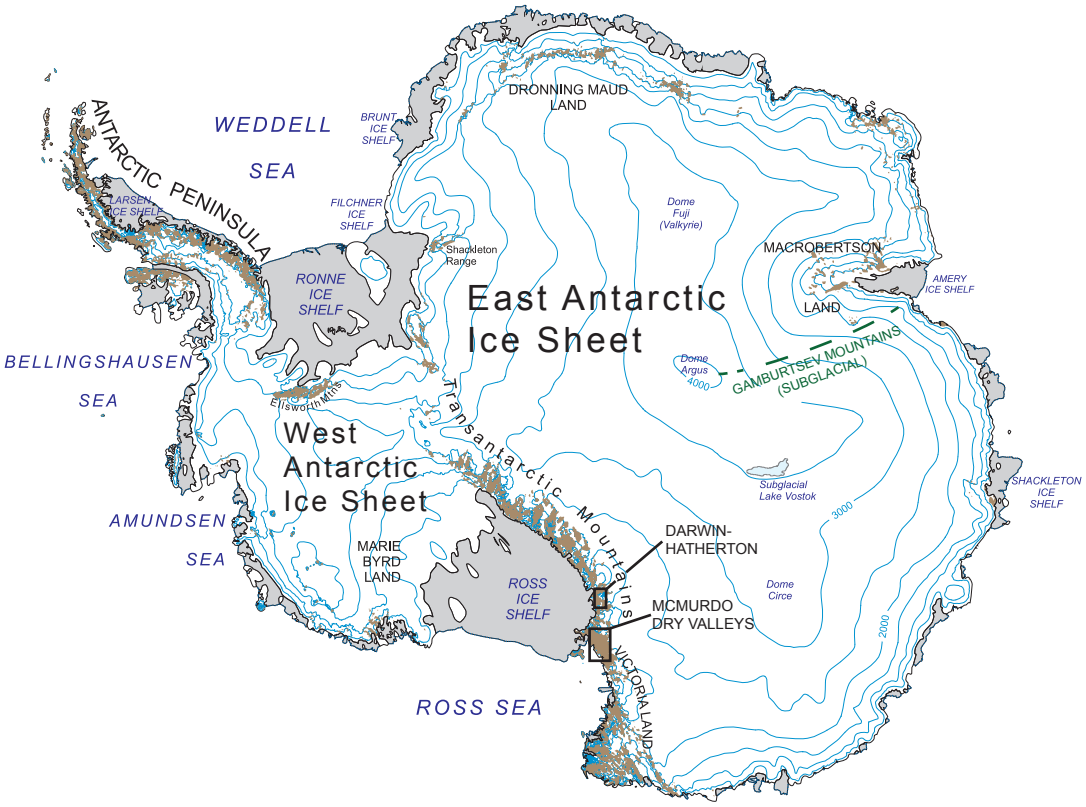

Figure 1.1: Map of the Antarctic continent - Showing East and West Antarctic ice sheets, fringing ice shelves and major topographic features. Areas in brown are ice-free. Adapted from the British Antarctic Survey (BAS) using data from the LandSAT Image Mosaic of Antarctic (LIMA) (www.lima.usgs.gov/documents/LIMA_overview_map.pdf)

In the lead up to the Last Glacial Maximum, a major advance of the WAIS introduced a significant volume of ice into the Ross Sea Embayment (RSE). Grounded West Antarctic ice, pushed out towards the continental margins and replaced the floating ice of the Ross Ice Shelf (RIS) (Anderson et al., 2013). During the same period, the EAIS is thought to have advanced at its coastal margins and thinned in the ice sheet interior. Although East Antarctic ice drained into the RSE *via* the outlet glaciers of the Transantarctic Mountains (Bockheim et al., 1989; Denton et al., 1989a), the buttressing of the WAIS against the TAMs effectively dammed glacier drainage and caused significant thickening to occur in the lower sections of the outlet glaciers (Bockheim et al., 1989; Golledge and Levy, 2011). This combination of minor EAIS thickening and a significantly thickened WAIS resulted in distinctive

glacier ice surface profiles, which represented the behaviour of both West and East Antarctic ice sheets. Therefore, glacial material deposited at outlet glacier margins during past glacial highstands like the LGM, delineate the upper limits of local as well as Antarctic ice sheet thicknesses (Bromley et al., 2010; Denton and Marchant, 2000; Di Nicola et al., 2012; Storey et al., 2010; Strasky et al., 2009; Todd et al., 2010).

This thesis focuses on the geomorphic evidence of ice sheet advance found in the Darwin Hatherton glacial system (DHGS), located within the Transantarctic Mountains (Figure 1.2). During three Antarctic field seasons (2007-2010), fieldwork was undertaken at four sites along both the Darwin and Hatherton glaciers. These included a range of glacial landscapes, including mountainous sites near the EAIS catchment and coastal sites proximal to the confluence of the Darwin Glacier with the Ross Ice Shelf.

The location and geomorphology of this glacial system is well suited as a research location for a number of reasons:

1. The system has one of highest concentrations of ice free areas outside of the McMurdo Dry Valleys.

2. The system contains a variety of glacial features and deposits used as evidence of past ice sheet thickness.

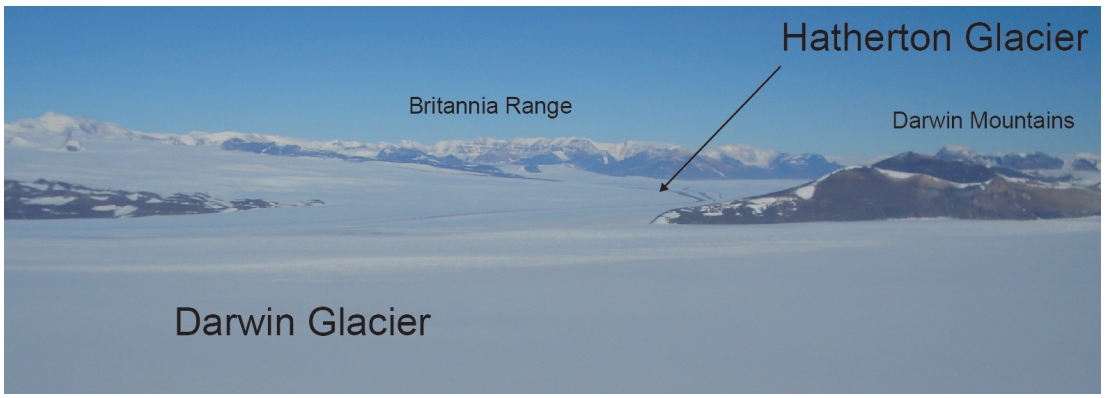

Figure 1.2: The Darwin and Hatherton glaciers - A view of the confluence of the Darwin and Hatherton glaciers, approximately midway through the system. Ice is flowing from right to left with the Darwin Glacier in the foreground and the Hatherton Glacier in the background. The two glaciers are separated by the Darwin Mountains and from the Byrd Glacier to the south by the Britannia Range.

3. The system plays a role in the drainage of the EAIS through the TAMs.

Previous work in this region by Denton (1979) and Bockheim et al. (1989) mapped the distribution of a well-defined sequence of glacial deposits, delineating the past positions of the Darwin and Hatherton glacier ice margin. The glacially transported boulders and cobbles found in these deposits reflect past changes in local ice thickness and position as well as acting as a proxy for East and West Antarctic ice sheet behaviour. Therefore, the geological record of ice sheet advance found in the landscapes flanking the Darwin and Hatherton glaciers are key sites for testing ice sheet models in this sector of the TAMs. To re-evaluate the Quaternary advances and retreats suggested by Bockheim et al. (1989), surface exposure dating (SED) using beryllium-10 (^{10}Be) and aluminium-26 (^{26}Al) terrestrial cosmogenic nuclides (TCN) is employed to date material representing the former extent of cold-based glacial margins. By collecting samples from the Bockheim et al. (1989) glacial deposits at various elevations above the current ice margin, the use of the 'mountain dipstick' technique (Mackintosh et al., 2007; Stone et al., 2003) can be used infer the elevation of past ice thickness. The technique has been successfully applied at sites throughout the Antarctic continent including the Ford Range (Stone et al., 2003) and the Antarctic Peninsula (Hodgson et al., 2012) in West Antarctica; the Prince Charles Mountains (Lilly, 2008), Transantarctic Mountains (Bromley et al., 2010; Todd et al., 2010) and the Ohio Range (Ackert et al., 2013) in East Antarctica.

1.1 Research aims

This thesis has two main aims, each with several specific research objectives.

1. Reconstructing the glacial history of the Antarctic ice sheets.
    - Understanding the glacial dynamics of the DHGS during the Pleistocene. Particularly during interglacials.
    - Re-evaluating the ice volume changes of the DHGS at the LGM and the ice surface profile suggested by Bockheim et al. (1989).
    - Comparing the Quaternary behaviour of the DHGS to other outlet glaciers in the TAMs. *i.e.* The Reedy and Ferrar glaciers.

- Using the DHGS as a direct measure of East and West Antarctic ice sheet behaviour.

2. Apply and assess the use of *insitu* cosmogenic nuclides and surface exposure dating in Antarctic settings.

   - To improve the understanding of the role that cold-based ice has on nuclide concentrations.
   - Understanding the limitations of the technique in high alpine and polar regions.
   - Using a dual-nuclide approach to identify samples that have undergone burial by ice.

1.2 Thesis structure

This thesis is divided into two parts. The first (Chapters 2-4) is comprised of literature reviews and discusses specific topics to provide the necessary background material for the following chapters. In the second, chapters are self-contained pieces of work that discuss site descriptions and results to address the specific research aims and objectives outlined in Section 1.1. The results of research carried out for this thesis is contained in Chapters 5-8. A breakdown of the individual chapter content is outlined below.

Chapter 2 discusses the technical aspects of surface exposure dating in polar environments. The first section introduces the source of cosmic rays, their interaction at the atmospheric and terrestrial level and the physics that govern how exposure ages are calculated. The second part of the chapter deals with the assumptions made in the interpretation of ages from a glacial feature and the considerations that must be made when using the technique in polar regions. Finally the methodology used in this research for the collection of samples is discussed.

Chapter 3 introduces the geological and glaciological setting of the Antarctic ice sheets, their evolution, past changes in ice volume and contribution to sea level rise, particularly during the LGM. The development of numerical glaciological models is discussed, including the role marine and terrestrial evidence has played in

constraining ice sheet extent and thickness. While initially at the continental scale, the focus switches to understanding the behaviour of the East and West Antarctic ice sheets within the Ross Sea Embayment.

Chapter 4 builds on the work presented in the previous chapter and concerns the regional setting of the Darwin and Hatherton glaciers. Key sections include climate, geology, glaciology and recent modelling results of past behaviour. Significantly, this chapter introduces the work of Bockheim et al. (1989), their interpretation of glacial drifts and the subsequent reconstruction of the LGM in this sector of the Transantarctic Mountains.

Chapters 5, 6 and 7 include field observations, SED results and their interpretations. Four sites along the DHGS, the Dubris and Bibra valleys, Lake Wellman, Roadend Nunatak and Diamond Hill, from EAIS catchment to the confluence with the Ross Ice Shelf are discussed. Within the framework of the Bockheim et al. (1989) glacial drifts, observations about the geology, geomorphology and range of glacial features at each site, combined with the interpretation of Quaternary SED exposure ages are discussed. Chapter 5 summarises the paper by Joy et al. (2014) and Chapter 6 that of Storey et al. (2010).

Chapter 8 summarises the results from the four field sites (Chapters 5-7) and discusses the DHGS as a whole as well as within the regional climatic framework. The DHGS is to the results from the Reedy Glacier, an outlet glacier in which exposure dating has been used to understand the Quaternary dynamics of the EAIS and WAIS in the southern Transantarctic Mountains. From these results, the past behaviour of the Antarctic ice sheets can be inferred.

Finally, the appendices are divided into a number of sections. The first contains sample information, accelerator mass spectrometry (AMS) results, calculated exposure ages and sample photos for Dubris and Bibra valleys (Chapter 5), Lake Wellman (Chapter 6), Roadend Nunatak and Diamond Hill (Chapter 7). The second section contains copies of published papers.

Chapter 2

Surface exposure dating in polar regions

Since the discovery of cosmic rays by Victor Hess in 1912, cosmic radiation has provided key insights into fundamental particle physics prior to the development of particle accelerators. It was the early work of Grosse (1934) who recognised that a suite of hypothetical "cosmic radio-elements" could form at the surface of the Earth due to interactions with cosmic rays. Libby et al. (1949) followed, identifying that ^{14}C, in measurable concentrations was being produced in the atmosphere in this manner. But the birth of surface exposure dating (SED) using terrestrial cosmogenic nuclides (TCNs) arrived with the pioneering work of Davis and Schaeffer (1955); a landmark study that first applied the use of a TCN, Chlorine-36 (^{36}Cl), as a tool to date glacial landscapes. Soon the relationship between erosion rates and TCN concentration was also recognised. Frohlich and Lubert (1973) suggested that erosion rates can be measured using a combination of ^{41}Ca and ^{39}Ar. Unfortunately, extremely low TCN production rates on the surface of the Earth, compared to that of the atmosphere, meant that these techniques were sparsely used.
In the 1980's, developments in accelerator mass spectrometers (AMS, Tuniz et al., 1998) led to instruments sensitive enough to measure TCNs in rock samples; thus the long theorised technique was now practical. In 1986/87, a landmark eight papers were released using cosmogenic ^{3}He, ^{21}Ne, ^{22}Ne, ^{10}Be, ^{26}Al and ^{36}Cl in terrestrial rocks (Craig and Poreda, 1986; Klein et al., 1986; Kurz, 1986; Marti and Craig, 1987; Nishiizumi et al., 1987a,b, 1986; Phillips et al., 1986). In the decades since, a number of additional TCNs (^{14}C, ^{41}Ca & ^{53}Mn), both stable and unstable, have been added and used to both date landscapes and quantify erosional processes

at the multi-million year scale. The process has become particularly important in the field of glacial geomorphology, where hundreds of studies have now used the technique to reconstruct glacier and ice sheet chronologies (See Balco, 2011 for a review).

2.1 Principles of surface exposure dating

2.1.1 Cosmic rays at the Earth's surface

The primary sources of galactic cosmic radiation (GCR), which have energies ranging from 100's of MeV to a few GeV, are generally thought to be the massive supernovae that exist within our galaxy (Diehl et al., 2006; Prantzos, 1993). The collapsing cores of these massive stars, thought to occur every ≈50 years, release streams of high energy nuclear particles, predominantly atomic nuclei but also including electrons and positrons. Accelerated by shock waves released during the supernovae explosions, GCR particles reach energies of 1-10^{10} GeV (Gosse and Phillips, 2001) before impinging on the upper surface of the Earth's atmosphere. Additionally, within our solar system cosmic rays are produced by the sun (known as solar cosmic rays), these are generally low energy (1-100 MeV) nuclei and electrons which are released during periods of enhanced solar activity. Due to their far lower energy than GCRs, they do not play a significant role in the production of TCNs (Masarik and Reedy, 1996). In the upper atmosphere, GCR is predominantly composed of protons (87%), alpha particles (≈12%) and a small percentage of heavier nuclei (Simpson, 1983).

The incoming primary proton generates a secondary cascade of nuclear interactions (Figure 2.1) as it interacts with atoms within the atmosphere. As these primary protons have energies far higher than that which bind nucleons in atomic nuclei (≈7-9 MeV), spallation reactions predominate; an impacting primary particle fragmenting a nucleon or a cluster of nucleons from the target particle. The secondary cascade exhibits a number of key characteristics:

1. A forward trajectory centred on the incoming ray, as product nucleons from the spallation reaction predominantly carry the incoming momentum in the same direction (Dorman et al., 1999).

2. A shift in composition from proton to neutron dominated flux due to ionization losses of protons as they travel through the atmosphere (Lal and Peters, 1967).

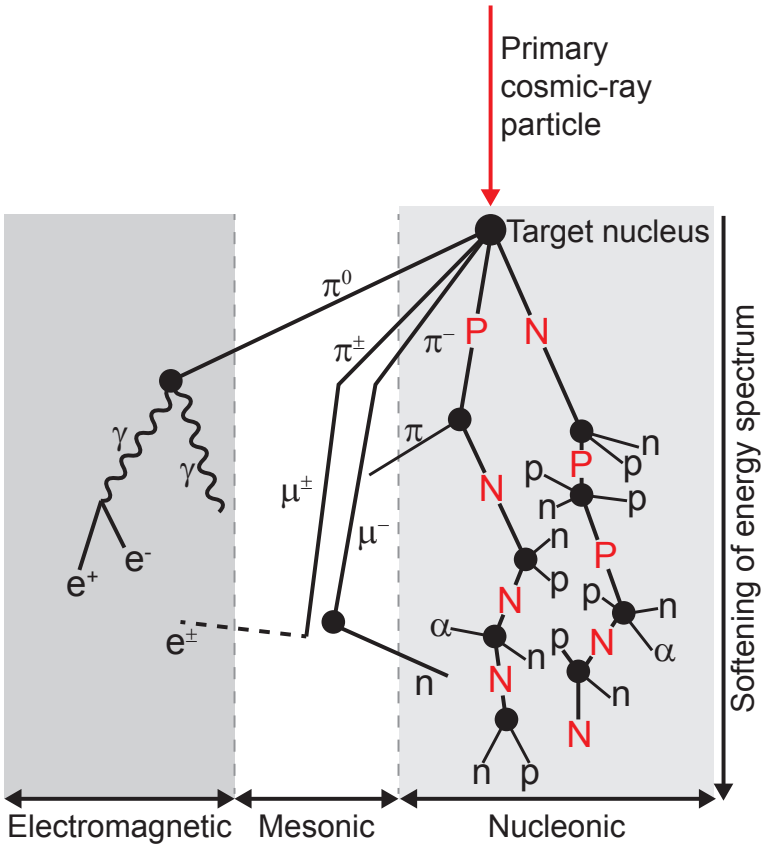

Figure 2.1: Secondary cosmic ray cascade in the atmosphere - The result of a single primary GCR proton entering the atmosphere. Adapted from Dunai (2010). Abbreviations used: n, neutron, p, proton (capital letters for particles carrying the nuclear cascade), α, alpha particle, $e^{\pm}$, electron or positron, γ, gamma ray photon, π, pion and μ, muon.

The secondary cascade also has three primary components, or pathways, that various particles follow (Dunai, 2010; Gosse and Phillips, 2001):

- Electromagnetic. Producing positrons and photons from the decay of mesons.
- Mesonic. Producing pions that rapidly decay to muons at high altitude (≈15 km) within the atmosphere.

- Nucleonic, also known as hadronic. Initially producing a proton, then neutron, dominated cascade.

Only the mesonic and nucleonic components play a role in the production of TCNs at the surface of the Earth, with nucleonic pathways dominating the total cosmic ray flux at sea level. Here the secondary GCR flux is composed mainly of neutrons (98%, Masarik and Beer, 2009), with an additional minor contribution at depth by fast muons (*i.e.* mesonic component). Additionally, secondary GCR flux varies spatially with the Earth's geomagnetic field, the specific elevation and latitude of a site affecting the intensity of the GCR flux (Section 2.1.4.1) and this plays a key role in the production rates of TCNs.

2.1.2 Aluminium-26 and beryllium-10 exposure dating

The development of high sensitivity accelerator mass spectrometers has opened a wide range of applications for the use of TCNs, particularly in sites where suitable material for radiocarbon dating is absent or beyond the age range of conventional thermo-luminescent dating techniques. Neotectonics and paleoseismicity (Bormann et al., 2012; Gosse, 2011), burial dating of sediments (Granger and Muzikar, 2001; Matmon et al., 2012) and dune field chronologies (Fujioka, 2012) are just a few examples of the many landscape studies that have used TCNs as a tool to quantify tectonic and geomorphic processes. One of the predominant applications of TCNs is in surface exposure dating (SED, also referred to as cosmogenic nuclide dating) of glacial deposits. SED employs a suite of *insitu* produced radionuclides (including ^{3}He, ^{10}Be, ^{26}Al, ^{36}Cl & ^{14}C) in surface material across a variety of target minerals at time scales from 10^{3}-10^{7} (*i.e.* 1 ka to 10 Ma) years. The technique allows the application of multiple nuclides with differing half-lives to examine burial histories and complex exposures (Section 2.2.1).

Two of the most common radionuclides for SED are beryllium-10 (^{10}Be) and aluminium-26 (^{26}Al), both having relatively well constrained production rates and concentrations within the measurement range of modern AMS facilities (Table 2.1). This combination of radionuclides is extensively used in Antarctic SED studies due to a robust analytical methodology and a maximum age of $\approx$5 Ma, well within the

Plio-Pleistocene.

Table 2.1: Attributes of beryllium-10 and aluminium-26 - Values used in exposure age calculations within this thesis. Production rates are scaled to sea level - high latitude (SLHL) using the scaling methods of Stone (2000) (see Balco et al. 2008, 'CRONUS')

Nuclide	Half-life (Ma)	Decay Constant	Production Rate (atm g^{-1} a^{-1})	Primary Targets
^{10}Be	1.31[a]	5.00 x 10^{-7}	4.60 $\pm$ 0.42[b]	^{16}O(n,4p3n), ^{16}O(μ^{-1},αpn) ^{28}Si(n,x), ^{28}Si(μ^{-1},x)
^{26}Al	0.71	9.90 x 10^{-7}	30.7 $\pm$ 2.8[c]	^{28}Si(n,p2n), ^{28}Si(μ^{-1},2n)

[a] The revised ^{10}Be half-life of Korschinek et al. (2010)
[b] Reflects a 10.6% downwards correction (Nishiizumi et al., 1991) to the previously accepted ^{10}Be production rate of 5.1 atm g^{-1} a^{-1} (Stone, 2000).
[c] Based on a ^{26}Al/^{10}Be production rate ratio of 6.75 (see Balco et al. 2008)

The spallation of ^{16}O and ^{28}Si nuclei produces ^{10}Be and ^{26}Al at known production rates (see Table 2.1 for the various nuclear reaction types) within quartz. An ideal SED target mineral for a number of reasons: A) It is extremely common in both the sandstones and granitoids ($\approx$40-98% SiO_2) of the Transantarctic Mountains (Section 4.2), B) highly resistant to weathering (both chemical & physical), C) relatively easy to prepare for analysis (for sample preparation methodology see Child et al., 2000; Mifsud et al., 2012) and D) the target composition density of silicon and oxygen atoms is well defined.
Additionally, the use of surface exposure dating at the Earth's surface relies on an understanding of a number of key factors:

- The secondary cosmic ray flux at the sample site as a function of elevation and latitude.
- Absolute production rate of the nuclide in the target mineral. This includes variations in the production rate due to sample geometry (*i.e.* depth, thickness and topographic horizon).
- The ability to measure accurately very low (x 10^{-15}) isotopic ratios.
- Sample history.

At its most basic, SED uses the measured TCN concentration (by AMS) and the known production rate to calculate the length of exposure time. This requires a number of assumptions to be made: A) That the sample has had no prior exposure (*i.e.* a simple exposure history), B) that the surface of the sample is not eroding and C) that the sample has maintained a constant geometry during irradiation. Lal (1991) laid the theoretical foundation and modern methodology for surface exposure studies. The concentration of a TCN varying over time being expressed in the relationship:

$$\frac{\partial N}{\partial t} = P_o e^{-\Lambda_x} - \varepsilon \frac{\partial N}{\partial x} - \lambda N \tag{2.1}$$

Where N is the number of atoms, t is time, P_0 is the TCN production rate at the surface of the sample, x is depth of the sample below the surface and Λ is the attenuation length (g cm^{-2}) for spallation reactions. The last two terms describe nuclide losses by radioactive decay *via* a decay constant (λ) and *via* erosion (ε) at the rock surface. For surface samples (*i.e.* x=0) and assuming no initial or inherited TCN concentration from prior exposure, then the solution to Equation 2.1 becomes:

$$N(t) = \frac{P_o}{\lambda + \rho\varepsilon/\Lambda}[1 - e^{-t(\lambda + \rho\varepsilon/\Lambda)}] \tag{2.2}$$

Where $N_{(t)}$ is number of TCN atoms at time t and ρ is the density of the sample material. Various factors to correct for topographic horizon (Section 2.1.4.3) and surface slope can now be included to correct a site specific production rate. In addition, a correction factor that integrates the cosmic ray flux over the sample thickness (Section 2.1.4.4) can also be included. Furthermore, by assuming that the rate of erosion (ε) is negligible over the time scale in question, as often is the case in Antarctica (Section 2.2.4), Equation 2.2 can be further simplified to:

$$N(t) = \frac{P}{\lambda}(1 - e^{-\lambda t}) \tag{2.3}$$

Once again, the variable P, is the effective sample specific production rate corrected for the various effects listed above. This simplified relationship between TCN concentration (N) and time of exposure (t) for the given ^{10}Be and ^{26}Al radioactive decay constants (λ) is shown in Figure 2.2.

As is expected, aluminium shows a far higher concentration than beryllium but shares a similar shaped inverse exponential curve, which are asymptomatic to the saturation (or equilibrium) values when t is greater than five or six half-lives (*i.e.* over the multi-million time scale). At ≈5-10 Ma, both nuclides show negligible increase in measurable concentration. At this equilibrium condition, production of new radionuclides is balanced by radioactive decay. If t is considerably greater than $1/\lambda$ then saturation occurs. Thus, the measured TCN concentration is controlled by the erosion rate such that from Equation 2.2 we get:

$$N_{equilibrium} = \frac{P}{(\lambda + \rho\epsilon/\Lambda)} \tag{2.4}$$

Hence for surfaces at steady-state that are undergoing erosion, the use of a TCN can determine the long term average erosion rate.

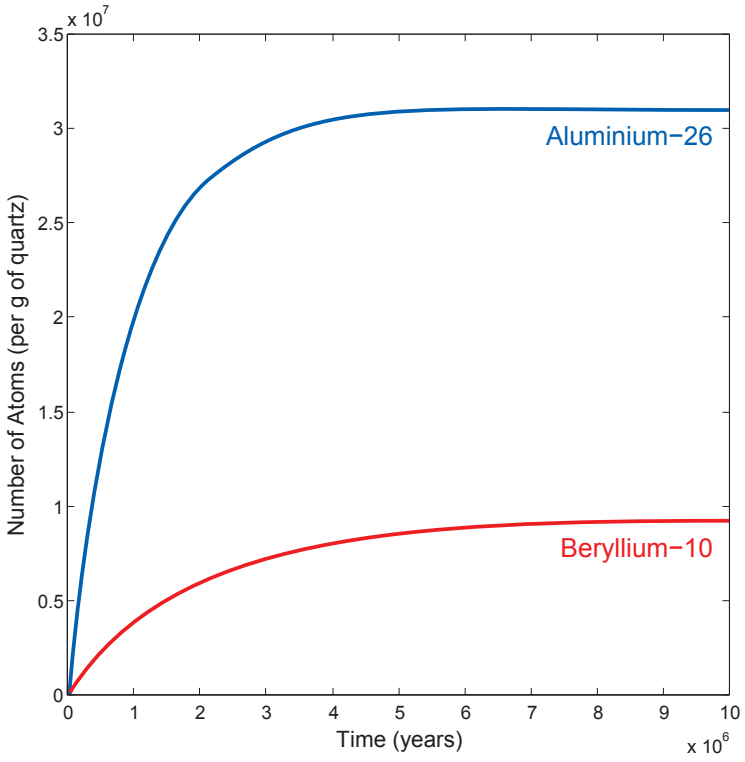

Figure 2.2: Theoretical accumulation of ^{10}Be and ^{26}Al - Using Equation 2.3, the SLHL values from Table 2.1 and assuming a situation with no erosion and a zero thickness sample.

2.1.2.1 The dual-nuclide approach

One of the assumptions made in the use of SED is that a sample has had a continuous exposure to cosmic rays since its emplacement. Unfortunately in high alpine and polar glacial settings, this is not always the case. In some cases, samples may have had undergone initial exposure, followed by a period of burial where production is halted for prolonged periods and finally a third stage of re-exposure (*i.e.* through reworking into younger glacial deposits or exhumation due to erosional processes). This three component exposure history is difficult to solve using a single TCN. To identify samples in which periods of partial or complete burial may have occurred (Section 2.2), a combination of TCNs with differing half-lives may be used. While exotic pairings such as ^{14}C/^{10}Be (White et al., 2011) or ^{10}Be/^{36}Cl (Phillips et al., 1997) can be used depending on the required application, the most commonly used dual-nuclides are ^{26}Al/^{10}Be (Gosse and Phillips, 2001). By plotting the ratio between two TCNs over time, total exposure and minimum burial times can be estimated. For the case of samples collected when buried (*i.e.* in caves or in depth profile studies) the solution assumes continuous exposure and then burial. However if the sample is collected today on the surface, this modelling is insufficient to allow a reliable estimate of the most recent exposure. The ratio between TCNs n and m as a function of time is given by:

$$R_{mn}(t) = \frac{N_m(t)}{N_n(t)} = \frac{P_m(0)(\lambda_n + \varepsilon/\Lambda_{f,e})(1 - exp[1 - exp(-\lambda_m + \varepsilon/\Lambda_{f,e})t])}{P_n(0)(\lambda_m + \varepsilon/\Lambda_{f,e})(1 - exp[1 - exp(-\lambda_n + \varepsilon/\Lambda_{f,e})t])} \quad (2.5)$$

Where N is the number of atoms of nuclide m or n at time t, P is the production rate, λ is the decay constant, Λ the attenuation length and ε is erosion. Note that as only production rates and half-lives differ, the two nuclides must have some significant difference between the two parameters. Therefore the use of stable noble gas nuclides (*i.e.* ^{3}He and ^{21}Ne) do not meet this requirement (Gosse and Phillips, 2001).

As ^{10}Be and ^{26}Al have significantly different half-lives (1.31 *vs* 0.71 Ma), Lal and Arnold (1985) proposed their use as paired nuclides. Additionally, during sample processing they can be separated in tandem from the same target mineral (quartz). Results are presented on a dual-nuclide plot (also known informally as a 'banana

plot') in which the ^{26}Al/^{10}Be ratio is plotted against ^{10}Be concentration (normalised to SLHL). Figure 2.3 shows the initial exposure line based on Equation 2.5 and assuming zero erosion. Simultaneously as ^{10}Be and ^{26}Al concentrations increase, each TCN inventory reaches equilibrium. ^{26}Al with a shorter half-life ($t_{1/2}$=0.7 Ma) reaching equilibrium first. This means with time, the ^{10}Be concentration continues to increase, whilst ^{26}Al is at saturation. This causes the ^{26}Al/^{10}Be ratio to decrease from its initial value of 6.7, which is defined by:

$$P_{Initial-ratio} = (P_{Al} * \Lambda_{Be})/(P_{Be} * \Lambda_{Al}) = \frac{P_{Al}}{P_{Be}} \tag{2.6}$$

To a value of:

$$P_{Final-ratio} = (P_{Al} * \Lambda_{Be})/(P_{Be} * \Lambda_{Al}) = \approx 3.4 \tag{2.7}$$

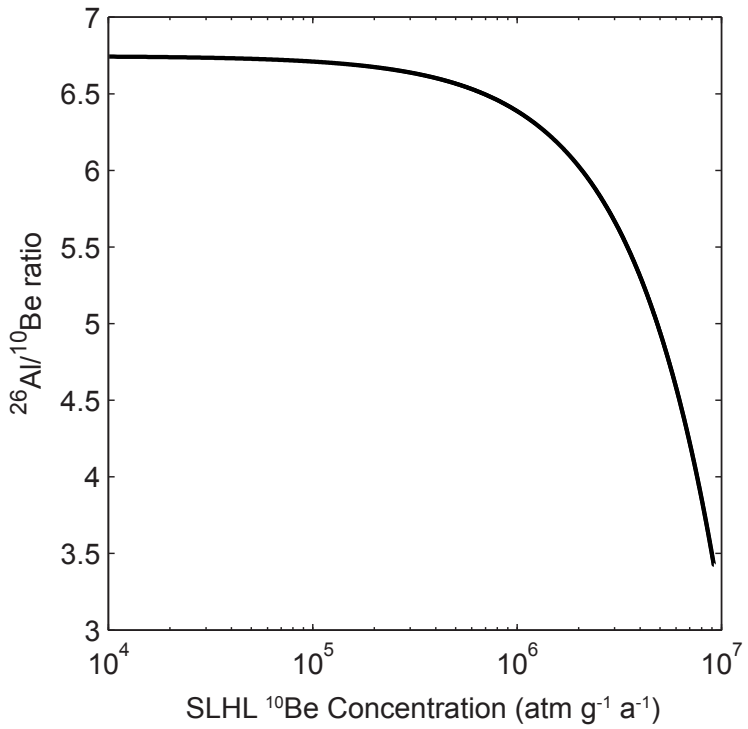

Figure 2.3: Theoretical ^{26}Al/^{10}Be ratios for a non-eroding sample - In a sample undergoing no erosion and a continuous exposure. Increasing ^{10}Be concentrations on the x axis can be thought of as an increase in time, With younger samples plotting on the exposure line to the left and older samples to the right.

At a SLHL ^{10}Be concentration of approximately 2x10^{7} atm g^{-1}, the sample is considered saturated, with nuclide production being offset by radioactive decay and any further changes in ratio virtually undetectable. For samples with a continuous exposure, but non-zero and constant erosion rate, the loss of ^{10}Be *via* erosion will cause saturation to occur at a lower ^{10}Be concentration and higher ^{26}Al/^{10}Be ratio. Exposure lines for a series of stable erosion rates (0.1, 0.2, 1, 2 and 5 mm ka^{-1}) are shown in Figure 2.4A. The banana shaped area that encompasses the exposure lines of these varying erosion rates as known as the 'steady-state erosion island'. The work of Lal (1991) and Nishiizumi et al. (1991) defined a number of areas in which a plotted sample could fall and their interpretation (Figure 2.4B).

1. Above the non-eroding exposure line. This area is known as the 'forbidden zone' as samples having ^{26}Al/^{10}Be ratios higher than this line are theoretically impossible. They cannot be explained by any combination of erosion, burial, exposure or inheritance and are likely due to problems in sample preparation and AMS measurement.

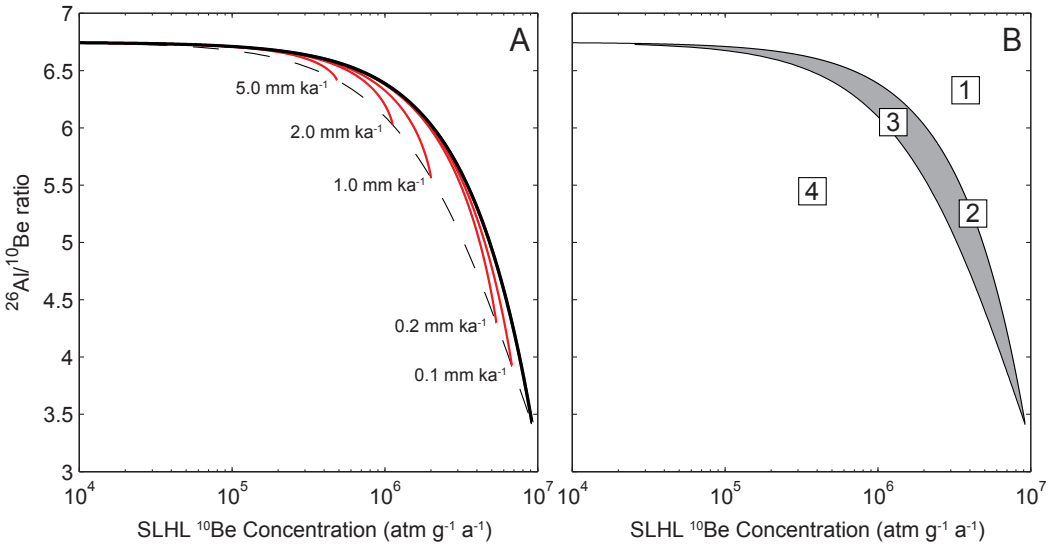

Figure 2.4: Theoretical ^{26}Al/^{10}Be ratios for an eroding sample - (A) In a sample undergoing stable erosion at different rates and a continuous exposure. (B) The area that bounds the end points of these erosion lines is known as the 'steady-state erosion island'. The numbers (1-4) refer to the four areas where samples of differing exposure histories can plot (see text).

2. On the non-eroding exposure line. These samples are highly unlikely to have undergone burial, erosion or inheritance.

3. Within the steady-state island. These samples reflect some combination of erosion and exposure, but not burial.

4. Beneath the steady-state island. These samples indicate some form or burial and/or periods of non-exposure.

With position #4, samples that undergo periods of burial can be isolated using a series of isochrons calculated for various burial ages (Figure 2.5). If a sample undergoes complete or partial burial (or shielding) the TCN with the lowest half-life will decay faster. This results in an anomalous offset in their ratio and plot beneath and to the left of their 'true' exposure position.

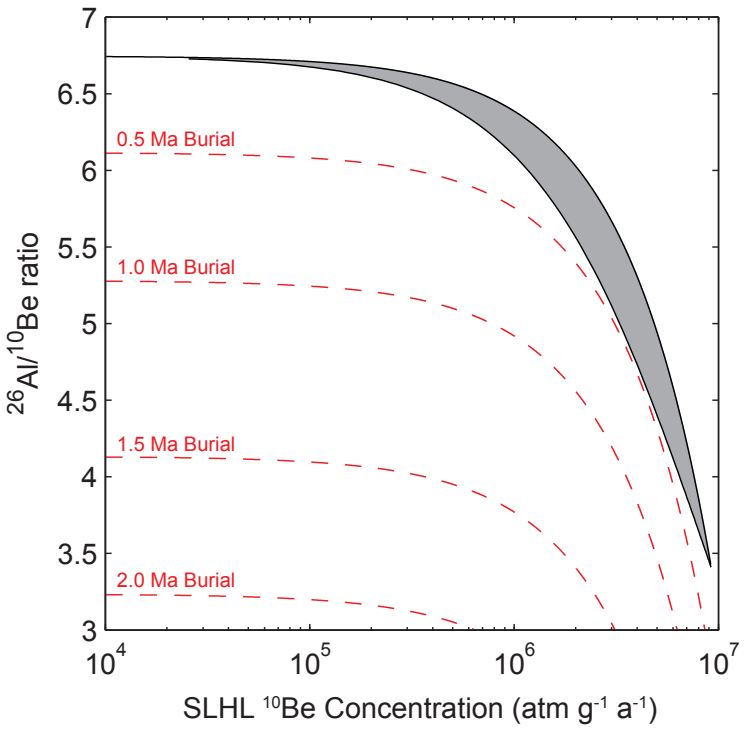

Figure 2.5: Theoretical ^{26}Al/^{10}Be burial isochrons - Samples undergoing periods of burial or shielding (>200 ka) would plot beneath the steady state island and line up with isocrons representing the total duration of burial.

Although ^{10}Be-^{26}Al is one of the most common TCN pairings used in determining total burial time via , its requires the understanding of a number of *caveats*:

1. The plots do not show how the sample arrived in that position. Only the total exposure and burial time of a sample can be estimated.

2. ^{26}Al/^{10}Be ratios can only identify samples having a burial signature of >200 ka which is determined by the analytical error in AMS measurement. This is an important point as burial time is twice as long as a Quaternary glacial cycle.

3. For samples displaying a unequivocal burial signal, exposure ages must be considered *apparent*. This is due to the true TCN concentration (*i.e.* produced during exposure) being reduced by radioactive decay during periods of burial.

4. The difficulty in obtaining high precision ^{26}Al AMS measurements. This is compounded by the relative low natural abundance of ^{26}Al and high concentrations of ^{27}Al and ^{26}Mg (an isomer of ^{26}Al) in sample material. Large ^{26}Al/^{10}Be ratio errors may make it hard to accurate identify whether a sample falls within the steady-state erosion island or below it.

For those samples collected on the surface, but have had prior episodes of burial, a third independent record is required to determine how the full exposure period is divided between pre and post-burial. To compensate for these shortfalls a number of additional techniques are being developed. For example, the work of Li et al. (2008) attempted to use stable isotope climate records (*i.e.* marine sediment and ice cores) as a constraint to model periods of final bedrock exposure after burial by ice sheets. By estimating periods of burial and exposure based on proxy records and comparing them to the ^{26}Al/^{10}Be ratio of a sample, a modelled trajectory is created. To address the limitation of the ^{26}Al/^{10}Be burial method being sensitive to only prolonged periods of burial (*i.e.* >200 ka), a different TCN with a much short half-life is required. The use of *insitu* ^{14}C ($t_{1/2}$ = 5.730 ka) is increasingly being used on LGM aged samples to identify shorter periods of burial and check

if the measured ^{10}Be concentration includes an inherited signal from a previous exposure (Briner et al., 2012; White et al., 2010).
Given the problems that can affect exposure age interpretation in glacial and polar environments (Section 2.2), the dual-nuclide approach is another tool that allows the identification of samples that have undergone periods of burial, or modification. A more subtle case is if the sample has undergone prior exposure without any burial and thus the measured concentrations will include an inheritance signal. In this scenario, both the ^{10}Be age and the ^{26}Al age will appear as self-consistent and show a normal exposure history. In a mixed population of material from both supraglacial (*i.e.* a prior exposure) and subglacial (*i.e.* eroded from beneath the glacier with no prior exposure history) material, if sufficient samples have been collected, the cumulative age of supraglacial material will most likely be higher than the average age of the subglacial material. In this scenario, a ^{14}C *insitu* measurement for the latter will verify the presence of inheritance in the former.

2.1.3 Antarctic TCN production rates

Key to the correct calculation of exposure ages from TCN concentrations is knowing accurately the cosmogenic production rates. Considering that ^{10}Be is predominantly produced by a single reaction pathway (nucleonic spallation), a wide range of production rate values have been used in Antarctica. Clark et al. (1995) used a value of 4.74, while (Brown et al., 1991) a value of 6.03 atoms per gram of quartz per year (atm g^{-1} a^{-1}). A value based on the early work of Nishiizumi et al. (1989).

The wide range in early production rate values can be explained by a number of factors:

1. Shielding by snow or ice (Section 2.2.2).
2. Temporal variations in geomagnetic paleointensity (see Gosse and Phillips, 2001 for a review).
3. Revised radiocarbon chronologies used to calibrate TCN production rates.

4. An overestimation of the muon contribution.

It has been recognized that #4 has been the primary cause in overestimating production rates, Brown et al. (1995) showed that the muon contribution was far less than previously thought and accordingly reduced it from 15 to 3%. Additionally the work of Stone (1999) identified discrepancies between various production rates at differing elevations. By normalising scaled production rates from a number of global sites, combined with the new muon contribution of 3%, the SLHL ^{10}Be production rate (for muon+spallation reactions) was revised downwards to 5.1 $\pm$ 0.3 atm g^{-1} a^{-1}. Stone (2000) also noted the variation between Antarctic and non-Antarctic production rates, publishing a new scaling scheme to account for the permanent low pressure system that surrounds Antarctica and other high latitude sites (Section 2.1.4.2). Questions about the original ^{10}Be half-life of 1.5 Ma (Fink and Smith, 2007; Nishiizumi et al., 2007) has led to a large improvement in increasing the reliability of both the accepted ^{10}Be half-life and ^{10}Be/^{9}Be ratio of AMS standard reference materials (SRMs). A recent revision by Nishiizumi et al. (2007) of the ^{10}Be/^{9}Be ratio in AMS SRMs has led to a 1.106 $\pm$ 0.012 reduction in the accepted nominal ratios. When this downward correction is applied to the ^{10}Be/^{9}Be value for the NIST-4325 SRM used at ANSTO, the revised ^{10}Be/^{9}Be ratio becomes 27900 $\pm$ 300 x 10^{-15}. This in turn reduces the 5.1 production rate of Stone (2000) to a value of 4.60 $\pm$ 0.42 atm g^{-1} a^{-1}. Currently this value is the best estimate for Antarctic production rates and is the value used in ^{10}Be calculations within this thesis.

More recently, a New Zealand ^{10}Be spallation production rate of 3.88 $\pm$ 0.1 atm g^{-1} a^{-1} has been suggested by Putnam et al. (2010). This value is significantly lower, 33%, than the value of Stone (1999). Due to questions about the applicability of the new NZ value in the Antarctic, nearly all works dealing with SED in Antarctica have used a SLHL production rate of 5.1 (pre AMS SRM change) or now 4.6 (Ackert et al., 2011; Fogwill et al., 2012; Lilly et al., 2010; White et al., 2010; Yamane et al., 2011). Studies on the production rate of ^{26}Al are closely linked with those of ^{10}Be, primarily due to the similarity in sample preparation and the ability to measure both nuclides in a single sample. Nishiizumi et al. (1989) measured the ^{26}Al/^{10}Be

production rate ratio at ≈6.0-6.1, although others have measured it as high as 6.1-6.5 (Kubik et al., 1998; Shulmeister et al., 2005). The PRIME-Z93-0221 SRM used at the ANSTO AMS facility has a nominal $^{26}Al/^{27}Al$ ratio of 16800 x10^{-15}. Currently the ^{26}Al production rate is set as 6.67 times the ^{10}Be production rate (Balco et al., 2008) this results in a ^{26}Al production rate of 30.7 $\pm$ 2.8 atm g^{-1} a^{-1} based on the Stone (2000) scaling. Both the quoted ^{10}Be and ^{26}Al total production rates include a 2.5% muon contribution at SLHL and are assigned errors of 10%. The muon production rate is scaled for elevation according to the methods described in Stone (2000).

2.1.4 Site specific scaling

To determine the TCN production rate at a sampling site, scaling factors must be applied to convert a nominal production rate at one chosen geographic location to the elevation and latitude of where the same is located. These scaling factors are used because of spatial variability in the local secondary GCR flux. This flux can vary from site to site based on cosmic ray shielding by the Earth's magnetic field (latitude) and the attenuation of GCR by the atmosphere (altitude). The location, to which all production rates are referenced to is sea level high latitude (>60°N and S at 0 masl). Dunai (2010) defines scaling as "..*a description of the influence of the Earth's and Sun's magnetic fields, and atmospheric mass on cosmogenic nuclide production rates*." The combination of a scaling factor and a calibrated SLHL nuclide production rate (PR_{SLHL} = 4.6 atm g^{-1} a^{-1}) allows the formulation of a local site-specific production rate. For example, a Stone (2000) scaling of 0.9622 for Christchurch New Zealand (43°S), gives a local production rate of 4.4 atm g^{-1} a^{-1} at sea level. These corrections are incorporated into a variety of differing scaling schemes (Desilets et al., 2006; Dunai, 2000, 2001; Lal, 1991; Lifton et al., 2005, 2008) which then require a number of additional sample specific corrections (Sections 2.1.4.3 & 2.1.4.4).

The scaling scheme used in this thesis is that of Lal (1991) with the later Antarctic corrections (for air pressure-elevation conversions) from Stone (2000). While this scaling scheme uses a relatively simple dipole approximation of geomagnetic field and may be less comprehensive or detailed as other scaling schemes, it is

sufficiently accurate for calculating Antarctic exposure ages in this thesis. In all scaling schemes the primary factors affecting site specific GCR flux and thus TCN production, are altitude and latitude.

2.1.4.1 Altitudinal variations

The path of secondary cosmic rays through the atmosphere is attenuated by interactions with the constituent atoms and hence, the magnitude of attenuation is related to the atmospheric density. Therefore as air pressure drops, so does attenuation leading to a rise of 1% in TCN production rates with every 10 metres of elevation gain (Lal, 1991). Scaling correction factors to compensate for this phenomenon are typically based on elevations above sea level to simplify SED. The scheme of Lal (1991) incorporates barometric pressure as a control on GCR intensity, with a conversion from altitude (in masl) to barometric pressure, using the standard atmosphere model of Lide (1999).

$$p(z) = P_s \exp\left\{ -\frac{gM}{R\zeta}[\ln T_s - \ln(T_s - \zeta z)] \right\} \tag{2.8}$$

Where P_s is atmospheric pressure at sea level (1013.25 hPa), g is gravitational acceleration, M the molar mass of air, R the gas constant, ζ an adiabatic lapse rate (0.0065° K m^{-1}) and T_s is the global average sea level temperature (288.15° K). But due to variability in global air pressures, the relationship between barometric pressure and altitude is not linear. In the Antarctic, sea level air pressures are 2-3% lower than the average atmospheric value at a range of altitudes (Figure 2.6). The permanent low pressure system (the mean Antarctic sea level pressure is 989 $\pm$ 5 hPa) caused by airflow across the ice sheets and a persistent temperature inversion layer makes the assumptions of the hydrostatic model of Lide (1999) invalid.

Radok et al. (1996) derived a modified altitude pressure relationship that incorporated temperature gradients across the inversion layer and used a mean sea level temperature of 250° K, 38° K lower than that normally used at lower latitudes. This was simplified by Stone (2000) to calculate $P_{Ant}(z)$, the Antarctic air pressure at a

given altitude z in metres (Equation 2.9):

$$p_{Ant}(z) = 989.1 \exp\left\{ - \frac{z}{7588} \right\} \tag{2.9}$$

This model fits well in a variety of Antarctic terrain, such as ice shelf and TAM sites up to 3200 masl. Stone (2000) also demonstrated the strength of the relationship by validation against 67 sites producing an RMS error of $\pm$3.0 hPa. The use of this method makes a number of assumptions:

- That the air pressures observed in the modern meteorological Antarctic record have been stable over the period of the calculated exposure age.
- That tectonic uplift and/or glacio-isostatic adjustment have not played a role in altering the elevation of a location over time (Section 2.2.3).

Stone (2000) also noted that due to a complex interplay between the two, the individual contributions might be hard to separate. Thus, to reduce their influence on exposure ages, a local calibrated production rate may be needed. All samples collected in this thesis, had altitudes measured by GPS ($\pm$10 m vertical accuracy) and where necessary measurements were crossed checked against digital elevation models (DEMs). Altitudes were subsequently converted to air pressures (hPa) *via* Equation 2.9.

2.1.4.2 Latitudinal variations

Of the most widely used scaling factors, that of Lal (1991), uses geographic coordinates, altitude and latitude to describe global variations in GCR flux. This assumes that the Earth's geomagnetic field is a simple dipole. Changes in the geomagnetic dipole intensity cause a variation with latitude of nuclear disintegrations within the atmosphere. High latitude sites (>60°) with near vertical geomagnetic field lines show little effect, while equatorial sites show a strong decrease. Lal (1991) demonstrated that low latitude sites (0-10°) can show a 14-74% decrease in nuclear disintegration rates with a 25-200% increase in dipole intensity. Additionally, as the geomagnetic field has shown significant changes in the last 800 ka (Guyodo and Valet, 1999), this temporal variability can have a significant impact on GCR flux.

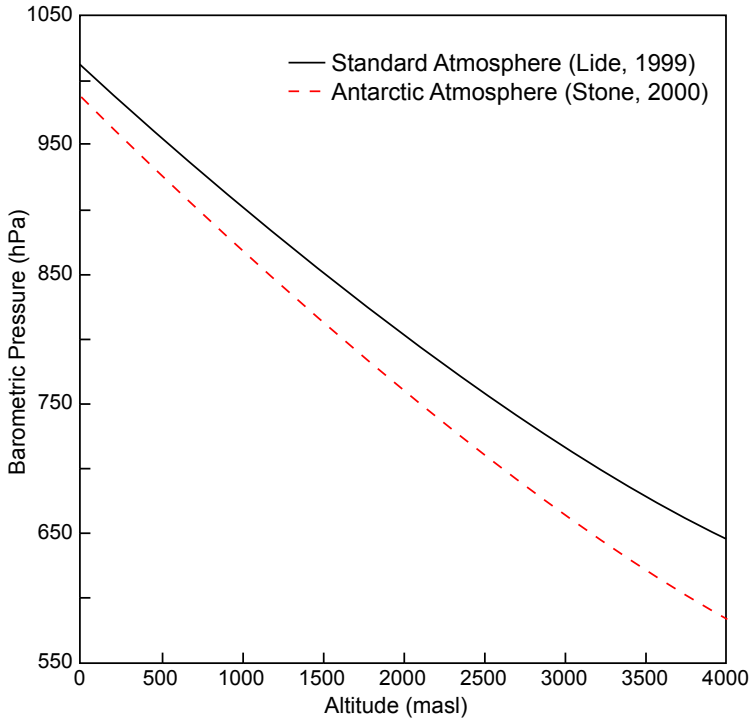

Figure 2.6: Air pressure-altitude relationship - Using the standard atmosphere models of Lide (1999)(Equation 2.8) and that of the Antarctic model of Stone (2000)(Equation 2.9).

Dunai (2001) showed that production rates increased by 17% at the equator over 50 ka due to the recorded geomagnetic field change as given by Guyodo and Valet (1999) (Figure 2.7). Due to this problem, a number of recent scaling schemes have incorporated time-variable scaling factors to account for paleo-magnetic variations (Desilets et al., 2006; Dunai, 2001; Lifton et al., 2005). The use of the Lal (1991) or Stone (2000) scaling schemes in high latitude sites are little effected by paleo-magnetic variations and thus would show negligible impacts to production rates. Hence in this thesis, corrections for paleo-magnetic dipole variations were deemed to be insignificant and not applied.

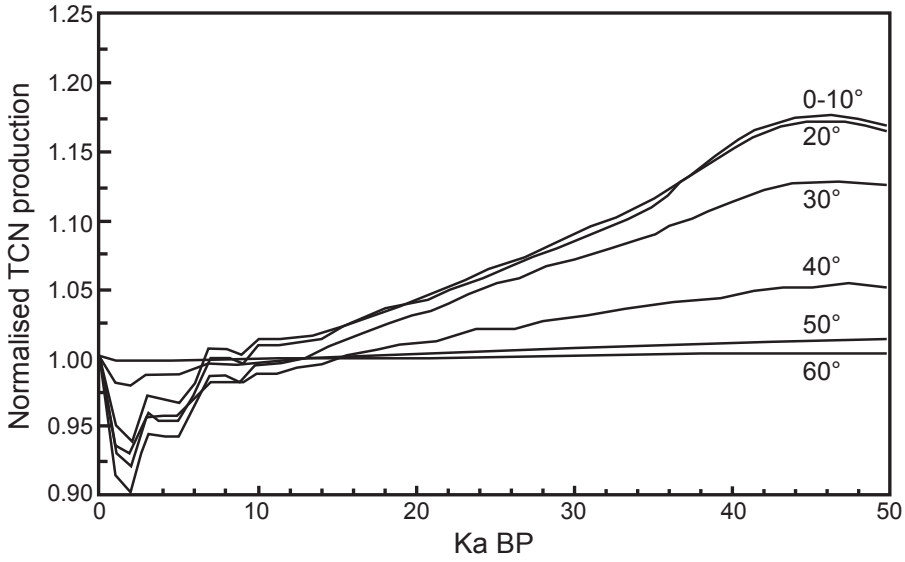

Figure 2.7: Temporal and spatial variability of production rates - Over the last 50 ka caused by changes in the geomagnetic field. Uses the scaling scheme of Dunai (2001) and the SINT-800 geomagnetic record of Guyodo and Valet (1999). Figure from Dunai (2001).

As previously shown, (Stone, 2000) replaced the altitude component of Lal (1991) using mean annual atmospheric pressure (Equation 2.9) thus producing a series of coefficients that are latitude dependant (Table 2.2). These coefficients can be used in a series of equations to calculate SLHL scaling for spallation (Equation 2.10) and muon (Equation 2.12) components from -20 to 6000 metres in altitude (1040-490 hPa).

$$S_\lambda(P) = a + b\exp[-P/150] + cP + dP^2 + eP^3 \tag{2.10}$$

Where $S_\lambda(P)$ is the spallation scaling factor, a, b, c, d, e are latitude dependant coefficients from Table 2.2 and P is air pressure from Equation 2.9.

$$M_\lambda(P) = M_{\lambda,1013.25}\exp\left[\frac{1013.25 - P}{242}\right] \tag{2.11}$$

Where S_λ and M_λ are the calculated spallation and muon contributions (Equation 2.10 & 2.12) and f_{sp} is the fraction of spallogenic production at sea level. Initial f_{sp} values for the muon production of ^{10}Be and ^{26}Al were estimated to be 0.844 and 0.826 respectively, incorporated into the scaling algorithms of Lal (1991). More

recently there have been a number of re-evaluations of the contributions of surface muons to total productions at SLHL. Lower values and thus lower muon capture contributions of 2-3% were first suggested for ^{10}Be based on deep depth profiles in bedrock (Brown et al., 1995). Stone (2000) suggested the use of 0.974 (^{10}Be) and 0.978 (^{26}Al) in his scaling scheme; these values have been used for SLHL muon production rate calculations and scaled appropriately for elevation to our sampling sites in this thesis. $M_\lambda(P)$ is the muon scaling factor, P is air pressure, 1013.25 is the standard sea level air pressure and 242 is the atmospheric muon attenuation factor from Rossi (1952), both values are in hPa. As most TCNs are produced by a mixture of spallation and muon capture, the final scaling of Stone (2000) for the production rate of isotope is given as:

$$F_\lambda(P) = f_{sp}S_\lambda(P) + (1 - f_{sp})M_\lambda(P) \tag{2.12}$$

The combination of altitude (*i.e.* air pressure) and latitude effects on the intensity of GCR and thus production rates is shown in Figure 2.8. High elevation and latitude sites show significantly higher scaling factors that other low elevation/latitude sites. Therefore, given that sample sites in the Transantarctic Mountains are at elevations over 2000 masl, TCN production will be enhanced by factors of ≈5. A benefit for younger Holocene samples where measured TCN concentrations will be low.

Table 2.2: Scaling equation coefficients - From Stone (2000).

Latitude λ	a	b	c	d	e	$M_{lat1013.25}$
0	31.8518	250.3193	-0.083393	7.4260x10^{-5}	-2.2397x10^{-8}	0.587
10	34.3699	258.4759	-0.089807	7.9457x10^{-5}	-2.3697x10^{-8}	0.600
20	40.3153	308.9894	-0.106248	9.4508x10^{-5}	-2.8234x10^{-8}	0.678
30	42.0983	512.6857	-0.120551	1.1752x10^{-4}	-3.8809x10^{-8}	0.833
40	56.7733	649.1343	-0.160859	1.5463x10^{-4}	-5.0330x10^{-8}	0.933
50	69.0720	832.4566	-0.199252	1.9391x10^{-4}	-6.3653x10^{-8}	1.000
$\leq$ **60**	71.8733	863.1927	-0.207069	2.0127x10^{-4}	-6.6043x10^{-8}	1.000

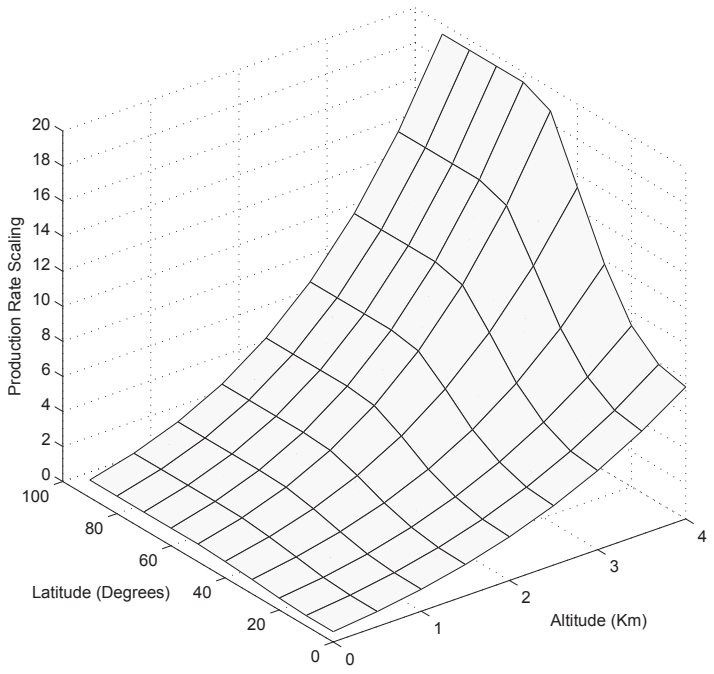

Figure 2.8: Latitude and altitude effects on production rates - X axis is latitude (0-90°), Z axis is elevation (Km above sea level) and the Y axis is the scaling factor of Stone (2000).

2.1.4.3 Topographic shielding

Calibration values of SLHL production rates are defined under conditions of maximum GCR flux that can be received on a horizontal sample surface. Hence, any object thick enough to block cosmic rays (*i.e.* obstruct a view of the sky), will correspondingly reduce the GCR flux and thus affect production rates. To account for this, the geometry of the viewable horizon must be calculated as a correction per sample site. As the bulk of GCR flux is predominantly be in the vertical axis due to the strong falloff of cosmic ray trajectory with increasing angle from vertical, the necessary corrections are usually small (>0.95) unless extreme topographies are encountered such as narrow canyon floors and cliff faces. For example, a sample shielded by an obstruction of 30° elevation for a full 360° rotation would have a correction factor of $\approx$0.95.

Dunne et al. (1999) calculated the total GCR flux received by a horizontally flat sample surface with a complete view of the sky as:

$$F_{Tot} = \int_{\phi=0}^{2\pi} \int_{\theta=0}^{\pi/2} I_0 sin^m(\theta) cos(\theta) d\theta d\phi \tag{2.13}$$

Where I_0 is the GCR intensity, ϕ is azimuth from the vertical direction, θ is elevation from the horizontal and m is an experimentally derived constant (typically m=2.3, Nishiizumi et al. 1989). Integrating Equation 2.13 gives:

$$F_{Max} = \frac{2\pi I_0}{m+1} \tag{2.14}$$

Where F_{Max} is the maximum GCR flux received by an object with an unshielded exposure. For a rectangular shaped obstruction, of height sin (θ_0) and width ($\Delta\phi$), the amount of shielded GCR can be calculated by:

$$F_{Shield} = F_{\theta_0 \Delta\phi} = \frac{\Delta\phi I_0}{m+1} sin^{m+1}(\theta_0) \tag{2.15}$$

Thus to account for obstructed GCR, a topographic shielding factor (C_T) can be calculated as the ratio of the remaining GCR flux ($F_{Max} - F_{Shield}$) against the maximum flux (F_{Max}). For n rectangular obstructions:

$$C_T = 1 - \frac{1}{2\pi} \sum_{i=1}^{n} \Delta\phi sin^{m+1}(\theta_i) \tag{2.16}$$

Equation 2.16 is generally considered to be applicable to *insitu* flat lying samples in situations where azimuth and elevations of the horizon can be measured in the field. While software based tools for the calculation of topographic shielding have been suggested (Codilean, 2006) and implemented in major geographic information systems (*r.horizon* in GRASS and solar radiation graphics in ArcGIS), the simplest method is that of Balco et al. (2008).

By estimating the approximate topography of the 360° horizon using breakpoints (Figure 2.9A), the CRONUS-Earth website (http://hess.ess.washington.edu) can calculate topographic shielding using two paired input vectors, such that each input pair is the azimuth and inclination of a given break point (Figure 2.9B). Topographic

corrections used in this thesis (Tables A.1, A.4, A.5, A.10, A.13 & A.14) were calculated in this way. Major horizon breakpoints were measured in the field using a Suunto compass and clinometer to an accuracy of $\pm 0.5^{\circ}$ for both azimuth and inclination.

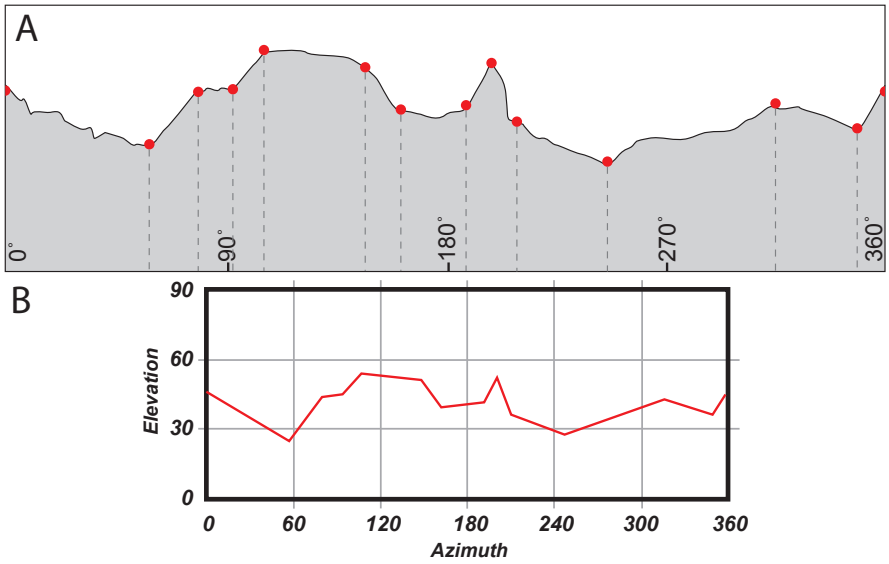

Figure 2.9: Correction for topographic shielding - (A) Simple point approximation of a 0-360° horizon. (B) CRONUS output with a shielding factor of 0.764.

2.1.4.4 Sample thickness corrections

The simplified production rate formula (Equation 2.3) assumes a sample thickness of zero, therefore a correction for the actual physical sample thickness must be applied. As the bottom sections of a sample are shielded by the entire mass of the sample, the upper sections in turn are shielded less (Figure 2.10).

To correct for this internal or 'self' shielding of GCR, Equation 2.17 provides a production rate correction factor resulting from the exponential decrease in high energy neutron flux with depth below the surface (Dunne et al., 1999) and integrated over the sample thickness.

$$C_z = \frac{P_0 \int_0^z e^{(-z\rho/\Lambda)} dz}{z} \tag{2.17}$$

Where the concentration of nucleons at depth d (cm) in a sample of thickness z (cm) is calculated using the surface production rate (P_0), the attenuation coefficient (Λ, typically 150 g cm^{-2}) for spallation reactions and the density (ρ, typically 2.7 g cm^{-3}) of the sample material.

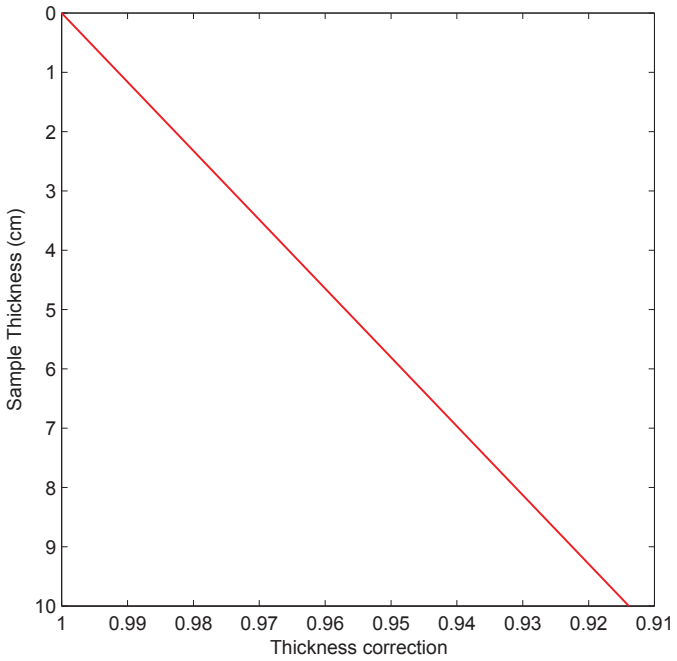

Figure 2.10: Sample thickness correction - correction to TCN production rate based on a sample density of 2.7 g cm^{-3} and a attenuation length of 150 g cm^{-2} using Equation 2.17.

2.2 Considerations with the use of SED in polar environments

While the use of TCNs in mid-latitude glacial landscapes is well proven (Balco, 2011; Fogwill and Kubik, 2005; Putnam et al., 2010; Shulmeister et al., 2005), polar glacial environments require additional considerations. With the use of the technique in these environments becoming increasing popular, understanding the influence of geomorphic and glaciological processes is essential to correctly interpret results. Erosion rates, unknown provenance of glacial material and preservation of prior exposure histories all play significant roles in affecting TCN con-

centrations and thus calculated exposure ages. In addition, cold-based glaciers can advance and retreat over landscapes without significant erosion or deposition creating episodes of partial, or complete burial (Atkins, 2013; Atkins et al., 2002; Bockheim, 2010). By considering the effect of these processes, a robust methodology for sample selection can be tailored for the polar regions.

2.2.1 Nuclide inheritance

The use of TCNs as a geochronological tool relies on a number of assumptions in order to calculate an exposure age from AMS radionuclide concentrations (Tuniz et al., 1998); primarily that samples from a single landform have:

- A zero-exposure history prior to deposition.
- A negligible, or independently well determined, erosion rate.
- Have not been altered by post depositional geomorphic or glaciological processes. *i.e.* altering the surface orientation and/or covering with sediment, snow and ice post-deposition.

In the Antarctic, these assumptions are often invalid. The probability of glacial material having a simple exposure history is often not sufficiently high enough to maximise their occurrence while collecting samples (*i.e.* give a exposure age directly related to the mean deposition age of the land form). As the majority of samples show some degree of prior exposure, a number of additional pathways must exist for older (or pre-exposed) material to be integrated into new deposits. The problems of sampling at the former margins of ice sheets, particularly those suspected of having poly-thermal basal conditions (*i.e.* a combination of warm and cold-based), was also recognised in the North Hemisphere ice sheets (Fabel et al., 2006; Stroeven, 2002; Stroeven et al., 2011). Therefore, knowledge of the processes that can produce a range of ages outside the true age of deposition is necessary for the correct interpretation of results. To understand the roles that pre and post depositional processes play on measured concentrations, Heyman et al. (2011) defined three conceptual models.

In the simple exposure model (Figure 2.11), the target material is initially completely shielded from cosmic rays and therefore has no pre-existing spallogenic TCN inventory. This material is then glacially plucked and deposited sub-aerially as constructional moraines and drift, at which time the production of TCNs starts to occur. As these materials undergo a common exposure history following deposition, they provide a suite of ages clustered around the true deglaciation age. Thus TCNs are only produced in the single period of exposure post-deposition.

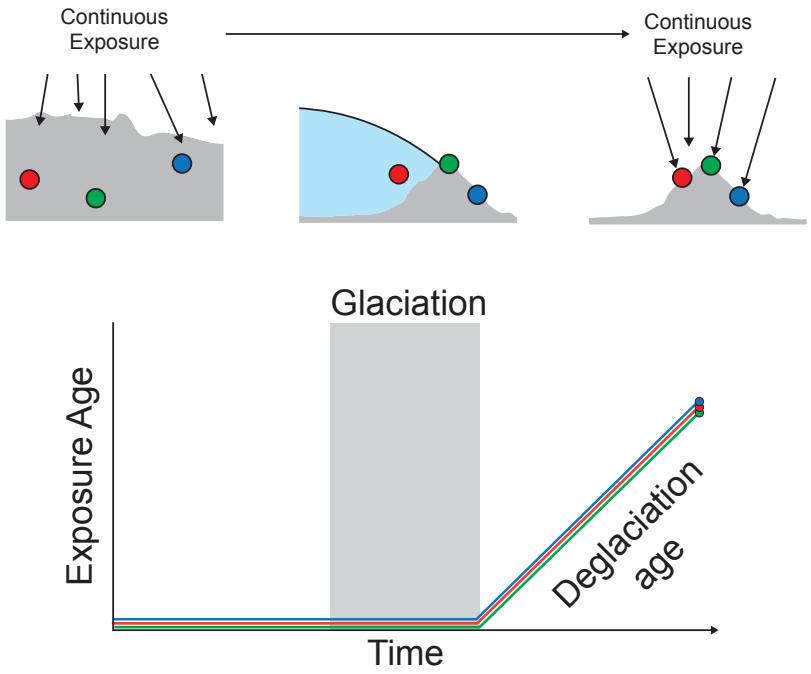

Figure 2.11: Simple cosmic ray exposure - Glacial material has no previous nuclide concentration and undergoes no post depositional processes. Adapted from Heyman et al. (2011).

The second model is the first of two scenarios in which samples have a complex exposure history (Figure 2.12). Prior to emplacement, the target material has already experienced some degree of cosmic ray exposure, likely due to exhumation from an older glacial deposit or incomplete shielding from cosmic rays prior to being sub-glacially entrained. After glacial transportation and deposition the material will continue accruing TCNs in addition to that from the original exposure period. The effect of this inheritance will be reflected in a higher measured nuclide concentration and thus an older (apparent) exposure age than expected. This prior

inheritance of nuclides is common in Antarctic SED studies, and has led to the interpretation in which the youngest sample at a given altitude is used as a minimum age. Older samples are considered as containing some form of prior TCN inventory and effectively ignored or treated as a maximum exposure age (Mackintosh et al., 2007; Stone et al., 2003).

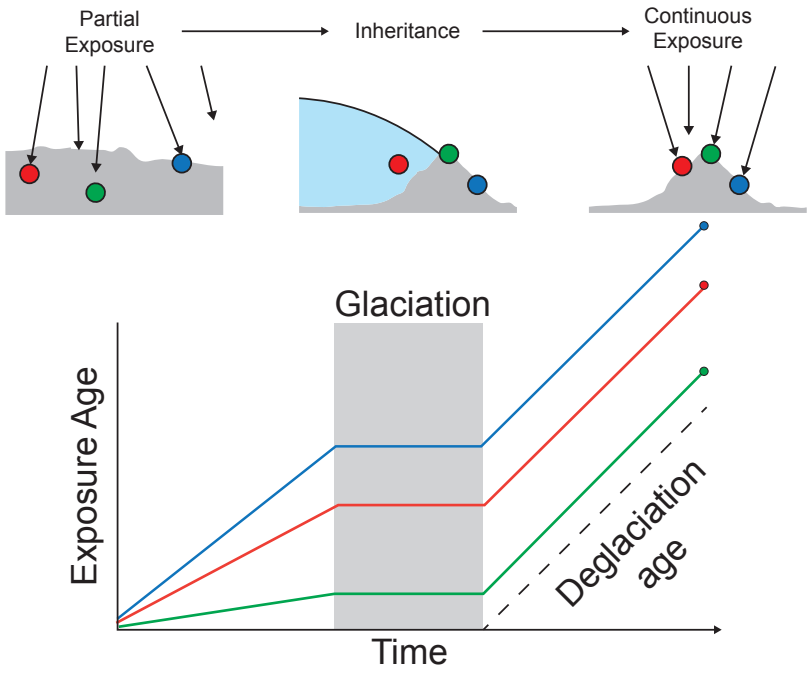

Figure 2.12: Complex cosmic ray exposure with inheritance - Glacial material has nuclide concentrations from previous exposure but undergoes no post depositional processes. Adapted from Heyman et al. (2011).

In the final model (Figure 2.13), material is completely shielded from cosmic ray irradiation prior to transport, thus having a zero exposure history at time of deposition. Where the model differs from that of a simple exposure (*i.e.* the first model described) is that TCN concentrations are modified following deposition by a variety of geomorphic surface processes. This is in contrast to the second model and leads to reduced TCN concentrations and hence the preference for a maximum age model to represent time of glacial retreat. The loss of TCNs can occur in a number of ways, all leading to a situation where exposure ages are younger than the expected value (Applegate et al., 2012).

- Erosion (either chemical or physical).
- Attenuation of cosmic rays by shielding (*i.e.* surface cover by sediment or snow).
- Attenuation of cosmic rays by reorientation of the initially exposed surface (*i.e.* by landform setting or mass movement).

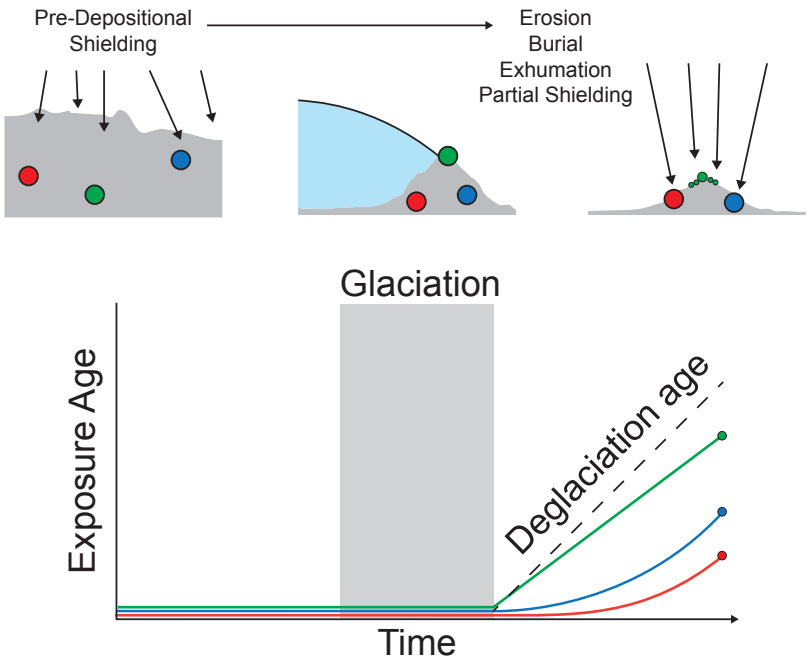

Figure 2.13: Complex cosmic ray exposure with erosion - Glacial material has no previous TCN inheritance but undergoes erosion and modification post deposition. Adapted from Heyman et al. (2011).

A variety of erosional processes can cause the loss of TCNs other than through radioactive decay. The extremely low Antarctic erosion rates (Section 2.2.4) can lead to a situation where, physical and biological weathering dominate over chemical (Hall et al., 2002). Decimetre scale spalling of parent boulders can occur *via* both freeze-thaw and biological interactions with endoliths and lichens (Budel et al., 2009; Guglielmin et al., 2011), producing clasts that have a mixture of TCN concentrations (Staiger et al., 2006). While erosion effectively removes TCN from the

surface of the target, post depositional shielding can be partial or full. If partial, exposure ages will be underestimated but production continues, albeit at an effective lower rate. If shielding is complete and production totally ceases, then radioactive decay is responsible for the loss of concentration. The result in the latter case is still an underestimate of the true age, but the ^{26}Al and ^{10}Be ages will no longer concur. In the absence of production (*i.e.* surface irradiation) ^{26}Al with its shorter half-life ($t_{1/2}$=0.7 Ma) decays faster. The result can be used to measure a burial age using a dual-nuclide plot (Section 2.1.2.1). Partial shielding typically occurs when material is buried by till, snow or ice cover (Section 2.2.2) followed by exhumation. These periods of partial or complete shielding are especially common in ice cored moraines and rock glaciers, where solifluction and mass movement processes can bury and exhume material (Briner et al., 2005). With the problem of inheritance so common in glacial environments, especially in Antarctica, the use of a two nuclide approach, such as a ^{26}Al/^{10}Be, allows the identification of samples (>200ka) affected by burial.

2.2.2 Burial by ice and water

With the possibility of ice and snow cover in polar and high alpine environments, the effect it has on shielding samples from GCR must be also be considered. In particular, cold-based ice can advance over and cover previously emplaced glacial landforms for an unknown period of time and then retreat, leaving it relatively unmodified (Atkins, 2013; Bockheim, 2010). As material density is the major factor in the attenuation of cosmic radiation, an understanding of local climate and glaciology is needed to correct for both perennial and ephemeral snow packs and ice that may have existed in the past. While the typical density of ice is approximately 0.912 g cm^{-3} at -10°C, snow is far more complicated as its density relies on a variety of meteorological surface processes (Fountain et al., 2009). Due to the spatial variability of Antarctic wind speeds and snow accumulation, a range of snow surface densities can exist on the continent; from 0.10 (Keys, 1980) to 0.38 g cm^{-3} (Kruetzmann et al., 2011; Lenaerts et al., 2012), with the upper value being more representative of windblown snow.

There are a number of methods used to calculate shielding corrections for snow, ice or sediment. All assume that the covering material is homogeneous and of uniform density throughout its depth. Only nuclear spallation reactions are considered in these corrections as muon reactions play only a minor role in the upper surfaces of rocks (density of ≈2.7 g cm^{-3}), let alone the lower densities of snow and ice. Therefore they are ignored in the calculation of these corrections (Kubik and Reuther, 2007).

When material is deposited on top of the target object, the incoming radiation is attenuated exponentially. Equation 2.17 is modified to reflect changes in production rate, not nuclide concentration.

$$P_s = P_0 e^{(-Z\rho/\Lambda)} \tag{2.18}$$

Where P_s is the production rate (atm g^{-1} a^{-1}) at the rock surface under a material thickness of Z (cm), which has a density of ρ (g cm^{-3}). P_0 is the initial production rate at the rock surface prior to material cover and Λ is the fast neutron attenuation length (g cm^{-2}) (Gosse and Phillips, 2001).

This approach assumes that the covering material has no temporal variation, and that the thickness of the cover has remained static over time. Another method integrates changes in thickness over time and is the preferred method for snow pack estimates (Gosse and Phillips, 2001). This time integrated approach can also be coupled to a local climate models or historic snow pack data, allowing the shielding correction to be calculated by paleo-climatic reconstructions (Schildgen et al., 2005).

$$s = \frac{1}{n}\sum_{i=1}^{n}(Z_b - Z_{s,i})\rho_{s,i}/\Lambda \tag{2.19}$$

Where s is the shielding correction, Z_b is the height of the sample surface (cm), n is the total period of time, Z_s is the height of the shielding at interval i, ρ is the density of the material (g cm^{-3}) and Λ is the fast neutron attenuation length (g cm^{-2}).

Figure 2.14 shows the effect of burial by different densities of snow, ice and water on a SLHL production rate of 4.6. As is expected, the most dense material (water) attenuates cosmic rays the most, with only a metre required on top of the rock

surface to reduce sample irradiation by ≈50%. Various densities of snow attenuate far less, a one metre cover reducing production rates by ≈20%.

Water coverage of bedrock is only an issue in a small number of sites in ice free areas like the MDVs (*i.e.* Miers, Taylor and Victoria valleys) where large pro-glacial lakes are suggested to have formed post-LGM (Hall et al., 2006; Hendy, 2000). But the role of cold-based glacier advances, where in some locations little to no evidence is left and the ephemeral nature of snow pack distribution are far harder to quantify. Fountain et al. (2009) measured annual precipitation rates in the MDVs ranging from 3-50 mm a^{-1} (water equivalent) and found a strong correlation between snow cover and the distance from coast. The duration of snow cover is also spatially variable, but overall sublimation/ablation far outweighs precipitation. At Lake Vida (Victoria Valley), snow lasts all winter and only a few weeks at Lake Bonney (Taylor Valley) (Fountain et al., 2009). Thus while the depth of burial by snow can theoretically play a role in the attenuation of local production rates (Figure 2.14) the limited thickness and duration of precipitation in the MDVs suggest that it is may be negligible. Given a maximum precipitation of 50 mm a^{-1} and snow lasting over winter (*i.e.* a three month period), a total yearly accumulation of 12.5 mm (water equivalent) would only affect production rates by 2-4%.

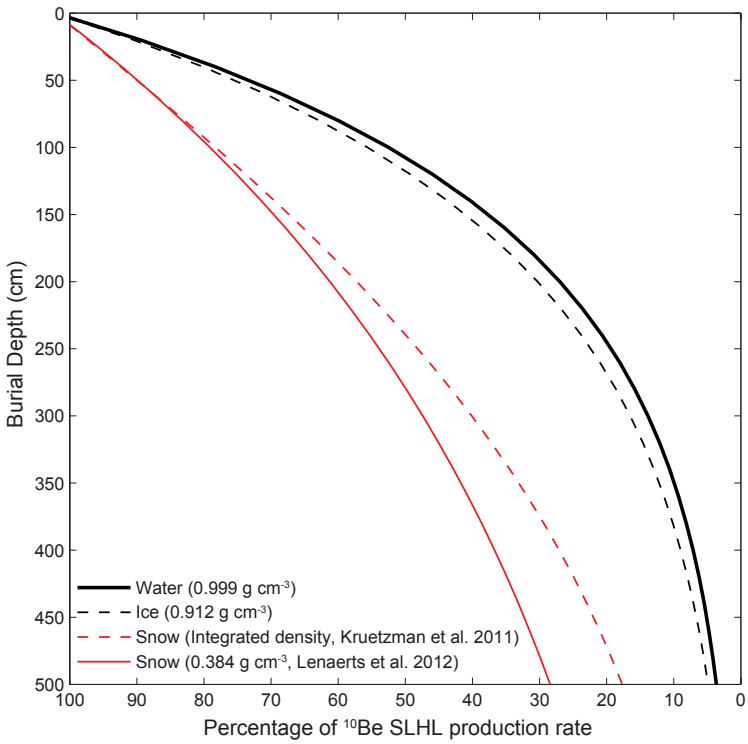

Figure 2.14: Attenuation of cosmic rays by snow and ice cover - The modelled effect of burial by water, ice and snow on a SLHL ^{10}Be production rate of 4.6 atm g^{-1} a^{-1}.

2.2.3 Changes in production rates by uplift

Given the location of the DHGS within the Transantarctic Mountains, the effect of tectonic uplift and glacio-isostatic adjustment (GIA) on both TCN production rates and the interpretation of glacial geomorphology must be considered. As a major factor in the scaling of TCN production rates, any change in the elevation of a sample will likewise affect the production of TCNs (Section 2.1.4.1). At sites where periods of past uplift are possible, the use of a constant production rate at the elevation of where the sample is found will lead to underestimates of the true age. The same goes for the use of glacial landscapes as a proxy for ice thickness. If a glacial deposit or landform is considered as the vertical limit of an ice advance, is it actually *insitu* or has it been deposited at a lower elevation and uplifted? This situation is especially pertinent for the interpretation of older deposits in stable locations, or young deposits in areas with high glacio-isostatic adjustment (GIA) rates.

The various scaling schemes (Dunai, 2001; Lal, 1991; Stone, 2000) undoubtedly show that uplift (*i.e.* a change in sample elevation) has an effect on TCN production rates. But the question must be raised, was there Quaternary uplift in this sector of the TAMs? And if so would it have a quantifiable effect on TCN production rates in collected samples. Tectonic uplift of the TAMs is believed to be sectional along the Ross Sea Embayment and while significant uplift occurred throughout the Cenozoic numerous lines of evidence suggest that the major activity of tectonic uplift had ceased by the Quaternary (Ackert and Kurz, 2004; Brook et al., 1995a; Sugden et al., 1999; Wilch et al., 1993). Superimposed on the tectonic signal is vertical elevation changes caused by GIA. The advance and retreat of late Quaternary ice sheets is responsible for an estimated several mm a^{-1} of vertical rebound (Ivins and James, 2005; James and Ivins, 1998). For the Scott Coast, Hall (2004) have published a relative sea level (RSL) curve based on radiocarbon evidence from raised beaches. The suggestion being that LGM ice retreat in the Ross Sea Embayment ($\approx$6.6 ka ^{14}C BP) has resulted in an estimated 32 metres of GIA in this coastal sector of the TAMs. A 32 metre change in elevation in a SLHL sample would result in a $\approx$3.5% increase in scaling factor and thus a corresponding increase in the local production rate. Using the Stone (2000) scaling scheme, this would cause an increase from 5.82 to 6.03 atm g^{-1} a^{-1} in the local production rate. Therefore, if the GIA occurred directly after ice retreat and assuming a rapid uplift, the sample would have spent the majority of its total exposure at the higher elevation and therefore not require correcting. If the reverse occurs (*i.e.* uplift occurs only years before the sample is collected), then the time spent at that elevation would not accurately reflect the history of the sample and would require a 3.5% increase in production rate.

Considering that significant debate surrounds the magnitude of both tectonic uplift and GIA in the TAMs (Brook et al., 1995b; Hall, 2004; Sugden et al., 1995) and given the range of ages from samples in this study (0.7 ka to 2.3 Ma), this thesis assumes the position taken by other SED studies in the Ross Sea Embayment (*i.e.* Di Nicola et al., 2012; Strasky et al., 2009; Todd et al., 2010), that tectonic uplift and GIA was minimal during the Quaternary. Therefore production rates are not corrected for elevation changes. Given that all SED results are minimum ages (*i.e.*

nil erosion), any uplift that may have occurred would only increase the age. One interesting counterpoint to this argument is from a recent study at the Reedy Glacier. Bromley et al. (2010) postulated that instead of high stand glacial deposits representing periods of increased ice volume, they actually represent a combination of GIA uplift and glacial down-cutting by the glacier. The decreasing age-elevation relationship seen in outlet glaciers falsely suggests glacial thinning, while no actual change in ice volume has occurred. Assuming that down-cutting would be maximised in periods of warm basal conditions, Stern et al. (2005) estimated that glacial down-cutting since the start of polar conditions has been accompanied by $\approx$1500 m of GIA.

2.2.4 Antarctic erosion rates

As discussed in Section 2.2.1 radionuclide concentrations can be reduced by radioactive decay and also by chemical and/or physical weathering processes of a surface. This results in an age underestimate and correcting for erosion rate will increase the measured exposure age. Thus being able to understand and quantify the loss of a materials surface, is key when attempting to date a surface's exposure to cosmic rays (Gosse and Phillips, 2001). Given our understanding of the longevity of the Antarctic environment and the cold arid conditions, erosion rates (even with some spatial variations) are extremely low, typically <0.6 m Ma^{-1} (Table 2.3). While comparable to other hyper-arid sites in Chile (<0.1 m Ma^{-1}, Nishiizumi et al., 2005) and Australia (<0.7 m Ma^{-1}, Bierman and Turner, 1995), these values are considerably lower than the 4-5 m Ma^{-1} observed in other deserts (Namib Desert, Cockburn et al., 1999 & Death Valley, Frankel et al., 2007).

One of the effects that erosion has on the surface of a rock is the lowering of nuclide concentrations due to loss of the actual rock surface. Simplified modelling of cosmogenic exposure (Equation 2.3) neglect erosion, therefore calculated ages are considered a minimum age. If the erosion rate can be determined *via* field or experimental methods, it can be added as a correction factor (Equation 2.2). It is by varying an assumed constant erosion rate that the lower bounds of the 'erosion island' used in dual-nuclide studies (Section 2.1.2.1) is calculated. If TCN concentrations are taken to represent steady-state or saturation, then using Equation 2.4

the maximum erosion rate for a sample can be estimated using:

$$\varepsilon = \left(\frac{P}{C} - \lambda\right)\frac{\Lambda}{\rho} \tag{2.20}$$

Where P is the site specific production rate (atm g^{-1} a^{-1}), C is the concentration of the nuclide in question (atm g^{-1}), λ is the TCN decay constant, Λ is the attenuation length (g cm^{-2}) and ρ is the material density (g cm^{-3}) (Gosse and Phillips, 2001).

Table 2.3: Antarctic erosion rates - Maximum modelled values from a number of surface exposure studies. The minimum erosion rate used in all studies for the calculation of exposure ages was 0 m Ma^{-1}.

Erosion Rate Max (m Ma^{-1})	Location	Study
<0.30	McMurdo Dry Valleys	Ivy-ochs et al. (1995)
<0.36	McMurdo Dry Valleys	Schaefer (1999)
<0.60	McMurdo Dry Valleys	Summerfield (1999)
<0.23	Northern Victoria Land	Oberholzer et al. (2003)
<0.35	Shackleton Range	Fogwill et al. (2004)
<0.67	Sor Rondane mountains	Matsuoka et al. (2006)
<0.65	Transantarctic Mountains	Strasky et al. (2009)
<0.52	Rauer Group	White et al. (2009)
<0.05	Transantarctic Mountains	Di Nicola et al. (2012)
<0.54	Antarctic Peninsular	Hodgson et al. (2012)
<0.57	Ohio Range	Mukhopadhyay et al. (2012)

Given the low rates of erosion observed in Antarctic rocks, a secondary problem is that without significant erosion, material exposed at the surface can be preserved for long periods of time *insitu*. Spalled or fractured material off the surface of an old boulder may have considerable TCN inheritance depending on the size of the apparent erratic. This is compounded by the fact that Antarctic glaciers typically do not have a well-developed hydrological system to 'flush' out older material from deposits, allowing older well preserved material with a pre-existing cosmogenic inventory, to be mixed in with freshly exhumed material.

2.2.5 Sampling methodology

Given the complications discussed in this chapter a robust sampling methodology for SED is necessary. The old adage 'Junk in, junk out' is especially pertinent, the choice of sample greatly affecting the outcome. Therefore a rigorous sample selection based on both the physical geometry of the sample, its location as well as an understanding of its geomorphic context in the glacial landscape are key to improving the precision of exposure ages, a reduction in complexity and thus a more robust interpretation.

The primary objective while sampling "..is to collect and describe the attributes of a sample that precisely represents the exposure history of a given landform." (Gosse and Phillips, 2001). Typically SED studies aim to correlate the concentration of a TCN (measured by AMS) to the timing of a geological event (*i.e.* tectonic uplift, fault rupture, glacial retreat). While a number of sampling strategies exist for the different uses of TCNs such as burial dating (Granger and Muzikar, 2001) and erosion studies (Summerfield, 1999), this section will concentrate on the sampling of glacial erratics and bedrock for surface exposure dating. In the Antarctic context,constructional features such as moraine ridges or boulder-belts (Figure 2.15) are inferred to represent periods of glacial still-stand where material has collected at stagnant or stationary ice margins (Atkins, 2013).

Glacial drifts are deposited during periods of recession, where material is draped over the underlying topography during the retreat of an ice margin. Both moraines and drifts, being a mix of various lithologies and clast sizes are highly vulnerable to recycling and reworking. The inclusion of previously exposed material containing an unknown TCN concentration into a new deposit infers both reworking (*i.e.* movement to a new location) and recycling (*i.e.* reused material). In either case, a multitude of processes can occur prior to deposition, such as burial, exhumation, rotation and cycles of reburial. Thus, the provenance of the material (*i.e* whether from a pre-existing moraine or subglacial bedrock), exposure history (simple or complex) and the processes pre-deposition are relative unknowns. This can lead to a situation where a moraine is a mixture of material containing both simple and complex exposures, a single co-eval landform having a wide range of ages older than what the true age of deposition was. A literature review by Putkonen and

Swanson (2003) showed that in published exposure ages, an average age range of 38% exists between the youngest and oldest samples within a single moraine. Therefore particular care must be taken to understand the glaciological and geological context of the landforms in question to ensure that a sample or samples are representative of the event that is being dated.

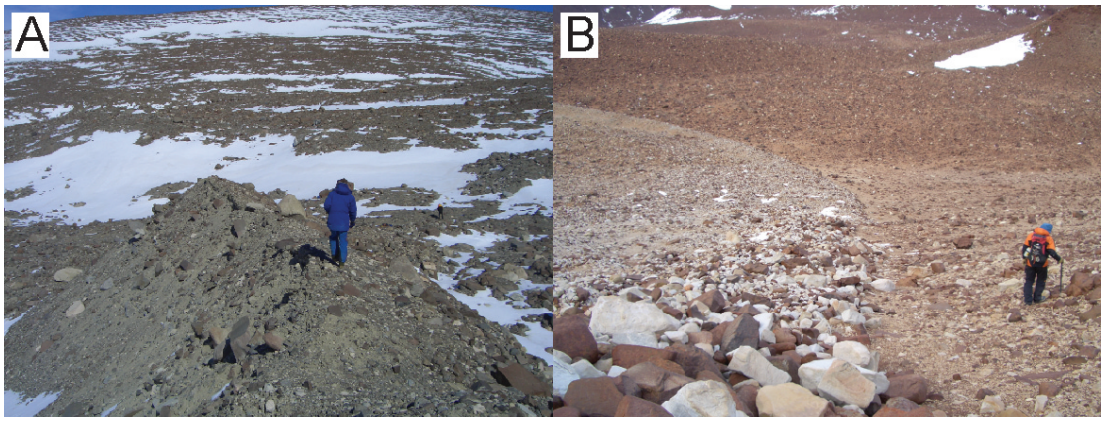

Figure 2.15: Examples of moraines within the Darwin Hatherton glacial system - (A) Matrix supported, poorly preserved asymmetrical moraine ridge within the Britannia Drift at Lake Wellman. (B) Clast supported boulder-belt moraine at the upper contact of the Britannia II Drift at Dubris Valley

For surface exposure dating, the choice of a suitable sample choice should consider a number of key criteria:

- The sample must be relevant to the geological problem in question.
- Sample lithology and mass. Typically the collected sample must contain a sufficient mass of the target mineral. 100 g of cleaned quartz is required for ^{10}Be and ^{26}Al analysis (Child et al., 2000).
- Surface geometry. The sampled surface should be horizontal, away from edges and have an unobstructed view of the sky.
- Stable since emplacement. The sample should be free from post-depositional movement.

Within the exposure dating community some debate exists concerning the size of the sampled boulder in glacial environments. Some studies suggesting that large

boulders (Stone et al., 2003), with enough weight to resist movement and remain stable are preferred (Figure 2.16A). In these cases the upper, preferably horizontal, surfaces of the boulders make ideal targets. The opposite has been suggested by other studies (Briner, 2009). In less stable sites, where material is likely to be mobile (*i.e.* collapsing ice cored moraines & talus slopes), surficial gravels, pebbles and cobbles <5 cm in diameter can be sampled (Figure 2.16B). Given the limited thickness of the sample, only minor attenuation of incoming cosmic rays will occur. Thus the clast, regardless of how much movement has occurred post-deposition, will have been irradiated on all surfaces equally.
Given the complex and problematic Antarctic glacial landscape, the sampling methodology may change on a site by site basis. In this thesis, once a sample has been selected, our collection methodology is as follows.

- Photographs and description of general site location, including slope and elevation (measured by GPS and confirmed by LIDAR when necessary).
- Photographs and description of boulder, including size, height of surface above ground, slope and underlying morphology and composition (*i.e.* bedrock, drift *etc.*).
- Upper surface to be collected marked, then removed using hammer and chisel. Sample is preferentially horizontal and away from edges if possible.
- Photographs and description of sample, including estimated mass; if surface or whole clast is collected, sample thickness (will require cutting down if >5 cm thick), surface weathering and slope.
- Topographic horizontal and shielding measured (Section 2.1.4.3).

This field data collected is summarised in the appendices (Tables A.1, A.4, A.5, A.10, A.13 & A.14).
As the SED ages from the Lake Wellman moraines were widely spread, we made the conscious decision in later fieldwork to sample directly from the drift surfaces themselves, the material appearing far more stable than the moraine ridges. In addition, instead of collecting multiple samples within a single location, we targeted

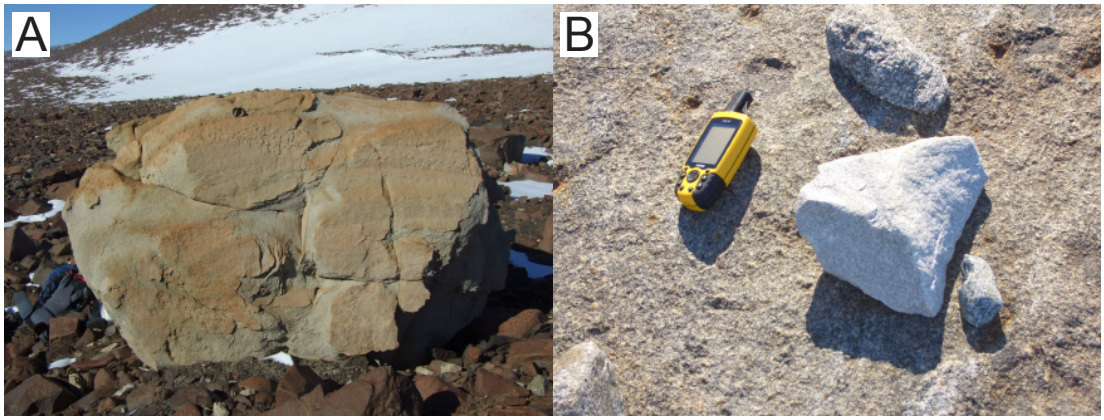

Figure 2.16: SED samples within the Darwin Hatherton glacial system - (A) Large sandstone erratic (2.0 x 1.7 x 2.0 m) emplaced on Britannia drift at Lake Wellman (Sample LW18.1). (B) Small granite clast (0.15 x 0.05 x 0.15 m) emplaced on striated bedrock at Diamond Hill on the Hatherton Glacier margin (DH7.4).

material within identifiable glacial drifts (as defined by Bockheim et al., 1989) at a variety of sites (in the case of the Dubris and Bibra valleys), in order to obtain a spatial spread of samples and also due to the total number of collected samples being limited by our permit.

2.2.5.1 Sampling of bedrock - boulder pairs

As demonstrated, glacially emplaced erratics of various sizes are preferred targets for surface exposure dating, particular those on stable bedrock platforms. While many studies have used this type of sample material for SED, only a limited number have considered matching the boulder or cobble with a sample from the underlying bedrock (Corbett et al., 2011; Delmas et al., 2008; Pallàs et al., 2006). As the erratic boulder and the underlying bedrock are likely to have differing amounts of prior cosmogenic exposure and post-exposure burial, they allow the testing of various exposure-burial hypothesises. Sampling methodology is the same as that for a single glacial erratic, but depending on proximity, the boulder may shield the bedrock from incoming cosmic rays. In this case, topographic shielding for the bedrock sample may have to be remeasured to account for shielding. In the Darwin Hatherton glacial system, only one site was suitable for this technique. At Diamond Hill, at the confluence of the Darwin Glacier and the Ross Ice Shelf, granitoid erratics

are found emplaced on stable bedrock and low slope (<10°) felsenmeers (block-fields). Five bedrock-boulder pairs (Figure 2.17 for examples) were sampled at this location.

The sampling of bedrock boulder-pairs combined with a dual-nuclide analysis (Section 2.1.2.1) can provide information not only on timing of the last advance but also on the degree to which the location may be affected by the advance of cold-based ice.

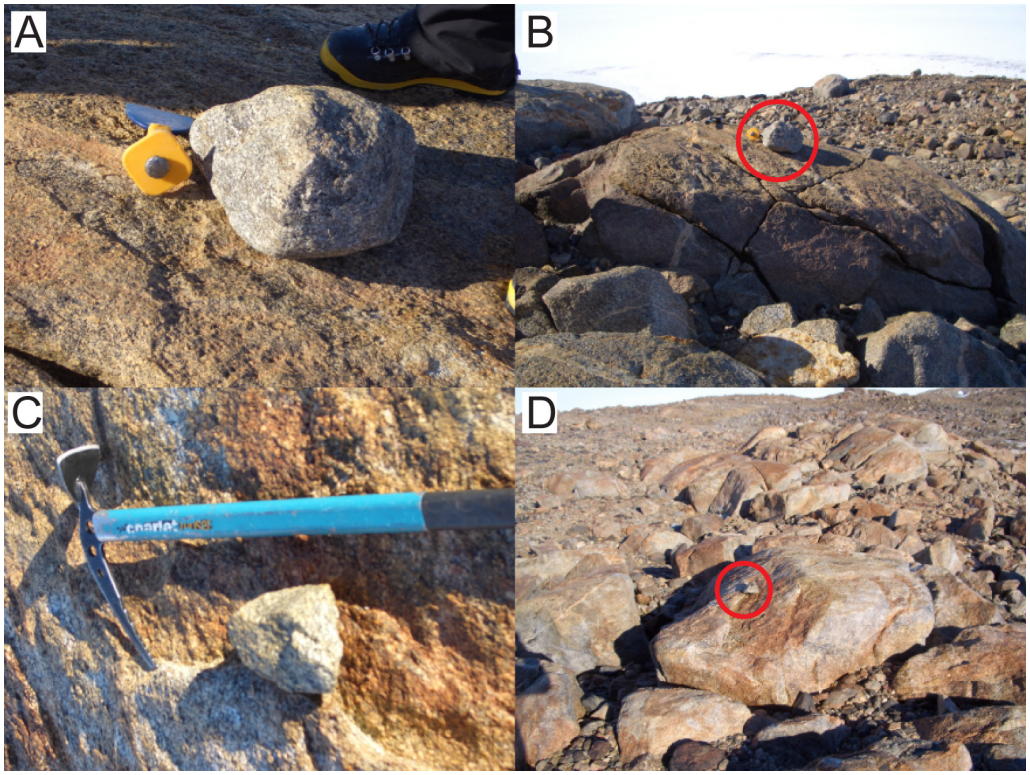

Figure 2.17: Examples of bedrock-boulder pairs - Samples for SED from Diamond Hill. (A) Granitic boulder DH6.2 emplaced on (B) granite bedrock platform, DH6.2B. (C) Granite cobble DH8.1 emplaced on (D) granitic felsenmeer, DH8.1B.

Chapter 3

The Antarctic ice sheets

The modern Antarctic and Greenland ice sheets, while smaller in volume than what was reached during the Last Glacial Maximum (LGM, ≈20-18 ka), still contain the majority of ice within the global cryosphere. In the Antarctic, two large ice sheets with a estimated ice volume of 24.7 x 10^6 km^3 cover up to 98% of the Antarctic continental land mass. The larger East Antarctic Ice Sheet (EAIS) containing 21.7 x 10^6 km^3, while the smaller West Antarctic Ice Sheet (WAIS) is 3 x 10^6 km^3 (Lythe and Vaughan, 2001). As well as playing a critical role in global climate, through the regulation and modification of both atmospheric and oceanographic systems (Ingólfsson, 2004), the Antarctic ice sheets are equivalent to ≈66 metres of sea level rise (Denton and Marchant, 2000). Hence the behaviour of the Antarctic ice sheets and their possible contribution to global sea levels have been recognised by the Intergovernmental Panel on Climate Change (IPCC) as a major concern in a warming world (IPCC, 2007).

Due to the limited geological records concerning the early Antarctic ice sheets, our understanding of their initiation and evolution during the mid-Tertiary are not well understood. The stable isotope record of Zachos et al. (2001) suggests that a switch from warmer to cooler climates at the Eocene/Oligocene boundary (≈35 Ma) lead to an increase in global ice volume, likely related to the Antarctic ice sheets. Glacio-marine sediment cores recovered from the western Ross Sea (Cape Ross Project) suggest that a dynamic EAIS existed by 24 Ma (For a review see Barrett 2007). The glaciological model of DeConto and Pollard (2003), focused on the early inception of the ice sheets, suggests that minor ice caps in Dronning Maud Land, the Transantarctic (TAMs) and Gamburtsev Mountains coalesced over

a 6 Ma period to form a proto-EAIS (Figure 3.1). Meanwhile, the early evolution of the WAIS is far less understood, with evidence of a grounded ice sheet within the Ross Sea Embayment variously placed as late Oligocene to late Miocene (Bart, 2003; Bartek et al., 1992; De Santis et al., 1999).

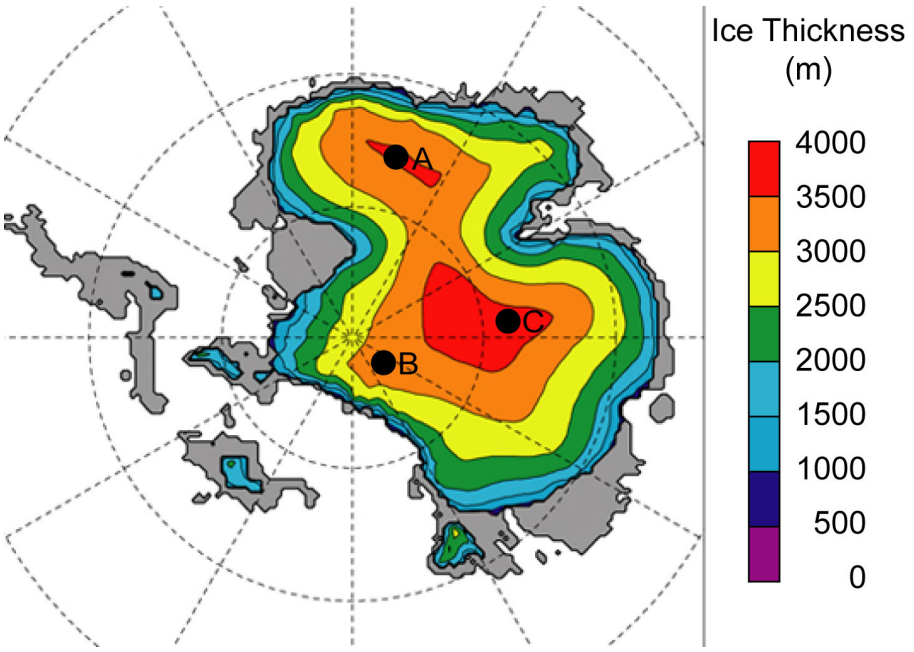

Figure 3.1: Reconstruction of an early Antarctic ice sheet - The glaciological model of DeConto and Pollard (2003) that shows the configuration of a proto-East Antarctic Ice Sheet at ≈28 Ma. The three initial centres of ice accumulation located in Dronning Maud Land (A), the Transantarctic (B) and Gamburtsev (C) mountains have now coalesced to form a major ice sheet. Ice thickness is measured in metres.

A number of climatic drivers are thought to have aided the formation of the ice sheets, instigating a change in global climate from 'hothouse' to 'icehouse' conditions (DeConto and Pollard, 2003). During this period tectonic reorganisation led to the opening of major seaways between Antarctica, Tasmania (Tasmanian Passage) and South America (Drake Passage) creating the Antarctic Circumpolar Current (ACC) and thermally isolating the continent (Exon et al., 2004; Scher and Martin, 2006). The ocean circulation models of Nong et al. (2000) support the cooling of the continent in this manner, with a reduction in southwards heat transport and decreased Southern Ocean sea surface temperatures (≈3°C). However, DeConto and Pollard (2003) suggested that the role of tectonics is secondary and

that global Paleogene cooling and the glaciation of Antarctica was driven by decreasing atmospheric CO_2. At the Oligocene/Eocene boundary atmospheric CO_2 concentrations dropped from ≈560-840 ppm to a near pre-industrial level of ≈280 ppm, this decrease resulted in a lowering of equilibrium line altitudes (ELAs) (DeConto and Pollard, 2003). In the high elevation regions of Antarctica, lowered ELAs combined with Milankovich cycles favourable for the accumulation of ice may have accelerated ice sheet formation. (Naish et al., 2001). However, our knowledge of the Quaternary configuration of the Antarctic ice sheets is limited compared to those of the Northern Hemisphere. The scarcity of high resolution Antarctic terrestrial records a significant stumbling block to accurate numerical modelling of the continent. Therefore, fundamental questions have arisen concerning the thickness and extent of the Antarctic ice sheets, particularly at the LGM, leading to varying estimates of ice volume (Section 3.2).

3.1 Antarctic ice sheet morphology

The Antarctic ice sheets are divided into the larger EAIS and smaller WAIS along the length of the TAMs, differences in glaciology and bedrock topography between the ice sheets significantly affecting their behaviour. Fringing the coastal margins of the ice sheets are a number of floating ice shelves, fed by ice draining from the EAIS and WAIS *via* outlet glaciers and ice streams. The Ross Ice Shelf is fed in this manner, predominantly by the ice streams draining the WAIS at the Siple Coast (*i.e.* the Mercer, Whillans and Kamb ice streams), combined with a minor EAIS contribution *via* the outlet glaciers of the TAMs (Thomas et al., 2013).

3.1.1 The East Antarctic Ice Sheet

The underlying bedrock topography of the EAIS is a central craton derived from the breakup of Gondwana (Fitzgerald, 2002) and comprises the bulk of the Antarctic land mass. Beneath the EAIS, bedrock elevations are predominantly above sea level (when corrected for isostatic rebound, *i.e.* Lythe and Vaughan 2001) reaching up to 2500 masl at the subglacial Gamburtsev Mountains that underlie the centre of the ice sheet (Bo et al., 2009). Approximately 400 sub-glacial lakes are also

observed, Lake Vostok with an estimated volume of 5400 km^3 is the largest and located under ≈4000 metres of ice (Siegert et al., 2012). Above these subglacial features is the vast East Antarctic polar plateau, where a number of high elevation ice domes (*i.e.* Dome Argus, Circe & Fuji) have coalesced to form a ridge-like ice divide having a maximum altitude of 4093 masl. The ice thickness in this region of the EAIS is estimated to be between 2800 and 4500 metres (Wright et al., 2008). From the polar plateau, ice drains towards the coast *via* a limited number of high velocity outlet glaciers and ice streams (Rignot et al., 2011), characterised by deeply incised bedrock channels, warm-basal ice conditions and terminations at coastal margins (Bamber, 2000). In the section of the TAMs that flanks the Ross Sea Embayment, the mountains block the majority of ice flow from East Antarctica. Thus, only a limited discharge of ice from the EAIS reaches the Ross Ice Shelf *via* a number of outlet glacial systems (*i.e.* the Beardmore, Ferrar, Darwin, Byrd, Skelton, Scott and Reedy). It is important to note that these outlet glaciers do not just drain ice from the EAIS/TAM boundary, but also farther inland; the Beardmore Glacier collects East Antarctic ice from a point 800 km from the coast *via* a number of large subglacial channels (Bamber, 2000).

3.1.2 The West Antarctic Ice Sheet

In direct contrast to the EAIS, the smaller WAIS has been shown as highly sensitive to climatic forcing with both extreme advances and retreats over the last 5 Ma (Naish et al., 2009; Pollard and DeConto, 2009). The dynamic nature of the WAIS was recognised early on by Mercer (1968) who stated that with future warming "*..the West Antarctic Ice Sheet will become a threat to coastal areas of the world within six metres of sea level.*". Concerns about the sensitivity of the WAIS to projected future warming are also shared by the global climate community (IPCC, 2007). Therefore to assess the time frame and likelihood of WAIS collapse, knowledge of past behaviour during both glacial and interglacial cycles is required.
Compared to the stable East Antarctic craton, the West Antarctic landmass is an archipelago of crustal blocks created during Gondwana breakup, with further modification driven by the continued rifting of the West Antarctic basin during the Cenozoic (Dalziel and Lawver, 2001). The differences in bedrock topography are

significant, the subglacial topography of Lythe and Vaughan (2001) shows the fragmented West Antarctic landmass separated by a network of paleo-seaways (Figure 3.2).

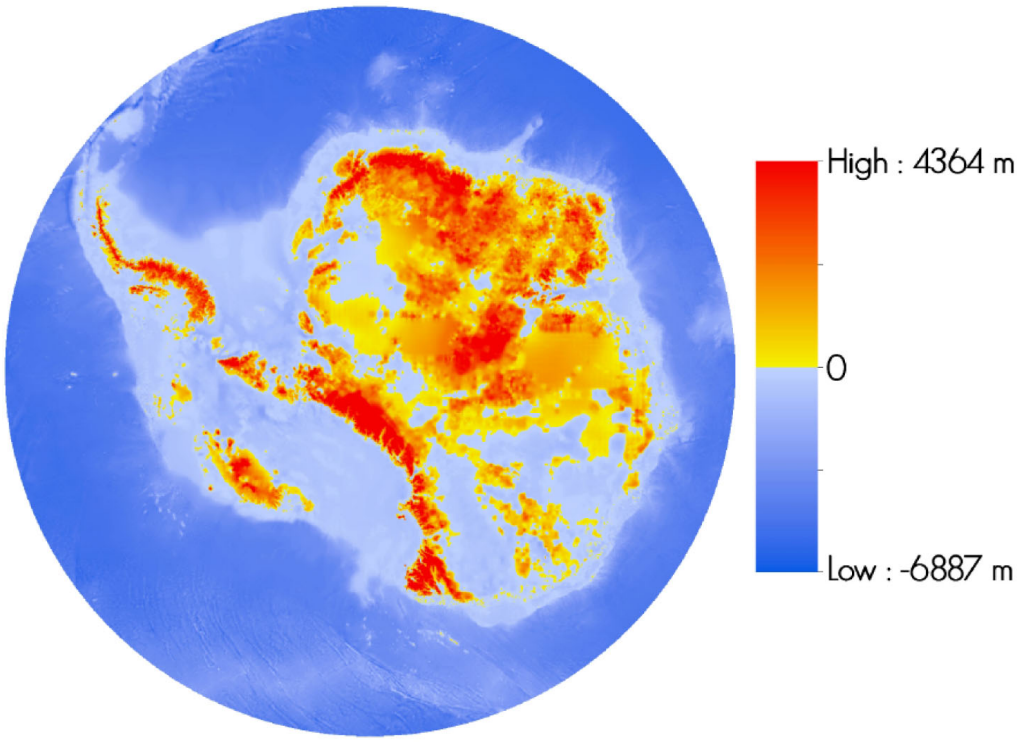

Figure 3.2: Bedrock topography of the Antarctic ice sheets - Bedrock topography uncorrected for isostatic uplift. Adapted from Lythe and Vaughan (2001).

Unlike the EAIS with its multiple high elevation domes, the WAIS has only a single plateau reaching ≈3000 masl, draining ice into three distinct regions: the Weddel Sea (*i.e.* into the Ronne Ice Shelf), the Ross Sea (*i.e.* into the Ross Ice Shelf) and the Amundsen/Bellinghausen Sea. As the average elevation of the WAIS is far lower than that of the EAIS, coastal storms can penetrate further into the interior of the ice sheet causing up to three times the level of snow accumulation compared to that of the EAIS (Bindschadler, 2006). Yet even with high accumulation rates, the mass balance of the WAIS is kept stable by a well-developed series of fast flowing, high discharge ice streams draining into ice shelves. Underlying the WAIS, the paleo-seaways are now large subglacial trenches filled with a large proportion of the total West Antarctic ice volume (1 x 10^6 km^3) (Lythe and Vaughan, 2001).

The largest trench, the Bentley Subglacial Basin, reaches depths of 2555 metres below sea level and it is here that WAIS ice is at its thickest. The basal ice found within these ice streams do not sit on bedrock, but on beds of soft subglacial sediments, possibly aiding in the basal sliding of discharged ice (MacAyeal, 1992). It is the marine aspect of the WAIS that makes it so sensitive to climate change, small increases in sea surface temperature and/or sea levels can cause ice loss to accelerate. The ice streams draining the interior and ice shelves buttressing ice sheet margins are particularly susceptible, with the destabilization of the ice sheet as a potential outcome (Joughin and Alley, 2011; Pollard and DeConto, 2009).

While there is a wealth of evidence supporting the presence of a WAIS during the mid Neogene (Bart, 2003; Bart and Anderson, 2000; Böhm et al., 2009), the initiation and early evolution of the ice sheet is far less constrained (Wilson et al., 2013). The geological record implies limited ice during the Oligocene, based on the subglacial volcanic deposits (hyaloclastilites) of LeMasurier and Rex (1983) and Wilch and McIntosh (2000). These studies suggest thin mountain glaciers centred on the Marie Byrd Land sector at 25-29 Ma, but could not rule out thickened continental ice sheets. During the mid to late Miocene, the WAIS had expanded to a size where grounded ice had entered the Ross Sea Embayment (Bart, 2003; Bartek et al., 1992; De Santis et al., 1999) and at times advanced to the continental shelf, creating widespread glacial unconformities (Anderson and Shipp, 2001). Evidence from the Weddel Sea implies similar behaviour to that of the Ross Sea Embayment, a WAIS larger than present eroding the continental margin (Anderson and Shipp, 2001).

3.2 The Antarctic contribution to LGM sea level rise.

The climate of the Last Glacial Maximum (LGM) has been intensely studied over the past four decades. It is defined as the most recent period of glacial conditions, in which both Northern and Southern Hemisphere ice sheets reached their maximum volume (Mix et al., 2001). The LGM reaching its peak at 20 ka for the Northern Hemisphere (NH), slightly later at 18 ka for Antarctica and the Southern

Ocean (Denton et al., 2010) and aligning to the marine isotope record of Shackleton (1987) as stage 2 (MIS-2). The LGM was the final phase of a 100 ka change from a warmer than present interglacial climate (≈125 ka, MIS-5) to full glacial conditions (Figure 3.3). During this period, a cooling climate aided the initiation and expansion of continental ice sheets. Water was effectively removed from the hydrological cycle and lowered global sea levels in proportion to growing ice sheet volumes with reconstructions of LGM eustatic sea levels (ESL) suggesting a drop of 125-135 metres below present (Fleming et al., 1998; Yokoyama et al., 2000). Immediately following the LGM, a rapid change in climate lead to the collapse of the NH ice sheets during an event known as Termination-I (NH, 20-7 ka) (Denton et al., 2010). Over a relatively short period of time, pulses of glacial meltwater were released into the Northern Atlantic Ocean, returning global sea levels to near modern values. The rapid change at the terminal phase of previous ice ages is thought to have been caused by a variety of forcing mechanisms ranging from: solar insolation (Denton et al., 2010), sea levels and temperatures (Adkins et al., 2002; Golledge et al., 2012; Mackintosh et al., 2011), atmospheric composition (Jouzel et al., 2007) and the retreat of the NH ice sheets (Carlson and Winsor, 2012; Peltier, 2004).

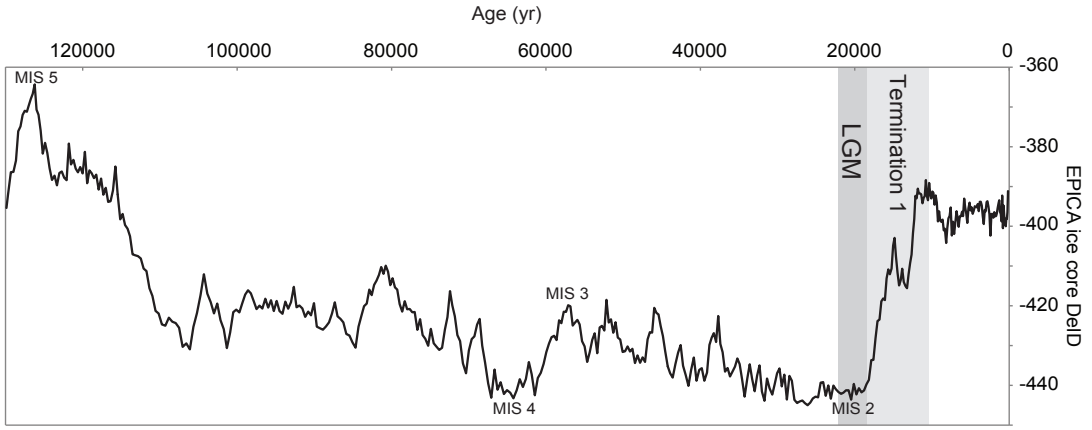

Figure 3.3: The last glacial cycle and LGM - 130,000 years of climate as seen in the EPICA ice core from Dome C in the EAIS (Jouzel et al., 2007). Negative deuterium isotope (^{2}H) values are used as a proxy for decreased air temperatures. Also marked are the marine isotope stages (MIS) of Shackleton (1987).

But while the volume of the Northern Hemisphere ice sheets and their contribution to post-LGM sea level rise is relatively well understood, the same cannot be said for Antarctica. Significant debate surrounds the volume and extent of the East and West Antarctic ice sheets at the LGM (See Table 3.1 for modelled estimates). Compared to the wealth of geological evidence constraining the NH ice sheets, direct evidence of Antarctic paleo-climate is limited to the marine record and rare ice-free coastal and mountainous areas. Various ice sheet models estimate the EAIS and WAIS to contain 57-66 m of sea level equivalent, so an understanding the role that post-LGM ice volume changes may have played in sea level rise is necessary.

To further complicate the situation, a significant mismatch appears to exist between post-LGM sea level rise and the calculated volumes of the Northern Hemisphere ice sheets, referred to as the 'Missing ice' problem (Yokoyama et al., 2000). When the modelled volumes of the LGM NH ice sheets are combined, an ESL change of 20-30 m is left unaccounted for (Figure 3.4). This shortfall is considered by many to be the Antarctic contribution, predominantly from the retreat of the LGM WAIS to its present position (Section 3.3). While the use of intermediate and far field ESL curves as a proxy for ice volume is problematic, several lines of evidence support the 'missing ice' theory (see Lilly, 2008 for a review).

The behaviour of the WAIS and EAIS is believed to be asynchronous across the continent, with both ice thickness and the position of maximum ice extent retreating and advancing at different times at different sites (Anderson, 2002; Anderson et al., 2013). Geological evidence suggests that deglaciation times varied regionally, some EAIS sites indicate deglaciation at 16-19 ka, while others later at <15 ka (Hall and Denton, 2000; Mackintosh et al., 2007; White et al., 2010). Therefore over the last 30 years a variety of numerical models have attempted to reconstruct the complex configuration of the LGM ice sheet and thus the Antarctic contribution to ESL post-LGM. A range of values from 6-37 metres of sea level equivalent (msle) being calculated (Table 3.1).

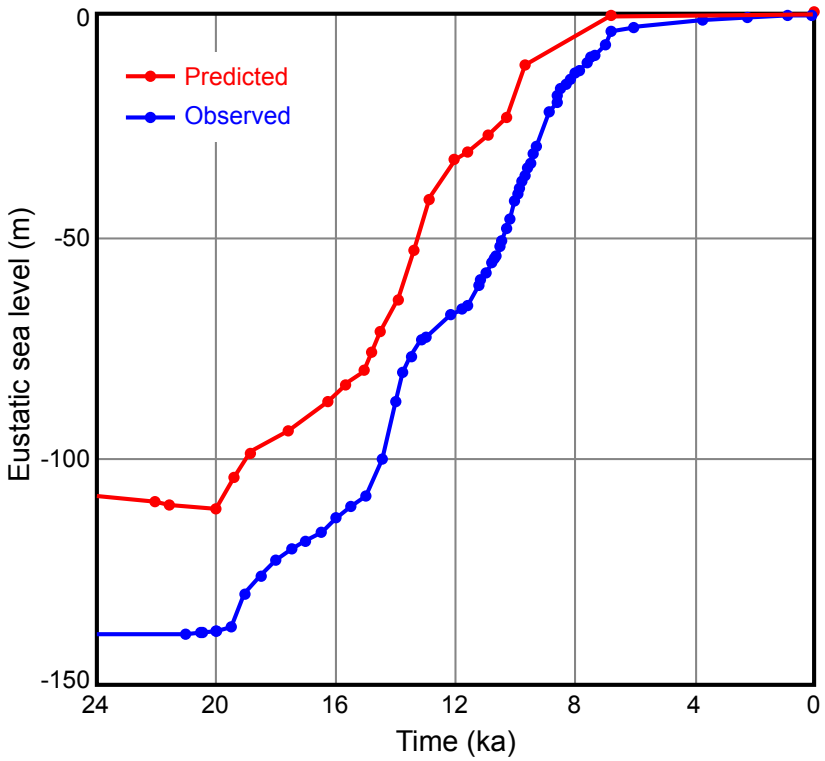

Figure 3.4: Observed *vs* modelled eustatic sea levels - The 'missing ice' problem as seen in a mismatch between observed (blue) and modelled (red) ESLs over the last 24 ka. Predicted values are based on the Pleistocene configuration of Northern Hemisphere ice sheets and use the Australian National University's glacio-isostatic model (*i.e.* Lambeck (2000); Lambeck et al. (2003); Yokoyama et al. (2000). Figure from Lilly (2008).

Table 3.1: Post-LGM eustatic sea level estimates - A small subset of numerical modelling results for the combined Antarctic ice sheets.

Year	Eustatic Sea Level (m)	Author
1988	37	Nakada and Lambeck (1988)
1990	12	Huybrechts (1990)
1991	25	Denton et al. (1991)
1991	26	Tushingham and Peltier (1991)
1999	6-13	Bentley (1999)
2000	20-30	Nakada (2000)
2001	6	Ritz et al. (2001)
2002	14	Denton and Hughes (2002)
2002	14-18	Huybrechts (2002)
2006	9.5-17.5	Philippon et al. (2006)
2009	12.5	Pollard and DeConto (2009)
2010	37 (max)	Saito and Abe-Ouchi (2010)
2011	10	Mackintosh et al. (2011)
2012	6.7	Golledge et al. (2012)
2012	7.5-10.5	Whitehouse et al. (2012)

While the mechanics and rheology of ice (Hooke, 2005), the modern ice sheet configuration and underlying bedrock topography (Bamber et al., 2009; Lythe and Vaughan, 2001) are well understood, the terminal position (*i.e.* maximum extent) and ice thickness are important and relatively poorly constrained parameters. The sparse geological evidence representing these parameters is a major limitation in the calibration of ice sheet models and thus the correct calculation of the Antarctic ESL contribution. While the marine record has become invaluable for determining the terminal ice position and timing of deglaciation from the continental shelf, the availability of terrestrial onshore records, in particular those of ice thickness in the interior regions of the continent are limited.

The record of WAIS extent based on marine geophysics and swath bathymetry (Heroy and Anderson, 2005; Licht and Andrews, 2002; Shipp and Domack, 1999), suggest an advance to a position at the outer continental shelf in many regions, especially within the basins currently occupied by ice shelves (*i.e.* Ross & Ronne). Meanwhile, the best evidence constraining the extent of the EAIS is located offshore at the Amery Ice Shelf (Mackintosh et al., 2011). The earliest CLIMAP re-

constructions of the Antarctic ice sheets (Stuiver et al., 1981) showed the LGM maximum extent at the continental margin. A later version by Denton et al. (1991) showed little interior growth, but thickening of ice at the periphery. Denton and Hughes (2002) produced a final version of the model with a revised LGM ice volume change of 14 msle. In contrast, the ANT3/4/5/6 models (Nakada, 2000; Nakada and Lambeck, 1988) show extensive thickening in the Weddel Sea, with ice advancing further out onto the continental slope than others (see Anderson, 2002 for a review).
Later models of the Antarctic ice sheets show a far smaller increase of ice volume at the LGM than earlier ones. The models of Golledge et al. (2012); Mackintosh et al. (2011); Pollard and DeConto (2009); Whitehouse et al. (2012) all calculate an ESL change of 6.7-10.5 msle. Possible reasons for this significant reduction in the modelled volume of ice are:

- An increase in computing power and the development of ice sheet models such as the Parallel Ice Sheet Model (PISM, http://www.pism-docs.org) and GLIMMER (Rutt et al., 2009).
- A recognition of the role that ice-ocean interactions play at marine ice sheet margins, particular during deglaciation (Denton et al., 1986a; Golledge et al., 2012; Mackintosh et al., 2011).
- A recognition that the interior portions of ice sheets respond asynchronously to coastal margins Ackert et al. (2013); Mackintosh et al. (2011).
- An increase in the number of marine and terrestrial geological records available to use as model calibration (see Anderson, 2002; Bentley, 2010 for reviews).

It is likely that the increase in the quantity and quality of geological records have made the greatest constraints, with modern glaciological models increasingly using a range of physical evidence to estimate ice sheet thicknesses and extent. A number of recent studies have used a multi-proxy approach to calibrate model outputs. For example, Mackintosh et al. (2011) used the chronology of terrestrial records (surface exposure ages & ^{14}C) for interior ice thicknesses and marine

records (swath bathymetry & sediment cores) for grounding line positions. Furthermore, maximum LGM ice thickness inferred from a variety of geological proxies at 38 interior sites were used by Golledge et al. (2012) to test the outputs of their ice sheet model.

3.3 Ice sheet behaviour in the Ross Sea Embayment

The Ross Sea Embayment (RSE), a marine basin reaching ≈1000 metres deep is located between the Transantarctic Mountains to the west and the Siple Coast to the east. The location of the RSE, at the intersection of the East and West Antarctic ice sheets, makes the region a key site in understanding the role of ice sheet expansion during the Quaternary, particularly the WAIS.

The modern setting of the RSE is one dominated by the Ross Ice Shelf (RIS), an area of 5.6 x 10^5 km^2 from its grounding line, at the Siple Coast, to its floating margin near the mouth of the embayment (Brunt et al., 2010). The ice shelf is predominantly fed by West Antarctic ice draining into the RSE *via* the ice streams of the Siple Coast, with a minor contribution by the EAIS. In the western flank of the TAMs are found the McMurdo Dry Valleys (MDVs). The largest ice free area on the continent, the MDVs comprise a number of complex valley systems and smaller glacier flanking sites. The variety of geological records used to infer past ice elevations makes the area unique and highly significant to our understanding of the RSE during the LGM.

3.3.1 The Ross Sea Embayment during the Pleistocene

Global isotope and eustatic sea level records have suggested that significant fluctuations in ice volume (Lisiecki and Raymo, 2005; Zachos et al., 2001) had occurred throughout the Pleistocene. How the Antarctic ice sheets, particularly the WAIS, reacted during 40 and 100 ka interglacial cycles is a key to understanding their behaviour in warmer than present conditions (Vaughan and Arthern, 2007). This is especially pertinent during the mid-Pleistocene transition with occurrence of the "super-interglacial" of MIS-31 (1.06-1.08 Ma, Raymo et al. 2006 & DeConto et al. 2012).

The WAIS has been shown to be especially sensitive during Pleistocene interglacials. Diatoms and high concentrations of meteoric ^{10}Be recovered from subglacial tills beneath the Whillians ice stream draining into the Ross Sea Embayment, indicate that presently grounded areas of the WAIS were once ice free (Scherer et al., 1998). Scherer et al. (1998) suggested that the area proximal to the ice-stream was in open water conditions, based on the occurrence of *Thalassiosira Antarctica*, at $\approx$480 ka. Age control for this event was based on a raised beach record from Barbados and Bermuda that suggested a collapsing WAIS contributed to the 20 metre sea level rise at the time (Hearty et al., 1999). The $\approx$1285 metre deep ANDRILL-1B core, taken from the sea floor beneath the Ross Ice Shelf in McMurdo Sound (Naish et al., 2009) was the first direct evidence of the glacial-interglacial behaviour of the WAIS in the Ross Sea Embayment. The work of McKay et al. (2012) suggested that the oscillating cycles of glacio-marine sedimentation observed in the core represented a transition from grounded ice sheet to ice shelf and that it had occurred least seven times over the last 800 ka. The interpretation and timing of the geological evidence is in good agreement with the numerical model of Pollard and DeConto (2009) that shows multiple WAIS collapse events over the last 5 Ma (Figure 3.5).

When combined the various records tell a compelling story (Figure 3.6). During interglacials oceanic δ^{18}O values decrease as sea surface temperature increased, the Vostok (Petit et al., 1999) and EPICA (Jouzel et al., 2007) ice core δ^{18}O values increased (*i.e.* less negative) inferring warming air temperatures and the Antarctic Ice Sheet model of Pollard and DeConto (2009) suggest that WAIS volume decreased as grounding lines retreated from the marine basins. In glacial periods the reverse is true, with cooler atmospheric and oceanic temperatures coinciding with an increase in WAIS volume.

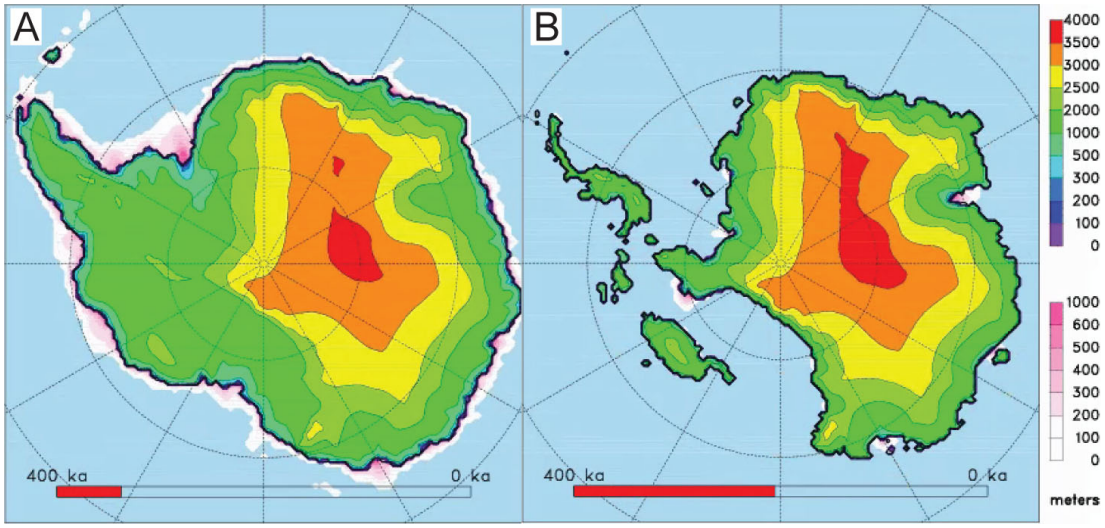

Figure 3.5: Modelled Antarctic ice sheet collapses and advances - Showing EAIS and WAIS advances and retreats modelled by Pollard and DeConto (2009). Examples of glacial maxima (A, ≈303 ka) and minima (B, ≈206 ka) during the Quaternary from Pollard and DeConto (2009).

McKay et al. (2012) confirms the suspected behaviour of the WAIS, as suggested by the work of Lisiecki and Raymo (2005), Pollard and DeConto (2009), Petit et al. (1999) and Jouzel et al. (2007) within the Ross Sea Embayment. The sedimentary record from the AND-1B core shows that a series of unconformities exist that corresponded to glacial periods (*i.e.* MIS-2) and when entering interglacials (*i.e.* MIS-5e & 31) the depositional environment switches from that of a glacial diamictite to a volcanoclastic mudstone, dominated by diatoms. The facies observed within the core suggested a depositional environment within McMurdo Sound that switched from a grounded ice sheet (*i.e.* unconformity), to ice margin proximal (*i.e.* subglacial diamictite), to ice margin distal (*i.e.* glacio-marine mudstones) and finally open water (*i.e.* volcaniclastic and diatomaceous). Importantly, these packages of facies repeat throughout the core and not only suggest multiple WAIS collapses (as suggested by Pollard and DeConto 2009) but that the timing of ice sheet advances and retreats is likely linked to 100 (pre-MPT) and 40 ka (Post-MPT) Milankovich cycles.

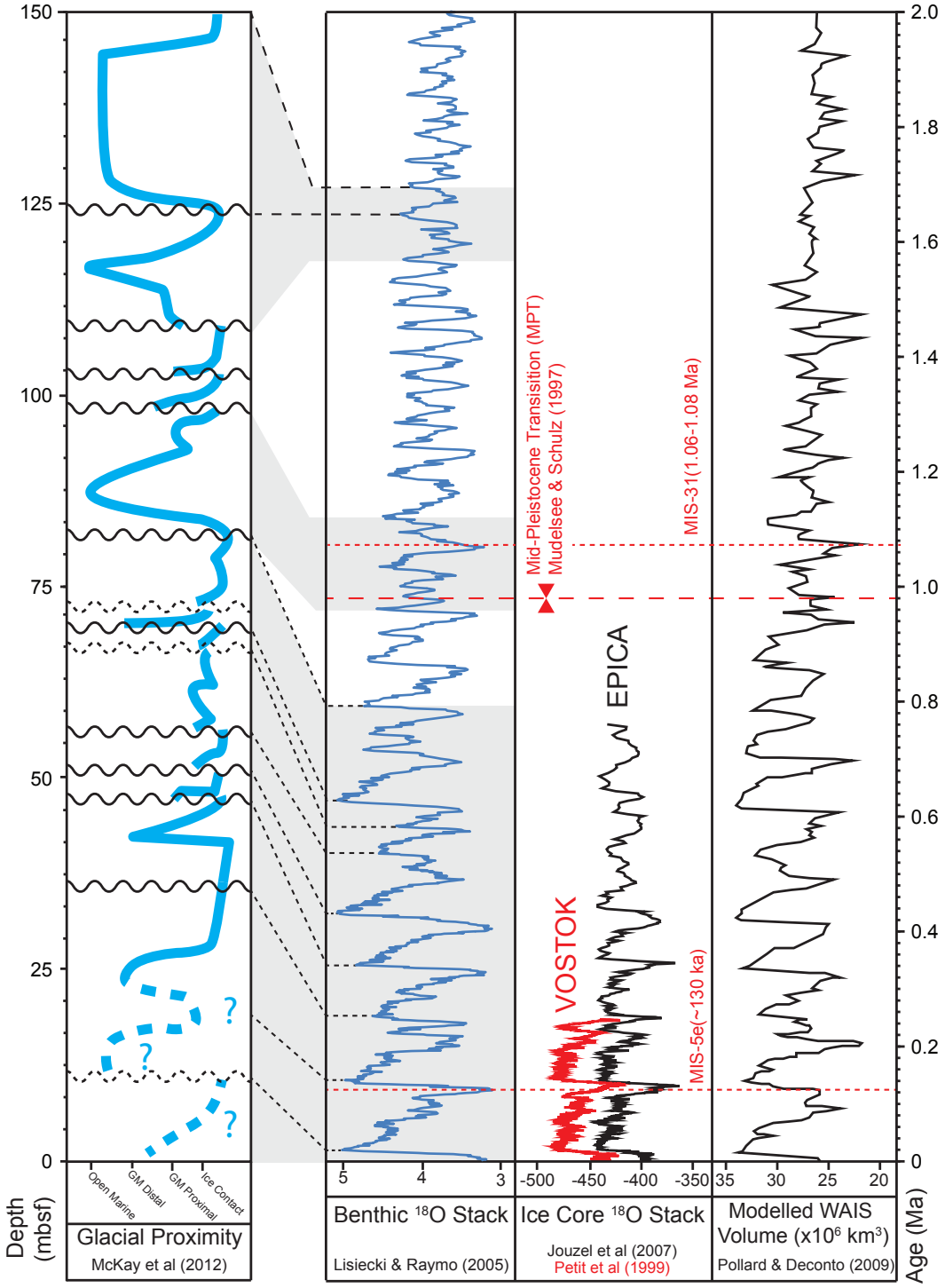

Figure 3.6: Pleistocene glacial behaviour - A number of marine and terrestrial records used as proxies or direct evidence of ice volume changes. From left to right; Glacio-marine conditions in the RSE as suggested by (McKay et al., 2012) (Note that scale is in metres beneath sea floor). The stacked benthic δ^{18}O isotope record of Lisiecki and Raymo (2005). The δ^{18}O isotope record from the Vostok (Petit et al., 1999) and EPICA (Jouzel et al., 2007) ice cores and modelled WAIS ice volume by Pollard and DeConto (2009) over the last 2 Ma. Adapted from McKay et al. (2012).

3.3.2 The Ross Sea Embayment during the LGM

The modelled LGM ice sheet of Denton and Hughes (2000, 2002) shows a configuration larger than the modern, with relatively little change in the continents interior, but with ice sheet margins expanded out close to the continental shelf edge (Figure 3.7). Leading up to the LGM, the maximum extent of grounded West Antarctic ice was ≈1200 kilometres northwards of its modern position at the Siple Coast with grounded West Antarctic ice filling the previously marine Ross Sea basin and replacing the floating Ross Ice Shelf. The expansion of WAIS ice up to the LGM is observed in both the geological record and demonstrated in numerical models. The grounded WAIS within the RSE, described by Thomas and Bentley (1978) as the 'Ross Ice Sheet', was equivalent to an estimated 4.6 msle increase in LGM ice volume. A significant increase when compared to the EAIS contribution of 9.4 msle. Given the breakdown by sector, the RSE (*i.e.* Ross Sea sector) contributed 32% of the total WAIS ice volume and 21% of the total Antarctic ice volume (*i.e.* WAIS + EAIS) at the LGM (Denton and Hughes, 2002). While evidence indicating the timing of glacial advance up the LGM is sparse, the maximum extent and retreat of grounded ice post-LGM within the RSE is well represented in the geological record. A number of lines of evidence, both terrestrial and marine, have aided in the various reconstruction of the LGM ice sheet configuration within the RSE.

- Marine
  - Swath bathymetry (Greenwood et al., 2012).
  - Glacio-marine sediment cores (McKay et al., 2008, 2012).
  - Marine geophysics (Shipp and Domack, 1999).
- Glaciological
  - WAIS ice cores (Brook et al., 2005; Morgan et al., 2002).
  - EAIS ice cores (Monnin et al., 2004; Rhodes et al., 2012; Stauffer et al., 2004).
- Terrestrial
  - Glacial geomorphology of the McMurdo Dry Valleys (Hall and Denton, 2000).

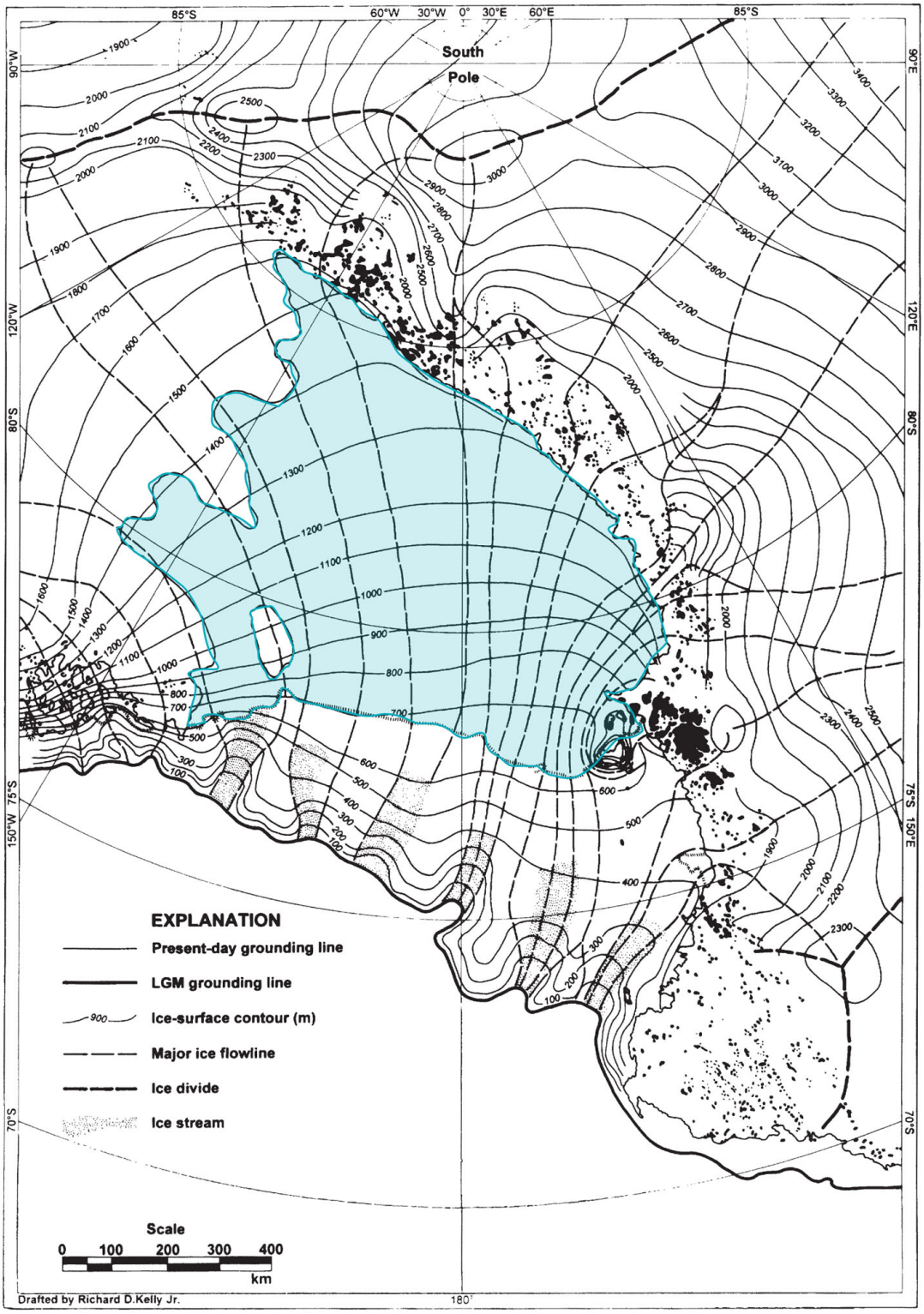

Figure 3.7: The LGM Ross Sea Embayment - A modelled LGM configuration by Denton and Marchant (2000). The blue shaded area represents the modern Ross Ice Shelf.

- Glacio-isostatically raised beaches (Butler, 1999).
- Regional sea level curves (Conway et al., 1999; Hall, 2004).
- Glacial geomorphology of TAM outlet glaciers (Bromley et al., 2012; Denton et al., 1989a; Marchant et al., 1994).

A variety of glaciological models have attempted to reconstruct the configuration of the LGM Antarctic ice sheets, but only two have focused on their behaviour within the RSE (*i.e.* Denton and Hughes, 2000 & Golledge et al., 2012). The Denton and Hughes (2000) model for the LGM configuration of the RSE relies heavily on geological evidence to constrain both the thickness and extent of grounded ice. The location and source of major ice flow was inferred using a combination of both terrestrial and marine data (see Denton and Marchant 2000 for a review). Drainage from EAIS catchments were modelled running through a number of key TAM glaciers; Titan Dome through the Beardmore Glacier (Denton et al., 1989a), Dome Circe though the Darwin-Hatherton (Bockheim et al., 1989) and Taylor Dome through the MacKay Glacier. Using geomorphic evidence on the sea bed of the RSE, ice flowlines were extrapolated out to the grounding line from the discharge point of glacial systems. Within McMurdo Sound, the flow of ice appears to be complex. Deposition of the Ross Sea Drift within the mouths of the MDVs suggests that the ice sheet flowed into the lower sections of formerly ice free valleys. The northwest flow of ice transported basaltic material from its source on Ross Island inland into the mouths of coastal valleys (Greenwood et al., 2012; Hall and Denton, 2000). The complexity of the RSE is also shown by Golledge et al. (2012), who offered a model which produced an overall grounding line position comparable to that of Denton and Hughes (2000), but highlighted inconsistencies in modelled ice thickness when compared to the geological evidence in the TAMs. The problem of modelling the MDVs is also commented on by Whitehouse et al. (2012), who note that many sites along the TAMs are poorly resolved by their model. A number of explanations were suggested, including the regions complex topography and the role of katabatic winds in keeping the valleys ice free (Whitehouse et al., 2012).
The geological evidence has been instrumental in our understanding of the retreat of the LGM ice sheet in the RSE. Conway et al. (1999) and later revisions by Hall et al. (2013) combining a large number of geophysical, geological and glaciological

records to suggest that the retreat of the WAIS grounding line was a 'swinging gate'. The eastern side of the ice sheet locked at the northern point of the Siple Coast, but the western side swinging to the south east until it reached the modern grounding line position (Figure 3.8).

The expanded WAIS was at its maximum extent at the continental shelf between 26.6-19.5 ka (Domack et al., 1999; Shipp and Domack, 1999), retreating back past Terra Nova Bay at 8 ka (Orombelli et al., 1990) to Ross Island between 11-7 ka ^{14}C BP (Conway et al., 1999; Domack et al., 1999). The glacio-marine ANDRILL cores collected from beneath McMurdo Sound also suggest a lifting of the grounding line in the region at 11-10 ka ^{14}C BP (McKay et al., 2012). The grounding line of the Conway et al. (1999) 'swinging gate' as it moved from Ross Island to its present position is only constrained by a limited number of data points. The first, at the Darwin-Hatherton glacial system (DHGS, Chapter 4), suggests that while the glacier had thickened during the LGM it had returned to near modern levels by $\approx$6.8 ka ^{14}C BP as the grounded ice margin moved southwards past the glacier mouth (Bockheim et al., 1989). The second point is from Roosevelt Island, a grounded ice dome within the RSE. Here seismic data and glaciological modelling suggest that the grounding line was north of the island at $\approx$3.2 ka BP (Conway et al., 1999). The final point is that of the Scott Glacier, where ice reached near modern levels by $\approx$2 ka (Hall et al., 2013; Todd et al., 2010). While the 'swinging gate' has been proven to be a viable hypothesis by glaciological models (Pollard and DeConto, 2009), the scarcity of data in the middle to southern parts of the RSE means that understanding the behaviour of outlet glaciers such as the DHGS can aid in constraining not only local ice sheet thickness, but also the timing of deglaciation within the RSE.

Figure 3.8: Post-LGM retreat of the Ross Ice Sheet - A revised version of Conway et al. (1999) by Hall et al. (2013). The 'Swinging gate' model starting at the LGM Grounding line position at Coulman Island (A), ice elevations (in masl) are inferred from geological evidence (Hall et al., 2013). The grounding line retreats past Terra Nova Bay (B, 8 ka), the McMurdo Dry Valleys (C, 7.8 ka), Hatherton Glacier (D, 6.8 ka), Beardmore Glacier (E), north of Roosevelt Island (F, 3.2 ka), Scott Glacier (G, 2 ka) until reaching its modern position (I).

3.3.3 Glaciers of the Transantarctic Mountains

The geological and glaciological setting of the TAMs has given rise to a variety of glacier styles that draining ice from both local catchments as well as ice sheets. Atkins (2013) broadly classified the cold-based glaciers observed within the TAMs into three classes:

1. Alpine glaciers, in which ice is sourced from small cirques and ice fields and discharged into ice-free valleys (*e.g.* The Meirs, Adams and Garwood glaciers in the Denton Hills). Typically narrow (<300 m) and less than 5 km long, these glaciers usually transport a minimal amount of supraglacial material and deposit only minor moraines at the ice margins. The terminal faces are characterised by a vertical ice wall and associated ice apron sitting on a variety of substrates (*i.e.* Glacial, fluvial and lacustrine). In the summer months, supraglacial meltwater can form complex meltwater channels draining down valley.

2. Piedmont glaciers. Large coastal ice fields feeding several broad lobes up to 4km wide into ice free valleys (*e.g.* Wilson Piedmont Glacier feeding the Victoria Lower Glacier in the MDVs). The ice margins are usually a mixture of morphologies, from vertical faces to low gradient ramps that rest on a variety of substrates and have complex ice cored moraines and meltwater channels at the margins.

3. Outlet glaciers that drain ice sheets *via* deeply incised channels or relict glacial valleys (*e.g.* Byrd Glacier in the TAMs). While having cold-based margins, some outlet glaciers have ice thick enough (>1000 m) in sections of their central trunks to reach pressure melting point and thus be warm-based. Typically the glacier margins are resting on bedrock or pre-existing glacial material and display a variety of morphologies, from vertical faces to ice sublimating ramps. Given the large catchment areas that feed outlet glaciers, they are particularly dynamic and show larger scale advances and retreats compared to alpine glaciers.

It is the outlet glaciers that are of particular interest in reconstructing past ice sheet dynamics within the TAMs. Elevation changes of East and West Antarctic ice causing the outlet glaciers draining into the RSE to display a number of characteristic behaviours. During glacial maxima, the ice surface of TAM outlet glaciers responded by:

- A major thickening in the lower to middle sections. As grounded West Antarctic ice advanced past the mouth of the outlet glacier, discharge was dammed and caused a wave of thickening to propagate up glacier.
- A minimal or even a reduction of ice in the upper parts of the glacier due to changes in the EAIS.
- A decrease in the steepness of the glacier profile as upper parts remain unchanged (or lowered), while lower parts thickened.

The majority of TAM outlet glaciers display a characteristic ice surface profile change during the LGM. Figure 3.9 shows the typical asymmetric thickening observed in reconstructed profiles for the Darwin, Beardmore and Scott glaciers; negligible change at the EAIS catchment and up to 1000 m of ice thickening at the confluence with the WAIS. This behaviour is supported by both glaciological models (Anderson et al., 2004; Golledge and Levy, 2011; Johnson and Staiger, 2007; Riger-Kusk, 2011) and terrestrial evidence (Ackert and Kurz, 2004; Bockheim et al., 1989; Bromley et al., 2012, 2010; Denton et al., 1989a; Marchant et al., 1994; Todd et al., 2010).

As the 'swinging gate' of Conway et al. (1999) retreated back to the Siple Coast, the buttressing effect of grounded ice was removed and glacier profiles gradually returned to an equilibrium position. The initial deglaciation of the northernmost outlet glaciers is thought to have started at 12.9 ka BP (Conway et al., 1999) and is still continuing today at the Reedy Glacier (a thinning of <0.02 m a^{-1}), the southernmost outlet glacier (Todd et al., 2010). While the Reedy Glacier may still show some continued response to deglaciation, glaciological models for the TAM outlet glaciers, suggest that for the most part, glaciers have reached equilibrium and have been at their current stable position for at least 1 ka (Anderson et al., 2004; Johnson and Staiger, 2007; Todd et al., 2010).

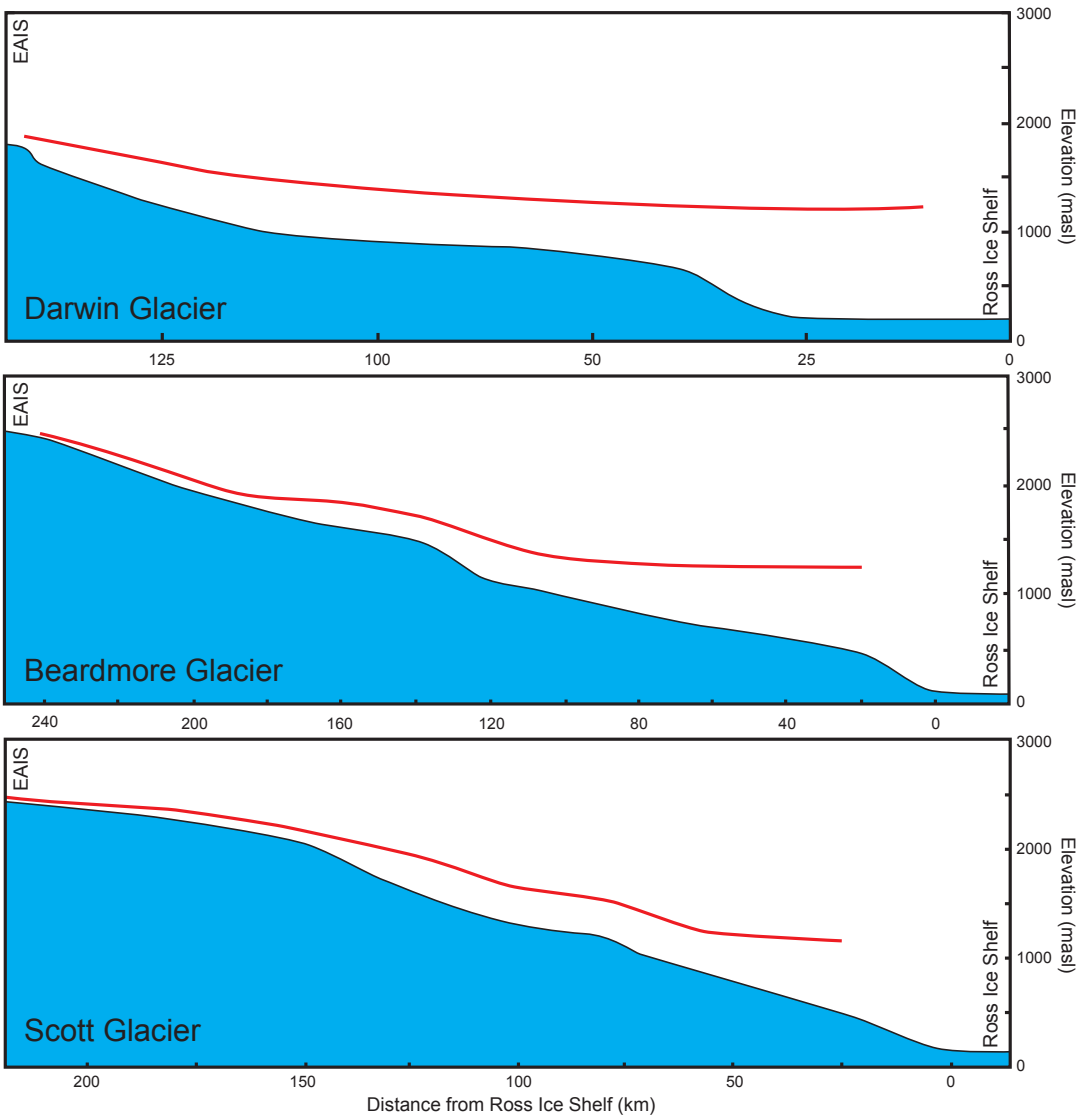

Figure 3.9: Modern and past outlet glacier profiles - Modern (blue) and suggested LGM (red) ice surface profiles for the Darwin-Hatherton, Beardmore and Scott glaciers. Based on a range of geomorphic evidence, the outlet glaciers show similar asymmetric thickening along their length, the maximum LGM ice thickening occurred proximal to the Ross Ice Shelf. Adapted from Bockheim et al. (1989), Denton et al. (1989a) and Bromley et al. (2012).

While a lack of data constraining the chronology, particularly in the middle sectors of the TAMs, is problematic, a number of numerical models have still provided insights into the RIS deglaciation during the Holocene (Denton and Hughes, 2000, 2002; Golledge et al., 2012). At the outlet glacier scale, a modelling study for the Darwin-Hatherton glacial system by Anderson et al. (2004) has suggested that a delayed glacier response to WAIS de-buttressing should be taken into account. The RIS grounding line retreating past the entrance to the DHGS as early as 7.9-7.7 ka BP, but the glacier did not return to its equilibrium profile until 6.8 ka BP.

3.3.4 Surface exposure evidence of Quaternary ice sheet behaviour

Until recently, absolute chronologies representing the deglaciation of the Antarctic ice sheets have been generally limited to the LGM and younger. Prior to the mid-1990s, the only suitable geochronological techniques available for geomorphological studies were radiocarbon (^{14}C) and optically stimulated luminescent (OSL) dating. The relative availability of radiocarbon dating, the nature of material to be sampled (*i.e.* lacustrine carbonates & preserved organic material) and the time span of interest led to a number of studies examining the WAIS deglaciation of the Ross Sea Embayment (*e.g.* Bockheim et al., 1989 & Hall and Denton, 2000). Unfortunately, the maximum $\approx$50 ka age range in radiocarbon dating (Reimer et al., 2009) is unsuitable for older glacial material. Thus, material deposited in moraines and drifts prior to the LGM have little to no age control and were mostly constrained by correlations to other similar deposits (*e.g.* Bockheim et al., 1989, Denton et al., 1989b & Moriwaki et al., 1992b).

Given the long history of mapping glacial deposits in the TAMs, surface exposure dating (SED, Chapter 2) has allowed the terrestrial glacial record to be extended back millions of years, making it a valuable tool in understanding the Quaternary behaviour of the Antarctic ice sheets (Balco, 2011). While the early use of SED in the Ross Sea Embayment was focused on dating the Sirius Group and glacial deposits within the MDVs, the use of the technique to constrain pre-LGM ice sheet behaviour was soon recognised. Using transects up valley (*i.e.* with the direction

of advancing ice) and vertically up nunataks and mountain peaks, a correlation between age and elevation can be made. Mackintosh et al. (2007) coined the phrase 'mountain dipsticks' to describe the vertical record of glacial erratics left by thinning ice. The use of SED in Antarctic deglaciation chronologies has also suggested that ice sheet thicknesses at the margins of the EAIS (Lilly et al., 2010; Mackintosh et al., 2007; Todd et al., 2010) and interior of the WAIS (Ackert et al., 2007, 2013) were less than predicted by glaciological models (Denton and Hughes, 2002; Huybrechts, 2002). The differences in suggested ice thicknesses have questioned the magnitude of the post-LGM Antarctic sea level contribution. Over the last few decades, a number of studies have used SED to investigate the older Quaternary glacial history of the East and West Antarctic ice sheets in the Ross Sea Embayment (Figure 3.10).

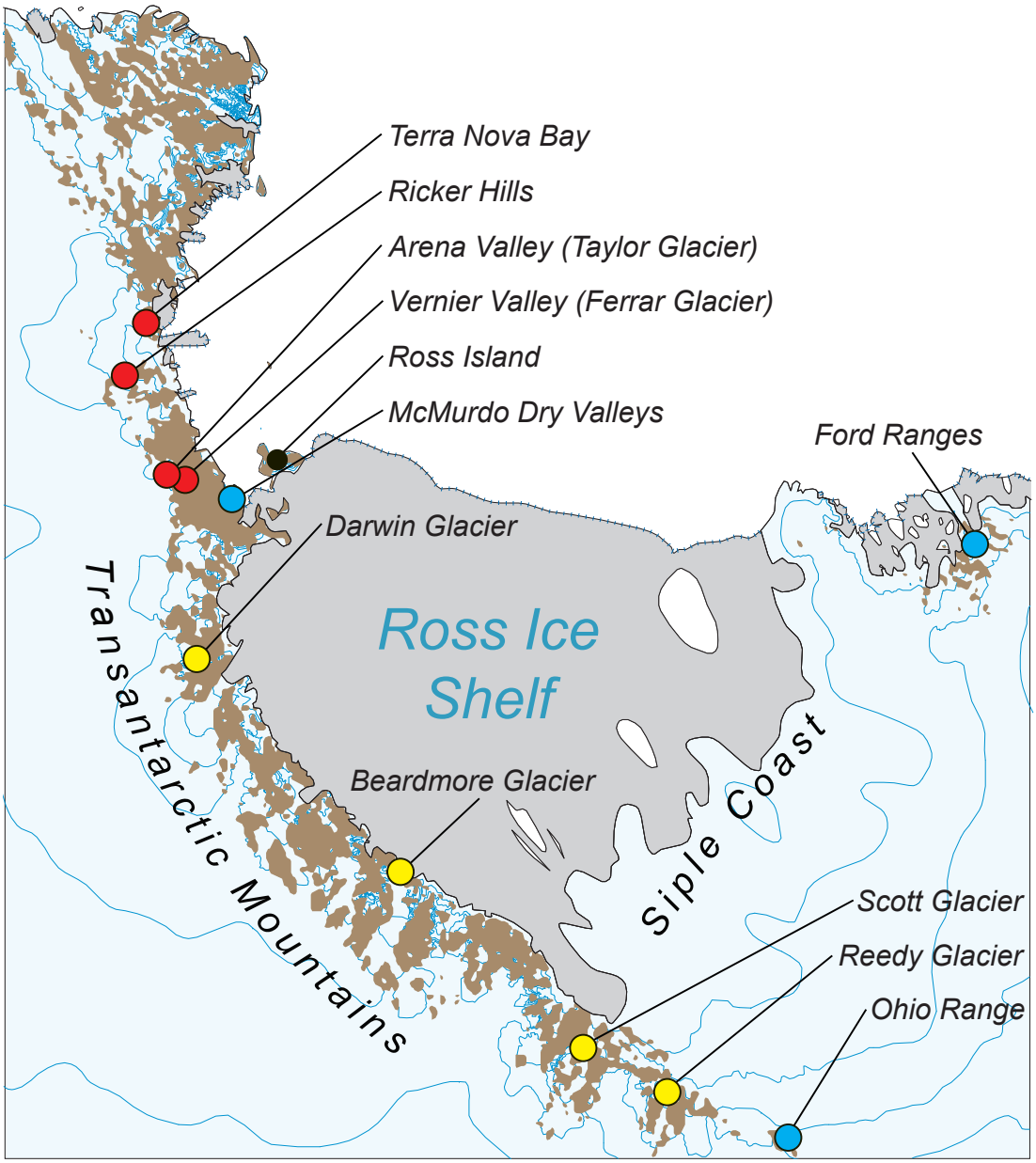

Figure 3.10: SED studies within the Ross Sea Embayment - Sites marked with coloured circles are locations where surface exposure dating has been used to study ice sheet behaviour (Section 3.3.4). The EAIS (red) sites of Vernier (Staiger et al., 2006) and Arena valleys (Brook and Kurz, 1993), Ricker Hills (Strasky et al., 2009) and Terra Nova Bay (Di Nicola et al., 2009). The WAIS sites (blue) are the Ross Sea Drift in the MDVs (Brook et al., 1995b), Ohio (Ackert et al., 1999, 2013) and Ford (Stone et al., 2003) ranges. The TAM outlet glaciers (yellow) of the Reedy (Bromley et al., 2010; Todd et al., 2010), Scott (Bromley et al., 2012) and Beardmore (Stone et al, pers comms).

3.3.4.1 West Antarctica

The Ross Sea Drift (RSD), a distinctive deposit observed on the coasts of the McMurdo Sound (Figure 3.11) was the target for an early surface exposure dating study in Antarctica (Brook et al., 1995b). The primary focus of this work was to revise and constrain the chronology and subdivide the RSD into younger (presumed to be post-LGM) and older deposits in the McMurdo Dry Valleys. The drifts were assumed to show a correlation between age (based on ^{14}C & U/Th dating) and distance from the coast, with the older drift material further up valley than the younger drift. A variety of TCNs were measured in basaltic (using olivine for ^{3}He) and granitic (using quartz for ^{10}Be & ^{26}Al) cobbles and boulders on the drift surface. The SED results ranged from 8-567 ka and while displaying a wide spread in ages, the ^{10}Be results appear to show a differentiation between younger and older units. The younger RSD have ages of 8-106 ka (n=19) and older RSD 104-567 ka (n=7,see Figure 3 in Brook et al. 1995b). Additionally, the mean ^{3}He age for the younger drift is 40 $\pm$ 8 (excluding one sample) and for the older 252 $\pm$ 62 ka. A key site in the Blue Glacier region (see Figure 1 in Brook et al. 1995b) marked the terminal moraine of the younger RSD and has a radiocarbon age of 14.4 $\pm$ 16 cal BP assigned to it (Stuiver et al., 1981). This ^{14}C age, from algal mats within an ice contact delta, is comparable to the SED results of Brook et al. (1995b); with mean ages of 15 $\pm$ 3 (^{3}He), 14 $\pm$ 2 (^{10}Be) and 16 $\pm$ 2 ka (^{26}Al). In both the younger and older RSD deposits, Brook et al. (1995b) suggested the spread of ages may represent multiple periods of glacial advance with the ice margin fluctuating in and out of the valley mouths instead of a single period of grounded ice. The importance of the RSD as an indicator of LGM ice limits within the McMurdo Sound region has been the focus of recent SED studies. Although still unpublished, the exposure ages from the University of Otago (NZ) and ANSTO, have shown a clear Holocene deglaciation with ^{10}Be ages of 5-9 ka (Fink, pers comms).

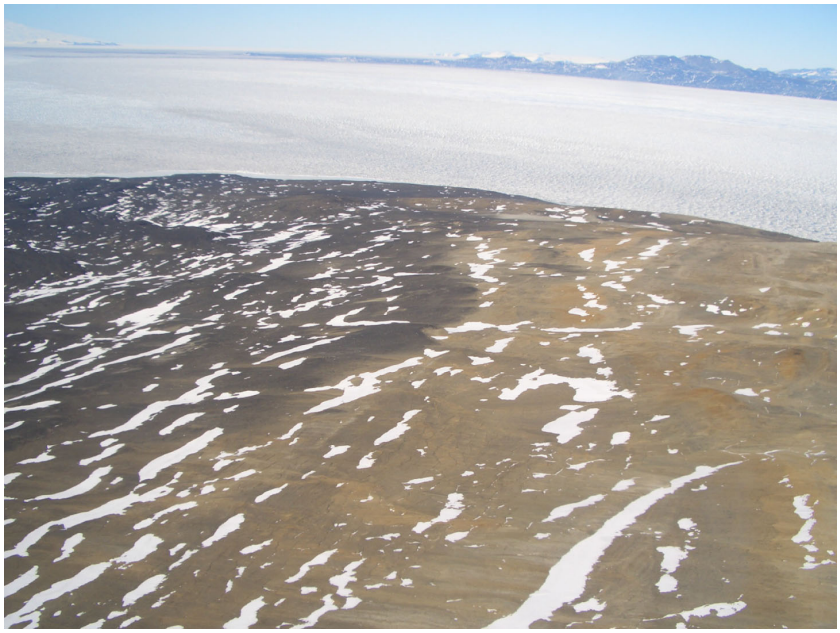

Figure 3.11: Ross Sea Drift at McMurdo Sound - The basalt rich Ross Sea Drift (darker material) deposited over granitic bedrock at the mouth of the Garwood Valley. The younger (LGM) RSD is the darkest coloured material to the far left and lies at a lower elevation to that of the older drift.

Away from the ice shelf and near to the northern tip of the Siple Coast in Marie-Byrd Land, Stone et al. (2003) investigated WAIS deglaciation in the Ford Ranges (Figure 3.10). The location, close to the northern margin of the ice sheet comprises a series of mountain peaks running inland from the coast into the WAIS (≈80 km). At seven of these nunataks (see Figure 1 in Stone et al. 2003), glacial material at elevation above the modern ice surface was sampled for SED. The ^{10}Be ages clearly show a trend of decreasing ice volume over the last 10 ka, however a small number of older samples (95-112 ka) outside this trend are assumed to be caused by prior exposure and therefore TCN inheritance. The SED ages suggest that the exposed upper parts of the Ford Ranges became ice free within the last 11 ka and as the height of the West Antarctic ice surface during its LGM expansion exceeded that of the highest elevation peaks, the upper limits of the LGM WAIS could not be ascertained. The data of Stone et al. (2003) suggested that proximal to the coast, the WAIS was at least 700 metres above its present level and that ≈80 km inland, the level was only ≈200 metres above present.

The results of Stone et al. (2003) differed considerably to the earlier work of Ackert et al. (1999). At Mt Waesche (≈400 km southeast of the Ford Ranges), maximum WAIS elevations were only 75 metres above the present ice surface and SED ages suggested that ice sheet thinning started at ≈10 ka. To understand the behaviour of the interior (as opposed to the coastal) parts of the WAIS, Ackert et al. (2007) used sites in the Ohio Range, 1000 km south of the Ford Ranges and located close to the WAIS ice divide. The results suggested only limited ice overflowing from the EAIS, therefore inferring that glacial material deposited at elevations above the modern ice surface was purely from the WAIS. The ^{10}Be and ^{3}He ages showed a WAIS ≈125 metres above present and thinning by ≈11.5 ka. As with Stone et al. (2003), Ackert et al. (2007) also recognised that due to the low Antarctic erosion rates and glacial recycling of pre-existing material, that the possibility of older ages (*i.e.* previously exposed material) may be expected. Thus only the youngest exposure ages at a given elevation were used. The exposure ages and reconstructed ice surface of Ackert et al. (2007) disagree with the glaciological models of Denton and Hughes (2002) in which a LGM WAIS thickening of 400 metres was suggested for the area. Ackert et al. (2013) revised their earlier work in the interior of the WAIS and combined it with the glaciological model based on the work of Pollard and DeConto (2009). A key finding from this revaluation was that WAIS interior ice elevations during the LGM may have been similar or lower than present. Additionally, that maximum WAIS thickening occurred during the mid-Holocene (≈5 ka), likely caused by an increase in precipitation. The exposure dataset for both locations (Mt. Waesche & Ohio Range) have an absence of LGM ages, instead clustering around ≈10, ≈40 and ≈80 ka (Ackert et al., 1999, 2007). The studies referred to in this section raise a number of significant points about the LGM dynamics of the WAIS:

1. At the WAIS interior (*i.e.* Ohio Range), LGM ice elevations were not as high as those at the coastal ice margins (i.e. Ford Ranges).

2. The thinning of the WAIS at coastal sites was ≈3 ka earlier than the interior, suggesting that ice was still thickening at interior sites after coastal sites were retreating.

3.3.4.2 East Antarctica

A number of ice free sites, at the margins of glaciers draining the EAIS, also contain glacial drifts thought to be deposited during the Quaternary. Brook and Kurz (1993) and Brown et al. (1991) investigated one such site, Arena Valley, on the south western flanks of the Taylor Glacier (Figure 3.10). Here a well preserved sequence of drift sheets and moraines demarcates previous advances of the cold-based Taylor Glacier margin. In order of age and distance from the ice margin, these are the Taylor-II, III and IV(a & b). Brook and Kurz (1993) expanded on the earlier results of Brown et al. (1991) with additional ^{10}Be and ^{3}He ages from sandstone clasts collected from the upper moraine contact of each drift sheet. The results show an ^{3}He age range of 0.7-1.3 Ma and may suggest that the Taylor-II ($\approx$113 ka) and III ($\approx$208 ka) were deposited in retreats from the MIS-5e and MIS-7 interglacials ($\approx$130 & 244 ka). Using the upper contact of the Taylor-IVb Drift, a maximum thickening of $\approx$500 metres and for the Taylor-IVa Drift, $\approx$250 metres can be inferred during 0.3-1.1 Ma. As in other Antarctic SED studies, Brook and Kurz (1993) noted that a wide spread in ages exists within drifts and also the different TCNs. The complexity of sampling material deposited at a cold-based margin, the level of reworked material and low erosion rates being the likely causes.

Fifteen kilometres south of Arena Valley, Staiger et al. (2006) used ^{3}He and ^{21}Ne TCNs to understand the past dynamics of the Ferrar Glacier (Figure 3.10). The Ferrar Glacier is connected to Taylor Glacier, but receives the majority of ice flux from the nearby Taylor Dome, only $\approx$80 km from McMurdo Sound. Although Taylor Dome is part of the EAIS, an increase of 100-200 metres is required for ice from the EAIS interior to override Taylor Dome. Therefore, the behaviour of the Ferrar Glacier is more likely to be sensitive to local changes in precipitation, only responding to large scale ice elevation changes of the EAIS (Staiger et al., 2006). Within Vernier Valley, four glacial drift sheets lie parallel to the ice contact margin and within the low elevation valley floor, with the oldest drifts assumed to be furthest from the ice margin. Using material collected from moraine ridges, the ^{21}Ne and ^{3}He results gave ages of 22-51 ka, 260-570 ka, 1.1 and 1.7-3.7 Ma for the four drifts. The SED results suggest an overall thinning of the Ferrar Glacier in Vernier

Valley from a glacial high stand (+125 m) during the Pliocene Climatic Optimum (3-4 Ma), but also does not preclude a fluctuating ice margin during this period. A key observation made by Staiger et al. (2006) was the lack of LGM aged material. One explanation was that the LGM Ferrar Glacier was thinner than its modern configuration and that a Holocene glacial advance buried any evidence of the LGM ice position.

At the Ricker Hills, the Quaternary behaviour and sensitivity of the EAIS to past climate change was the primary focus of Strasky et al. (2009). ^{10}Be and ^{21}Ne SED was used to date glacial material at elevations above the modern David Glacier (See Figures 1 & 2 in Strasky et al. (2009)). A sequence of four glacial drifts were previously described and mapped at the study site, 100 km inland from the RSE and on the margin of the EAIS. Baroni et al. (2008) suggested that the youngest two drifts were Holocene to LGM aged, while the two oldest were deposited during the Pleistocene. The highest elevation drift was observed overriding a warm-based till deposited during the Oligocene (Baroni et al., 2008). While small patches of the Holocene drift were found flanking the modern ice margin, no exposures of the LGM drift was observed. The older Pleistocene deposits being widely distributed within the field area. ^{21}Ne exposure ages for the oldest drifts were 70-120 and 603-900 ka. The erratic boulders within the oldest drift suggest a Pleistocene high-stand, with East Antarctic ice $\approx$500 metres above the present David Glacier at 1.1-1.4 Ma. As the upper limits of the drift coincide with a glacial trim-line and undisturbed deposits of the warm-based till, it would suggest that this level is the maximum achieved during the Pleistocene and that the upper parts of the nunatak have remained ice free since the Miocene.

Di Nicola et al. (2009) applied exposure age dating to the ice free nunataks and peaks found in Terra Nova Bay (Figure 3.10). The upper elevations of Mt Browning and Mt Abbot (760 & 1022 masl) are delineated by a well-defined glacial trimline, suggested to represent the maximum limits of East Antarctic ice. This interpretation is supported by the preserved alpine topography and the lack of glacial erratics above the trimline, while beneath it, a sequence of glacial drifts (Baroni and Orombelli, 1989; Orombelli et al., 1991). A bedrock sample above and glacial erratics below the trimline have ^{10}Be, ^{26}Al and ^{21}Ne exposure ages from 9.2-1891 ka. The bedrock sample from the summit of Mt Abbott has the oldest age of the

dataset at 1.9 Ma, but using a higher erosion rate (0.17 m Ma^{-1}), the age extends out to 3.8 Ma. In contrast, a group of ages strongly cluster around ≈140 ka, while the lowest elevation samples contain the youngest age (9.2 ka) and fit well with the suggested Holocene age for the deposit.

These studies all appear to suggest that the EAIS, at least in the Ross Sea sector of the TAMs, has shown significant thickening during past warm periods. Outlet glaciers draining the EAIS all appear to show an overall reduction in ice volume since the Plio-Pleistocene. LGM deposits are absent at all sites and all show an increase in ice volume during the Holocene, in particular the Ferrar.

3.3.4.3 Outlet glaciers

Only a limited number of studies have used SED to understand glacial response to changes in ice sheet thickness in outlet glaciers along the TAMs. While the work of Todd et al. (2010) and Bromley et al. (2010) at the Reedy Glacier was not the first to use SED in the TAMs, they were the first to use it longitudinally along the entire glacier profile (Figure 3.12). The Reedy Glacier is the southernmost outlet glacier of the TAMs and drains the EAIS into the Mercer ice stream, ≈50 km inland from the WAIS grounding line. Five ice-free areas (in order of distance from the WAIS, Quartz Hills, Caloplaca Hills, Polygon Spur, Mims Spur and Hatcher Bluffs) and five nunataks both proximal and distal from the confluence of the Reedy and the WAIS were visited and samples collected for SED (see Figure 1 in Todd et al. 2010 for a regional map). Within these areas, Bromley et al. (2010) had mapped and redefined a sequence of cold-based glacial drifts originally described by Mercer (1968). From youngest to oldest: the Reedy-III and Reedy-A though E, with ^{10}Be ages ranging from 6.8 ka to 4.9 Ma. The SED ages of Bromley et al. (2010) were focused on the older Reedy drifts and suggest a late Pliocene age for the Reedy E (>5 Ma), found at ≈600 metres above the present ice surface at Quartz Hills and ≈300 m at Polygon Spur. Younger drifts also appear to show a strong age-elevation relationship. The Reedy-D with an SED age of 2.5 Ma, Reedy-C ≈700 ka and the Reedy B 135-166 ka; elevations of the upper drifts limits all decrease with age (Figure 3.12).While older deposits have been used to infer past ice thicknesses

of outlet glaciers, Bromley et al. (2010) suggested an alternative, that the upper margin of the drift sheets does not represent ice thickness. Instead they suggested a combination of glacio-isostatic uplift and coeval down-cutting of the glacier has exaggerated the elevations above the modern ice surface (Section 2.2.3).

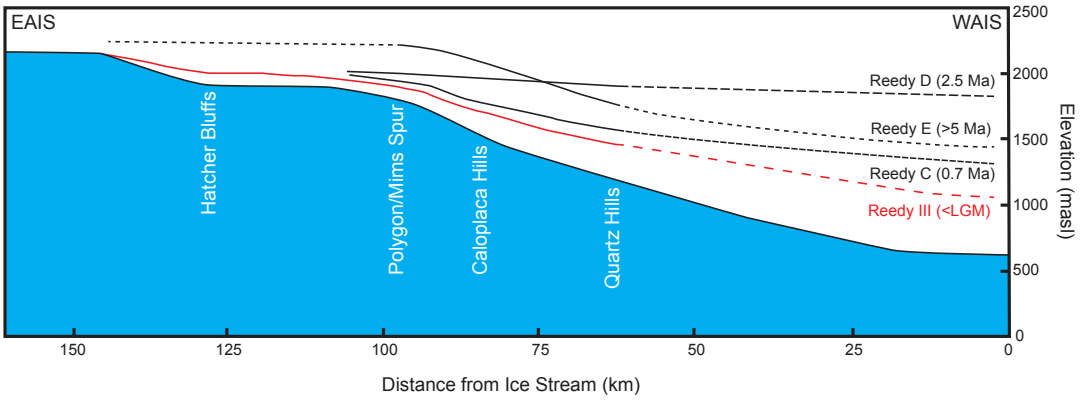

Figure 3.12: Former ice surfaces of the Reedy Glacier - Ice surface reconstructions for the Reedy Glacier based on the glacial drift sequences of Bromley et al. (2010). The blue area represents the modern ice surface, while the red line is the reconstructed LGM surface based on the Reedy III Drift (Todd et al., 2010). Dashed lines are extrapolated surfaces based on the last available piece of available geological evidence (Quartz Hill in most cases). Note that the Reedy B surface has been omitted for clarity.

Aside from the work of Bromley et al. (2010), which concentrated on mapping and dating the older drifts, Todd et al. (2010) examined the Reedy-III, the youngest of the drifts and assumed to have been deposited during the retreat of the WAIS post-LGM. As with the LGM profile of the Hatherton Glacier by Bockheim et al. (1989), the WAIS thickness in the lower regions of the glacier has been extrapolated downstream from the last piece of geological evidence. In the case of the Reedy Glacier, from the Quartz Hills, located mid-way down the length of the glacier (see Figure 1 in Todd et al. 2010). The exposure ages of Todd et al. (2010) from the Reedy-III show that the LGM WAIS had thickened by 450-800 metres and had propagated back midway into the glacier (Quartz Hills, see Figure 3.12). The maximum ice elevation (1060-1400 masl) is lower than the 1700 masl suggested for the area by Denton and Hughes (2002) and Huybrechts (2002) and suggests an over estimation of modelled West Antarctic ice volume. West Antarctic ice in the lower parts of the Reedy Glacier (inferred from Quartz Hill) is thought to have

reached its maximum thickness prior to 17 ka, staying at this level for at least 3 ka, but thickening throughout the glacier did not occur at the same time. The maximum ice elevation was reached later with proximity to the EAIS, 14.7-10 ka at Caloplaca Hills, 9.1-7.7 ka at Mims Spur and ≈7.7 ka at Hatcher Bluffs. At the closest site to the EAIS (Hatcher Bluff) ice was only a maximum of 60 metres above the modern glacier at the LGM. Todd et al. (2010) suggest that at the LGM a grounded WAIS caused a wave of thickened to propagate upstream, but ice at the head of the glacier was thinning due to reduced EAIS accumulation. During the Holocene the reverse occurred, as the WAIS grounding line moved south and Reedy Glacier ice thinned, while an increase in EAIS accumulation may have caused thickening in the upper parts of the glacier, removing any evidence of the LGM ice limits. The exposure ages suggest that rapid deglaciation has occurred in the lower parts of the Reedy Glacier, with ≈100 metres of loss since 7-8 ka. Additionally, material collected at the very margins of the Reedy Glacier mouth show only a 20 metre drop in the ice surface over the last 1 ka.

A number of other research programs continue to use SED ages to examine the LGM evolution of outlet glaciers at the Beardmore and Scott glaciers (Figure 3.10). Tentative results from the Beardmore Glacier (Stone et al, pers comms) have suggested that Mt Hope (900 masl), a nunatak at the mouth of the glacier was overridden by ice during the LGM, providing a minimum elevation to the 1250 metres of thickening suggested in this region of the TAMs (Denton et al., 1989a). South of the Beardmore at the Scott Glacier, Bromley et al. (2012) have described and mapped glacial drifts observed at the flanks of the glacier. Unfortunately SED results from this location have not yet been published (Stone et al, in prep), therefore drift ages are predominantly based on clast weathering and morphology similar to the approach of Bockheim et al., 1989) and correlation to other similar deposits (*i.e.* the Reedy-III to the Ross Sea Drift).

The studies reviewed here allow several conclusions to be drawn about the use of the SED technique in Antarctic ice free environments, particularly at cold-based margins

- The high percentage of material with prior exposure.
- Judicial sample collection and interpretation of exposure ages.
- The strength of the technique in unravelling ice sheet histories beyond that possible by radiocarbon dating (≈50 ka).
- The use of dual-nuclides for identifying those samples with complex burial histories.

Furthermore, the reviewed studies collectively provide important information for constraining the Cenozoic behaviour of the WAIS and EAIS in the RSE. Important points that are especially pertinent for studying the DHGS are:

- The LGM EAIS was similar sized or smaller than present.
- EAIS thickening during the Holocene due to increased accumulation rates.
- Significantly elevated EAIS ice surfaces during the Pleistocene.
- A significantly thickened WAIS during the LGM.
- The interior parts of an LGM WAIS may have been thinner than present.
- WAIS thickness along the TAMs are overestimated in a number of numerical models

Chapter 4

The Darwin Hatherton glacial system

The Darwin Hatherton glacial system (DHGS) is a medium-sized outlet glacial system located within the Transantarctic Mountains (TAMs) at 80°S, 160°E. Two major glaciers, the Darwin Glacier and its smaller tributary, the Hatherton, drain the high elevation plateau of the EAIS (≈2200 masl) into the low elevations of the Ross Embayment (≈80 masl) (Figure 4.1). The system is not only one of the largest ice-free areas outside of the McMurdo Dry Valleys (MDVs), but also contains a suite of well-preserved glacial deposits used as evidence of former ice sheet extent (Bockheim et al., 1989). As the terrestrial records of EAIS and WAIS dynamics are rare, usually limited to ice-free mountainous and coastal regions, the DHGS is a key site for validating ice sheet models in this sector of the TAMs (Denton and Hughes, 2002).

Historically, the area has been visited regularly since its initial survey by the Commonwealth Transantarctic Expedition in 1958 and has been the focus of a number of diverse scientific studies: glacial geology (Bockheim et al., 1989; Denton, 1979), soil chemistry (Aislabie et al., 2012), glaciology (Anderson et al., 2004; Hughes and Fastook, 1981), regional climate (Zawar-Reza et al., 2010), meteorite falls (Kamp and Lowe, 1982; Kirkbride et al., 1991) and terrestrial ecosystems (Howard-Williams et al., 2010; Magalhaes et al., 2012).

4.1 Regional setting

The outlet glaciers of the TAMs lie in a unique position bridging a geological and morphological barrier between East and West Antarctica. The initial tectonic formation of the TAMs is thought to have begun at ≈55 Ma and continued throughout

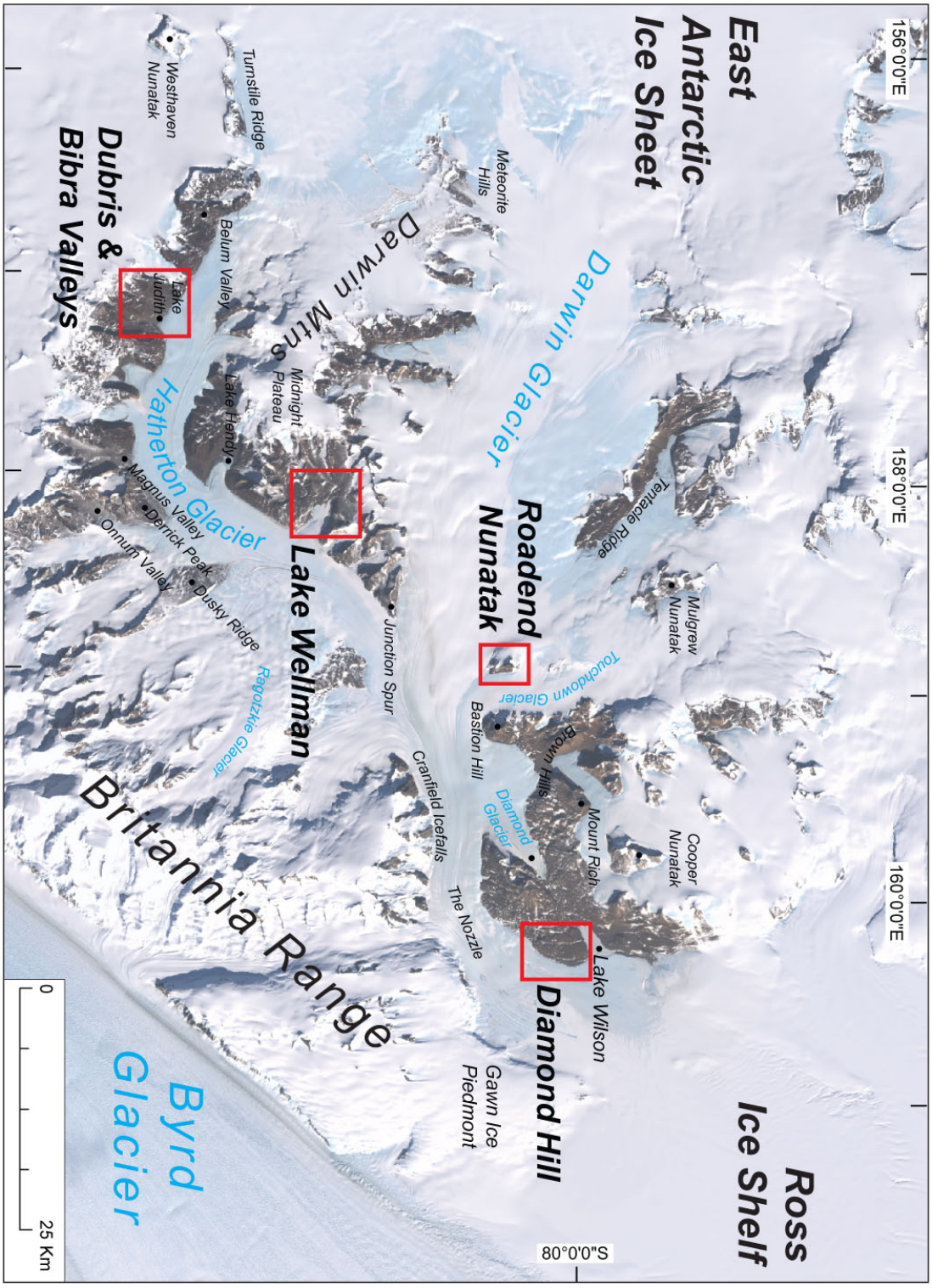

Figure 4.1: Regional map - The Darwin Hatherton glacial system. Areas outlined in red are the study sites discussed in chapters 5 (Dubris Valley Area), 6 (Lake Wellman) and 7 (Diamond Hill and Roadend Nunatak).

the Eocene/Oligocene (Barrett et al., 1991; Fitzgerald, 1992). An early hypothesis by Denton (1979) for the evolution of Darwin-Byrd region, suggested that the TAMs were uplifted through a pre-existing ice sheet. Unfortunately, this theory requires the presence of significant ice prior to the uplift, a scenario that glaciological models disagree with. DeConto and Pollard (2003) showed that the formation of the first minor ice sheets in central East Antarctica likely occurred during the Oligocene, although the timing of the initial TAM uplift (≈55 Ma) may not be tightly constrained. Regardless of the mechanism of formation, Denton (1979) observed three major classes of landform in the DHGS:

- Deep incised valley systems that cut across the TAMs and drain ice from the East Antarctic into the Ross Ice Shelf (Figure 4.2A).
- Short valleys with cirque like headwalls that fringe ice covered plateaus. The cirques were formed by a combination of alpine style glaciations and ice advancing over dolerite escarpments (Figure 4.2B).
- Isolated nunataks. Horn or tabular shaped exposures of granite or dolerite (Figure 4.2C).

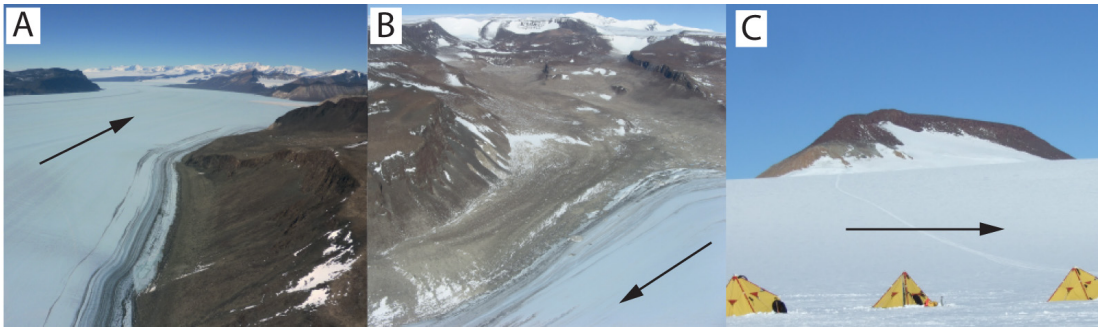

Figure 4.2: Major landscapes of the DHGS - (A) Deeply incised central trunk of the Hatherton Glacier. Looking east towards Derrick Peak. (B) Oblique view of the Dubris Valley and it's cirque headwall within the Britannia Range display the typical morphology of the flanking ice-free valleys. (C) The exposed bedrock of Roadend Nunatak, Darwin Glacier in the foreground. Arrows indicate direction of ice flow.

This combination has resulted in a landscape typical of those that flank the outlet glaciers of the TAMs. In the case of the DHGS, 4000 km^2 of ice-free plateaus and valleys that contain evidence of the past glaciological and climatic conditions of the region.

4.2 Geology of the Transantarctic Mountains

The geometry of the Antarctic continent has been predominantly driven by changes in both geographic position and configuration of its plate boundaries since the breakup of Gondwana (Fitzgerald, 2002). The movement of the continent to its present position and the opening of the Drake Passage have led to the thermal isolation of the landmass. This combination has created the climatic conditions observed today, that of a hyper-arid polar desert (Lawver et al., 1992). Therefore the geology of the Transantarctic Mountains (TAMs) is intrinsically linked to the tectonic and climatic evolution of the continent and in particular the Ross Sea Embayment (RSE, Section 3.3).

The TAMs are one of the largest mountain ranges on Earth, stretching approximately 3500 km across the continent and reaching elevations of up to 4500 masl. Located on the margin of the West Antarctic rift system, the TAMs are comprised of series of asymmetric tilt blocks with sizes in the order of several hundred kilometres long, divided by grabens and transfer faults (Fitzgerald, 2002). In the Darwin Glacier section of the TAMs, Haskell et al. (1964) and Grindley and Laird (1969) mapped three primary groups of rocks in addition to what they interpreted as Quaternary surficial deposits. The composition of these Quaternary glacial drifts (Section 4.6.1) reflects the distribution of various bedrock lithologies. In the lower sections of the DHGS, proximal to the Ross Ice Shelf, bedrock is predominantly granitoids of the Granite Harbour Intrusives, while at the confluence of the Darwin and Hatherton glaciers; Ferrar dolerite dominates as the major outcropping lithology. Outcrops of Beacon sandstone are limited to relatively thin lenses within the upper parts of the Darwin Mountains and Britannia Range (Grindley and Laird, 1969; Haskell et al., 1964) (Figure 4.3).

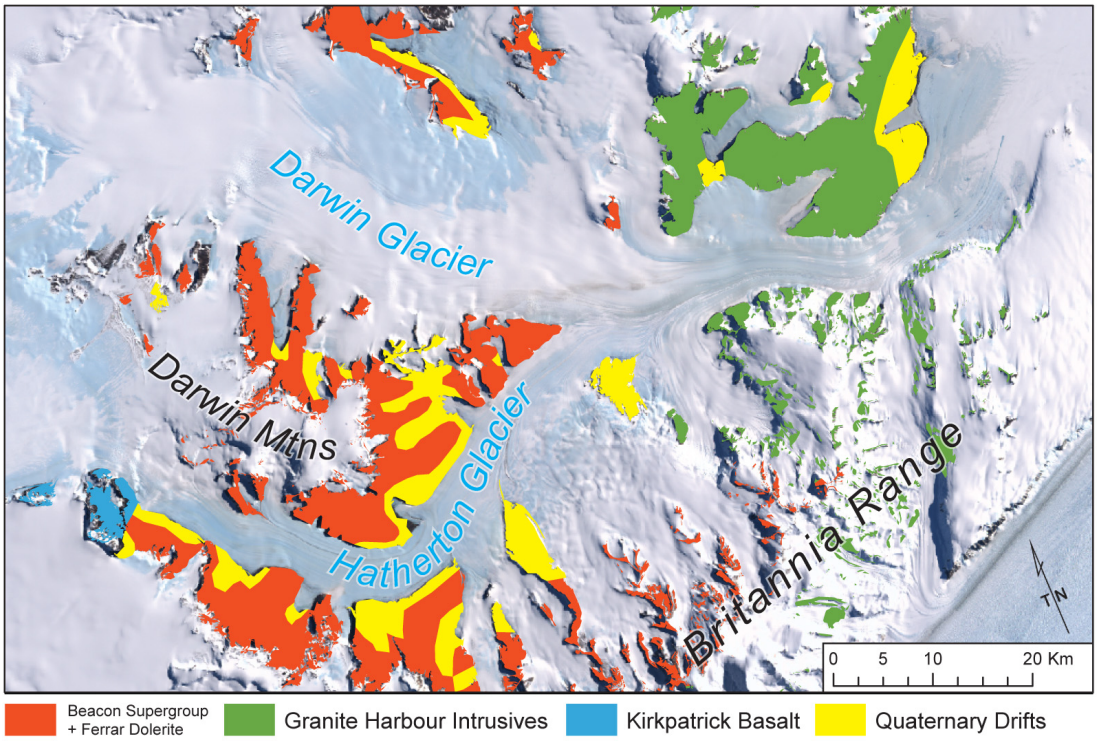

Figure 4.3: Geology of the DHGS - Regional map of the DHGS showing the distribution of the major lithologies. Granitoids (green) are the predominant lithology to the east, while dolerite and limited exposure of sandstone to the west (red). The distribution of bedrock plays a key role in composition of the Quaternary drifts (yellow) found throughout the DHGS. Adapted from Grindley and Laird (1969).

4.2.1 Granite Harbour Intrusives

During the period of mountain building known as the Ross Orogeny, Cambrian aged granitoids were intruded by multiple plutons producing a mixture of metamorphic and igneous lithologies (Federico et al., 2006). These rocks, known as the Granite Harbour Intrusives, are the underlying basement geology of the DHGS. The upper contact of the basement is an erosional surface formed during the uplift of the TAMs, when a 100 My period of regional erosion formed the Kukuri peneplain (Fitzgerald, 2002). This unconformity is overlain by lithologies of the Beacon Supergroup.

Located in the lower parts of the DHGS, the Granite Harbour Intrusives outcrop at Diamond (Figure 4.4A) and Bastion hills, the southern flanks of the Britannia Range and Cooper Nunatak. As well as bedrock exposures, the Granite Harbour

Intrusives are also commonly found as clasts within drift sheets. While extremely common throughout the lower sections of the DHGS (Figure 4.4B), granitic material is rare in the drifts of the upper DHGS. The Granite Harbour Intrusives were subdivided geochemically by Simpson and Cooper (2002) into the Darwin calcic suite, the Cooper granodiorite and the Foggy Dog Granite Suite. The rocks are variously described as a mix of medium to coarse grained granites to granodiorites, with an unfoilated to gneissic banding. At Diamond Hill the lithology is also found commonly with extensive veins of quartz and in places, pegmatite feldspars are present.

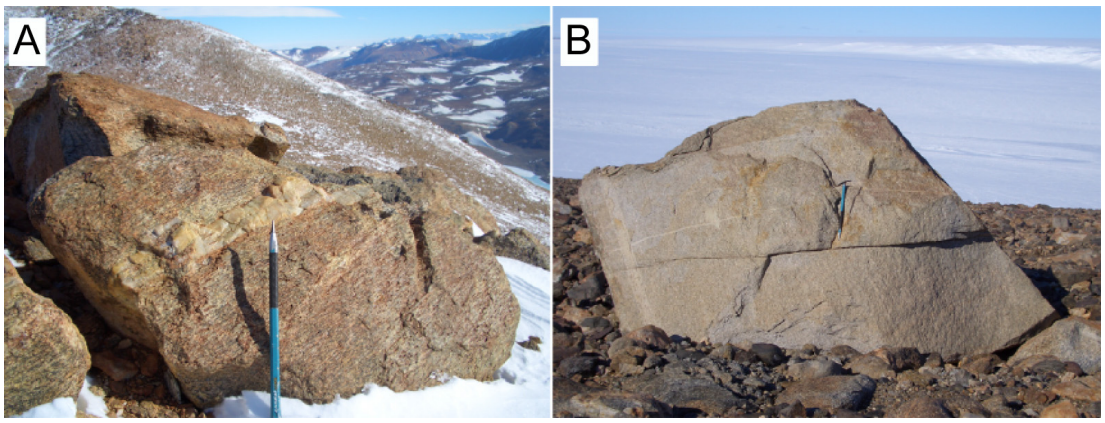

Figure 4.4: Granite Harbour Intrusives - Examples of the varied lithologies within the GHI observed in the eastern parts of the DHGS. (A) Coarse grained bedrock exposure, with quartz vein (≈20 cm wide) near the summit of Diamond Hill. (B) Large (<3 m) fine-grained erratic emplaced on older granitic drift at Diamond Hill.

4.2.2 Beacon Supergroup

The Beacon Supergroup has a maximum thickness of ≈3 km and contains a number of lithologically diverse members. In the Darwin Mountains, Haskell et al. (1964) identified fluvio-glacial tills, coal measures and sandstones ranging in age from the Devonian to the late Permian (Figure 4.5A). Clasts and boulders of Beacon (or Hatherton) Sandstone, a sub group of the Beacon Formation, are commonly observed within the glacial drifts of the DHGS, predominantly in the upper parts of the Hatherton Glacier (Figure 4.5B). The sandstone is described as a orthoquartzite containing additional secondary quartz and originally deposited in a

combination of fluvial, lacustrine and sub-aerial environments (Woolfe, 1993). In outcrops and boulders cleaved along bedding planes, cross-bedding structures and abundant trace fossils (*i.e. Beaconites antarcticus*) are also observed (Barrett et al., 1971). The rock is highly visible within drifts, due to its characteristic light colour, especially when emplaced as glacial erratics on bedrock exposures of dolerite. As the sandstone has an extremely high level of quartz (>95%) it makes an excellent target material for surface exposure dating (Chapter 2).

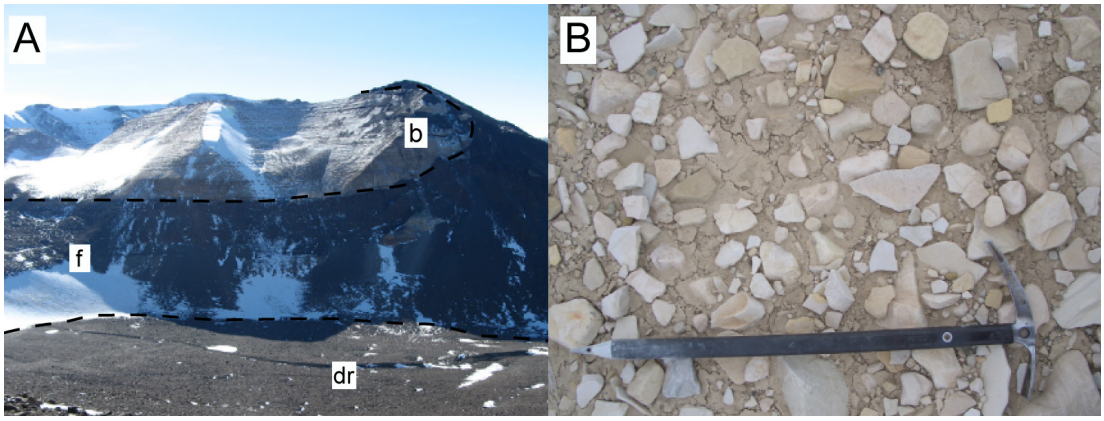

Figure 4.5: Beacon Sandstone - (A) Exposure of Beacon (b) at Lake Wellman, clearly shown intruded by a dolerite sill (f). The lower valley floor is draped with glacial drift (dr). (B) Hatherton Drift at the mouth of the Dubris Valley is comprised entirely of Beacon clasts.

4.2.3 Ferrar Dolerite

A widespread flood basalt province, dated at 177 $\pm$ 2 Ma and attributed to the Gondwana breakup, produced the intrusive Ferrar Dolerite and its extrusive counterpart the Kirkpatrick Basalt (Heimann et al., 1994). Within the TAMs the Ferrar is a distinctive lithology, observed as an extensive network of large, semi-horizontal sills and dykes intruding though the Beacon Supergroup and to a lesser extent, the basement. The dolerite is described as a fine-grained mafic lithology, containing augite, pigeonite and plagioclase in a quartz, K-feldspar and Fe-Ti oxide matrix (Morrison and Reay, 2004). The Ferrar has a distinctive outcrop distribution within the DHGS. Exposed outcrops and nunataks to the west of Junction Spur are predominantly Ferrar (Figure 4.6A), with only thin lenses of both Beacon Sandstone and the Misthound Coal Measures observed in some escarpments (Haskell

et al., 1964).The Kirkpatrick Basalt only occurs in a small region within the western Britannia Range. The Ferrar Dolerite is also commonly observed in glacial drifts throughout the DHGS. Cobbles and boulders of varying sizes (0.1-5 m) are found emplaced as glacial erratics within all drift sheets, regardless of age (Figure 4.6B).

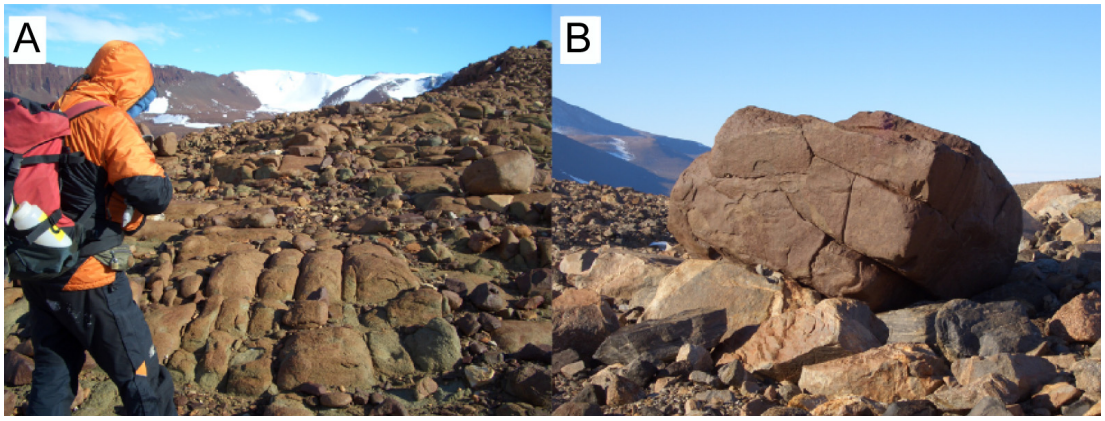

Figure 4.6: Ferrar Dolerite - (A) Weathered bedrock exposure on the Danum Platform. Large columnar escarpments (≈200 m high) are visible on the upper left of the photo. (B) Dolerite erratic emplaced on granitic bedrock at Diamond Hill.

4.3 Climate

The ice-free areas of the TAMs, such as the McMurdo Dry Valleys (MDVs), are known to be an environment of extremes. Classed as hyper-arid cold polar deserts, the MDVs have low relative-humidity, annual precipitation, surface snow cover measurements and are dominated by strong katabatic winds (Marchant and Head, 2007). A strong spatial gradient in meteorological conditions is observed from the high elevation areas close to East Antarctica, to the low elevation coastal parts flanking the Ross Ice Shelf. Wind strength decreases and both relative humidity and precipitation increase with proximity to the coast (Fountain et al., 2009). While the MDVs are one of the most studied locations on the continent, due to both the unique environment and ecosystems (Cary et al., 2010) and have a good modern record of meteorological observations (Doran et al., 2002), the climate of the DHGS is far less understood. Due to a lack of a long term meteorological record, a small number of short to medium term instrumental measurements comprise the

bulk of our understanding of climate within the DHGS. The longest climate record (2004-2011) in the DHGS is from an automated weather station (AWS) installed in the lower section of the Darwin Glacier (Brown Hills)(http://www.lgp.aq). This record was later extended by the addition of a number of short term summer AWS installations by the University of Canterbury (Zawar-Reza et al., 2010).

The instrumental record indicates a climate dominated by topographically controlled katabatic winds, spilling off the East Antarctic Plateau and channelled down-glacier to the Ross Ice Shelf. The Brown Hills AWS (79°50.113S, 159°19.122E, 300 masl) shows a three year (2005-2007) average wind speed of ≈5-10 m s^{-1}, with the strongest winds reaching ≈35 m s^{-1} from a WSW direction (≈250° true degrees) (Figure 4.7A). A strong seasonal signal is also evident during the summer months when the katabatics weaken, coinciding with an increase in the frequency of low velocity north-easterlies (Figure 4.7B). Temperature at the Brown Hills site is also seasonally variable, reaching as high as +5°C in summer, while in winter, temperatures of -40°C are not uncommon (Figure 4.7C). The temperature differential between upper and lower parts of the DHGS may also be reflected in the availability of free water. Glacial meltwater is scarce in the upper parts of the Hatherton Glacier, while lower parts of the Darwin Glacier, particularly Diamond Hill, ponds and pools are common.

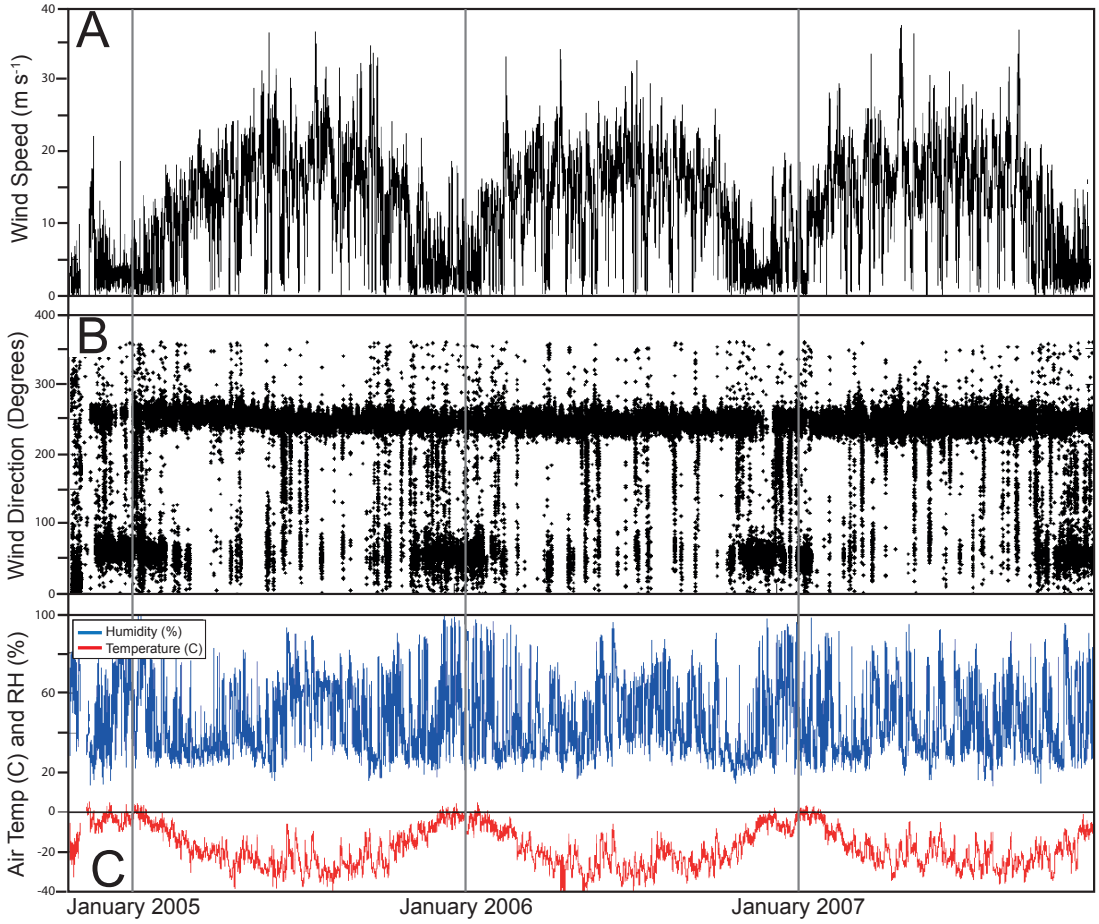

Figure 4.7: 2005-2007 climate data for the DHGS - Data from the Brown Hills AWS in the lower DHGS. Clear seasonal trends are observed in (A) Wind speed (m s^{-1}), (B) Wind direction (true degrees) and (C) Relative Humidity (%, blue) and Air Temperature (°C, red). Compared to winter, summer periods show warmer temperatures, lower wind speeds and a switching east-northeast to westerly wind direction. Data from http://www.lgp.aq.

4.4 Weathering features

Due to the nature of the ice-free Antarctic desert environment, a combination of low relative humidity and surface moisture leads to extremely low erosion rates of 0-0.7 m Ma^{-1} (see Section 2.2.4 for a discussion) and thus the exceptional preservation of small scale glacial features. Therefore the relationship between the environment, climate and geomorphic processes that led to the distinctive styles of weathering observed in ice-free areas such as the DHGS must be understood. This is especially important when applying a technique such as surface exposure dating (Chapter 2), in which erosion plays a key role in reducing the concentration of radionuclides on a surface (Gosse and Phillips, 2001).
Weathering in polar regions has previously thought to have been based on a number of key tenets, that:

1. Mechanical weathering, especially freeze-thaw, is the major process and inhibited by low temperatures.

2. Chemical weathering is only a minor contributor, if at all (Elliott, 2006).

3. A number of minor processes also contribute to weathering, in particular: physio-mechanical processes, such as salt weathering and wind erosion are aided by physio-chemical reactions such as hydration, hydrolysis and redox (Goudie, 1994)

Hall et al. (2002) suggested that this is a simplistic way of viewing the situation and that the spatial and temporal variation of available moisture may also be a key factor. As observed in high temperature deserts, chemical weathering is limited by lack of moisture, not by temperature. Therefore the rocks within the DHGS, in which climate is dominated by strong katabatic winds and low temperatures, primarily weather from thermal stress and rare freeze-thaw cycles. Additional chemical weathering processes may also play a limited role in sites where moisture is available.

A number of distinct styles of weathering products observed throughout the landscape of the DHGS are created by these processes and can be interpreted as indicators of past and present climate.

4.4.1 Fracturing by freeze-thaw and thermal stress

As one of the principal methods of mechanical erosion, freeze-thaw occurs in environments where temperature gradients cross the freezing point of water and there is an availability of surface moisture. The formation of ice generates, or propagates, macro to micro scale fractures within a rock surface and the subsequent cycles of freeze-thaw continues the weakening process (Matsuoka and Murton, 2008). In low temperature polar deserts, like those of the TAMs, it has been suggested that freeze-thaw would be inhibited by the lack of moisture (Hall, 2004). The work of Matsuoka et al. (1996) in the Sør Rondane Mountains, suggest that while the majority of mountainous ice-free areas were too arid to support freeze-thaw processes, there was enough moisture within small micro-climatic zones. These were identified as:

- Rock walls adjacent to snow packs.
- Areas proximal to pond and lake margins.
- Till material (<0.2 m thick) on ice cored moraines.

As the distribution of these zones may be limited within Antarctic ice-free areas, the process of thermal stress may be an important alternative to explain the variety of rock fracturing features observed away from the DHGS ice margins. Thermal stress occurs when a high temperature gradient exists between the rock surface, heated by solar radiation and the thermally isolated subsurface, causing differential expansion of minerals. As quartz has a thermal expansion twice that of feldspars (Ishimaru and Yoshikawa, 2000), the quartz rich (>50%) sandstones and granites occurring in the DHGS would be especially susceptible to this form of weathering, The erosion of a rock surface by thermal stress can occur *via* two principal drivers (Elliott, 2006):

1. Thermal fatigue. Caused by gradual cycles of heating and cooling.

2. Thermal shock. Caused by rapid changes in temperature.

While thermal stress and freeze-thaw may be caused by different environmental mechanisms, the expansion and stress in a rock produces similar weathering products; macro and micro scale fracturing along bedding and cleavage planes.

Observed throughout the DHGS are rocks shattered and fractured in this style, found in a variety of climatic micro environments, both distal and proximal to the ice margin (Figure 4.8A & 4.8B). Sites near the ice margins, or within the Hatherton Drift (Section 4.6.1.1) can be moisture rich, with low elevation coastal sites (*i.e.* Diamond Hill) showing relative humidity up to 80-90% even within the winter months (Figure 4.7C). These ice proximal sites along the length of the DHGS, regardless of elevation, generally share common glacio-hydrological features: ponds, lakes, ice cored moraines and lateral meltwater channels. All sources of moisture that in the summer months can be available for freeze-thaw weathering. In sites at elevation above and distal to the Darwin and Hatherton glaciers, arid polar desert conditions are the norm, with moisture sources being limited to snow transported by the westerly katabatics and the resulting seasonal snow melt (Bockheim et al., 1989). Here, thermal stress as a mechanism for weathering is far more likely, given the dry environment (Figure 4.8C).

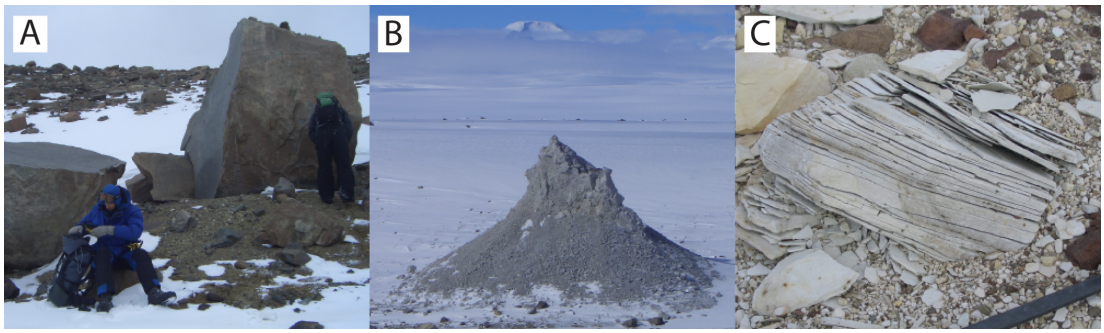

Figure 4.8: Examples of freeze-thaw and thermal stress weathering - (A) Block of granite fractured in half at Lake Wellman. (B) Large block (≈10 m high) of sandstone weathered in place on the surface of Lake Wellman with a distinct debris cone forming around base. (C) 'Playing card' thermal fracturing of sandstone within the Danum Drift at Dubris Valley.

4.4.2 Tafoni weathering

Tafoni, also known as cavernous weathering, is identified by its distinctive irregular cavities, arches and curved surfaces (Jennings, 1968). The widespread geographical distribution of tafoni in a variety of substrates and climates, has led to continuing debate about the genesis of the weathering features (Turkington and Phillips, 2004). In cold environments, the mechanical weathering processes controlling initiation and strength of tafoni development have been given as: thermal stress, salt weathering and freeze-thaw (Hall, 2004). It is through a combination of these processes that quartz crystals are preferentially fractured over feldspar, causing the granular disaggregation and exfoliation of the surface structure (French and Guglielmin, 2000). Aided by turbulent winds at ground level, loose material is then removed, causing further mechanical weathering within the cavities and predominantly eroding the underside of boulders (Strini et al., 2008). Given that freeze-thaw is assumed to be the primary method of weathering in polar settings and that the resulting angular fractures are diagnostic of the process, the curved and spheroidal features observed in tafoni seems anomalous. Therefore it has been suggested that freeze thaw may only play a minor role in the fracturing of quartz crystals (Hall, 2004), with thermal stress now commonly cited as the key geomorphic process (Strini et al., 2008). In addition, biological communities, such as endolithic algae and lichen, have also been suggested by Guglielmin et al. (2005); Hall et al. (2008) as playing a role in micro-fracturing.

In Antarctica, tafoni has been observed at many ice-free sites within both mountainous (Matsuoka, 1995; Matsuoka et al., 2006; Mukhopadhyay et al., 2012; Summerfield, 1999) and coastal areas (French and Guglielmin, 2000; Kiernan et al., 2009; White et al., 2009). The key factors linking these areas being: high winds, low temperatures and geology. Granite and sandstone are the predominant lithologies with observed tafoni, with only minor surface pitting (<3 cm deep) observed in dolerite bedrock and boulders.

Tafoni occurring in boulders and bedrock exposures are observed throughout the DHGS, but are increasingly common in the lower parts of the Darwin Glacier, especially at Diamond Hill (Figure 4.9A). Here granite has a pseudo-karst appearance with overhangs, cavities, pronounced weathering pits (up to 0.3 m deep) and show

a distinct reddish coloured weathering rind caused by the oxidation of iron. The amount of tafoni observed at Diamond Hill is unsurprising given that granites seem to be particularly susceptible to this form of weathering (Guglielmin et al., 2005; Una Alvarez, 2008). Well-developed examples, found within similar granitic lithologies, are also observed within the MDVs (Marchant and Head, 2007).

In the upper parts of the Darwin and Hatherton glaciers, exposures of granite are extremely limited, therefore the only examples of tafoni observed are from sandstone erratics and some rare bedrock outcrops. One such feature is found close to Lake Wellman, where a ≈10 m high glacial tor of dolerite, capped with Beacon Sandstone is found exposed at a ridge top (Figure 4.9B). This outcrop appears to have very similar morphology and weathering to that seen in the Dubris Valley area (Figure 4.9C):

- An orange coloured weathering rind (≈3 mm).
- Multiple cavities (<0.4 m) undercutting the upper surface, within which is found a 'rotten' or crumbling under-surface.
- An accumulation of small angular clasts known as 'grus' (French and Guglielmin, 2000) and limited amounts of visible salt efflorescence.

Figure 4.9: Examples of tafoni weathering - (A) Granite erratic at Diamond Hill. (B) Sandstone tor above Lake Wellman. (C) Sandstone erratic on the Danum Platform.

4.5 Glaciology

The Byrd catchment draining through this sector of the TAMs is estimated to have an area of ≈997 Mkm^2, but only a fraction of the ≈30 Gt a^{-1} (Rignot et al., 2008) discharge passes through the DHGS, the majority flowing through the Byrd Glacier to the south. Due to subglacial bedrock topography, the size of the DHGS catchment is estimated to be 9150 km^2 (Riger-Kusk, 2011). This value, based on the 1 km^2 digital elevation model (DEM) of Bamber et al. (2009), is a 15% increase over that used in the earlier glaciological model of Anderson et al. (2004). The maximum elevation of the DHGS, at the margins of the EAIS is ≈2200 masl, while the lowest point, at the convergence with the RIS, is ≈80 masl.

Ice flow from the EAIS is the predominant driver of the system, with the bulk of ice moving though the DHGS and discharging into the floating Ross Ice Shelf, the total ice flux is estimated to be ≈1.03 km^3 a^{-1} (Humbert et al., 2005). An additional small contribution to total discharge is also supplied by minor valley glaciers (*i.e.* the Touchdown & Ragotzkie) draining local mountain catchments into the system.

4.5.1 Ice velocity

The first ice velocity measurements of the DHGS, were undertaken at Junction Spur by Hughes and Fastook (1981). The Hatherton Glacier was measured at 30-50 m a^{-1}, the Darwin Glacier at 40-60 m a^{-1} and a third measurement site at the Nozzle, an area of the Darwin Glacier that narrows downstream of the Darwin and Hatherton glacier convergence, was 110-130 m a^{-1}. A modern glaciological modelling study of the DHGS by Anderson et al. (2004), found that while output velocities compared well to the upstream Darwin Glacier measurement, the Hatherton Glacier results were considerably lower than the physical measurements of Hughes and Fastook (1981).

Differential global positioning system (DGPS) measurements were used by Riger-Kusk (2011) to measure surface velocities in a number of positions within the DHGS. Upstream of Junction Spur, Darwin Glacier velocities were an average of 24 m a^{-1}, while downstream increased to a maximum of 179 m a^{-1} at the nozzle. Once ice had passed this narrow section, velocities slowed at the grounding line of the

Darwin Glacier. Unfortunately, due to a small number of measurements (n=3) and low temporal resolution (three days), measurements from the Hatherton Glacier were less robust, with a range of 2.3-11.8 m a^{-1}.

The differences in velocity and ice flux between the Darwin and Hatherton glaciers is likely caused by the bedrock topography and thus ice thickness within the catchment. Surface and aerial ground penetrating radar (GPR) profiles of the DHGS, show a distinct area of ice thinning at the head of the Hatherton Glacier (Figure 4.10). A subglacial bedrock ridge restricts the Hatherton Glacier to a maximum thickness of <200 metres, effectively reducing ice flow into the glacier. However, the Darwin Glacier has incised a deeper channel (≈1200 m) allowing an increased flow of ice compared to that of the Hatherton. The identification of this bedrock dam in the Hatherton Glacier has implications to its past dynamics, as a decrease in EAIS ice thickness, would starve the glacier of ice flow. This may result in the Hatherton Glacier behaving to changes in EAIS elevation changes differently compared to that of the Darwin Glacier and suggests that Hatherton Glacier dynamics may have been significantly different in the past (Riger-Kusk, 2011).

Figure 4.10: Ice thickness within the DHGS - Aerial and GPR data corrected for firn from Riger-Kusk (2011). Darwin Glacier is the upper and Hatherton Glacier is the lower channel. Area outlined in red marks the subglacial ridge restricting ice flow into the Hatherton Glacier.

4.5.2 Basal conditions

To interpret the ice-free landscapes that flank the DHGS and the drift sequences of Bockheim et al. (1989) (Section 4.6.1), an understanding of the underlying glaciological conditions that control both the flow behaviour and the deposition of glacial sediments is required; a key parameter being the thermal regime of a glacier.

Anderson et al. (2004) produced the first glaciological model to explore the basal properties of the DHGS, suggesting that given the calculated ice thickness that a change from cold to warm-based thermal regimes occurred at the confluence of the glaciers. The inference being that the Hatherton Glacier was predominantly cold-based, while the Darwin Glacier was warm-based.

Both the models of Anderson et al. (2004) and Riger-Kusk (2011) suggested that during the LGM, conditions at the ice-bedrock interface along the length of the DHGS altered and that in the main flow, a combination of warm and cold-based ice existed. Given an accurate snapshot of the bedrock topography and glaciological conditions from the nested model of Riger-Kusk (2011)(Figure 4.11A) a number of conclusions about the present basal conditions within the present DHGS can be made (Table 4.1).

This leads to an interesting scenario. As EAIS and WAIS ice thicknesses are known to have fluctuated in the past (Mackintosh et al., 2011; Pollard and DeConto, 2009), any changes within the DHGS catchment would not only be reflected in the surface elevations of the Darwin and Hatherton Glaciers, but also the thermal regime. This is especially important when considering a situation such as the Hatherton Glacier, a slow moving glacier predominantly controlled by subglacial topography and thus extremely sensitive to changes in ice flux. Modelled outputs for the LGM (Riger-Kusk, 2011) show only minor changes to the Hatherton Glacier, but major alterations to the basal conditions of the Darwin Glacier (Figure 4.11B). As EAIS ice is known to be much thicker in the early Pleistocene than the LGM (Bockheim et al., 1989), a situation may have occurred where increased ice flux and thus ice loading, would cause the Hatherton Glacier to have areas of basal ice above the pressure melting point (Figure 4.11 & Table 4.1). This relationship between ice thickness and basal regime has also been observed at the Ferrar and Taylor

glaciers, where warm-based conditions are found when ice thickness is greater than ≈900 m (Golledge and Levy, 2011; Hubbard et al., 2004).

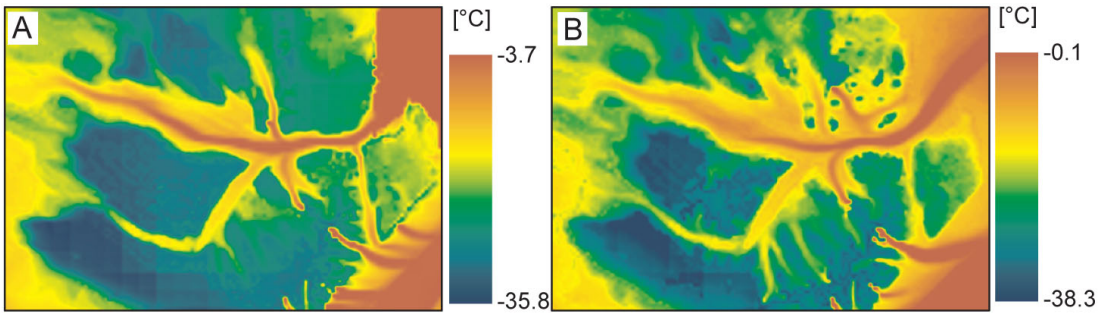

Figure 4.11: Basal temperatures within the DHGS. - (A) Present and (B) LGM basal conditions from the 3D nested model of Riger-Kusk (2011). The Darwin Glacier is the upper and the Hatherton the lower ice flow.

Table 4.1: Present basal characteristics of the Darwin and Hatherton glaciers - Showing the major differences between the two glaciers. From Riger-Kusk (2011).

	Darwin	**Hatherton**
Velocity	High	Low
Temperature	-0.5 to -12°C	-10 to -25°C
Ice thickness	750 to 1200m	200 to 800m
Pressure melting point	Above	Below
Thermal Regime	Warm	Cold

4.5.2.1 Evidence of past thermal regimes

The concept of fluctuating basal conditions in the Hatherton Glacier is also supported by geological evidence that suggest periods of warm-based ice observed in areas that are presently cold-based (Storey et al., 2010). The drifts of both the Darwin and Hatherton glaciers contain a number of classic glacial features created under warm and wet basal conditions. While some studies have shown that erosion can occur in cold-based glaciers (Atkins et al., 2002; Cuffey et al., 2000; Lloyd Davies et al., 2009), the predominant thermal regime for erosional basal conditions are warm-based. When basal temperatures are above the pressure melting point, sliding is the predominant method of glacier movement (Shreve, 1984). When wet basal sediments are overridden by debris rich ice, clast on clast movement leads to

the striating and plucking of material in the direction of ice flow (Benn and Evans, 2006) (Figure 4.12). This typically occurs under conditions of high basal shear stress in fast moving warm-based ice. In the mid to lower parts of the DHGS, elongated and striated boulders as well as glacially polished and striated bedrock exposures are observed at glacier flanking sites. Boulders and bedrock of this nature are a key diagnostic in determining warm basal conditions (Benn and Evans, 2006). While there is evidence that some striations can be produced under cold-based ice (Atkins, 2002; Atkins et al., 2002), such crude cold-based striae are very different from the fine striations generated under warm-based conditions and are not observed in conjunction with the levels of faceting seen in bullet shaped boulders. While extremely rare, striated boulders and bedrock of this nature are found in the DHGS in all lithologies. Figures 4.12A and 4.12B are examples observed within the Britannia and Diamond drifts at the DHGS and display glacially polished surfaces and striations indicating the direction of ice flow. Glacially transported boulders can also show evidence of material removed, or plucked, from their ends by ice, causing angular to sub-angular faceting; a classic lee-stoss asymmetrical clast morphology being produced. While glacial features, such as striations and chipping of edges are well preserved within glacier marginal deposits (*i.e.* Hatherton and Britannia), preservation is extremely low, even non-existent in the older Danum and Isca drifts.

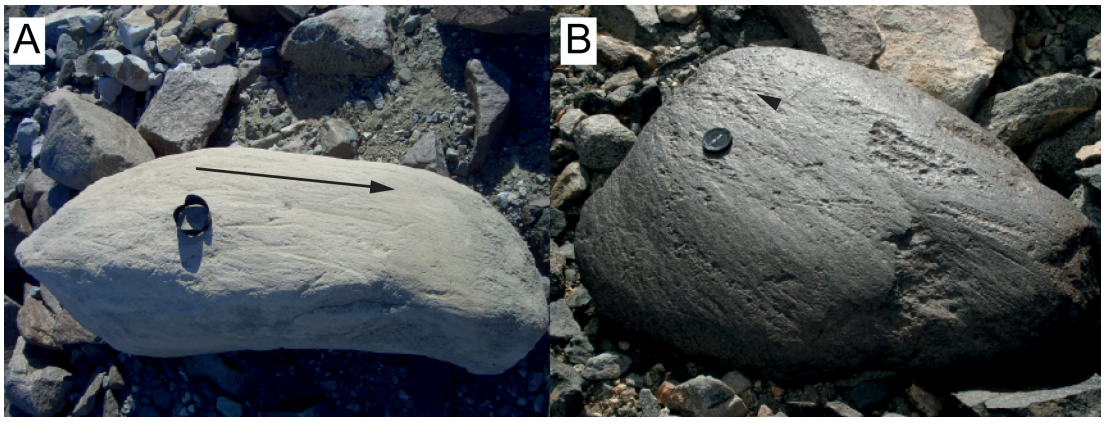

Figure 4.12: Examples of relict boulders - Striated and plucked boulders in the DHGS that are indicative of warm basal conditions. (A) Beacon sandstone in the Hatherton Drift at Lake Wellman. (B) Dolerite within the Diamond Drift at Diamond Hill. Arrows indicated inferred ice flow direction.

Another product of warm basal conditions within the DHGS are exposures of glacial tills. Diagnostic of wet sediment-basal ice interactions, tills are a product of three primary processes: lodgement, sublimation/ablation and deposition (Benn and Evans, 2006). In the TAMs, glacial deposits such as the Ricker Hills Tillite (Baroni and Fasano, 2006) and Peleus Till (Prentice et al., 1993) have been used to infer periods of warm-based glaciation during the Neogene.

At the modern cold-based margin of the Hatherton Glacier at Bibra Valley, large blocks (2-3 m) of frozen till are being deposited at the glacier margin (Figure 4.13A). The till shows a typical bi-modal distribution of grain sizes, with unsorted cobbles and boulders within a stratified matrix of sand, silts and clays (*c.f.* Boggs 2006). The boulders and cobbles within the tills are typically sub-angular to rounded striated clasts of Beacon Sandstone and Ferrar Dolerite. Away from the glacier margin, within the Britannia Drift, rare deposits of a similar nature are found superimposed on cold-based drift deposits at elevations up to 300 m above the Hatherton Glacier. The sedimentology of these deposits suggests a similar origin to that observed at the ice margin, but while the ice marginal sites are well preserved, those at elevation display some degree of weathering (Figure 4.13B), with the material disaggregating into smaller chunks in obvious debris cones. Given this limited weathering, it may suggest only a limited period of time has elapsed since redeposition.

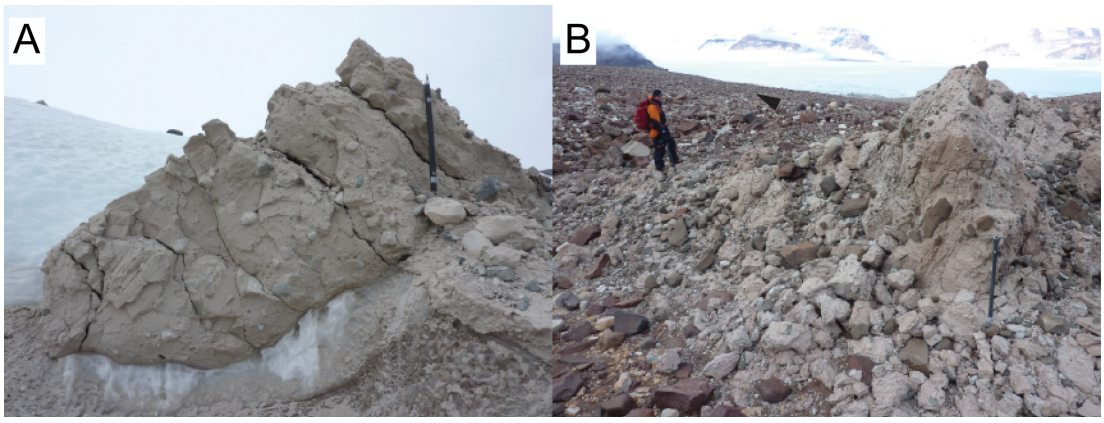

Figure 4.13: Examples of relict glacial till - (A) Frozen block of till, displaying typical warm-based features, being deposited at the modern margin of the Hatherton Glacier at Bibra Valley. (B) A similar till deposit weathering within the upper Britannia-I Drift on the Danum Platform.

This evidence suggests that warm basal conditions may have existed during the past in the deeper parts of the Hatherton Glacier and have been transported englacially to be deposited at the modern cold-based margin. As the model of Riger-Kusk (2011) shows that the central trunk of the Hatherton Glacier was still cold-based at the LGM, the inference is that the creation and subsequent transportation of this material was likely to be from older glaciations. Relict warm-based material being redeposited during cold-based advances is clearly shown by the exhumation of till at the modern cold-based margin of the Hatherton Glacier. Therefore, while a limited amount of material from a warm-based origin is found within the drift sheets of Bockheim et al. (1989), the process of deposition is entirely from cold-based ice.

While the predominant view in glaciology is that cold-based glaciers have the ability to preserve the underlying sediments and bedrock (Davis et al., 2006; Kleman, 2007; Sugden et al., 2005), recent studies have now shown that glaciological processes exist in which cold-based ice can also produce a range of glacial features (Atkins et al., 2002; Fitzsimons, 2003; Waller et al., 2012). Given the differing nature of the basal processes involved, these are very different in style to those generated under warm basal conditions.

In the DHGS, the evidence supporting the advance of cold-based ice is usually in the form of thin patchy glacial drifts (or minor reworking of older drifts) and the emplacement of boulder belt moraines at stagnant ice margins overlying older, minimally disturbed surfaces. In many cases this evidence is extremely subtle, thus exposure ages showing complex histories need to be interpreted with an appreciation of the products formed under cold basal conditions (Di Nicola et al., 2009; Strasky et al., 2009). Atkins (2013) discussed a variety of cold-based features within the TAMs. While not all of these are observed at glacier marginal sites in the DHGS, the four main classes of features are applicable:

- Erosional features. These include crude striations, scrapes and grooves (Figure 4.14A) as well as abrasions and irregular scuff marks on stross side of boulders.

- Depositional products. Thin patchy drifts, clast supported boulder belt moraines, ice-cored moraines and isolated scattered boulders. All of these

features are extremely common at sites on the margin of the Hatherton Glacier (Section 4.6.1).

- Deformational features. Overturned and glacially reworked boulders (Figure 4.14B)

- Preservation features. Areas of flattened ground compressed by the weight of the overriding cold-based ice (Figure 4.14C), these often occur in combination with overturned and scuffed boulders. Undeformed buried soils showing recycled ventifacts are also commonly observed (Bockheim, 2010; Bockheim et al., 1989).

Figure 4.14: Examples of cold-based landscape modification - Examples from the Dubris and Bibra valleys. (A) Large horizontal slab of Beacon Sandstone displaying unweathered crude linear grooves, arrows indicates direction of ice flow. (B) Overturned dolerite boulder, the underside displaying significantly less desert varnish than the upper. (C) Compressed ground in the Hatherton Drift. Large boulder appears 'pushed' into the flattened surface.

4.6 Glacial history of the Darwin Hatherton glacial system

While the inception of the DHGS may differ from that of the McMurdo Dry Valleys, in that the landscape was initially carved glacially, not fluvially as in the case of the MDVs (Sugden et al., 1995, 1999), both show evidence of extensive glacial modification. In particular, a series of distinctive glacial deposits, used to constrain the past dynamics of the DHGS, have been correlated to other sites within the

TAMs (Moriwaki et al., 1992b), leading to the Conway et al. (1999) 'swinging gate' model of post-LGM ice retreat within the Ross Embayment (Section 3.3).
The mapping of glacial drifts within the DHGS by Bockheim et al. (1989) allowed the reconstruction of longitudinal ice elevation profile (Figure 4.15). It shows that during the Quaternary the heavy influence of ice buttressing by a grounded WAIS effectively dammed ice drainage and caused significant thickening in the lower reaches of the DHGS. Geological evidence indicates the downstream thickening at the ice shelf confluence, was up to 1000m above present during the late Quaternary and perhaps a similar thickness during the LGM based on ^{14}C dating (Bockheim et al., 1989; Denton, 1979). These dropped to near modern levels as the grounding line of the WAIS retreated past the mouth of the DHGS at $\approx$6.8 ka BP (Conway et al., 1999). However, only minor thickening is evident proximal to the catchment suggesting that EAIS dynamics may have also played a role in glacier profile fluctuations. As the longitudinal profile of the DHGS has fluctuated during these periods of WAIS and EAIS advance and retreat, ice has likewise advanced and retreated into the mouths of the flanking valleys. The degree of ice advance within these tributary valleys is dependent on the thickness of the DHGS and thus the dynamics of the ice sheets. Glacial deposits located in the ice-free areas flanking the upper reaches of the DHGS (*i.e.* Lake Wellman, Dubris and Bibra valleys) likely act as an archive of previous EAIS glacial advances while those in the lower reaches (*i.e.* Diamond Hill, Roadend Nunatak) reflect the WAIS.

4.6.1 Glacial drifts

Denton (1979), followed by Bockheim et al. (1989) and Storey et al. (2010) investigated and mapped four distinct glacial deposits at a number of sites within the DHGS, forming a clear stratigraphic sequence. Bockheim et al. (1989) named them, from youngest to oldest: Hatherton, Britannia, Danum and Isca. The distribution of these drifts throughout the DHGS are not continuous; the youngest drifts, located at low elevations alongside the margins of the DHGS can be clearly traced from valley to valley, while the older, located at elevations above and distal to the modern ice margin are more patchy and discontinuous. Isolated occurrences of individual drifts were identified at a number of locations along the DHGS (*i.e.* Derrick

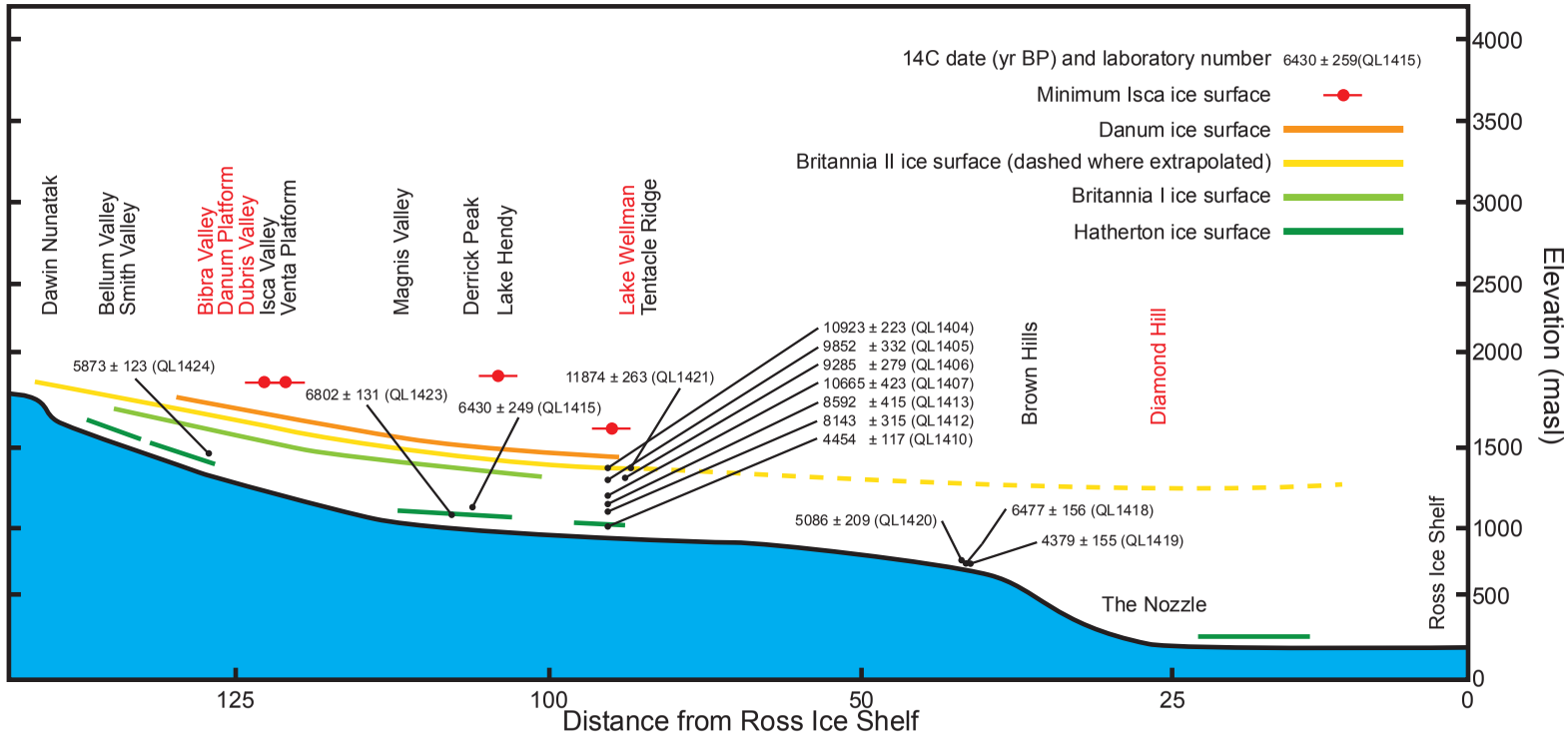

Figure 4.15: Reconstructed ice surfaces of the DHGS - Longitudinal ice surfaces along a transect running through the Hatherton and Darwin Glaciers and into the Ross Ice Shelf. Adapted from Bockheim et al. (1989). All stated ^{14}C ages are calibrated. Samples QL-1401, QL-1402, QL-1403, QL-1408, QL-1409, QL-1411, QL-1414, QL-1416, QL-1417 and QL-1422 omitted as per Bockheim et al. (1989). Sites visited as part of this research marked in red.

Peak, Tentacle Ridge and Magnus Valley), the best preserved examples predominantly found in the mountains flanking the Hatherton Glacier; type sections are located at Lake Wellman and Dubris Valley (Bockheim et al., 1989). Outside of these areas, especially near the confluence of the Darwin Glacier and Ross Ice Shelf (*i.e.* Brown Hills and Diamond Hill), the identification of these drifts was less clear and thus were classed as undifferentiated (Bockheim et al., 1989).
A combination of glacial geomorphology and soil development studies were used to define individual drift surfaces, with abrupt morphological changes and moraine ridges representing their maximum extent. Boulder belt moraines, typically formed at the terminal and lateral margins of cold-based glaciers (Ackert et al., 2011; Bockheim, 2010), represent periods of glacial still-stand, while the more widespread drifts (*i.e.* thin surficial deposits), were deposited as cold-based ice advanced into and sublimated within valleys (Storey et al., 2010).
At Lake Wellman and Dubris Valley several trends are observed within the sequence, related to elevation and distance from the ice margin:

- Increasing drift age (Bockheim et al., 1989; Storey et al., 2010)
- An increase in the amount and degree of weathering.
- Decreasing preservation of glacial features such as striations.
- An increase in desert pavement surfaces.
- An increase in soil development (Bockheim, 2010; Bockheim et al., 1989)

The striking difference between drifts is a product of these characteristics, with weathering, soil development and landscape preservation all directly linked to distance from the glacier and thus age. This evidence supports the hypothesis of both Bockheim et al. (1989) and Storey et al. (2010) that the drift sequence represents an overall retreat of the DHGS from a past glacial high-stand position, represented by the Isca drift, to the levels observed today. Within this time period, ice advances and retreats deposited the Danum, Britannia and Hatherton drifts into the tributary valleys alongside the DHGS.

4.6.1.1 Hatherton Drift

The youngest of the sequence, the Hatherton Drift, is found at ice proximal sites along the flanks of the DHGS and is characterised by fresh angular clasts with minimal weathering. The drift contains frequent perched boulders and in the lower sections (*i.e.* with decreasing distance to the RIS) can contain clasts showing evidence of glacial processes such as plucking and striations. Within the low elevation areas of the Dubris and Bibra valleys (DBV), the Hatherton Drift displays a remarkable variety of glacial geomorphology: Ice-cored moraines draped with thin clast rich cold-based glacial deposits, debris cones, ice-marginal ponds and kettle holes are all observed (Figure 4.16). The upper extent of the drift, estimated from a digital elevation model (DEM) of the area, is 33-172 metres above Lake Wellman ($\approx$794 masl) and at the DBV 43-138 metres above the Hatherton Glacier Margin (Lake Judith, $\approx$1120 masl). This equates to an average elevation of $\approx$85 metres above the modern ice margin, higher than the 20-70 metres at Lake Wellman suggested by Bockheim et al. (1989).

Figure 4.16: Hatherton Drift at Bibra Valley - Abundant ice cored debris cones and ponds at the Hatherton Glacier. At this location the Hatherton Drift is predominantly composed of sandstone clasts.

Bockheim et al. (1989) observed that the drift was not lithologically uniform and that its composition differed with proximity to the catchment. In the upper parts of the Hatherton Glacier (*i.e.* Dubris Valley and Lake Wellman), the drift is predominantly angular sandstone and dolerite clasts within a unconsolidated thin sandy deposit (Figure 4.17A); while in the lower sections (*i.e.* Diamond Hill), angular to sub-angular granites and gneisses are dominant (Figure 4.17B).

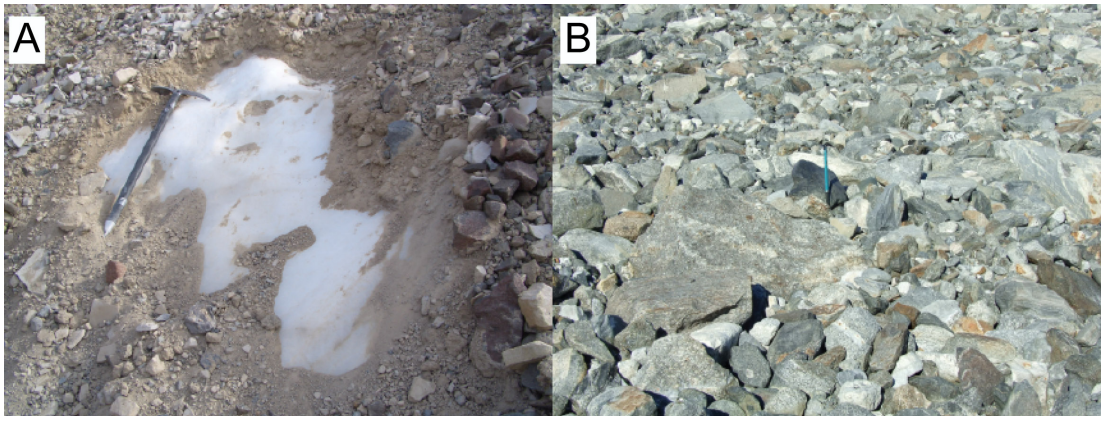

Figure 4.17: Hatherton Drift - Two examples at the ice margin. (A) Sandstone rich ice-cored deposit at the mouth of the Dubris Valley. Note thin (<0.1 m) sandy deposit over ice cored moraine. (B) Granite rich deposit at Diamond Hill. Generally clast supported material on top of ice cored moraines.

4.6.1.2 Britannia Drift

The Britannia Drift has been used in the DHGS to constrain ice sheet dynamics during the global LGM period as defined by the marine record (Denton and Hughes, 2002; Denton and Marchant, 2000). Bockheim et al. (1989) subdivided the Britannia into two, with the Britannia-I deposited over the older Britannia-II drift during a later glacial re-advance. The drift is predominantly sub-rounded to sub-angular boulders of sandstone and dolerite, with rare clasts of granite; the Britannia-I containing a higher proportion of dolerite compared to the Britannia-II. Similar to the Hatherton Drift, the Britannia is also characterised by well-preserved constructional features, with hummocky terrain, matrix supported moraines, boulder belts and emplaced glacial erratics common at low elevations above modern glacier margins. Throughout the drift are matrix poor, clast rich boulder belts, a classic cold-based

feature formed at stagnant terminal and lateral ice margins (Atkins et al., 2002; Bockheim, 2010; Bockheim et al., 2008).

In the DBV, the Britannia-II Drift was assumed to be deposited by an expanding Hatherton Glacier during the Antarctic LGM (≈15-20 ka). The maximum extent of this unconfirmed LGM advance is represented by an extremely well-defined boulder-belt moraine contact with the older Danum surface, observed at elevations up to 320 meters above the present Hatherton Glacier. The contact is sinuous and nearly continuous throughout the valley bottoms and ridges of the Lake Wellman and Dubris Valleys. In contrast to the still-stand generated boulder-belts, glacial drifts deposited during periods of gradual retreat and/or sublimation have a patchy distribution throughout the Dubris and Bibra valleys. In some places it is thick and buries the underlying older surfaces (Bockheim, 2010; Bockheim et al., 1989), while in others there is only a scattering of boulders and a minor reworking of the original drift surface.

As the upper contact of the Britannia Drift has been used to constrain LGM ice thickness for the DHGS, the Lake Wellman and DBV sites are highly important. Both sites preserve the upper limits of the Britannia, but are morphologically different. At Lake Wellman a well-defined matrix supported moraine marks the upper contact with the underlying Danum (Figures 4.18A & 4.18B), while in the Dubris Valley, the terminal position is marked by a thin drift sheet and associated boulder belt (Figures 4.18C & 4.18D). At Lake Wellman, the Britannia was only mapped as a single deposit, while in the DBVs, both surficial morphology (Figure 4.18C) and the soil profiles of Bockheim et al. (1989) suggest a subdivision; an older deposit known as Britannia-II (B-II) and a younger, the Britannia-I (B-I) Drift (Figure 4.18D). Bockheim et al. (1989) suggesting that given the radiocarbon chronology (Section 4.7.1), that the Britannia-II was LGM and the Britannia-I post-dated the LGM, but may have also been a re-advance of Hatherton ice during the same glaciation.

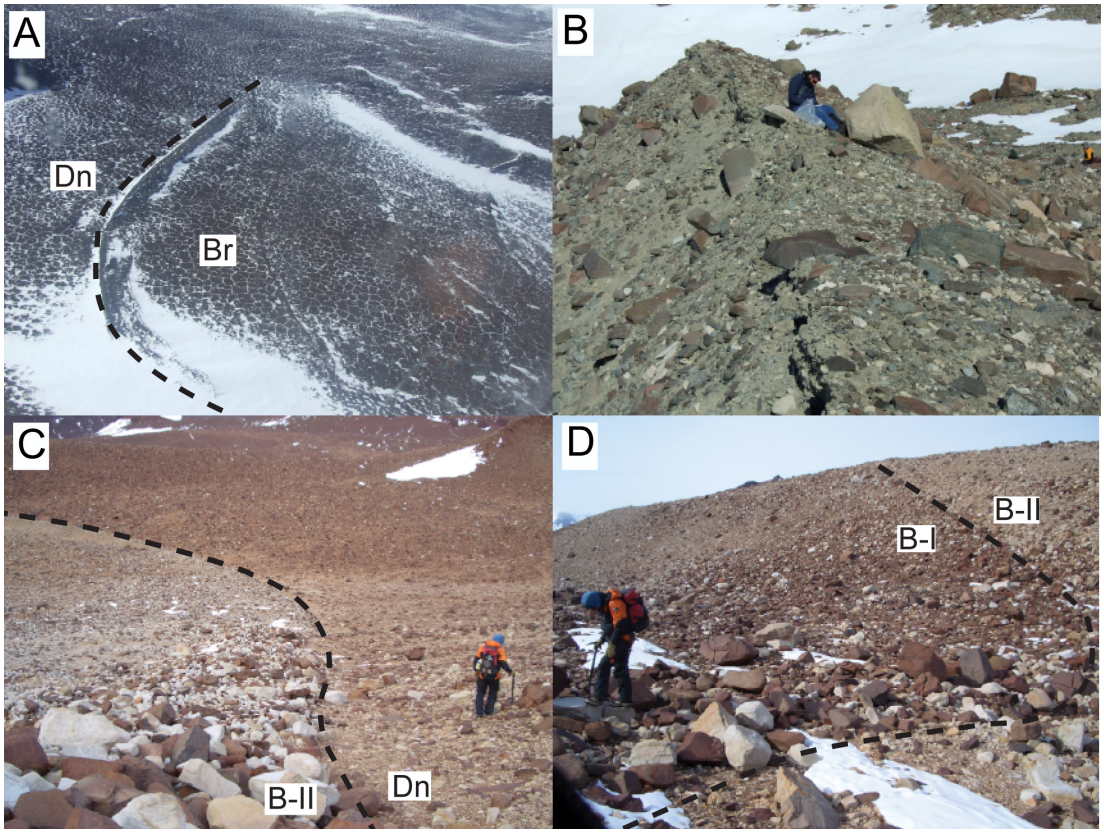

Figure 4.18: Britannia Drift - At Lake Wellman (A) Moraine 2 at the upper contact of the Britannia (Br) and Danum drifts (Dn) at ≈1065 masl. (B) Close up view of the unstable matrix supported moraine. The Britannia Drift at Dubris Valley. (C) The distinct clast supported upper contact of the Britannia-II (B-II) with the older underlying Danum Drift. (B) The poorly defined contact between the Britannia-I (B-I) and Britannia-II drifts. Note the higher percentage of dolerite in the B-I.

4.6.1.3 Danum and Isca drifts

The Danum and Isca drifts are the oldest mapped deposits within the DHGS, found at altitudes greater than ≈300 m above the modern ice margin. While the Danum-Isca contact is relatively well constrained, the upper Isca contact is not as clear, the poorly defined contact blending with older pre-Isca and late Quaternary undifferentiated deposits at high elevations above the modern ice margin (Bockheim et al., 1989).

The older drifts in the Lake Wellman and DBV show a significant difference in geomorphology compared to those at the ice margins. Constructional glacial features

are virtually absent, with only a limited number of poorly preserved moraines being observed. Additionally, the landscape is dominated by patterned ground and desert pavements (Figure 4.19), features usually associated with advanced weathering and drift age (Bockheim, 2010). Soil development in the Danum/Isca drifts is also far more advanced than those at lower elevations (*i.e.* Britannia and Hatherton), with soils showing increased salt levels, weathering and depth of staining (Aislabie et al., 2012). Bockheim et al. (1989) subdivided the Isca into an older (V) and younger (IV) members, giving them a mid-Quaternary age with the Isca-V representing the initial stages of DHGS damming by a grounded WAIS and Isca-IV a later alpine glaciation. Compared to the Danum (Figure 4.19A), the Isca (Figure 4.19B) shows a higher degree of weathering. Dolerite clasts show surface pitting and wind polishing, while boulders of beacon sandstone display wind polishing, weathering rinds and a range of tafoni weathering. Commonly observed in the Isca are dolerite surface clasts showing signs of ventifacton, with moderately developed faceting and wind-parallel grooves that indicate the occurrence of long term aeolian processes (Knight, 2008).

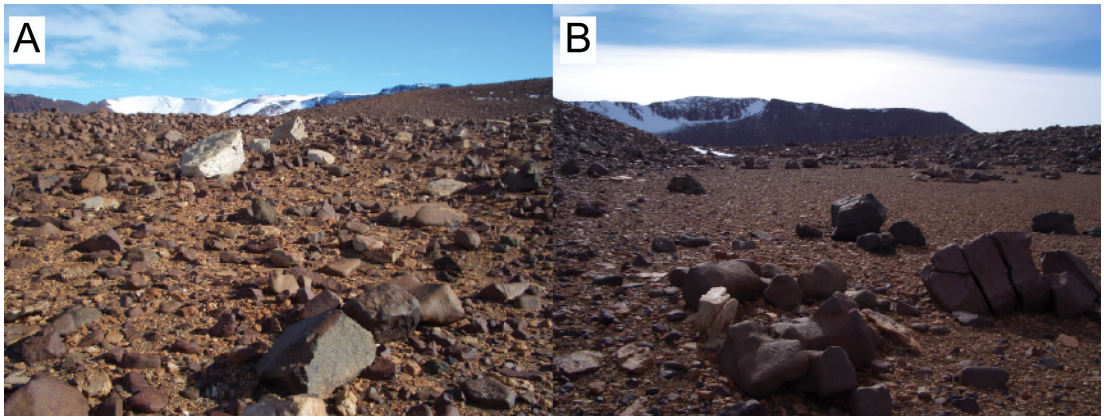

Figure 4.19: Danum and Isca drifts - Differences in drift morphology observed on the Danum Platform (A) Danum Drift and (B) a well-developed area of desert pavement in the Isca Drift.

4.7 Geological chronologies

4.7.1 Radiocarbon dating

Radiocarbon ages of algae located within the Hatherton and Britannia drifts form the basis of the Bockheim et al. (1989) chronology. It was suggested by Sugden et al. (2006) that in the rising temperatures that occurred post-LGM, the availability of seasonal free water increased as ice retreated. The formation of pro-glacial lakes, ponds and meltwater channels in areas that were formally ice covered, now permitted the growth of blue-green algae at lake margins. Therefore the growth of algal mats can used as a proxy for the minimum age of ice retreat, the assumption being that increased moisture, at a level able to initiate algal growth, post-dated the removal of ice at that location. Bockheim et al. (1989) collected 24 algal samples at seven ice-free sites along the DHGS, the majority of samples from the Lake Wellman (n=9) and Derrick Peak areas (n=6) and predominantly within the Britannia Drift. Examples of these paleo-pond margins, where patches of dessicated algae are found (Figure 4.20) are common in both locations.

Figure 4.20: Dessicated algae at the modern Hatherton Glacier margin - Located within the Hatherton Drift at Lake Wellman.

Key to the reconstruction of LGM ice surfaces by Bockheim et al. (1989) were transects covering a range of elevations above the present ice margin. As these algae rich sites were taken to represent pro-glacial lakes and thus the former extent of an enlarged DHGS, site elevations can be used to infer minimum ice thickness. The use of radiocarbon ages, in addition to the geomorphic evidence of distinct drift sequences, suggested a post-LGM chronology for the Britannia and Hatherton drifts within the DHGS.

To compare the radiocarbon chronology of Bockheim et al. (1989) and the surface exposure ages of this work and others, radiocarbon dates (^{14}C BP) have been converted into calendar ages (cal BP). Using the methodology of Verleyen et al. (2011), the uncalibrated dates of Bockheim et al. (1989) have been converted to upper and lower calibrated ages (at 2σ) using the CALIB 6.1 software (http://calib.qub.ac.uk/calib/). As carbon came from a purely terrestrial source, correction for the marine reservoir effect was not needed (Jull et al., 2012) and as all ages were younger than 11 ka ^{14}C BP, the Southern Hemisphere atmospheric calibration (SHcal04) curve was used (McCormac et al., 2004). Table 4.2 contains the original uncalibrated results, as well as those for the ages calibrated with the SHcal04 curve. As the maximum age for^{14}C dating is $\approx$50 ka, using the IntCal09 curve (Reimer et al., 2009), the chronology would be limited to the Holocene and late Pleistocene. Thus algal ages for the Danum and Isca are not possible using this technique. Based on the limiting radiocarbon ages and field mapping, the overall chronology assigned by Bockheim et al. (1989) was early Holocene for the Hatherton, post-LGM and LGM for Britannia (I and II) and MIS-6 and older for Danum and Isca. The age for the Danum is based on a correlation to the Marshall Drift, a deposit flanking the Taylor Glacier and sharing similar weathering and soil characteristics (Denton et al., 1989b).

Table 4.2: Calibrated radiocarbon results from the DHGS - From Bockheim et al. (1989). Calibrated using CALIB 6.1 (www.calib.qub.ac.uk/calib/)

Laboratory Number	Location	Drift	Calibration Curve	Uncalibrated Age (^{14}C BP)	Uncalibrated Error (^{14}C BP)	Calibrated Upper (cal BP)	Calibrated Lower (cal BP)	Mean Age	Mean Age (ka)
QL-1404	Lake Wellman	Britannia-II	SHcal04	9620	60	10700	11145	10923	10.9
QL-1405	Lake Wellman	Britannia	SHcal04	8790	140	9520	10184	9852	9.9
QL-1406	Lake Wellman	Britannia	SHcal04	8430	140	9006	9564	9285	9.3
QL-1407	Lake Wellman	Britannia	SHcal04	9420	140	10242	11087	10665	10.7
QL-1413	Lake Wellman	Britannia	SHcal04	7770	180	8177	9007	8592	8.6
QL-1411	Lake Wellman	Britannia	SHcal04	5740	90	6298	6668	6483	6.5
QL-1412	Lake Wellman	Britannia	SHcal04	7400	170	7828	8458	8143	8.1
QL-1408	Lake Wellman	Britannia	SHcal04	4010	50	4235	4533	4384	4.4
QL-1409	Lake Wellman	Britannia	SHcal04	1710	40	1416	1691	1554	1.6
QL-1410	Lake Wellman	Hatherton	SHcal04	4040	40	4337	4570	4454	4.5
QL-1424	Bibra Valley	Britannia-I	SHcal04	5210	40	5750	5995	5873	5.9
QL-1423	Onum Valley	Britannia	SHcal04	6020	50	6671	6933	6802	6.8
QL-1421	Tentacle Ridge	Britannia	SHcal04	10250	60	11611	12136	11874	11.9
QL-1401	Derrick Peak	Britannia	SHcal04	4890	40	5470	5655	5563	5.6
QL-1402	Derrick Peak	Britannia	SHcal04	4960	40	5584	5736	5660	5.7
QL-1403	Derrick Peak	Britannia	SHcal04	4700	100	5042	5590	5316	5.3
QL-1415	Derrick Peak	Britannia	SHcal04	5670	120	6181	6678	6430	6.4
QL-1416	Derrick Peak	Britannia	SHcal04	4320	50	4623	4971	4797	4.8
QL-1417	Derrick Peak	Britannia	SHcal04	3660	90	3683	4154	3919	3.9
QL-1414	Derrick Peak	Hatherton	SHcal04	2130	40	1926	2151	2039	2.0
QL-1418	Brown Hills	Britannia	SHcal04	5740	50	6321	6633	6477	6.5
QL-1419	Brown Hills	Britannia	SHcal04	4000	60	4223	4534	4379	4.4
QL-1420	Brown Hills	Britannia	SHcal04	4510	60	4877	5294	5086	5.1
QL-1422	Magnis Valley	Hatherton	SHcal04	5270	40	5901	6177	6039	6.0

For the Britannia Drift, ^{14}C ages range from 1.4-12.1 with a mean value of 6.8 ka cal BP (n=21). The oldest sample was located at Tentacle Ridge (QL-1421), the youngest (QL-1409) at Lake Wellman and one was definitively classed as Britannia-II (QL-1404), dating to 10.7-11.1 ka cal BP. At Lake Wellman, Britannia ages ranged from 1.5-11.1 ka cal BP (n=9) along a transect covering an elevation range of up to 250 meters above the lake ($\approx$794 masl). An age-elevation plot (Figure 4.21) shows a strong positive linear relationship between the two variables (r^2=0.92). The oldest sample (QL-1404, 11.1-10.9 ka cal BP) was taken approximately 240 metres above the lake near a prominent moraine near the upper contact of the Britannia Drift. Only a limited number of samples (n=3) were taken from the younger Hatherton Drift, at Lake Wellman (QL-1410), Magnis Valley (QL-1422) and Derrick Peak (QL-1414). Ages here were all mid Holocene, ranging from 4.3-6.2 ka cal BP. The interpretation of the results for the DHGS by Bockheim et al. (1989) was that ice retreated from its maximum LGM limit at least 10.7-11.8 ka cal BP and reached a position near the modern Hatherton margin by 6.4-6.8 ka cal BP.

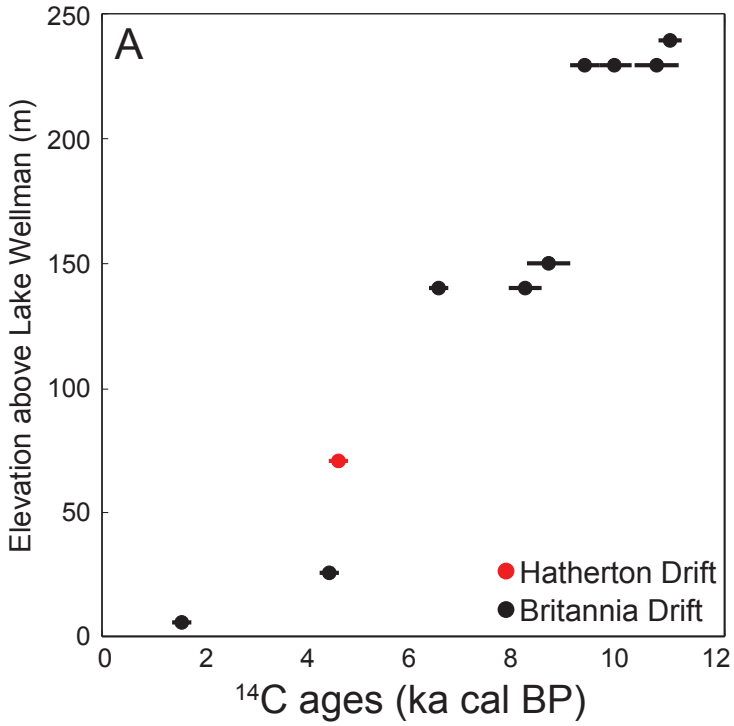

Figure 4.21: Lake Wellman Britannia Drift radiocarbon ages - Calibrated age *vs* elevation plot. Sample elevations are in metres above Lake Wellman and from Figure 4 in Bockheim et al. (1989).

At all other sites, including Derrick Peak, a clear age-elevation relationship was not observed; therefore results were used purely as a minimum age of Hatherton ice recession from the area. The Lake Wellman results, being the strongest in the dataset, are the key pieces of evidence used by Bockheim et al. (1989) to constrain LGM ice thickness in the upper parts of the DHGS.

However a number of unanswered questions remain about the radiocarbon LGM chronology. A significant overlap exists in ages between the oldest Hatherton age (QL-1422, 5.9-6.2 ka cal BP) and the youngest Britannia (QL-1409, 1.4-1.7 ka cal BP). Within the dataset, nearly 30% of Britannia dates overlap with those from the Hatherton. While mention is made of the lithological differences between the Hatherton Drift at either end of the DHGS, the reasons for morphologically and geochemically distinct drifts having the same ages is not discussed by Bockheim et al. (1989). A possible explanation may lie in the applicability of algae as a proxy

for ice recession. Bockheim et al. (1989) suggested that the radiocarbon ages represented a minimum age for the recession of the ice margin. Given that algal growth actually represents the availability of free water, not the retreat of ice, algae would rapidly grow when moisture reached a key threshold (Kennedy, 1993). This may occur well after ice has retreated from the site, with changes in climate a possible driver for increased moisture availability. While the relationship between ice recession and algal growth is supported in the MDVs, within the context of ice impounded lakes (Sugden et al., 2006), in alpine environments like the DHGS, the relationship is far less certain (Storey et al., 2010).

4.7.2 Correlation to other glacial deposits

To aid in the creation of a chronology applicable along the length of the TAMs and a model of ice sheet retreat for the Ross Sea Embayment, the drifts of the DHGS were correlated to others within the TAMs (Bockheim et al., 1989; Denton et al., 1989a; Denton and Marchant, 2000). The glacial deposits that flank outlet glaciers margins within the TAMS share similar characteristics; ice-free sites are hyper arid-polar deserts in similar geologic settings with comparable drift morphology and lithology (Bockheim et al., 1989). Therefore if drifts are of a similar nature and at a similar elevation above the modern ice margin, it has been suggested that they are co-eval deposits in the same glacial event. Moriwaki et al. (1992b) summarised the work of Denton et al. (1989a) and others, correlating the drifts of six sites including the DHGS (Figure 4.22). While the Britannia and Hatherton drifts were constrained by an absolute radiocarbon chronology (Section 4.7.1), older drifts had relative ages assigned to them. The Danum drift was the only other drift assigned a age range byBockheim et al. (1989) who suggested the Danum as MIS-6 and correlated with the Marshall drift in the MDVs and the Meyer Drift at the Beardmore Glacier (Denton et al., 1989a).

With the development of new geochronological techniques, drift ages have been questioned and refined, Brook et al. (1993), using ^{3}He and ^{10}Be exposure dating proposed that the Taylor II and III in the MDVs correlated to the Danum and thus may be 200 ka and not the MIS 6 age suggested by Bockheim et al. (1989). Bockheim et al. (1989) state when discussing the Britannia-I and II drifts "...we

leave open the possibility that a new numerical dating technique may show that these drifts represent separate glacial events." and in addition suggested that the Britannia-II may possibly be MIS-4 and not MIS-2 as the radiocarbon chronology indicated.

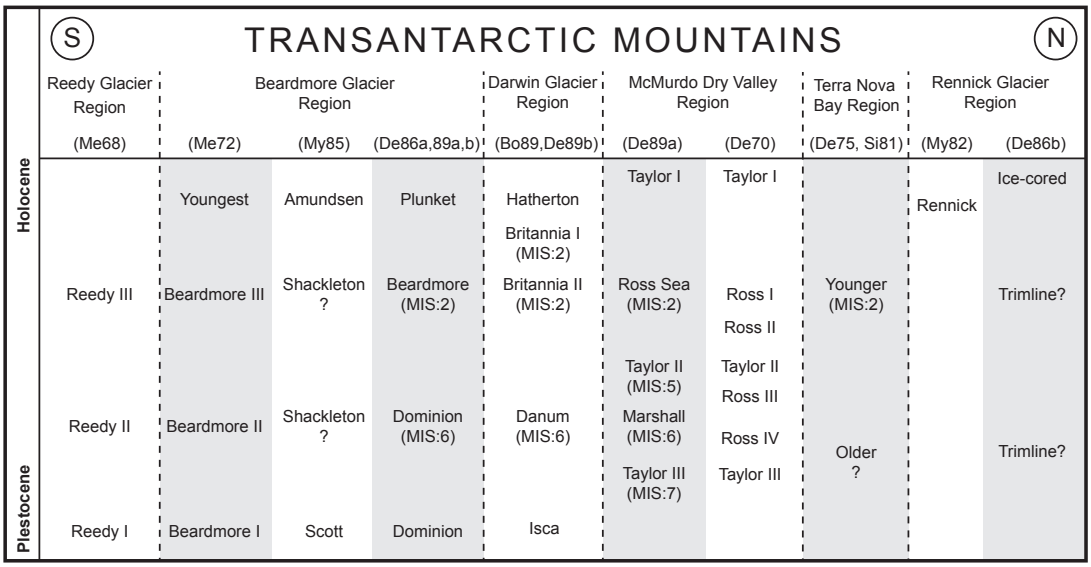

Figure 4.22: Suggested correlation of glacial drifts - Selected glacial events and drifts within the Transantarctic Mountains from Moriwaki et al. (1992b). Cited works are De70 (Denton et al., 1970), De75 (Denton et al., 1975), De86a (Denton et al., 1986a), De86b (Denton et al., 1986b), De89a (Denton et al., 1989a), Be89b (Denton et al., 1989b), Bo89 (Bockheim et al., 1989), Me68 (Mercer, 1968), Me72 (Mercer, 1972), My82 (Mayewski, 1982), My85 (Mayewski et al., 2013) and Si81 (Stuiver et al., 1981).

4.7.3 Meteorites

Another method of testing the Denton (1979) and Bockheim et al. (1989) chronology came from an unexpected source. In 1978, a University of Waikato field party mapped the geology of Derrick Peak, an area flanking the Hatherton Glacier in the Britannia Range (Figure 4.1). On an exposed bedrock terrace within the Quaternary Danum-Isca drifts of Denton (1979), 16 iron meteorites (DRP78001-16) were discovered at elevations up to 500 metres above the present Hatherton Glacier (Kamp and Lowe, 1982); additional material was also discovered during further expeditions to the area in 1988 (Kirkbride et al., 1991)(meteorites DRP88017-25) and

2000 (AMTMET, http://curator.jsc.nasa.gov/antmet/)(meteorites DRP00200-201), a total of ≈400 kg of material.

Trace element analysis classified the 1978 and 1988 meteorites as type IIb octahedrites, having comparable gallium, nickel and cobalt concentrations (Clark, 1982; Malvin et al., 1984). Distinctive surface weathering was another shared characteristic with the meteorites appearing to have been *insitu* at the surface or partially buried for a extended period. While the upper surfaces are irregular, wind polished and display weathering pits (Figure 4.23), the buried underside shows evidence of corrosion, attributed to soil moisture content (Clark, 1982). Given the geochemical, metallographic and weathering evidence, it was concluded that the meteorites came from a single large shower (Kirkbride et al., 1991) and that final deposition was at the margin of an enlarged Hatherton Glacier (Kamp and Lowe, 1982).

Figure 4.23: Meteorite DRP-880020 - 63 kg iron meteorite discovered at Derrick Peak by Kirkbride et al. (1991)(photo credit: Museum of Canterbury).

The 1978 and 1988 finds were located on a 500 m wide glacially cut bench on the northern slopes of Derrick Peak. The highest elevation meteorites were found emplaced on exposed bedrock (Beacon or Ferrar), while those at lower elevations within the Isca Drift. A small number of meteorites were also found in the very

upper parts of the Danum drift on Derrick Peak (Kamp, pers comm) and in Onnum Valley (Kirkbride et al., 1991). As the bulk of the meteorites were located within the glacial drift limits of Bockheim et al. (1989), their age of deposition (*i.e.* 'terrestrial age') was used in an attempt to further constrain the glacial chronology of the area. A key development being the use of cosmogenic radionuclides to date a meteorites terrestrial exposure. Nine of the meteorites collected in 1978 (DRP 78001-9) had exposure ages of 0.9 (*via* $^{36}Cl/^{10}Be$) to 1 Ma (*via* $^{10}Be/^{26}Al$) (Nishiizumi et al., 1987a); while there was some variability in measured radionuclide concentrations between samples (see Table 1 in Nishiizumi et al. (1987a)) a final terrestrial age of 1 $\pm$ 0.1 Ma was obtained for the group (Nishiizumi et al., 1989), agreeing with the conclusion of Kamp and Lowe (1982) that the meteorites arrived in a single fall.

As Bockheim et al. (1989) suggested a MIS-6 age from the Danum and older for the Isca, the cosmogenic results are significantly older than expected when compared to the glacial chronology. While Kirkbride et al. (1991) did not definitively answer the question, three scenarios were postulated to explain this variation.

1. The glacial chronology of Bockheim et al. (1989) was incorrect.
2. The glacial deposits in which the Meteorites were located in were incorrectly identified (*i.e.* Kamp and Lowe 1982; Kirkbride et al. 1991).
3. The terrestrial ages of Nishiizumi et al. (1989, 1987a) were incorrect. Either by measurement/analytical errors or by incorrectly interpreting the exposure history of the meteorite.

Due to this debate, the use of the Derrick Peak meteorites as an aid to validate the glacial chronology of Bockheim et al. (1989) remains in doubt.

Chapter 5

Glacial history of the Dubris and Bibra valleys.

This Chapter summarises the 2013 paper (Accepted Manuscript):
A 2 million year glacial chronology of the Hatherton Glacier, Antarctica and implications for the size of the East Antarctic Ice Sheet at the Last Glacial Maximum.
Joy, K., Fink, D., Storey, B.C. & Atkins, C.
Journal of Quat Sci Rev. (Appendices section B.1)
My contribution to this paper is outlined in the University of Canterbury "Co-Authorship Form" located on page v of this thesis.

5.1 Locality description and geomorphology

The Dubris and Bibra valleys (DBV, 80°S, 156°E) are two ice free regions of ≈60 km^2 that flank the Hatherton Glacier in the Britannia Range about 25 km from the EAIS catchment region. They form a series of steep sided (>45°) U-shaped glacially excavated valleys with floors that slope towards the modern ice margin of the Hatherton Glacier and which are separated by a flat topped ridge, the Danum Platform. Strong katabatic winds channel into the valleys from the EAIS plateau leaving the area almost completely ice free with only a few small semi-permanent snow patches present. The dominant bedrock lithology is the Ferrar Dolerite with minor exposures of sandstone and coal measures of the Beacon Supergroup (Haskell et al., 1964). Warm-based alpine-type glaciations during the late Miocene most likely sculpted the dominant valleys (Denton and Sugden, 2005) prior to a regional change to cold-based conditions (Lewis et al., 2007). Subse-

quent glacial events during the Quaternary involved incursion of the cold-based margin of the Hatherton Glacier ice up into the valley. This is evidenced by extensive and numerous glacial drifts and boulder-belt moraines ranging from the modern ice elevation of 1100 masl to ≈1600 masl. These drifts are predominantly comprised of sandstone, dolerite and rare granite clasts. Given the scarcity of sandstone exposures within the DBV and the high proportion in glacial deposits, it is clear that this material had been glacially transported from its source into the valleys. Due to the DBVs proximity to the EAIS, only a limited distance is available for rock fall generated supraglacial material to be collected by the Hatherton Glacier and then deposited within the valleys; beyond this distance, no other nunataks or outcrops exist. A wide range of geomorphological features are found within the valleys, the most distinctive being a sequence of 'bathtub ring' contours of near continuous boulder-belt moraine ridges that often demarcate the five drifts of Bockheim et al. (1989) deposited across the valleys. In order of distance from the modern ice margin and thus age, these are the Hatherton, Britannia-I, Britannia-II, Danum and Isca (Figure 5.1).

The major drift contacts show variation in both elevation and distance from the modern ice margin when comparing the relatively low relief valleys to the higher elevation ridges. For example, the Britannia-II / Danum drift contact is located 70 Metres lower but 1 km farther up valley than the same contact traced onto the Danum Platform, reflecting the topographic influence on the past position of the Hatherton Glacier margin as it encroached into the area (Figure 5.2). There is also a clear trend of decreasing preservation of glacially constructed features (*i.e.* ice cored moraines, debris cones, kettle holes, boulder belts and paleo-lakes) with elevation. The geomorphology of the older high elevation deposits is far less diverse, more weathered and has a subdued topography compared to the younger drifts at lower elevations. The youngest of the deposits, the Hatherton drift, which extends from the current ice margin at 1100 masl to at most 1200 masl, is characterised by irregular ice-cored terrain covered by a thin layer of fine grained sediment and carapace of sandstone cobbles. Abundant ice-cored debris cones, kettle holes, moraine ridges and some rare discrete blocks of frozen till are found within this zone while in the Isca and Danum drifts, the oldest deposits, none of these features are observed.

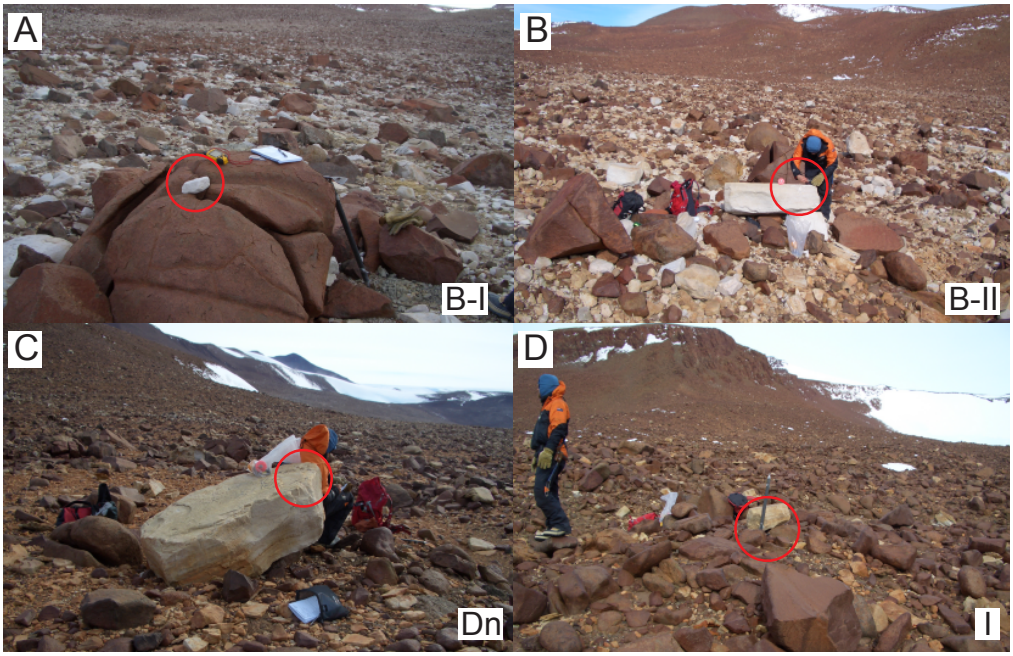

Figure 5.1: Glacial drifts in the Dubris and Bibra valleys - Typical view of the Britannia-I (B-I), Britannia-II (B-II), Danum (Dn) and Isca (I) glacial drifts. All samples (shown circled) were Beacon sandstone boulders or clasts, emplaced on drift surfaces or perched on large dolerite platforms. (A) BV3.1 in the Britannia-I Drift (Bibra Valley). (B) DP4.1 in the Britannia-II Drift (Danum Platform). (C) DP5.1 in the Danum Drift (Danum Platform) and (D) DV1.1 in the Isca Drift (Dubris Valley). Full sample descriptions and locations are in Table A.1.

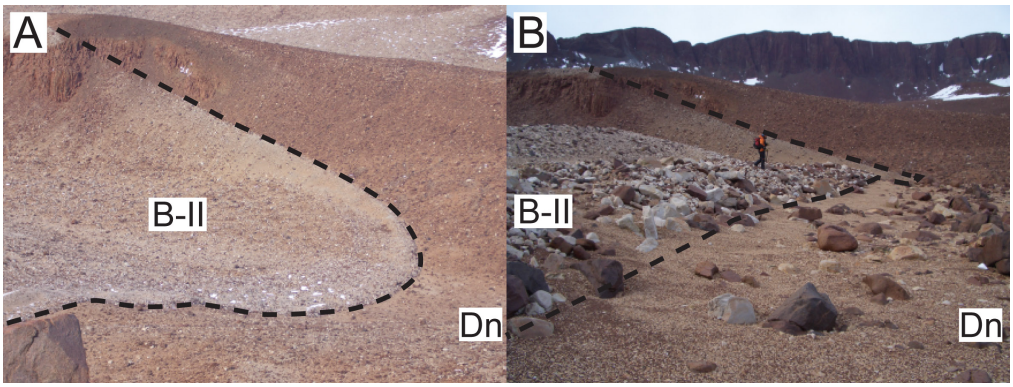

Figure 5.2: Britannia-II and Danum drifts in the Dubris Valley - Oblique (A) and closeup (B) of the Britannia-II (B-II) and Danum (Dn) drift contact margin. The valley width at this location (DV3.1) is approximately 700 metres. Previously assigned ages for the Britannia-II are LGM and for the Danum Drift MIS-6 according to Bockheim et al. (1989). ^{10}Be surface exposure ages on the Britannia-II are ≈110-130 ka and on the Danum Drift a minimum age of ≈0.6 Ma. The direction of intruded Hatherton Glacier ice advance is left to right.

5.2 Surface exposure dating

5.2.1 Results

Eighteen glacial erratics were sampled from the mapped drifts at elevations ranging from 1255 to 1620 masl with the highest sample (DP6.1) ≈500 m above the present ice margin of 1100 masl (Figure 5.3 & 5.4). Thirteen exposure ages from the Britannia and five from the older Danum and Isca drifts were tested for spatial age distribution across the DBV. To be consistent with other Antarctic studies that cite exposure ages, we initially adopt a minimum age model. This infers, as a function of elevation, that measured concentrations of ^{10}Be and ^{26}Al reflect the minimum timing of deposition based on a zero erosion exposure. Our calculated ^{10}Be exposure ages range from 4.9 ka to 2 Ma and fall into four distinct age groupings. These align well with the established glacial drift stratigraphy of Bockheim et al. (1989) for the four drifts but with very different absolute age ranges. The oldest two groups of ^{10}Be, 0.5 to 2 Ma (n=5), are all contained within the Isca and Danum Drifts. The younger two age groups, Britannia-II, 122.9 to 130.7 ka (n=5) is MIS-5 and hence definitively pre-LGM and Britannia-I, 4.9 to 8.0 ka (n=8) is Holocene. The transects at Dubris Valley, Danum Platform and Bibra Valley all show a positive age-elevation relationship, with r^2 values of 0.53, 0.86 and 0.92 respectively. As an aid to identify samples which have experienced uninterrupted sub-aerial exposure and are thus consistent with our prerequisite to constrain minimum ages at a given elevation, a ^{26}Al/^{10}Be dual-nuclide plot is used (Section 2.1.2.1). Of the 18 samples only BV3.1, DP1.2 and possibly DV5.2 display depressed ^{26}Al/^{10}Be ratios that imply periods of burial (Figure 5.5). For young samples where decay is negligible, the ^{26}Al/^{10}Be concentration ratio should be equivalent to the ^{26}Al/^{10}Be production rate ratio (*i.e.* 30.7/4.6 = 6.7). For the eight eligible DBV samples with ages less than 0.2 Ma (rejecting BV3.1 and DP1.2), we get 6.4 $\pm$ 0.4, consistent with other Southern Hemisphere and Antarctic production rate ratio values (Bentley et al., 2006; Shulmeister et al., 2005).

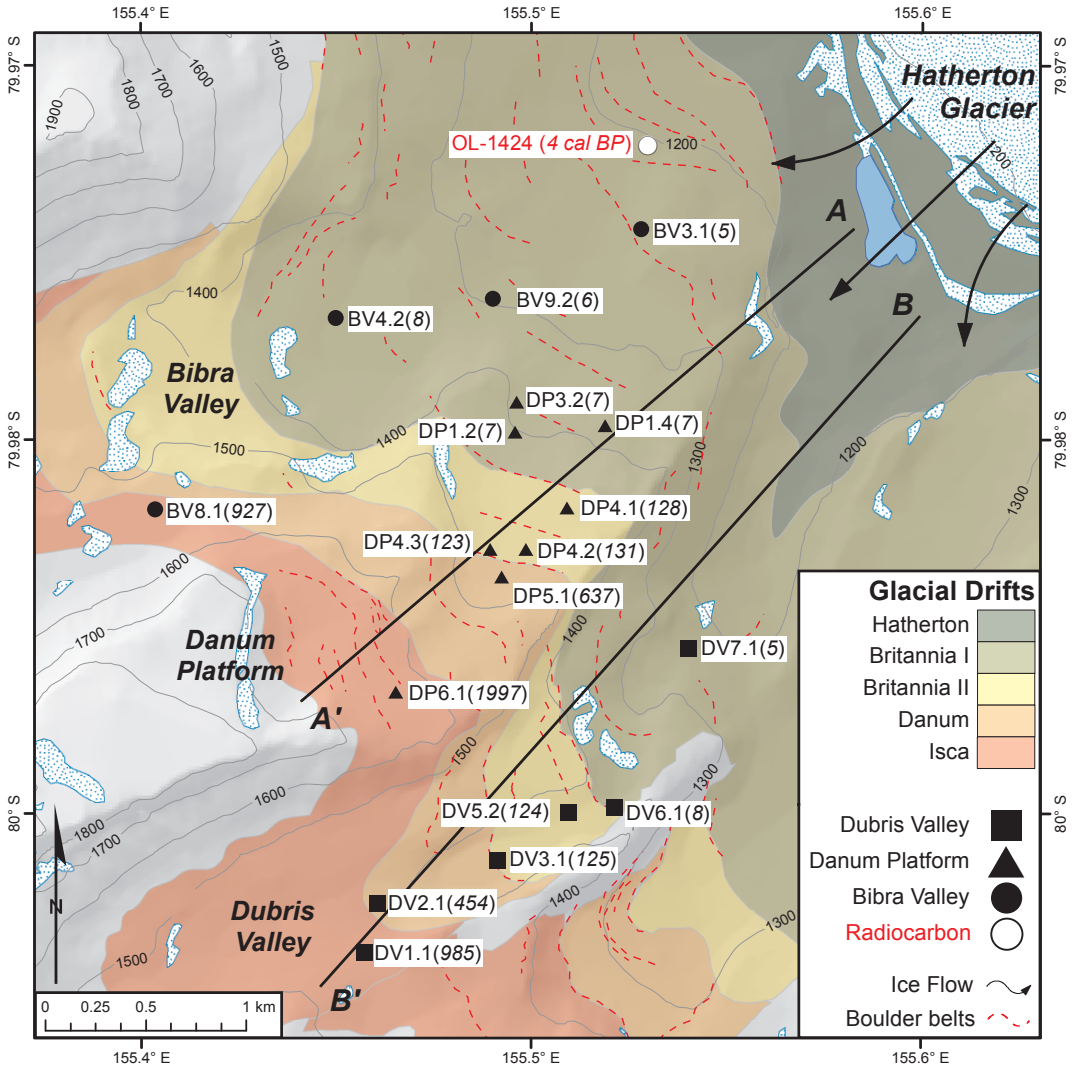

Figure 5.3: Map of the Dubris and Bibra Valleys - The study location bordering the southern margin of the Hatherton Glacier in the Britannia Range approximately 25 km from the EAIS. The stratigraphic definitions and relative positions of the five drift sheets are taken from Bockheim et al. (1989) and have been adjusted based on our field work. Moraine ridges from field mapping and interpretation of satellite imagery.

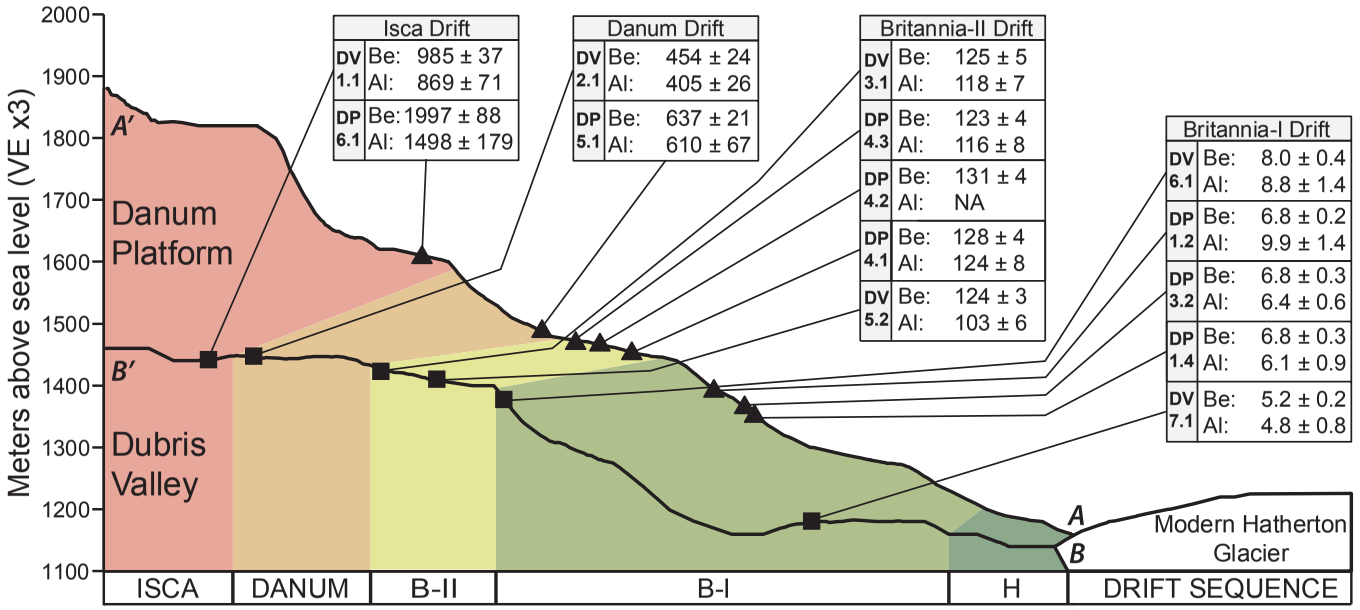

Figure 5.4: Transect profiles for the Dubris and Bibra valleys - Schematic representation of elevation *vs* drift relationship for the Danum Platform (A-A‘) and Dubris Valley (B-B‘). The Bibra Valley ^{10}Be exposure ages are omitted for clarity (5, 6 and 8 ka for Britannia-I and 927 ka for Isca). Drift contacts are adapted from Bockheim et al. (1989) and ^{10}Be and ^{26}Al exposure ages given in kiloyears (ka). Vertical exaggeration is x3 and age errors include production rate errors (see Tables A.2 & A.3).

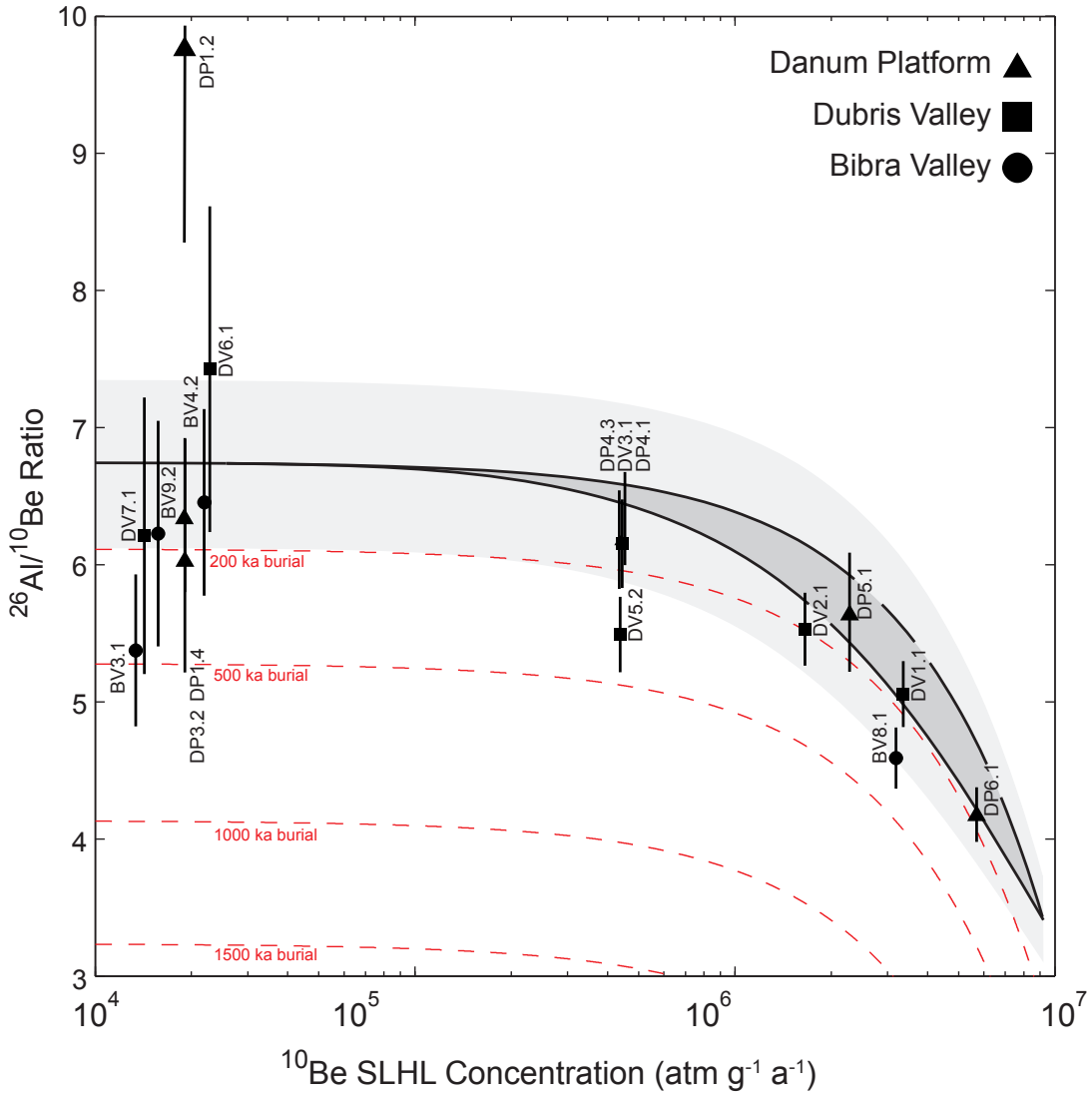

Figure 5.5: Dual-nuclide plot for the DBV SED samples - ^{26}Al/^{10}Be results of all 17 samples from Danum Platform, Dubris and Bibra valleys (Tables A.2 & A.3). The steady state erosion island is bordered by a 9% error in SLHL ^{26}Al and ^{10}Be production rate measurements (*i.e.* 30.7 and 4.6 atm/g/a respectively). All samples, except DP1.2, fall within the shaded region that represents continuous exposure and absence of any complex burial history. The shaded $\pm 1\sigma$ uncertainty region is determined from the error in the measured average ^{26}Al/^{10}Be concentration ratio (6.7 $\pm$ 0.4) of samples exposed for <100 ka (or 5 x 10^6 atoms g^{-1}) and which is effectively equivalent to the ^{26}Al/^{10}Be production rate ratio. Sample DP4.2 has not been plotted due to failed ^{27}Al measurement.

5.2.1.1 Britannia drifts

The Britannia Drift is composed entirely of sandstone and dolerite clasts with a mix of weathering features and shapes. The drift sheet forms a patchy cover on the landscape but is widely distributed throughout the DBV and is divided into two units (Bockheim et al., 1989). The Britannia-II Drift extends up to 4 km into the DBV from the modern ice margin and overlies the Danum Drift displaying a distinct boulder belt moraine at its most distal limit. The Britannia-I Drift also covers a wide area and forms a patchy drift sheet overlying the Britannia-II Drift. However, the boundaries of Britannia-I Drift are poorly defined and in many places indistinguishable. While the drifts show similar sedimentology, a number of key differences are observed in the field. The Britannia-II Drift contains no perched erratics, yet in the Britannia-I Drift, they are common, with occasional fresh abrasions and small deposits of sand and clasts noted on the stoss side of some boulders, typical of cold-based glacial deposition (Atkins, 2013; Atkins et al., 2002) indicating that the two drifts were deposited by different glacial events. Our exposure age results confirm the subdivision of the Britannia Drift into two units, an older (Britannia-II Drift) and younger deposit (Britannia-I Drift) (Figure 5.6A). The Britannia-II exposure ages across the entire DBV are grouped tightly ranging from 123 to 131 ka, a mean age of 126.0 $\pm$ 3.2 ka (1σ error, n=5) placing this deglaciation phase of the Hatherton at Termination-II and within MIS-5. Although we have no independent measure of the mean erosion rate for these Beacon Sandstone erratics, applying a reasonable value of 0.5 mm ka^{-1} based on other Antarctic studies, would raise the non-zero exposure age from 126 to 133 ka. An upper limit choice would be 1.0 mm ka^{-1} taking the Britannia-II age to maximum of 145 ka. The younger Britannia-I ages range from 4.9 to 8.0 ka with a mean age of 6.5 $\pm$ 1.2 ka (1σ error, n= 8) indicating glacial retreat in the mid-Holocene period, similar to the finding of Stone et al. (2003) in Marie Byrd Land. Cumulative probability plots (Lowell, 1995) were also used to analyse grouped Britannia Drift ages (Figures 5.6B & 5.6C). The Britannia-I Drift ages display a quasi-bimodal profile with enhanced probability in the ranges $\approx$7.5 $\pm$ 1.0 ka and at 5.5 $\pm$ 0.5 ka. It is difficult to determine if this bi-modality relates to two glacial events during the early to mid-Holocene or is a result of insufficient sampling and/or a large geological variability in age determi-

nation. However, we note that the five samples from Britannia-II are well defined by a single normal distribution with a 1σ error of only 3%.

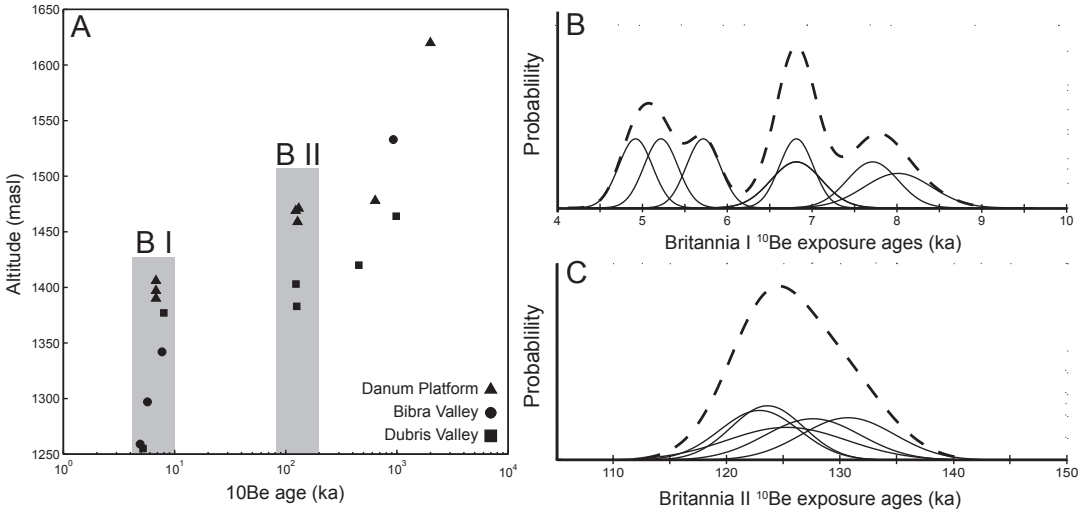

Figure 5.6: Density distribution plots for the Britannia drifts - Elevation versus ^{10}Be exposure ages for samples from the Danum Platform, Dubris and Bibra valleys (Figure A). The average exposure age error (external error, see Tables A.3, A.8, A.9,A.12, A.17 & A.18) is 10% or approximately the size of the point markers for all but the oldest sample (DP6.1, 15.3%). The shaded regions contain samples belonging to the Britannia-I (B-I) and Britannia-II (B-II) drifts. Samples outside these areas are from the Isca and Danum drifts. Figures B and C are density distribution plots for Britannia drift ^{10}Be ages. Solid black lines are based on 1σ Gaussian errors derived from the total analytical (internal) error per sample, ranging from 2.6% to 5%. The dashed lines are cumulative distributions for the all samples designated as Britannia-I (Figure B, mean $\pm 1\sigma$, 6.5 $\pm$ 1.2 ka) and Britannia-II (Figure C, mean $\pm 1\sigma$, 126.0 $\pm$ 3.2 ka).

5.2.1.2 Isca and Danum drifts

The Isca and Danum drifts were differentiated by Bockheim et al. (1989) on the basis of surface weathering characteristics and buried paleosols containing in-situ ventifacts. Both drifts contain abundant areas of desert pavement with wind polished and iron stained sandstone boulders. Dolerite ventifacts with well-developed facets are commonly embedded in the pavement surface. A few large sandstone erratics (<4 m) can also be found emplaced on pavement or bedrock with extensive taffoni (cavernous) weathering and wind polishing (desert varnish). The older Isca Drift is widely distributed throughout much of the high elevation and ice distal parts of the DBV and is often found overlain by the younger Danum Drift. The oldest

^{10}Be ages in our dataset are obtained from the Isca and Danum drifts. Samples BV8.1, DV1.1 and DP6.1 from the Isca Drift have exposure ages of 0.9 $\pm$ 0.1, 1 $\pm$ 0.1 and 2 $\pm$ 0.3 Ma. While samples collected from the Danum Drift, (DP5.1 and DV2.1) have ^{10}Be ages of 637 $\pm$ 69 and 454 $\pm$ 50 ka. Although the upper limit was not located, our Isca ages may represent the younger portions of a much thicker Plio-Pleistocene advance.

5.3 Implications for glacial chronology

As the ^{26}Al/^{10}Be paired data shows no clear burial signal, we take the simplest case that ^{10}Be concentrations of all samples represent predominately a continuous exposure history and that the upper regions of the DBV have not been overridden by ice for at least 1 Ma (or if using a maximum age model 2 Ma). The Isca Drift was deposited by an enlarged Hatherton Glacier at least 500 m above its modern elevation which advanced 4-5 km up into the DBV. Using a minimum, zero-erosion rate age model, we assign a minimum deglaciation age of $\approx$1 Ma for the deposition of the Isca Drift. Based on the limited number of samples from the Danum Drift (n=2), a minimum age of $\approx$450 ka is assigned which suggests deglaciation prior to MIS 11. The age spread recorded between the two older drifts suggest periods of either static ice volume or very slow deglaciation. The age range for the Danum and Isca drifts is in stark contrast to the strongly clustered ages observed in the younger drifts. Exposure ages within the Britannia Drifts show little to no variation between valleys or with altitude, suggesting episodes of rapid loss of ice *via* sublimation across the DBV area.

Based on ^{10}Be exposure ages, the Britannia-II Drift, inferred to be LGM in age by Bockheim et al. (1989), is older with a mean age of $\approx$126 ka, suggesting an MIS-5 deglaciation phase coinciding with a warming Antarctic climate commensurate with Termination-II (Stenni et al., 2010). Although identifying the Britannia-I from the Britannia-II *via* colour, lithology and weathering features were not always possible, the presence of perched glacial erratics on larger boulders or on bedrock was a key indicator in distinguishing the two deposits. Exposure ages from all the eight Britannia-I samples give early to mid-Holocene ages, in agreement with the minimum radiocarbon age of 6 ka cal BP (Bockheim et al., 1989) from a low

elevation sample, QL-1424 at ≈1200 masl in the Bibra Valley (Figure 5.3). The large age difference at DBV between Britannia-I (≈6 ka) and Britannia-II (≈126 ka) clearly supports the classification of the Britannia into two different phases of Hatherton Glacier and/or ice sheet volume changes. We suggest that cold-based Hatherton ice, advanced over a portion of the underlying Britannia-II Drift with only minimal deposition or disturbance (Britannia-I). This advance acted as a glacial 'salt and pepper shaker' depositing Britannia-I erratics on the older Britannia-II Drift, creating a composite drift. Additional evidence of this overriding includes the presence of crude abrasion on the stoss side of weathered boulders and occasional overturned or rotated boulders within the Britannia-I drift limit. Similar subtle features related to cold-based glacier overriding (Atkins, 2013; Atkins et al., 2002; Lloyd Davies et al., 2009) and minimal reworking of older surfaces (Bockheim, 2010) have been documented in other areas on the TAMs. Compared to the narrow deglaciation age for the Britannia-II Drift, the Britannia-I Drift ages have a distribution that can be interpreted in two ways: a single population with a mean age of 6.5 $\pm$ 1.2 ka (1σ error, n=8) suggesting a single stage of deglaciation occurred or a multi stage retreat with peaks at 7.5 and 5.5 ka continuing until 4.8 ka. Our preferred interpretation is that of the multi stage deglaciation model, which is supported by mapping the glacial geomorphology from satellite imagery and field observations which show numerous small moraine ridges across the Britannia-I Drift in proximity to the current ice-edge of Hatherton Glacier. Combined with the clear bi-modal ^{10}Be exposure ages for the Britannia-I Drift„ we propose a period of slow retreat from an advance prior to 7.8 ka and weak advances or stillstands at 6.8 and 5.2 ka where material at the ice contact margin accumulated, forming boulder-belt moraine ridges. Holocene ages are also identified in glacial drifts 850 km south of the DBV at the Reedy Glacier (85.5°S). At EAIS proximal sites (Mims Spur and Hatcher Bluff), the Reedy-III Drift was deposited at ≈4-9 ka during the last retreat from a Reedy Glacier 140-50 metres thicker than present (Todd et al., 2010). The presence of thickened ice at these sites is suggested to be caused by a short lived glacial maxima at ≈8.6 ka and possibly also at 3.5 ka (Todd et al., 2010). Therefore, given the overlap in age ranges, we correlate the Reedy-III Drift with the Britannia-I Drift, instead of the previously assigned Britannia-II (Bockheim et al., 1989; Moriwaki et al., 1992a).

From its maximum advance into the DBV since at least ≈0.5 Ma (*i.e.* MIS-16), we estimate a cumulative vertical reduction in Hatherton ice thickness of about 400 m. A reduction of ≈100 m occurred between the deposition of the Danum and subsequent Britannia-II Drift at about 120 ka (MIS-6 or 5) and only a further 50 m from Britannia-II to Britannia-I at the early Holocene. In contrast, over the next 5 kiloyears across the mid-Holocene, the Hatherton Glacier ice thickness is reduced by ≈220 m at deposition of the Hatherton Drift and finally, ≈30 m over the past few kiloyears to today's present margin.

5.3.1 The Dubris and Bibra valleys at the LGM

Identification of drift or other glacial deposits with an unequivocal LGM exposure age was not observed at the DBV regardless of age-elevation model. The Britannia-II Drift, previously assumed to be LGM by Bockheim et al. (1989), clearly shows minimum MIS-5 exposure ages and the Britannia-I Drift at DBV is early-mid Holocene. At Lake Wellman, the youngest Britannia (I and II) age was 35 ka, whilst that for the Hatherton Drift was <2 ka. At both DBV and Lake Wellman, there is neither direct field evidence nor a clustered population of exposure ages representing an ice advance at the LGM. Therefore, the question must then be posed as to where the maximum ice limits were during the LGM period and why are they absent within the five mapped drifts which span the full time period between mid-Holocene to early Pleistocene at the DBV. Our data indicate that during the LGM, no EAIS ice entered the Hatherton Glacier suggesting that LGM ice thickness of the EAIS in this locality is similar to today's observed ice volume or possibly even smaller. This is in contrast to that predicted by the Denton and Hughes (2002) model and more in agreement with Golledge and Levy (2011), Mackintosh et al. (2011) and Hein et al. (2011) who suggest smaller East Antarctic ice volumes during the LGM, particularly in the ice sheet interiors (Lilly et al., 2010). The SED results suggest that Hatherton Glacier ice incursion into the DBV is predominantly influenced by EAIS ice overspill through the TAMs.

5.4 Major conclusions

- Mapped drifts were deposited by cold-based ice at the margins of the Hatherton Glacier which periodically expanded into the DBV.
- The Hatherton Glacier retreated from its high-stand position no later than the minimum Isca Drift age of 0.99 Ma. Approximately 400 vertical metres of ice reduction has occurred since the mid-Pleistocene and ≈50% of this loss in ice surface elevation (*i.e.* ≈200 m) has occurred since the early-Holocene at about 7-8 ka.
- The Britannia-II Drift, previously defined as LGM based on limiting radiocarbon ages of ≈10 ka cal BP, correlates to a retreat from a MIS-5e highstand with a mean zero-erosion exposure age of 126.0 $\pm$ 2.9 ka (1σ error, n=5). The Britannia-I Drift shows a bimodal retreat during the early to mid-Holocene occurring at ≈7.5 and 5.5 ka, although a single retreat at 6.5 $\pm$ 1.2 ka is also plausible.
- No evidence of LGM ice incursion from the Hatherton into the DBV was identified from our ^{10}Be exposure ages, suggesting that the EAIS during the LGM may have been lower than observed today

Chapter 6

Glacial history of the Lake Wellman area

This Chapter summarises the 2010 paper:
Cosmogenic nuclide exposure age constraints on the glacial history of the Lake Wellman area, Darwin Mountains, Antarctica.
Storey, B. C., Fink, D., Hood, D., Joy, K., Shulmeister, J., Riger-Kusk, M. & Stevens, M. I.
Antarctic Science 2013, 22(06), 603-618 (Appendices section B.2)
My contribution to this paper is outlined in the University of Canterbury "Co-Authorship Form" located on page vi of this thesis.

6.1 Locality description and geomorphology

The Lake Wellman area (77.9°S, 156.9°E) is found approximately 12 km upstream from the confluence of the Hatherton and Darwin glaciers and ≈60 km downstream from the EAIS. The ice free valleys and glacial cirques in the region flank the Hatherton Glacier and reach elevations of 1700-1800 masl within the Darwin Mountains. Lake Wellman lies at the modern margin of the Hatherton Glacier and key to this research is that the area contains one of the better preserved sequences of the glacial drifts in the DHGS identified by Bockheim et al. (1989) and is the location from which their radiocarbon deglaciation chronology is based (Sections 4.6.1 and 4.7.1). Bockheim et al. (1989) estimated the upper limit of the Hatherton Drift (Figure 6.1A) was 20-70 m above the present surface of Lake Wellman, the Britannia Drift (Figure 6.1B) extended a further 450 m above the Hatherton, and the

Danum Drift (Figure 6.1C) 50-100 m above the Britannia limit. Above the Danum, at high elevation sites within the Lake Wellman area is the oldest drift, the Isca (Figure 6.1D). This effectively suggested that the total ice thickening at the time of deposition of the Danum Drift sheet was about 600 m higher than the current elevation at Lake Wellman (≈800 masl) and using a modern Hatherton ice surface altitude of 960 masl, an ice thickness of at least 500 m greater than today.

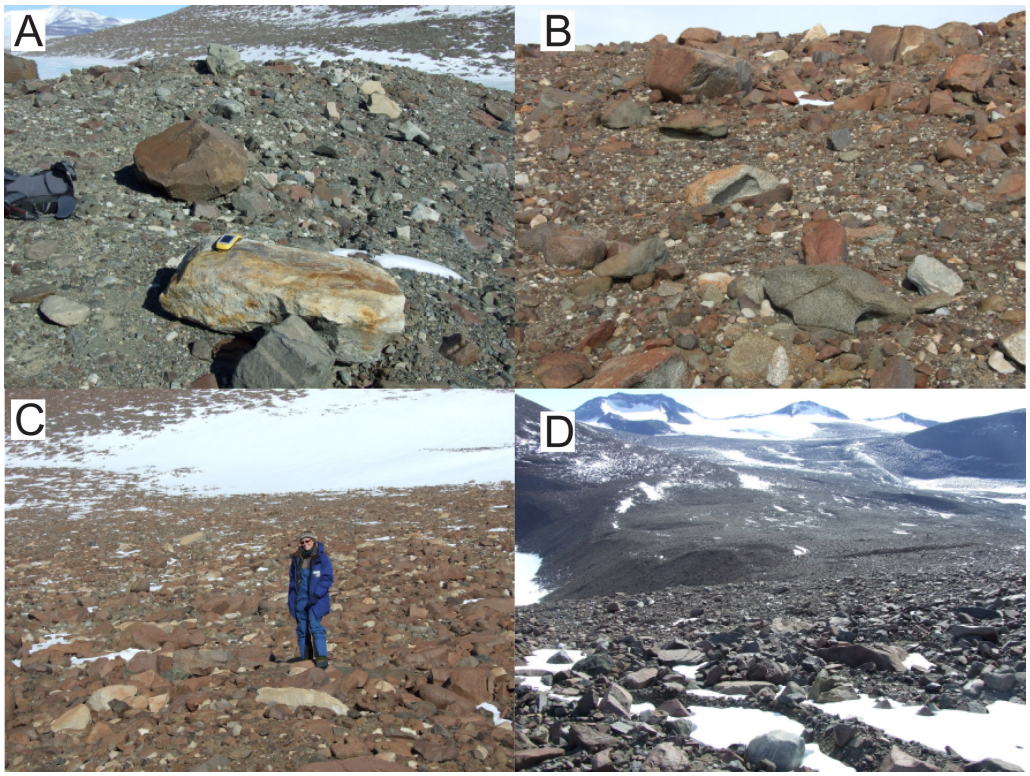

Figure 6.1: Glacial drifts at Lake Wellman - The four drifts defined by Bockheim et al. (1989), separated based on differences in weathering, lithology and soil development. In order of age, youngest to oldest with suggested ages by Bockheim et al. (1989) in brackets. (A) Hatherton Drift at site LW25 (Holocene) (B) Britannia Drift at site LW2 (MIS-2). (C) Danum Drift at site LW15 (MIS-6). (D) Isca Drift at site LW12 (Pleistocene).

Within the drifts, a number of key geomorphological features are noted:

1. Moraine ridges and boulder lines are found at both upper drift contacts and within glacial drifts. The youngest drift, the Hatherton, has prominent moraine ridges (Moraine-1 at an elevation of ≈800 masl, Figure 6.2A) within its ice-cored hummocky terrain, while another large moraine separates the Britannia and Danum drifts (Moraine-2 at an elevation of ≈1060 masl, Figure 6.2B).

2. A correlation between the morphological preservation of individual drift sheets, distance from the ice margin and age according to Bockheim et al. (1989). The percentage of surface modified boulders (*i.e.* fractured, pitted, and spalled) and development of surface varnishing and cavernous weathering (tafoni) increases with drift age, while the percentage of perched, striated and plucked boulders decreases. These latter features are more common in the younger drift sheets closer to the ice margin, particularly the Hatherton and Britannia.

3. While the upper contacts that define the overlapping of a younger drift with a older one are relatively well preserved in the Lake Wellman area, in places they can be subdued and poorly preserved. In particular, the boundary between the Danum and the Isca, the oldest observed drifts, appears to be gradual as opposed to a sharp contact.

4. The Britannia Drift was mapped by Bockheim et al. (1989) as a single extensive deposit following a major glacial advance. This is in contrast to the Britannia observed in the Dubris and Bibra valleys (Chapter 5), where Bockheim et al. (1989) divided it into two separate events. The Britannia-II, interpreted as MIS-2 and the later Britannia-I, interpreted as Holocene.

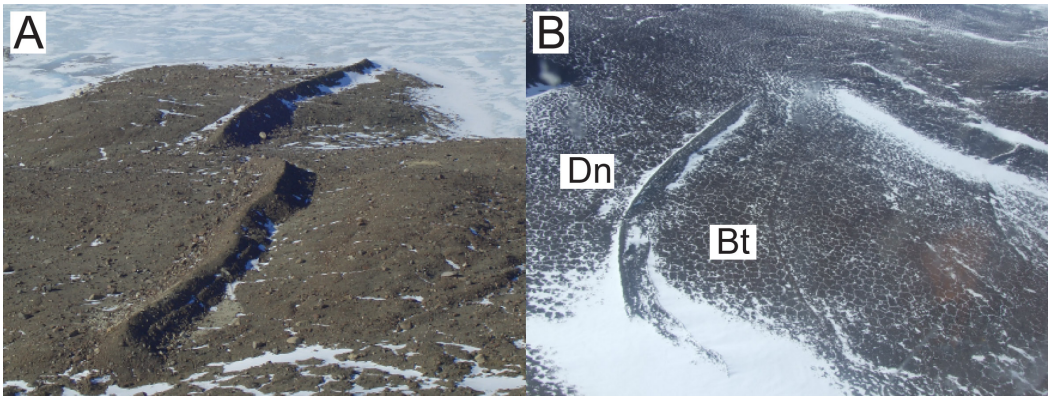

Figure 6.2: Moraines at Lake Wellman - Large asymmetric moraine ridges observed both proximal (A) and distal (B) to the modern ice margin. (A) Moraine-1 within the Hatherton Drift next to Lake Wellman. Ridge is 2-3 m high and ≈760 m long. (B) Moraine-2 at the upper contact between the Britannia (Bt) and Danum (Dn) drifts. Ridge is 7-11 m high and ≈11 m long. Advancing ice moves from right to left in both images.

6.2 Surface exposure dating

Using satellite imagery and the mapped glacial contacts of Bockheim et al. (1989), the morphology of the drifts and moraines were closely examined with a particular focus on the selection of sites suitable for SED sampling (Figure 6.3). We collected glacially transported sandstone and granitic erratics exposed on the upper surfaces of the four drifts to determine *insitu* ^{10}Be and ^{26}Al surface exposure ages. The samples came from two elevation transects from the modern ice surface to the highest altitude glacial drift (Fig. 6.3). Transect A-A' includes erratics from the Hatherton (including Moraine-1), Britannia, Danum and what Bockheim et al. (1989) defined as an "undifferentiated drift". Transect B-B' covered the Britannia (including Moraine-2), Danum and Isca drifts. Stable, rounded sandstone and granite clasts, in open sky settings, were preferentially sampled because they demonstrate glacial transport, minimize the likelihood of inheritance and are less likely to have moved since deposition (see Section 2.2 for a discussion). Samples that exhibited signs of post-depositional reorientation or partial burial by sediment were avoided and preferentially small erratics perched on larger stable boulders were sampled. Tables A.4 and A.5 (in appendices) provide locations and descriptions of erratics selected for dating.

6.2.1 Results

Transect A-A' ^{10}Be exposure ages ranged from 1 ka-2.3 Ma, and from 16-415 ka for transect B-B' (Tables A.6 & A.7 for AMS results, tables A.8 & A.9 for exposure ages). Corresponding ^{26}Al ages for A-A' ranged from 0.7 ka-2 Ma and from 31-340 ka for B-B'. For four samples (LW11.1 and LW9.3 on transect A-A'; LW14.1 & LW14.3 on transect B-B') ^{26}Al ages are not available due to laboratory failures in the analysis of ^{27}Al or unreliable AMS determinations of ^{26}Al/^{27}Al ratios. In general, the oldest ages occur at highest elevations with the youngest ages closest to the present ice surface (Figure 6.4), but neither of the two transects show an entirely consistent age-elevation trend.

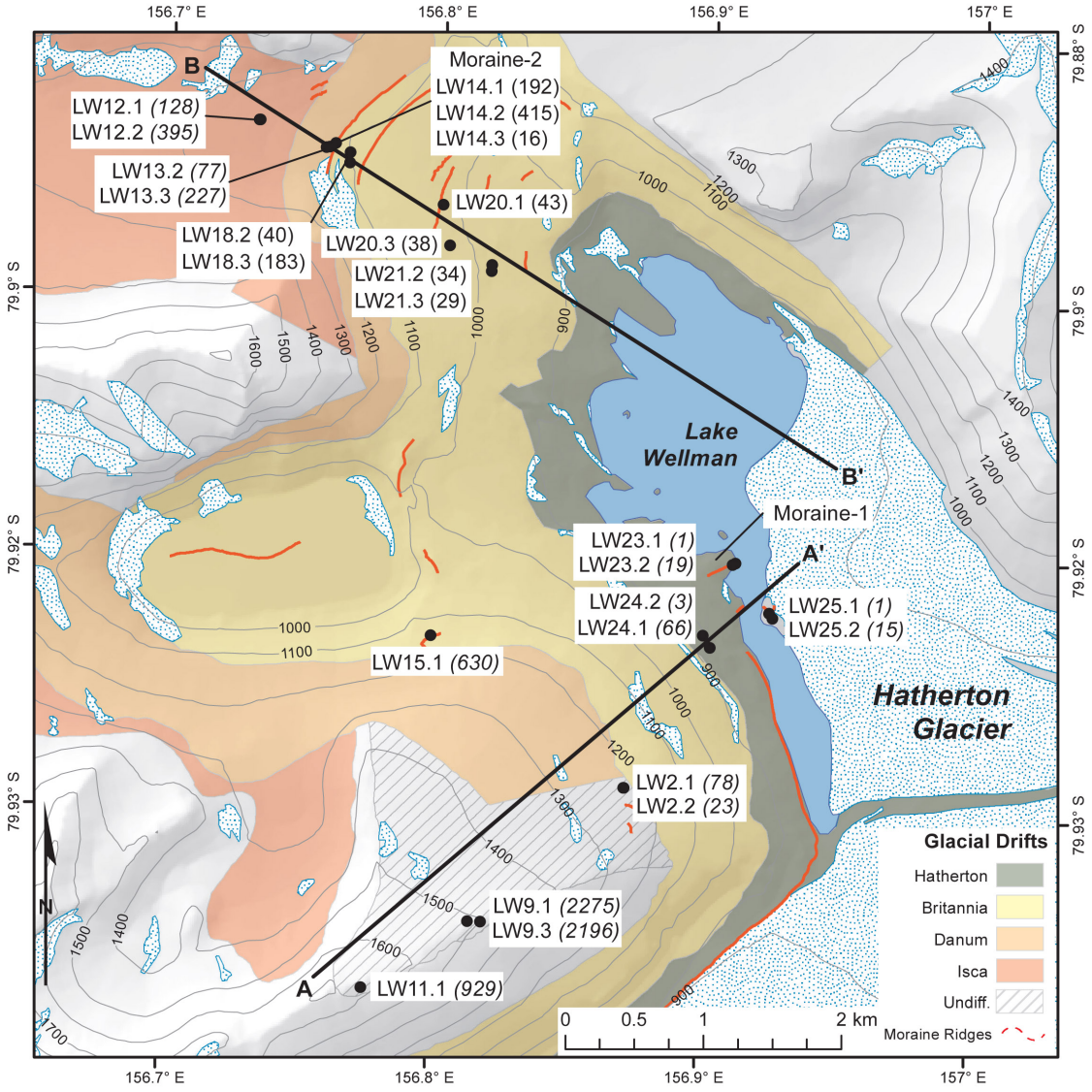

Figure 6.3: Map of the Lake Wellman area - Showing the distribution of the four main drift sequences after Bockheim et al. (1989). Black bold lines A-A' and B-B' represent altitudinal transects along which samples were collected for SED. Sample sites are labelled, followed by bracketed ^{10}Be ages in ka. Hatherton Glacier ice flows from bottom-left to top-right in a direction semi-parallel to transect A-A'.

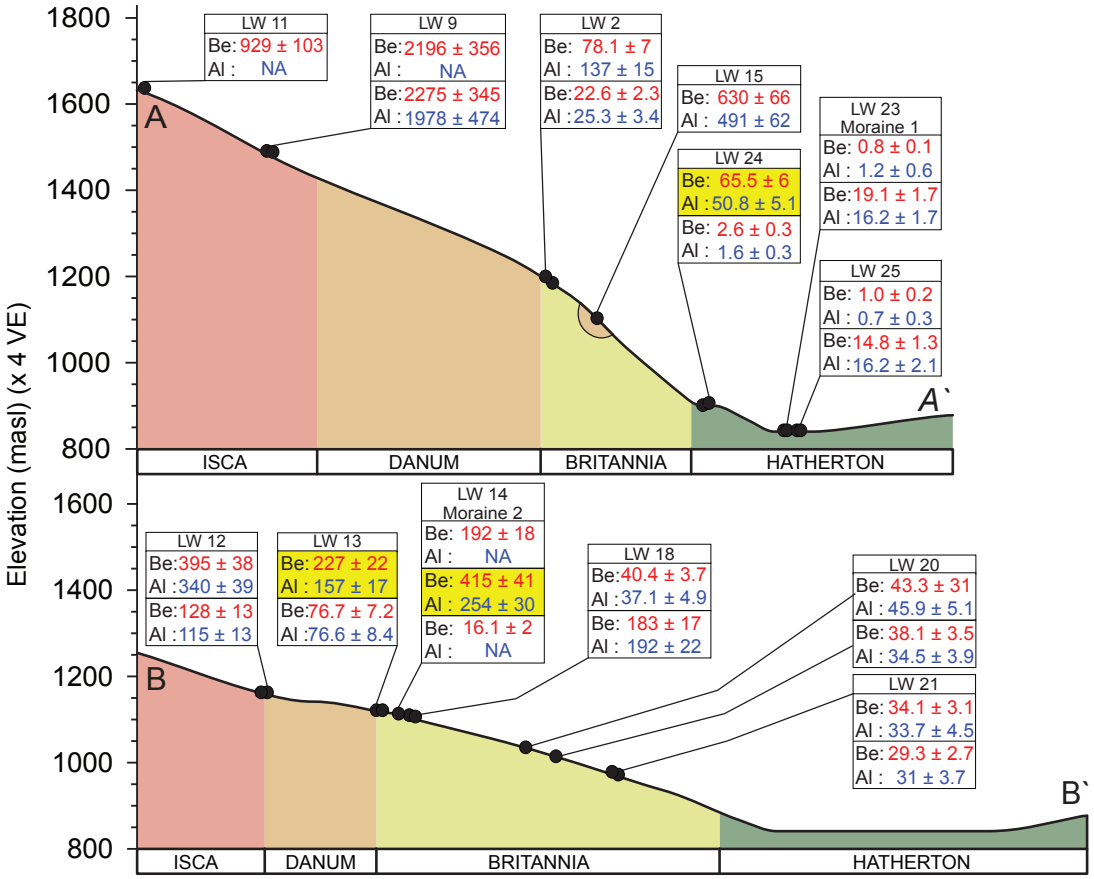

Figure 6.4: Transect exposure age profiles for Lake Wellman - ^{10}Be and ^{26}Al exposure ages for analysed samples from transect A-A' and B-B'. All ages are given in ka. Red numbers represent ^{10}Be and blue ^{26}Al ages. Yellow boxes indicate samples that reflect a distinct burial history, based on depressed ^{26}Al/^{10}Be ratios (see Figure 6.5). Note that site LW15, while at a similar elevation to the Britannia Drift, is designated Danum Drift.

Complexities in the exposure history of erratics are clearly evident at Lake Wellman, including a wide spread of ages and a subset of samples clearly showing periods of burial (Figure 6.5). Despite the observation of overall increasing age with elevation, these complexities preclude a definitive conclusion regarding the specifics of ice volume changes of the Hatherton Glacier. However we can apply model constraints on age-elevation trends to qualify the relative ice volume changes over time. An approach to achieve a plausible chronology of Hatherton ice volume change assumes that selecting either the youngest or oldest ages from each site (or drift) defines the possible end members of age-elevation models. In a minimum age model, older erratics at lower than expected elevations are presumably due to excessive inheritance, whilst for a maximum age model, younger erratics can appear at higher elevations due to resetting, post-depositional modification or cold-based deposition over older surfaces. We filter the sample population by first applying a criteria, based on a plot of $^{26}Al/^{10}Be$ ratios versus normalized SLHL ^{10}Be concentrations (Figure 6.5), to identify the subset of samples deemed inappropriate for inclusion.

Three samples, namely LW14.2 (located on the apex of Moraine-2), LW13.3 and LW24.1, of the plotted 17 show unequivocal evidence for a complex exposure with burial. $^{26}Al/^{10}Be$ ratios for these three samples falling well within the defined burial zone of Figure 6.5. For example, LW14.2 (^{10}Be 415 $\pm$ 41 ka; ^{26}Al 254 $\pm$ 30 ka) shows a considerable integrated history of pre-exposure, burial (>0.5 Ma), and an unspecified final re-exposure. Within the criteria of overlapping 1σ analytical error for the $^{26}Al/^{10}Be$ ratio and respective 1σ error envelope for the exposure-erosion island (due to a 9% uncertainty in production rates), the remaining 14 samples can be deemed to be consistent with an interpretation of continuous exposure. Samples LW23.1, 24.2, and 25.1 (where ^{10}Be ages are less than 2-3 ka and hence burial calculations are not appropriate) and LW2.1 (which has an ^{26}Al age larger than the ^{10}Be age by more than 2σ) are not shown in Figure 6.5.

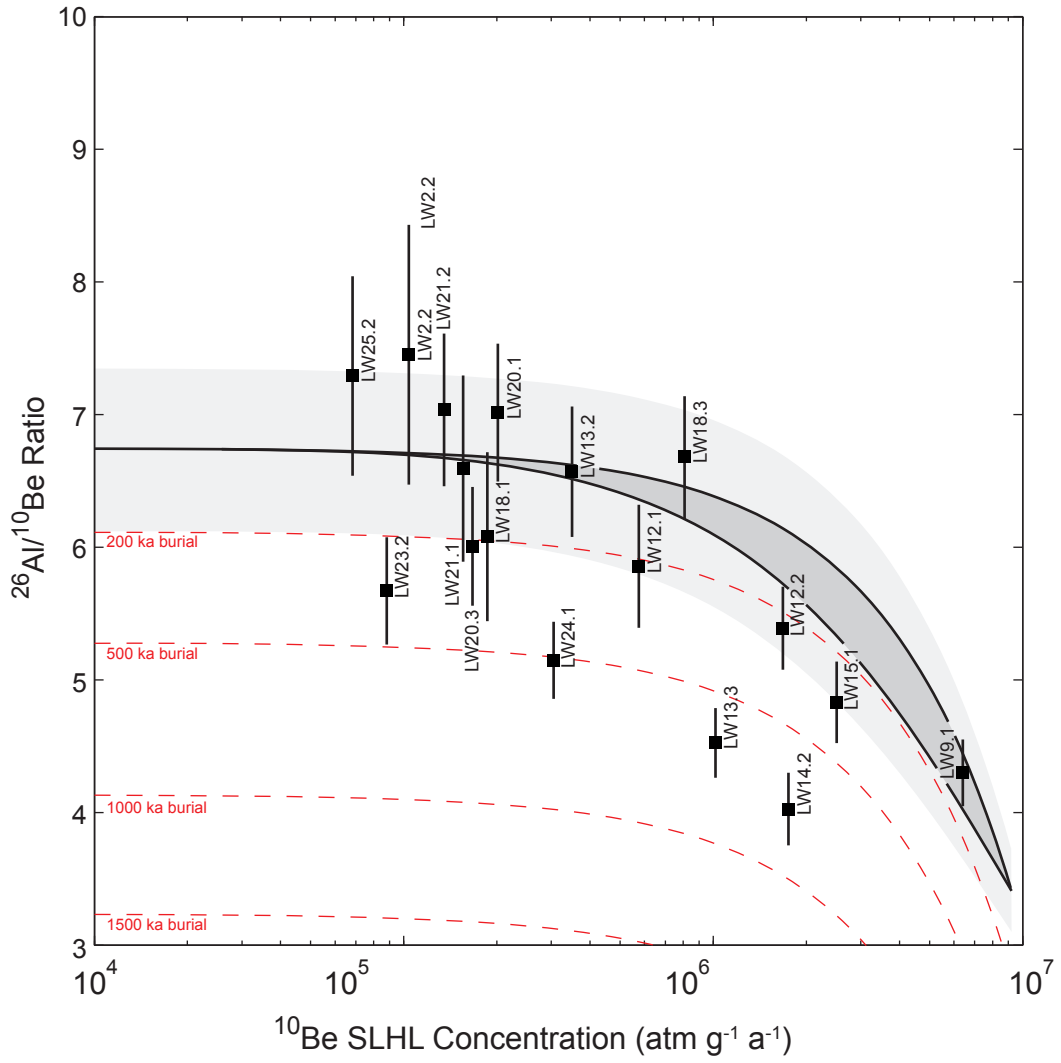

Figure 6.5: Dual-nuclide plot for Lake Wellman SED samples - A plot of ^{26}Al/^{10}Be ratios versus normalized SLHL ^{10}Be concentrations showing the exposure history of analysed samples The upper black curve represents continuous exposure at zero erosion, while the lower black curve steady state erosion. Exposed surface samples undergoing erosion will fall within the two loci defining an area termed the steady-state exposure island (Dark grey). Burial isochrons of 200 ka, 500 ka, 1 Ma and 1.5 Ma are also shown. Error bars are derived from analytical errors only. Samples LW13.3, 14.2 and 24.1 show an unequivocal burial signal, whereas in contrast that for LW23.2, LW20.3, LW18.1 and LW12.1 are uncertain given that the minimum detectable burial age is 150-200 ka. The light grey area represents a $\pm$ 9% error in ^{26}Al and ^{10}Be production rates (Balco et al., 2008).

For the Lake Wellman dataset, which demonstrates multiple glacial cycles and is restricted to erratics on drift sheets, a maximum age model also requires consideration. It appears to be more consistent with the overall field observations and the extended million year exposure age scale than an alternate interpretation based on minimum ages. We also apply a second filter by rejecting the remaining two of the three samples collected from Transect B-B' at site LW14 on the surface of the unconsolidated Moraine-2 (Figure 7.4B). The results from LW14 exhibit the most complexity in exposure age interpretation. We feel this is justified on the basis that:

1. Neither of these two samples unfortunately is reported with an ^{26}Al age.
2. The three ^{10}Be ages come from samples in very close proximity to each other.
3. Moraine-2 showed strong evidence of surface modification and deformation. Likely due to being sediment rather than clast supported

Moraine-2 is a composite feature likely resulting from either multiple advances (perhaps over a time period of 30-400 ka) or a single event deposited material with prior cosmogenic inventory. Either suggestion confirms our field observations that the moraine is still undergoing a continuous process of modification, via a mix of solifluction, deflation and mass movement. It is also important to note that the three rejected samples from Moraine-2 (LW14) are all small cobbles or boulders in comparison to the other larger than metre-sized erratics from transect B-B'.

6.2.1.1 Hatherton Drift

No samples from Hatherton Drift were available for collection on transect B-B'. Two of the three lowest elevation sites at 850 masl on transect A-A' (*i.e.* LW23, LW25), are effectively at the ice contact margin of the present Hatherton Glacier and the Lake Wellman shoreline. LW23 samples were taken from the apex of Moraine-1 (Figure 7.4A). The third site, LW24 (895 masl), is adjacent to the boundary of the Hatherton and Britannia drifts and only 50m above the surface of Lake Wellman (note that the modern elevation of the central axis of Hatherton Glacier is at 960 masl). Exposure ages (either ^{10}Be or ^{26}Al) for all six samples (n=2 per site), show a striking complexity in the A-A' transect. The ^{10}Be ages from each pair of samples

from each of the three sites are incompatible with each other but show a bimodal distribution. ^{10}Be ages for three of the samples cluster together between 0.8 and 2.6 ka, whereas two others are 14.8 $\pm$ 1.3 and 19.1 $\pm$ 1.7 ka. Respective ^{26}Al ages for each of these five samples show a similar pattern. The sixth sample, LW24.1, with a ^{10}Be age of 65.5 $\pm$ 6 ka is inconsistent with this trend and shows a distinct burial signal (Figure 6.5). Our options for Hatherton Drift are:

1. In the minimum age model, that it is a late Holocene - modern deposition (*i.e.* younger than 2-3 ka), older ages are rejected due to inheritance equivalent to 15 ka.

2. In the maximum age model, the drift is defined by the 14.8 $\pm$ 1.3 and 19.1 $\pm$ 1.7 ka ^{10}Be exposure ages of LW25.2 and LW23.2 respectively. The near zero ages being rejected on the basis of recent exhumation and post-depositional modification. Therefore the last local glacial maximum of Hatherton Glacier occurred between 15-19 ka.

When the Storey et al. (2010) paper was first published, the older ages for site LW23 and LW25 (#2) were the preferred interpretation for the Hatherton Drift. This conclusion was based on the abundant evidence of reworked boulders in the Hatherton Drift where striated and weathered surfaces have been fragmented, chipped and fresh surfaces exposed. However since then, results from other sites in the DHGS (Diamond Hill & the Dubris and Bibra valleys) have allowed a further revision of the Hatherton Drift age (discussed in Chapters 5 & 7). Therefore scenario #1, that of the Hatherton drift at Lake Wellman as being a late-Holocene deposit is now the preferred interpretation using a minimum age model. Choosing a young age for the Hatherton Drift leads to the question of the location of the local LGM advance at Lake Wellman. Of the eight samples within the next oldest drift, Britannia, only one resembles an LGM age (*i.e.* 23 ka at LW2.2), and five from transect B-B' show a well constrained pre-LGM age for the Britannia Drift of 35.6 $\pm$ 1.5 ka.

6.2.1.2 Britannia Drift

Applying the same procedure gives estimates of a minimum and maximum ^{10}Be Britannia Drift age of 23 $\pm$ 3 ka and 183 $\pm$ 17 ka (n=8). These age boundaries are consistent with the respective minimum and maximum deduced for the older Danum and Isca drifts. However, an alternate and sounder estimate is offered for the age of Britannia Drift that acknowledges the statistical age distribution of five of the eight ages. The three pairs of samples from three sites in transect B-B' below the elevation of Moraine-2 were collected along the upper 1 km width of the Britannia Drift covering an elevation range of 981-1087 masl. Five of these six ^{10}Be ages show a well constrained cluster from 29.3 $\pm$ 2.7 to 43.3 $\pm$ 4.1 ka. This is statistically consistent with a single population with mean age and 1σ error of 37.0 $\pm$ 5.5 ka and a weighted mean age of 35.6 $\pm$ 1.5 ka; a similar result is obtained for the ^{26}Al ages (35.5 $\pm$ 1.9 ka). The single outlier, sample LW18.3 (183 $\pm$ 17 ka), which actually determines the maximum Britannia age, appears to be five times older than the mean Britannia age (n=5). A second approach is based on the remaining two samples (LW2.1 and LW2.2 from transect A-A') which gives a minimum Britannia age of 23 $\pm$ 3 ka (as above) or maximum age of 78 $\pm$ 7 ka. These two age limits for Britannia bracket the spread in the ages of the five samples (*i.e.* 29 to 43 ka) used to calculate the single population mean age.

6.2.1.3 Danum Drift

Two sites at intermediate elevations of 1100 masl are associated with Danum Drift. On transect A-A', lying 1 km off the main axis site is LW15 (n=1) and from transect B-B', site LW13 (n=2) is up-slope and adjacent to Moraine-2. We presume that Moraine-2 marks the maximum ice extent of the younger Britannia Drift over the older Danum. Selection of either a minimum ^{10}Be age of 77 ka for LW13.2 or a maximum age of 630 ka (LW15.1) for the Danum Drift deposition are both consistent with respect to stratigraphic age increasing with altitude based on the same age model criteria when applied to the Isca Drift. However, as LW15.1 does not lie directly on the main A-A' axis, a tentative maximum age of 230 ka is assigned from LW13.3, but note that this sample shows divergent ^{10}Be and ^{26}Al ages.

6.2.1.4 Isca Drift

Based on a maximum age selection, the three samples from LW11 and LW9 at the highest elevation (1575 masl), record the oldest ^{10}Be ages of the full dataset; 0.9 $\pm$ 0.1, 2.2 $\pm$ 0.4 and 2.3 $\pm$ 0.3 Ma respectively. These two sites lie within undifferentiated drift but their locations, being at the same altitude and directly adjacent to Isca Drift, are consistent with a far more extensive volume of Hatherton Glacier during the early to mid-Pleistocene and suggest a 1-2 Ma age retreat for the Isca. In transect B-B', the highest elevation samples (LW12 at 1155 masl) give widely different ^{10}Be exposure ages of 128 $\pm$ 13 and 395 $\pm$ 38 ka (with concordant ^{26}Al ages). The latter exposure age being the oldest of the B-B' transect and is far younger than the oldest A-A' transect age (LW9, 2.2 Ma at 1500 masl). Although the LW12 ages are clearly divergent, they demonstrate a minimum glaciation age for Isca Drift of between 130-400 ka, equivalent to MIS-6 or MIS-10. With a ^{26}Al exposure age near saturation (at zero erosion) for LW9.1 and equivalent ^{10}Be age for adjacent sample LW9.2, it is difficult to explain such old ages to be a result solely due to inheritance. Therefore, it appears that no ice has advanced over this location for at least the past 1 Ma and more probably over the past 2 Ma.

6.3 Implications for glacial chronology

At its maximum ice extent $\approx$2.2 million years ago in the Pliocene, ice was at least 800 m thicker than the present ice level at Lake Wellman or 680 metres thicker than the ice reference surface for Hatherton Glacier today. We suggest, based on the volume and extent of glacial debris that warm based ice blanketed the whole area at this time. We do not rule out re-advances of the ice, in fact, the discordant ages of Isca drift material between the two transects suggests that the lower elevation Isca site on transect B was re-occupied by ice $\approx$400 ka in the mid to late-Pleistocene and that a single designation for this drift may be somewhat unhelpful. According to our preferred interpretation, the Danum drift appears to be 230 ka and most likely is MIS-8 although a Late Quaternary age ($\approx$75 ka) cannot be discounted from the data. Moraine-2, if deposited by Britannia drift at $\approx$35 ka indicates

the elevation to which ice reached during the last major ice expansion in this area. This is 500 m lower than the major overriding ice event in the mid-Pliocene.

6.3.1 The Lake Wellman area at the LGM

Our strongest constraint on the Britannia Drift (suggested being of LGM age by Bockheim et al., 1989), downhill of Moraine-2 comes from the tightly clumped five ages of LW18, LW20, and LW21 of 35 ka (omitting LW18.3). This is compatible with observations from elsewhere in East Antarctica that demonstrate maximum last glaciation ice extent well before the LGM (Gore et al., 2001). The LGM limit appears to be restricted to the Hatherton drift whose upper limits are at an elevation just 50 meters above the modern ice sheet surface. This indicates that the magnitude of LGM ice at this location may have been minor. In fact there is no conclusive evidence that LGM ice was ever above modern limits as the pre-Holocene ages from LW23, LW24 and LW25 are deglaciation ages and may relate to a post-LGM thickening as precipitation increased on the polar plateau after the end of the cold dry LGM phase.

6.4 Major conclusions

- The maximum recorded ice thickness of the Hatherton Glacier in the Lake Wellman area was at least 690m thicker than the modern elevation of the Hatherton Glacier surface.

- The Isca Drift was deposited by a Pliocene advance of an outlet glacier of the East Antarctic Ice Sheet more than 2.2 million years ago.

- The Danum Drift, based on a maximum age scenario, was deposited at 630 ka, but an MIS-4 age ($\approx$75 ka) is also possible.

- The ages for the Britannia Drift suggest that the last substantial thickening of ice in this area occurred prior to 30-45 ka (MIS-3); ice thinning progressively after that time.

- The Hatherton Drift represents ice volume changes from LGM through to the late Holocene. While a maximum age model for the Hatherton Drift suggests that local LGM ice volume was only slightly thicker than present, the preferred interpretation from minimum exposure ages infers that it represents a late-Holocene ice advance.

Chapter 7

Glacial history of Diamond Hill and Roadend Nunatak

7.1 Locality description and geomorphology

7.1.1 Diamond Hill

The 1340 metre high Diamond Hill (79.9°S, 159.5°E) is a ≈40 km^2 ice free area, bordered to the east by the Ross Ice Shelf (RIS) and to the south by the Darwin Glacier (Figure 7.1). Low elevation sites at Diamond Hill were previously visited by Bockheim and Wilson (1979), but areas close to the upper limits (1200 masl) of the LGM WAIS suggested by Bockheim et al. (1989) were not (Denton, pers comm). Therefore, field work in 2008-2009 was focused on interpreting the glacial deposits and establishing the past history of the WAIS at Diamond Hill.

Compared to the variety of glacial features (*i.e.* drift sheets, moraines, boulder belts and debris cones) observed at sites on the margins of the Hatherton Glacier further up valley, the glacial features at Diamond Hill are relatively sparse and subdued. Geological mapping of the area by Haskell et al. (1964) and Grindley and Laird (1969) show that the majority of the Diamond Hill area is composed of granitic bedrock, with Quaternary ice-cored moraines, drifts and tills found on the eastern side below ≈200 masl. The four component sequence of glacial drifts observed by Bockheim et al. (1989) at Lake Wellman, Dubris and Bibra valleys are conspicuously absent from the two sites visited in the lower parts of the DHGS (*e.g.* Diamond Hill & Roadend Nunatak). Instead the Quaternary drift material at Diamond Hill is suggested by Bockheim et al. (1989) to be of a similar age to the Britannia

Drift found at sites throughout the Darwin Hatherton glacial system (DHGS, see Chapter 4). This correlation is based on a limited area of undifferentiated material in the Brown Hills (West of Diamond Hill, Figure 7.1) that displays similar soil development to that of the Britannia-II. Bockheim et al. (1989) suggested that the location of the drift, at elevation no more than 50 metres above the modern Darwin Glacier, was consistent with the thickened LGM ice hypothesised at this location. Additionally, radiocarbon ages obtained from algal mats preserved within the drift at Brown Hills suggest an ice retreat from the area at 5-6.6 ka cal BP (Bockheim et al., 1989), similar to the age proposed for the Britannia Drift at Lake Wellman (Section 4.7.1).

Figure 7.1: Regional map of the lower Darwin Glacier - Showing the field work areas of Diamond Hill and Roadend Nunatak visited in 2008-2009 and other locations discussed in text. Sites marked in red (DH7 & DH9) are Hatherton Drift ice-marginal sites discussed in Section 7.1.1.1, see Figure 7.7 for detailed views of both areas.

Using the extent of the mapped Quaternary drift (Grindley and Laird, 1969) and observations from the 2008-2009 field season, three discrete geomorphic subunits were identified and mapped at Diamond Hill, which are referred to in this work, from lowest to highest in elevation, as the Hatherton Drift, Diamond Drift and Upper Drift.

7.1.1.1 Hatherton Drift (<150 masl)

Throughout the low (<150 masl) elevations of Diamond Hill, a conspicuous glacial drift limit is observed. This drift is characterised by a fresh, un-weathered, grey

coloured appearance and is predominantly comprised of angular to sub-angular granitic and granite-gneissic clasts (Figure 7.2). Typically the drift is relatively thin (<0.5 m), clast supported and observed overlaying both ice and exposures of weathered bedrock.

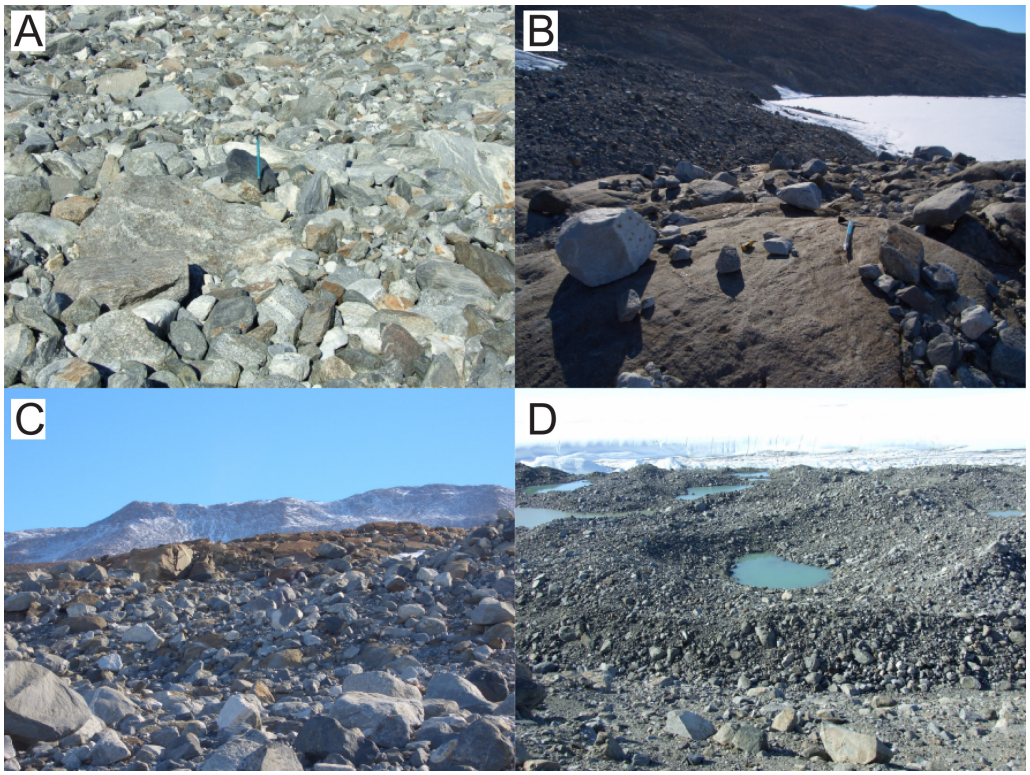

Figure 7.2: The Hatherton Drift at Diamond Hill - Unweathered glacial deposit observed at elevations <150 masl at the margins of Diamond Hill with the Darwin Glacier and Ross Ice Shelf. (A) Fresh sub-angular granitic drift at the glacier margin. (B) Glacial erratics deposited on striated bedrock at site DH7. (C) Upper contact of the Hatherton Drift (foreground) with older weathered bedrock (background). (D) Ice-cored moraine and kettle holes at DH9 near the RIS margin.

Although lithologically different to the predominantly Beacon Sandstone composition of the Hatherton Drift found in other locations (*i.e.* Lake Wellman and Dubris Valley), the drift is tentatively correlated to the Hatherton Drift of Bockheim et al. (1989) based on:

- The position of the drift relative to the modern ice margin.
- Lack of weathering and soil development.

- Angularity of clasts.
- Lack of fine grained sediments.

The areal extent of the drift is limited compared to the other identified drifts observed at Diamond Hill. The Hatherton Drift is deposited in a narrow (≈400 m wide) strip bordering from modern ice margin at the RIS (≈80 masl) up to the contact with the older Diamond Drift (≈120-150 masl). Two ice marginal sites, DH7 and DH9 (Figure 7.1), were visited within the Hatherton Drift and while angularity, weathering characteristics and elevation were similar, the variety of observed glacial features was significantly different between sites.

The more southerly site, DH7, is located near the grounding line of the DHGS and directly adjacent to the 'Nozzle', where Darwin Glacier ice reaches its highest velocity (≈180 m a^{-1}, Riger-Kusk 2011) before discharging into the low velocity RIS. The Hatherton Drift at this site is characterised by a thin surficial deposit, predominantly boulder to cobble sized, but often underlain by a thin layer of fine sediment and sand. At its lowest elevation at the ice margin, a series of bedrock outcrops, such as tors, whalebacks and extended platforms are overlain with a variety of glacial debris. These exposures are striated, display limited glacial polish and have a scattering of glacially emplaced material on their upper surfaces, such as pebbles, cobbles and boulders of various lithologies; this being a key characteristic of the site (Figure 7.2B). The Hatherton Drift also displays a number of trends with elevation, distance from ice margin and presumably age:

- An increase in drift thickness.
- A decrease in preservation of striated bedrock.
- An increase in bedrock weathering.
- A reduction in sediment content.

These suggest that over time the volume of deposited material at this site has been decreasing. At lower elevations, bedrock exposures only have a limited amount of perched cobbles and boulders and well preserved glacial polish and striations are common. As the upper elevations of the drift (<120-150 masl) are approached,

glacial material thickens (<0.5 m), individual clasts display more weathering and the drift sheet drapes around and up to the margins of weathered bedrock exposures (Figure 7.2C).

Near site DH9 and south of Lake Wilson (Figure 7.1) on the eastern side of Diamond Hill, the topography flanking the relatively static margin of the RIS is low lying and flat compared to that of the sloping (10-25°) Darwin Glacier side. At DH9, the general appearance of the Hatherton Drift is also similar to that of site DH7 (*i.e.* un-weathered, sub-angular and grey coloured), but absent are the bedrock exposures with perched cobbled observed at the Darwin Glacier margin. Instead the Hatherton Drift is characterised by a group of hummocky ice-cored moraines containing numerous kettle holes and ponds (Figure 7.2D). The areal extent of ice-cored drift at this site is effectively impounded between the RIS ice margin to the east and to the west by a large older moraine complex at a slightly higher elevation, the only one observed in the Diamond Hill area. At this location, the older moraine ridge also delineates the Hatherton Drift from the lower section of the next unit, the Diamond Drift. As viewed from both sites (DH7 & DH9), only rare examples of supra-glacial material appear on the surfaces of the RIS and Darwin Glacier.

7.1.1.2 Diamond Drift (150-450 masl)

Above the Hatherton Drift at ≈150 masl a distinct change in colour and clast morphology occurs (Figure 7.2C). Grindley and Laird (1969) mapped the majority of Diamond Hill as exposed granitic bedrock, however based on our mapping between ≈150-450 masl another geomorphic unit is evident. This drift appears distinct from those at Lake Wellman and Dubris Valley and is informally labelled in this thesis as the Diamond Drift. Widely dispersed in the south-eastern parts of Diamond Hill above site DH7, the lower section of the Diamond Drift has been overlain by the Hatherton Drift, but towards higher elevations of ≈450 masl, the drift material thins exposing in various localities the underlying bedrock (Section 7.1.1.3). One of the key characteristics of the Diamond Drift is the relatively high level of weathering in the sub-angular to rounded boulders and cobbles compared to that of the Hatherton Drift. Granitic clasts have a distinctive orange iron staining and varnish (Figure 7.3A), tafoni and surficial weathering pits (up to 0.4 m deep) are very

common, with the development of these features increasing with elevation (Figure 7.3B). Large glacially transported granite and dolerite erratics (<3 m, Figure 7.3C) are extremely common at lower drift elevations. Smaller perched boulders typically emplaced on large exposures of polished and striated bedrock or feldsmeers are also common. Throughout the Diamond Drift, boulders show crude striations, chipping and post depositional rotation, all suggested by Atkins (2013) as evidence of landscape modification by cold-based ice advances.

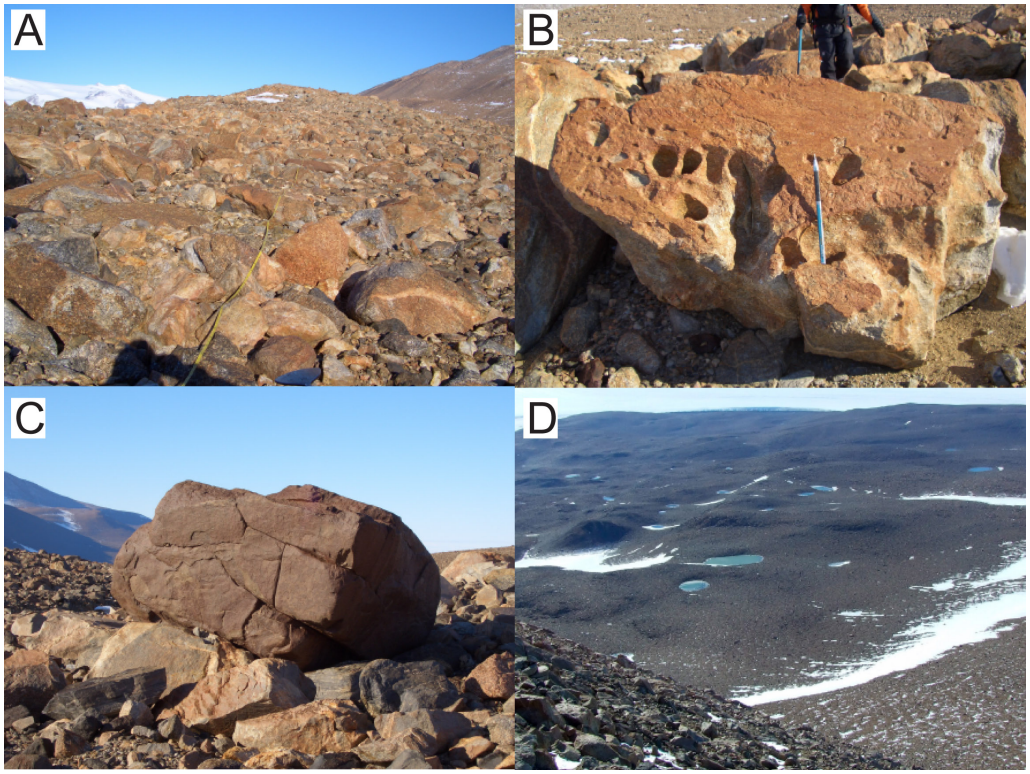

Figure 7.3: The Diamond Drift at Diamond Hill - (A) Typical appearance of the Diamond Drift between ≈150-450 masl. (B) Large granite erratic showing well developed weathering features such as tafoni and pitting. (C) Large dolerite (≈2 m) and granite erratics (<1 m) emplaced together on the Diamond Drift. (D) Overlooking the ponds and patterned ground commonly observed in the upper parts of the Diamond Drift.

While the Diamond Drift has a similar sedimentology to the Hatherton at the Darwin Glacier margin (*i.e.* a thin subdued carpet of material draped around bedrock exposures), the degree of weathering is evidence for a far older deposit. Few glacial features are observed in the Diamond Drift compared to that of the Hatherton. The landscape above 150 masl is typically gently sloped, undulating and intersected

by gullies and bedrock ridges. At higher elevations up to ≈500 masl, numerous shallow ponds and small lakes (Webster-Brown et al., 2010) are surrounded by limited areas of patterned ground (Figure 7.3D). Another notable feature of the Diamond Drift is that the surface appears to be compressed and surficial clasts are 'locked' together. This surface texture is similar to peri-glacial areas observed in the Dubris and Bibra valleys (Chapter 5), where small areas of compacted glacial debris is observed, commonly on slopes. The cause of this morphology was attributed by Atkins (2013) to vertical compression during the advance and presence of cold-based ice. The observation of this feature within the larger areal extent of the Diamond Drift may suggest periods of non-erosive ice cover along the length of the Hatherton Glacier.

Other than the drift itself, there are no obvious moraine ridges or boulder belts apart from a moraine complex at site DH9 bordering the RIS. This series of moraines ≈2-3 km long, extends from the southern margin of Lake Wilson and along the eastern side of Diamond Hill (Figure 7.4A), where the maximum moraine height of ≈12-14 m above the Hatherton Drift is reached at site DH9 (Figure 7.4B). This moraine marks the lower boundary between the younger ice-cored Hatherton Drift and the older Diamond Drift. The moraine is flat topped and has a asymmetric profile, with the steepest side (>45°) sloping towards the Hatherton Drift and RIS margin (Figure 7.4C). The west side of the moraine has a far more gentle slope (<30°) and at site DH9, evidence of a small lake impounded behind the moraine is observed. Two samples were collected for SED (DH9.1 & DH9.4) from the apex of the moraine. Clasts at this location show significantly more weathering, rounding and iron-staining than those from the Hatherton Drift. This difference can be clearly seen in Figure 7.4C, where older material on the right is clearly differentiated from the Hatherton Drift on the left. While the elevation of this site (≈76 masl) is below that assigned to the upper limits of the Hatherton Drift (≈120-150 masl), the contrast in clast weathering and morphology suggests that the moraine was constructed from material sourced from the Diamond Drift or is of a similar age.

Given the numerous exposures of bedrock, particularly in the upper parts of the Diamond Drift, questions might be raised about the provenance of the material that comprises the drift; whether it is glacially transported from the upper regions of the DHGS, locally derived material repositioned and modified by glacial activity

or *insitu* Diamond Hill regolith. A number of lines of evidence suggest that this material has a glacial origin:

- Large glacially emplaced dolerite boulders. No bedrock outcrops of Ferrar are found within the Diamond Hill area.
- Striated, bullet shaped clasts, indicative of warm basal conditions are found both embedded within and emplaced upon the drift surface.
- Perched erratics on striated bedrock.

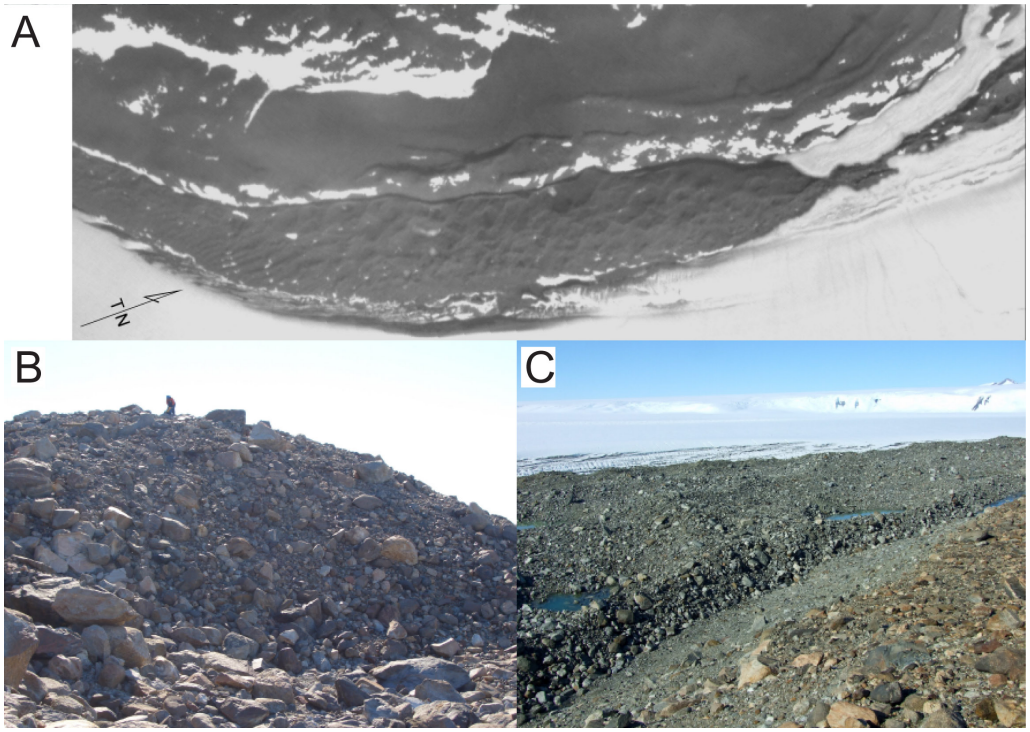

Figure 7.4: Moraine ridge observed at the RIS margin - Detail of the only moraine ridge found at Diamond Hill, acting as a demarcation between the Hatherton and Diamond drifts in this area. (A) ALOS satellite imagery of the moraine ridge complex and the ice-cored Hatherton Drift deposited between the ice margin and moraine ridge. (B) The moraine ridge at its most southern point. Here at site DH9 it is ≈12-14 metres above the Hatherton Drift. Note the person standing on the upper moraine surface for scale. (C) Looking from the upper moraine surface across the Hatherton Drift towards the north. RIS is in the background. A distinct difference in weathering is observed between the moraine surface (Diamond Drift, right) and the Hatherton Drift (left).

7.1.1.3 Upper Drift (>450 masl).

Above 450 masl the Diamond Drift gradually thins exposing a larger proportion of the underlying bedrock with a far reduced coverage of glacial drift deposits. The exposed bedrock is granite-gneiss intersected with abundant diorite dykes and veins of quartz (Figure 7.5A), typical of the Granite Harbour Intrusives (Section 4.2.1) observed in the TAMs. The landscape of this unit over its lower elevations of 450-550 masl is a mixture of bedrock and colluvium with the exposed ridge tops heavily weathered with extensive desert varnishing and iron staining (Figure 7.5B). The higher elevations (>550 masl) of Diamond Hill are comprised of a series of elevated plateaus separated by debris mantled bedrock ridges, predominantly comprised of *insitu* weathered clasts and small patches of regolith.

When compared to the Diamond Drift, outcrops displaying tafoni weathering are very rare, the little that is observed near (1000-1200 masl) or on the summit of Diamond Hill (> 1200 masl) is either poorly developed or ill-preserved (Figure 7.5C). This tafoni shows both an extremely limited distribution and degree of weathering compared to that observed at similar elevations in some other coastal TAM sites. Tafoni at the Denton Hills and McMurdo Dry Valleys, in a similar setting to Diamond Hill, display extremely well-developed and complex morphologies in their bedrock exposures.

Within the exposed bedrock above $\approx$450 masl, there was only limited evidence of glaciation. Compared to the Diamond and Hatherton Drift, no striated bedrock, no bullet shaped clasts and no dolerite erratics were observed. A few rare granitic erratics, emplaced on bedrock exposures were observed at elevations up to $\approx$930 masl. Sample DH11.1 (Figure 7.5D), the highest elevation erratic collected for SED, was relatively fresh looking but still had a distinctive orange weathering rind. It should be noted that this sample was also the only collected close to the suggested 1100 masl LGM ice limit suggested by Bockheim et al. (1989) and Denton et al. (1989a).

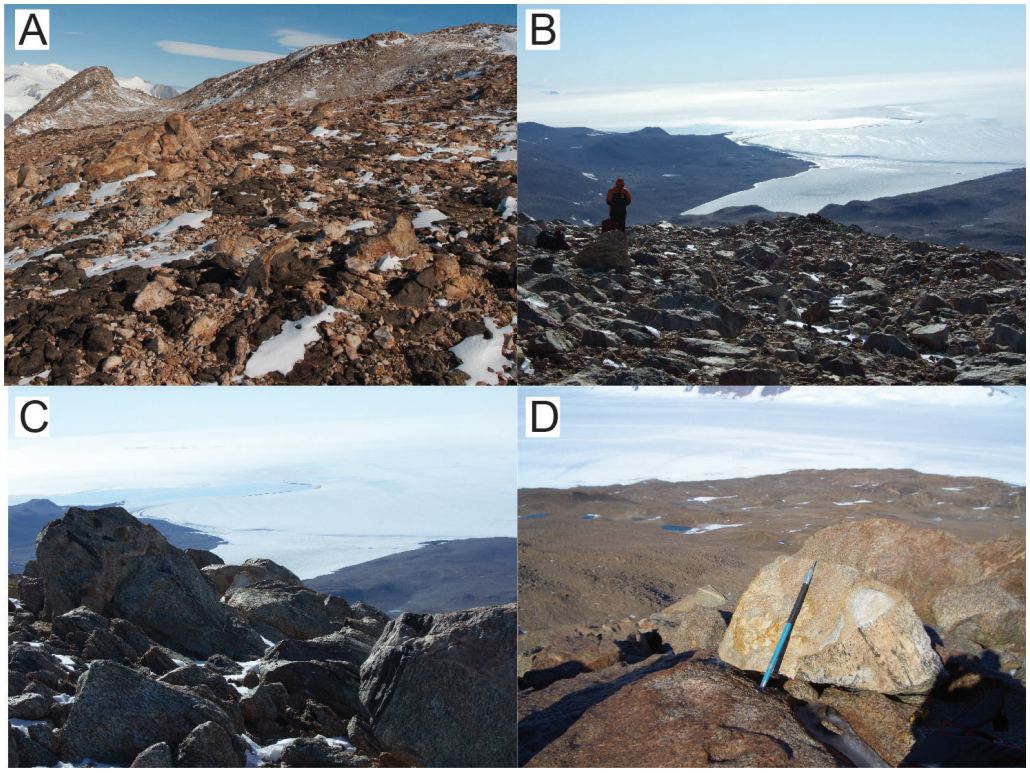

Figure 7.5: Bedrock exposures at Diamond Hill - (A) An *insitu* weathered dolerite dyke (dark material) within granite bedrock. (B) Typical low relief bedrock surface observed in high elevation parts of Diamond Hill. Looking to the northeast across Lake Wilson to the Ross Ice Shelf (≈600-1000 masl). (C) Poorly developed tafoni in granite-gneiss at 1250 masl (near the Diamond Hill summit). (D) Fine-grained granite erratic emplaced on weathered granite-gneiss bedrock overlooking the Diamond Drift. Sample DH11.1 within the Upper Drift at ≈930 masl.

7.1.2 Roadend Nunatak

Roadend Nunatak (78.9°S, 158.0°E) is found 20 km upstream from Diamond Hill, between the Brown Hills and the Darwin Mountains (Figure 7.1). The small nunatak is a 5 km^2 exposure of dolerite and granitic bedrock reaching an elevation of ≈1350 masl. The nunatak has a distinctive shape, the western side sloping gently down to the ice surface of the Darwin Glacier, but the eastern side steeply drops down to the smaller Touchdown Glacier (Figure 7.6A). The original outcropping lithology, the Beacon Supergroup, has been completely eroded (Faure and Mensing, 2011), leaving a near horizontal plateau entirely comprised of heavily weathered boulders and bedrock exposures of Ferrar Dolerite (Figure 7.6B). Faure and Mensing (2011)

suggested that from observations taken during the 1978/1979 field season that the upper surface of Roadend Nunatak was free of any evidence of past glaciation. In a 2008/2009 visit to the site, the drifts of (Bockheim et al., 1989) were not observed, but three rare granite boulders were found on the upper surface (Figure 7.6C).

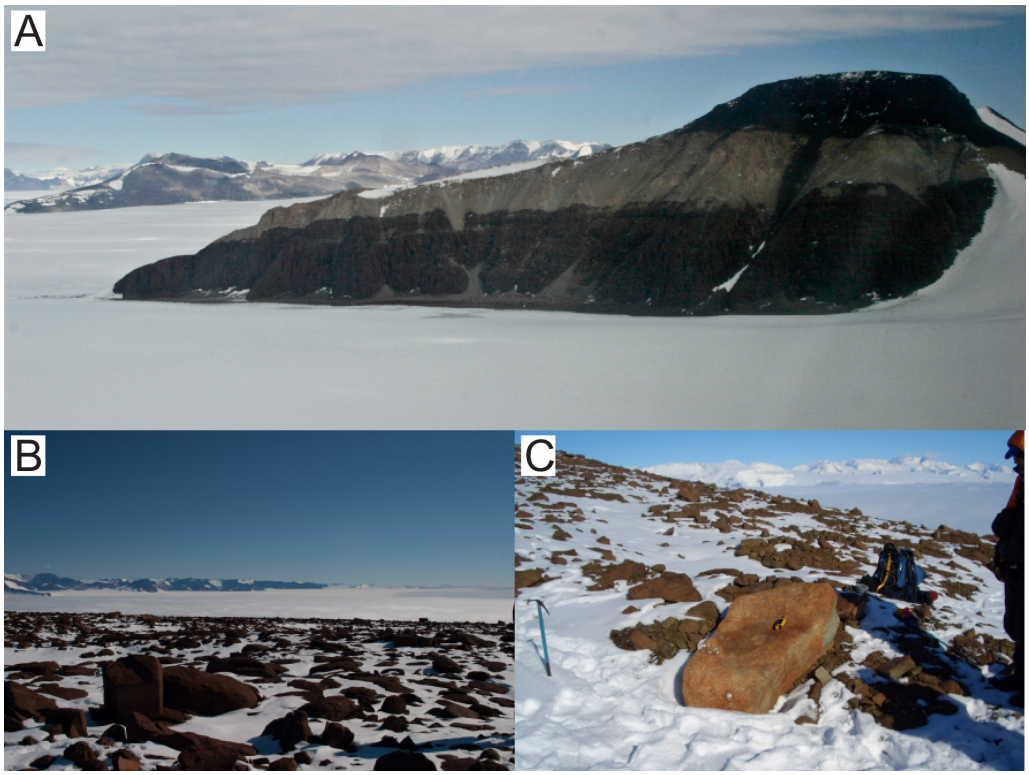

Figure 7.6: Roadend Nunatak - (A) The truncated western side of Roadend Nunatak, showing near horizontal layers of granite and intruded dolerite sills. Touchdown glacier is in the foreground, Darwin Glacier and Junction Spur in the background. (B) The eroded dolerite surface of the Kukri Penneplain on the summit plateau. (C) RE1.2, one of two granite erratics collected for SED at ≈1340 masl on the plateau of Roadend Nunatak.

7.2 Surface exposure dating

At Lake Wellman and Dubris Valley the defined drifts of Bockheim et al. (1989) provided a constraint on our sampling strategy. In the absence of these identifiable drifts at Diamond Hill, samples were collected as a function of elevation, distance to ice margin and the glacial mapping conducted in 2008/2009 (as described in

Section 7.1). A total of 28 erratic and bedrock samples were collected at Diamond Hill (Tables A.13 to A.18). The majority (n=21) were from large exposed boulders, small cobbles perched on bedrock outcrops and erratics directly from sub-aerially exposed material on the drift surfaces. Additionally a small number (n=7) of bedrock samples (Section 7.2.1.4) were also combined with erratic samples as part of a bedrock-boulder pairing (n=5, see Section 2.2.5.1). Samples were collected along three altitudinal transects; A-A‘ from 80-1000 (n=11), B-B‘ from 80-1200 (n=12) and C-C’ from 70-650 masl (n=5) (Figures 7.7A & 7.8). These covered Upper, Diamond and Hatherton drifts (including bedrock sample) and crossed the 1100 masl LGM limit suggested by Bockheim et al. (1989). Two samples in transect C-C’ (DH9.1 and DH9.4), were collected from the apex of the large moraine found at the margin of the RIS (Figure 7.4). In the low elevation sections of the Hatherton Drift (*i.e.* Site DH7) cobbles and small boulders perched on stable bedrock outcrops and platforms protruding above the drift surface were preferred SED targets, based on a similar methodology to that used at Lake Wellman, Dubris and Bibra valleys. In the Diamond Drift and Upper Drift above 450 masl, samples were large boulders either emplaced on bedrock platforms or exposed within drift surfaces. Our sampling strategy at Diamond Hill collected surface material from the largest possible erratics, providing a maximum height above the drift surfaces.

At Roadend Nunatak, two granitic boulders, RE1.1 and RE1.2, were sampled for SED (Table A.10), both were $\approx$2 m long, had sub-rounded morphology and distinctive orange weathering rinds (Figures 7.7B & 7.6C).

As with all sites in the DHGS, the susceptibility of deposited material to recycling and/or periods of burial by cold-based ice, necessitates a dual-nuclide approach (Section 2.1.2.1). Use of this technique assists in the identification of samples with complex exposure histories, which include a period or periods of burial greater than 200 ka, by measuring a second *insitu* cosmogenic nuclide. Twenty five out of the 28 total samples were successfully processed for ^{26}Al alongside ^{10}Be, with ^{26}Al AMS or ^{27}Al ICP-OES measurement failures in the remaining three samples (DH7.1, DH5.2 and DH11.1).

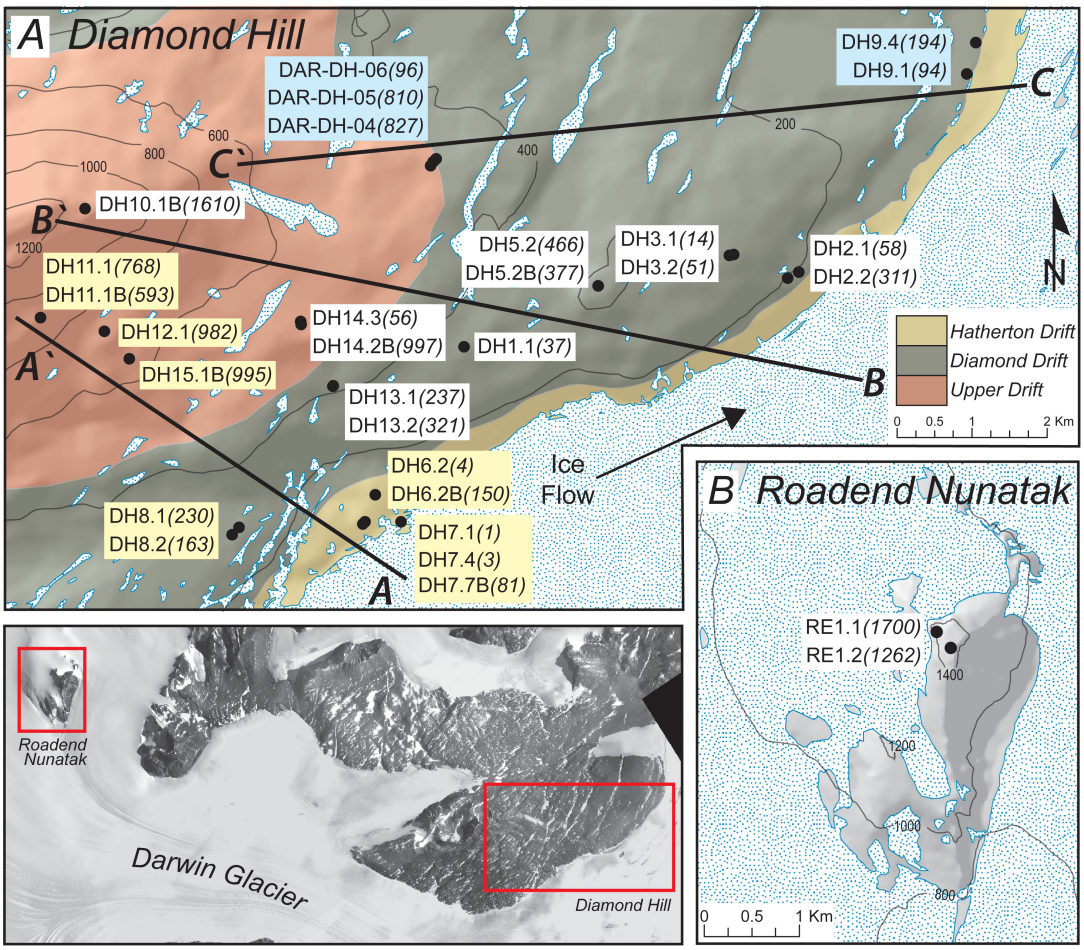

Figure 7.7: Map of the Diamond Hill and Roadend Nunatak areas - (A) Diamond Hill. Black bold lines A-A', B-B' and C-C' represent altitudinal transects along which samples were collected for SED (See Figure 7.8 for profiles). (B) Roadend Nunatak. SED sample sites are labelled in black, followed by bracketed ^{10}Be ages in ka. Darwin Glacier ice flows from a south-westerly direction into the RIS.

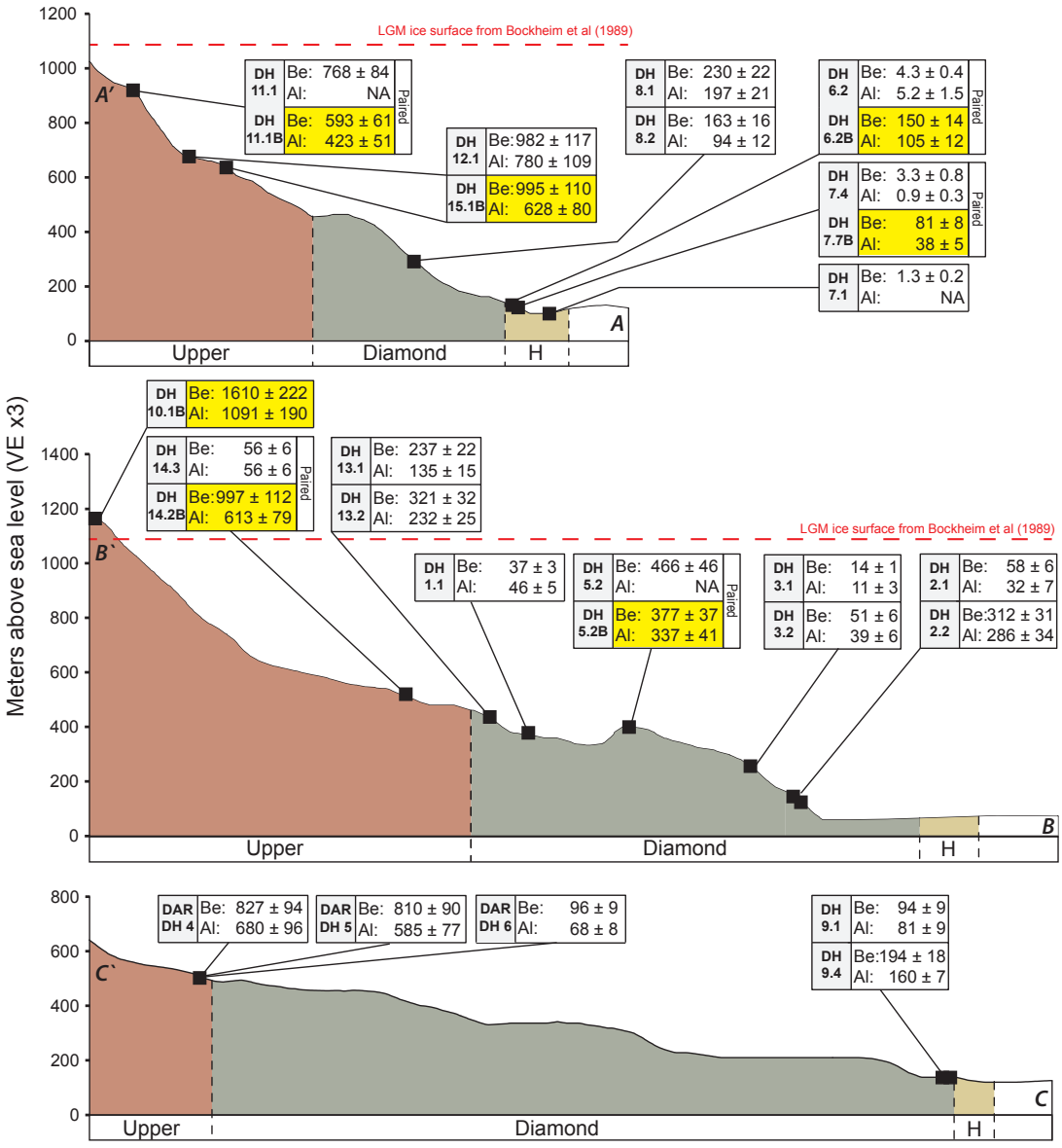

Figure 7.8: Transect exposure age profiles for Diamond Hill - ^{10}Be and ^{26}Al exposure ages (in ka) for analysed samples from transect A-A', B-B' and C-C'. Yellow boxes indicate bedrock samples and if they are paired, the corresponding perched erratic sample is given. Sample and site data (Tables A.13 & A.14), AMS results (Tables A.15 & A.16) and exposure ages (Tables A.17 & A.18) are included in the appendices.

7.2.1 Diamond Hill results

The complete SED dataset for Diamond Hill of 21 erratics and 7 bedrock samples gives ^{10}Be ages from 1 ka to 1.6 Ma, a minimum and maximum age range similar to those from Lake Wellman (0.8 ka -2.3 Ma) and the Dubris and Bibra valleys (5 ka-2 Ma). Transects A-A', B-B' and C-C' give minimum ^{10}Be age ranges of 1-768 ka, 14 ka-1.6 Ma and 94-827 ka respectively from a mixture of erratic and bedrock samples. As with other sites in the DHGS, a similar trend of oldest age at the highest elevation was found, but a wide variation in age-elevation relationships exists outside of the oldest and youngest ages (Figure 7.7A & 7.8).

7.2.1.1 Hatherton Drift (<150 masl)

Erratic samples from the Hatherton Drift (n=3), collected at elevations from 91-146 masl (transect A-A') provide ^{10}Be minimum ages of 1.3, 3.3 and 4.3 ka (DH7.1, DH7.4 & DH6.2, Table 7.1). Given the young ages of these samples, statistical uncertainty and the relatively large impact on ^{26}Al/^{27}Al background corrections, an interpretation of burial history is inconclusive.

Table 7.1: Hatherton Drift erratic ages at Diamond Hill - Complete details of samples are given in Tables A.13-A.18.

Sample ID	Elevation (masl)	^{10}Be age (ka)	^{26}Al age (ka)
DH7.1	91	1.3 ± 0.2	-
DH7.4	132	3.3 ± 0.8	0.9 ± 0.3
DH6.2	146	4.3 ± 0.4	5.2 ± 1.5

7.2.1.2 Diamond Drift (150-450 masl)

The majority of collected erratics come from the Diamond Drift and show a complex spread of erratic ages, from 14-466 ka (n=12, Table 7.2). The SED ages correlate extremely poorly over the full 150-450 masl elevation range of this drift, having a r^2 of 0.1. A subset (*i.e.*samples located between 330-450 masl, n=6) show a strong correlation with elevation (r^2 of 0.94). These four sites cover an elevation spread of $\approx$40% of this drift. Despite the strength of this relationship and

recognising that it reflects only half of the data, the lack of an overall and definitive age-elevation relationship poses a significant impediment to the interpretation of the drift. Additionally 6 of the 11 erratics (sample DH5.2 failed for ^{26}Al) collected from the Diamond Drift show discordant ^{26}Al and ^{10}Be ages which indicate complex exposure and burial histories prior to their last exposure. Of the remaining six samples (excluding DH1.1), DH9.1, DH9.4, DH8.1, DH2.2 and including bedrock sample DH5.2B (see Table 7.4) plot either in or below the stable erosion island in a dual nuclide plot (Figure 7.9). This indicates that the exposure histories of these five samples can either be interpreted as:

1. A period (or periods) of maximum burial (*i.e.* <200 ka). As defined by the ^{26}Al/^{10}Be production rate ratio error.

2. A continual simple exposure history.

Table 7.2: Diamond Drift erratic ages at Diamond Hill - Complete details of samples are given in Tables A.13-A.18 in the appendices. Note that bedrock ages from within this drift are in Table 7.4.

Sample ID	Elevation (masl)	^{10}Be age (ka)	^{26}Al age (ka)
DH9.1	76	94 $\pm$ 9	81 $\pm$ 9
DH9.4	88	194 $\pm$ 18	160 $\pm$ 17
DH2.1	184	58 $\pm$ 6	32 $\pm$ 7
DH2.2	194	311 $\pm$ 31	286 $\pm$ 34
DH8.1	283	230 $\pm$ 22	197 $\pm$ 21
DH8.2	283	163 $\pm$ 16	94 $\pm$ 12
DH3.2	334	51 $\pm$ 6	39 $\pm$ 6
DH3.1	335	14 $\pm$ 1	11 $\pm$ 3
DH1.1	352	37 $\pm$ 3	46 $\pm$ 5
DH13.1	397	237 $\pm$ 22	135 $\pm$ 15
DH13.2	417	321 $\pm$ 32	232 $\pm$ 25
DH5.2	428	466 $\pm$ 46	-

In summary: basically all bar four erratic samples can be considered as buried and re-exhumed, which effectively allows little to no conclusion of drift age deposition. Using the remaining four samples gives a drift age of between 100 to 300 ka.

Additional to samples collected from the Diamond Drift surface, two samples were also collected from the moraine complex at the RIS margin. The youngest, DH9.1 (94 ka), is a perched erratic and DH9.4 (194 ka) a boulder sub-aerially exposed on the upper moraine. Both samples show depressed $^{26}Al/^{10}Be$ ratios, but their position within the 9% production rate error suggests either a simple exposure history (Figure 7.9) or a minimum duration of burial (<200 ka) then exhumation. As DH9.1 and DH9.4 plot beneath the same burial isochron (200 ka), it may also suggest that both samples have undergone a similar burial history. Unfortunately, as clear burial signals (*i.e.* discordant $^{26}Al/^{10}Be$ ratios) are only reflected after >200 ka of total shielding, the significance of these results may be inconclusive. Given the proximity of these samples to the ice margin, a complex history of morainal material being recycled and/or reworked by advancing RIS ice must be considered as a high possibility.

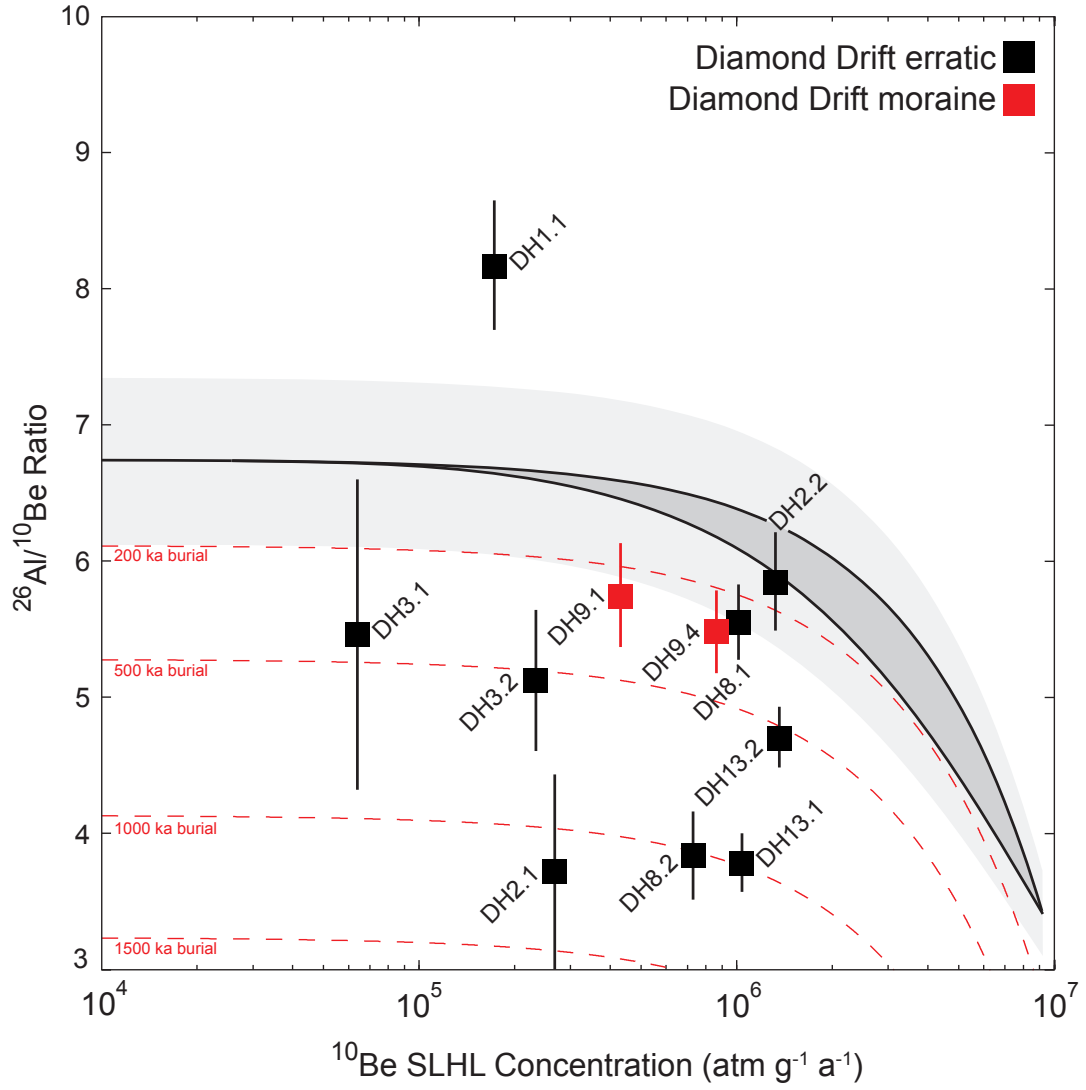

Figure 7.9: Dual-nuclide plot for the Diamond Drift SED samples - A plot of ^{26}Al/^{10}Be ratios versus normalized SLHL ^{10}Be concentrations showing the exposure history of analysed samples. Exposed surface samples undergoing erosion will fall within the steady-state exposure island. Burial isochrons of 200 ka, 500 ka, 1 and 1.5 Ma (dashed red curves) are also shown. Error bars are derived from analytical errors only and the light grey area enclosing the steady state exposure island represents a $\pm$ 9% error in ^{26}Al and ^{10}Be production rates (Balco et al., 2008). Sample DH5.2 not shown due to a failed ^{27}Al measurement.

7.2.1.3 Upper Drift (>450 masl)

From the higher elevation parts of Diamond Hill (>450 masl), six glacially emplaced boulders show ^{10}Be ages from 55.8 to 982 ka (Table 7.3, n=6). As with the lower elevation Diamond Drift, a lack of age-elevation relationship exists within this unit. The oldest sample (DH12.1) with a ^{10}Be age of 982 ka is found several hundred metres lower than DH11.1, the highest elevation erratic observed at Diamond Hill (930 masl) with a younger age of 768 ka. In stark contrast to this age scale, the youngest samples collected above 450 masl, DAR-DH-06 (461 masl) and DH14.3 (550 masl) have ages of 96 and 56 ka. Thus the erratics collected above 450 masl display a quasi bi-modal age grouping, with the youngest ^{10}Be ages (56 & 96 ka) significantly different to the older group (n=4, 768-982 ka). Additionally, DAR-DH-04 (827 ka) and DAR-DH-05 (96 ka) were collected within a limited distance (*i.e.* hundreds of metres) of each other. As with those from the Diamond Drift, some samples show an age discordance in ^{26}Al/^{10}Be ratios (Figure 7.10). Four of the six samples from the Upper Drift are older than 760 ka and plot beneath the lower right of the erosion curve. DH12.1, DAR-DH-4 and DAR-DH-5 demonstrably plot within error of the stable erosion island, while DH14.2 plots beneath. Of the remaining two younger samples, DH14.3 is situated within error of the stable erosion island and DAR-DH-06 lies beneath the 500 ka burial isochron.

Table 7.3: Upper Drift erratic ages at Diamond Hill - A summary of Tables A.13-A.18.

Sample ID	Elevation (masl)	^{10}Be age (ka)	^{26}Al age (ka)
DAR-DH-5	443	810 ± 90	585 ± 77
DAR-DH-4	449	827 ± 94	680 ± 96
DAR-DH-6	461	96 ± 9	68 ± 8
DH14.3	550	56 ± 6	56 ± 6
DH12.1	734	982 ± 117	780 ± 109
DH11.1	930	768 ± 84	-

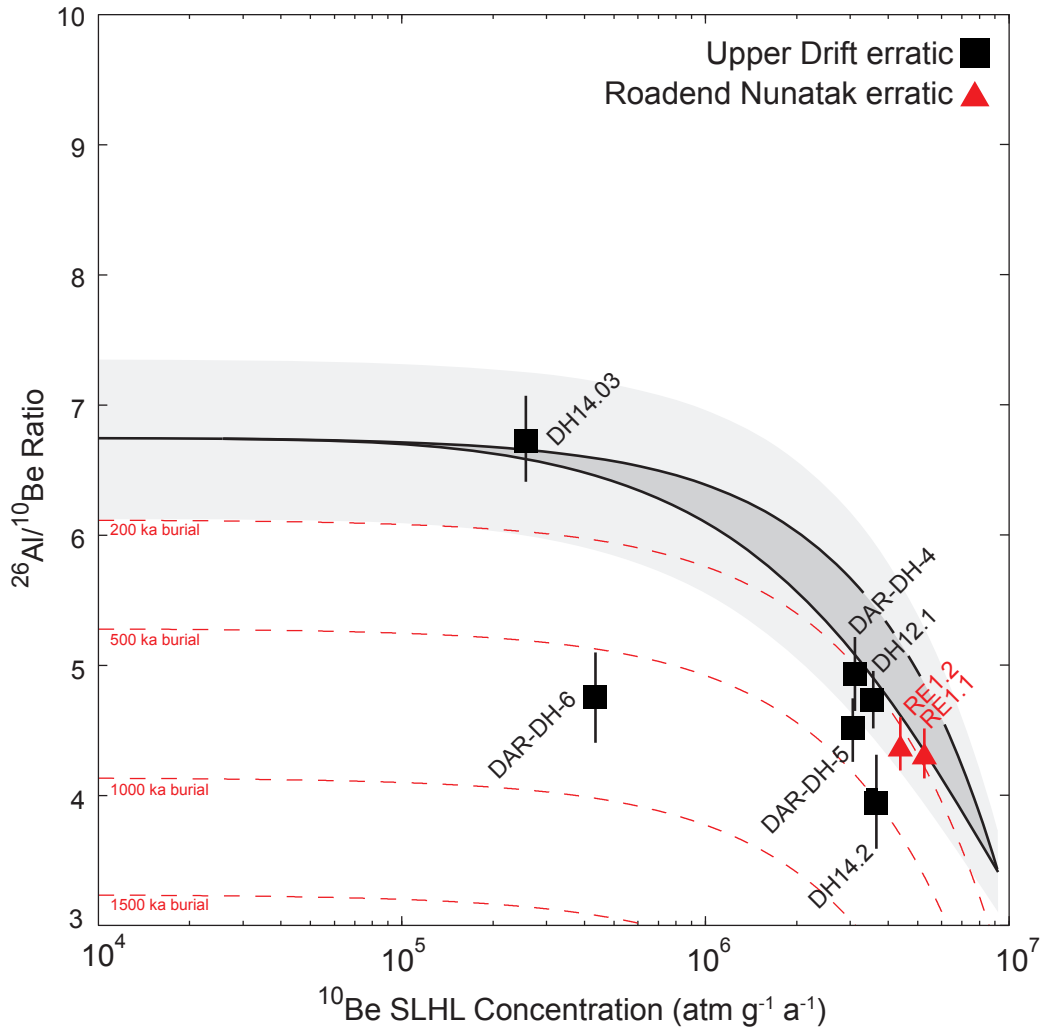

Figure 7.10: Dual-nuclide plot for the Upper Drift and Roadend Nunatak SED samples - A plot of ^{26}Al/^{10}Be ratios versus normalized SLHL ^{10}Be concentrations showing the exposure history of analysed samples. Exposed surface samples undergoing erosion will fall within the steady-state exposure island. Burial isochrons of 200 ka, 500 ka, 1 and 1.5 Ma (dashed red curves) are also shown. Error bars are derived from analytical errors only and the light grey area represents a $\pm$ 9% error in ^{26}Al and ^{10}Be production rates (Balco et al., 2008). Sample DH11.1 is omitted due to no Al measurements.

7.2.1.4 Bedrock

The seven bedrock samples from Diamond Hill show a strong correlation between apparent ^{10}Be age and elevation. Transect A-A' having a 81-995 ka (n=4) age spread while transect B-B' ages (n=3) are from 377 ka to 1.6 Ma (Table 7.4), with r^2 values of 0.61 (A-A') and 0.87 (B-B') respectively. When transects are combined, the entire set of bedrock samples (n=7) gives a r^2 value of 0.72. Only one sample (DH11.1B) can be considered an outlier with respect to increasing age with elevation. Five of the seven bedrock samples predominantly show ^{26}Al/^{10}Be ratios that suggest periods of burial (Figure 7.11). Only one sample, DH5.2B (377 ka) and perhaps DH10.1B (1.6 Ma), have overlapping ^{26}Al and ^{10}Be ages and plot within the 9% error of the stable-erosion island (Figure 7.11), these two bedrock samples suggest a simple exposure history. The burial age *vs* elevation relationship observed in bedrock samples can be explained by a long term decrease in total ice volume with elevation over multiple glacial cycles.

Table 7.4: Diamond Hill bedrock SED ages - Bedrock collected from transects A-A' and B-B'.

Sample ID	Elevation (masl)	Drift	^{10}Be age (ka)	^{26}Al age (ka)	Burial (ka)
DH7.7B	125	Hatherton Drift	81 $\pm$ 8	38 $\pm$ 5	1500
DH6.2B	148	Hatherton Drift	150 $\pm$ 14	105 $\pm$ 12	$\approx$700
DH5.2B	428	Diamond Drift	377 $\pm$ 37	337 $\pm$ 41	200
DH14.2B	554	Upper Drift	997 $\pm$ 112	613 $\pm$ 79	500
DH15.1B	666	Upper Drift	995 $\pm$ 110	628 $\pm$ 80	500
DH11.1B	930	Upper Drift	593 $\pm$ 61	423 $\pm$ 51	200
DH10.1B	1192	Upper Drift	1610 $\pm$ 222	1091 $\pm$ 190	<200

As bedrock samples displaying extended periods of burial (>200 ka) reflect a loss of TCNs via deep burial by ice, their exposure ages as defined by TCN concentrations alone must be considered 'apparent' with ^{10}Be and ^{26}Al concentrations not accurately reflecting the true length of exposure. A glacial environment such as Diamond Hill is one where West Antarctic ice has fluctuated from modern levels to glacial high-stands (such as the LGM) over many cycles in the past few million years. Therefore, samples at low elevations would be expected to covered by more ice for longer periods of time (*c.f.* those at higher elevations) thus the longer periods

of burial in low elevation samples. High elevation samples would be the first to be uncovered and thus have the least burial. This elevation-burial relationship at ice sheet margins has also been observed at another EAIS site, the Groves Mountains (73°S, 75°E). Lilly et al. (2010) showed that oscillating glacial-interglacial cycles superimposed over a steady linear decrease in ice volume, caused a characteristic shift in TCN concentrations. A hint of this relationship in the bedrock samples collected at Diamond Hill (Table 7.4) seems to be evident.

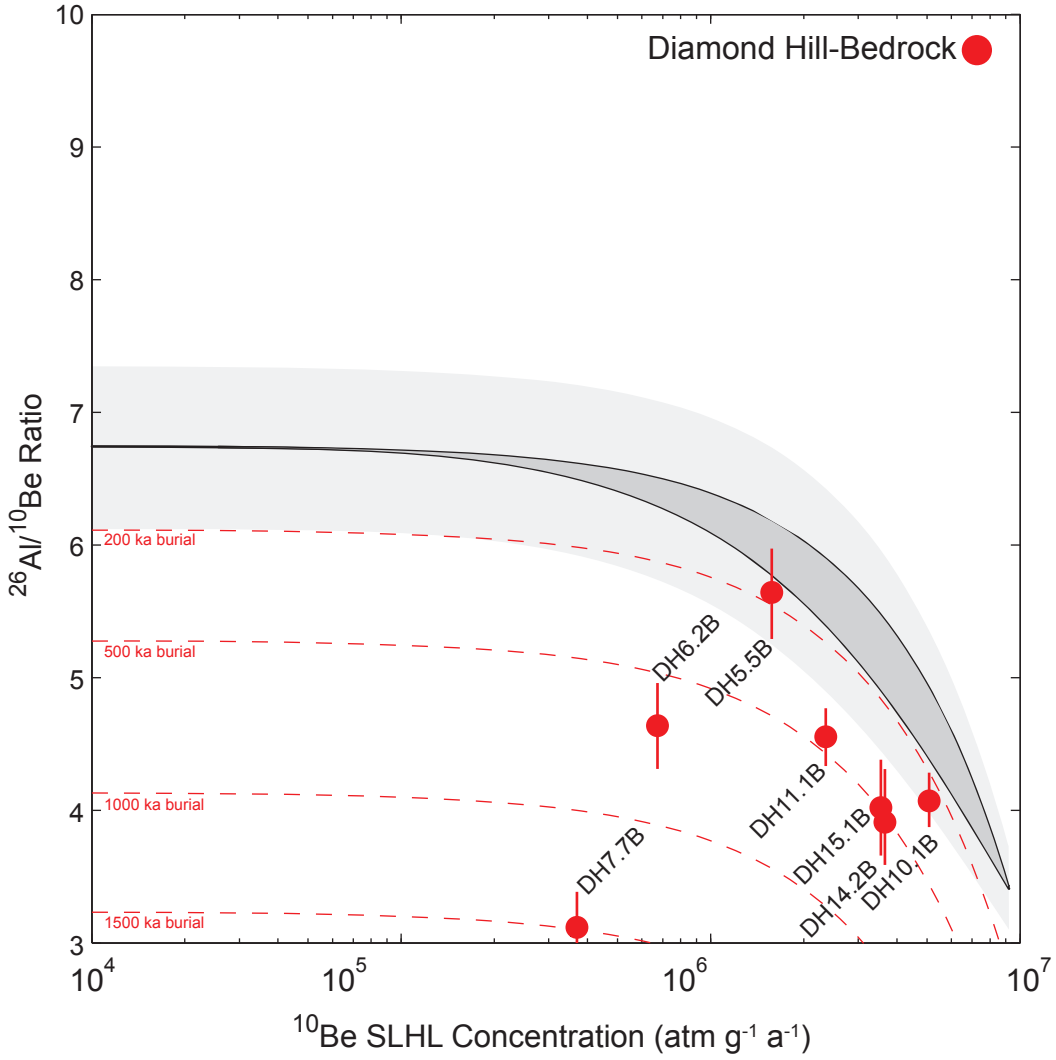

Figure 7.11: Dual-nuclide plot for the bedrock SED samples - A plot of ^{26}Al/^{10}Be ratios versus normalized SLHL ^{10}Be concentrations showing the exposure history of analysed bedrock samples. Exposed surface samples undergoing erosion will fall within the steady-state exposure island. Burial isochrons of 200 ka, 500 ka, 1 and 1.5 Ma (dashed red curves) are also shown. Error bars are derived from analytical errors only and the light grey area represents a $\pm$ 9% error in ^{26}Al and ^{10}Be production rates (Balco et al., 2008).

7.2.2 Roadend Nunatak results

Glacial erratic samples RE1.1 and RE1.2, from the upper eroded surface of Roadend nunatak give minimum ^{10}Be ages of 1.7 and 1.3 Ma respectively and have ^{26}Al/^{10}Be ratios that locate them within the 9% error bands of the stable-erosion island (Figure 7.11). Both samples were collected at almost the same elevation from the Nunatak's upper plateau and strongly suggest that the highest elevations of Roadend Nunatak were ice free by the mid-Pleistocene, about 1.5 Ma ago. It is important to note that no other granite boulders were observed on the upper surface and as the source of the granite erratics only outcrop to the east and north-east of Roadend Nunatak (*i.e.* between the Brown Hills and the Ross Ice Shelf), there are only three possible explanations to explain the occurrence of this material.

1. Sub or supra-glacial material has been transported westwards from Diamond Hill.

2. Material has been eroded subglacially from beneath the EAIS and transported eastwards through the DHGS (either Darwin or Hatherton glaciers).

3. Sub or supra-glacial material has been transported from the Cook Mountains southwards via the Touchdown Glacier.

As a reversal in the direction of ice is required for scenario #1, only the last two explanations for the transportation of the material appear valid. Even if an enlarged Touchdown Glacier is thought to be the cause (#3), the elevation of the Roadend erratics and the location of Roadend Nunatak within the DHGS would still imply that past mid-Pleistocene ice levels would have been a minimum of 400-600 metres higher than present.

7.3 Principal component analysis of Diamond Hill exposure ages

Given the wide geological scatter observed within the Diamond Hill exposure ages, a statistical technique such as principal component analysis (PCA) may show

trends not obvious in dual-nuclide plots. PCA is a multivariate statistical technique that transforms possibly correlated sample characteristics (either observed or measured) into a new set of uncorrelated variables. Abdi and Williams (2010) state that the primary goals of PCA are to:

- Extract the most important information from the dataset.
- Reduce the size of the dataset by keeping only this important information.
- Simplify the description of the dataset.
- Analyse the structure of the observations and variables.

To meet these goals, principal components are created to preserve the variation while reduce the dimensionality of the initial dataset (Jolliffe, 2005). While the technique has been commonly used in biological and palaeontological studies (Hammer and Harper, 2008), Hein et al. (2013) applied the technique in a glacial setting to identify patterns within a exposure age dataset from the Shackleton Glacier in West Antarctica. Using PCA, correlations between elevation, ^{10}Be age, degree of weathering and sample exposure history (*i.e.* complexity) were observed (see Figure 8 in Hein et al. 2013).

Hein et al. (2013) used a relatively simple approach to characterising samples, ranking lithology, shape, size, weathering, elevation, surface slope, stability, ^{10}Be age and exposure history as integers. For the Diamond Hill dataset this methodology is slightly modified (Table 7.5). Sample shape and size are ignored as they appear to play only a minor role (As shown by Hein et al. 2013), while surface slope and stability are irrelevant to the Diamond Hill dataset (samples were all collected on low slope and high stability surfaces). In addition, ^{26}Al and ^{10}Be concentrations are added to ensure correlation with their corresponding ages (For complete list see Table A.19 in appendices).

PCA analysis of the Diamond Hill dataset was done in the PAST3 software (http://folk.uio.no/ohammer/past/) using a correlation matrix and biplot axes scaled to the eigenvalues. Biplots represent the dataset in two dimensional space using the first two components (PC1=x & PC2=y) and plots both table rows (*i.e.* individual data points) and columns (*i.e.* vectors) simultaneously. This process allows the

visual analysis of possible correlations within the glacial erratic (Figure 7.12A) and bedrock datasets (Figure 7.12B). When the datasets are compared a number of striking observations are noted.

- The individual samples (Red dots) within bedrock and erratic biplots exhibit little to no clustering.
- The similarity in vector direction and magnitude between the two datasets.

Within the two datasets, the vectors somewhat group and thus show correlations between a number of variables. In the case of the erratics (Figure 7.12A), exposure history, weathering and elevation are all positively correlated, their near vertical position between quadrants 1 and 2 shows the influence of principal component two (y axis). The second group containing ^{10}Be and ^{26}Al age and concentration are strongly correlated and predominantly influenced by principal component one (x axis). The results of the PCA analysis suggest that the two groups appear to be poorly correlated (>90°), with only ^{10}Be concentration showing a medium to weak correlation with elevation and weathering. Given the wide scatter and limited correlation in age-elevation plots (Figure 7.8) the lack of correlation between ^{10}Be age and elevation is unsurprising, as is the correlation between weathering, elevation and exposure history.

Table 7.5: Geomorphological criteria for principal components analysis - Integer ranking for Diamond Hill samples (see appendix A.19 for values). Ice elevation at Diamond Hill is defined as 60 masl (Ross Ice Shelf). Methodology is based on Hein et al. (2013).

Weathering		**Elevation above ice (m)**		**^{10}Be & ^{26}Al Exposure (ka)**		**Exposure History**		**^{10}Be & ^{26}Al Conc (x10^6)**	
1	Very low	1	0-100	1	0-100	0	No ratio	1	0-2
2	-	2	101-200	2	101-200	1	Simple	2	2-4
3	Low	3	201-300	3	201-300	2	Complex	3	4-6
4	-	4	301-400	4	301-400			4	6-8
5	Medium	5	401-500	5	401-500			5	8-10
6	-	6	501-600	6	501-600			6	10-12
7	High	7	601-700	7	601-700			7	12-14
		8	701-800	8	701-800			8	14-16
		9	801-900	9	801-900			9	16-18
		10	>901	10	>901			10	>18

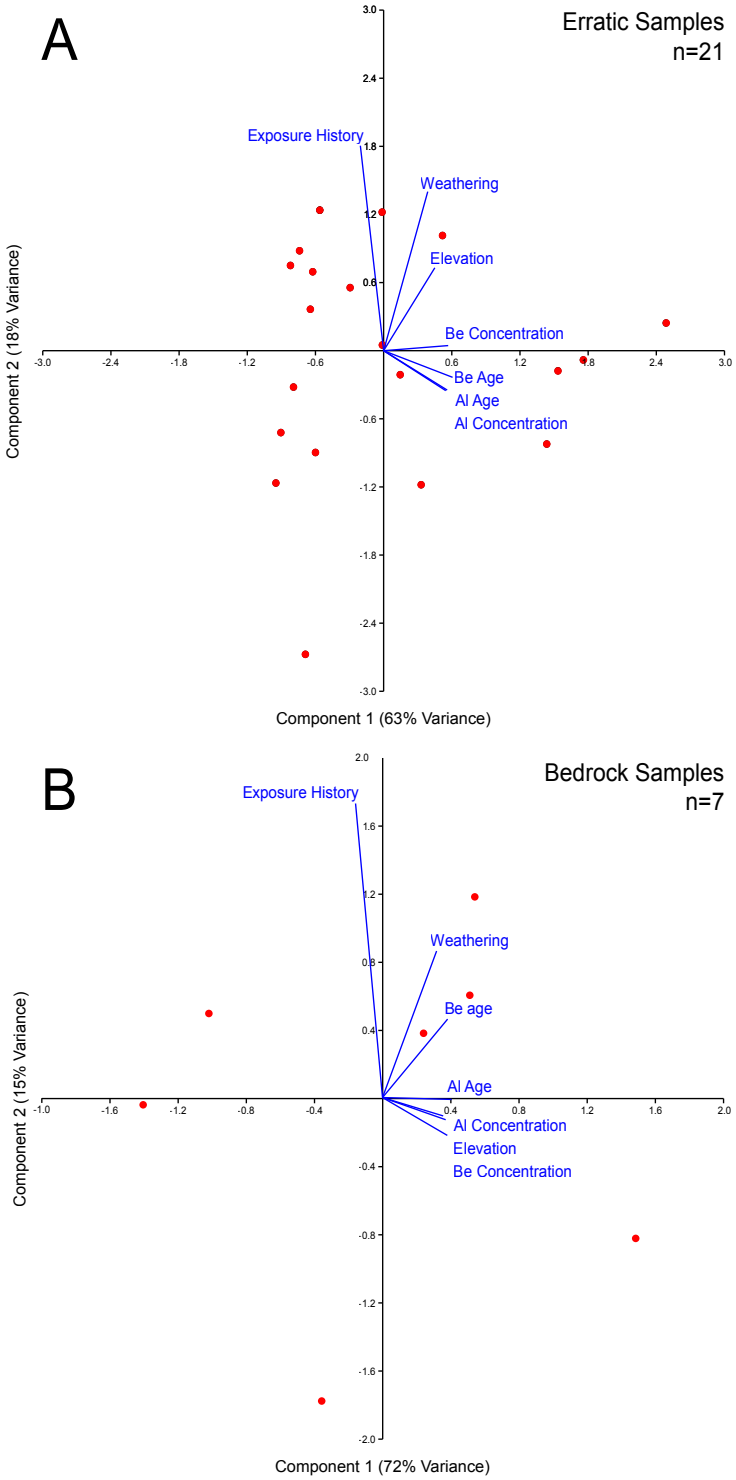

Figure 7.12: PCA biplots - Eigenvalue scaled results for Diamond Hill erratics (A) and bedrock (B). Variance explained by each principal component is listed on the axes (Total variance of 81% for erratics & 87% for bedrock). The direction and length of the vectors (Blue lines) are based on the initial sample criteria given in Table 7.5 and allow the visualisation of possible correlations. The most strongly correlated variables clustering along similar directions.

The bedrock dataset tells a slightly different story, although vector angles are similar to the erratic dataset, elevation and ^{10}Be age are switched. Thus the two groups of correlated variables are exposure history, weathering and ^{10}Be age (again influenced by PC2) and ^{26}Al age and concentration, ^{10}Be concentration and elevation (influenced by PC1). The cause of the switch in variables is unknown as ^{10}Be age appears to correlate well with elevation (Table 7.4), but may be due to the inverse correlation between exposure history and elevation (more burial observed in lower elevation samples). More puzzling is the lack of correlation between the ^{10}Be age and ^{10}Be concentration.

Initial observations suggest that both bedrock and erratic samples, even with similar exposure ages, have not undergone the same combination of geomorphic processes. This is expected, particularly in the case of the erratics, in sample with complex exposure histories and unknown transport pathways within the glacial system. The results show strong correlations between exposure history, weathering and elevation, similar to the results of Hein et al. (2013).

Although the use of PCA based on the methodology of Hein et al. (2013) may be useful in finding correlations between geomorphological observations, it should be noted that in datasets dominated by samples with complex exposure histories, its use may be less valid. As discussed in Chapter 2, TCN concentration in buried samples will start decreasing *via* radioactive decay when completely shielded from cosmic rays. As the decreased TCN concentration now longer accurately reflects the *true* exposure age, it can only be represent the *apparent* exposure age of a sample. The Diamond Hill dataset contains a high proportion of material with complex exposure histories (55%) and thus any correlation between geomorphological observations (*i.e.* weathering, elevation *etc*) and exposure age would be meaningless. Although correlations in samples with simple exposure history and thus true exposure ages are unaffected, the high likelihood of complex material within Antarctic SED datasets make this a significant problem when using PCA in this method. The use of exposure ages in this manner may partly explain the correlations observed in the Diamond Hill data.

7.4 Implications for glacial chronology

Compared to sites flanking the Hatherton Glacier, in particular the Dubris and Bibra valleys, the SED dataset for Diamond Hill is far more complex and shows a far higher proportion of samples displaying depressed $^{26}Al/^{10}Be$ ratios; *i.e.* the majority of Diamond Hill erratics and bedrock have experienced an extensive (>200 ka) burial history prior to their last exposure. In fact without considering the 9% error band in the exposure and erosion curves of Figures 7.9, 7.10 and 7.11, only four or five samples could be defined as having a continuous simple exposure, with the remainder (n=24) showing some signs of burial ranging from not less than 200 ka to 1.5 Ma. This observation strongly restricts our ability to arrive at simple interpretations of Diamond Hill's glacial history in terms of the apparent ^{10}Be exposure ages of the analysed samples.

With the lack of a clear age-elevation relationship in collected erratics and the very high likelihood of recycled material being incorporated into drifts, only those samples with demonstrable simple exposure histories can be used to constrain drift age. Thus samples with ^{10}Be and ^{26}Al ages within error, or those that plot within the stable-erosion island are preferentially used to determine ice thickness over time. By using this method and a minimum age model (*i.e.* youngest age at a given elevation), samples are assumed to have a subglacial origin and thus reflect time of deposition commencing from the time when glacier ice retreated or thinned. At the margins of cold-based ice, this deposition would result in the formation or the addition of new material to pre-existing drift sheets. Unfortunately such material with a constant exposure history may have also experienced a period of supraglacial transport. Observations of the Darwin Glacier ice surface at Diamond Hill showed only limited supraglacial material and suggests that the bulk of material exhumed at the modern ice margin is of a subglacial origin. Whether the modern glacier can be used as an analogue for past depositional environments is unknown, given that ice discharge, velocity and basal regimes have altered in the past.

As with the other sites studied in this thesis which flank the Hatherton Glacier (*i.e.* Lake Wellman and Dubris Valley), the ^{10}Be results at Diamond Hill show a unequivocal Pleistocene glacial highstand significantly thicker than present. The higher elevation sectors of Diamond Hill (>1200 masl) and Roadend Nunatak (>1340 masl)

became ice free at least 1.3-1.7 Ma. During this period, ice at Diamond Hill was at least 1100 metres above the present surface of the RIS (≈70 masl) and at Roadend Nunatak, ≈640 m above today's Darwin Glacier (≈800 masl). The presence of thickened ice during the Quaternary at Diamond Hill is also supported by the apparent bedrock exposure ages, all which show discordant $^{26}Al/^{10}Be$ ratios representing periods of burial which increase with decreasing bedrock elevation. This trend of bedrock burial history must result from cycles of thick long term ice cover, full exposure and long term overall ice volume reduction. Additionally, as bedrock sample DH10.1B, collected at the highest elevation 1200 masl, displays a modelled burial of ≈200 ka, it would suggest that thickened West Antarctic ice was far greater than even that suggested for the LGM. Given the thickness of ice and the length of burial observed in this bedrock sample, it suggests that during the late Neogene the summit of Diamond Hill may have been overridden by ice for an extended period of time.

The spread of apparent ages, magnitude of burial age and number of buried samples collected from the Diamond and Upper drifts limits their usefulness as proxies for the deposition of the drifts, but allows an examination of ice sheet volume changes. Thus, only a small number of samples, *i.e.* those demarcating upper limits and those displaying minimal burial, can be used. At elevations above ≈ 450 masl on Diamond Hill and using a minimum age model, the highest collected erratic shows that ice retreated below 930 masl at 768 ka (DH11.1, no ^{26}Al) and below 550 masl at 56 ka (DH14.3, no burial). A number of erratics were also deposited at lower elevations on bedrock outcrops, suggesting that material is either derived from local bedrock, or glacially recycled material. For example, sample DH12.1 (734 masl, no burial), the oldest erratic found at Diamond Hill, with a ^{10}Be age of 981 $\pm$ 86 ka is comparable to that of bedrock collected at slightly lower elevations (DH14.2B & DH15.1B).

For any of the scenarios that imply significantly thickened ice on Diamond Hill, the presence of the moraine ridges (DH9) at the RIS margin must also be explained. As the sampled boulders are demonstrably old (94-194 ka), only two explanations are plausible.

1. The moraine is a relict feature and has been preserved under a cold-based

advance. To obtain this level of preservation, it would imply only a limited amount of thickened ice covering the feature.

2. The moraine is constructed of reworked and recycled material post-LGM. While the feature looks old, it may actually be a recent feature composed of old material. Thus the two SED ages, 94 & 194 ka, may reflect prior exposure and not the features that date deposition.

Given the evidence, the latter explanation is favoured. The 1000 m of thickened West Antarctic ice suggested by Bockheim et al. (1989) at this location would preclude any preservation of the feature sub-glacially.
Additionally, $^{26}Al/^{10}Be$ ratios of samples collected from the moraine apex suggest that the feature is comprised of material with a variety of exposure histories. Sample DH9.1 has a simple exposure history and possibly of a supraglacial original and DH9.4, a complex exposure history inferring some period of burial (Figure 7.9). There are still unanswered questions about the glacial environment the feature was emplaced in. The stoss side of the moraine, proximal to the Hatherton Drift, is steep, unstable and poorly preserved compared to the lee side within the Diamond Drift. Therefore to produce the unusual moraine morphology, an explanation may be that a post-LGM advance of RIS ice has bulldozed material and created the asymmetric moraine face. As ice, buttressed against the stoss side of the moraine, started to retreat or thin during the early to mid-Holocene ($\approx$5-10 ka), the Hatherton Drift was deposited. While this explanation is plausible, Figure 7.4A shows that additional moraines, which display branching in the northern parts of the area, lie behind the ice cored moraine and are within the Diamond Drift. Thus their formation must be caused by a scenario of multiple advances, post-LGM and prior to $\approx$5 ka.
In contrast to the complexities observed in the Diamond Drift SED results at Diamond Hill, the interpretation of the Hatherton Drift is relatively simple. The extensive deposits observed at the margins of the DHGS and RIS along the flanks of Diamond Hill give early to mid-Holocene exposure ages (1.4-4.3 ka). Although this glacial material is lithologically different to the Hatherton Drift observed at Lake Wellman (*i.e.* predominantly granite *vs* sandstone composition) the exposure ages are very similar (0.8-2.6 ka, n=3). Thus, the occurrence of the Hatherton Drift at

Diamond Hill suggests a minor ice advance prior to ≈4 ka in the lower elevation sectors of the DHGS.

7.4.1 Diamond Hill at the LGM

The LGM ice surface at Diamond Hill is constrained by two points, the suggested 1100 masl level of Bockheim et al. (1989) and Denton et al. (1989a) and the 14 ka ^{10}Be SED age (DH3.1) at 335 masl. Bockheim et al. (1989) extrapolated their inferred LGM glacier ice surface profile for the Hatherton Glacier downstream from the closest available location of geological evidence to the RIS to determine a 1000 m of thickening; a technique also used for the reconstruction of the LGM Beardmore Glacier (Denton et al., 1989a). Recent SED ages by Todd et al. (2010) for the Reedy Glacier in the south-east of the Ross Embayment, suggests a LGM thickening of 500 m, a value several hundred metres less than what is predicted by the regional LGM models of Denton and Hughes (2002) and Huybrechts (2002). The work of Todd et al. (2010) would appear to agree with the DHGS models of Anderson et al. (2004) and Riger-Kusk (2011) that suggest a smaller ice volume (a maximum thickness of 700 to 900 m) than Bockheim et al. (1989). As the grounded ice margin of the WAIS is suggested to have passed the mouth of the DHGS at ≈7 ka (Bockheim et al., 1989; Conway et al., 1999; Hall et al., 2013), an estimated overall loss of ≈ 250 metres of ice is required since 13.8 ka (if the re-advance that deposited the Hatherton Drift is ignored). This equates to a lowering of the WAIS ice surface at Diamond Hill of ≈0.04 m a^{-1} during a 6.8 ka period. Unfortunately, given the lack of LGM ages in the SED dataset for both Diamond Hill and Roadend Nunatak no additional evidence of the maximum LGM ice sheet thickness can be contributed to this debate.

7.5 Major conclusions

- The high elevation sectors of Diamond Hill (>1100 masl) and Roadend Nunatak (>1300 masl) have been exposed for a minimum 1.2-1.7 Ma. The thickness of the DHGS at this point in time would have been ≈ 1000 m at

Diamond Hill above today's RIS and ≈ 600 m at Roadend Nunatak above the modern Darwin Glacier.

- Evidence of Pleistocene glacial erratics (≈768 ka) emplaced at 930 masl on Diamond Hill.
- As with other sites in the DHGS, while no unequivocal SED evidence of LGM ice extent is observed, it cannot be ruled out.
- Ice retreated from 330 masl at Diamond Hill at 13.8 ka, with a loss of ≈250 metres over 6.8 ka.
- The RIS/DHGS deposited the Hatherton Drift at Diamond Hill between 1.4-4.3 ka prior to retreat to its present position.
- A retreat of the RIS/DHGS at 1.4-4.3 ka suggests <40 m of ice loss at Diamond Hill during the late-Holocene.
- Compared to SED datasets from the Hatherton Glacier, a far more complex spread of ages is observed. At Diamond Hill, samples with prior TCN inheritance and burial histories ranging from 0.2-1.5 Ma dominate the sample population.
- A trend of increasing burial age with decreasing elevation in bedrock samples. Similar to that observed at other EAIS sites (*i.e.* Lilly et al. 2010).
- PCA analysis of bedrock and erratic geomorphology show a strong correlation between elevation and weathering.

Chapter 8

Quaternary history of the Darwin Hatherton glacial system

8.0.1 Prior exposure of glacial material

A striking observation in the Darwin Hatherton glacial system (DHGS) exposure age dataset is the increasing percentage of samples displaying discordant $^{26}Al/^{10}Be$ ratios (*i.e.* burial) with distance from the glacier catchment (Figure 8.1). This observation leads to a conclusion of an increase in previously exposed or recycled material, with distance of glacial transport.

Sites closest to the catchment display the 'cleanest' signal. Deposited glacial material, either as erratics or drifts, appears to have the least chance of having a prior exposure history. In contrast, sites near the lower part of the system display higher spread of older ages and material with divergent $^{26}Al/^{10}Be$ ratios. The DBV, the closest location to the EAIS catchment, is the most well defined dataset (Figure 8.1A), with clear groups of exposure ages and free of samples displaying a definitive burial (>200 ka). At Lake Wellman, an additional $\approx$30 km downstream, a change in the spread of exposure ages is seen. Even within defined groups (*i.e.* drifts), exposure ages show a wider range, less clustering and more samples suspected of burial (Figure 8.1B). Finally, a further 60 km downstream at Diamond Hill, past the confluence of the Darwin and Hatherton glaciers, the dataset appears very different. Apart from those very young samples within the Hatherton Drift, samples from the Diamond and Upper drifts show a large geological scatter, little correlation between exposure age and elevation and most show extensive burial ages (Figure 8.1C). This 'dirty' dataset is likely a product of the increased availability of material

with complex exposure histories to be recycled, incorporated and transported by the glacier.

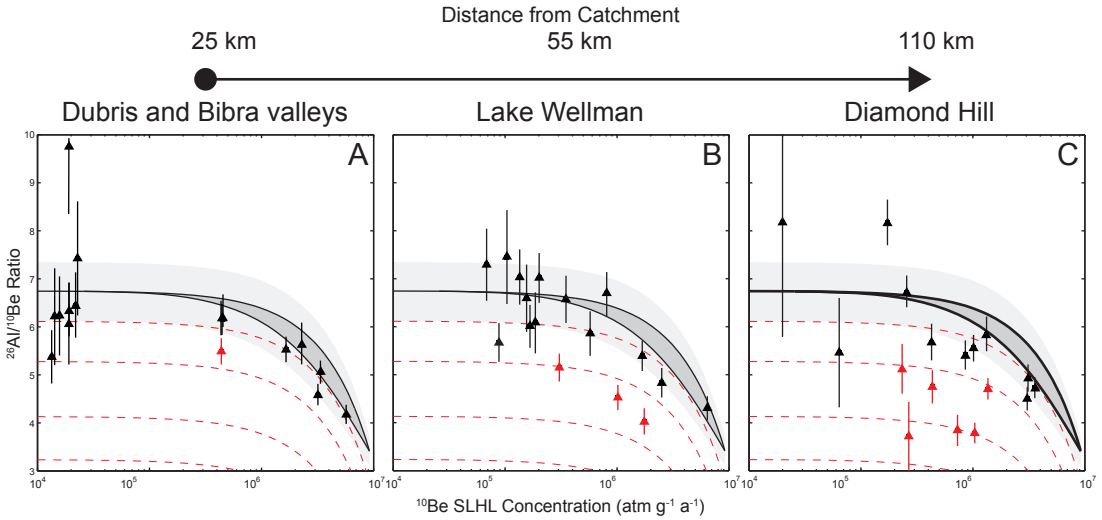

Figure 8.1: Dual-nuclide plots for DHGS erratic samples - Showing the increasing spread of ages and erratic samples with a definitive burial signal (red) with distance from the EAIS.

A number of explanations may explain the differences observed between sites in the upper and lower parts of the DHGS (*e.g.* the DBV *vs* Diamond Hill), as well those that are relatively close together (*e.g.* the DBV *vs* Lake Wellman).

1. Changing basal conditions of the DHGS. As the Hatherton Glacier is completely cold-based and the Darwin Glacier is partially warm-based, an increase in ice thickness would allow more of the Darwin Glacier to reach the pressure melting point. This may also be reflected in a higher quantity of eroded warm-based material being deposited at the cold-based margins.

2. Sampling methodology. Over the three seasons of fieldwork, an appreciation for the role cold-based processes play became apparent. At Lake Wellman (the first site visited) sampling was far less aware of cold-based geomorphology compared to that of the DBV (the last site visited). Viewing the landscape through a 'cold-based lens' may have reduced the sampling of reworked glacial material.

Another factor that may have an effect on distribution of exposure ages within the DGHS is the variability of ice flux and velocity of the Hatherton Glacier. The geophysical surveys and glaciological modelling of Riger-Kusk (2011) suggest that a subglacial bedrock ridge exists directly across the main trunk of the upper Hatherton Glacier (Figure 8.2). At this location an expanded EAIS spills into the Hatherton Glacier.

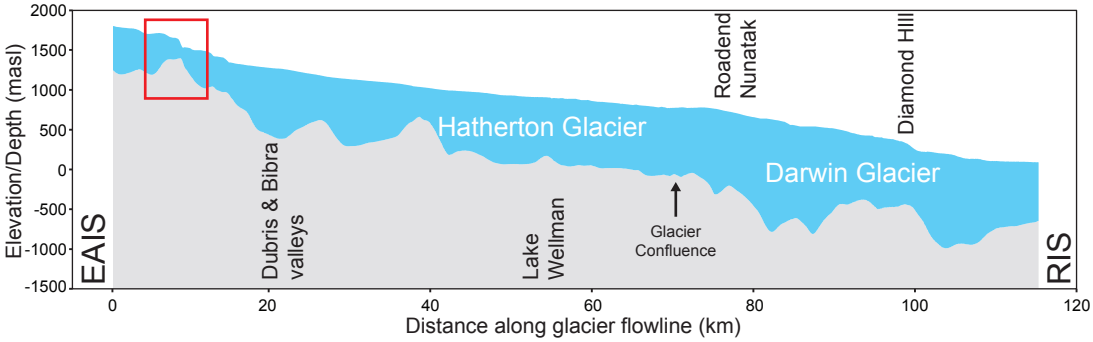

Figure 8.2: Bedrock and present ice surface profile for the DHGS - Based on the firn corrected ice thickness model of Riger-Kusk (2011). The red box highlights the subglacial ridge cutting across the main Hatherton Glacier ice flow and is the same area shown in figure 4.10.

This subglacial ridge would have restricted ice flow into the system, a possible explanation for the significantly different ice velocities and thicknesses seen in the Darwin Glacier compared to the Hatherton. On the down valley side of the ridge, the Hatherton Glacier is ≈500 metres thick, while directly above it, ice thins to ≈180 metres, the minimum observed in the central trunk of the glacier. If the interior sections of the EAIS thinned during the LGM, as is suggested by Staiger et al. (2006) and Golledge and Levy (2011), the ridge may restrict ice flow into the Hatherton Glacier. With the constraint provided by the topographic ridge, ice velocity and flux may be highly sensitive to nearby EAIS fluctuations. In the extreme case, the ridge may have the ability to completely starve the glacier of ice, thus stopping flow and accentuating the retreat signal in the DBV during periods of EAIS minima. As the bedrock ridge is only located across the Hatherton, the Darwin Glacier would be far less sensitive to changes in EAIS elevations. Johnson and Staiger (2007) show the path that an englacial (*i.e.* within a glacier) or supraglacial (*i.e.* on the glacier surface) clast takes on its way downstream is dependent on

velocity and this significantly effects the variability of irradiation. A decrease in ice velocity is shown to cause a upward movement within the ice column, possibly exhuming subglacial material. The reverse is also shown to occur, with an increase in ice velocity causing a downward ice flow, thus possibly burying previously exposed material (Johnson and Staiger, 2007). A side effect of this process may be that the transport time for glacial material may vary depending on climatic conditions. During periods of low glacial flow rates, supraglacial material generated from rockfalls might accumulate at the surface of a stagnant Hatherton Glacier. Johnson and Staiger (2007) show that climate driven glacier dynamics play a major role in the transport of supra and subglacial material. The model of Johnson and Staiger (2007) shows that a supraglacial clast moving downstream on the surface of the Ferrar Glacier running under a simulated Pliocene configuration has a significantly shorter exposure time (≈55 ka) than that of a clast on the Ferrar Glacier under LGM conditions (≈88 ka, Figure 8.3).

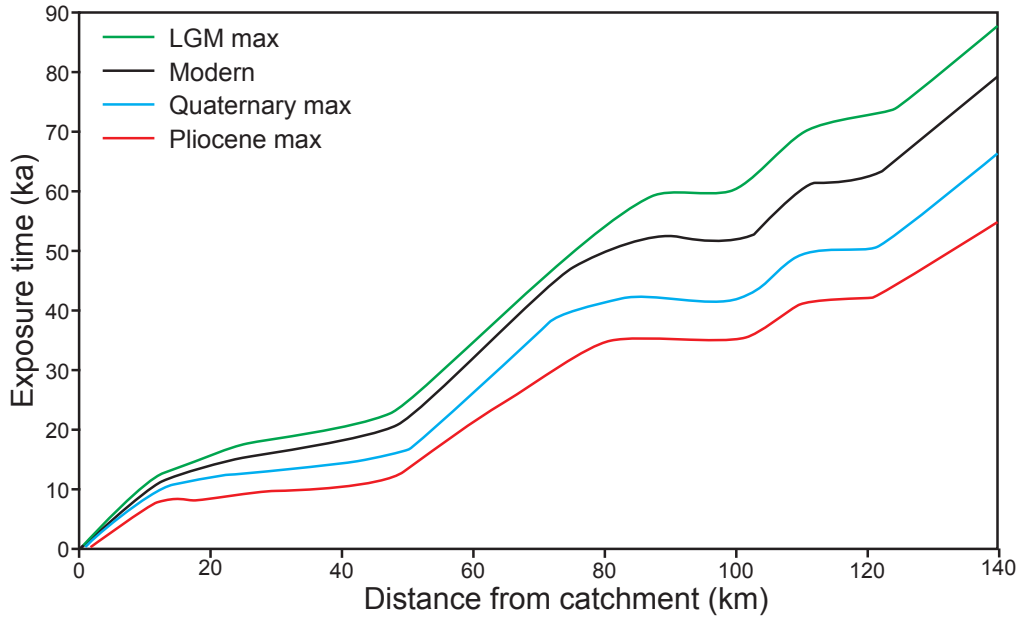

Figure 8.3: Modelled exposure times for supraglacial material - Based on a modelled Ferrar Glacier by Johnson and Staiger (2007) for a number of climatic periods.

Whether the bedrock ridge could effectively dam glacial flow is a matter of debate. At the Ferrar Glacier, a number of subglacial ridges with a similar morphology (40

& ≈200 metres of ice cover) to that observed at the Hatherton Glacier exist in the bedrock topography. Johnson and Staiger (2007) suggested that with a thinning of the glacier profile, ice flow could be retarded or possibly completely restricted during glacial minimas, the bedrock feature starves the glaciers downstream sections of ice. Their model also suggests that at these areas of thinning, the restriction of flow and decrease in velocity may cause an upwelling of older basal ice, also exhuming subglacial material. As velocity slows with proximity to the bedrock ridge, an increase of collected supraglacial, as well as freshly exposed subglacial material, may occur. During these periods of reduced EAIS and thinning ice in the Hatherton Glacier, rockfall generated supraglacial material could increasingly accumulate on the glacier surface and as the EAIS starts to re-thicken, the material would be transported downstream. If this pulse of supraglacial (and possibly exhumed subglacial) material is then deposited at a cold-based margin, a high level of geological scatter in ages would be expected. The scenario would also be further exacerbated by the inclusion of sub and englacial material, representing a true deglaciation age, within the deposit.

While the effect of subglacial 'damming' is a compelling explanation, a number of later glaciological models of the Taylor (Kavanaugh and Cuffey, 2009; Kavanaugh et al., 2009) and Ferrar glaciers (Golledge and Levy, 2011) disagree. Instead, the models suggest that flow would still occur even in a situation where the surface of the glacier has dropped below the level of the ridge and that EAIS ice should simply 'cascade' over the ridge top. In the modelled Ferrar Glacier by Golledge and Levy (2011), ice thickens on the stoss side and accelerates over the crest of the subglacial ridges. This appears to be the reverse of the Johnson and Staiger (2007) model, which suggested a slowing of ice over the feature.

Whatever the outcome of the debate, the role ice velocity has in the residence time of supraglacial material is an important consideration, with slow flowing glaciers generating considerable exposure times. Due to the DBVs proximity to the EAIS, only a limited distance (≈26 km) is available for supraglacial material to be sourced, as beyond this distance no other nunataks or outcrops exist. The low velocity of the Hatherton, ≈8 m a^{-1}, would allow a maximum residence time of supraglacial material, having continuous surface exposure from last possible source to depo-

sition in the DVA, of ≈3.3 ka. If the scenario is extrapolated downstream to Lake Wellman, the exposure time increases to ≈7 ka.

8.1 Interpretation of glacial drifts within the DHGS

Samples collected for SED were collected from a range of elevations along the length of the DHGS, from freshly exposed material directly adjacent to the glacier margin (*i.e.* Hatherton Drift), to older glacial deposits up to 800 metres above it (*i.e.* Isca Drift). The majority of our exposure age dataset are from within the Bockheim et al. (1989) sequence of glacial drifts (n=41 from Lake Wellman, Diamond Hill & the DBV). In addition, a number of bedrock (n=7 from Diamond Hill), moraine ridge (n=7 from Lake Wellman & Diamond Hill), previously undescribed drifts (n=16 from Diamond Hill) and glacial erratics (n=2, Roadend Nunatak) were also collected.
The complete dataset of 73 ^{10}Be and 65 ^{26}Al paired exposure ages collected at four sites along the length of the DHGS show a ^{10}Be age range of 1 kato 2.3 Ma and ^{26}Al from 1 ka to 2 Ma. Figure 8.4 plots the combined ^{10}Be dataset (all erratics and bedrock samples from Lake Wellman, Roadend Nunatak, Diamond Hill and the Dubris and Bibra valleys) against sample elevation. A local ice datum is used, allowing the normalisation and comparison of sample and drift elevations between sites. As suggested by Bockheim et al. (1989) and observed at other outlet glaciers in the TAMs (*i.e* the Reedy & Scott), a trend of increasing age with elevation is clear. Although there is a wide scatter within each site, the dataset shows a weak, but positive, age-elevation relationship when grouped *via* site, with an r^2 value of 0.52 (Figure 8.4A). When grouped with respect to the drifts of Bockheim et al. (1989), a similar pattern is seen (Figure 8.4B). Removing bedrock and samples designated as outliers, the r^2 value for age-elevation based on drift sequence increases to 0.59. In addition to this age-elevation relationship, samples collected from within individual drift sheets also display various degrees of clustering. Samples defined as Hatherton Drift (including those from Diamond Hill) plot distinctly in a low elevation/young age section of Figure 8.4B, separate from the older drifts. Within the older Britannia-II (≈125 ka), Danum and Isca drift samples, a clear overlap is observed, possibly due to a small number of samples from each drift with outlier ages. Within these groups, all display a generally poor relationship

between drift elevation and age with the Isca, Britannia and Hatherton drifts having r^2 values of 0.41, 0.23 and 0.04, while the Danum Drift has a higher value of 0.6. The lack of consistency that is observed in the exposure ages from Lake Wellman and the DBV may suggest that the drift correlations of Bockheim et al. (1989) may be incorrect and need revising.

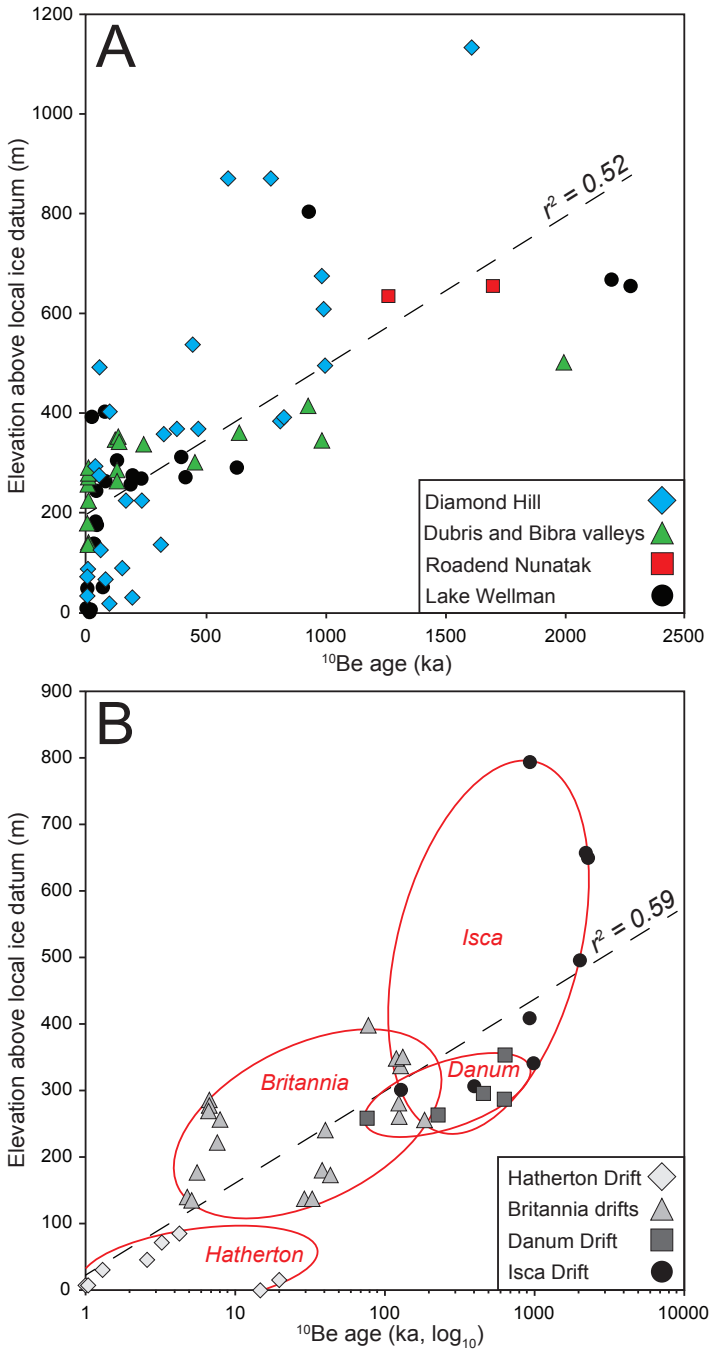

Figure 8.4: Age *vs* elevation plots for all samples - (A) Complete ^{10}Be age dataset, containing all samples collected from Lake Wellman, the DBV, Roadend Nunatak and Diamond Hill. (B) Erratic samples for all sites that have been included as part of the Bockheim et al. (1989) drift sequence (x-axis presented as a log scale for clarity). Note that bedrock samples and those considered outliers are excluded from Figure (B). The elevation in both Figures (A) and (B) is defined as the sample height in metres above a local ice datum. For the Lake Wellman area, the Lake Wellman ice surface at 794 masl. For the DBV, Lake Judith at 1120 masl. For Roadend Nunatak, the Darwin Glacier at 780 masl and for Diamond Hill, the Ross Ice Shelf at 60 masl.

8.1.1 Glacial drift exposure age chronology

One of the aims of this thesis was to re-evaluate the ice volume changes and glacial chronology suggested by Bockheim et al. (1989). Therefore SED results for the drifts, previously dated using radiocarbon ages obtained from preserved pro-glacial algal mats (Section 4.7.1), are compared between drift exposures at a number of key sites. Although the Bockheim et al. (1989) drifts were mapped at other locations throughout the DHGS (*i.e.* Tentacle Ridge, Brown Hills, Onnum & Magnis valleys, see Figure 4.1), within this thesis only Lake Wellman and the DBV were visited and these two sites contained the entire sequence of glacial deposits. Therefore, only one of the four glacial drifts described by Bockheim et al. (1989) was observed at locations outside of the Hatherton Glacier. Apart from the glacier marginal deposit described at Diamond Hill (Section 7.1.1.1) and correlated to the Hatherton Drift, observations of the Isca, Danum and Britannia drifts are limited to Lake Wellman, Dubris and the Bibra valleys.

8.1.1.1 Hatherton Drift

Of the glacial deposits mapped in the DHGS, the Hatherton Drift has a distribution that can be followed along the entire length of the glacier. The primary composition of the drift varies depending on its location along the system, a transition from sandstone (at the DBV) to granitic (at Diamond Hill) with increasing distance from the EAIS. While the dominant lithology of the drift alters, its defining characteristic, that of fresh unweathered clasts is the same at all sites. Eight samples (excluding one outlier, LW24.1) from the Hatherton Drift at Lake Wellman (Section 6.2.1.1) and Diamond Hill (Section 7.2.1.1) give ^{10}Be ages of 0.7-19 ka at elevations from 1-86 metres above the local ice datum (Table 8.1). As six of the eight have ages younger than 4.3 ka (Figure 8.5) these form the basis for our preferred mid to late Holocene age. Our preferred interpretation is that the Hatherton Drift represents a late Holocene glacial retreat starting at 4.3 ka. This scenario is consistent with the youngest limiting SED (4.8 ka) and radiocarbon ages ($\approx$6 ka, QL-1424) for the Britannia-I Drift at the DBV .

Table 8.1: Hatherton Drift SED ages - Combined ages from Lake Wellman and Diamond Hill. Elevation is defined as the height in metres above a local ice datum. For the Lake Wellman area, the datum is the Lake Wellman ice surface at 794 masl. For Diamond Hill, the Ross Ice Shelf at 60 masl. Samples marked in red are those considered to be outliers.

Sample ID	Location	Elevation	^{10}Be age	^{26}Al age
LW25.2	Lake Wellman	1 m	15 ka	16 ka
LW23.2	Lake Wellman	5 m	19 ka	16 ka
LW23.1	Lake Wellman	7 m	0.8 ka	1.2 ka
LW25.1	Lake Wellman	8 m	1.0 ka	0.7 ka
DH7.1	Diamond Hill	31 m	1.1 ka	-
LW24.2	Lake Wellman	47 m	2.6 ka	1.6 ka
LW24.1	Lake Wellman	50 m	66 ka	51 ka
DH7.4	Diamond Hill	72 m	3.3 ka	0.9 ka
DH6.2	Diamond Hill	86 m	4.3 ka	5.2 ka

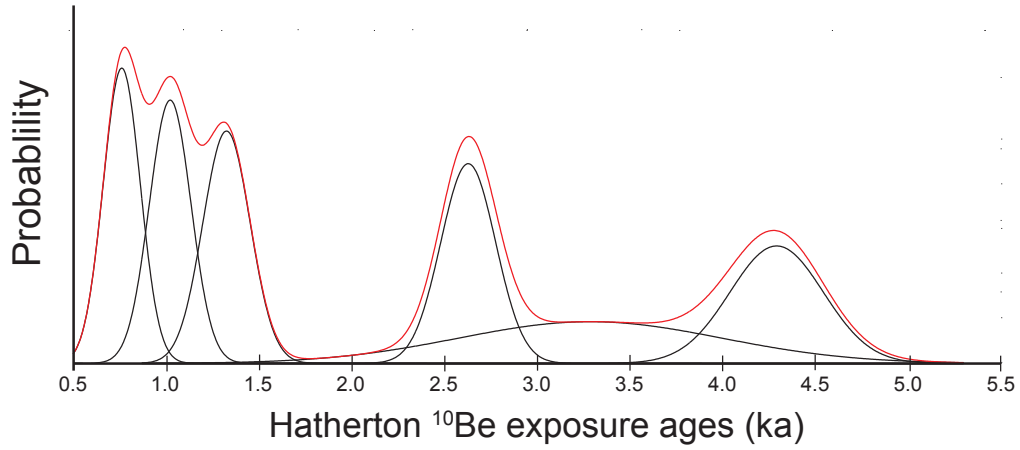

Figure 8.5: Density distribution plot for Hatherton Drift samples - Solid black lines are based on 1σ Gaussian errors derived from the total analytical (internal) error per sample, ranging from 3 to 22%. The red lines are cumulative distributions for the all samples designated as Hatherton Drift from Lake Wellman and Diamond Hill.

8.1.1.2 Britannia drifts

The Britannia Drift SED results show the greatest complexity in exposure ages in any of the Bockheim et al. (1989) drifts and therefore raise a problem in their comparison between Lake Wellman and the DBV, only ≈30 km apart. At the DBV, Bockheim et al. (1989) separated the Britannia into two discreet units (Britannia-I & Britannia-II), but at Lake Wellman the differentiation was not as clear. The field observations of Bockheim et al. (1989) were unable to subdivide the drift and

therefore mapped the Britannia as a single homogeneous drift sheet.
Twenty three samples (excluding one outlier) from the Britannia Drift at both sites and collected at elevations from 135-400 metres above the local ice datum have ^{10}Be ages from 5-182 ka (Table 8.2). The exposure ages from the DBV (Section 5.2.1.1) are the most coherent of any site within the DHGS and display the strongest evidence of ice sheet influence on the behaviour of the Hatherton Glacier. Both the Britannia-I Drift (≈5-8 ka) and Britannia-II (≈124-131 ka) drifts display tightly clustered ages, in direct contrast to those from Lake Wellman (Section 6.2.1.2).
At Lake Wellman, an age range of 16-193 ka is obtained for the Britannia, with a statistically significant cluster of five ages at 29-43 ka (Figure 8.6). Because of the vast differences in age distribution observed between Lake Wellman and the DBV, the ^{10}Be ages for the Britannia drift can be interpreted in two ways.

1. Using a minimum age model, LGM ice at Lake Wellman had retreated to a point 271 meters above the modern glacier by 16 ka. Although this scenario closely fits that of Bockheim et al. (1989), it suggests that all other ages reflect some degree of burial and/or complex exposure history. The strongly clustered five ages at the DBV (≈125 ka) would also have to be discounted.

2. Treating the 16 ka date as an outlier, the Britannia Drift, at both sites would then represent a retreat of ice at a maximum ≈190 ka, but more likely ≈126 ka, based on the cluster of ages at the DBV (Britannia-II). This retreat probably continued until the LGM, with a period of increased deposition represented by a re-advance or prolonged stillstand at ≈35 ka at Lake Wellman.

The first scenario hinges on a single sample collected from the apex of an unstable moraine. Although the use of the sample cannot be completely excluded in interpretations, its reliability is questioned. The preferred interpretation is that of scenario #2, with the exposure ages suggesting that the Britannia Drift at Lake Wellman is not an LGM deposit. At the DBV, the Britannia-I ages represent a completely separate younger glacial event; The mid Holocene ages suggest a re-advance of the Hatherton Glacier that occurred post-LGM, with an enlarged Hatherton Glacier retreating at 8-5 ka and depositing the Britannia-I. It is also possible that the Britannia at Lake Wellman represents a retreat from a MIS-3 (30-45 ky) ice advance,

while the Britannia-I and II represent retreat from ≈MIS-5e and early-Holocene advances. Therefore the drifts are common in name only.

Table 8.2: Britannia Drift SED ages - Combined ages from Lake Wellman and the DBV. Elevation is defined as height in metres above a local ice datum. For the Lake Wellman area, the datum is the Lake Wellman ice surface at 794 masl. For the DBV, Lake Judith at 1120 masl. The sample marked in red is considered to be an outlier.

Sample ID	Location	Elevation	^{10}Be age	^{26}Al age
DV7.1	DBV	135 m	5.2 ka	4.8 ka
LW21.1	Lake Wellman	136 m	34 ka	34 ka
LW21.2	Lake Wellman	137 m	29 ka	31 ka
BV3.1	DBV	139 m	4.9 ka	3.9 ka
LW20.1	Lake Wellman	173 m	43 ka	46 ka
BV9.2	DBV	177 m	5.7 ka	5.3 ka
LW20.3	Lake Wellman	180 m	38 ka	35 ka
BV4.2	DBV	222 m	7.7 ka	7.4 ka
LW18.1	Lake Wellman	242 m	40 ka	37 ka
LW18.3	Lake Wellman	256 m	183 ka	192 ka
DV6.1	DBV	257 m	8.0 ka	8.8 ka
DV3.1	DBV	263 m	125 ka	118 ka
LW14.2	Lake Wellman	270 m	415 ka	254 ka
DP1.4	DBV	270 m	6.8 ka	6.1 ka
LW14.3	Lake Wellman	271 m	16 ka	-
LW14.1	Lake Wellman	274 m	192 ka	-
DP3.2	DBV	277 m	6.8 ka	6.4 ka
DV5.2	DBV	283 m	124 ka	103 ka
DP1.2	DBV	286 m	6.8 ka	9.9 ka
DP4.1	DBV	339 m	128 ka	124 ka
DP4.3	DBV	349 m	123 ka	116 ka
DP4.2	DBV	351 m	131 ka	-
LW2.2	Lake Wellman	392 m	23 ka	25 ka
LW2.1	Lake Wellman	401 m	78 ka	137 ka

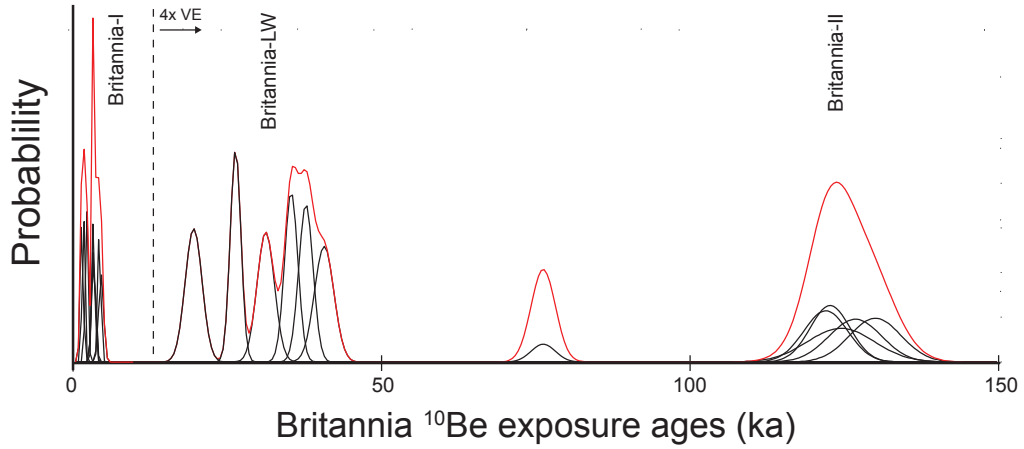

Figure 8.6: Density distribution plot for Britannia Drift samples - Solid black lines are based on 1σ Gaussian errors derived from the total analytical (internal) error per sample, ranging from 3 to 9%. The red lines are cumulative distributions for the all samples designated as Britannia Drift from Lake Wellman and the DBV. The probability value (x axis) for samples older than 10 ka are vertically exaggerated by a factor of four. Samples LW14.1 and 18.3 (192 & 183 ka) are omitted for clarity.

8.1.1.3 Danum Drift

The second oldest deposit mapped in the DHGS is the Danum Drift (Section 4.6.1.3), suggested by Bockheim et al. (1989) as being deposited during MIS-6 ($\approx$ 140-190 ka). Our exposure ages for the Danum Drift suggest an exposure far older than the suggested 130-185 ka. Although the least constrained event in the dataset, the Danum Drift ages range from 77-637 ka (Table 8.3) at elevations of 260-358 metres above the Hatherton Glacier. The upper age of the Danum is constrained by the oldest ages from both Lake Wellman and the DBV (Figure 8.7).

Table 8.3: Danum Drift SED ages - Combined ages from Lake Wellman, Dubris and Bibra valleys. Elevation is defined as height in metres above a local ice datum. For the Lake Wellman area, the datum is the Lake Wellman ice surface at 794 masl. For the DBV, Lake Judith at 1120 masl. Samples marked in red are those considered to be outliers.

Sample ID	Location	Elevation	^{10}Be age	^{26}Al age
LW13.2	Lake Wellman	261 m	77 ka	77 ka
LW13.3	Lake Wellman	267 m	227 ka	157 ka
LW15.1	Lake Wellman	291	630 ka	491 ka
DV2.1	Dubris & Bibra valleys	300 m	454 ka	405 ka
DP5.1	Dubris & Bibra valleys	358 m	637 ka	610 ka

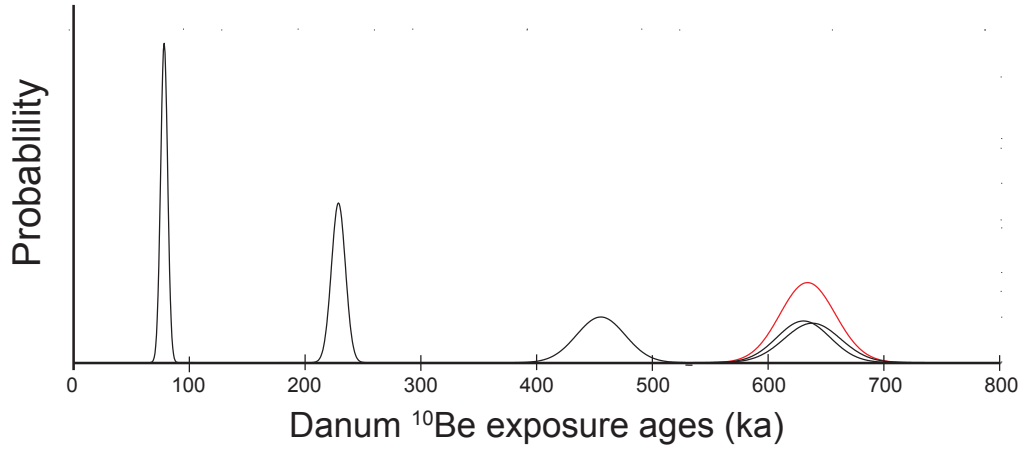

Figure 8.7: Density distribution plot for Danum Drift samples - Solid black lines are based on 1σ Gaussian errors derived from the total analytical (internal) error per sample, ranging from 3 to 5%. The red lines are cumulative distributions for the all samples designated as Danum Drift from Lake Wellman and Diamond Hill.

8.1.1.4 Isca Drift

The Isca Drift (Section 4.6.1.3) is the highest elevation deposit described at the Hatherton Glacier and its upper limits were not observed at either Lake Wellman or the DBV. As exposure ages were only collected within the lower sections of the Isca (*i.e.* at elevations above the contact with the Danum Drift) any inferences of ice thickness must be considered a minimum and that ice in these locations was presumably much thicker in the past.

Six samples designated as Isca Drift have SED ages ranging from 0.9-2.3 Ka (Table 8.4) and display strong clustering at $\approx$1 Ma and >2 Ma (Figure 8.8). The drift appears to be deposited during a retreat of Hatherton Glacier ice between 0.9-2.2 Ma. During this time, the ice was a minimum of 500-700 metres of ice thicker than present at the DBV and Lake Wellman. The meteorite exposure ages of Nishiizumi et al. (1989) from Derrick Peak (Section 4.7.3), also fall within the range suggested for the Isca (1-2 Ma), albeit at the lower end. Samples collected by Kamp and Lowe (1982) and Kirkbride et al. (1991) close to the Danum/Isca drift boundary all display ages of 0.9-1 Ma. At the time, the meteorite exposure ages were discounted due to the assumed MIS-6 age of the underlying drifts, but based on the new exposure

age data, they appear to be consistant and suggest the lower limit of the Isca was deposited at ≈1 Ma.

Table 8.4: Isca Drift SED ages - Combined ages from Lake Wellman, Dubris and Bibra valleys. Elevation is defined as height in metres above a local ice datum. For the Lake Wellman area, the datum is the Lake Wellman ice surface at 794 masl. For the DBV, Lake Judith at 1120 masl. Samples marked in red are those considered to be outliers.

Sample ID	Location	Elevation	^{10}Be age	^{26}Al age
LW12.1	Lake Wellman	305 m	128 ka	115 ka
LW12.2	Lake Wellman	310 m	395 ka	340 ka
DV1.1	Dubris & Bibra valleys	344 m	985 ka	869 ka
BV8.1	Dubris & Bibra valleys	413 m	927 ka	699 ka
DP6.1	Dubris & Bibra valleys	500 m	1997 ka	1498 ka
LW9.1	Lake Wellman	656 m	2275 ka	1978 ka
LW9.3	Lake Wellman	663 m	2196 ka	-
LW11.1	Lake Wellman	801 m	929 ka	-

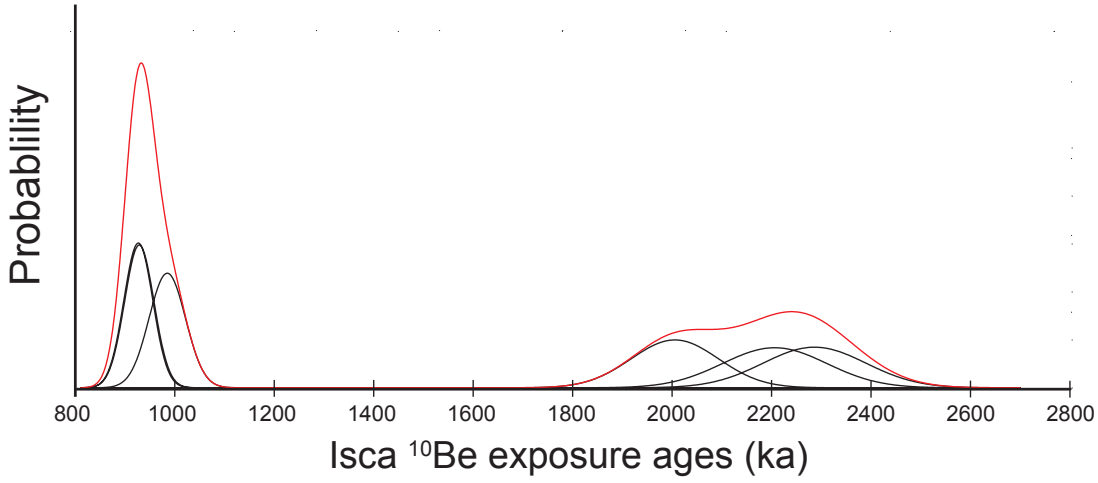

Figure 8.8: Density distribution plot for Isca Drift samples - Solid black lines are based on 1σ Gaussian errors derived from the total analytical (internal) error per sample, ranging from 3% to 5%. The red lines are cumulative distributions for the all samples designated as Isca from Lake Wellman and the Dubris and Bibra valleys.

8.2 Quaternary behaviour of the DHGS

The ^{10}Be chronology presented in this thesis for the DHGS is in partial agreement with that suggested by Bockheim et al. (1989). The exposure ages show conclusively that deposition of the Hatherton Drift occurred during the Holocene and for the Isca Drift, the mid to late Pleistocene. The Danum and Britannia drifts shows ages far older than the MIS-6 and the LGM ages inferred by Bockheim et al. (1989), although it should be noted that in the DBV, Bockheim et al. (1989) suggested that the Britannia-I post-dated the Britannia-II.

The DBV results show clear evidence of the EAIS influence in the upper DHGS region and allows strong conclusions to be made concerning EAIS dynamics during interglacials. Unfortunately, this outcome is in stark contrast to the uncertainty in age interpretation in the lower parts of the DHGS due to the wide geologic scatter and complexity in exposure ages. The high frequency of reworked material and clasts preserving a prior exposure history that is observed in the Diamond Hill exposure ages precludes a conclusion about the dynamics of the WAIS, particularly during the LGM. However our results can be compared to the Reedy Glacier (Section 3.3.4.3), another outlet glacier system in the TAMs, located $\approx$1100 km to the south east of the DHGS. It is the only other glacial system with a large number of exposure ages showing the influence of the EAIS and WAIS on glacier ice surface elevations. Given the importance of the Reedy Glacier geological record, the work of Todd et al. (2010) and Bromley et al. (2010) are key to our understanding of both glacier behaviour and the timing of ice sheet retreat in the southern most sector of the TAMs.

8.2.1 Pre-LGM (2.2 Ma-22 ka)

Of the glacial sequence described by Bockheim et al. (1989), the Danum, Isca, Britannia (Lake Wellman) and Britannia-II (DBV) all have exposure ages that predate the LGM. As samples with the oldest ages are generally those at the highest elevations, it would suggest that that DHGS ice was considerably thicker in the past. Exposure ages from the Isca Drift suggest that the upper DHGS was ice free by 1-2 Ma, while its lowermost sections appear to have thinned slightly later, for example

their higher elevations at Roadend Nunatak and Diamond Hill becoming exposed at ≈1.6 Ma. Additionally, a time transgressive ice surface reconstruction for this period (1.6-2.2 Ma, Figure 8.9) displays the characteristic asymmetric thickening observed at other TAM outlet glaciers. Hatherton Glacier ice reached at least +500 metres at the DBV and +1100 metres above the Darwin Glacier at Diamond Hill. In the upper parts of the DHGS, at Lake Wellman and the DBV, the retreat appears to have continued until at least 1 Ma. As highlighted previously, the lack of a clear correlation to the Bockheim et al. (1989) drifts within the Diamond Hill exposure ages is likely due to the high proportion of reworked clasts. Hence correlations between the older pre-LGM exposure ages and glacial drifts are restricted to Lake Wellman and the DBV at Hatherton Glacier.

The deposition of the Danum Drift is interpreted to represent a separate glacial event from the Isca Drift, related to a re-advance of the Hatherton Glacier. From a glacial high-stand position reached between 0.6-1 Ma (see Table 8.3), ice retreated until at least 400 ka. During these mid-late Pleistocene glacial high-stands, it is possible that basal conditions within the Hatherton Glacier were predominantly warm based, with the presence of significantly thickened ice (500 m above modern) in the central trunk of the glacier reaching pressure melting point. Episodes of warm basal conditions would be accompanied by the production of subglacial material eroded from the base of the glacier. At glacial minima, thinner glacier margins would be cold based, but material exhibiting warm based characteristics (*i.e.* striae, glacially polished and bullet shaped boulders) could be transported en-glacially and deposited at cold-based margins (Atkins, 2013). This is observed in the DHGS, where boulders displaying evidence of warm basal conditions are observed within the Danum, Isca, Diamond and Upper drifts (Section 4.5.2.1).

The last glacial event to pre-date the LGM is the Britannia-II Drift, only observed in the DBV. Here, a cold based advance occurring between 130-192 ka reached ≈250-350 metres above the present Hatherton Glacier. The spatial distribution of the exposure ages throughout the drift show that a relatively sudden retreat occurred at ≈125 ka. While the exposure ages paint a convincing deglaciation story, the retreat may have continued much longer, possibly until the LGM. The striking ^{10}Be age grouping for the Britannia-II at the DBV is not observed in the Britannia Drift dataset for Lake Wellman. The lack of similar ages between the two

sites may suggest the thickening observed at the DBV was limited to EAIS proximal sites. A local ice thickening of the EAIS may have caused an advance into the DBV but was insufficient to impact the ice surface elevation of the Hatherton Glacier at Lake Wellman. Equally important is the conclusion that the lack of similar ages between the two sites raises questions about the applicability of soil development studies as a tool to demarcate glacial deposits.

When compared to the exposure age chronology for the Reedy Glacier by Bromley et al. (2010), the older DHGS ages show a strikingly similar drift age pattern (Table 8.5).

Table 8.5: Exposure ages from the Reedy Glacier and DHGS - A comparison of ^{10}Be ages from mapped glacial drifts in the DHGS to those of Bromley et al. (2010) at the Reedy Glacier. Note that samples deemed as outliers in both datasets have been omitted.

Location	Drift	^{10}Be age
Reedy Glacier	Reedy-E	1173-4932
Reedy Glacier	Reedy-D	2459
DHGS	Isca	926-2275
Reedy Glacier	Reedy-C	695-778
DHGS	Danum	454-637
Reedy Glacier	Reedy-B	135-166
DHGS	Britannia-II	123-192

While not implicitly stated by Bromley et al. (2010) it appears that samples were preferentially collected at the uppermost drift limits (*i.e.* at similar elevations). Therefore the oldest exposure ages within drifts at the Reedy Glacier may represent the initial start of glacial retreat. If this is the case, they can provide an insight into the upper limits of the exposure age groupings observed at the DHGS. As shown in Table 8.5, the maximum drift ages correlate very well with those from the Reedy Glacier. Therefore, a tentative suggestion is that at the Hatherton Glacier, the Isca, Danum and Britannia II maximum drift ages (*i.e.* beginning of retreat following advance) are $\approx$2.5, 0.8 and 0.17 Ma respectively and are correlative to Reedy C, D and B respectively.

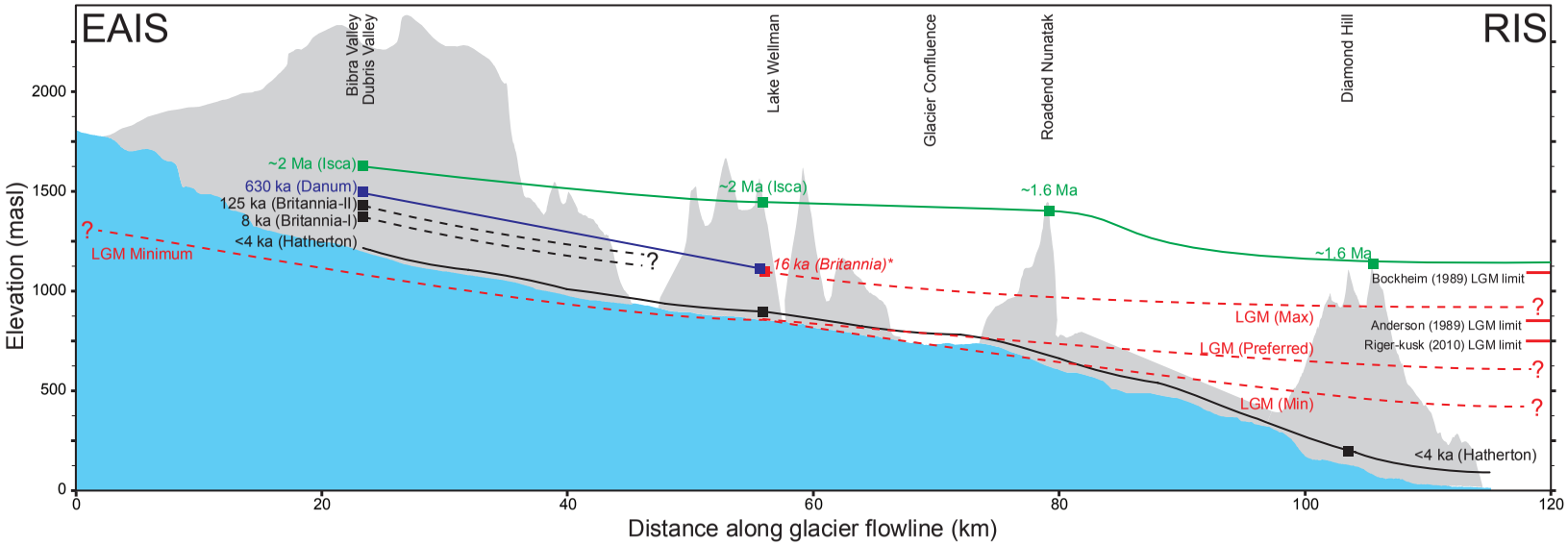

Figure 8.9: Reconstructed ice surfaces for the DHGS - Reconstructed paleo-ice surfaces based on exposure ages for the Plio-Pleistocene (Isca), mid-Pleistocene (Danum) and Holocene (Britannia-I & Hatherton drifts). While evidence to reconstruct the LGM surface of the DHGS was sparse, tentative minimum and maximum ice surface reconstructions have been given based on geomorphological observations. The Maximum scenario uses the maximum limits of glacial drift observed at Diamond Hill (upper Drift) and the single 16 ka age (considered to be unreliable) at Lake Wellman. The minimum LGM ice scenario (considered the more likely) is based on the maximum elevation of the Diamond Drift at Diamond Hill and a ice elevation near the modern Lake Wellman. As the EAIS is suggested to be thinner than present in the latter scenario, the paleo-ice elevation below the modern Hatherton Glacier during the LGM is purely schematic.

8.2.2 LGM (22-10 ka)

One of the most interesting observations in the full SED dataset from the DHGS is the conspicuous absence of LGM aged deposits, although they are not precluded at Diamond Hill. Given the scale of ice sheet thickening within the Ross Sea Embayment, a predominance of exposure ages related to the late Quaternary retreat of the WAIS should be expected. Instead, only four of the 73 ^{10}Be ages are within the 20-10 ka range. The lack of evidence pertaining to the timing and magnitude of the DHGS during the LGM ice occurs at all sites along the length of the DHGS and poses the question of why these ages are not observed in our dataset. Explanations for the 'missing' LGM evidence include:

1. Glacial advances during the LGM were predominantly cold-based and therefore only a limited amount of material was deposited during ice retreat.

2. The magnitude of East and West Antarctic ice sheet thickening at the LGM is was far smaller than currently assumed or perhaps LGM ice thickness was lower than today.

3. The sampling methodology employed in this thesis (Section 2.2.5) failed to collect material deposited during the LGM retreat.

However material was sampled from within drifts (the DBV) and from glacial erratics on bedrock platforms (Diamond Hill), this being the methodology suggested by Stone et al. (2003) and followed by Todd et al. (2010) and Bromley et al. (2010) at the Reedy Glacier. Hence the conclusion points to a combination of scenario #1 and #2 as the principal causes for the absence of LGM deposits. If the sampling methodology is considered robust, then the inference would be that the majority of material deposited at Diamond Hill has a complex exposure and preservation of a prior TCN inventory. This characteristic was not observed at sites closer to the catchment.

At the Dubris and Bibra valleys, the lack of a identifiable LGM signal, combined with a clear separation between the Britannia-I (8-5 ka) and the Britannia-II ($\approx$125 ka) drifts tells an interesting story. As the DBV is the closest site to the EAIS ($\approx$36 km) it may be the least affected by the upstream propagation of thickening caused

by the damming of the DHGS and therefore only reflects changes in the EAIS. The interpretation of the Britannia drifts in the DBV is that the Britannia-II represents a glacial retreat at ≈125 ka to a position at the LGM that is lower than the modern Hatherton Glacier. Post-LGM there was a major Holocene advance (Britannia-I) that covered any evidence of the maximum LGM limit.
At Lake Wellman, three samples with exposure ages that may represent the retreat of LGM ice were collected. Sample LW14.3, collected from the Britannia Drift limit marked by Moraine-2 (1065 masl), has a ^{10}Be age of 16 ka and can be interpreted in two ways:

- A true value that represents the initial LGM deglaciation. The Hatherton Glacier during the LGM reached the Britannia upper limit (1065 masl) as suggested by Bockheim et al. (1989).
- A sample with a complex exposure history that has either undergone erosion and/or burial.

The unstable, matrix supported nature of the moraine the sample was collected from the older ages (192 & 415 ka, samples LW14.1 &14.2) obtained from samples in close proximity, suggests the age should be treated as an outlier and therefore is rejected. In addition, LW14.2 shows a burial age of ≈750 ka. The remaining two samples (LW23.2 & LW25.2) were sampled from within the Hatherton Drift at the Lake Wellman ice margin (≈794 masl). As with sample LW14.3 (Moraine-2), the unstable nature of the moraine-1 means that samples are likely to have some form of complex exposure history or post depositional modification, possibly due to exhumation or clast rotation. As support for this assertion, here at sites LW23 and LW25 on Moraine-1, two other adjacent samples gave ^{10}Be ages of 0.8 and 1.0 ka. If the two exposure ages (19.1 & 14.8 ka) are taken at face value, it suggests that the Hatherton Drift at Lake Wellman may well be an LGM deposit and that ice reached a maximum of 50 metres above Lake Wellman. The preferred interpretation is that the ages are reworked LGM clasts (LW23.2 shows a burial signal) incorporated into the Holocene aged Hatherton Drift. This would mean that the LGM ice limits were not much different than the modern Hatherton Glacier. The exposure ages suggest that, similar to the DBV, Lake Wellman was not overrun by

ice during the LGM. They may also suggest that the upstream thickening of the DHGS, caused by the WAIS grounding line buttressing the glacier discharge, may not have propagated as far as Lake Wellman as per the interpretation of Bockheim et al. (1989).

But while a EAIS smaller (or a similar size) than present may be a plausible explanation for sites near the DHGS catchment (*i.e.* the DBV & Lake Wellman), , it does not explain the observations at Diamond Hill. As modelled LGM ice is 1000-700 metres above the present RIS at this location (Anderson et al., 2004; Bockheim et al., 1989; Riger-Kusk, 2011) the likelihood of little to no LGM debris being deposited is low. The mapping of the Upper Drift at Diamond Hill (Section 7.1.1.3), where one would expect to locate LGM deposits (if models are correct) shows that the highest elevation at which glacial erratics are found is ≈930 masl (DH11.1). If the exposure ages can be ignored (max 468 ka), then the maximum sample elevation can be used as a proxy for the upper limit for past ice thickening. As the high elevation sections of Diamond Hill (>1200 masl) show little to no recent evidence of overriding ice, the emplacement of the Upper Drift would suggest that ice has not been higher than 900 masl for at least 1.6 Ma (based on the bedrock exposure age of sample DH10.1B).

Using a similar methodology, an alternate scenario that uses the upper limits of the Diamond Drift can also occur. As the deposition of the Diamond Drift (Section 7.1.1.2) post-dates that of the Upper Drift, it may be a more suitable geological proxy for thickened ice. As the Upper Drift limits only reach ≈450-550 masl, it would infer a far smaller ice thickness (≈390-490 m) than that suggested in the numerical models (Anderson et al., 2004; Riger-Kusk, 2011). In summary, the complexity of the Diamond Hill ^{10}Be dataset and the lack of LGM aged material, this thesis can only make limited conclusions about the timing and scale of West Antarctic ice in the lower sections of the DHGS. Based on the geomorphic evidence and a single ^{10}Be age, the WAIS at Diamond Hill is tentatively constrained by:

- A maximum LGM ice thickness of ≈870 metres based on the limits of the Upper Drift. This is defined is by sample DH11.1, the highest emplaced erratic observed at Diamond Hill (930 masl) and assumes that nearly all of its cosmogenic inventory (≈768 ka) represents prior exposure.

- Similarly, a minimum LGM ice thickness of ≈370 metres based on the maximum limits of the Diamond Drift (430 masl). This assumes all bar one sample (DH3.1) of nine (with ages of 37-466) represents prior exposure.
- The 13.8 ka date of sample DH3.1 (335 masl) within the Diamond Drift.

This would suggest that West Antarctic ice at the LGM reached an elevation of 930-430 masl and had lowered to ≈335 masl by 13.8 ka (Figure 8.9). Although, if the upper limit of 900 metres is assumed, then the deposition of the Diamond Drift at a lower elevation must also now be explained; possibly during a post-LGM re-advance and/or a period of increased deposition.

When the lack of LGM exposure ages is compared to that of the Reedy Glacier, significant differences in the spread of ages are observed. The Reedy-III Drift, mapped at Mims Spur, Calopaca and Quartz Hills, was originally suggested as being deposited during the retreat of LGM ice by Mercer (1968); the exposure ages of Todd et al. (2010) support this. Of the ^{10}Be ages assigned to the Reedy-III (see Tables 1 & 2 in Todd et al. 2010), 12 of the 32 samples (38%) are between 20-10 ka, with a further nine samples having a mean age of ≈8.6 ka. The remaining 11 samples, with ages from 25-117 ka, are excluded from the Todd et al. (2010) LGM interpretation (≈17 ka) for the Reedy-III based on the assumption that samples have a complex exposure history.

As the exposure ages of Todd et al. (2010) suggest that the Reedy-III Drift (correlated to the Britannia Drift by) represents the retreat of thickened ice at the LGM, the question still remains regarding the absence of LGM glacial deposits in the DHGS.

8.2.2.1 Modelled behaviour of the DHGS during the LGM

Numerous terrestrial, marine and geological records have now shown the advance and retreat of a significantly thickened WAIS into the Ross Sea Embayment at the LGM. Although the position and extent of grounded ice is well understood (Anderson et al., 2013), the magnitude of ice thickening within the RSE is poorly constrained. As thickness of West Antarctic ice at the mouth of the DHGS has previously been inferred by only a small number of radiocarbon ages and an extrapolated ice surface (Bockheim et al., 1989), the use of newer geochronological

techniques (*i.e.* SED) has the potential to further constrain the magnitude of LGM ice thickness. The exposure age chronology for the upper reaches of the DHGS LGM ice surface based on this thesis points to a rather unexpected and exciting conclusion - that Hatherton LGM ice was lower, or at the most similar to today. In contrast, exposure ages at the confluence of the RIS and the DHGS are inconclusive. However extrapolating our Hatherton Glacier LGM surface (see Figure 8.9) indicates that at the RIS, ice thickening was lower (by ≈300 metres) than previously suggested based on radiocarbon ages.

Within the TAMs, the strongest evidence for a smaller WAIS at the LGM, as suggested by Anderson et al. (2004), comes from Todd et al. (2010) and Bromley et al. (2012). The Reedy and Scott glaciers (Section 3.3.4.3), although located much farther south than the DHGS (≈85°S) are the closest which contain relatively well dated records. At the Reedy Glacier, a recent suite of exposure ages (Todd et al., 2010) suggests a 17-38% overestimation in the thickness of a LGM WAIS in the southernmost TAMs. Using the upper limits of the Reedy-III Drift, which the exposure ages show to be of LGM age, a maximum WAIS ice surface of 1062-1400 masl is suggested (+450 to 800 m). This is in contrast to the 1700 masl predicted in the Denton and Hughes (2002); Denton and Marchant (2000) and Huybrechts (2002) models of LGM ice sheet thickness. A similar finding is shown at the Scott Glacier by Bromley et al. (2012). Mapping of the Scott-I Drift suggests that during the LGM, West Antarctic ice at the mouth of the Scott Glacier reached 1100 masl (+1000 m). This is in disagreement with older models that show an LGM ice surface at this location of 1600 (Denton and Hughes, 2002) to 2000 masl (Ritz et al., 2001). Furthermore, the LGM ice thickness shown in later glaciological models (Mackintosh et al., 2011; Whitehouse et al., 2012) broadly concur with the results of Bromley et al. (2012). Therefore, as the geological evidence from the Reedy and Scott glaciers both suggest that the WAIS was not as thick as modelled with a 17-45% overestimation. This finding is similar to the recommendations of this thesis for the DHGS. Therefore it can be assumed with some confidence that West Antarctic ice at the mouth of the DHGS was thinner than the 1200 masl suggested by Bockheim et al. (1989) as deduced from ^{10}Be exposure ages.

For the DHGS, two glaciological models exist that infer LGM ice thickness, both suggesting ice elevations lower than that of Bockheim et al. (1989). The work of An-

derson et al. (2004) used a simple one dimensional flow line model to reconstruct a number of glacier surfaces at the LGM. By using the upper limits of the Britannia Drift surface, an equilibrium glacier profile using a grounded ice sheet thickness of 800 $\pm$ 100 metres ($\approx$900 masl) above the modern ice shelf, was deemed the best fit. This value is $\approx$25% lower than the 1200 masl, previously suggested. The later model of Riger-Kusk (2011) used a different approach for the DHGS. Geophysical surveys of subglacial topography and ice thickness of DHGS were used in conjunction with continental (All-Antarctic model) and regional (3D Nested model) scale models of the DHGS. The results show that a thickening of 0-80 for EAIS and 600-700 metres for WAIS would have been required to raise the Hatherton Glacier up to the limit of the Britannia-II Drift (at the DBV) during the LGM. This value is $\approx$40% lower than the 1200 masl previously suggested. While the models of Riger-Kusk (2011) suggest that the EAIS was little changed from the present, they also show that the upstream propagation of ice could reach the Britannia Drift limit at the DBV. Hence the major outcome of this model is that grounded West Antarctic ice at the mouth of the DHGS is the sole contributor to the behaviour of the DHGS during the LGM. The conclusion being that the EAIS contributed little to the LGM and subsequent deglaciation.

The numerical models of Anderson et al. (2004) and Riger-Kusk (2011) both show a thinner WAIS than that suggested by Bockheim et al. (1989) and the models of Denton and Hughes (2002); Denton and Marchant (2000). The 600-800 metres of modelled WAIS thickening broadly concurs with our observations and mapping of glacial drifts at Diamond Hill. In contrast, the exposure age chronology and geomorphological observations at the DBV strongly disagree that ice reached the Britannia-II Drift limit ($\approx$126 $\pm$ 3 ka) during the LGM.

8.2.3 Holocene (<10 ka)

The RSE during the Holocene experienced a number of climatic optima (Masson-Delmotte, 2000; Steig et al., 2000) that are reflected in the geological record Verleyen et al. (2011). Given the fluctuating nature of climate during this period and its effect on ice accumulation, it is unsurprising that the Holocene exposure ages indicate strong variations in ice thicknesses. In contrast to the lack of ages

related to the LGM retreat of the WAIS, evidence of Holocene ice thickening is observed at almost all sites along the DHGS. Two glacial events, represented by the Britannia-I and Hatherton drifts, are clearly defined in the Holocene exposure age chronology. At the DBV, the occurrence (and absence) of glacial drifts, tells a complex story. Following a LGM glacial lowstand at elevations below the modern Hatherton Glacier, the exposure age chronology and the relationship between the Britannia-II, Britannia-I and Hatherton drifts within the DBV during the Holocene suggests (Figure 8.10).

- A re-advance of ≈250 vertical metres of ice between the LGM and 8 ka (Figure 8.10B & Britannia-I Drift). This is followed by a retreat at 5-8 ka to a elevation lower or similar than the present Hatherton Glacier (Figure 8.10D); followed by.

- A re-advance of 50 metres at ≈5 ka (Figure 8.10E & Hatherton Drift), then a retreat back to the present glacier position (Figure 8.10F).

The strong Holocene age grouping observed within the Britannia-I at the DBV is absent at Lake Wellman. Therefore, it may suggest that the increase in ice thickness that deposited the Britannia-I was localised to the upper reaches of the Hatherton Glacier and is unrelated to the WAIS driven thickening observed downstream. This increase in Hatherton Glacier ice flux is likely related to increased snow accumulation and thickening in East Antarctica (Petit et al., 1999). Postdating the Britannia-I Drift is the youngest recessional deposit observed in the DHGS, the Hatherton Drift. The Hatherton Drift has a extremely fresh looking and unweathered appearance compared to all other observed drifts in the DHGS and contains the youngest exposure ages in our dataset, 0.7-4.3 ka. A maximum elevation of 50-85 metres above the present ice margin is reached by the drift, with the thickest (*i.e.* highest elevation) deposit located at Diamond Hill. A similar, yet less pronounced, asymmetric thinning is observed within the other drift sheets. The Hatherton Drift is likely to represent a minor re-advance of the DHGS in the mid-late Holocene. Furthermore, the limited thickness of the Hatherton Drift and young exposure ages, suggests that the DHGS was approaching its equilibrium ice profile by ≈4.3 ka.

Similarities in the DHGS Holocene ^{10}Be exposure ages are observed when compared to those at the Reedy Glacier. Todd et al. (2010) suggests that a thickening EAIS at the head of the Reedy Glacier covered any evidence of the LGM and created a mid to late Holocene high-stand. The lower sections of the Reedy Glacier (*i.e.* proximal to the WAIS) started thinning at ≈13 ka, whereas the upper sections (*i.e.* proximal to the EAIS) continued thickening. At sites close to the EAIS (*i.e.* Hatcher Bluff, Mims and Polygon spurs), exposure ages show that ice started retreating from its high-stand position, 140 metres above the present Reedy Glacier, at 5.3-9.1 ka. Both the scale of ice thinning and initial timing of deglaciation is similar to that observed in the Britannia-I Drift at the DBV. The recessional deposits mapped at the ice margins of the Reedy Glacier also reflect a similar thinning history to that of the Hatherton Drift. Material deposited at the ice margins along the length of the Reedy Glacier have exposure ages from 0.6-4 ka and suggest that the Reedy Glacier has thinned by ≈50 metres, while the DHGS a maximum of 80 metres over the same time period (<4.3 ka).

8.3 Implications for Antarctic ice sheet dynamics

One of the key aims of this thesis was to use the DHGS as a proxy to understand East and West Antarctic ice sheet behaviour. Although our exposure age chronology is inconclusive in some aspects, particularly concerning the LGM configuration of the WAIS, it does provide some insights of suggested ice sheet behaviour. Our best understanding of how the Antarctic ice sheets have reacted to glacial/interglacial climates are the models of Mackintosh et al. (2011) and Golledge et al. (2012), that reconstruct the Antarctic continent at the LGM and throughout the Holocene. While the modelled East and West Antarctic ice sheets appear to have behaved similarly, differences occur between the ice sheet interiors and the coastal margins.

- Coastal ice sheet margins
  - Advance and thicken during glacial (*i.e.* colder) periods.
  - Retreat and thin during interglacial (*i.e.* warmer) periods.

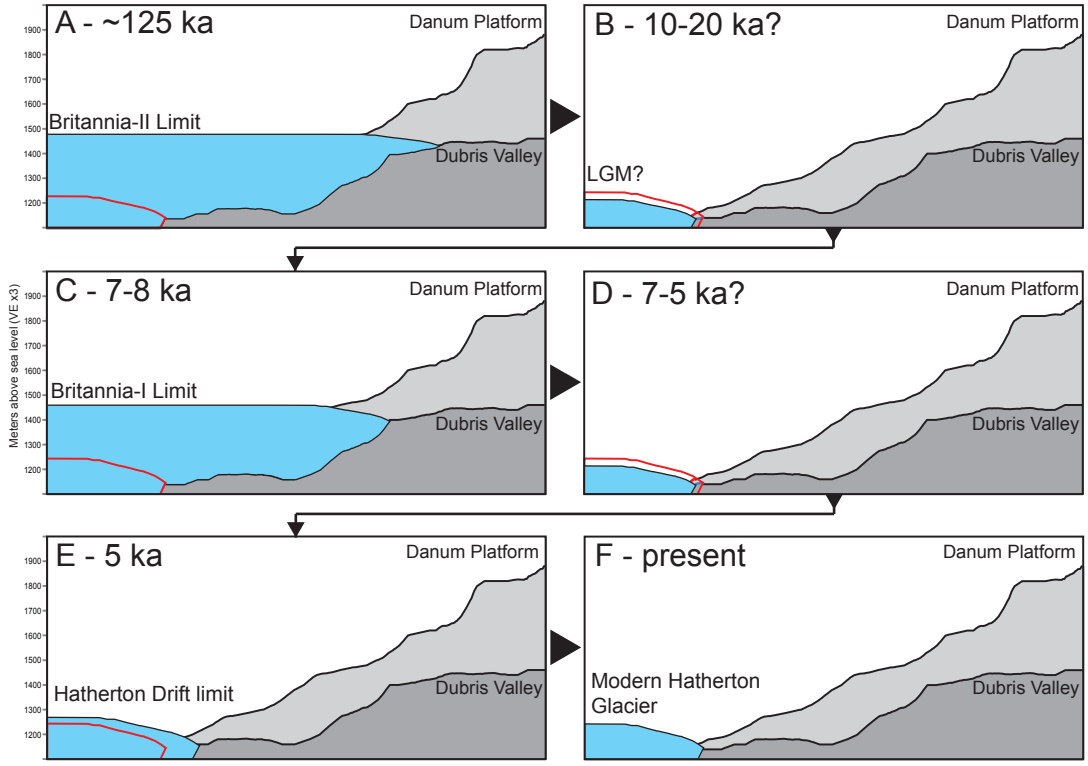

Figure 8.10: Holocene Hatherton Glacier fluctuations in the DBV - South east profile across the DBV, showing the ice margin of the Hatherton Glacier as it advances up valley (left to right). Suggested ice thicknesses at various times. (A) ≈125 ka, (B) 10-20 ka, (C) 7-8 ka, (D) 5-7 ka, (E) 5 ka and (F) the present. Ice surface elevations are based on the mapped positions of drift upper limits. The red line represents the profile of the modern day Hatherton Glacier in the DBV.

- Ice sheet interiors
  - Thin during glacial (*i.e.* colder) climates.
  - Thicken during interglacial (*i.e.* warmer) climates.

This asynchronous ice sheet behaviour is driven by a number of factors. Advances and retreats (*i.e.* thickening and thinning) of the coastal margins are caused by fluctuations in sea surface temperature (*i.e.* melt rates), sea levels (*i.e.* stress on fringing ice shelves) and increased precipitation (*i.e.* an increase in low pressure systems). On the other hand, the dynamics of the ice sheet interiors appear to be purely driven by accumulation rates (*i.e.* snowfall). The model of Mackintosh

et al. (2011) shows that in the warming climate since the LGM, the bulk of ice loss has come from coastal margins, while the interiors (particularly the EAIS) have thickened (Figure 8.11). At the LGM, the reverse is the case, with expanded coastal margins (as seen in the WAIS advance into the RSE) and a thinning of the interiors (as seen in the WAIS by Ackert et al. 2013).

Apart from a reliable Holocene exposure age interpretation at Diamond Hill (*i.e.*

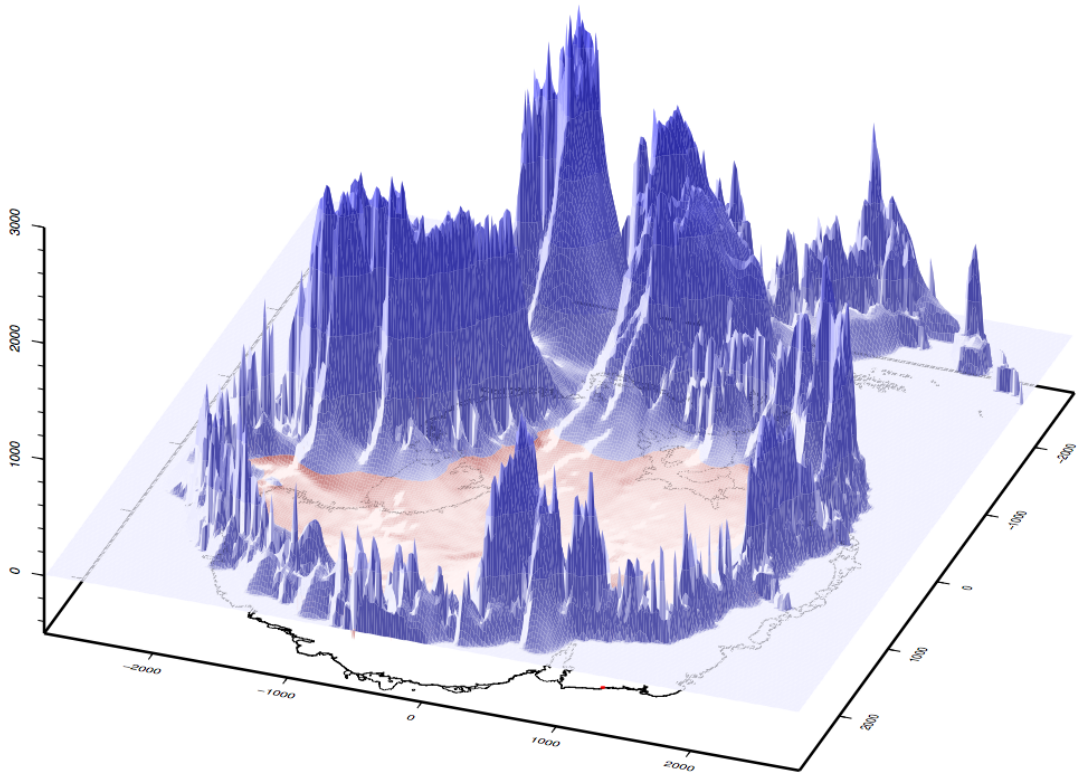

Figure 8.11: Modelled ice loss since the LGM - The model of Mackintosh et al. (2011) that shows the majority of ice volume loss in the last 20 ka has come from the coastal margins of the WAIS and to a lesser extent the EAIS margin. In contrast, the interior portions of the EAIS have thickened.

the Hatherton Drift), further inferences of pre-Holocene WAIS-RIS behaviour is not possible due to the large percentage of material recycled and with complex exposure histories. Therefore, any interpretation of ice sheet dynamics is limited to the DBV, where the dataset is most clear. While the model of Riger-Kusk (2011) suggests that the thickening of the DHGS, caused by the WAIS, reached as far

upstream as the DBV, our exposure ages strongly disagree. This is supported by the EAIS proximal sites of the Reedy Glacier, in which drift limits and exposure ages suggest EAIS thickening post-LGM. Therefore, the position is taken that ice surface fluctuations observed at the DBV are largely influenced by the EAIS, although most likely this may not be the case further downstream at Lake Wellman.

The interpretation of the Britannia-II, Britannia-I and Hatherton drift limits within the DBV suggest a dynamic EAIS with a number of events related to EAIS thickening shown in the geological record. Critically, the *absence* of geological evidence can suggest periods of EAIS thinning, with the glacier retreating below that of the present Hatherton Glacier margin. The Britannia-II ^{10}Be results give a mean age of 126 $\pm$ 3 ka and suggests a retreat from a warm MIS5e high-stand (Figure 8.12). This explanation is plausible as (A) the retreat coincides with a switch to a cooler climate (heading towards MIS-5d, $\approx$115 ky) and (B) occurs when West Antarctic ice volumes are at a minimum (Pollard and DeConto, 2009) and eustatic sea levels are at a maximum (Rohling et al., 2008). The upper limits of the Britannia-II drift at the DBV exposure age gives a maximum ice thickness increase of 260-350 metres at $\approx$130 ka, ice retreating at a rate no less than 0.0026-0.0035 m a^{-1} to reach a minimum extent at LGM.

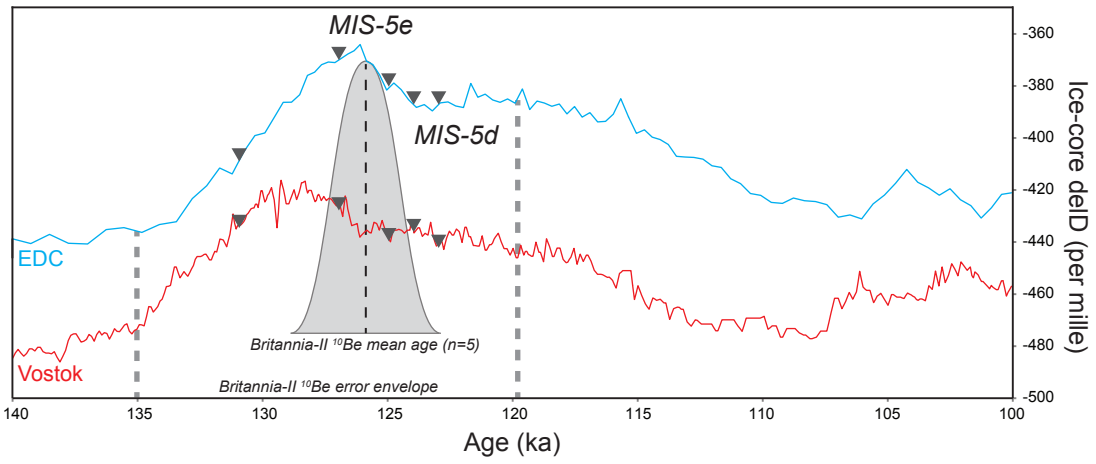

Figure 8.12: Britannia-II Drift ages compared to the stable isotope record - The ^{10}Be exposure ages for the Britannia-II (black triangles) compared to the EPICA Dome C (EDC, red) and Vostok (blue) deuterium ice core records. The grey dashed lines represent the upper and lower exposure age errors based on the youngest and oldest ages within the cluster. Gaussian curve defines the mean age and error for the Britannia-II (126 $\pm$ 3 ka).

As previously discussed, the lack of LGM evidence at the DBV is undoubtedly due to a EAIS with an upper ice elevation lower than today. The evidence, or more correctly the lack of evidence, that supports a thinner LGM EAIS is in agreement with geological records and numerical models at other TAM outlet glaciers. The Reedy (Todd et al., 2010) and Ferrar (Golledge and Levy, 2011) glaciers all show evidence of a reduction of ice during the LGM at the head of the glacier, or a Holocene thickening that has covered all evidence of the minimal LGM position. As the nature of the Britannia-I deposit is one of a cold based advance with only minimal deposition (*i.e.* the glacial salt and pepper shaker), it suggests the bulk of material within the limits defined by the Britannia-I is actually minimally reworked or preserved Britannia-II Drift. For this scenario to occur, LGM ice must have been less extensive than the subsequent Hatherton Drift.

The Holocene behaviour of the Hatherton Glacier fluctuated rapidly within a relatively short time frame. Figure 8.13 shows the timing of Holocene events in the exposure age record of the DHGS and Reedy Glacier (Todd et al., 2010) as well as, for background information, climatic events defined in the ice core (Masson-Delmotte, 2000; Steig et al., 2000) and geological records of the McMurdo Dry Valleys (Verleyen et al., 2011). As there is significant overlap between the Holocene warming and cooling events recorded in the ice core records and exposure ages, identifying the actual drivers of advance and retreat is difficult and not the purpose of this overlap of different records. The Britannia-I represents a major re-advance of ice into the DBV, reaching a maximum of 130-280 metres above the modern glacier. Although the timing of advance is relatively well constrained, it must occur post-LGM but pre-date the oldest Hatherton Drift deposition age. The time frame suggests that it is likely that the advance occurred during the early Holocene thermal optimum (11.5-9 ka, Masson-Delmotte 2000). The Britannia-I exposure ages show ice retreat from its upper limits at 8-5 ka and may be related to the short period of strong cooling identified by Steig et al. (2000) at $\approx$9.5 ka. This timing may also fit with the deglaciation of the upper Reedy Glacier, 9-7.7 ka at Mims Spur, but is also consistent with Polygon Spur. As with the Britannia-II Drift, the Britannia-I may represent another example of EAIS thickening during a warm period, localised to the upper parts (*i.e.* DBV) of the Hatherton Glacier.

The youngest deposit in the DHGS, the Hatherton Drift, is observed at Lake

Wellman, Diamond Hill as well as the DBV (but not sampled here). In contrast to the other deposits which are only observed in limited exposures, the Hatherton Drift appears to be related to a thickening event along the entire glacier length. As the deposit represents a re-advance over the underlying Britannia-I at the DBV, it also implies that the Britannia-I had retreated to a ice limit similar to that of the present day, or at least below the Hatherton Drift (+50 m, see Figure 8.10). Riger-Kusk (2011) suggested that as the WAIS had retreated past the mouth of the DHGS (≈6.8 ka, Conway et al. 1999), the Hatherton Glacier had nearly returned to its equilibrium profile, thereby indicating that the only possible cause of the Hatherton Glacier thickening was the EAIS. While this suggestion is plausible, it raises the question why a minor thickening is observed throughout the glacier while the thickening related to the Britannia-I and Britannia-II did not. The Hatherton Drift exposure ages from 0.7-4.3 (excluding the two older samples from Lake Wellman) correlate well with the recessional deposits observed at the Reedy Glacier (Todd et al., 2010). Both are of a similar thickness and timing and given their distance apart (1100 km) must be caused by the same climatic driver. A possible explanation may be a small EAIS increase (+10-80 m) during the second climatic optimum (Masson-Delmotte, 2000) at 3-7 ka.

Understanding the behaviour of the ice sheet interiors, compared to that of the coastal margins, suggests that the distribution of ice volume is not as simple as thought. This may play a major role in our understanding of the Antarctic ice sheets contribution in past sea level rises, particularly during the LGM. During the decrease in WAIS volume observed during interglacials, predominantly in the marine basins (*i.e.* Ross Sea Embayment) and margins, may be been partially offset by the ice volume increase within the interior EAIS. Thus the predicted Antarctic contribution to Holocene sea level rise may be smaller than thought and suggests that the Northern Hemisphere ice sheets were the major source.

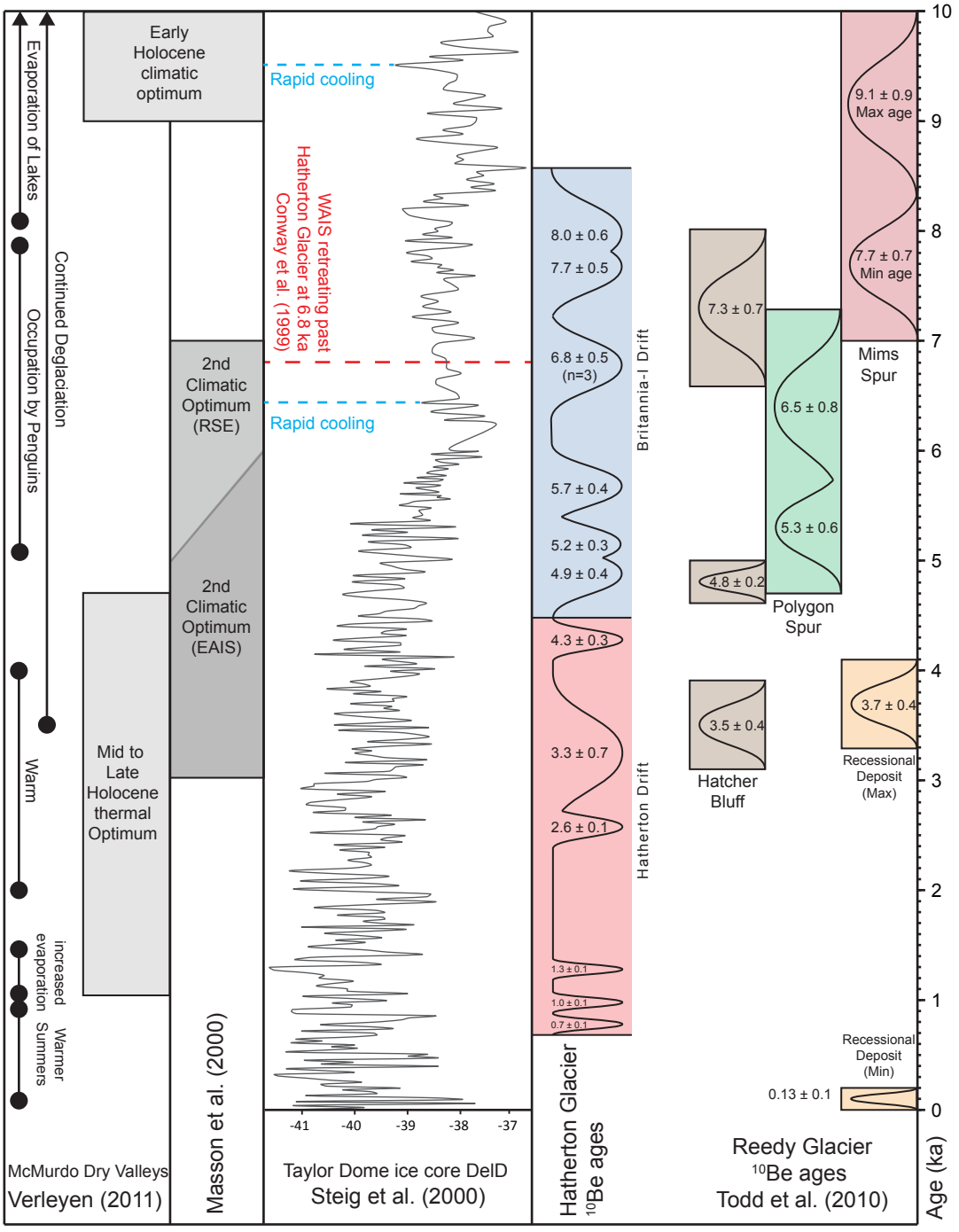

Figure 8.13: The RSE during the Holocene - A summary of the major climatic and environmental events observed in geological (Verleyen et al., 2011) and ice core records (Masson-Delmotte, 2000; Steig et al., 2000). The Holocene exposure ages from the Britannia-I and Hatherton drifts in the DHGS and from three sites (Hatchers Bluff, Mims and Polygon Spur) at the Reedy Glacier Todd et al. (2010) are included. The red dashed line represents the 6.8 ka age suggested by Conway et al. (1999) for the retreat of the WAIS grounding line past the DHGS. The blue dashed lines represent the two short periods of cooling identified by Steig et al. (2000) in the Taylor Dome ice core.

Chapter 9

Conclusion

With significant differences in glaciology, the Darwin and Hatherton glaciers show a clear distinction in glacial deposits and landforms. The Hatherton Glacier with slow moving ice and a cold-based central trunk is flanked by an ice free landscape containing a variety of moraines, boulder belts and clearly defined glacial drift sheets. In the lower, fast flowing sections of the Darwin Glacier, the reverse is the case. Material deposited at the glacier margins is predominantly reworked material emplaced as ice cored moraine or cobbles on bedrock outcrops, with constructional glacial features extremely rare.

The work contained in this thesis from the Darwin Hatherton glacial system has used the technique of surface exposure dating (SED) to define a new Quaternary glacial chronology and revise the early work of Bockheim et al. (1989). Based on SED ages from glacial material deposited during periods of past glacial thickening, our new chronology aids in constraining the timing and magnitude of East Antarctic ice sheet advances and retreats in this sector of the TAMs.

At all sites along the Darwin Hatherton glacial system, ice was at its thickest during the late-Pliocene to early-Pleistocene. At the Hatherton Glacier, the Isca drift represents a retreat at 1-2 Ma from a glacial highstand that reached at least 500 metres above the modern glacier. At the confluence of the Darwin Glacier and Ross Ice Shelf, a bedrock sample near the summit of Diamond Hill has an apparent age of 1.6 Ma and may suggest that the WAIS has overrun the upper parts of Diamond Hill in the past. Although the SED results were inconclusive about the timing of WAIS deglaciation, the geomorphological evidence tentatively supports a LGM configuration smaller than previously suggested, similar in magnitude to that suggested by the glaciological models of Anderson et al. (2004) and Riger-Kusk

(2011). Our research provides important insights to the field of exposure dating concerning the use of the technique in polar environments. The complexity involved in interpreting ages from material deposited at cold-based margins requires an understanding of the burial history and transportation of glacial material along an outlet glacial system.

9.1 Key outcomes

9.1.1 Reconstructing the glacial history of the Antarctic ice sheets

- Geomorphological field mapping of key glacial drift contacts at four sites along the DHGS: the Dubris and Bibra valleys, Lake Wellman, Roadend Nunatak and Diamond Hill.

- A general trend of oldest ages at the highest elevations. This infers that periods of maximum ice thickening in the DHGS has been during the Plio-Pleistocene.

- No equivocal evidence of the LGM was found at any site along the DHGS.

- The EAIS is suggested to have thickened during interglacial and thinned during glacial climates. The WAIS appears to have the opposite response, retreating in warm periods and advancing during cold periods.

- Ice surface reconstructions that suggest:

  - A retreat from $\approx$700-1000 meters of Pleistocene ice thickening at 1.6-2.2 Ma.
  - A tentative WAIS thickening of 500-900 metres at the mouth of the Darwin Glacier during the LGM.
  - A LGM EAIS that was thinner than present, but thicker during the Holocene.
  - That during warm periods, the EAIS thickened within the DBV. The Britannia-I and Britannia-II drifts were deposited during retreats from glacial highstands at 125 and 8 ka.
  - The Antarctic contribution to post-LGM sea level rise may be less than thought.

9.1.2 Apply and assess the use of *insitu* cosmogenic nuclides and surface exposure dating in Antarctic settings

- Seventy three glacial erratic and bedrock samples were collected, with ^{10}Be ages from 0.7 ka to 2.2 Ma.
- The use of a dual nuclide ^{26}Al/^{10}Be approach to identify samples that have undergone a period or periods of burial.
- The importance of understanding cold-based glacial deposits when sampling for SED in Antarctica.
- A clear increase in glacial debris displaying complex exposure histories with distance from catchment.
- An inability to create a coherent suite of exposure ages between glacial drifts assumed to be coeval.
- Exposure ages that suggest the type section for the Britannia Drift in the DBV is not LGM, although it is widely used in many glaciological models as evidence of LGM ice thickness in this sector of the TAMs.
- The ability of low velocity outlet glaciers to accumulate and transport supraglacial material.
- The LGM signal in the DHGS dataset is far less clear when compared to other outlet glaciers (*i.e.* the Reedy Glacier).

9.2 Further work

With considerable interest in the behaviour of the Antarctic ice sheets by the geoscience community, the research presented in this thesis has raised a number of new questions. *What mechanisms do low velocity glaciers use in transporting supra and en-glacial material? What constraints does the flow regime of an outlet have on the age spread of exposed material? How did the Antarctic ice sheets behave to climate change prior to the LGM?*

The Antarctic LGM remains a critical period in our understanding of how ice sheets behaved in the transition from cold to warm climates. With the limited number of terrestrial records of ice thickness in the Ross Sea Embayment, further work is required to map and evaluate the products of the LGM cold-based glacial margins. As the thickness of the LGM WAIS is still not full constrained, neither is the Antarctic contribution to sea level rise. During the completion of this thesis, a large gap in the time span covered by glaciological models was also noted. While there is a strong focus on modelling the Antarctic ice sheets at the LGM and through Termination-I, only a limited amount of research is published on the Plio-Pleistocene. The geological community is expanding the focus beyond the LGM, using new techniques such as SED to constrain the magnitude and timing of past ice sheet behaviour. It is hoped that the modelling community will also see the value of this approach.

Appendices

Appendix A

Sample and site descriptions

A.1 Dubris Valley Area

A.1.1 Sample, AMS and exposure age results

Table A.1: Dubris Valley Area site data

Drift Sequence [a]	Sample ID	Location		Elevation (masl)	Sample Type [b]	Sample Dimensions (LxWxH cm)	Sample Thickness (cm)	Thickness Correction [c]	Topographic Shielding [d]
		Latitude (S)	Longitude(E)						
Britannia I	BV3.1	79.9733	155.5278	1259	Sst-BD-WC	10x10x5	5	0.956	0.999
Britannia I	BV9.2	79.9767	155.4093	1297	Sst-BD-WC	15x10x5	5	0.956	0.998
Britannia I	BV4.2	79.9780	155.4494	1342	Sst-BD-WC	20x10x5	5	0.956	0.991
Britannia I	DV7.1	79.9917	155.5391	1255	Sst- BD-S	25x25x25	5	0.956	0.994
Britannia I	DV6.1	79.9983	155.5204	1377	Sst- BD-S	120x80x50	3	0.973	0.996
Britannia I	DP1.4	79.9827	155.5182	1390	Sst- BD-S	200x150x80	3	0.973	0.999
Britannia I	DP3.2	79.9817	155.4961	1397	Sst- BD-S	20x30x10	5	0.956	0.999
Britannia I	DP1.2	79.9817	155.4956	1406	Sst-BD-WC	15x10x5	5	0.956	0.998
Britannia II	DV5.2	79.9983	155.5088	1403	Sst- BD-S	80x100x80	3	0.973	0.997
Britannia II	DV3.1	80.0000	155.4908	1383	Sst- BD-S	17x10x7	2	0.982	0.99
Britannia II	DP4.3	79.9880	155.4890	1469	Sst- BD-S	80x80x30	3	0.973	0.999
Britannia II	DP4.1	79.9850	155.5091	1459	Sst- BD-S	120x120x60	5	0.956	0.999
Britannia II	DP4.2	79.9883	155.4986	1471	Sst- BD-S	30x30x15	3	0.973	0.999
Danum	DV2.1	80.0000	155.4603	1420	Sst-BD-WC	15x15x5	5	0.956	0.992
Danum	DP5.1	79.9893	155.4926	1478	Sst- BD-S	150x150x80	2	0.982	0.998
Isca	BV8.1	79.9867	155.4033	1533	Sst- BD-S	30x40x25	3	0.973	0.993
Isca	DV1.1	80.0067	155.4577	1464	Sst- BD-S	35x20x25	4	0.965	0.997
Isca	DP6.1	79.9950	155.4647	1620	Sst- BD-S	60x35x20	2	0.982	0.999

[a] Glacial drifts defined by Bockheim et al. (1989).
[b] Sample type. Quartz (Qzt), granitoid (Grt) or sandstone (Sst). Bedrock (BD), boulder (B), surface (S) or whole clast (WC) samples.
[c] Based on an attenuation length of 150 g cm^{-2} and a rock density of 2.7 g cm^{-3}.
[d] Based on M=2.3 (see section 2.1.4.3).

Table A.2: Dubris Valley area AMS results

Sample ID	ANSTO Be Cathode	ANSTO Al Cathode	$^{10}Be/^{9}Be$ Ratio ($1e^{-15}$) [a]	$^{10}Be/^{9}Be$ Error ($1e^{-15}$) [b]	$^{26}Al/^{27}Al$ Ratio ($1e^{-15}$) [c]	$^{26}Al/^{27}Al$ Error ($1e^{-15}$) [b]	Quartz Mass (g)	^{9}Be Carrier Mass (mg) [d]	^{27}Al Concentration (ppm) [e]
BV3.1	B4203	A2133	171	8	119	11	72.09	0.5449	175
BV9.2	B4204	A2134	192	6	190	24	69.8	0.5618	152
BV4.2	B4205	A2135	264	7	143	14	69.58	0.567	291
DV7.1	B4202	A2132	173	6	79	12	70.41	0.5512	321
DV6.1	B4206	A2136	293	13	135	21	69.08	0.5541	388
DP1.4	B4208	A2138	251	9	107	14	71.22	0.5739	343
DP3.2	B4209	A2139	246	11	180	14	70.42	0.5731	213
DP1.2	B4211	A2141	269	7	255	36	75.62	0.5637	232
DV5.2	B4210	A2140	4536	35	5867	126	71.44	0.5695	102
DV3.1	B4207	A2137	4879	167	2189	58	71.34	0.5284	305
DP4.3	B4217	A2147	4480	64	2620	96	69.79	0.5921	270
DP4.1	B4215	A2145	4972	112	5293	150	69.92	0.5402	138
DP4.2	B4219	A2148	5323	102	2485	64	74.06	0.5624	FAIL
DV2.1	B4213	A2143	19082	852	8125	130	70.12	0.4466	248
DP5.1	B4220	A2149	34174	512	12989	812	80.65	0.4168	231
BV8.1	B4221	A2150	38916	313	12393	213	70.38	0.4473	275
DV1.1	B4216	A2146	40759	740	17289	244	69.47	0.4162	214
DP6.1	B4222	A2151	78735	842	22205	325	69.98	0.4067	258

[a] Measured against NIST SRM-4325 with a nominal value of 27900 x 10^{-15}.

[b] The quoted 1σ error is the larger of total statistical error or weighted error in mean. Additional 2% (1σ) error added in quadrature based on reproducibility of AMS standard measurements.

[c] Measured against SRM PRIME-Z93-0221 with a nominal value of 16800 x 10^{-15}.

[d] Concentration of ^{9}Be carrier solution made from beryl crystal with $^{10}Be/^{9}Be$ ratio of $<5x10^{-15}$.

[e] Measured by ICP-OES in a 1-2 g solution of dissolved quartz in HF.

Table A.3: Dubris Valley area exposure age results

Sample ID	^{10}Be Concentration (x 10^3 atm g^{-1})	^{10}Be Error (x 10^3 atm g^{-1})	^{26}Al Concentration (x 10^3 atm g^{-1})	^{26}Al Error (x 10^3 atm g^{-1}) [a]	Minimum ^{10}Be Age (ka) [b]	Minimum ^{10}Be Age Error (ka) [c]	Minimum ^{26}Al Age (ka) [d]	Minimum ^{26}Al Age Error (ka) [c]	^{26}Al/^{10}Be Ratio	^{26}Al/^{10}Be Error
BV3.1	86	5	465	48	4.9	0.5 (0.2)	3.9	0.5 (0.4)	5.4	0.6
BV9.2	103	4	645	86	5.7	0.5 (0.2)	5.3	0.8 (0.7)	6.3	0.8
BV4.2	144	5	933	99	7.7	0.7 (0.3)	7.4	1.0 (0.7)	6.5	0.7
DV7.1	91	4	564	92	5.2	0.5 (0.2)	4.8	0.9 (0.7)	6.2	1.0
DV6.1	157	8	1172	189	8	0.8 (0.4)	8.8	1.6 (1.4)	7.5	1.2
DP1.4	135	6	823	117	6.8	0.7 (0.3)	6.1	1.0 (0.8)	6.1	0.9
DP3.2	134	7	856	76	6.8	0.7 (0.3)	6.4	0.8 (0.5)	6.4	0.6
DP1.2	134	5	1320	194	6.8	0.6 (0.2)	9.9	1.6 (1.4)	9.8	1.4
DV5.2	2417	57	13313	674	123.6	11.6 (3.2)	102.7	10.8 (5.4)	5.5	0.3
DV3.1	2415	99	14923	790	125.3	12.5 (5.3)	117.6	12.7 (6.5)	6.2	0.3
DP4.3	2540	67	15771	924	122.9	11.6 (3.5)	115.8	12.8 (7.1)	6.2	0.4
DP4.1	2567	81	16337	880	127.6	12 (4.2)	123.6	13.2 (6.8)	6.4	0.3
DP4.2	2702	80	NA	NA	131	12.5 (4.1)	NA	NA	NA	NA
DV2.1	8123	406	45059	2187	454.3	49.4 (24.3)	404.7	47.3 (22.8)	5.5	0.3
DP5.1	11804	318	66957	5191	637.2	68.9 (21.0)	609.8	96.2 (63.1)	5.7	0.4
BV8.1	16530	393	75986	3719	926.8	104.6 (28.8)	698.6	97.0 (47.1)	4.6	0.2
DV1.1	16320	470	82718	3966	984.5	113.4 (36.4)	869	128.9 (61.6)	5.1	0.2
DP6.1	30582	758	127838	6150	1996.5	306 (87.1)	1497.5	325.4 (155.9)	4.2	0.2

[a] Error in ^{26}Al concentration includes a 4% error in ICP-OES measurement of Al concentration in quartz.

[b] ^{10}Be decay constant = 5.00 x 10^{-7} ($t_{1/2}$ =1.387 Ma), ^{10}Be production rate = 4.60 $\pm$ 0.42 atoms g a^{-1}. Site specific production rate based on Stone (2000) scaling.

[c] Age error includes a 9% standard error in sea-level high latitude production rate in quadrature with total analytical AMS error (Bracketed).

[d] ^{26}Al decay constant = 9.90 x 10^{-7} ($t_{1/2}$ = 0.70 Ma), ^{26}Al production rate = 30.7 $\pm$ 2.8 atoms g a^{-1}.

A.1.2 Exposure dating sample photos


BV3.1(Left) and BV4.2(Right)


BV8.1(Left) and BV9.2(Right)


DP1.2(Left) and DP1.4(Right)


DP3.2(Left) and DP4.1(Right)


DP4.2(Left) and DP4.3(Right)

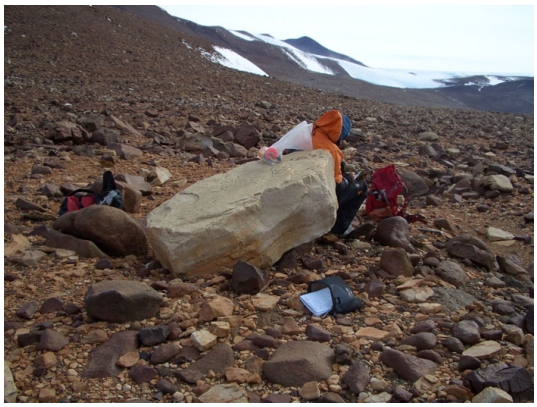


DP5.2(Left) and DP6.1(Right)

DV1.1(Left) and DV2.1(Right)

DV3.1(Left) and DV5.2(Right)

DV6.1(Left) and DV7.1(Right)

A.2 Lake Wellman

A.2.1 Sample, AMS and exposure age results

Table A.4: Lake Wellman site data 1

Drift Sequence [a]	Sample ID	Location		Elevation (masl)	Sample Type [b]	Sample Dimensions (LxWxH cm)	Sample Thickness (cm)	Thickness Correction [c]	Topographic Shielding [d]
		Latitude (S)	Longitude(E)						
Isca	LW11.1	79.9448	156.7755	1646	Grt-B-S	174x105x84	5	0.9563	0.995
Isca	LW9.1	79.9404	156.8194	1501	Sst-B-S	256x290x130	5	0.9563	0.995
Isca	LW9.3	79.9404	156.8144	1508	Grt-B-S	130x170x45	2	0.9866	0.995
Britannia	LW2.1	79.9316	156.8715	1246	Grt-B-S	800x500x300	6	0.9479	0.995
Britannia	LW2.2	79.9316	156.8713	1237	Sst-B-WC	12x12x10	10	0.9152	0.995
Danum	LW15.1	79.9220	156.7986	1136	Sst-B-S	105x156x185	4	0.9648	0.985
Hatherton	LW24.1	79.9223	156.9021	895	Grt-B-S	115x160x50	5	0.9563	0.995
Hatherton	LW24.2	79.9216	156.8993	892	Grt-B-S	86x93x52	3	0.9735	0.995
Moraine 1	LW23.1	79.9168	156.9109	852	Sst-B-S	33x18x14	3	0.9735	0.995
Moraine 1	LW23.2	79.9169	156.9099	850	Grt-B-WC	12x8x5	5	0.9521	0.995
Hatherton	LW25.1	79.9200	156.9238	852	Grt-B-S	125x86x44	5	0.9563	0.995
Hatherton	LW25.2	79.9204	156.9251	845	Sst-B-S	125x96x45	5	0.9563	0.995

[a] Glacial drifts defined by Bockheim et al. (1989).
[b] Sample type. Quartz (Qzt), granitoid (Grt) or sandstone (Sst). Bedrock (BD), boulder (B), surface (S) or whole clast (WC) samples.
[c] Based on an attenuation length of 150 g cm^{-2} and a rock density of 2.7 g cm^{-3}.
[d] Based on M=2.3 (see section 2.1.4.3).

Table A.5: Lake Wellman site data 2

Drift Sequence [a]	Sample ID	Location		Elevation (masl)	Sample Type [b]	Sample Dimensions (LxWxH cm)	Sample Thickness (cm)	Thickness Correction [c]	Topographic Shielding [d]
		Latitude (S)	Longitude(E)						
Isca	LW12.1	79.8888	156.7315	1150	Sst-B-S	174x105x84	1	0.9648	0.990
Isca	LW12.2	79.8888	156.7313	1155	Grt-B-S	180x212x84	6	0.9479	0.990
Danum	LW13.2	79.8905	156.7574	1107	Sst-B-S	180x211x103	5	0.9563	0.995
Danum	LW13.3	79.8905	156.7562	1112	Grt-B-S	158x157x93	3	0.9778	0.995
Moraine 2	LW14.1	79.8906	156.7593	1119	Sst-B-WC	10x6x8	5	0.9563	0.995
Moraine 2	LW14.2	79.8907	156.7593	1115	Sst-B-S	24x60x51	5	0.9563	0.995
Moraine 2	LW14.3	79.8907	156.7592	1115	Sst-B-S	17x17x8	5	0.9563	0.995
Britannia	LW18.1	79.8908	156.7650	1087	Sst-B-S	290x177x203	5	0.9563	0.990
Britannia	LW18.3	79.8914	156.7648	1101	Grt-B-S	180x83x110	5	0.9563	0.990
Britannia	LW20.1	79.8940	156.7998	1018	Sst-B-S	220x177x106	3	0.9735	0.995
Britannia	LW20.3	79.8967	156.8025	1025	Grt-B-S	150x110x60	3	0.9735	0.995
Britannia	LW21.1	79.8979	156.8183	981	Grt-B-S	74x93x84	3	0.9778	0.995
Britannia	LW21.2	79.8983	156.8181	982	Sst-B-S	177x78x56	3	0.9778	0.995

[a] Glacial drifts defined by Bockheim et al. (1989).
[b] Sample type. Quartz (Qzt), granitoid (Grt) or sandstone (Sst). Bedrock (BD), boulder (B), surface (S) or whole clast (WC) samples.
[c] Based on an attenuation length of 150 g cm^{-2} and a rock density of 2.7 g cm^{-3}.
[d] Based on M=2.3 (see section 2.1.4.3).

Table A.6: Lake Wellman AMS results 1

Sample ID	ANSTO Be Cathode	ANSTO Al Cathode	$^{10}Be/^{9}Be$ Ratio ($1e^{-15}$) *a*	$^{10}Be/^{9}Be$ Error ($1e^{-15}$) *b*	$^{26}Al/^{27}Al$ Ratio ($1e^{-15}$) *c*	$^{26}Al/^{27}Al$ Error ($1e^{-15}$) *b*	Quartz Mass (g)	^{9}Be Carrier Mass (mg) *d*	^{27}Al Concentration (ppm) *e*
LW11.1	B3313	A1788	31726	338	129332	2422	50.20	0.4043	FAIL
LW9.1	B3314	A1789	48356	665	20005	540	51.06	0.4404	270
LW9.3	B3315	A1790	52066	655	183145	2771	50.13	0.4087	FAIL
LW2.1	B3453	A1811	3467	28	2108	84	75.09	0.4097	304
LW2.2	B3316	A1791	1010	60	383	40	76.55	0.4042	313
LW15.1	B3312	A1787	22282	510	8484	251	75.49	0.4153	211
LW24.1	B3446	A1804	2982	39	7944	167	100.05	0.3989	23
LW24.2	B3450	A1808	122	6.5	224	31	99.85	0.3998	27
LW23.1	B3451	A1809	26	3.9	19	10	99.97	0.5157	236
LW23.2	B3311	A1786	763	13.5	1002	47	92.35	0.4064	57
LW25.1	B3452	A1810	44	5	43	16.3	100.24	0.4107	62
LW25.2	B3448	A1806	606	12.1	297	26	93.95	0.4028	193

a Measured against NIST SRM-4325 with a nominal value of 27900 x 10^{-15}.

b The quoted 1σ error is the larger of total statistical error or weighted error in mean. Additional 2% (1σ) error added in quadrature based on reproducibility of AMS standard measurements.

c Measured against SRM PRIME-Z93-0221 with a nominal value of 16800 x 10^{-15}.

d Concentration of ^{9}Be carrier solution made from beryl crystal with $^{10}Be/^{9}Be$ ratio of <5x10^{-15}.

e Measured by ICP-OES in a 1-2 g solution of dissolved quartz in HF.

Table A.7: Lake Wellman AMS results 2

Sample ID	ANSTO Be Cathode	ANSTO Al Cathode	$^{10}Be/^{9}Be$ Ratio ($1e^{-15}$) *a*	$^{10}Be/^{9}Be$ Error ($1e^{-15}$) *b*	$^{26}Al/^{27}Al$ Ratio ($1e^{-15}$) *c*	$^{26}Al/^{27}Al$ Error ($1e^{-15}$) *b*	Quartz Mass (g)	^{9}Be Carrier Mass (mg) *d*	^{27}Al Concentration (ppm) *e*
LW12.1	B3304	A1779	5405	246	2183	88	76.19	0.4048	233
LW12.2	B3305	A1780	14867	136	16646	460	75.22	0.4133	80
LW13.2	B3306	A1781	3121	87	838	40	75.21	0.4018	395
LW13.3	B3307	A1782	9164	81	26986	660	75.22	0.4017	25
LW14.1	B3761	NA	4195	52	NA	NA	45.38	0.4440	NA
LW14.2	B3308	A1783	18775	204	8095	357	89.63	0.3991	125
LW14.3	B3762	NA	375	33	NA	NA	44.95	0.4310	NA
LW18.1	B3447	A1805	1877	30	1741	157	87.91	0.4065	92
LW18.3	B3449	A1807	9465	114	13661	628	100.23	0.4058	57
LW20.1	B3444	A1802	2407	65	984	46	108.40	0.4038	193
LW20.3	B3309	A1784	1942	27	1330	69	100.38	0.4104	109
LW21.1	B3310	A1785	1703	56	696	62	100.05	0.4037	196
LW21.2	B3445	A1803	1501	24	662	42	104.85	0.4133	190

a Measured against NIST SRM-4325 with a nominal value of 27900 x 10^{-15}.

b The quoted 1σ error is the larger of total statistical error or weighted error in mean. Additional 2% (1σ) error added in quadrature based on reproducibility of AMS standard measurements.

c Measured against SRM PRIME-Z93-0221 with a nominal value of 16800 x 10^{-15}.

d Concentration of ^{9}Be carrier solution made from beryl crystal with $^{10}Be/^{9}Be$ ratio of <5x10^{-15}.

e Measured by ICP-OES in a 1-2 g solution of dissolved quartz in HF.

Table A.8: Lake Wellman exposure age results 1

Sample ID	^{10}Be Concentration (x 10^3 atm g^{-1})	^{10}Be Error (x 10^3 atm g^{-1})	^{26}Al Concentration (x 10^3 atm g^{-1})	^{26}Al Error (x 10^3 atm g^{-1}) [a]	Minimum ^{10}Be Age (ka) [b]	Minimum ^{10}Be Age Error (ka) [c]	Minimum ^{26}Al Age (ka) [d]	Minimum ^{26}Al Age Error (ka) [c]	^{26}Al/^{10}Be Ratio	^{26}Al/^{10}Be Error
LW11.1	17077	423	NA	NA	929.0	102.6 (29.2)	NA	NA	NA	NA
LW9.1	27874	732	120356	6400	2275.0	344.6 (102.6)	1978.0	474 (244.2)	4.3	0.3
LW9.3	28369	728	NA	NA	2196.0	355.8 (104.1)	NA	NA	NA	NA
LW2.1	1264	30	14307	870	78.1	7.0 (1.9)	137.0	15.0 (8.5)	11.3	0.7
LW2.2	356	23	2678	310	22.6	2.3 (1.3)	25.3	3.4 (2.7)	7.5	1.0
LW15.1	8192	262	39895	2180	630.0	66.3 (23.1)	491.0	61.6 (32.3)	4.9	0.3
LW24.1	795	21	4128	210	65.5	6.0 (1.8)	50.8	5.1 (2.5)	5.2	0.3
LW24.2	33	2	137	20	2.6	0.3 (0.1)	1.6	0.3 (0.2)	4.2	0.7
LW23.1	9	1	100	50	0.8	0.1 (0.1)	1.2	0.6 (0.6)	11.0	6.0
LW23.2	224	6	1281	80	19.1	1.7 (0.5)	16.2	1.7 (1.0)	5.7	0.4
LW25.1	12	1	60	10	1.0	0.1 (0.1)	0.7	0.2 (0.2)	5.0	1.3
LW25.2	174	5	1279	130	14.8	1.3 (0.4)	16.2	2.1 (1.5)	7.4	0.8

[a] Error in ^{26}Al concentration includes a 4% error in ICP-OES measurement of Al concentration in quartz.

[b] ^{10}Be decay constant = 5.00 x 10^{-7} ($t_{1/2}$ =1.387 Ma), ^{10}Be production rate = 4.60 $\pm$ 0.42 atoms g a^{-1}. Site specific production rate based on Stone (2000) scaling.

[c] Age error includes a 9% standard error in sea-level high latitude production rate in quadrature with total analytical AMS error (Bracketed).

[d] ^{26}Al decay constant = 9.90 x 10^{-7} ($t_{1/2}$ = 0.70 Ma), ^{26}Al production rate = 30.7 $\pm$ 2.8 atoms g a^{-1}.

Table A.9: Lake Wellman exposure age results 2

Sample ID	^{10}Be Concentration (x 10^3 atm g^{-1})	^{10}Be Error (x 10^3 atm g^{-1})	^{26}Al Concentration (x 10^3 atm g^{-1})	^{26}Al Error (x 10^3 atm g^{-1}) [a]	Minimum ^{10}Be Age (ka) [b]	Minimum ^{10}Be Age Error (ka) [c]	Minimum ^{26}Al Age (ka) [d]	Minimum ^{26}Al Age Error (ka) [c]	^{26}Al/^{10}Be Ratio	^{26}Al/^{10}Be Error
LW12.1	1919	97	11335	690	128.0	13.1 (6.5)	115.0	12.6 (7.2)	5.9	0.5
LW12.2	5460	132	29708	1590	395.0	37.9 (10.6)	340.0	38.9 (20.1)	5.4	0.3
LW13.2	1114	40	7389	490	76.7	7.2 (2.8)	76.6	8.4 (5.0)	6.6	0.5
LW13.3	3271	79	14975	780	227.0	21.9 (6.1)	157.0	17.2 (8.7)	4.6	0.3
LW14.1	2743	70	NA	NA	192	18.0 (5.2)	NA	NA	NA	NA
LW14.2	5587	139	22671	1440	415.0	40.7 (11.6)	254.0	30.0 (17.5)	4.1	0.3
LW14.3	240	22	NA	NA	16	2.0 (1.4)	NA	NA	NA	NA
LW18.1	580	16	3571	360	40.4	3.7 (1.1)	37.1	4.9 (3.6)	6.2	0.7
LW18.3	2561	65	17300	1120	183.0	16.9 (4.9)	192.0	22.0 (13)	6.8	0.5
LW20.1	599	21	4242	280	43.3	4.1 (1.5)	45.9	5.1 (3)	7.1	0.5
LW20.3	531	14	3221	220	38.1	3.5 (1.1)	34.5	3.9 (2.4)	6.1	0.5
LW21.1	459	18	3046	300	34.1	3.3 (1.4)	33.7	4.5 (3.3)	6.6	0.7
LW21.2	396	11	2807	220	29.3	2.7 (0.8)	31.0	3.7 (2.4)	7.1	0.6

[a] Error in ^{26}Al concentration includes a 4% error in ICP-OES measurement of Al concentration in quartz.

[b] ^{10}Be decay constant = 5.00 x 10^{-7} ($t_{1/2}$ =1.387 Ma), ^{10}Be production rate = 4.60 $\pm$ 0.42 atoms g a^{-1}. Site specific production rate based on Stone (2000) scaling.

[c] Age error includes a 9% standard error in sea-level high latitude production rate in quadrature with total analytical AMS error (Bracketed).

[d] ^{26}Al decay constant = 9.90 x 10^{-7} ($t_{1/2}$ = 0.70 Ma), ^{26}Al production rate = 30.7 $\pm$ 2.8 atoms g a^{-1}.

A.2.2 Exposure dating sample photos


LW2.1(Left) and LW2.2(Right)


LW9.1(Left) and LW9.3(Right)


LW11.1(Left) and LW12.1(Right)

LW12.2(Left) and LW13.2(Right)

LW13.3(Left) and LW14.1(Right)

LW14.2(Left) and LW14.3(Right)


LW15.1(Left) and LW18.1(Right)


LW18.3(Left) and LW20.1(Right)


LW20.3(Left) and LW21.1(Right)

LW21.2(Left) and LW23.1(Right)

LW23.2(Left) and LW24.1(Right)

LW24.2(Left) and LW25.1(Right)

LW21.5(Left)

A.3 Roadend Nunatak

A.3.1 Sample, AMS and exposure age results

Table A.10: Roadend Nunatak site data

Drift Sequence [a]	Sample ID	Location		Elevation (masl)	Sample Type [b]	Sample Dimensions (LxWxH cm)	Sample Thickness (cm)	Thickness Correction [c]	Topographic Shielding [d]
		Latitude (S)	Longitude(E)						
Undifferentiated	RE1.1	79.7992	158.0360	1433	Grt-B-S	120x100x30	5.0	0.9563	0.9990
Undifferentiated	RE1.2	79.7979	158.0294	1412	Grt-B-S	80x130x50	5.0	0.9563	0.9990

[a] Glacial drifts defined by Bockheim et al. (1989).
[b] Sample type. Quartz (Qzt), granitoid (Grt) or sandstone (Sst). Bedrock (BD), boulder (B), surface (S) or whole clast (WC) samples.
[c] Based on an attenuation length of 150 g cm^{-2} and a rock density of 2.7 g cm^{-3}.
[d] Based on M=2.3 (see section 2.1.4.3).

Table A.11: Roadend Nunatak AMS results

Sample ID	ANSTO Be Cathode	ANSTO Al Cathode	$^{10}Be/^{9}Be$ Ratio ($1e^{-15}$) *a*	$^{10}Be/^{9}Be$ Error ($1e^{-15}$) *b*	$^{26}Al/^{27}Al$ Ratio ($1e^{-15}$) *c*	$^{26}Al/^{27}Al$ Error ($1e^{-15}$) *b*	Quartz Mass (g)	^{9}Be Carrier Mass (mg) *d*	^{27}Al Concentration (ppm) *e*
RE1.1	B4214	A2144	54100	1019	83664	505	69.57	0.4484	54
RE1.2	B4212	A2142	34049	610	63867	563	70.94	0.5838	58

a Measured against NIST SRM-4325 with a nominal value of 27900 x 10^{-15}.

b The quoted 1σ error is the larger of total statistical error or weighted error in mean. Additional 2% (1σ) error added in quadrature based on reproducibility of AMS standard measurements.

c Measured against SRM PRIME-Z93-0221 with a nominal value of 16800 x 10^{-15}.

d Concentration of ^{9}Be carrier solution made from beryl crystal with $^{10}Be/^{9}Be$ ratio of <5x10^{-15}.

e Measured by ICP-OES in a 1-2 g solution of dissolved quartz in HF.

Table A.12: Roadend Nunatak exposure age results

Sample ID	^{10}Be Concentration (x 10^3 atm g^{-1})	^{10}Be Error (x 10^3 atm g^{-1})	^{26}Al Concentration (x 10^3 atm g^{-1})	^{26}Al Error (x 10^3 atm g^{-1}) [a]	Minimum ^{10}Be Age (ka) [b]	Minimum ^{10}Be Age Error (ka) [c]	Minimum ^{26}Al Age (ka) [d]	Minimum ^{26}Al Age Error (ka) [c]	^{26}Al/^{10}Be Ratio	^{26}Al/^{10}Be Error
RE1.1	23304	681	100667	4653	1700	229.7 (74.6)	1301.2	230.5 (107.2)	4.3	0.2
RE1.2	18726	537	82403	3845	1262	153.5 (49.1)	933.0	139.7 (65.5)	4.4	0.2

[a] Error in ^{26}Al concentration includes a 4% error in ICP-OES measurement of Al concentration in quartz.

[b] ^{10}Be decay constant = 5.00 x 10^{-7} ($t_{1/2}$ =1.387 Ma), ^{10}Be production rate = 4.60 $\pm$ 0.42 atoms g a^{-1}. Site specific production rate based on Stone (2000) scaling.

[c] Age error includes a 9% standard error in sea-level high latitude production rate in quadrature with total analytical AMS error (Bracketed).

[d] ^{26}Al decay constant = 9.90 x 10^{-7} ($t_{1/2}$ = 0.70 Ma), ^{26}Al production rate = 30.7 $\pm$ 2.8 atoms g a^{-1}.

A.3.2 Exposure dating sample photos

RE1.1(Left) and RE1.2(Right)

A.4 Diamond Hill

A.4.1 Sample, AMS, exposure age and PCA tables

Table A.13: Diamond Hill site data 1

Drift Sequence [a]	Sample ID	Location		Elevation (masl)	Sample Type [b]	Sample Dimensions (LxWxH cm)	Sample Thickness (cm)	Thickness Correction [c]	Topographic Shielding [d]
		Latitude (S)	Longitude(E)						
Hatherton	DH7.1	79.8850	159.3819	91	Grt-B-WC	300x300x30	3	0.973	1.000
Hatherton	DH7.7B	79.8852	159.3649	125	Qzt-BD-S	Bedrock	4	0.965	1.000
Hatherton	DH7.4	79.8853	159.3639	132	Grt-B-S	105x76x45	5	0.956	1.000
Hatherton	DH6.2	79.8829	159.3692	146	Grt-B-S	25x25x20	5	0.956	1.000
Hatherton	DH6.2B	79.8829	159.3692	148	Grt-BD-S	Bedrock	3	0.973	1.000
Diamond	DH2.1	79.8627	159.5668	184	Grt-B-S	130x220x125	2	0.982	1.000
Diamond	DH2.2	79.8632	159.5617	194	Grt-B-S	40x30x30	4	0.965	1.000
Diamond	DH8.1	79.8860	159.3048	283	Grt-B-WC	15x10x10	5	0.956	1.000
Diamond	DH8.2	79.8867	159.3016	283	Grt-B-S	100x100x200	3	0.973	1.000
Diamond	DH3.2	79.8616	159.5334	334	Qzt-B-S	400x400x200	4	0.969	1.000
Diamond	DH3.1	79.8614	159.5354	335	Grt-B-S	600x400x400	3	0.973	1.000
Diamond	DH1.1	79.8701	159.4088	352	Qzt-B-S	270x80x120	5	0.956	1.000
Diamond	DH13.1	79.8738	159.3470	397	Grt-B-S	48x38x20	5	0.956	1.000
Diamond	DH13.2	79.8739	159.3469	417	Grt-B-S	60x30x35	5	0.956	1.000
Diamond	DH5.2	79.8646	159.4714	428	Grt-B-S	60x60x60	5	0.956	1.000
Diamond	DH5.2B	79.8646	159.4714	428	Qzt-BD-S	Bedrock	5	0.956	1.000

[a] Glacial drifts defined by Bockheim et al. (1989).
[b] Sample type. Quartz (Qzt), granitoid (Grt) or sandstone (Sst). Bedrock (BD), boulder (B), surface (S) or whole clast (WC) samples.
[c] Based on an attenuation length of 150 g cm^{-2} and a rock density of 2.7 g cm^{-3}.
[d] Based on M=2.3 (see section 2.1.4.3).

Table A.14: Diamond Hill site data 2

Drift Sequence [a]	Sample ID	Location		Elevation (masl)	Sample Type [b]	Sample Dimensions (LxWxH cm)	Sample Thickness (cm)	Thickness Correction [c]	Topographic Shielding [d]
		Latitude (S)	Longitude(E)						
Diamond moraine	DH9.1	79.8454	159.6425	76	Grt-B-S	20x20x15	5	0.956	1.000
Diamond moraine	DH9.4	79.8428	159.6463	88	Grt-B-S	30x30x30	6	0.948	1.000
Upper Drift	DAR-DH-05	79.8548	159.3904	443	Grt-B-S	150x150x70	3	0.973	0.983
Upper Drift	DAR-DH-04	79.8551	159.3893	449	Grt-B-S	150x130x100	3	0.973	0.983
Upper Drift	DAR-DH-06	79.8545	159.3918	461	Grt-B-S	210x370x150	1	0.991	0.983
Upper Drift	DH14.3	79.8686	159.3304	550	Grt-B-S	25x18x12	5	0.956	0.997
Upper Drift	DH14.2B	79.8688	159.3307	554	Qzt-BD-S	Bedrock	5	0.956	1.000
Upper Drift	DH15.1B	79.8723	159.2492	666	Qzt-BD-S	Bedrock	5	0.956	0.990
Upper Drift	DH12.1	79.8700	159.2369	734	Grt-B-S	100x60x50	5	0.956	1.000
Upper Drift	DH11.1	79.8691	159.2062	930	Grt-B-S	100x80x65	3	0.973	1.000
Upper Drift	DH11.1B	79.8691	159.2062	930	Qzt-BD-S	Bedrock	4	0.965	1.000
Upper Drift	DH10.1B	79.8598	159.2254	1192	Grt-BD-S	Bedrock	2	0.982	1.000

[a] Glacial drifts defined by Bockheim et al. (1989).
[b] Sample type. Quartz (Qzt), granitoid (Grt) or sandstone (Sst). Bedrock (BD), boulder (B), surface (S) or whole clast (WC) samples.
[c] Based on an attenuation length of 150 g cm^{-2} and a rock density of 2.7 g cm^{-3}.
[d] Based on M=2.3 (see section 2.1.4.3).

Table A.15: Diamond Hill AMS results 1

Sample ID	ANSTO Be Cathode	ANSTO Al Cathode	$^{10}Be/^{9}Be$ Ratio ($1e^{-15}$) *a*	$^{10}Be/^{9}Be$ Error ($1e^{-15}$) *b*	$^{26}Al/^{27}Al$ Ratio ($1e^{-15}$) *c*	$^{26}Al/^{27}Al$ Error ($1e^{-15}$) *b*	Quartz Mass (g)	^{9}Be Carrier Mass (mg) *d*	^{27}Al Concentration (ppm) *e*
DH7.1	B3787	A1978	22	2	NA	NA	93.84	0.5172	FAIL
DH7.7B	B3882	A1980	1513	23	1896	137	99.67	0.4926	37
DH7.4	B3881	A1979	42	10	77	28	68.22	0.4958	22
DH6.2	B3785	A1976	60	3	134	38	90.41	0.6099	75
DH6.2B	B3786	A1977	2621	18	3630	189	105.74	0.5683	54
DH2.1	B3780	A1970	1065	35	551	102	76.00	0.4178	119
DH2.2	B3781	A1971	5264	78	5040	200	75.50	0.4180	101
DH8.1	B3788	A1981	3765	33	26766	519	80.33	0.5081	15
DH8.2	B3883	A1982	2428	28	1236	86	69.94	0.5040	164
DH3.2	B3880	A1973	819	74	974	99	70.53	0.5042	93
DH3.1	B3782	A1972	290	9	153	32	75.02	0.4173	173
DH1.1	B3779	A1969	798	12	4428	157	76.18	0.4150	24
DH13.1	B3794	A1989	3272	32	1006	33	59.79	0.5012	311
DH13.2	B3885	A1990	5303	115	8223	90	71.82	0.5022	64
DH5.2	B3783	A1974	7834	35	21920	634	76.44	0.5125	FAIL
DH5.2B	B3784	A1975	7971	92	13650	543	75.21	0.4094	54

a Measured against NIST SRM-4325 with a nominal value of 27900 x 10^{-15}.

b The quoted 1σ error is the larger of total statistical error or weighted error in mean. Additional 2% (1σ) error added in quadrature based on reproducibility of AMS standard measurements.

c Measured against SRM PRIME-Z93-0221 with a nominal value of 16800 x 10^{-15}.

d Concentration of ^{9}Be carrier solution made from beryl crystal with $^{10}Be/^{9}Be$ ratio of $<5x10^{-15}$.

e Measured by ICP-OES in a 1-2 g solution of dissolved quartz in HF.

Table A.16: Diamond Hill AMS results 2

Sample ID	ANSTO Be Cathode	ANSTO Al Cathode	$^{10}Be/^{9}Be$ Ratio ($1e^{-15}$) *a*	$^{10}Be/^{9}Be$ Error ($1e^{-15}$) *b*	$^{26}Al/^{27}Al$ Ratio ($1e^{-15}$) *c*	$^{26}Al/^{27}Al$ Error ($1e^{-15}$) *b*	Quartz Mass (g)	^{9}Be Carrier Mass (mg) *d*	^{27}Al Concentration (ppm) *e*
DH9.1	B3789	A1983	1375	22	3506	170	100.44	0.5946	40
DH9.4	B3790	A1984	2771	27	6537	211	99.91	0.5913	41
DAR-DH-05	B2484	A1694	8041	195	32960	950	47.44	0.5044	35
DAR-DH-04	B2483	A1693	14212	440	20847	727	80.47	0.4950	62
DAR-DH-06	B2485	A1695	1461	28	1586	89	59.56	0.5064	112
DH14.3	B3795	A1992	635	28	1743	44	50.26	0.6158	90
DH14.2B	B3886	A1991	12538	80	56667	238	71.44	0.6369	23
DH15.1B	B3796	A1993	10345	84	13040	115	51.62	0.6113	114
DH12.1	B3793	A1988	10867	369	62719	800	51.73	0.6204	29
DH11.1	B3884	A1986	23910	140	18111	369	76.04	0.4128	FAIL
DH11.1B	B3792	A1987	8479	51	33412	527	49.88	0.6085	42
DH10.1B	B3791	A1985	35501	182	41042	420	53.30	0.4264	84

a Measured against NIST SRM-4325 with a nominal value of 27900 x 10^{-15}.

b The quoted 1σ error is the larger of total statistical error or weighted error in mean. Additional 2% (1σ) error added in quadrature based on reproducibility of AMS standard measurements.

c Measured against SRM PRIME-Z93-0221 with a nominal value of 16800 x 10^{-15}.

d Concentration of ^{9}Be carrier solution made from beryl crystal with $^{10}Be/^{9}Be$ ratio of <5x10^{-15}.

e Measured by ICP-OES in a 1-2 g solution of dissolved quartz in HF.

Table A.17: Diamond Hill exposure age results 1

Sample ID	^{10}Be Concentration (x 10^3 atm g^{-1})	^{10}Be Error (x 10^3 atm g^{-1})	^{26}Al Concentration (x 10^3 atm g^{-1})	^{26}Al Error (x 10^3 atm g^{-1}) [a]	Minimum ^{10}Be Age (ka) [b]	Minimum ^{10}Be Age Error (ka) [c]	Minimum ^{26}Al Age (ka) [d]	Minimum ^{26}Al Age Error (ka) [c]	^{26}Al/^{10}Be Ratio	^{26}Al/^{10}Be Error
DH7.1	8	1	NA	NA	1.3	0.2 (0.1)	NA	NA	NA	NA
DH7.7B	5	1	1563	134	81	7.5 (2.3)	37.5	4.6 (3.2)	3.1	0.3
DH7.4	21	5	38	14	3.3	0.8 (0.7)	0.9	0.3 (0.3)	1.9	0.7
DH6.2	27	2	223	64	4.3	0.4 (0.3)	5.2	1.5 (1.4)	8.2	2.4
DH6.2B	942	22	4389	305	150.4	14.2 (3.9)	105.2	12.3 (7.5)	4.7	0.3
DH2.1	391	154	1466	280	58.4	5.7 (2.4)	32.4	6.8 (6.2)	3.7	0.7
DH2.2	1948	52	11381	690	311.5	30.5 (9.2)	286.2	34.4 (19.4)	5.8	0.4
DH8.1	1592	382	8850	440	230.1	21.7 (6)	196.7	21.3 (10.4)	5.6	0.3
DH8.2	1169	295	4520	377	163.3	15.5 (4.5)	93.9	11.8 (8)	3.9	0.3
DH3.2	391	37	2018	224	50.8	6.5 (4.7)	39.0	5.5 (4.3)	5.2	0.6
DH3.1	108	4	591	128	13.8	1.3 (0.5)	11.2	2.6 (2.4)	5.5	1.2
DH1.1	291	8	2380	138	37.4	3.4 (1)	45.9	4.8 (2.6)	8.2	0.5
DH13.1	1833	45	6992	394	237.3	22.5 (6.3)	134.9	14.6 (7.8)	3.8	0.2
DH13.2	2478	77	11684	550	321.2	31.7 (10.8)	231.6	25.1 (11.9)	4.7	0.2
DH5.2	3510	80	NA	NA	466.3	46.4 (12.4)	NA	NA	NA	NA
DH5.2B	2900	73	16343	992	377.0	36.9 (10.6)	336.8	41 (23.1)	5.6	0.3

[a] Error in ^{26}Al concentration includes a 4% error in ICP-OES measurement of Al concentration in quartz.

[b] ^{10}Be decay constant = 5.00 x 10^{-7} ($t_{1/2}$ =1.387 Ma), ^{10}Be production rate = 4.60 $\pm$ 0.42 atoms g a^{-1}. Site specific production rate based on Stone (2000) scaling.

[c] Age error includes a 9% standard error in sea-level high latitude production rate in quadrature with total analytical AMS error (Bracketed).

[d] ^{26}Al decay constant = 9.90 x 10^{-7} ($t_{1/2}$ = 0.70 Ma), ^{26}Al production rate = 30.7 $\pm$ 2.8 atoms g a^{-1}.

Table A.18: Diamond Hill exposure age results 2

Sample ID	^{10}Be Concentration (x 10^3 atm g^{-1})	^{10}Be Error (x 10^3 atm g^{-1})	^{26}Al Concentration (x 10^3 atm g^{-1})	^{26}Al Error (x 10^3 atm g^{-1}) *a*	Minimum ^{10}Be Age (ka) *b*	Minimum ^{10}Be Age Error (ka) *c*	Minimum ^{26}Al Age (ka) *d*	Minimum ^{26}Al Age Error (ka) *c*	^{26}Al/^{10}Be Ratio	^{26}Al/^{10}Be Error
DH9.1	544	15	3104	207	94.1	8.7 (2.7)	80.7	9.0 (5.4)	5.7	0.4
DH9.4	1096	27	5957	334	193.6	18 (5.1)	160.4	17.4 (9.3)	5.4	0.3
DAR-DH-05	5714	188	25751	1394	810.1	90.2 (32.2)	584.8	77.4 (40.4)	4.5	0.2
DAR-DH-04	5843	223	28852	1661	827.1	94.3 (37.9)	679.7	95.6 (52.1)	4.9	0.3
DAR-DH-06	830	24	3965	287	95.7	9.1 (3.0)	68.3	8.0 (5.0)	4.8	0.3
DH14.3	520	26	3505	183	55.8	5.6 (2.7)	56.4	5.8 (2.9)	6.7	0.4
DH14.2B	7470	174	29548	1360	997.3	112.4 (30.4)	612.7	78.9 (36.6)	4.0	0.2
DH15.1B	8187	195	33049	1542	994.7	110.4 (30.4)	628.4	80.3 (37.6)	4.0	0.2
DH12.1	8710	354	41251	1962	981.8	117.1 (49.4)	779.9	109.4 (52)	4.7	0.2
DH11.1	8675	201	NA	NA	768.1	84.1 (22.7)	NA	NA	NA	NA
DH11.1B	6913	160	31493	1526	592.5	61.4 (16.6)	422.9	51.1 (24.6)	4.6	0.2
DH10.1B	18981	435	77397	3634	1610.3	222.0 (59.5)	1090.5	190.0 (89.4)	4.1	0.2

a Error in ^{26}Al concentration includes a 4% error in ICP-OES measurement of Al concentration in quartz.

b ^{10}Be decay constant = 5.00 x 10^{-7} ($t_{1/2}$ =1.387 Ma), ^{10}Be production rate = 4.60 $\pm$ 0.42 atoms g a^{-1}. Site specific production rate based on Stone (2000) scaling.

c Age error includes a 9% standard error in sea-level high latitude production rate in quadrature with total analytical AMS error (Bracketed).

d ^{26}Al decay constant = 9.90 x 10^{-7} ($t_{1/2}$ = 0.70 Ma), ^{26}Al production rate = 30.7 $\pm$ 2.8 atoms g a^{-1}.

A.4.2 Exposure dating sample photos


DH1.1(Left) and DH2.1(Right)


DH2.2(Left) and DH3.1(Right)


DH3.2(Left) and DH5.2/DH5.2B(Right)


DH6.2(Left) and DH7.1(Right)


DH7.4(Left) and DH7.7B(Right)


DH8.1(Left) and DH8.2(Right)


DH9.1(Left) and DH9.4(Right)


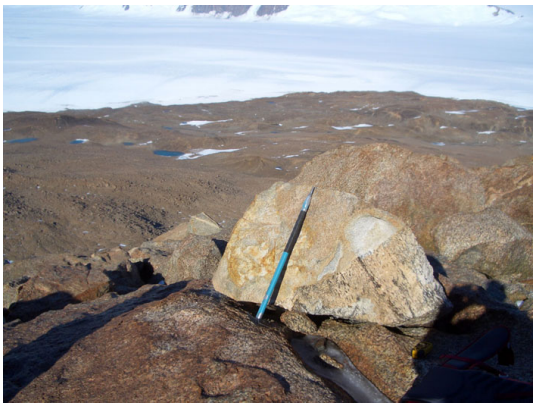

DH10.1B(Left) and DH11.1(Right)


DH12.1(Left) and DH13.1(Right)


DH13.2(Left) and DH14.3(Right)


DH15.1B(Left) and DAR-DH-04(Right)

DAR-DH-05(Left) and DAR-DH-06(Right)

Table A.19: Diamond Hill PCA rankings - Based on values from Table 7.5.

Sample ID	Type	Weathering	Elevation	Be Age	Al Age	Exposure History	Be Concentration	Al Concentration
DH1.1	Erratic	6	3	1	1	2	1	2
DH2.1	Erratic	5	2	1	1	2	1	1
DH2.2	Erratic	6	2	4	3	1	1	6
DH3.1	Erratic	5	3	1	1	2	1	1
DH3.2	Erratic	6	3	1	1	2	1	2
DH5.2	Erratic	5	4	5	NA	0	2	NA
DH5.2B	Bedrock	3	4	4	4	1	2	9
DH6.2	Erratic	4	1	1	1	1	1	1
DH6.2B	Erratic	4	1	2	2	2	1	3
DH7.1	Erratic	2	1	1	NA	0	1	NA
DH7.4	Erratic	5	1	1	1	1	1	1
DH7.7B	Erratic	3	1	1	1	2	1	1
DH8.1	Erratic	6	3	3	2	1	1	5
DH8.2	Erratic	4	3	2	1	2	1	3
DH9.1	Erratic	3	1	1	1	1	1	2
DH9.4	Erratic	4	1	2	2	1	1	3
DAR-DH-4	Erratic	7	4	9	7	1	3	10
DAR-DH-5	Erratic	5	4	9	6	1	3	10
DAR-DH-6	Erratic	4	5	1	1	2	1	2
DH10.1B	Bedrock	5	10	10	10	1	10	10
DH11.1	Erratic	6	9	8	NA	0	5	NA
DH11.1B	Bedrock	4	9	6	5	2	4	10
DH12.1	Erratic	7	7	10	8	1	5	10
DH13.1	Erratic	6	4	3	2	2	2	3
DH13.2	Erratic	6	4	4	3	2	3	6
DH14.2B	Bedrock	5	5	10	7	2	4	10
DH14.3	Erratic	6	5	1	1	1	1	2
DH15.1B	Bedrock	4	7	10	7	2	5	10

Appendix B

Published papers

B.1 Journal of Quaternary Science (2011)

A 2 million year glacial chronology of the Hatherton Glacier, Antarctica and implications for the size of the East Antarctic Ice Sheet at the Last Glacial Maximum.

Joy, K., Fink, D., Storey, B. C. & Atkins C.(2013). Journal of Quaternary Science, 83, 46-57.

Quaternary Science Reviews xxx (2013) 1–12

Contents lists available at ScienceDirect

Quaternary Science Reviews

journal homepage: www.elsevier.com/locate/quascirev

A 2 million year glacial chronology of the Hatherton Glacier, Antarctica and implications for the size of the East Antarctic Ice Sheet at the Last Glacial Maximum

Kurt Joy [a,*], David Fink [b], Bryan Storey [a], Cliff Atkins [c]

[a] Gateway Antarctica, University of Canterbury, Private Bag 4800, Christchurch, New Zealand
[b] Institute for Environmental Research, ANSTO, PMB1, Menai 2234, Australia
[c] School of Geography, Environment and Earth Sciences, Victoria University of Wellington, P.O. Box 600, Wellington, New Zealand

ARTICLE INFO

Article history:
Received 17 May 2013
Received in revised form
25 October 2013
Accepted 25 October 2013
Available online xxx

Keywords:
Hatherton Glacier
Antarctica
East Antarctic Ice Sheet
Cosmogenic ^{10}Be and ^{26}Al exposure dating
Reduced Last Glacial Maximum ice sheet volume

ABSTRACT

A series of distinct glacial deposits flanking the margins of the upper Hatherton Glacier, an outlet glacier in the central Transantarctic Mountains, are used to constrain the behaviour of the Antarctic ice-sheets. Cosmogenic exposure ages of 18 erratics from four glacial drifts covering the ice free Dubris and Bibra valleys, range in age from 5 to 1997 ka. Our results document four glacial advance and retreat events superimposed on an overall long-term ice thickness reduction of about 500 m since the mid-Pleistocene. The lack of field evidence and absence of LGM exposure ages in the glacial deposits of the Hatherton Glacier supports our conclusion that at the LGM the East Antarctic Ice Sheet was of similar size, or may have been slightly smaller, than present. Minimum exposure ages from the oldest two glacial events, represented by the Isca and Danum drifts, are ~1–2 Ma and ~0.5 Ma respectively. The Britannia-II Drift, previously assumed to mark the maximum extent of the Last Glacial Maximum advance, has a mean ^{10}Be age of 126 ± 3.2 ka ($n = 5$). Ages from the younger Britannia-I Drift suggest that since the mid-Holocene (6.5 ± 1.2 ka, $n = 5$), approximately 200 m of additional ice has been lost.

1. Introduction

Key to understanding the impact of future climate change on global sea level is the ability to model ice sheet response to atmospheric and oceanic warming. Measurement of past configurations of the Antarctic ice sheet margins have been used to validate model outputs in order to improve predictions (Denton and Hughes, 2002; Pollard and DeConto, 2009; Mackintosh et al., 2011; Golledge et al., 2012). For example, the debate surrounding the magnitude of Antarctic ice melt contribution to the ~120 m rise in global mean sea level (Peltier and Fairbanks, 2006) since the Last Glacial Maximum (LGM) approximately 20,000 years ago has been a central topic in the development of these glaciological models. While much evidence of former ice sheet extent can be found in the off-shore marine sedimentary record (Shipp et al., 1999; Mackintosh et al., 2011; McKay et al., 2012), the onshore terrestrial evidence is restricted to the coastal margins. Here, thinning ice sheets and outlet glaciers modify the exposed bedrock of the flanking mountain ranges and isolated nunataks (Brook et al., 1995; Denton and Marchant, 2000; Hall et al., 2000; Gore et al., 2001; Fink et al., 2006).

Fluctuations in the longitudinal profiles of outlet glaciers, especially those draining through the Transantarctic Mountains (TAMs) into the Ross Sea Embayment were directly influenced by the dynamics of both the EAIS and WAIS (Denton and Hughes, 2002; Anderson et al., 2004; McKay et al., 2009; Talarico et al., 2012). During the LGM the West Antarctic ice sheet (WAIS) is known to have advanced into the Ross Sea Embayment under glacial conditions and retreated with the warming that followed (Anderson, 2002; Hall et al., 2013), yet the behaviour of the East Antarctic Ice Sheet (EAIS) interior during this period is far less understood. Within the mountain ranges flanking the TAM outlet glaciers, a complex distribution of glacially transported debris has been deposited at various elevations as moraines, scattered glacial erratics and expanses of boulder drifts or till (Marchant et al., 1994; Staiger et al., 2006; Swanger et al., 2011). The presence of these deposits is interpreted as direct evidence of past glacial thickening driven by changes in ice sheet volume (Denton and Marchant, 2000).

The Darwin and Hatherton glaciers are one of the many drainage systems of the EAIS across the TAMs and were used in the Denton and Hughes (2002) LGM reconstruction of the Ross Sea

* Corresponding author.
E-mail address: Kurt.Joy@pg.Canterbury.ac.nz (K. Joy).

0277-3791/$ – see front matter © 2013 Published by Elsevier Ltd.
http://dx.doi.org/10.1016/j.quascirev.2013.10.028

Embayment. The Dubris and Bibra valleys (DBV), situated within the Britannia Range on the southern flank of the upper Hatherton Glacier, have periodically been inundated with Hatherton Glacier ice during periods of EAIS expansion. These alpine-type side-entrant valleys contain a sequence of glacial deposits previously used to constrain past fluctuations of the EAIS and WAIS in this sector of the TAMs during the Quaternary (Bockheim et al., 1989). A major transition in our ability to quantify the timing of past Antarctic ice sheet fluctuations, its thickness and lateral extent, hence providing a geochronological context to reconstruct paleo ice sheet dynamics, is the increasing application of cosmogenic exposure dating.

The location and geomorphology of the glacial drifts were mapped using the terminology of Bockheim et al. (1989) and samples collected for ^{10}Be and ^{26}Al surface exposure dating. Our procedures and methodology are equivalent to that employed by Storey et al. (2010) who carried out a similar study at Lake Wellman located on the northern flank of the Hatherton Glacier a further ~30 km downstream towards the Ross Ice Shelf. In that study, Storey et al. (2010) presented a ^{10}Be–^{26}Al chronology of ice volume change at Lake Wellman which supported an LGM ice thickness to be no more than 50 m higher compared to the modern Hatherton Glacier ice elevation; an order of magnitude lower than previously assumed. As this result has many implications for the regional evolution of the WAIS and EAIS during the LGM and Termination-I, it is critical to assess whether such a reduction in LGM ice volume occurred over a wider region of the Britannia Range of the TAMs and along the Darwin and Hatherton glaciers. Therefore, to quantify the timing of past Hatherton Glacier ice volume changes and to re-evaluate the Bockheim et al. (1989) radiocarbon chronology, we apply the technique of in-situ surface exposure dating to the glacial deposits of the DBV.

2. The Darwin–Hatherton glacial system

The Darwin–Hatherton glacial system (DHGS) is a medium-sized outlet glacier system comprised of two glaciers; the larger Darwin and its smaller tributary, the Hatherton (Fig. 1). Separated from the Byrd Glacier to the south by the Britannia Range, the DHGS drains the EAIS through the TAMs into the floating Ross Ice Shelf. While the glaciers of the DHGS share the same catchment, variations in sub-glacial bedrock topography restrict ice flow from the EAIS into the Hatherton Glacier. Surface ice velocities of <5–8 m a^{-1} have been measured for the Hatherton Glacier while those of the Darwin Glacier range from ~20 to 180 m a^{-1} (Riger-Kusk, pers. comm). Numerical modelling and geophysical surveys of glacier flow infer that while basal conditions in the central trunk of the Darwin Glacier reach pressure melting point, the thinner Hatherton Glacier is predominantly cold-based (Anderson et al., 2004; Riger-Kusk, pers. comm). Geological evidence observed at Lake Wellman (Fig. 1) supports this theory, with striated, plucked and faceted clasts, typical of warm based glaciers, suggesting that parts of the Hatherton Glacier have experienced a variety of basal conditions in the past (Storey et al., 2010). These observations are relevant to the interpretation of cosmogenic exposure ages obtained in this study and those reported from Lake Wellman. A longitudinal ice elevation profile for the LGM was reconstructed by Bockheim et al. (1989) based on minimum radiocarbon ages and shows the influence of ice buttressing by a grounded WAIS (see Fig. 7 in Bockheim et al., 1989). As the grounding zone of the WAIS advanced into the Ross Embayment, displacing the floating Ross Ice Shelf with grounded ice at its confluence with the DHGS, the impedance to DHGS ice flow increased resulting in a significant thickening in the lower to middle reaches of the glacier profile (Anderson et al., 2004). Coupled with the available geological evidence (Denton, 1979; Bockheim et al., 1989), the buttressed profile indicated that downstream thickening at the ice shelf confluence was up to 1000 m above present, dropping to near modern levels as the WAIS grounding line retreated past the mouth of the DHGS at ~7 ka (Conway et al., 1999; Hall et al., 2013). In direct contrast to this interpretation, the recent suite of exposure ages obtained from Lake Wellman by Storey et al. (2010) suggest that no such thickening on this scale occurred at LGM times but rather, the surface of Hatherton Glacier was elevated 800 m above present day ice during the early to mid-Pleistocene (1–2 Ma). Glacial–interglacial oscillations of the Hatherton Glacier are superimposed on an overall long-term trend of ice surface lowering that has continued up to the late Holocene.

2.1. Dubris and Bibra valleys

The Dubris and Bibra valleys (DBV) at 80°S, 156°E, are two ice free regions of ~60 km^2 that flank the Hatherton Glacier in the Britannia Range (Fig. 1) about 25 km from the EAIS catchment

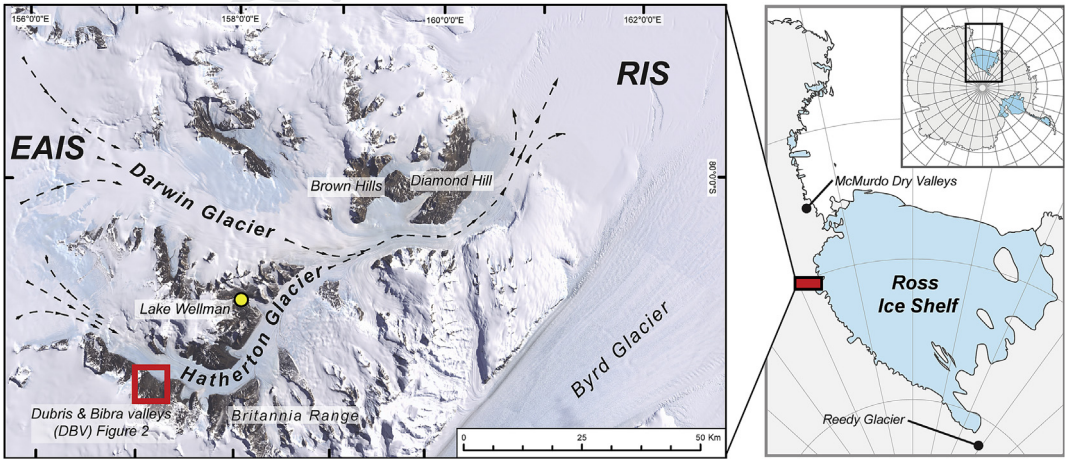

Fig. 1. Regional maps showing the location of field sites within the Darwin–Hatherton glacial system (DHGS) and its position within the Ross Embayment. The Dubris Valley study area, on the southern flank of the Hatherton Glacier, is shown in the red square. The yellow circle denotes the Lake Wellman site where Storey et al. (2010) have conducted a similar study of past ice volume. The DHGS system flows eastward through the Transantarctic Mountains draining the East Antarctic Ice Sheet (EAIS) into the Ross Ice Shelf (RIS). The Britannia Range separates the DHGS from the Byrd Glacier to the south. (For interpretation of the references to colour in this figure legend, the reader is referred to the web version of this article.)

Please cite this article in press as: Joy, K., et al., A 2 million year glacial chronology of the Hatherton Glacier, Antarctica and implications for the size of the East Antarctic Ice Sheet at the Last Glacial Maximum, Quaternary Science Reviews (2013), http://dx.doi.org/10.1016/j.quascirev.2013.10.028

region. They form a series of steep sided (>45°) U-shaped glacially excavated valleys with floors that slope towards the modern ice margin of the Hatherton Glacier and which are separated by a flat topped ridge, the Danum Platform. Strong katabatic winds channel into the valleys from the EAIS plateau leaving the area almost completely ice free with only a few small semi-permanent snow patches present. The dominant bedrock lithology is the Ferrar Dolerite with minor exposures of sandstone and coal measures of the Beacon Supergroup (Haskell et al., 1964).

Warm-based alpine-type glaciations during the late Miocene most likely sculpted the dominant valleys (Denton and Sugden, 2005) prior to a regional change to cold-based conditions (Lewis et al., 2007). Subsequent glacial events during the Quaternary involved incursion of the cold-based margin of the Hatherton Glacier ice up into the valley. This is evidenced by extensive and numerous glacial drifts and boulder-belt moraines ranging from the modern ice elevation of 1100 masl to ~1600 masl. These drifts are predominantly comprised of sandstone, dolerite and rare granitic clasts (Fig. 2). Given the scarcity of sandstone exposures within the DBV and the high proportion in glacial deposits, it is clear that this material had been glacially transported from its source into the valleys. Due to the proximity of the DBV to the EAIS, only a limited distance is available for rock fall generated supra-glacial material to be collected by the Hatherton Glacier and then deposited within the valleys; beyond this distance, no other nunataks or outcrops exist.

2.2. Radiocarbon based glacial chronologies

Bockheim et al. (1989) described and mapped the distribution of four glacial deposits (drifts and boulder belt moraines) within the DHGS, using a combination of surface morphology, clast weathering and soil geochemistry; from youngest to oldest these are named as, Hatherton, Britannia, Danum and Isca drifts. Based on minimum radiocarbon ages and field mapping, the overall chronology assigned by Bockheim et al. (1989), were early Holocene for the Hatherton Drift, post-LGM and LGM for the Britannia drifts and MIS-6 and older for Danum and Isca drifts, respectively. Subsequently, the Britannia Drift has been used in the DHGS to constrain ice sheet dynamics of during the global LGM and Termination-I as defined by the marine record (Denton and Marchant, 2000; Denton and Hughes, 2002). Bockheim et al. (1989) subdivided the Britannia Drift into two advances, with the Britannia-II Drift representing an LGM advance and the Britannia-I Drift deposited over the older Britannia-II Drift during a later (post-LGM) glacial re-advance. The maximum extent of the Britannia-II advance is represented by an extremely well-defined boulder-belt moraine contact margin with the older and distinctly more weathered Danum surface (Fig. 3). This is observed at elevations up to 320 m above the present Hatherton Glacier. The contact is sinuous and continuous throughout the valley floor and ridges of the DBV. In contrast to the boulder belts, the glacial drifts deposited have a patchy and irregular distribution throughout the area. The drift material in some places is thick and buries the underlying older surfaces (Bockheim et al., 1989), while in others there is only a scattering of boulders and a minor reworking of the original drift surface, typical of cold-based glacial deposition (Atkins, 2013).

LGM ice thickness modelling of the DHGS was based on minimum ages obtained from radiocarbon dating of algal mats located within the Hatherton and Britannia drifts along the DHGS. These mats form at the margins of former pro-glacial lakes and ponds following glacier retreat, providing increased availability of seasonal free water and permitting the growth of blue-green algae (Sugden et al., 2006). For the Britannia event, Bockheim et al. (1989) suggest retreat from its maximum extent occurred at least 10.2–12.1 ka cal BP and reached a position near the modern Hatherton margin by 6.3–6.8 ka cal BP. However, there is a wide variation in Britannia Drift ages throughout the DHGS, with the youngest being

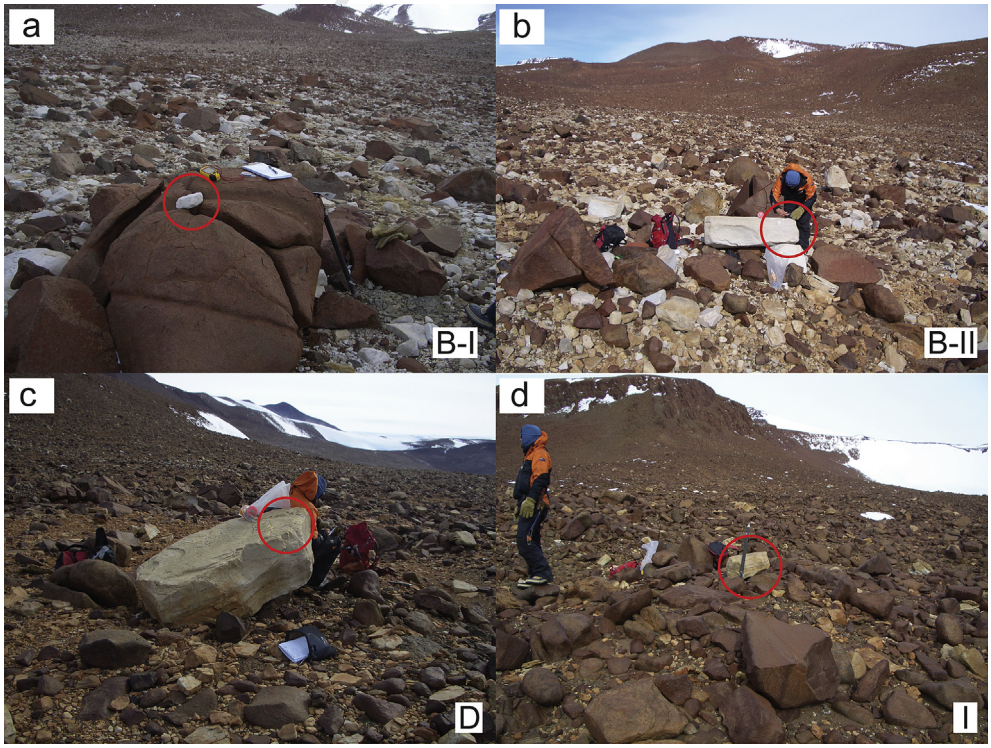

Fig. 2. Typical view of the Britannia-I (B-I), Britannia-II (B-II), Danum (D) and Isca (I) glacial drifts encounted in the Dubris and Bibra Valleys. All samples (shown circled) were Beacon sandstone boulders or clasts, emplaced on drift surface or perched on large dolerite platforms. a) BV3.1 in the Britannia-I Drift (Bibra Valley). b) DP4.1 in the Britannia-II Drift (Danum Platform). c) DP5.1 in the Danum Drift (Danum Platform) and d) DV1.1 in the Isca Drift (Dubris Valley). Full sample descriptions and locations are in Table 1.

Please cite this article in press as: Joy, K., et al., A 2 million year glacial chronology of the Hatherton Glacier, Antarctica and implications for the size of the East Antarctic Ice Sheet at the Last Glacial Maximum, Quaternary Science Reviews (2013), http://dx.doi.org/10.1016/j.quascirev.2013.10.028

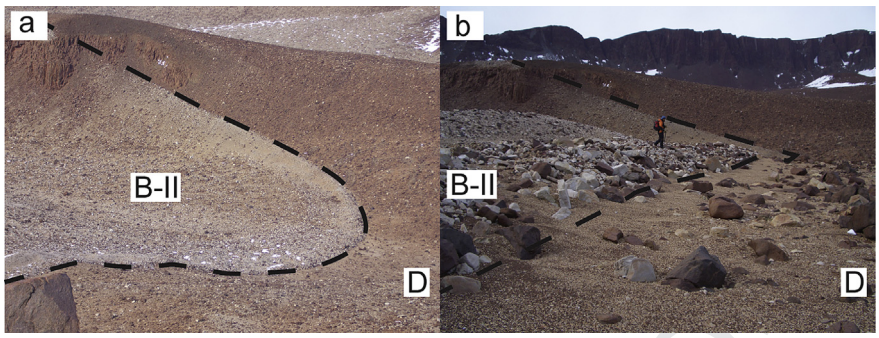

Fig. 3. Oblique (a) and closeup (b) of the Britannia-II (B-II) and Danum (D) drift contact margin in the Dubris Valley. The valley width at this location (DV3.1) is approximately 700 m. Previously assigned ages for the Britannia-II are LGM and for the Danum drift MIS-6 according to Bockheim et al. (1989). ^{10}Be surface exposure ages on the Britannia-II are ~110–130 ka and on the Danum drift a minimum age of ~1 Ma. The direction of intruded Hatherton Glacier ice advance is left to right.

5.9–6.2 ka cal BP. These samples (QL1418, QL1419 and QL1420) from the Brown Hills near the confluence of the Darwin Glacier and Ross Ice Shelf, overlap with those obtained in the younger Hatherton Drift. From the DBV, there is only one radiocarbon age which underpins the above glacial chronology. This sample (QL-1424), taken from the Britannia-I Drift at the mouth of the Bibra Valley, dates to 5.9–6.0 ka cal BP (Bockheim et al., 1989). Although Bockheim et al. (1989) correctly postulated that the radiocarbon ages represent a minimum age for the recession of the ice margin; there is a high uncertainty in the long-term preservation of algal mats post-retreat and a probability of activation of algal mats predominately during the warmer Holocene period, independent of drift deposition age.

2.3. Cosmogenic nuclide based glacial chronologies

The radiocarbon glacial chronology of Bockheim et al. (1989) was re-assessed by Storey et al. (2010) at Lake Wellman on the northern flank of Hatherton Glacier using in-situ surface exposure dating (SED, Gosse and Phillips, 2001) and Accelerator Mass Spectrometry (AMS, Tuniz et al., 1998). Paired ^{10}Be and ^{26}Al surface exposure ages for mapped Hatherton and Britannia drifts (Storey et al., 2010) present a significantly different chronology to that of the Bockheim et al. (1989) radiocarbon ages. From 23 granitoid and sandstone samples collected over the four distinct drift types, a minimum exposure age model placed the Hatherton Drift as late-Holocene (n = 3 samples, 0.8–2.6 ka) and the Britannia Drift to pre-LGM at 37.0 ± 5.5 ka (n = 5, one outlier). The older drift sequences give ^{10}Be age ranges of 77–630 ka for the Danum and 929–2275 ka for the Isca (Storey et al., 2010).

The SED based chronology of Storey et al. (2010) and resultant age versus elevation profile challenged the predicted LGM ice thickness profile given by Denton and Hughes (2002) and Bockheim et al. (1989). Specifically, Storey et al. (2010) suggested that the volume of DHGS ice proximal to the EAIS was similar to or only slightly larger than that observed today and a reduction in the predicted LGM EAIS ice advance through the TAMs. Our paper provides an additional SED dataset nearer the ice source of the DHGS at the DBV where the four drifts have been observed to test the glacial chronology of both Bockheim et al. (1989) and Storey et al. (2010).

3. Methodology

3.1. Sample selection

With an increasing prevalence of exposure dating studies in Antarctica, it is important to recognise the specific problems that can arise when the technique is applied in polar conditions where ice sheet dynamics play a role in generating and transporting glacial debris. Uncertainty in the initial cosmogenic nuclide inventory, provenance and accumulation of supra and sub-glacial material during transport, post depositional modification (*i.e.* boulder orientation, exhumation through eroding glacial till), cold-based ice overriding of previously deposited debris and low erosion rates of <1 m Ma^{-1} (Summerfield, 1999) all can influence exposure age calculations. Partial recycling of previously exposed material into younger moraines and patchy deposition of younger moraines on older surfaces or passive burial by cold-based ice can lead to complex and sometimes contradictory ages from a single co-eval landform (Strasky et al., 2008; Bromley et al., 2010; Storey et al., 2010; Todd et al., 2010). Therefore, to minimise potential problems associated with clast reworking and to offer an increased likelihood of determining the true deglaciation age of a glacial landform, sample selection criteria that consider a cold-based depositional environment are highly relevant.

As the glacial drifts of the DBV represent periods of past glacial thickening, the "mountain dipstick" method (Stone et al., 2003; Mackintosh et al., 2007) was employed. Using a combination of published field maps (Bockheim et al., 1989) and high resolution satellite imagery, key moraine contacts and other geomorphic features of the Britannia, Danum and Isca drifts were mapped (Fig. 4). Samples were taken along elevation transects up-valley from the present Hatherton Glacier margin (~1100 masl) up to the headwall of the Dubris (~1350 masl) and Bibra valleys (~1450 masl). A third transect along the Danum Platform, which separates the two valleys, reached an elevation of 1620 masl. The use of transects that crossed drift sheets and major contacts allowed the analysis of age–elevation relationships, a retreat chronology and the reconstruction of former ice thickness within the DBV. In total, 18 samples were collected from the Danum Platform (n = 8), Dubris (n = 6) and Bibra valleys (n = 4). Based on drift sheet mapping, 13 samples came from the Britannia Drifts and five from the older Danum and Isca drifts. No samples were taken from the Hatherton Drift as it consisted predominately of ice cored moraine with frequent evidence of post depositional modification by mass-movement and solifluction that rendered sampling for exposure dating unreliable.

Typically in SED studies, samples from ice marginal moraines, bedrock exposures (Lilly et al., 2010) or emplaced glacial erratics (Stone et al., 2003) are favoured. Sediment supported moraines in the DBV are subdued and poorly preserved and morphologically similar to those at Lake Wellman (Storey et al., 2010). However the unstable nature of these moraine ridges suggested significant glacial reworking and/or post-depositional modification. This is evident in the excessive age spread seen in such deposits at Lake Wellman (See Figs. 4 and 7 in Storey et al., 2010). Therefore, to ensure the post depositional stability of samples, Beacon

Please cite this article in press as: Joy, K., et al., A 2 million year glacial chronology of the Hatherton Glacier, Antarctica and implications for the size of the East Antarctic Ice Sheet at the Last Glacial Maximum, Quaternary Science Reviews (2013), http://dx.doi.org/10.1016/j.quascirev.2013.10.028

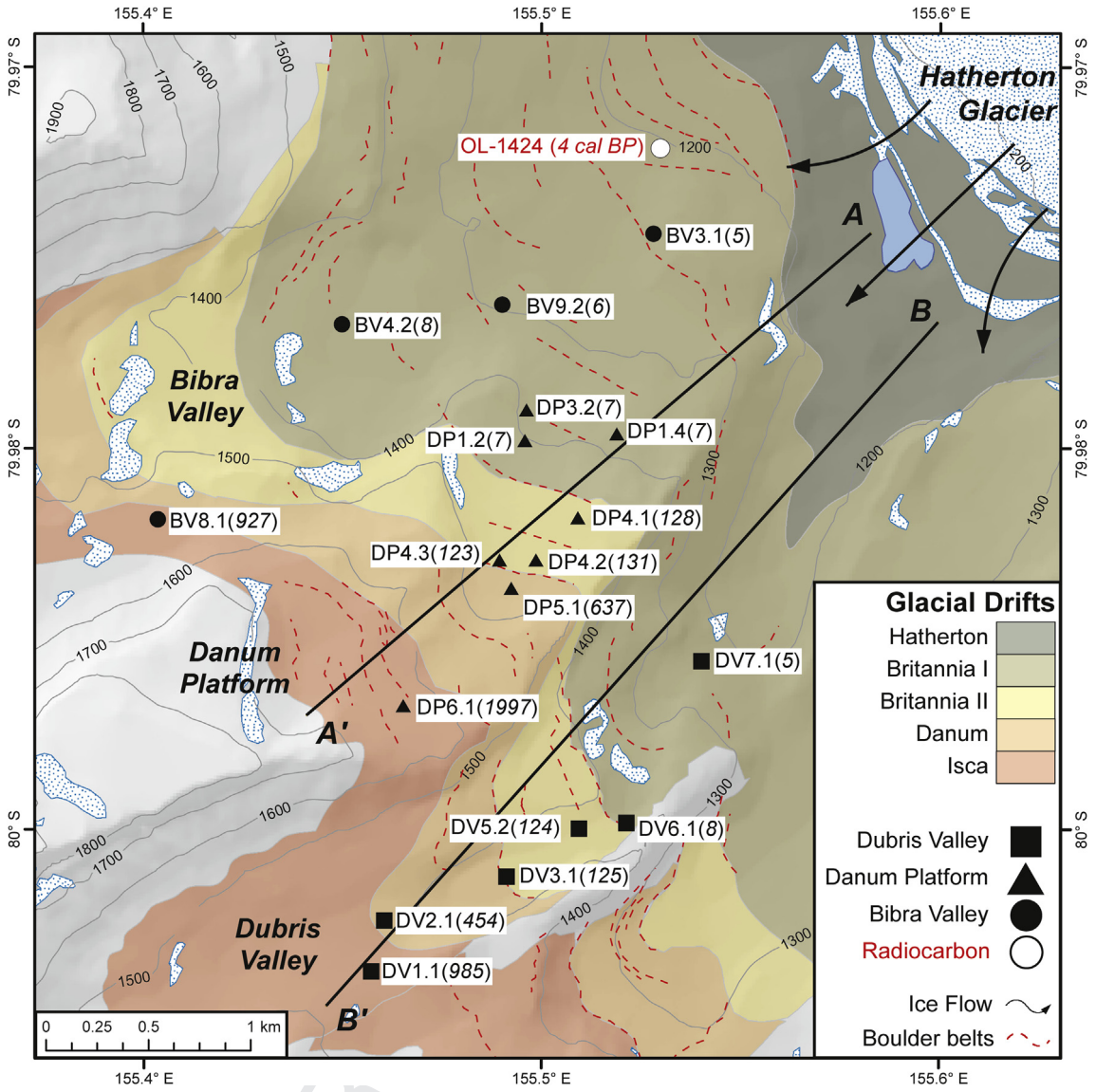

Fig. 4. Map of the Dubris and Bibra Valleys and Danum Platform bordering the southern margin of the Hatherton Glacier in the Britannia Range approximately 25 km from the EAIS. The stratigraphic definitions and relative positions of the 5 drift sheets are taken from Bockheim et al. (1989) and have been adjusted based on our field work. Moraine ridges from field mapping and interpretation of satellite imagery. Up valley transects for the Danum Platform (A–A′) and Dubris Valleys (B–B′) are presented in Fig. 4. Cosmogenic exposure ages (in brackets after sample ID) and radiocarbon ages are stated in integer kiloyears (ka).

Sandstone (>95% quartz) and boulders positioned above the drift surface, or cobbles emplaced on stable and flat boulders (>2 m) were preferentially sampled. At sites where this was not possible, exposed boulders and cobbles from desert pavements both proximal and distal to the drift contact were carefully selected and sampled instead. In addition, we have paid close attention to the glacial geomorphology, in particular the often subtle features of erosion, reworking and deposition associated with cold-based glaciers (Atkins et al., 2002; Lloyd-Davies et al., 2009; Atkins, 2013) to minimise potential problems related to exposure inheritance, clast recycling and exhumation after prolonged burial by ice.

At each site the geometry of the viewable sky was measured from the sample surface to correct for both topographic and self-shielding as per Balco et al. (2008). An attenuation length of 150 g cm^2 and a rock density of 2.7 g cm^3 were also used to correct for sample surface thickness. Sample elevations were converted to air pressure as per Stone (2000), due to the measured Antarctic altitude–pressure relationship deviating from that of the standard atmospheric model. Site specific production rates were calculated based on the sea level high latitude (SLHL) scaling scheme of Stone (2000). Table 1 summarises sample data and local corrections to ^{10}Be and ^{26}Al production rates.

3.2. Sample preparation and AMS measurement

Samples were prepared at the University of Canterbury cosmogenic preparation laboratory following the Australian Nuclear Science and Technology Organisation (ANSTO) procedure for quartz separation, cleaning and oxide extraction (Child et al., 2000; Mifsud et al., 2012). Once processed, targets were measured for ^{10}Be and ^{26}Al at the ANTARES AMS facility at ANSTO (Fink and Smith, 2007). ^{10}Be was normalised against the NIST-4325 standard reference material (^{10}Be/^{9}Be ratio of 27,900 × 10^{-15}) and ^{26}Al against PRIME-Z93-0221 (^{26}Al/^{27}Al ratio of 16,800 × 10^{-15}) (Table 2). A detailed discussion can be found in Storey et al. (2010).

Please cite this article in press as: Joy, K., et al., A 2 million year glacial chronology of the Hatherton Glacier, Antarctica and implications for the size of the East Antarctic Ice Sheet at the Last Glacial Maximum, Quaternary Science Reviews (2013), http://dx.doi.org/10.1016/j.quascirev.2013.10.028

Table 1
Sample and site descriptions for the Dubris and Bibra Valley region.

Drift sequence [a]	Sample ID	Location		Elevation (masl)	Sample type[b]	Sample dimensions (L × W × H cm)	Sample thickness (cm)	Sample shielding correction[c]	Topographic shielding correction
		Latitude (S)	Longitude (E)						
Britannia I	BV3.1	79.9733°	155.5278°	1259	Clast on dolerite boulder	10 × 10 × 15	5	0.956	0.999
Britannia I	BV9.2	79.9767°	155.4093°	1297	Clast on dolerite boulder	15 × 10 × 5	5	0.956	0.998
Britannia I	BV4.2	79.9780°	155.4494°	1342	Clast on beacon boulder	20 × 10 × 5	5	0.956	0.991
Britannia I	DV7.1	79.9917°	155.5391°	1255	Clast on boulder	25 × 25 × 25	5	0.956	0.994
Britannia I	DV6.1	79.9983°	155.5204°	1377	Boulder	120 × 80 × 50	3	0.973	0.996
Britannia I	DP1.4	79.9827°	155.5182°	1390	Boulder	200 × 150 × 80	3	0.973	0.999
Britannia I	DP3.2	79.9817°	155.4961°	1397	Clast on dolerite boulder	20 × 30 × 15	5	0.956	0.999
Britannia I	DP1.2	79.9817°	155.4956°	1406	Clast on dolerite boulder	15 × 10 × 15	5	0.956	0.998
Britannia II	DV5.2	79.9983°	155.5088°	1403	Boulder	80 × 100 × 80	3	0.973	0.997
Britannia II	DV3.1	80.0000°	155.4908°	1383	Clast	17 × 10 × 7	2	0.982	0.990
Britannia II	DP4.3	79.9880°	155.4890°	1469	Boulder	80 × 80 × 30	3	0.973	0.999
Britannia II	DP4.1	79.9850°	155.5091°	1459	Boulder	120 × 120 × 60	5	0.956	0.999
Britannia II	DP4.2	79.9883°	155.4986°	1471	Clast	30 × 30 × 15	3	0.973	0.999
Danum	DV2.1	80.0000°	155.4603°	1420	Clast	15 × 15 × 5	5	0.956	0.992
Danum	DP5.1	79.9893°	155.4926°	1478	Boulder	150 × 100 × 80	2	0.982	0.998
Isca	BV8.1	79.9867°	155.4033°	1533	Small Boulder	30 × 40 × 25	3	0.973	0.993
Isca	DV1.1	80.0067°	155.4577°	1464	Large clast	35 × 30 × 25	4	0.965	0.997
Isca	DP6.1	79.9950°	155.4647°	1620	Boulder	60 × 35 × 20	2	0.982	0.999

[a] Glacial drifts defined by Bockheim et al. (1989) and confirmed by field mapping in 2009.
[b] Sample type indicates whether whole clast or boulder surface was sampled. The lithology of all samples was Beacon sandstone.
[c] Based on an attenuation length of 150 g cm^2 and a rock density of 2.7 g cm^3.

Total production rates at sea-level and high latitude of 30.7 ± 9% and 4.6 ± 9% atoms g^{-1} a^{-1} for ^{26}Al and ^{10}Be respectively were used (Lilly et al., 2010; Storey et al., 2010). This value for ^{10}Be incorporates the 10.6% downward revision reported by Nishiizumi et al. (2007) due to the re-evaluation of the nominal ^{10}Be/^{9}Be ratio for NIST-4325. While there is a recent New Zealand ^{10}Be spallation production rate of 3.85 ± 3% (Putnam et al., 2010), it is significantly lower, by 17%, than the ^{10}Be production rate given above. Due to uncertainty about the applicability of the lower SLHL ^{10}Be production rate in the Antarctic and in order to maintain consistency with other Antarctic exposure age studies (Lilly et al., 2010; White et al., 2011; Yamane et al., 2011; Fogwill et al., 2012; Ackert et al., 2013), we prefer to maintain use of the greater production rate for ^{10}Be Exposure ages were calculated using a ^{10}Be decay constant of 4.99 × 10^{-7} a^{-1}, based on the half-life value of 1.387 ± 0.012 Ma (Korschinek et al., 2010) and 9.89 × 10^{-7} a^{-1} for ^{26}Al based on a half-life of 0.70 Ma (Nishiizumi, 2004).

4. Results

The DBV contains a wide range of geomorphological features, the most distinctive being a sequence of "bathtub ring" contours of near continuous boulder-belt moraine ridges that often demarcate the five phases of mapped glacial drifts deposited across the valleys (Figs. 3 and 4). The major drift contacts show variation in both elevation and distance from today's ice margin when comparing the relatively low relief valleys to the higher elevation ridges (Fig. 4). For example, the Britannia-II/Danum Drift contact is located 70 m lower but 1 km farther up valley than the same contact traced onto the Danum Platform, reflecting the topographic influence on the paleo position of the Hatherton Glacier margin as it encroached into the area (Fig. 5).

There is also a clear trend of decreasing preservation of glacially constructed features (*i.e.* ice cored moraines, debris cones, kettle holes, boulder belts and paleo-lakes) with increasing elevation and distance from the ice margin. The geomorphology of the older high elevation deposits is far less diverse, more weathered and has a subdued topography compared to the younger drifts at lower elevations.

The youngest deposit, the Hatherton Drift, which extends from the current ice margin at 1100 masl to at most 1200 masl, is characterised by irregular ice-cored terrain covered by a thin layer of fine grained sediment and carapace of sandstone cobbles. Abundant ice-cored debris cones, kettle holes, moraine ridges and some rare discrete blocks of frozen till are found within this zone while in the Isca and Danum drifts, the oldest deposits, none of these features are observed.

4.1. Surface exposure ages

Eighteen glacial erratics were sampled from the mapped drifts at elevations ranging from 1255 to 1620 masl with the highest sample (DP6.1) ~500 m above the present ice margin of ~1100 masl (Figs. 4 and 5). Thirteen exposure ages from the Britannia and five from the older Danum and Isca drifts were tested for spatial age distribution across the DBV. To be consistent with other Antarctic studies that cite exposure ages, we initially adopt a minimum age model. This infers, as a function of elevation, that measured concentrations of ^{10}Be and ^{26}Al reflect the minimum timing of deposition based on a zero erosion exposure. Our calculated ^{10}Be exposure ages range from 4.9 to 1997 ka (Table 3) and fall into four distinct age groupings. These align well with the established glacial drift stratigraphy of Bockheim et al. (1989) for the four drifts but with very different absolute age ranges. The oldest two groups of ^{10}Be ages, 454 to 1997 ka ($n = 5$), are all contained within the Danum and Isca drifts. The younger two age groups, Britannia-II, 122.9–130.7 ka ($n = 5$) is MIS-5 and hence definitively pre-LGM and Britannia-I, 4.9–8.0 ka ($n = 8$) is Holocene. The transects at Dubris Valley, Danum Platform and Bibra Valley all show a positive age–elevation relationship, with r^2 values of 0.53, 0.86 and 0.92 respectively.

As an aid to identify samples which have experienced uninterrupted sub-aerial exposure and are thus consistent with our prerequisite to constrain minimum ages at a given elevation, a ^{26}Al/^{10}Be dual nuclide plot is used. This technique has been successfully employed in similar Antarctic studies (Storey et al., 2010; White et al., 2011) to detect those samples showing periods of pre-exposure followed by prolonged burial and re-exposure (Fig. 6). Samples having complex exposure histories (*i.e.* cycles of exposure-burial) and thus classed as outliers will have depressed ^{26}Al/^{10}Be ratios which are discordant from ratios of acceptable samples. Outliers will plot below the region bounded by continuous

Please cite this article in press as: Joy, K., et al., A 2 million year glacial chronology of the Hatherton Glacier, Antarctica and implications for the size of the East Antarctic Ice Sheet at the Last Glacial Maximum, Quaternary Science Reviews (2013), http://dx.doi.org/10.1016/j.quascirev.2013.10.028

Table 2
AMS results for Dubris and Bibra Valley region.

Sample ID	ANSTOBe Cathode	ANSTOAl Cathode	$^{10}Be/^{9}Be$ ratio[a,b] ($\times 10^{-15}$)	$^{26}Al/^{27}Al$ ratio[b,c] ($\times 10^{-15}$)	Quartz mass (g)	^{9}Be carrier mass[d] (mg)	^{27}Al concentration (ppm)
BV3.1	B4203	A2133	170.7 ± 7.9 (4.7%)	119.0 ± 11.1 (9.3%)	72.09	0.5449	175.0
BV9.2	B4204	A2134	191.6 ± 6.2 (3.2%)	190.0 ± 23.8 (12.5%)	69.80	0.5618	152.0
BV4.2	B4205	A2135	264.2 ± 6.6 (2.5%)	143.4 ± 13.7 (9.6%)	69.58	0.5670	291.4
DV7.1	B4202	A2132	172.9 ± 6.4 (3.7%)	78.7 ± 12.4 (15.7%)	70.41	0.5512	321.0
DV6.1	B4206	A2136	292.8 ± 13.0 (4.4%)	135.1 ± 20.9 (15.4%)	69.08	0.5541	388.5
DP1.4	B4208	A2138	250.6 ± 9.5 (3.8%)	107.5 ± 14.4 (13.4%)	71.22	0.5739	342.8
DP3.2	B4209	A2139	246.4 ± 11.0 (4.5%)	179.7 ± 13.6 (7.6%)	70.42	0.5731	213.4
DP1.2	B4211	A2141	269.1 ± 6.9 (2.6%)	255.4 ± 35.6 (13.9%)	75.62	0.5637	231.5
DV5.2	B4210	A2140	4536 ± 35 (0.8%)	5867. ± 126 (2.1%)	71.44	0.5695	101.7
DV3.1	B4207	A2137	4879 ± 167 (3.4%)	2189 ± 58 (2.7%)	71.34	0.5284	305.4
DP4.3	B4217	A2147	4480 ± 64 (1.4%)	2620 ± 96 (3.6%)	69.79	0.5921	269.7
DP4.1	B4215	A2145	4972 ± 112 (2.2%)	5293 ± 150 (2.8%)	69.92	0.5402	138.3
DP4.2	B4219	A2148	5323 ± 102 (1.9%)	2485 ± 64 (2.6%)	74.06	0.5624	FAIL
DV2.1	B4213	A2143	19082 ± 852 (4.5%)	8125 ± 130 (1.6%)	70.12	0.4466	258.4
DP5.1	B4220	A2149	34174 ± 512 (1.5%)	12989 ± 812 (63%)	80.65	0.4168	230.9
BV8.1	B4221	A2150	38916 ± 313 (0.8%)	12393 ± 213 (1.7%)	70.38	0.4473	274.7
DV1.1	B4216	A2146	40759 ± 740 (1.8%)	17289 ± 244 (1.4%)	69.47	0.4162	214.3
DP6.1	B4222	A2151	78735 ± 843 (1.1%)	22205 ± 325 (1.5%)	69.98	0.4067	257.9

[a] Measured against NIST SRM-4325 with a nominal value of 27900 × 10^{-15}; AMS ratio is the weighted mean of repeat measurements.
[b] Error is the larger of total statistical error or weighted error in mean. All ratios corrected for chemistry processing blanks: for $^{10}Be/^{9}Be$ (4.2 ± 2.9) × 10^{-15} ($n = 4$, 2 targets) and for $^{26}Al/^{27}Al$ (20 ± 10) × 10^{-15} ($n = 3$, 1 target).
[c] Measured against SRM PRIME-Z93-0221 with a nominal value of 16800 × 10^{-15}.
[d] ^{9}Be spike from solution of beryl crystal with 1385 ± 1% μg ^{9}Be/g solution.

exposure and steady state maximum erosion, which in Fig. 6 includes a ±1σ error band (~± 15%) in the $^{26}Al/^{10}Be$ production rate ratio (*i.e.* ±9% error per nuclide). Of the 18 samples only BV3.1, DP1.2 and possibly DV5.2, display depressed $^{26}Al/^{10}Be$ ratios that imply periods of burial. For young samples where decay is negligible, the $^{26}Al/^{10}Be$ concentration ratio should be equivalent to the $^{26}Al/^{10}Be$ production rate ratio (*i.e.* 30.7/4.6 = 6.7). For the eight eligible DBV samples with ages less than 0.2 Ma (rejecting BV3.1 and DP1.2), we get 6.4 ± 0.4, consistent with other Southern Hemisphere and Antarctic production rate ratio values (Shulmeister et al., 2005; Bentley et al., 2006).

4.1.1. Pre-last glacial cycle deposits – the Isca and Danum drifts

The Isca and Danum drifts were differentiated by Bockheim et al. (1989) on the basis of surface weathering characteristics and buried paleosols containing in-situ ventifacts. Both drifts contain abundant areas of desert pavement with wind polished and iron stained sandstone boulders. Dolerite ventifacts with well-developed facets are commonly embedded in the pavement surface. A few large sandstone erratics (<4 m) can also be found emplaced on pavement or bedrock with extensive taffoni (cavernous) weathering and wind polishing (desert varnish). The older Isca Drift is widely distributed throughout much of the high elevation and ice distal parts of the DBV and is often found overlain by the younger Danum Drift.

The oldest ^{10}Be ages in our dataset are obtained from the Isca and Danum drifts. Samples BV8.1, DV1.1 and DP6.1 from the Isca Drift have exposure ages of 927 ± 105, 985 ± 113 and 1997 ± 306 ka. While samples collected from the Danum Drift (DP5.1 and DV2.1) have ^{10}Be ages of 637 ± 69 and 454 ± 50 ka. Although the upper limit was not located, our Isca ages may represent the younger portions of a much thicker Plio-Pleistocene advance.

4.1.2. Post-last glacial cycle deposits – the Britannia-I and II drifts

The Britannia Drift is composed entirely of sandstone and dolerite clasts with a mix of weathering features and shapes. The drift sheet forms a patchy cover on the landscape but is widely distributed throughout the DBV and is divided into two units

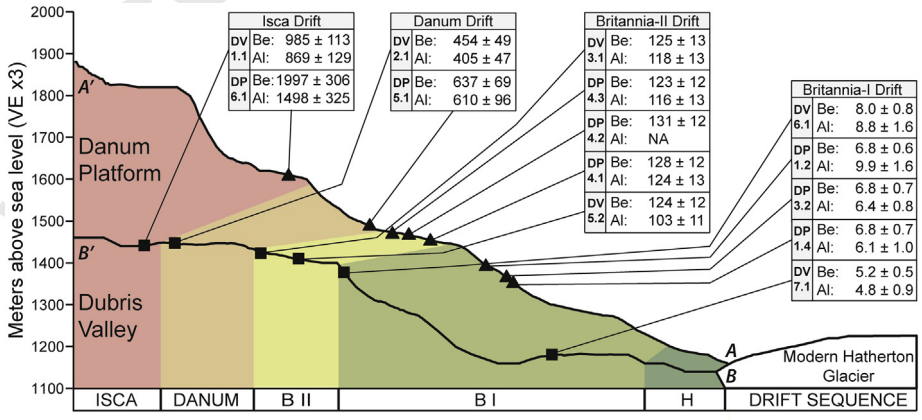

Fig. 5. Schematic representation of elevation vs drift relationship for the Danum Platform (A–A′) and Dubris Valley (B–B′). The Bibra Valley ^{10}Be exposure ages are omitted for clarity (5, 6 and 8 ka for Britannia-I and 927 ka for Isca). Drift contacts are adapted from Bockheim et al. (1989) and ^{10}Be and ^{26}Al exposure ages given in kiloyears (ka). Vertical exaggeration is ×3 and age errors include production rate errors (see Table 3).

Please cite this article in press as: Joy, K., et al., A 2 million year glacial chronology of the Hatherton Glacier, Antarctica and implications for the size of the East Antarctic Ice Sheet at the Last Glacial Maximum, Quaternary Science Reviews (2013), http://dx.doi.org/10.1016/j.quascirev.2013.10.028

Table 3
Dubris and Bibra Valley exposure ages based on a zero erosion model.

Drift sequence [a]	Sample ID	^{10}Be concentration[b] (atm g^{-1}) ($\times 10^3$)	^{26}Al concentration[b] (atm g^{-1}) ($\times 10^3$)	Minimum ^{10}Be exposure age[c,e] (ka)	Minimum ^{26}Al exposure age[d,e] (ka)	^{26}Al/^{10}Be ratio
Britannia I	BV3.1	86 ± 4	465 ± 48	4.9 ± 0.5 (0.2)	3.9 ± 0.5 (0.4)	5.4 ± 0.6
Britannia I	BV9.2	103 ± 4	645 ± 86	5.7 ± 0. 5 (0.2)	5.3 ± 0.8 (0.7)	6.3 ± 0.9
Britannia I	BV4.2	144 ± 5	933 ± 99	7.7 ± 0.7 (0.3)	7.4 ± 1.0 (0.7)	6.5 ± 0.7
Britannia I	DV7.1	90 ± 4	564 ± 92	5.2 ± 0.5 (0.2)	4.8 ± 0.9 (0.7)	6.2 ± 1.1
Britannia I	DV6.1	157 ± 8	1172 ± 189	8.0 ± 0.8 (0.4)	8.8 ± 1.6 (1.4)	7.5 ± 1.3
Britannia I	DP1.4	135 ± 6	822 ± 117	6.8 ± 0.7 (0.3)	6.1 ± 1.0 (0.8)	6.1 ± 0.9
Britannia I	DP3.2	134 ± 7	856 ± 76	6.8 ± 0.7 (0.3)	6.4 ± 0.8 (0.5)	6.4 ± 0.7
Britannia I	DP1.2	134 ± 5	1320 ± 194	6.8 ± 0.6 (0.2)	9.9 ± 1.6 (1.4)	9.8 ± 1.5
Britannia II	DV5.2	2417 ± 57	13313 ± 674	124 ± 12 (4)	103 ± 11 (5)	5.5 ± 0.3
Britannia II	DV3.1	2415 ± 99	14922 ± 790	125 ± 13 (5)	118 ± 13 (6)	6.2 ± 0.4
Britannia II	DP4.3	2540 ± 67	15771 ± 924	123 ± 12 (4)	116 ± 13 (7)	6.2 ± 0.4
Britannia II	DP4.1	2567 ± 81	16337 ± 880	128 ± 12 (4)	124 ± 13 (7)	6.4 ± 0.4
Britannia II	DP4.2	2702 ± 79	NA	131 ± 13 (4)	NA	NA
Danum	DV2.1	8123 ± 406	45059 ± 2187	454 ± 50 (24)	405 ± 47 (23)	5.5 ± 0.4
Danum	DP5.1	11804 ± 318	66957 ± 5191	637 ± 69 (21)	610 ± 96 (63)	5.7 ± 0.5
Isca	BV8.1	16530 ± 393	75987 ± 3719	927 ± 105 (29)	699 ± 97 (47)	4.6 ± 0.3
Isca	DV1.1	16320 ± 470	82718 ± 3966	985 ± 113 (36)	869 ± 129 (62)	5.1 ± 0.3
Isca	DP6.1	30582 ± 758	127838 ± 6150	1997 ± 306 (87)	1498 ± 325 (156)	4.2 ± 0.2

[a] Glacial drifts defined by Bockheim et al. (1989) and confirmed by field mapping in 2009.
[b] Additional 2% error added in quadrature based on reproducibility of AMS standard measurements for both ^{26}Al and ^{10}Be and 1% error in ^{9}Be spike solution concentration. Error in ^{26}Al concentration includes an additional 4% error in ICP-OES measurement of Al concentration in quartz mass.
[c] ^{10}Be decay constant = 5.00×10^{-7} ($t_{½}$ = 1.387 Ma) ^{10}Be SLHL production rate = 4.60 ± 0.42 atoms/g/year.
[d] ^{26}Al decay constant = 9.90×10^{-7} ($t_{½}$ = 0.70 Ma), ^{26}Al SLHL production rate = 30.7 ± 2.8 atoms/g/year.
[e] Age error includes a 9% uncertainty in sea-level high latitude production rates in quadrature with total analytical AMS error. Errors given in parenthesis are analytical age errors only.

(Bockheim et al., 1989). The Britannia-II Drift extends up to 4 km into the DBV from the modern ice margin and overlies the Danum Drift displaying a distinct boulder belt moraine at its most distal limit. The Britannia-I Drift also covers a wide area and forms a patchy drift sheet overlying the Britannia-II Drift. However, the boundaries of Britannia-I Drift are poorly defined and in many places indistinguishable. While the drifts show similar sedimentology, a number of key differences are observed in the field. The Britannia-II Drift contains no perched erratics, yet in the Britannia-I Drift, they are common, with occasional fresh abrasions and small deposits of sand and clasts noted on the stoss side of some boulders, typical of cold-based glacial deposition (Atkins et al., 2002; Atkins, 2013) indicating that the two drifts were deposited by different glacial events.

Our exposure age results confirm the subdivision of the Britannia Drift into two units, an older (Britannia-II Drift) and younger deposit (Britannia-I Drift) (Fig. 7). The Britannia-II exposure ages across the entire DBV are grouped tightly ranging from 123 to 131 ka, a mean age of 126.0 ± 3.2 ka (1σ error, $n = 5$) placing this deglaciation phase of the Hatherton Glacier at Termination-II and within MIS-5. Although we have no independent measure of the mean erosion rate for these Beacon Sandstone erratics, applying a reasonable value of 0.5 mm ka^{-1} based on other Antarctic studies, would raise the non-zero exposure age from 126 to 133 ka. An upper limit choice would be 1.0 mm ka^{-1} taking the Britannia-II age to maximum of 145 ka. The younger Britannia-I Drift ages range from 4.9 to 8.0 ka with a mean age of 6.5 ± 1.2 ka (1σ error, $n = 8$) indicating glacial retreat in the mid-Holocene period, similar to the finding of Stone et al. (2003) in Marie Byrd Land. Cumulative probability plots (Lowell, 1995) were also used to analyse grouped Britannia Drift ages (Fig. 7b and c). Five samples from Britannia-II Drift are well defined by a single normal distribution with a 1σ error of only 3%. However, the Britannia-I Drift ages display a quasi–bimodal profile with enhanced probability in the ranges ~7.5 ± 1.0 ka and at 5.5 ± 0.5 ka. It is difficult to determine if this bi-modality relates to two glacial events during the early to mid-Holocene or is a result of insufficient sampling and/or a large geological variability in age determination.

5. Discussion

5.1. Isca and Danum drifts

As the ^{26}Al/^{10}Be paired data shows no clear burial signal in the older samples, we take the simplest case that ^{10}Be concentrations of all samples represent a continuous exposure history and that the highest elevations in the DBV have not been overridden by ice for at least 1 Ma (or if using a maximum age model 2 Ma). The Isca Drift was deposited by an enlarged Hatherton Glacier at least 500 m above its modern elevation which advanced 4–5 km up into the DBV. Using a minimum, zero-erosion rate age model, we assign a minimum deglaciation age of 930 ka for the deposition of the Isca Drift. Based on the limited number of samples from the Danum Drift ($n = 2$), a minimum age of ~450 ka is assigned which suggests deglaciation prior to MIS 11. The age spread recorded between the two older drifts suggest periods of either static ice volume or very slow deglaciation. The age range for the Danum and Isca drifts is in stark contrast to the strongly clustered ages observed in the younger drifts. Exposure ages within the Britannia Drifts show little to no variation between valleys or with altitude, suggesting episodes of rapid loss of ice via sublimation across the DBV area.

Our ^{10}Be chronology at DBV is in full agreement with that deduced from Lake Wellman by Storey et al. (2010). At Lake Wellman, exposure ages from Isca Drift ranged from 930 to 2275 ka and while the Danum Drift was relatively unconstrained in their dataset, the preferred interpretation was ~630 ka though a minimum age of 220 ka was still plausible. The combined set of exposure ages from Lake Wellman and the DBV concurs with the Bockheim et al. (1989) conclusion that each of these drifts was deposited at similar times at both DBV and at Lake Wellman. However, our new ^{10}Be chronology demonstrates unequivocally that the drifts are far older than their previously assumed minimum MIS-6 (185–130 ka) age.

5.2. Britannia-II drift

Based on ^{10}Be exposure ages, the Britannia-II Drift, inferred to be LGM in age by Bockheim et al. (1989), is older with a mean age of

Please cite this article in press as: Joy, K., et al., A 2 million year glacial chronology of the Hatherton Glacier, Antarctica and implications for the size of the East Antarctic Ice Sheet at the Last Glacial Maximum, Quaternary Science Reviews (2013), http://dx.doi.org/10.1016/j.quascirev.2013.10.028

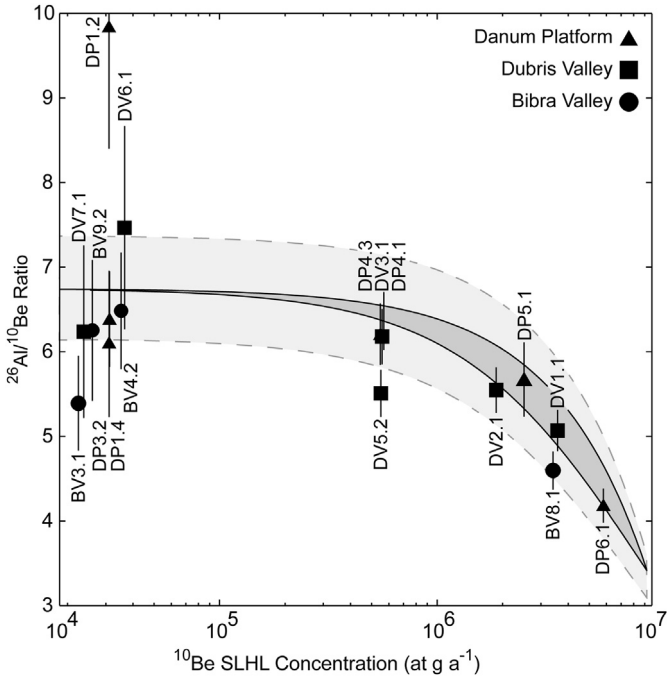

Fig. 6. Dual nuclide plot of all 17 samples from Danum Platform, Dubris and Bibra valleys showing steady state erosion island bordered by a 9% error in SLHL ^{26}Al and ^{10}Be production rate measurements (i.e. 30.7 and 4.6 atm/g/a respectively). All samples, except DP1.2, fall within the shaded region that represents continuous exposure and absence of any complex burial history. The shaded $\pm 1\sigma$ uncertainty region is determined from the error in the measured average ^{26}Al/^{10}Be concentration ratio (6.7 ± 0.4) of samples exposed for <100 ka (or 5×10^6 atoms g^{-1}) and which is effectively equivalent to the ^{26}Al/^{10}Be production rate ratio. Sample DP4.2 has not been plotted due to failed ^{27}Al measurement.

~126 ka, suggesting an MIS-5 deglaciation phase coinciding with a warming Antarctic climate commensurate with Termination-II (Stenni et al., 2010). The MIS-5 Britannia age at DBV differs significantly from the 35 ± 1.5 ka age for the Britannia-II Drift provided by Storey et al. (2010). One explanation may be due to the lack of differentiation between the older and younger phases of the Britannia deposits at Lake Wellman, which Bockheim et al. (1989) mapped as a single homogenous drift sheet, in contrast to the clear geomorphic difference between the Britannia-I and II observed in the DBV.

Although identifying the Britannia-I from the Britannia-II via colour, lithology and weathering features was not always possible, the presence of perched glacial erratics on larger boulders or on bedrock was a key indicator in distinguishing the two deposits. Exposure ages from all the eight Britannia-I samples give early to mid-Holocene ages, in agreement with the minimum radiocarbon age of 6 ka cal BP (Bockheim et al., 1989) from a low elevation sample, QL-1424 at ~1200 masl in the Bibra Valley (See Fig. 4). The large age difference at DBV between Britannia-I (~6 ka) and Britannia-II (~126 ka) clearly supports the classification of the Britannia drifts into two different phases of Hatherton Glacier and/or ice sheet volume changes. We suggest that cold-based Hatherton Glacier ice advanced over a portion of the underlying Britannia-II Drift with only minimal deposition or disturbance (Britannia-I Drift). This advance acted as a glacial 'salt and pepper shaker' depositing Britannia-I erratics on the older Britannia-II Drift, creating a composite drift. Additional evidence of this overriding includes the presence of crude abrasion on the stoss side of weathered boulders and occasional overturned or rotated boulders within the Britanna-I Drift limit. Similar subtle features related to cold-based glacier overriding (Atkins et al., 2002; Lloyd Davies et al., 2009; Atkins, 2013) and minimal reworking of older surfaces (Bockheim, 2010) have been documented in other areas on the TAMs.

5.3. Britannia-I and Hatherton drifts

Compared to the narrow deglaciation age for the Britannia-II Drift, the Britannia-I Drift ages have a distribution that can be interpreted in two ways: a single population with a mean age of 6.5 ± 1.2 ka (1σ error, $n = 8$) suggesting a single stage of

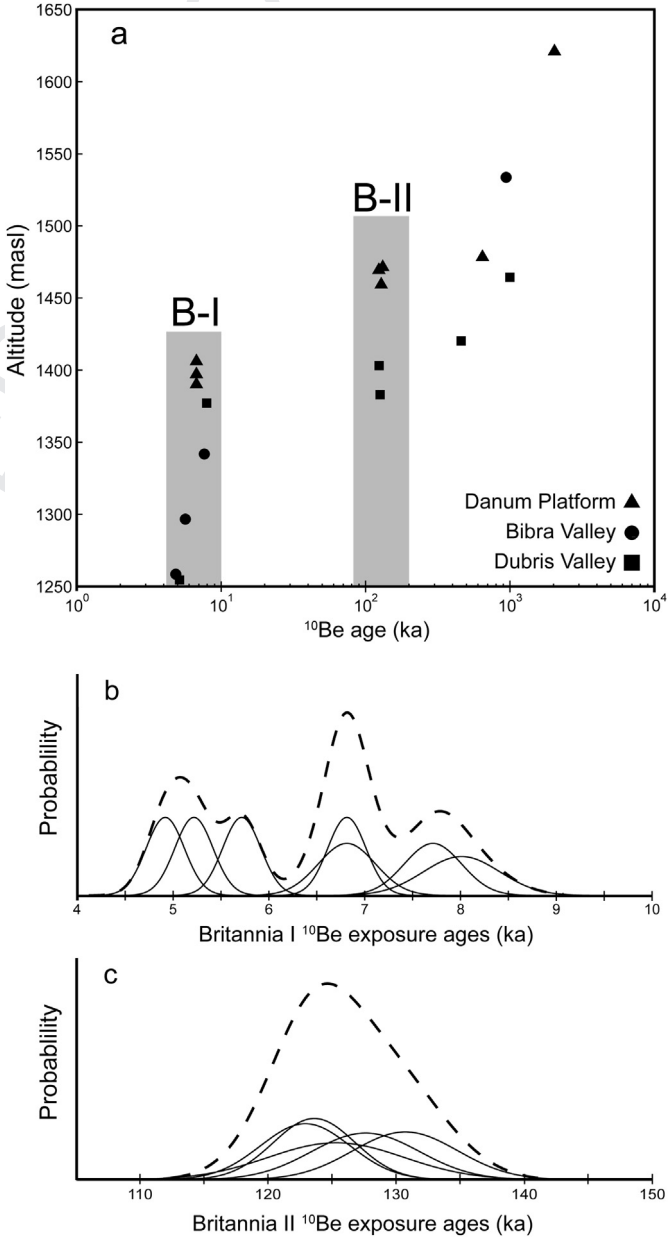

Fig. 7. Elevation versus ^{10}Be exposure ages for samples from the Danum Platform, Dubris and Bibra valleys (a). The average exposure age error (external error, see Table 3) is 10% or approximately the size of the point markers for all but the oldest sample (DP6.1, 15.3%). The shaded regions contain samples belonging to the Britannia-I (B-I) and Britannia-II (B-II) drifts. b and c are density distribution plots for Britannia drift ^{10}Be ages. Solid black lines are based on 1σ gaussian errors derived from the total analytical (internal) error per sample, ranging from 2.6% to 5%. The dashed lines are cumulative distributions for the all samples designated as Britannia-I (b, mean $\pm 1\sigma$, 6.5 ± 1.2 ka) and Britannia-II (c, mean $\pm 1\sigma$, 126.0 ± 3.2 ka).

Please cite this article in press as: Joy, K., et al., A 2 million year glacial chronology of the Hatherton Glacier, Antarctica and implications for the size of the East Antarctic Ice Sheet at the Last Glacial Maximum, Quaternary Science Reviews (2013), http://dx.doi.org/10.1016/j.quascirev.2013.10.028

deglaciation occurred or alternatively, a multi-stage retreat with peaks at 7.5 and 5.5 ka continuing until 4.8 ka. Our preferred interpretation is that of the multi stage deglaciation model, which is supported by mapping the glacial geomorphology from satellite imagery and field observations which show numerous small moraine ridges across the Britannia-I Drift in proximity to the current ice-edge of Hatherton Glacier. Combined with the clear bimodal ^{10}Be exposure ages for the Britannia-I Drift, we propose a period of slow retreat from an advance prior to 7.8 ka and weak advances or stillstands at 6.8 and 5.2 ka where material at the ice contact margin accumulated, forming boulder-belt moraine ridges. As the Britannia-I Drift was not mapped in Lake Wellman, there are no corresponding ^{10}Be ages from Storey et al. (2010). The Hatherton Drift runs parallel along the contact margin of the Hatherton Glacier, but was not sampled in the DBV. We therefore use the ^{10}Be dates of 0.7–2.3 ka from Storey et al. (2010) at Lake Wellman which suggest a retreat from an advance prior to 2.3 ka. These results are consistent with both the minimum ^{10}Be age of 4.8 ka for the Brittania-I Drift and the minimum radiocarbon age of ~6 ka (Bockheim et al., 1989). Holocene ages are also identified in glacial drifts 850 km south of the DBV at the Reedy Glacier (85.5°S). At EAIS proximal sites (Mims Spur and Hatcher Bluff), the Reedy-III Drift was deposited at ~4–9 ka during the last retreat from a Reedy Glacier 140–50 m thicker than present (Todd et al., 2010). The presence of thickened ice at these sites is suggested to be caused by a short lived glacial maxima at ~8.6 ka and possibly also at 3.5 ka (Todd et al., 2010). Therefore, given the overlap in age ranges, we correlate the Reedy-III Drift (at EAIS proximal sites) with the Britannia-I Drift, instead of the previously assigned Britannia-II Drift (Bockheim et al., 1989; Moriwaki et al., 1992).

5.4. Hatherton Glacier ice thickness reduction since mid-Pleistocene and the size of LGM ice in the DBV

The elevation and position of drift contacts within the DBV allows inferences to be made concerning Hatherton Glacier ice elevations during previous glacier high stands. The boulder belt moraines and boundaries between the four drifts trace out complex elevation contours which define the up-valley expansion of the Hatherton Glacier. Within the DBV these margins are more ice distal than their counterparts on the Danum Platform. When measured against the surface geometry of the modern Hatherton Glacier margin, estimates can be made of changes in ice thicknesses over the past ~1 Ma based on the ^{10}Be glacial chronology previously described.

From its maximum advance into the DBV since at least ~0.5 Ma (*i.e.* MIS-16), we estimate a cumulative reduction in Hatherton ice thickness of about 400 m. A reduction of ~100 m occurred between the deposition of the Danum and subsequent Britannia-II Drift at about 120 ka (MIS-6 or 5) and only a further 50 m from Britannia-II to Britannia-I at the early Holocene. In contrast, over the next 5 kiloyears across the mid-Holocene, the Hatherton Glacier ice thickness is reduced by ~220 m at deposition of the Hatherton Drift and finally, ~30 m over the past few kiloyears to today's present margin. We attribute the difference in ^{10}Be exposure ages observed in the Britannia drifts between the DBV (~7 & 125 ka) and Lake Wellman (~35 ka) as the result of the different glacier dynamics controlling WAIS and EAIS ice sheet flow into the Hatherton Glacier. The proximity to the EAIS may have resulted in the DBV having a far more dynamic and rapid response to ice-sheet fluctuations than that of Lake Wellman, ~30 km downstream and hence the differentiation between Britannia-II and Britannia-I drifts is more discernible.

We note that in both the study by Storey et al. (2010) and in this work, identification of drift or other glacial deposits with an unequivocal LGM exposure age was not observed regardless of age-elevation model. The Britannia-II Drift, previously assumed to be LGM by Bockheim et al. (1989), clearly shows minimum MIS-5 exposure ages and the Britannia-I Drift at DBV is early-mid Holocene. At Lake Wellman, the youngest Britannia (I and II) age was 35 ka, whilst that for the Hatherton Drift was <2 ka. At both DBV and Lake Wellman, there is neither direct field evidence nor a clustered population of exposure ages representing an ice advance at the LGM. Therefore, the question must then be posed as to where the maximum ice limits were during the LGM period and why are they absent within the five mapped drifts which span the full time period between mid-Holocene to early Pleistocene. Our data indicate that during the LGM, no EAIS ice entered the Hatherton Glacier suggesting that LGM ice thickness of the EAIS in this locality is similar to today's observed ice volume or possibly even smaller. This is in contrast to that predicted by the Denton and Hughes (2002) model and more in agreement with Golledge and Levy (2011), Mackintosh et al. (2011) and Hein et al. (2011) who suggest smaller East Antarctic ice volumes during the LGM, particularly in the ice sheet interiors (Lily et al, 2010). The SED results suggest Q1 that Hatherton Glacier ice incursion into the DBV is predominantly influenced by EAIS ice overspill through the TAMs. This is in contrast to the ice history at Lake Wellman, situated in the lower reaches of the DHGS where the Hatherton Glacier is far more sensitive to ice volume changes resulting from WAIS expansion. At this downstream location, the buttressing of the DHGS by a grounded WAIS caused thickening of ice to propagate upstream past the confluence of the Darwin and Hatherton glaciers towards Lake Wellman (Storey et al., 2010). Other factors, such differences in valley geometry, basal topography of the Hatherton Glacier compared to adjacent outlet glaciers and unknown changes in EAIS flow over the Transantarctic Mountains in the past may also contribute to reducing LGM ice volume in the Hatherton Glacier.

6. Conclusions

Surface exposure ages from glacial deposits in the Dubris and Bibra valley region show an overall but irregular decrease in Hatherton Glacier ice volume at least over the past 1–2 Ma as recorded by minimum exposure ages from the Isca Drift. The decline in ice volume was punctuated by at least four glacial advance/retreat events (Danum, Britannia-II, Britannia-I and Hatherton Drifts). Ranging from the early-Pleistocene to the mid-Holocene, our exposure ages cover a time span from 1997 to 5 ka.

Minimum exposure ages for the four sampled drifts show a decrease in age with decreasing elevation (1620–1255 masl) and distance to the modern ice margin. The oldest glacial retreat events are represented by the Isca Drift, occurring between 0.93 and 2 Ma, followed by the subsequent deposition of the Danum Drift, sometime during 0.45–0.64 Ma. Younger glacial events represented by the Britannia-II and Britannia-I drifts have clearly different geomorphology and were deposited at 125 and 5–8 ka respectively. These age groups are consistent with the exposure age based chronology established at Lake Wellman (Storey et al., 2010) and follow the glacial stratigraphy deduced by Bockheim et al. (1989), but differ significantly in their absolute age ranges.

Within the Dubris and Bibra valleys, proximal to the EAIS in the upper Hatherton Glacier, our results show that:

- Mapped drifts were deposited by cold-based ice at the margins of the Hatherton Glacier which periodically expanded into the DBV.
- The Hatherton Glacier retreated from its high-stand position no later than the minimum Isca Drift age of 0.99 Ma. Approximately 400 vertical metres of ice reduction have occurred since the

Please cite this article in press as: Joy, K., et al., A 2 million year glacial chronology of the Hatherton Glacier, Antarctica and implications for the size of the East Antarctic Ice Sheet at the Last Glacial Maximum, Quaternary Science Reviews (2013), http://dx.doi.org/10.1016/j.quascirev.2013.10.028

mid-Pleistocene and ~50% of this loss in ice surface elevation (*i.e.* ~200 m) has occurred since the early -Holocene at about 7–8 ka.

- The Britannia-II Drift, previously defined as LGM based on limiting radiocarbon ages of ~10 ka cal BP, correlates to a retreat from a MIS-5e highstand with a mean zero-erosion exposure age of 126.0 ± 2.9 ka (1σ error, $n = 5$). The Britannia-I Drift shows a bimodal retreat during the early to mid-Holocene occurring at ~7.5 and 5.5 ka, although a single retreat at 6.5 ± 1.2 ka is also plausible.
- No evidence of LGM ice incursion from the Hatherton into the DBV was identified from our ^{10}Be exposure ages, suggesting that the EAIS during the LGM may have been lower than observed today. This finding is in agreement with the Lake Wellman results of Storey et al. (2010).

Acknowledgements

This research was funded by grants from Antarctica New Zealand for logistic support, the Australian Institute of Nuclear Science and Engineering and ANSTO's CcASH Project (to DF) for AMS measurements (AINGRA09009). We thank Rob Spiers and James Oram at the University of Canterbury cosmogenic preparation lab and Charles Mifsud and Toshiyuki Fujioka at ANSTO. We also thank David Sugden and Gary Wilson for their constructive comments which greatly enhanced the final manuscript. KJ also thanks AINSE, Helicopters NZ and Gateway Antarctica for their post-graduate research scholarships.

References

Ackert, R.P., Putnam, A.E., Mukhopadhyay, S., Pollard, D., DeConto, R.M., Kurz, M.D., Borns, H.W., 2013. Controls on interior West Antarctic Ice Sheet elevations: inferences from geologic constraints and ice sheet modelling. Quat. Sci. Rev. 65, 26–38. http://dx.doi.org/10.1016/j.quascirev.2012.12.017.

Anderson, B., Hindmarsh, R.C.A., Lawson, W.J., 2004. A modelling study of the response of Hatherton Glacier to Ross Ice Sheet grounding line retreat. Glob. Planet. Change 42, 143–153.

Anderson, J.B., 2002. The Antarctic Ice Sheet during the Last Glacial Maximum and its subsequent retreat history: a review. Quat. Sci. Rev. 21, 49–70.

Atkins, C.B., Barrett, P.J., Hicock, S.R., 2002. Cold glaciers erode and deposit: evidence from Allan Hills, Antarctica. Geology 30, 659–662.

Atkins, C.B., 2013. Geomorphological Evidence of Cold-based Glacier Activity in South Victoria Land, Antarctica. In: Geological Society, London, Special Publications, vol. 381.

Balco, G., Stone, J.O., Lifton, N., Dunai, T.J., 2008. A complete and easily accessible means of calculating surface exposure ages or erosion rates from ^{10}Be and ^{26}Al measurements. Quat. Geochronol. 3 (3), 174–195.

Bentley, M.J., Fogwill, C.J., Kubik, P.W., Sugden, D.E., 2006. Geomorphological evidence and cosmogenic ^{10}Be/^{26}Al exposure ages for the Last Glacial Maximum and deglaciation of the Antarctic Peninsula Ice Sheet. Geol. Soc. Am. Bull. 118 (9–10), 1149–1159.

Bockheim, J.G., Wilson, S.C., Denton, G.H., Andersen, B.G., Stuiver, M., 1989. Late Quaternary ice-surface fluctuations of Hatherton Glacier, Transantarctic Mountains. Quat. Res. 31 (2), 229–254.

Bockheim, J.G., 2010. Soil preservation and ventifact recycling from dry-based glaciers in Antarctica. Antarct. Sci. 22 (4), 409–417.

Brook, E.J., Kurz, M.D.T., Ackert, R.P., Raisbeck, G.M., Yiou, F., 1995. Cosmogenic nuclide exposure ages and glacial history of late Quaternary Ross Sea Drift in McMurdo Sound, Antarctica. Earth Planet. Sci. Lett. 131 (1–2), 41–56.

Bromley, G.R.M., Hall, B.L., Stone, J.O., Conway, H., Todd, C.E., 2010. Late Cenozoic deposits at Reedy Glacier, Transantarctic Mountains: implications for former thickness of the West Antarctic Ice Sheet. Quat. Sci. Rev. 29 (3–4), 384–398. http://dx.doi.org/10.1016/j.quascirev.2010.02.001.

Child, D., Elliott, G., Mifsud, C., Smith, A.M., Fink, D., 2000. Sample processing for earth science studies at ANTARES. Nucl. Instrum. Methods Phys. Res. B 172 (1–4), 856–860.

Conway, H., Hall, B.L., Denton, G.H., Gades, A.M., Waddington, E.D., 1999. Past and future grounding-line retreat of the West Antarctic ice sheet. Science 286, 280–283.

Denton, G.H., 1979. Glacial history of the Byrd-Darwin Glacier area, Transantarctic Mountains. Antarct. J. U.S. 14 (5), 57–58.

Denton, G.H., Marchant, D.R., 2000. The geologic basis for a reconstruction of a grounded ice sheet in McMurdo Sound, Antarctica, at the Last Glacial Maximum. Geogr. Ann. A 82 (2–3), 167–211.

Denton, G.H., Hughes, T., 2002. Reconstructing the Antarctic Ice Sheet at the Last Glacial Maximum. Quat. Sci. Rev. 21 (1–3), 193–202.

Denton, G.H., Sugden, D.E., 2005. Meltwater features that suggest Miocene ice-sheet overriding of the Transantarctic Mountains in Victoria Land, Antarctica. Geogr. Ann. A 87 (1), 67–85.

Fink, D., Mckelvey, B., Hambrey, M.J., Fabel, D., Brown, R., 2006. Pleistocene deglaciation chronology of the Amery Oasis and Radok Lake, northern Prince Charles Mountains, Antarctica. Earth Planet. Sci. Lett. 243 (1–2), 229–243.

Fink, D., Smith, A.M., 2007. An inter-comparison of ^{10}Be and ^{26}Al AMS reference standards and the ^{10}Be half-life. Nucl. Instrum. Methods Phys. Res. B 259 (1), 600–609.

Fogwill, C.J., Hein, A.S., Bentley, M.J., Sugden, D.E., 2012. Do blue-ice moraines in the Heritage Range show the West Antarctic ice sheet survived the last interglacial? Palaeogeogr. Palaeoclimatol. Palaeoecol. 335–336, 61–70.

Golledge, N.R., Levy, R.H., 2011. Geometry and dynamics of an East Antarctic Ice Sheet outlet glacier, under past and present climates. J. Geophys. Res. 116 (F3), F03025.

Golledge, N.R., Fogwill, C.J., Mackintosh, A., Buckley, K.M., 2012. Dynamics of the last glacial maximum Antarctic ice-sheet and its response to ocean forcing. PNAS 1309 (40), 16052–16056.

Gore, D.B., Rhodes, E.J., Augustinus, P.C., Leishman, M.R., Colhoun, E.A., Rees-Jones, J., 2001. Bunger Hills, East Antarctica: Ice free at the Last Glacial Maximum. Geology 29 (12), 1103–1106.

Gosse, J.C., Phillips, F.M., 2001. Terrestrial in-situ cosmogenic nuclides: theory and application. Quat. Sci. Rev. 20 (14), 1475–1560.

Hall, B.L., Denton, G.H., Hendy, C.H., 2000. Evidence from Taylor Valley for a grounded ice sheet in the Ross Sea, Antarctica. Geogr. Ann. A 82 (2–3), 275–303.

Hall, B.L., Denton, G.H., Stone, J.O., Conway, H., 2013. History of the Grounded Ice Sheet in the Ross Sea Sector of Antarctica during the Last Glacial Maximum and the Last Termination. In: Geological Society, London, Special Publications, vol. 381. http://dx.doi.org/10.1144/SP381.5.

Haskell, T.R., Orombelli, G., Prebble, W.M., 1964. Basement and sedimentary geology of the Darwin Glacier area. In: ADIE, J.R. (Ed.), SCAR – IUGS. Symposium of Antarctic Geology. Cape Town, South Africa.

Hein, A., Fogwill, C., Sugden, D., Xu, S., 2011. Glacial/interglacial ice-stream stability in the Weddell Sea embayment, Antarctica. Earth Planet. Sci. Lett. 307 (1), 211–221.

Korschinek, G., Bergmaier, A., Faestermann, T., Gerstmann, U.C., Knie, K., Rugel, G., Wallner, A., Dillmann, I., Dollinger, G., Von Gostomski, C.L., 2010. A new value for the half-life of ^{10}Be by heavy-ion elastic recoil detection and liquid scintillation counting. Nucl. Instrum. Methods Phys. Res. B 268 (2), 187–191.

Lewis, A.R., Marchant, D.R., Ashworth, A.C., Hemming, S.R., Machlus, M.L., 2007. Major middle Miocene global climate change: evidence from East Antarctica and the Transantarctic Mountains. Geol. Soc. Am. Bull. 119 (11), 1449–1461.

Lilly, K., Fink, D., Fabel, D., Lambeck, K., 2010. Pleistocene dynamics of the interior East Antarctic ice Sheet. Geology 38, 703–706.

Lloyd Davies, M.T., Atkins, C.B., Van der Meer, J.M., Barrett, P.J., Hicock, S.R., 2009. Evidence for cold-based glacial activity in the Allan Hills, Antarctica. Quat. Sci. Rev. 28, 3124–3137.

Lowell, T.V., 1995. The application of radiocarbon age estimates to the dating of glacial sequences: an example from the Miami sublobe, Ohio, U.S.A. Quat. Sci. Rev. 14, 85–99.

Mackintosh, A., Golledge, N.R., Domack, E.W., Dunbar, R., Leventer, A., White, D.A., Pollard, D., DeConto, R.M., Fink, D., Zwartz, D., Gore, D.B., Lavoie, C., 2011. Retreat of the East Antarctic Ice Sheet during the last glacial termination. Nat. Geosci. 4 (3), 195–202.

Mackintosh, A., White, D.A., Fink, D., Gore, D.B., Pickard, J., Fanning, P.C., 2007. Exposure ages from mountain dipsticks in Mac. Robertson Land, East Antarctica, indicate little change in ice-sheet thickness since the Last Glacial Maximum. Geology 35 (6), 551–554.

Marchant, D.R., Denton, G.H., Bockheim, J.G., Wilson, S.C., Kerr, A.R., 1994. Quaternary changes in level of the upper Taylor Glacier, Antarctica: implications for paleoclimate and East Antarctic Ice Sheet dynamics. Boreas 23, 29–43.

McKay, R., Browne, G., Carter, L., Cowan, E., Dunbar, G., Krissek, L., Naish, T., Powell, R., Reed, J., Talarico, F., Wilch, T., 2009. The stratigraphic signature of the late Cenozoic Antarctic Ice Sheets in the Ross Embayment. Geol. Soc. Am. Bull. 121 (11–12), 1537–1561.

McKay, R.M., Naish, T.R., Powell, R., Barrett, P.J., Scherer, R.P., Talarico, F., Kyle, P., Monien, D., Kuhn, G., Jackolski, C., Williams, T., 2012. Pleistocene variability of Antarctic Ice Sheet extent in the Ross Embayment. Quat. Sci. Rev. 34, 93–112.

Mifsud, C., Fujioka, T., Fink, D., 2012. Extraction and purification of quartz in rock using hot phosphoric acid for in situ cosmogenic exposure dating. Nucl. Instrum. Methods Phys. Res. B 294, 203–207.

Moriwaki, K., Yoshida, Y., Harwood, D., 1992. Cenozoic glacial history of Antarctica—a correlative synthesis. In: Yoshida, Y., Kaminuma, K., Shiraishi, K. (Eds.), Recent Progress in Antarctic Earth Science. Terra Scientific Publishing, Toyko, pp. 773–780.

Nishiizumi, K., 2004. Preparation of ^{26}Al AMS standards. Nucl. Instrum. Methods Phys. Res. B 223–224 (0), 388–392.

Nishiizumi, K., Imamura, M., Caffee, M., Southon, J., Finkel, R.C., Mcaninch, J., 2007. Absolute calibration of ^{10}Be AMS standards. Nucl. Instrum. Methods Phys. Res. B 258 (2), 403–413.

Please cite this article in press as: Joy, K., et al., A 2 million year glacial chronology of the Hatherton Glacier, Antarctica and implications for the size of the East Antarctic Ice Sheet at the Last Glacial Maximum, Quaternary Science Reviews (2013), http://dx.doi.org/10.1016/j.quascirev.2013.10.028

Peltier, W.R., Fairbanks, R.G., 2006. Global glacial ice volume and Last Glacial Maximum duration from an extended Barbados sea level record. Quat. Sci. Rev. 25 (23–24), 3322–3337.

Pollard, D., DeConto, R.M., 2009. Modelling West Antarctic Ice Sheet growth and collapse through the past five million years. Nature 458, 329–332.

Putnam, A.E., Schaefer, J.M., Barrell, D.J.A., Vandergoes, M., Denton, G.H., Kaplan, M.R., Finkel, R.C., Schwartz, R., Goehring, B.M., Kelley, S.E., 2010. In-situ cosmogenic ^{10}Be production-rate calibration from the Southern Alps, New Zealand. Quat. Geochronol. 5 (4), 392–409.

Shipp, S., Anderson, J.B., Domack, E.W., 1999. Late Pleistocene–Holocene retreat of the west Antarctic ice-sheet system in the Ross Sea: Part 1—Geophysical results. Geol. Soc. Am. Bull. 111 (10), 1517–1536.

Shulmeister, J., Fink, D., Augustinus, P.C., 2005. A cosmogenic nuclide chronology of the last glacial transition in North-West Nelson, New Zealand—new insights in Southern Hemisphere climate forcing during the last deglaciation. Earth Planet. Sci. Lett. 233 (3–4), 455–466.

Staiger, J., Marchant, D.R., Schaefer, J.M., Oberholzer, P., Johnson, J., Lewis, A., Swanger, K., 2006. Plio-Pleistocene history of Ferrar Glacier, Antarctica: implications for climate and ice sheet stability. Earth Planet. Sci. Lett. 243 (3–4), 489–503.

Stenni, B., Blunier, T., Cattani, O., Chappellaz, J., Cheng, H., Dreyfus, G., Edwards, R.L., Falourd, S., Govin, A., Kawamura, K., Johnsen, S.J., Jouzel, J., Landais, A., Lourantou, A., Marshall, G.J., Minster, B., Mudelsee, M., Pol, K., Selmo, E., Waelbroeck, C., 2010. Abrupt change of Antarctic moisture origin at the end of termination II. Proc. Natl. Acad. Sci. 107, 12091–12094.

Stone, J.O., 2000. Air pressure and cosmogenic isotope production. J. Geophys. Res. 105, 753–759.

Stone, J.O., Balco, G., Sugden, D.E., Caffee, M., Sass, L.C., Cowdery, S., Siddoway, C., 2003. Holocene deglaciation of Marie Byrd Land, West Antarctica. Science 299, 99–102.

Storey, B.C., Fink, D., Hood, D., Joy, K., Shulmeister, J., Riger-Kusk, M., Stevens, M.I., 2010. Cosmogenic nuclide exposure age constraints on the glacial history of the Lake Wellman area, Darwin Mountains, Antarctica. Antarc. Sci. 22, 603–618.

Strasky, S., Di Nicola, L., Baroni, C., Salvatore, M.C., Baur, H., Kubik, P.W., Schlüchter, C., Wieler, R., 2008. Surface exposure ages imply multiple low-amplitude Pleistocene variations in East Antarctic Ice Sheet, Ricker Hills, Victoria Land. Antarc. Sci. 21, 59–69.

Sugden, D.E., Bentley, M.J., O Cofaigh, C., 2006. Geological and geomorphological insights into Antarctic Ice Sheet evolution. Philos. Trans. A Math. Phys. Eng. Sci. 364, 1607–1625.

Summerfield, M.A., 1999. Long-term rates of denudation in the Dry Valleys, Transantarctic Mountains, southern Victoria Land, Antarctica based on in-situ-produced cosmogenic ^{21}Ne. Geomorphology 27 (1–2), 113–129.

Swanger, K., Marchant, D.R., Schaefer, J.M., Winckler, G., Head, J.W., 2011. Elevated East Antarctic outlet glaciers during warmer-than-present climates in southern Victoria Land. Glob. Planet. Change 79 (1–2), 61–72.

Talarico, F.M., McKay, R.M., Powell, R.D., Sandroni, S., Naish, T., 2012. Late Cenozoic oscillations of Antarctic ice sheets revealed by provenance of basement clasts and grain detrital modes in ANDRILL core AND-1B. Glob. Planet. Change 96-97, 23–40.

Todd, C.E., Stone, J.O., Conway, H., Hall, B.L., Bromley, G.R.M., 2010. Late Quaternary evolution of Reedy Glacier, Antarctica. Quat. Sci. Rev. 29, 1328–1341.

Tuniz, C., Bird, J.R., Fink, D., Herzog, H.G., 1998. Accelerator Mass Spectrometry: Ultrasensitive Analysis for Global Science, first ed. CRC Press, Boca Raton, Florida, USA.

White, D.A., Fülöp, R.H., Bishop, P., Mackintosh, A., Cook, G., 2011. Can in-situ cosmogenic 14C be used to assess the influence of clast recycling on exposure dating of ice retreat in Antarctica? Quat. Geochronol. 6 (3–4), 289–294.

Yamane, M., Yokoyama, Y., Miura, H., Maemoku, H., Iwasaki, S., Matsuzaki, H., 2011. The last deglacial history of Lützow-Holm Bay, East Antarctica. J. Quat. Sci. 26, 3–6.

Please cite this article in press as: Joy, K., et al., A 2 million year glacial chronology of the Hatherton Glacier, Antarctica and implications for the size of the East Antarctic Ice Sheet at the Last Glacial Maximum, Quaternary Science Reviews (2013), http://dx.doi.org/10.1016/j.quascirev.2013.10.028

B.2 Antarctic Science (2010)

Cosmogenic nuclide exposure age constraints on the glacial history of the Lake Wellman area, Darwin Mountains, Antarctica.

Storey, B. C., Fink, D., Hood, D., Joy, K., Shulmeister, J., Riger-Kusk, M., & Stevens, M. I. (2010). Antarctic Science, 22 (06), 603-618.

Antarctic Science 22(6), 603–618 (2010) © Antarctic Science Ltd 2010 doi:10.1017/S0954102010000799

Cosmogenic nuclide exposure age constraints on the glacial history of the Lake Wellman area, Darwin Mountains, Antarctica

B.C. STOREY[1], D. FINK[2], D. HOOD[1], K. JOY[1], J. SHULMEISTER[3], M. RIGER-KUSK[1] and M.I. STEVENS[4]

[1]*Gateway Antarctica, University of Canterbury, Private Bag 4800, Christchurch, New Zealand*
[2]*Institute for Environmental Research, ANSTO, PMB1, Menai 2234, Australia*
[3]*Geography, Planning and Environmental Management, University of Queensland, St Lucia 4072, Australia*
[4]*South Australian Museum, SA 5000, and School of Earth and Environmental Sciences, University of Adelaide, SA 5000, Adelaide, Australia*
Bryan.storey@canterbury.ac.nz

Abstract: We present direct terrestrial evidence of ice volume change of the Darwin and Hatherton glaciers which channel ice from the Transantarctic Mountains into the Ross Ice Shelf. Combining glacial geomorphology with cosmogenic exposure ages from 25 erratics indicates a pre-LGM ice volume at least 600 m thicker than current Hatherton ice elevation was established at least 2.2 million years ago. In particular, five erratics spread across a drift deposit at intermediate elevations located below a prominent moraine feature mapped previously as demarcating the LGM ice advance limits, give a well-constrained single population with mean ^{10}Be age of 37.0 ± 5.5 ka (1σ). At lower elevations of 50–100 m above the surface of Lake Wellman, a further five samples from within a younger drift deposit range in exposure age from 1 to 19 ka. Our preferred age model interpretation, which is partly dependent on the selection of a minimum or maximum age-elevation model, suggests that LGM ice volume was not as large as previously estimated and constrains LGM ice elevation to be within ± 50 m of the modern Hatherton Glacier ice surface, effectively little different from what is observed today.

Received 9 March 2010, accepted 30 August 2010

Key words: cosmogenic exposure dating, Last Glacial Maximum, Latitudinal Gradient Project

Introduction

The spatial and temporal evolution of past Antarctic ice sheets has had a major influence on the development of polar ecosystems within ice-free regions of Antarctica. The cycle of advance and retreat of Antarctic ice sheets would have necessarily eradicated most terrestrial life during ice sheet maxima with recolonization following their retreat and possibly longer-term preservation of only a very small subset of flora and fauna (Adams *et al*. 2006, Stevens *et al*. 2006, Convey & Stevens 2007, Convey *et al*. 2008). On the assumption that major continental ice sheet advances, including the Last Glacial Maximum (LGM), overran ice-free habitats and coastal oases, most terrestrial life would have been wiped out, with the exception of sub-surface bacteria. On this basis, one can then postulate that there may be a relationship between the biodiversity of a glacial landscape and its glacial history. A few ice-free terrestrial environments, such as the McMurdo Dry Valleys region, have existed within the Transantarctic Mountains for up to 10–12 million years (Sugden *et al*. 2006), although many more are likely.

However, in order to investigate the idea of a correlation between ice sheet size and biodiversity, the large uncertainties in the extent and thickness of formerly expanded ice sheets (Bentley 1999), particularly at the LGM (Mackintosh *et al*. 2007) require attention. Computer models of the past behaviour of the Antarctic ice sheet based on glaciological, marine and physical inputs have provided conflicting pictures (Bentley 1999, Denton & Hughes 2002, Huybrechts 2002). Confounding these efforts is the scarcity of terrestrial evidence, particularly in East Antarctica, due to the limited number of coastal mountain ice-free regions and their lack of datable material, particularly for radiocarbon dating. In parallel with these modelling uncertainties, reductions in the calculated volumes of the Laurentide and Fennoscandian ice caps appear to account for only a portion of the observed ~120 m rise in global sea level since LGM times.

In the absence of any direct and/or local evidence for the volume of ice in Antarctica at the global LGM, early estimates were mostly based on the difference between known sea level change, and the known (Northern Hemisphere) ice sheets (Nakada & Lambeck 1988). As more direct evidence from the continent becomes increasingly available, estimates of the volume of grounded ice in Antarctica at the LGM are becoming correspondingly much smaller, particularly in East Antarctica. While it is clear from grounding line studies (Conway *et al*. 1999) that there were significant expansions of the West Antarctic Ice Sheet (WAIS) in the Ross Sea region, investigations on the main East Antarctic Ice Sheet (EAIS) have indicated relatively small ice sheet increases during the LGM (Gore *et al*. 2001, Mackintosh *et al*. 2007). Similarly, isostatic rebound along the McMurdo Sound coast based on

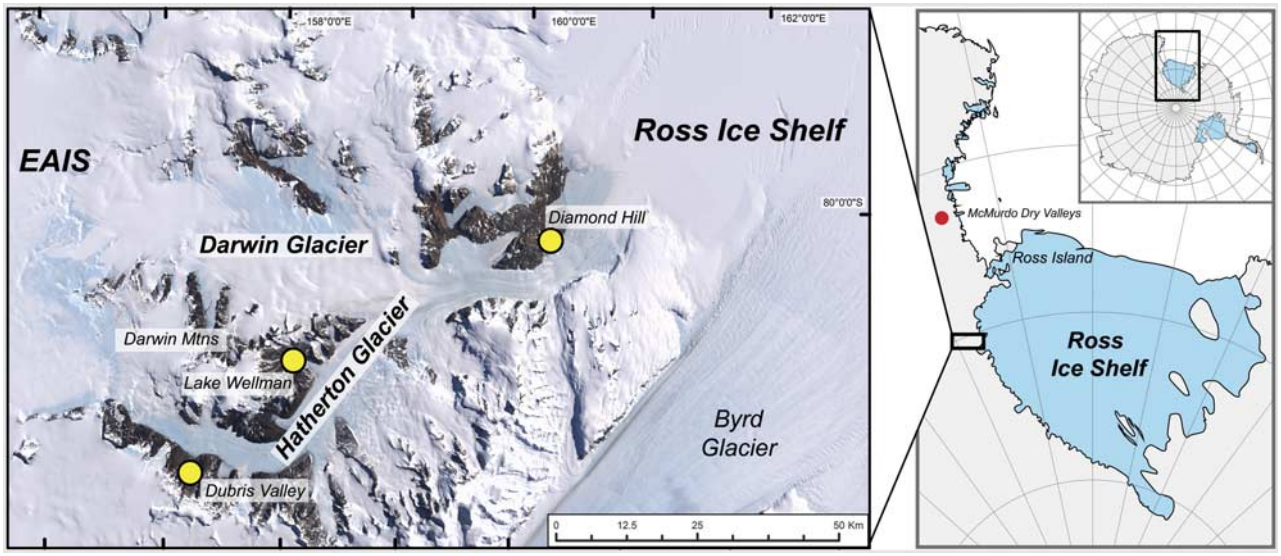

Fig. 1. Regional map (left figure) showing the location of Lake Wellman within the Hatherton and Darwin glacial system which discharges into the Ross Ice Shelf. Inset (right figure) shows location of Hatherton Glacier region (small black rectangle) with respect to Dry Valleys region of the Transantarctic Mountains (red dot). Diamond Hill and Dubris Valley are other field sites targeted for cosmogenic exposure dating.

raised beach elevations (Butler 1999) suggest minimal isostatic loading during the same period.

This paper provides new geological evidence of ice sheet extent and thickness over at least the past few hundred thousand, and perhaps the past two million years within a sector of the Transantarctic Mountains in order to better constrain computer model estimates of palaeo-ice sheet changes. We describe the glacial history based on new *in situ* cosmogenic nuclide exposure ages of an ice-free region in the Darwin Mountains on the edge of the Hatherton Glacier, referred to as the Lake Wellman area (Fig. 1). The location is one of the study sites along the Latitudinal Gradient Project of the Transantarctic Mountains (Howard-Williams *et al.* 2006). The set of 25 cosmogenic exposure ages of erratics collected along two altitudinal transects allows estimates of ice volume changes of the Hatherton Glacier which, at the spatial resolution examined here, constrains ice sheet models and provides input into the biogeographic and evolutionary history of the Darwin Mountains region. Previous work from the Lake Wellman area of the Transantarctic Mountains has been used to support a "big ice" view of Antarctic glacial expansion at the LGM (Denton & Hughes 2002). Our results have strong implications for the role of the Ross Ice Shelf in ice sheet volume calculations at the LGM.

The Lake Wellman area

The Hatherton Glacier flows from the EAIS into the lower Darwin Glacier, which in turn discharges ice into the Ross Ice Shelf (Fig. 1). The Darwin–Hatherton system is an important outflow glacier system that connected the East and West Antarctic ice sheets during previous glacial maxima. The advance and retreat of the Hatherton is recorded in well-preserved glacial moraines that are found in numerous side entrant valleys of the Darwin Mountains along the length of the glacier. Ice-free cirques and valleys in the Darwin Mountains are cut into Palaeozoic sandstones of the Beacon Supergroup and thick dolerite sills of the Jurassic Ferrar Supergroup (Haskell *et al.* 1964). In the vicinity of Lake Wellman, a large currently ice-free area had previously been completely or partially covered by ice (Bockheim *et al.* 1989) resulting in multiple drift sheets deposited by palaeo-advances of the Hatherton Glacier. These deposits were mapped in the late 1970s by Bockheim *et al.* (1989) who identified five drift sheets that occur discontinuously in the ice-free regions extending over an elevation range of about 800 m from the edge of Lake Wellman, which is at 845 m above sea level (m a.s.l.) (Fig. 2). From youngest to oldest, with increasing distance from the present day margins of Lake Wellman, these are: 1) Hatherton, 2) Britannia I, 3) Britannia II, 4) Danum, and 5) Isca.

Currently, the altitude of the ice surface of the Hatherton Glacier at midstream is 960 m a.s.l. Bockheim *et al.* (1989) estimated the upper limit of the Hatherton drift to have been 20–70 m above the present surface of Lake Wellman, the Britannia drift to extend a further 450 m above the Hatherton, and the Danum to be 50–100 m above the Britannia drift limit. This effectively suggested that the total ice thickening at the time of deposition of the Danum drift sheet was about 600 m higher than the current elevation defined by Lake Wellman and given a modern Hatherton ice surface altitude of 960 m a.s.l., an ice thickness of at least 500 m greater than today. The drift sheets are described as lithologically uniform dominated by dolerite and sandstone boulders of variable size and shape

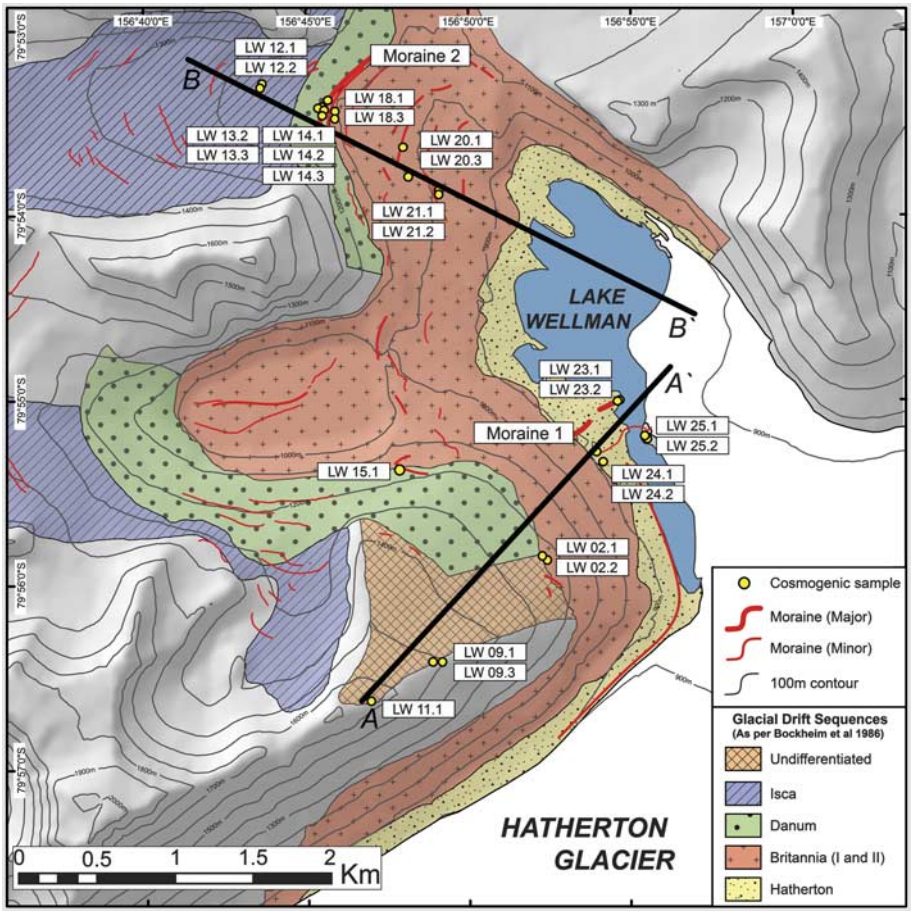

Fig. 2. A geomorphological map of the Lake Wellman area showing the distribution of the four main drift sequences after Bockheim *et al.* (1989). Black bold lines A–A' and B–B' represent altitudinal transects along which samples were collected from glacial deposits for exposure age dating. Sample sites are designated by rectangular boxes labelled as LW xx. Aerial photographs of moraines 1 and 2 are shown in Fig. 4. Hatherton Glacier ice flows from bottom-left to top-right in a direction semi-parallel to transect A–A'.

(Fig. 3) in unconsolidated gravel and sandy matrix. There are a few granitic erratics that have been transported into the area by ice; granite does not crop out locally in the Darwin Mountains. Prominent moraine ridges and boulder lines both separate and occur within the drift sheets (Fig. 2). Individual drift sheets show increasingly poor morphological preservation with distance (i.e. age) from the current ice surface. The percentage of surface modified boulders (varnished, fractured,

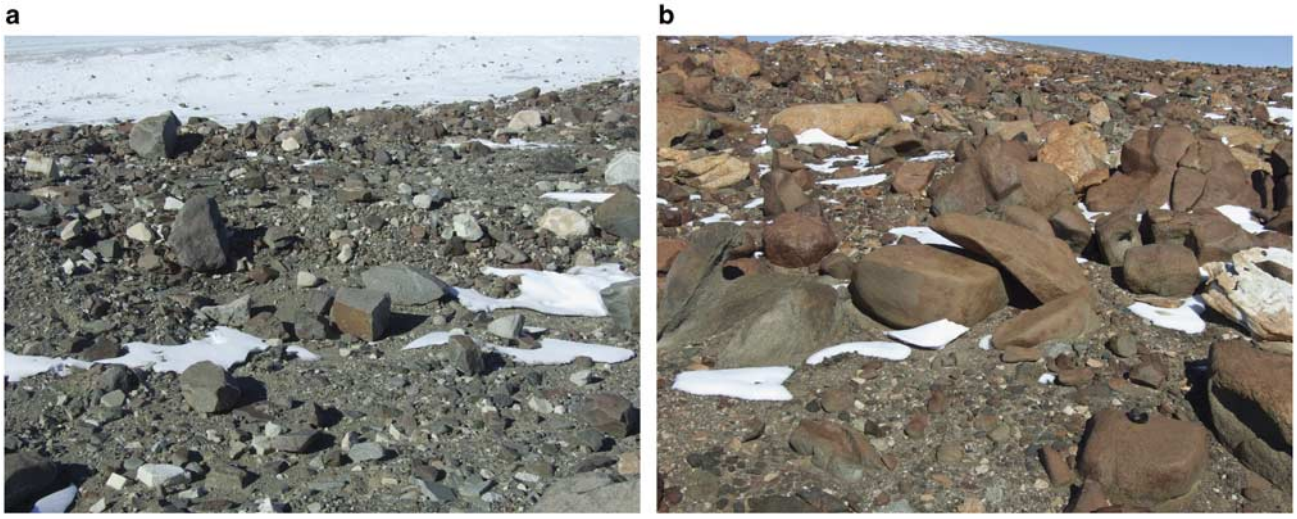

Fig. 3. Photographs showing the surface characteristics of **a.** the Hatherton, and **b.** the Isca drifts. The older Isca drift shows extensive surface weathering and desert tarnish whereas the younger Hatherton drift shows minimal weathering, glacial striations and more angular debris.

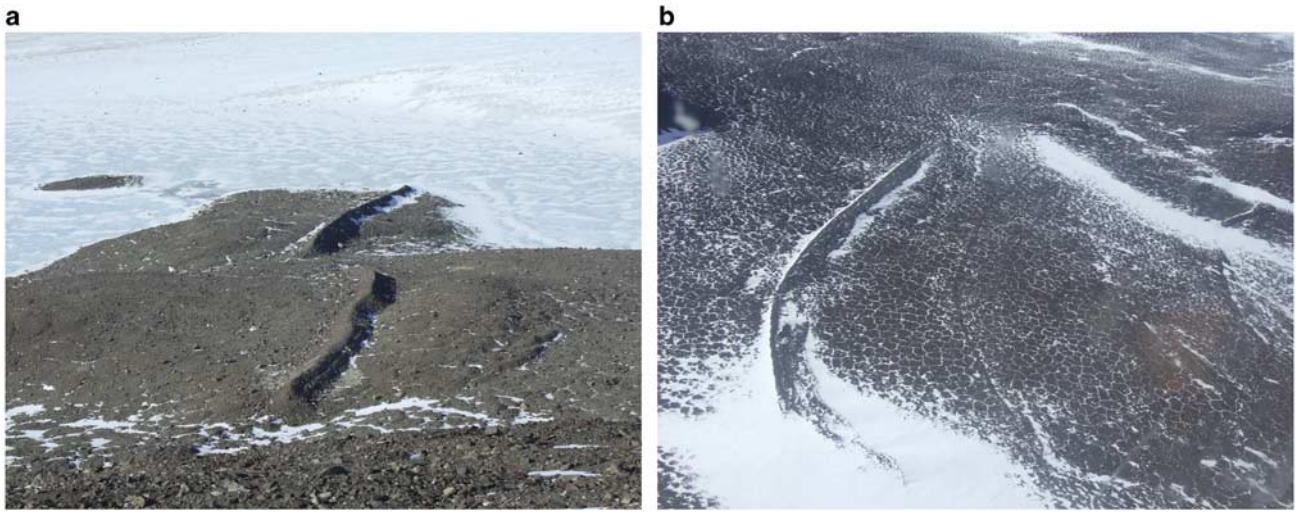

Fig. 4. Photographs showing the main features of **a.** Moraine 1 on the Hatherton drift, and **b.** Moraine 2 at the boundary of the Britannia and Danum drifts.

pitted, and spalled) increases progressively from the Hatherton to the Isca drifts. The varnishing and cavernous weathering (tafoni) also increases with age. Perched, striated and plucked boulders are more common in the younger drift sheets, particularly the Hatherton and Britannia drifts. The Hatherton drift has prominent moraine ridges (Fig. 4, marked as Moraine 1 on Fig. 2) and ice-cored hummocky terrain. A prominent moraine ridge separates the Britannia and Danum drifts (Fig. 4, see Moraine 2 on Fig. 2). This ridge has an asymmetric profile, is 1130 m long, 11 m high and 6 m wide and is made up of angular to sub-rounded moderately weathered clast-supported sandstone and dolerite boulders with rare granite clasts. The boundary between the Danum and the oldest drift, Isca, is not obvious in the Lake Wellman area, and in addition, in the Lake Wellman area it is not possible to distinguish the Britannia I from the Britannia II drift. Bockheim *et al.* (1989) concluded they were part of the same major glaciation event even though they were distinguishable in other locations.

Age of drift sheets

Bockheim *et al.* (1989) used ^{14}C dating of blue green algae among and beneath surface clasts on the Hatherton and Britannia drift surfaces to provide minimum ages for glacial recession. On the assumption that these algae grew in former lakes or ponds on the drift surfaces and that they had been preserved since the last glacial retreat, Bockheim *et al.* (1989) concluded that ice retreated from its maximum advance position on the Britannia drift prior to 9420–10 250 cal yr BP, that the Hatherton drift is older than 5270 cal yr BP and that the ice was near its present configuration by 5740–6020 cal yr BP. These radiocarbon ages have been used by Conway *et al.* (1999) to suggest that the WAIS damned the entrance to the Darwin–Hatherton glacial system during Britannia times (i.e. prior to ~10 ka) and that the Hatherton drift was deposited when its grounding line retreated further southward than the junction between the Darwin Glacier and the Ross Ice Shelf at about 6 ka, allowing the floating Ross Ice Shelf to fill the volume vacated by the receding WAIS. From correlations with drift in the McMurdo Sound region and from the local ^{14}C ages, Bockheim *et al.* (1989) assigned an early Holocene age for the Hatherton drift, a LGM age for the Britannia drift and marine isotope stage (MIS) 6 for the Danum drift (140–160 ka). They correlate Britannia drift with the Ross Sea drift representing the limit of ice at the LGM.

As pointed out by Bockheim *et al.* (1989), radiocarbon ages of these algae deposits can only provide a minimum age for the drifts as the algae grow in seasonally wet depressions and lakes on the glacial landforms after ice evacuation. In the Dry Valleys of southern Victoria Land, the inference of a direct relationship between the recession of the ice and the growth of the algae is supported by the geomorphological context of moraine impoundment of lakes (Sugden *et al.* 2006). In the Darwin area, however, the geomorphological context is much less certain and the algal ages reflect the onset of the availability of seasonal water rather than necessarily, ice retreat. Moreover, there is no means by which to determine the long-term preservation of algae. Clearly, to quantify the scale of ice sheet advance, its timing and the embedded phenomenon of glacial refugia, a more secure and reliable method is required to determine the age of the drift sheets. In this setting, only surface exposure dating (SED) using *in situ* cosmogenic radionuclides (CRN) ^{10}Be and ^{26}Al provides the opportunity to directly date glacial features.

Sampling and analyses

The area was remapped from satellite images and extensively ground truthed using the map of Bockheim *et al.* (1989)

Table I. Sample and site description for samples from Lake Wellman, Hatherton Glacier in the Darwin Mountains, Antarctica.

Sample name	Glacial drift sequence (1)	Location Latitude (S)	Longitude (E)	Elevation (m) a.s.l.	above Lake Wellman (2)	Sample type	Sample dimensions (cm)	Thickness (cm)	Topographic Shielding (3)
Transect A									
LW 11.1	Isca	79°56'41.594	156°46'32.068	1646	801	Granite	174 x 105 x 84	5.0	0.995
LW 09.1	Isca	79°56'25.702	156°49'10.135	1501	656	Sandstone	256 x 290 x 130	5.0	0.995
LW 09.3	Isca	79°56'25.675	156°48'52.191	1508	663	Granite	130 x 170 x 45	1.5	0.995
LW 02.1	Britannia	79°55'53.771	156°52'17.670	1246	401	Granite	800 x 500 x 300	6.0	0.995
LW 02.2	Britannia	79°55'53.774	156°52'16.794	1237	392	Sandstone	12 x 12 x 10	10.0	0.995
LW 15.1	Danum	79°55'19.236	156°47'54.995	1136	291	Sandstone	105 x 156 x 185	4.0	0.985
LW 24.1	Hatherton	79°55'20.608	156°54'07.684	895	50	Granite	115 x 160 x 50	5.0	0.995
LW 24.2	Hatherton	79°55'17.811	156°53'57.691	892	47	Granite	86 x 93 x 52	3.0	0.995
LW 23.1	Moraine 1	79°55'00.826	156°54'39.387	852	7	Sandstone	33 x 18 x 14	3.0	0.995
LW 23.2	Moraine 1	79°55'01.111	156°54'35.643	850	5	Granite	12 x 8 x 5	5.0	0.995
LW 25.1	Hatherton	79°55'12.344	156°55'25.965	852	7	Granite	125 x 86 x 44	5.0	0.995
LW 25.2	Hatherton	79°55'13.445	156°55'30.546	845	0	Sandstone	125 x 96 x 45	5.0	0.995
Transect B									
LW 12.1	Isca	79°53'19.798	156°43'53.586	1150	305	Sandstone	174 x 105 x 84	1.0	0.990
LW 12.2	Isca	79°53'19.785	156°43'52.768	1155	310	Granite	180 x 212 x 84	6.0	0.990
LW 13.2	Danum	79°53'25.813	156°45'26.798	1107	262	Sandstone	180 x 211 x 103	5.0	0.995
LW 13.3	Danum	79°53'25.933	156°45'22.423	1112	267	Granite	158 x 157 x 93	2.5	0.995
LW 14.1	Moraine 2	79°53'26.403	156°45'33.541	1119	274	Sandstone	10 x 6 x 8	5.0	0.995
LW 14.2	Moraine 2	79°53'26.546	156°45'33.807	1115	270	Sandstone	24 x 60 x 51	5.0	0.995
LW 14.3	Moraine 2	79°53'26.629	156°45'33.400	1115	270	Sandstone	17 x 17 x 8	5.0	0.995
LW 18.1	Britannia	79°53'26.942	156°45'54.120	1087	242	Sandstone	290 x 177 x 203	5.0	0.990
LW 18.3	Britannia	79°53'29.376	156°45'53.633	1101	256	Granite	180 x 83 x 110	5.0	0.990
LW 20.1	Britannia	79°53'38.668	156°47'59.290	1018	173	Sandstone	220 x 177 x 106	3.0	0.995
LW 20.3	Britannia	79°53'48.224	156°48'09.117	1025	180	Granite	150 x 110 x 60	3.0	0.995
LW 21.1	Britannia	79°53'52.584	156°49'06.008	981	136	Granite	74 x 93 x 84	2.5	0.995
LW 21.2	Britannia	79°53'53.970	156°49'05.287	982	137	Sandstone	177 x 78 x 56	2.5	0.995

(1) Associated drift sequence nomenclature according to Bockheim *et al*. (1989)
(2) Lake Wellman is at 845 m a.s.l. equivalent to the lowest altitude sample, LW 25.2. The altitude of the modern ice surface of Hatherton Glacier is defined as 960 m a.s.l.
(3) Attenuation length = 150 g cm^2 , rock density = 2.7 g cm^3

as a base. The morphology and sedimentology of the drifts and moraines were closely examined with a particular focus on the SED sample sites. We collected glacially transported sandstone and granitic erratics exposed sub-aerially on the upper surfaces of the four drifts described above from the Lake Wellman area to determine *in situ* ^{10}Be and ^{26}Al cosmogenic exposure ages. The samples came from two elevation transects, from modern ice surface to the highest altitude glacial drift (Fig. 2). Transect A–A' includes erratics from the intersection of the modern day ice surface, from the Hatherton (including Moraine ridge 1), Britannia and Isca drifts, whilst transect B–B' covers erratics from the Britannia drift, the prominent Moraine ridge 2, Danum and Isca drifts. Stable, rounded sandstone and granite clasts, in open sky settings, were preferentially sampled because they demonstrate glacial transport, minimize the likelihood of inheritance and are less likely to have moved since deposition. Samples that (to the best of our knowledge) exhibited signs of post-depositional re-orientation or partial burial by sediment or periglacial weathering were avoided. In some cases, small erratics perched on larger stable boulders were sampled. Table I gives locations and descriptions of those erratics selected for dating.

In order to supplement SED sampling data, sedimentological characteristics were compiled for the area around the sample sites. This was achieved using a 50 m transect at each general sampling location with individual clasts sampled at 1 m intervals along the transect (i.e. $n = 50$) for lithology, angularity, size and weathering characteristics (a full dataset is presented in Hood 2010). For 'drift' samples, transects were run parallel to the slope so that each transect represented a discrete elevation. For moraines, transects were taken from the crest and followed the trend of the crest line. A summary of lithology and angularity data are presented in Figs 5 & 6. Dolerite is the modal lithology in all samples, with lesser percentages of gabbro, granite, sandstone, basalt and gneiss. While there is no definitive trend with elevation the following two points should be noted. Firstly, Ferrar Dolerite and Beacon Supergroup sandstones are, or at least could be, of local provenance, but all samples contain lithologies (notably granite) that do not crop out in the Lake Wellman area. Secondly, while lithologies are not systematically different,

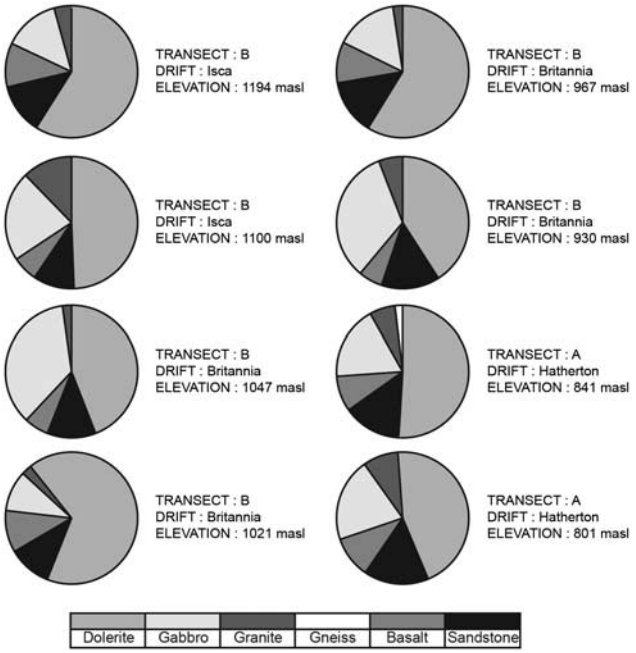

Fig. 5. Pie diagrams showing the proportion of different lithologies within the glacial drifts at different elevations within the Lake Wellman area.

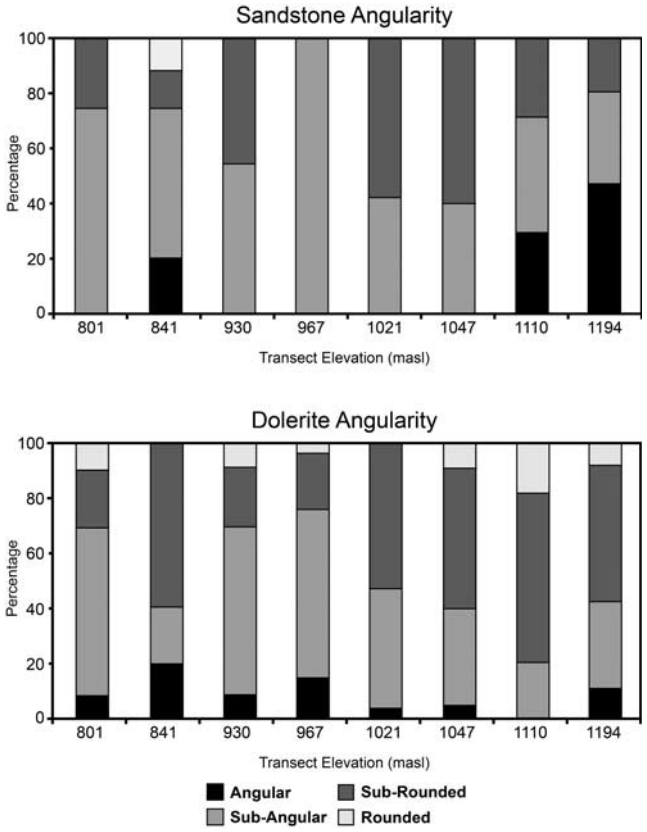

Fig. 6. Angularity histograms for dolerite and sandstone clasts within the glacial drifts in the Lake Wellman area.

some of the other characteristics are. Angularity measurements based on the 6-point Power's index indicate that there are differences between lower elevation samples and higher elevation samples. The angularity measurements need to be compared within, rather than between, lithologies and consequently only for dolerite are sample sizes statistically valid. For dolerite, the samples can be delineated into more rounded material above 1000 m and less rounded below (Fig. 6). For sandstones, the same trend is replicated, though even more strongly, and a further sub-division of the samples from above 1100 m with those from 1000–1100 m is suggested (Fig. 6).

Exposure age measurements and calculations

Cosmogenic targets for ^{10}Be and ^{26}Al were prepared at the University of Canterbury preparation laboratory following protocols and procedures provided by the Australian Nuclear Science and Technology Organisation (ANSTO) (Child *et al.* 2000). Once processed, ^{10}Be and ^{26}Al concentrations were measured in 25 quartz samples at the ANTARES Accelerator Mass Spectrometer (AMS) facility at ANSTO (Fink & Smith 2007). Table II gives the results of all the AMS measurements and Table III the calculated exposure ages.

Each set of eight unknown samples were processed with full chemistry procedural blanks for ^{10}Be and for ^{26}Al prepared from commercially purchased 1000 ppm ICP standard Be and Al solutions. The mean ^{10}Be/^{9}Be chemistry blank was 34.6 ± 5.0 (1σ) x 10^{-15} ($n = 6$, 3 targets) and mean ^{26}Al/^{27}Al chemistry blank was 27.8 ± 14.0 (1σ) x 10^{-15} ($n = 4$, 2 targets). The same 1000 ppm ICP Be solution was used as carrier for ^{10}Be samples. Aluminium concentrations in purified quartz solutions were measured by ICP-OES with a representative uncertainty of ± 4%. Reproducibility of native Al assay in duplicate solutions were < 2% for all samples. Apart from three of the 25 samples measured, final AMS ratios after normalization to standard reference materials ranged from 606 to 52 060 x 10^{-15} for ^{10}Be/^{9}Be and from 297 to 183 150 x 10^{-15} for ^{26}Al/^{27}Al. Total analytical errors for ^{10}Be concentrations (atoms per gram quartz) ranged from 0.9% to 4.5% and for ^{26}Al concentrations from 1.5% to 9.0%. Three samples gave very low AMS ratios - these were LW 23.1, LW 24.2 and LW 25.1 with ^{10}Be /Be ratios of (26 ± 4, 122 ± 7 and 44 ± 5) x 10^{-15} respectively, and ^{26}Al/Al ratios of (19 ± 10, 224 ± 31 and 43 ± 16) x 10^{-15}, respectively.

Given the relatively large spread in both ^{10}Be/^{9}Be and ^{26}Al/^{27}Al ratios (about 10^{3}), care was taken to asses ion-source cross-contamination by frequent measurement of cathodes loaded with Nb metal powder which was used as a mixing agent for the Be and Al oxide powders. Independent repeat AMS measurements per sample were combined as weighted means selecting the larger of the mean standard error or total statistical error. The final analytical error

Table II. Results of AMS measurement for ^{10}Be and ^{26}Al for the Lake Wellman samples.

Sample name	^{10}Be/^{9}Be ratio (x 10^{-15}) (1)	^{10}Be/^{9}Be error (x 10^{-15}) (2)	^{26}Al/^{27}Al ratio (x 10^{-15}) (3)	^{26}Al/^{27}Al error (x 10^{-15}) (2)	Quartz mass (g)	^{9}Be carrier mass (mg)	Al concentration (ppm)
Transect A							
LW 11.1	31 726	338	129 332	2422	50.20	0.4043	n.a.
LW 09.1	48 356	665	20 005	540	51.06	0.4404	270
LW 09.3	52 066	655	183 145	2771	50.13	0.4087	n.a.
LW 02.1	3467	28	2108	84	75.09	0.4097	304
LW 02.2	1010	60	383.0	40	76.55	0.4042	313
LW 15.1	22 282	510	8484	251	75.49	0.4153	211
LW 24.1	2982	39	7944	167	100.05	0.3989	23
LW 24.2	122.4	6.5	223.8	31.0	99.85	0.3998	27
LW 23.1	26.4	3.9	18.9	10.0	99.97	0.5157	236
LW 23.2	762.8	13.5	1002	47	92.35	0.4064	57
LW 25.1	44.0	5.0	43.2	16.3	100.24	0.4107	62
LW 25.2	605.9	12.1	296.9	26.0	93.95	0.4028	193
Transect B							
LW 12.1	5405	246	2183	88	76.19	0.4048	233
LW 12.2	14 867	136	16 646	460	75.22	0.4133	80
LW 13.2	3121	87	838	40	75.21	0.4018	395
LW 13.3	9164	81	26 986	660	75.22	0.4017	25
LW 14.1	4195	52	n.a.		45.38	0.4440	n.a.
LW 14.2	18 775	204	8095	357	89.63	0.3991	125
LW 14.3	374.6	33.0	n.a.		44.95	0.4310	n.a.
LW 18.1	1877	30	1741	157	87.91	0.4065	92
LW 18.3	9465	114	13 661	628	100.23	0.4058	57
LW 20.1	2407	65	984	46	108.40	0.4038	193
LW 20.3	1942	27	1330	69	100.38	0.4104	109
LW 21.1	1703	56	696	62	100.05	0.4037	196
LW 21.2	1501	24	662	42	104.85	0.4133	190

(1) Measured against NIST SRM-4325 with a nominal value of $27\,900 \times 10^{-15}$. Final AMS ratio from weighted mean of repeat measurements.
(2) The quoted 1σ error is the larger of total statistical error or weighted error in mean. Additional 2% (1σ) error added in quadrature based on reproducibility of AMS standard measurements.
(3) Measured against SRM PRIME-Z93-0221 with a nominal value of $16\,800 \times 10^{-15}$.

includes (in quadrature) a 2% systematic variability in repeat measurement of AMS standards (Fink & Smith 2007). Nishiizumi *et al*. (2007) have recently presented revised nominal values of ^{10}Be/^{9}Be isotopic ratios for AMS standard reference materials (SRMs) which resulted in a 1.106 ± 0.012 factor reduction in their previously accepted nominal ratios. This in turn mandates corresponding reductions in sea level high latitude (SLHL) spallation calibration scaling factors (summarized in table 6 of Balco *et al*. (2008) for various scaling models). Similarly, we apply the same 10.6% reduction in the value of the AMS SRM for ^{10}Be, NIST-4325, in use at the ANTARES AMS Facility (Fink & Smith 2007). AMS ^{10}Be concentrations presented in this work are normalized to NIST-4325 with a revised nominal ^{10}Be/^{9}Be value of $27\,900 \pm 300 \times 10^{-15}$, and ^{10}Be exposure ages are calibrated with a SLHL production rate based on Stone-Lal scaling methods (Stone 2000) reduced from 5.10 (including a 2.5% muon component production) to 4.60 atoms/g/yr. Final ^{26}Al concentrations are normalized to AMS SRM PRIME-Z93-0221, with a nominal ^{26}Al/^{27}Al value of $16\,800 \times 10^{-15}$. ^{26}Al exposure ages are calibrated with a SLHL production rate based on Stone-Lal scaling methods (Stone 2000) of 30.7 atoms/g/yr (including a 2.5% muon component production). Errors of 10% are assigned to both the ^{10}Be and ^{26}Al SLHL production rates which are propagated in quadrature with the total analytical AMS errors in cosmogenic concentrations. We use the new published ^{10}Be half-life (Korschinek *et al*. 2009) of 1.387 ± 0.012 Ma and an ^{26}Al half-life of 0.70 Ma.

Corrections to site specific production rates due to horizon topographic shielding of cosmic rays were no larger than 1% and negligible. Sample thicknesses ranged from 1.5–6 cm. Thickness corrections were carried out by integrating the effective flux over the sample thickness resulting in a maximum correction of 0.950 (using $\Lambda = 150\,\mathrm{g\,cm^2}$ and $\rho = 2.7\,\mathrm{g\,cm^3}$). Corrections for seasonal snow cover or erosion of boulder surface were not included.

Results and discussion

Interpreting exposure ages of erratics

The application of cosmogenic exposure dating in regions where ice sheets are the principal agent of bedrock sculpting and transport of erratics, requires an appreciation

Table III. ^{10}Be and ^{26}Al cosmogenic exposure ages based on zero erosion.

Sample name	Glacial drift sequence	^{10}Be (atoms g^{-1}) (x 10^3)	^{10}Be error (atoms g^{-1}) (x 10^3)	^{26}Al (atoms g^{-1}) (x 10^3)	^{26}Al error (atoms g^{-1}) (x 10^3) (1)	Minimum ^{10}Be exposure age (ka) (2)	Exposure age error (ka) (3)	Minimum ^{26}Al exposure age (ka) (4)	Exposure age error (ka) (3)	^{26}Al/^{10}Be ratio	^{26}Al/^{10}Be error
Transect A											
LW 11.1	Isca	17 077	423	n.a.		929	103	n.a.		n.a.	
LW 09.1	Isca	27 874	732	120 356	6400	2275	345	1978	474	4.32	0.26
LW 09.3	Isca	28 369	728	n.a.		2196	356	n.a.		n.a.	
LW 02.1	Britannia	1264	30	14 307	870	78.1	7.0	137	15	11.32	0.74
LW 02.2	Britannia	356.3	22.7	2678	310	22.6	2.3	25.3	3.4	7.52	0.98
LW 15.1	Danum	8192	262	39 895	2180	630	66	491	62	4.87	0.31
LW 24.1	Hatherton	794.6	20.6	4128	210	65.5	6.0	50.8	5.1	5.20	0.29
LW 24.2	Hatherton	32.8	1.9	136.7	20.0	2.6	0.3	1.6	0.3	4.17	0.65
LW 23.1	Moraine 1	9.1	1.4	100.1	50.0	0.8	0.1	1.2	0.6	10.99	6.03
LW 23.2	Moraine 1	224.3	6.4	1281	80	19.1	1.7	16.2	1.7	5.71	0.41
LW 25.1	Hatherton	12.0	1.4	59.8	10.0	1.0	0.2	0.7	0.3	4.97	1.31
LW 25.2	Hatherton	173.6	5.2	1279	130	14.8	1.3	16.2	2.1	7.36	0.76
Transect B											
LW 12.1	Isca	1919	97	11 335	690	128	13	115	13	5.91	0.47
LW 12.2	Isca	5460	132	29 708	1590	395	38	340	39	5.44	0.32
LW 13.2	Danum	1114	40	7389	490	76.7	7.2	76.6	8.4	6.63	0.50
LW 13.3	Danum	3271	79	14 975	780	227	22	157	17	4.58	0.26
LW 14.1	Moraine 2	2743	70	n.a.		192	18	n.a.		n.a.	
LW 14.2	Moraine 2	5587	139	22 671	1440	415	41	254	30	4.06	0.28
LW 14.3	Moraine 2	240.1	21.8	n.a.		16.1	2.0	n.a.		n.a.	
LW 18.1	Britannia	580.2	16.0	3571	360	40.4	3.7	37.1	4.9	6.16	0.65
LW 18.3	Britannia	2561	65	17 300	1120	183	17	192	22	6.75	0.47
LW 20.1	Britannia	599.1	21.0	4242	280	43.3	4.1	45.9	5.1	7.08	0.53
LW 20.3	Britannia	530.6	14.0	3221	220	38.1	3.5	34.5	3.9	6.07	0.45
LW 21.1	Britannia	459.2	18.0	3046	300	34.1	3.3	33.7	4.5	6.63	0.71
LW 21.2	Britannia	395.5	11.0	2807	220	29.3	2.7	31.0	3.7	7.10	0.59

(1) Error in ^{26}Al concentration includes a 4% error in ICP-OES measurement of Al concentration in quartz mass.
(2) ^{10}Be decay constant = 5.00 x 10^{-7} ($t_{\frac{1}{2}}$ = 1.387 Ma), ^{10}Be production rate = 4.60 +/- 0.42 atoms/g/year (see text for details).
(3) Age error includes a 9% standard error in sea level high latitude production rate in quadrature with total analytical AMS error.
(4) ^{26}Al decay constant = 9.90 x 10^{-7} ($t_{\frac{1}{2}}$ = 0.70 Ma), ^{26}Al production rate = 30.7 +/- 2.8 atoms/g/year.

of the various factors which can modify the cosmic ray exposure dose of a transported boulder following deposition on an exposed bedrock surface following ice retreat (Sugden *et al*. 2005). These factors address the assumption that the measured radionuclide concentration directly reflects simple and continuous exposure. Given the higher likelihood of cold-based ice activity in the Polar Regions, it is not uncommon to observe young erratics perched on ancient bedrock surfaces (Briner *et al*. 2003). The near-absence of sub glacial bedrock erosion due to non-sliding cold-based ice allows long-term accumulation and partial preservation of cosmogenic nuclide inventories from previous exposures. The most recent advance may well deposit entrained erratics with minimal inheritance, yet not erode sub-glacially or alter previously deposited moraines (Miller *et al*. 2002, Stroeven *et al*. 2002, Fabel *et al*. 2006). The observational evidence for cold-based ice overriding can be as subtle as minor differences in the degree of surface weathering across subdued demarcation trim lines (Sugden *et al*. 2005).

In other Antarctic studies, erratic and bedrock exposure ages as a function of altitude from ice edge to mountain peak (Stone *et al*. 2003, Mackintosh *et al*. 2007, Lilly *et al*. 2010) have become an effective method to estimate local ice volume of the most recent advance. Nunataks protruding today through the ice sheet can thus act as 'dipsticks' of historic ice thickness. In the absence of inheritance, these exposure ages should trace out a monotonic relationship of increasing age with altitude. The prevalence of a varying and unknown component of inheritance in the cosmogenic nuclide inventory often negates such a simplistic expectation, as recycled erratics or those freshly plucked from bedrock can be re-deposited with an inheritance signal and may not always represent exposure since last ice advance. This forces a working hypothesis to be that the youngest erratic age at the highest elevation best represents minimum (or zero) inheritance and hence the limit of the most recent advance (Bentley *et al*. 2006, Mackintosh *et al*. 2007). Unfortunately, such a scheme requires judicious and multiple sampling. Stone *et al*. (2003) in attempting to map Holocene ice volume profiles in Marie Byrd Land, Antarctica, provided 10 erratic ages from Mount Rea over an elevation span from 610 to

780 m a.s.l., to be confronted with exposure ages ranging from 10.4–112 ka showing no correlation to elevation. The single erratic with the lowest exposure age (10.4 ka) at 715 m was deemed as the best choice to locate early Holocene ice elevation for comparison to late Holocene ages at lower altitudes at other coastal nunataks. This example highlights the complexity of exposure dating in environments where transported debris can be recycled and partially preserved over repetitive glaciations.

In some cases, the sampling of erratic-bedrock pairs can provide information not only on timing of the last advance but also on the degree to which the locality is affected by passage of cold-based ice. Alternatively, the processes of moraine stabilization, post-depositional re-orientation or long-term debris cover will generate apparent young exposure ages (Gosse & Phillips 2001, Putkonen & Swanson 2003, Briner *et al*. 2005). If this process dominates the geomorphological glacial landscape, then selecting the older exposure ages may be more representative of ice advance than selecting the youngest exposure ages if inheritance dominates. In addition, the measurement of a ^{26}Al concentration paired with ^{10}Be in the same quartz sample allows determination of a ^{26}Al/^{10}Be ratio. Non-concordant ages between these two isotopic systems, as demonstrated by plots of ^{26}Al/^{10}Be ratios versus ^{10}Be, can then be used to identify samples which exhibit extensive burial histories (or more specifically, pre-irradiation followed by burial and then re-exposure). Although such identification requires burial histories in excess of 150–200 ka, it at least can qualify the *a priori* use of a sample's ^{10}Be exposure age as reflecting continuous exposure. It is important to note that a subset of recycled samples which have concordant isotope ages (within the usual error criteria of 2σ overlap), and thus would be classified as those with a "continuous exposure" (i.e. have not undergone a 3-stage exposure history), may well have an inheritance component. For these samples, both the ^{26}Al and ^{10}Be age would fall outside acceptable error limits of the mean moraine age based on the majority of other moraine samples. However, in the absence of a corresponding ^{26}Al age, ^{10}Be ages which lie more than 2σ or 3σ above the mean population age for a given glacial feature, will always carry some uncertainty as to its reliability and basis for rejection. A similarly 'deviant' ^{26}Al age in the same sample verifies the erratic as an outlier but more so, provides sound justification for removing the sample from the averaging process.

Only a limited number of Antarctic glacial studies provide ^{26}Al-^{10}Be exposure age pairs (Bentley *et al*. 2006, Fink *et al*. 2006, Mackintosh *et al*. 2007, Lilly *et al*. 2010). This has more to do with the fact that the large majority of cosmogenic studies in Antarctica have focussed on its LGM ice history making ^{26}Al measurements rather ineffective as an indicator of burial in comparison to increasing the population of ^{10}Be samples. Moreover, due to technical aspects, it is difficult in young aged samples to achieve the required statistical precision in the ^{26}Al/^{10}Be ratio to identify burial. These considerations with respect to ^{26}Al ages become far more relevant and beneficial when exposure ages exceed ~ 100 ka, because both the total error in the ^{26}Al/^{10}Be ratio decreases and burial histories and boulder recycling are more likely in older samples. An added complication within this work relates to the absence of minimally modified glaciated bedrock surfaces to allow bedrock-erratic pairs to be collected. The Lake Wellman area is dominated by a carpet of extensive and thick diamict in the form of drift sheets containing sub-angular clasts and boulders of varying dimensions, orientations and with varying degrees of weathering. The few prominent unconsolidated moraines overlie drift sheets that are discontinuous, making sample selection all the more difficult. In the absence of erratics on bedrock, the next level of choice were large, blocky and flat-surfaced erratics however there remains the uncertainty of exhumation, drift stabilization and freeze-thaw as a further factor driving exposure ages younger. In this study we attempt to apply these various approaches in evaluating and interpreting zero-erosion model exposure ages for ^{10}Be and ^{26}Al with due concern for the complexities of the glacial geomorphology inherent in polar studies using cosmogenic isotopes for dating. The zero erosion model applied to the assumption that the analysed samples have experienced no erosion.

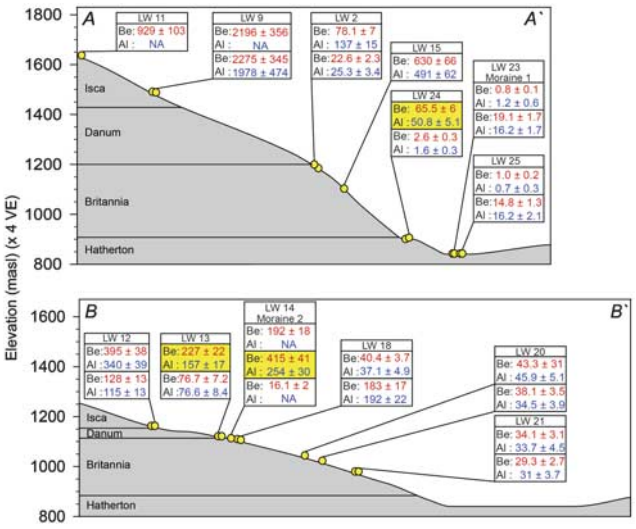

Fig. 7. Elevation versus ^{10}Be and ^{26}Al exposure ages for analysed samples from transect A-A' and B-B'. All ages are given in ka. Red numbers represent ^{10}Be ages and blue ^{26}Al ages. Yellow boxes indicate samples that reflect a burial history.

Exposure age results

Transect A–A' ^{10}Be exposure ages ranged from 0.8–2275 ka, and from 16–415 ka for transect B–B'. Corresponding ^{26}Al ages for A–A' ranged from 0.7–1978 and from 31–340 for B–B'. For four samples (LW 11.1, LW 9.3 on transect A–A';

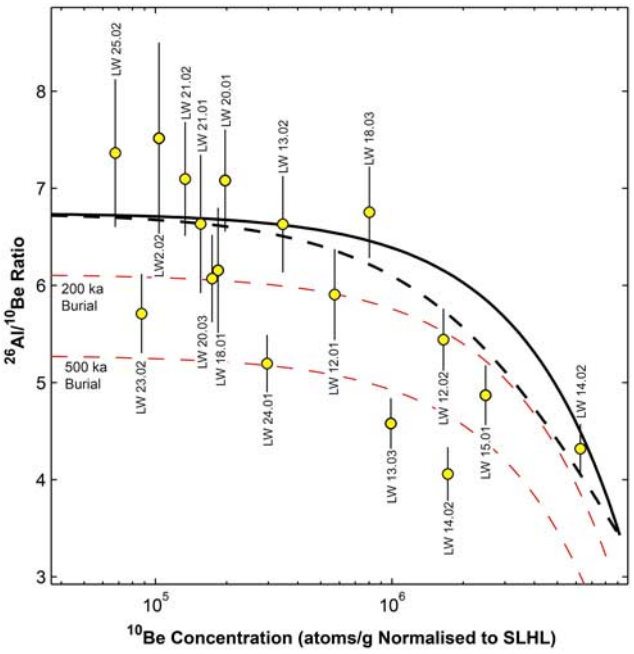

Fig. 8. A plot of ^{26}Al/^{10}Be ratios versus normalized SLHL ^{10}Be concentrations showing the exposure history of analysed samples The upper bold black curve represents continuous exposure at zero erosion, the lower dashed black curve steady state erosion. Exposed surface samples undergoing erosion will fall within the two loci defining an area termed the steady state exposure-erosion island. Burial isochrons of 200 ka (red thin red curve) and 500 ka (dashed red curve) are also shown. Error bars are derived from analytical errors only. Error envelopes for the exposure-erosion island (based on production rate ratio errors for ^{10}Be and ^{26}Al of about ± 7–9%) are not shown. Samples LW 13.3, 14.2 and 24.1 show an unequivocal burial signal, whereas in contrast that for LW 23.2, LW 20.3, LW 18.1 and LW 12.1 are uncertain given that the minimum detectable burial age is 150–200 ka.

LW 14.1 and LW 14.3 on transect B–B') ^{26}Al ages are not available due to laboratory failures in either ICP measurement of aluminium in purified quartz or unacceptably high aluminium concentrations which prevented reliable AMS determination of a ^{26}Al/Al ratio.

In general, the oldest ages occur at highest elevations with the youngest ages closest to the present ice surface (Fig. 7), but neither of the two transects show an entirely consistent age-elevation trend. Complexities in the exposure history of erratics, as described above, are clearly evident at Lake Wellman. Despite the observation of increasing age with elevation, these complexities preclude a definitive conclusion to be given regarding the evolution of changes in ice volume of Hatherton glacier. Given the large spread in ages (1–2220 ka), common glacial drifts mapped over different elevation ranges for transects A–A' and B–B', and samples with complex exposure histories, our approach to achieve a plausible and reasonable chronology of Hatherton ice volume changes assumes that selecting either the youngest or oldest ages from each site (or drift) defines the possible end-members of age-elevation models. Basically this means that for a minimum age model, older erratics at lower than expected elevations are presumably due to excessive inheritance, whilst for a maximum age model, younger erratics can appear at higher elevations due to resetting or post-depositional modification. We filter our sample population by first applying a criteria, based on a plot of ^{26}Al/^{10}Be ratios versus normalized SLHL ^{10}Be concentrations (Fig. 8), to identify the subset of reworked samples deemed inappropriate for inclusion. Three samples, namely LW 14.2 (sited on the apex of Moraine 2), LW 13.3 and LW 24.1, of the plotted 17 show unequivocal evidence for a complex exposure with burial as the ^{26}Al/^{10}Be ratio for these three samples all fall well within the defined burial zone of Fig. 8. For example, LW 14.2 (^{10}Be 415 ± 41 ka; ^{26}Al 254 ± 30 ka) shows a considerable integrated history of pre-exposure, extended burial larger than 0.5 Ma, and an unspecified final stage re-exposure. Within the criteria of overlapping 1σ analytical error for the ^{26}Al/^{10}Be ratio and respective 1σ error envelope for the exposure-erosion island (due to ~ 10% uncertainty in production rates), the remaining 14 samples are consistent with an interpretation of continuous exposure. Samples LW 23.1, 24.2, and 25.1 (where ^{10}Be ages are less than 2–3 ka) and LW 02.1 (which has an ^{26}Al age larger than the ^{10}Be age by more than 2σ) are not shown in Fig. 8.

Bentley *et al.* (2006) applied a similar methodology to their exposure ages in a study to measure timing of local LGM and deglaciation of the Antarctic Peninsula. About five of the 29 samples were designated as complex, and of the remaining 24, all but three ranged in age from 7–60 ka. Their smaller age distribution and focus on last deglaciation made their choice of a minimum age model plausible as it is most unlikely to get a post-LGM or late-glacial age younger than last deglaciation. However, for our Lake Wellman dataset, which evidently demonstrates multiple glacial cycles over a far longer period of time and which is restricted to erratics on drift sheets, a maximum age model requires consideration as it appears to be more consistent with the overall field observations and the extended million year exposure age scale than an alternate interpretation based on minimum ages.

We also apply a second filter by rejecting the remaining two of the three samples collected from Transect B–B' at site LW 14 on the surface of an unconsolidated moraine labelled as Moraine 2 in Fig. 2 and pictured in Fig. 4b. The results from LW 14 exhibit the most complexity in exposure age interpretation. We feel this is justified on the basis that a) neither of these two samples is reported with a ^{26}Al age, b) the 3 ^{10}Be ages were collected in very close proximity to each other and range from 16.1 ± 2.0 ka, 192 ± 18 ka to 415 ± 41 ka, and c) Moraine 2 showed strong characteristics of surface modification and deformation being predominately matrix rather than boulder

or clast supported. Most probably Moraine 2 is a composite feature resulting from multiple advances (perhaps over a time period of 30–400 ka) and is undergoing a continuous process of modification. It is interesting to note that the three rejected samples from Moraine 2 can all be considered as small cobbles in comparison to the other metre-sized erratics from transect B–B'.

Exposure age interpretation and chronology of glacial drifts

Isca drift. Based on a maximum age selection, the three samples from LW 11 and LW 09 at the highest elevations, ~ 1575 m, record the oldest ^{10}Be ages of the full dataset; 929 ± 103 ka, 2196 ± 356 and 2275 ± 345 ka, respectively. These two sites lie within undifferentiated drift but their locations, being at the same altitude and directly adjacent to Isca drift, are consistent with a far more extensive volume of Hatherton Glacier during the early–mid Pleistocene suggesting a 1–2 Ma age for Isca. In transect B–B', highest elevation samples at LW 12 (1155 m) give widely different ^{10}Be exposure ages of 128 ± 13 and 395 ± 38 ka (with concordant ^{26}Al ages), the latter exposure age is the oldest of the B–B' transect and is far younger than the oldest A–A' transect age of 2.2 Ma at 1500 m. Although the LW 12 ages are clearly divergent, they demonstrate a minimum glaciation age for Isca drift of between 130–400 ka, equivalent to MIS 6 or MIS 10. With a near ^{26}Al saturation exposure age (at zero erosion) for LW 09.1 and equivalent ^{10}Be age for adjacent sample LW 09.2, it is difficult to explain such old ages to be a result solely of inheritance. Thus we conclude that no ice has advanced over this location for at least the past 1 Ma and more probably over the past 2 Ma.

Danum drift. Two sites at intermediate elevations of ~1100 m are associated with Danum drift; a single sample from LW 15 which lies 1 km off the main axis of transect A–A', and two samples from LW 13 on transect B–B' up-slope and adjacent to Moraine 2. We presume that Moraine 2 marks the ice advance limits of the younger Britannia drift over the older Danum drift. Selection of either a minimum ^{10}Be age of 77 ka for LW 13.2 or a maximum age of 630 ka (LW 15.1) for the Danum drift deposition are both consistent with respect to stratigraphical age increasing with altitude based on the same age model criteria when applied to the Isca drift. However, as LW 15.1 does not lie directly on the main A–A' axis, we tentatively can assign a maximum 230 ka ^{10}Be age from LW 13.3 but note that this sample shows discordant ^{10}Be and ^{26}Al ages.

Britannia drift. Applying the procedure above to estimate a minimum and maximum Britannia drift age from eight available samples (LW 18, 20, 21, transect B–B'; and LW 2, transect A–A') results in a minimum ^{10}Be age of 23 ± 3 ka or maximum of 183 ± 17 ka. Again, these two age boundaries for Britannia drift are consistent with the respective minimum and maximum age boundaries deduced above for the two older Danum and Isca drifts. However, we offer an alternate and sounder estimate for the age of Britannia drift which acknowledges the statistical age distribution or clustering of five of the eight ages. The three pairs of samples from three sites in transect B–B' below the elevation of Moraine 2 were collected along the upper 1 km width of the Britannia drift covering an elevation range of 981–1087 m. Five of these six ^{10}Be ages show a well constrained clustered age range from 29.3 ± 2.7 ka to 43.3 ± 4.1 ka which is statistically consistent with a single population of mean age and 1σ age error of 37.0 ± 5.5 ka and a weighted mean age of 35.6 ± 1.5 ka (± 5%) (a similar result is obtained for the ^{26}Al ages, 35.5 ± 1.9 ka). The single outlier, sample LW 18.3 at 183 ± 17 ka, which actually determines Britannia's 'maximum' age hence appears to be five times larger than the mean Britannia age determined from the other five samples. A second approach to estimating Britannia drift age based on the remaining two samples (LW 2.1 and 2.2 from transect A–A') gives a minimum Britannia age of 23 ± 3 ka (as above) or maximum age of 78 ± 7 ka. These two age limits for Britannia bracket the spread in the ages of the five samples (i.e. 29 to 43 ka) used to calculate the single population mean age.

Hatherton drift. No samples from Hatherton drift were available for collection on transect B–B'. Two of the three lowest elevation sites at ~ 850 m on transect A–A', i.e. LW 23, LW 25, are effectively at the ice contact margin of today's Hatherton Glacier with the shoreline of Lake Wellman. LW 23 samples were taken form the apex of a moraine labelled as Moriane 1 in Fig. 2 and pictured in Fig. 4a. The third site, LW 24 at 895 m, is adjacent to the boundary of Hatherton and Britannia drift and only 50 m above the surface of Lake Wellman. We note that today's elevation of the central axis of Hatherton Glacier is at ~ 960 m. Exposure ages (either ^{10}Be or ^{26}Al) for all six samples (two per site), show a striking complexity in the A–A' transect. The ^{10}Be ages from each pair of samples from each of the three sites are incompatible with each other but interestingly show a bimodal distribution. ^{10}Be ages for three of the samples cluster together between 0.8 and 2.6 ka, whereas two others are 14.8 ± 1.3 and 19.1 ± 1.7 ka. Respective ^{26}Al ages for each of these five samples show a similar pattern. The sixth sample, LW 24.1, with a ^{10}Be age of 65.5 ± 6 ka is inconsistent with this trend and shows a distinct burial signal (Fig. 8). Our options for Hatherton drift are, according to a minimum age model, that it is a late Holocene - modern deposition (i.e. younger than 2–3 ka), older ages being rejected due to inheritance equivalent to ~ 15 kyrs. If in turn, the Hatherton drift age is defined by the 14.8 ± 1.3 and 19.1 ± 1.7 ka exposure ages (^{10}Be) of LW 25.2 and LW 23.2 respectively, the near-zero ages are

rejected on the basis of recent exhumation and post-depositional modification. Hence, based on a model of maximum site ages, the last local glacial maximum of Hatherton Glacier occurred between ~15–19 ka. In addition, we favour the older ages for site LW 23 and LW 25 because there is abundant evidence of reworked boulders in the Hatherton drift where striated and weathered surfaces have been fragmented, chipped and fresh surfaces exposed. Choosing the latter option leads to the question of the location of the (global) LGM advance at Lake Wellman because of the eight samples within the next oldest drift, Britannia, only one resembles an LGM age, i.e. ~23 ka (LW 2.2), and five from transect B-B' show a well constrained pre-LGM age for the Britannia drift of 35.6 ± 1.5 ka.

Age models

For both transects A–A' and B–B', the selection of either maximum or minimum ages describe age-elevation trends which are chrono-stratigraphically consistent for the four glacial drift deposits. Cosmogenic exposure ages generally follow a decreasing age trend with decreasing elevation but do not follow the defined chronologic definitions presented by Bockheim *et al*. (1989). Choosing a scenario wherein large-scale inheritance is not the dominant process distorting ages appears to provide overall a more robust and consistent chronostratigraphic interpretation of glacial ice advance. Rejecting samples displaying burial and using a model of maximum ^{10}Be age at given site elevations gives a LGM age (15–20 ka) for Hatherton drift, a MIS 3 (30–40 ka) age for the Britannia drift, an age range of 230 to 630 ka for the Danum drift and at least 395 ka, and more probably 2 Ma, for the Isca drift. The important features we conclude from this interpretation is that multiple glaciations spanning at least the past 2 Ma up to altitudes of 1500 m (or 600 m above present day ice level) have occurred through the Lake Wellman area and ice volume at the LGM may have been considerably smaller than previously assumed and, perhaps, no larger than we observe today. Choosing the alternate minimum age model forces the age scale from Isca to Hatherton drifts to contract into the Last Glacial Cycle (i.e. ~ the last 130 kyrs), places Danum drift at 77 ka (i.e. MIS 4), Britannia drift at 23 ka which precedes by ~2–3 ka the global LGM maximum Antarctic cold period at 19–20 ka (based on Antarctic ice cores) and requires Hatherton glacial expansion in the late Holocene. With this interpretation, ice volume history prior to the last interglacial (or more likely MIS 6 if we include a reasonable erosion rate for exposure age correction) is not recorded at Lake Wellman, and ice volume at LGM would be ~ 300 m higher in elevation than current ice elevation of Hatherton Glacier.

Fig. 9. Bullet shaped rocks. The direction of ice flow with respect to the rock is from left to right. The clasts are strongly faceted and striated and are indicative of warm based ice.

Although the prevalence of inheritance in Antarctic studies is well noted (Stone *et al*. 2003, Bentley *et al*. 2006), the ease of its identification has largely been confined to datasets focussed on LGM or Holocene ice sheet deglaciation, where even short-term recycling of glacial debris can readily result in old-age outliers. In our case, by selecting minimum ages, unreasonable values of inheritance of up to 2 Ma are required. Apart from Isca, estimates of inheritance ages from ~ 20–60 kyr (Hatherton drift samples) or even as large as 150 kyr (Danum drift) would appear to be acceptable, but this conclusion neglects the well-clustered mean exposure age of 35.6 ± 1.5 ka (error in mean) for the five of six Britannia drift samples distributed along transect B–B'. The 1σ age error for these five clustered samples is only ± 5 ka and considering the complexity in age groupings for all other drifts, is our strongest evidence to support our preference for caution in taking minimum ages. Interestingly, it appears in this region where the dominant form of glacial debris is large and extensive drift sheets of heterogeneous-sized matrix, that erratics on the surface of the drift (such as those from sites LW 18, 20 and 21) may offer a more reliable target for cosmogenic exposure age studies than moraines that overly them.

The Lake Wellman area is draped in a substantial but unknown thickness of 'drift' materials. Bedrock outcrops are sparse. All the evidence in the field area suggests that active wet based ice has flowed over the areas examined in this study. The evidence comes from the following sources:

1. The physical appearance and characteristics of some of the individual clasts suggests that material transport was by wet based flow. These include classic bullet shaped clasts with faceted faces and crag and tail features preserved (Fig. 9). These striated bullet shaped rocks and clasts are common in the Lake Wellman area. They occur from the modern ice surface to elevations of 1550 m. Cumulatively they are diagnostic of wet based ice. The remaining evidence is ancillary.
2. The lithologies preserved in all the drifts and moraines include rock types, most notably granite, that do not crop out in the Lake Wellman area indicating transport over large distances (Figs 5 & 6).
3. The preservation of relatively large, very distinct terminal moraines with, in some cases, near angle of repose slopes also supports the interpretation of relatively fast moving ice. These include both symmetrical and asymmetrical ridges, suggesting at least localized push and dump moraines (Fig. 4). In fact, the thick drift sequences themselves are indicative of debris rich ice and again suggest relatively fast flowing erosive ice.
4. The preferred interpretation using the maximum ^{10}Be exposure ages per site suggests that the population of drift material with inheritance is low and failure of older moraine samples to deliver reliable ages due to active surface modification; both support wet based ice passage. The thick carpet of glacial drift may represent basal debris whereas the linear moraine ridges most likely represent supraglacial material.

We cannot, of course, discount the possibility that some advances, or parts thereof, may be cold based, but the evidence for wet based ice in this area at some stages in its history is convincing.

Implications of the chronology for glacial history and diversity

At its maximum ice extent ~ 2.2 million years ago in the Pliocene, ice was at least ~ 1650 m a.s.l. or 800 m above the present surface of Lake Wellman which, in reference to the modern ice surface of Hatherton Glacier, is equivalent to 690 m increase in ice thickness. We suggest, based on the volume and extent of glacial debris that warm based ice blanketed the whole area at this time. We do not rule out readvances of the ice, and the discordant ages of Isca drift material between the two transects suggests that the lower elevation Isca site on transect B was re-occupied by ice ~ 400 ka in the mid- to late-Pleistocene and that a single designation for this drift may be somewhat unhelpful. The deposition age for Danum drift is not well constrained from our dataset, but according to our preferred interpretation, appears to be ~ 630 ka, although a Late Quaternary age (~ 75 ka) cannot be discounted from our data. Moraine 2, at an elevation of 1115 m a.s.l. (~ only 60 m above present day Hatherton ice surface), if deposited by Britannia drift at ~ 35 ka indicates the extent of increased ice thickness during the last major ice expansion in this area. This is 500 m lower compared to the ice thickness recorded by the major overriding ice event in the mid Pliocene. Our strongest constraint on the Britannia Drift, downhill of this ridge comes from the tightly clumped five ages of LW 18, 20, and 21 of 35 ± 5 ka. This is highly compatible with observations from elsewhere in East Antarctica that demonstrate maximum last glaciation ice extent well before the LGM (Gore *et al*. 2001).

The LGM limit appears to be restricted to the Hatherton drift whose upper limits are at an elevation just 50 m above the modern ice sheet surface. This indicates that LGM ice increase at this location was a minor phenomenon. In fact there is no conclusive evidence that LGM ice was ever above modern limits as the pre-Holocene ages from LW 23 and 25 are deglaciation ages and may relate to a post-LGM thickening as precipitation increased on the polar plateau after the end of the cold dry LGM phase.

The spatial resolution of glacial models and ice volume reconstructions has failed to detect the geographical distribution of glacial refugia (ice-free) in Antarctica. Clearly, the terrestrial biota indicates that refugia were more widespread and provides novel constraints that can be

highly informative for reconstructing the past glacial history of Antarctica (Stevens *et al*. 2006, Convey & Stevens 2007, Convey *et al*. 2009). For many areas of the continent there are no field data estimates for previous ice sheet thicknesses (Bentley *et al*. 2006) which restrict our ability to identify potential refugial locations or regions. Notable exceptions include the Dry Valleys of the Transantarctic Mountains of southern Victoria Land, where geomorphology supports ice-free conditions throughout the last 12–10 Ma (Sugden *et al*. 2006).

Much of what we know about the terrestrial biodiversity comes from the Dry Valley region yet other regions, such as in northern Victoria Land and the Beardmore and Shackleton glaciers, show similarly isolated biological signals (Brundin 1970, Adams *et al*. 2006, Stevens & Hogg 2006, Stevens *et al*. 2007). Indications from the Darwin Mountains, however, show that overall biota was sparse (see also Ruprecht *et al*. 2010). The significance of limited biodiversity (diversity and abundance) may not immediately seem obvious. However, a lack of biotic presence integrated with the Darwin Mountains glacial history shown here does in fact tell us a lot about the requirements necessary for colonization (and persistence) of flora and fauna associated with Antarctic soils, and these links provide a critical step forward in understanding the requirements and persistence of terrestrial life in Antarctica.

The paradigm of eradication of terrestrial biota during glacial maxima has been questioned (Stevens *et al*. 2006, Convey *et al*. 2009) and suggestions made for interdisciplinary research to integrate across geology, glaciology and biology (Convey *et al*. 2008, 2009). The Lake Wellman area shows a great deal of habitat modification with ice thickness ~ 800 m higher than its current level with some of the terrain ice-free for up to two million years, indicating that the glacial eradication dominated and did not support significant refugia for Antarctic terrestrial biota. This conclusion also has implications for the length of time required for terrestrial biota to recolonize post-glacial retreat and the gradual sequence (succession) of recolonizers necessary to 'prepare' a viable habitat in Antarctica; a question that has not been addressed in Antarctica.

Conclusions

We have successfully applied the technique of cosmogenic surface exposure dating in the Lake Wellman region of the Hatherton Glacier, East Antarctica, resulting in a constrained glacial chronology that spans the last two million years of glaciations. Geomorphic field observations show that active ice (perhaps wet based) has scoured the region transporting boulders and depositing thick drift sheets over numerous glacial cycles. From the set of 25 erratics from two orthogonal altitudinal transects, 16 provided paired ^{10}Be and ^{26}Al ages that confirm a simple continuous period of exposure (four failed to give a ^{26}Al age). Their mean exposure ages increase as a function of increasing elevation above current ice sheet surface, indicating a long-term decrease in ice volume of the Antarctic ice sheet moving over the Transantarctic Mountains since the Late Pliocene.

In contrast to mid-latitude, temperate alpine glacial systems, the frequency of erratics in the Polar Regions with a considerable degree of inheritance or burial histories resulting from preservation of multiple exposure periods and reworking of pre-exposed sub-glacial debris, respectively, can be significant. This will always limit the reliability of interpretations. Nevertheless, based on two simple age models - choosing the youngest erratic age at each elevation site or the oldest, there are sufficient reliable results to substantially modify the indirect chronology of Bockheim *et al*. (1989).
We conclude that:

- The maximum recorded ice thickness of the Hatherton Glacier in the Lake Wellman area was at least 690 m thicker than today's elevation of the Hatherton Glacier surface. The oldest drift (Isca) was deposited by a Pliocene advance of an outlet glacier of the East Antarctic Ice Sheet more than 2.2 million years ago. The next youngest drift, Danum drift, based on a maximum age scenario, was deposited at ~ 630 ka, but an age commensurate with MIS 4 at approximately 75 ka is also possible.

- In contrast to these older drifts, the Britannia drift is relatively well constrained by our data. It clearly indicates that the last substantial thickening of ice in this area occurred at ~ 35 ka, or more precisely between ~ 45 ka to ~ 30 ka during MIS 3, with the ice thinning progressively after that time. According to the elevation spread of the ages from the Britannia drift, the ice thickness at MIS 3 was not that much different from that during the Danum glaciation.

- Independent of the assumptions of age model distributions, ice volume changes from LGM through to the late Holocene are represented at Wellman by the youngest and smallest surface area drift - the Hatherton drift. Accordingly, using maximum ages per site, the increase in ice volume at the global LGM or during the last inter-glacial transition from 20–10 ka, can at most result in an ice thickness 50 m larger than the modern ice sheet surface. The set of minimum exposure ages on the Hatherton drift range from ~ 0.5 to ~ 3 ka and hence we cannot rule out the possibility that the Hatherton drift is a late Holocene deglaciation event. All these data suggest that ice at the LGM in the Lake Wellman area was substantially less thick than previously postulated.

Acknowledgements

We are very grateful to the excellent field support from Antarctica New Zealand as part of the Latitudinal Gradient

Project (LGP). In particular, we thank S. Gordon, I. Millar, R. Türk and M. Knox for logistics and/or field planning and assistance. We also thank Paul Brody for identification of algae. We are very grateful to the reviewers who provided very useful suggestions to improve the manuscript. We acknowledge financial support for this work from AINSE and from ANSTO's CcASH project 0203v (Cosmogenic Climate Archives of the Southern Hemisphere).

References

Adams, B.J., Bardgett, R.D., Ayres, E., Wall, D.H., Aislabe, J., Bamforth, S., Bargagli, R., Cary, C., Cavacini, P., Connell, L., Convey, P., Fell, J.W., Frati, F., Hogg, I.D., Newsham, K.K., O'donnel, A., Russell, N., Seppelt, R.D. & Stevens, M.I. 2006. Diversity and distribution of Victoria Land biota. *Soil Biology and Biochemistry*, **38**, 3003–3018.

Balco, G., Stone, J.O., Lifton, N.A. & Dunai, T.J. 2008. A complete and easily accessible means of calculating surface exposure ages or erosion rates from ^{10}Be and ^{26}Al measurements. *Quaternary Geochronology*, **3**, 174–195.

Bentley, M.J. 1999. Volume of Antarctic ice at the Last Glacial Maximum and its impact on global sea level change. *Quaternary Science Reviews*, **18**, 1569–1595.

Bentley, M.J., Fogwill, C.J., Kubik, P.W. & Sugden, D.E. 2006. Geomorphological evidence and cosmogenic 10Be/26Al exposure ages for the Last Glacial Maximum and deglaciation of the Antarctic Peninsula Ice Sheet. *Geological Society of America Bulletin*, **118**, 1149–1159.

Bockheim, J.G., Wilson, S.C., Denton, G.H., Andersen, B.G. & Stuiver, M. 1989. Late Quaternary ice-surface fluctuations of Hatherton Glacier, Transantarctic Mountains. *Quaternary Research*, **31**, 229–254.

Briner, J.P., Kaufman, D.S., Manley, W.F., Finkel, R.C. & Caffee, M.W. 2005. Cosmogenic exposure dating of late Pleistocene moraine stabilization in Alaska. *Geological Society of America Bulletin*, **117**, 1108–1120.

Briner, J.P., Miller, G.H., Davis, P.T., Bierman, P.R. & Caffee, M. 2003. Last Glacial Maximum ice sheet dynamics in Arctic Canada inferred from young erratics perched on ancient tors. *Quaternary Science Reviews*, **22**, 437–444.

Brundin, L. 1970. Antarctic land faunas and their history. *In* Holdgate, M.W., *ed*. *Antarctic ecology*. London: Academic Press, 41–54.

Butler, E.R.T. 1999. Process environments on modern and raised beaches in McMurdo Sound, Antarctica. *Marine Geology*, **162**, 105–120.

Child, D., Elliot, G., Mifsud, C., Smith, A.M. & Fink, D. 2000. Sample processing for earth science studies at ANTARES. *Nuclear Instruments & Methods in Physics Research*, **172**, 856–860.

Convey, P. & Stevens, M.I. 2007. Antarctic biodiversity. *Science*, **317**, 1877–1878.

Convey, P., Gibson, J.A.E., Hillenbrand, C.-D., Hodgson, D.A., Pugh, P.J.A., Smellie, J.L. & Stevens, M.I. 2008. Antarctic terrestrial life; challenging the history of the frozen continent? *Biological Reviews*, **83**, 103–117.

Convey, P., Stevens, M.I., Hodgson, D.A., Smellie, J.L., Hillenbrand, C.-D., Barnes, D.K.A., Clarke, A., Pugh, P.J.A., Linse, K. & Cary, C. 2009. Exploring biological constraints on the glacial history of Antarctica. *Quaternary Science Reviews*, **28**, 3035–3048.

Conway, H., Hall, B.L., Denton, G.H., Gades, A.M. & Waddington, E.D. 1999. Past and future grounding-line retreat of the West Antarctic Ice Sheet. *Science*, **286**, 280–283.

Denton, G.H. & Hughes, T.J. 2002. Reconstructing the Antarctic Ice Sheet at the Last Glacial Maximum. *Quaternary Science Reviews*, **21**, 193–202.

Fabel, D., Fink, D., Fredinc, O., Harbord, J., Land, M. & Stroeven, A.P. 2006. Exposure ages from relict lateral moraines overridden by the Fennoscandian ice sheet. *Quaternary Research*, **65**, 136–146.

Fink, D. & Smith, A. 2007. An inter-comparison of ^{10}Be and ^{26}Al AMS reference standards and the ^{10}Be half-life. *Nuclear Instruments and Methods in Physics Research*, **B259**, 600–609.

Fink, D., McKelvey, B., Hambrey, M., Fabel, D. & Brown, R. 2006. Pleistocene deglaciation chronology of the Radok Lake basin, Amery Oasis, northern Prince Charles Mountains, Antarctica. *Planetary Science Letters*, **243**, 229–243.

Gosse, J.C. & Phillips, F.M. 2001. Terrestrial *in situ* cosmogenic nuclides: theory and application. *Quaternary Science Reviews*, **20**, 1475–1560.

Gore, D.B., Rhodes, E.J., Augustinus, P.C., Leishman, M.R., Colhoun, E.A. & Rees-Jones, J. 2001. Bunger Hills, East Antarctica: ice free at the Last Glacial Maximum. *Geology*, **29**, 1103–1106.

Haskell, T.R., Kennett, J.P. & Prebble, W.M. 1964. Basement and sedimentary geology of the Darwin Glacier area. *In* Adie, R.J., *ed. Antarctic geology*. Amsterdam: North-Holland Publishing Company, 348–351.

Hood, D. 2010. *The Pleistocene glacial history of the Lake Wellman area, Darwin Mountains, Antarctica*. MSc thesis, Department of Geological Sciences, University of Canterbury, Christchurch, New Zealand, 168 pp. [Unpublished].

Howard-Williams, C., Peterson, D., Lyons, W.B., Cattaneo-Vietti, R. & Gordon, S. 2006. Measuring ecosystem response in a rapidly changing environment: the Latitudinal Gradient Project. *Antarctic Science*, **18**, 465–471.

Huybrechts, P. 2002. Sea-level changes at the LGM from ice-dynamic reconstructions of the Greenland and Antarctic ice sheets during the glacial cycles. *Quaternary Science Reviews*, **21**, 203–231.

Korschinek, G., Bergmaier, A., Faestermann, T., Gerstmann, U.C., Knie, K., Rugel, G., Wallner, A., Dillmann, I., Dollinger, G., von Gostomski, C.L., Kossert, K., Maiti, M., Poutivtsev, M. & Remmert, A. 2009. A new value for the half-life of ^{10}Be by heavy-ion elastic recoil detection and liquid scintillation counting. *Nuclear Instruments and Methods in Physics Research, B*, **268**, 187–191.

Lilly, K., Fink, D., Fabel, D. & Lambek, K. 2010. Pleistocene dynamics of the interior East Antarctic ice sheet. *Geology*, **38**, 703–706.

Mackintosh, A., White, D., Fink, D., Gore, D.B., Pickard, J. & Fanning, P.C. 2007. Exposure ages from mountain dipsticks in Mac. Robertson Land, East Antarctica, indicate little change in ice-sheet thickness since the Last Glacial Maximum. *Geology*, **35**, 551–554.

Miller, G.H., Wolfe, A.P., Steig, E.J., Sauer, P.E., Kaplan, M.R. & Briner, J.P. 2002. The Goldilocks dilemma: big ice, little ice, or "just-right" ice in the eastern Canadian Arctic. *Quaternary Science Reviews*, **21**, 33–48.

Nakada, M. & Lambeck, K. 1988. The melting history of the late Pleistocene Antarctic ice sheet. *Nature*, **333**, 36–40.

Nishiizumi, K., Imamura, M., Caffee, M.W., Southon, J.R., Finkel, R.C. & McAninch, J. 2007. Absolute calibration of ^{10}Be AMS standards. *Nuclear Instruments and Methods in Physics Research*, **B258**, 403–413.

Putkonen, J. & Swanson, T. 2003. Accuracy of cosmogenic ages for moraines. *Quaternary Research*, **59**, 255–261.

Ruprecht, U., Lumbsch, H.T., Brunauer, G., Green, T.G.A. & Türk, R. 2010. Diversity of *Lecidea* (Lecideaceae, Ascomycota) species revealed by molecular data and morphological characters. *Antarctic Science*, **21**, 10.1017/S0954102010000477.

Stevens, M. & Hogg, I.D. 2006. Contrasting levels of mitochondrial DNA variability between mites (Penthalodidae) and sprigtails (Hypogastruridae) from the Trans-Antarctic Mountains suggest long-term effects of glaciation and life history on substitution rates, and speciation processes. *Soil Biology & Biochemistry*, **38**, 3171–3180.

Stevens, M.I., Greenslade, P., Hogg, I.D. & Sunnucks, P. 2006. Southern Hemisphere springtails: could any have survived glaciation of Antarctica? *Molecular Biology & Evolution*, **23**, 874–882.

STEVENS, M.I., FRATI, F., MCGAUGHRAN, A., SPINSANTI, G. & HOGG, I.D. 2007. Phylogeographic structure suggests multiple glacial refugia in northern Victoria Land for the endemic Antarctic springtail *Desoria klovstadi*, (Collembola, Isotomidae). *Zoologica Scripta*, **36**, 201–212.

STONE, J.O. 2000. Air pressure and cosmogenic isotope production. *Journal of Geophysical Research*, **105**, 753–759.

STONE, J.O., BALCO, G.A., SUGDEN, D.E., CAFFEE, M.W., SASS, L.C., COWDERY, S.G. & SIDDOWAY, C. 2003. Holocene deglaciation of Marie Byrd Land, West Antarctica. *Science*, **299**, 99–102.

STROEVEN, A.P., FABEL, D., HÄTTESTRAND, C. & HARBOR, J. 2002. A relict landscape in the centre of Fennoscandian glaciation: cosmogenic radionuclide evidence of tors preserved through multiple glacial cycles. *Geomorphology*, **44**, 145–154.

SUGDEN, D.E., BENTLEY, M.J. & COFAIGH, C.Ó. 2006. Geological and geomorphological insights into Antarctic ice sheet evolution. *Philosophical Transactions of the Royal Society*, **A364**, 1607–1625.

SUGDEN, D.E., BALCO, G., COWDERY, S.G., STONE, J.O. & SASS, L.C. 2005. Selective glacial erosion and weathering zones in the coastal mountains of Marie Byrd Land, Antarctica. *Geomorphology*, **67**, 317–334.

Bibliography

Abdi, H. and Williams, L. (2010). Principal component analysis. *Wiley Interdisciplinary Reviews: Computational Statistics*, 2(4):433–459. 177

Ackert, R., Barclay, D., Borns, H., Calkin, P., Kurz, M., Fastook, J., and Steig, E. (1999). Measurements of past ice sheet elevations in interior West Antarctica. *Science*, 286(5438):276–280. 74, 77

Ackert, R. and Kurz, M. (2004). Age and uplift rates of Sirius Group sediments in the Dominion Range, Antarctica, from surface exposure dating and geomorphology. *Global and Planetary Change*, 42(1-4):207–225. 41, 70

Ackert, R., Mukhopadhyay, S., Parizek, R., and Borns, H. (2007). Ice elevation near the West Antarctic Ice Sheet divide during the Last Glaciation. *Geophysical Research Letters*, 34(21):L21506. 73, 77

Ackert, R., Mukhopadhyay, S., Pollard, D., DeConto, R., Putnam, A., and Borns, H. (2011). West Antarctic Ice Sheet elevations in the Ohio Range: Geologic constraints and ice sheet modelling prior to the last highstand. *Earth and Planetary Science Letters*, 307(1-2):83–93. 22, 110

Ackert, R., Putnam, A., Mukhopadhyay, S., Pollard, D., DeConto, R., Kurz, M., and Borns, H. (2013). Controls on interior West Antarctic Ice Sheet Elevations: inferences from geologic constraints and ice sheet modeling. *Journal of Quaternary Science*, 65:26–38. 5, 59, 73, 74, 77, 215

Adkins, J., McIntyre, K., and Schrag, D. (2002). The salinity, temperature, and δ18O of the glacial deep ocean. *Science*, 298:1769–1773. 55

Aislabie, J., Bockheim, J., Mcleod, M., Hunter, D., Stevenson, B., and Barker, G. (2012). Microbial biomass and community structure changes along a soil development chronosequence near Lake Wellman , southern Victoria Land. *Antarctic Science*, 24(2):154–164. 85, 115

Anderson, B., Hindmarsh, R., and Lawson, W. (2004). A modelling study of the response of Hatherton Glacier to Ross Ice Sheet grounding line retreat. *Global and Planetary Change*, 42(1-4):143–153. 70, 72, 85, 100, 102, 184, 208, 210, 211, 221

Anderson, J. (2002). The Antarctic Ice Sheet during the Last Glacial Maximum and its subsequent retreat history: a review. *Journal of Quaternary Science*, 21(1-3):49–70. 56, 59

Anderson, J., Kirshner, A., and Simms, A. (2013). Constraints on Antarctic Ice Sheet configuration during and following the last glacial maximum and its episodic contribution to sea-level rise. *Geological Society, London, Special Publications*, 381. 2, 3, 56, 209

Anderson, J. and Shipp, S. (2001). Evolution of the West Antarctic Ice Sheet. In Bindschadler, R., editor, *The West Antarctic Ice Sheet: Behaviour and environment.*, pages 45–57. American Geophysical Union., Washington, DC. 54

Applegate, P., Urban, N., Keller, K., Lowell, T., Laabs, B., Kelly, M., and Alley, R. (2012). Improved moraine age interpretations through explicit matching of geomorphic process models to cosmogenic nuclide measurements from single landforms. *Quaternary Research*. 35

Atkins, C. (2002). Cold-based glacial abrasion features. *Unpublished report. Victoria University of Wellington, Wellington, New Zealand*, pages 127–148. 104

Atkins, C. (2013). Geomorphological evidence of cold-based glacier activity in South Victoria Land, Antarctica. *Geological Society, London, Special Publications*, 381. 33, 37, 44, 69, 106, 132, 135, 158, 159, 203

Atkins, C., Barrett, P., and Hicock, S. (2002). Cold glaciers erode and deposit: evidence from Allan Hills, Antarctica. *Geology*, 30(7):659–662. 33, 103, 104, 106, 113, 132, 135

Augustin, L., Barbante, C., Barnes, P., Baroni, C., Bigler, M., Castellano, E., Cattani, O., Chappellaz, J., Dahl-Jensen, D., Delmonte, B., Dreyfus, G., Durand, G., Falourd, S., Fischer, H., Flückiger, J., Hansson, M., Huybrechts, P., Jugie, G., Johnsen, S., Jouzel, J., Kaufmann, P., Kipfstuhl, J., Lambert, F., Lipenkov, V., Littot, G., Longinelli, A., Lorrain, R., Maggi, V., Masson-Delmotte, V., Miller, H., Mulvaney, R., Oerlemans, J., Oerter, H., Orombelli, G., Parrenin, F., Peel, D., Petit, J., Raynaud, D., Ritz, C., Ruth, U., Schwander, J., Siegenthaler, U., Souchez, R., Stauffer, B., Steffensen, J., Stenni, B., Stocker, T., Tabacco, I., Udisti, R., van de Wal, R., van den Broeke, M., Weiss, J., Wilhelms, F., Wolff, E., and Zucchelli, M. (2004). Eight glacial cycles from an Antarctic ice core. *Nature*, 429(6992):623–8. 1

Balco, G. (2011). Contributions and unrealized potential contributions of cosmogenic-nuclide exposure dating to glacier chronology, 1990âĂŞ2010. *Journal of Quaternary Science*, 30(1-2):3–27. 10, 32, 72

Balco, G., Stone, J., Lifton, N., and Dunai, T. (2008). A complete and easily accessible means of calculating surface exposure ages or erosion rates from 10Be and 26Al measurements. *Quaternary Geochronology*, 3(3):174–195. 13, 23, 30, 146, 170, 172, 175

Bamber, J. (2000). Widespread complex flow in the interior of the Antarctic Ice Sheet. *Science*, 287(5456):1248–1250. 52

Bamber, J., Gomez-Dans, J., and Griggs, J. (2009). A new 1 km digital elevation model of the Antarctic derived from combined satellite radar and laser data âĂŞ Part 1: Data and methods. *The Cryosphere*, 3(1):101–110. 58, 100

Baroni, C. and Fasano, F. (2006). Micromorphological evidence of warm-based glacier deposition from the Ricker Hills Tillite (Victoria Land, Antarctica). *Journal of Quaternary Science*, 25(9-10):976–992. 105

Baroni, C., Fasano, F., Giorgetti, G., Salvatore, M., and Ribecai, C. (2008). The Ricker Hills tillite provides evidence of Oligocene warm-based glaciation in Victoria Land, Antarctica. *Global and Planetary Change*, 60:457–470. 79

Baroni, C. and Orombelli, G. (1989). Glacial geology and geomorphology of Terra Nova Bay (Victoria Land, Antarctica). *Memorie della Società Italiana*, 33(1987):171–193. 79

Barrett, P. (2007). Cenozoic climate and sea level history from glacimarine strata off the Victoria Land coast, Cape Roberts Project, Antarctica. *Glacial Sedimentary Processes and Products*, 39:259–287. 49

Barrett, P., Hambrey, M., and Robinson, P. (1991). Cenozoic glacial and tectonic history from CIROS-1, McMurdo Sound. In Crame, J. and Thomson, J., editors, *Geological Evolution of Antarctica.*, pages 285–291. Cambridge University Press. 87

Barrett, P., Kohn, B., Askin, R., and McPherson, J. (1971). Preliminary report on Beacon Supergroup studies between the Hatherton and Mackay Glaciers , Antarctica. *New Zealand Journal of Geology and Geophysics*, 14(3):605–614. 91

Bart, P. (2003). Were West Antarctic Ice Sheet grounding events in Ross Sea a consequence of East Antarctic Ice Sheet expansion during the middle Miocene? *Earth and Planetary Science Letters*, 216:93–107. 50, 54

Bart, P. and Anderson, J. (2000). Relative temporal stability of the Antarctic ice sheets during the late Neogene based on the minimum frequency of outer shelf grounding events. *Earth and Planetary Science Letters*, 182(3):259–272. 54

Bartek, L., Sloan, L., Anderson, J., and Ross, M. (1992). Evidence from the Antarctic continental margin of late Paleogene ice sheets: A manifestation of plate reorganization and synchronous changes in atmospheric circulation over the emerging Southern Ocean? In Prothero, D. and Berggren, W., editors, *Eocene-Oligocene Climatic and Biotic Evolution.*, pages 131–159. Princeton University Press., Princeton, New Jersey, USA. 50, 54

Benn, D. and Evans, J. (2006). *Glaciers and glaciations*. Arnold, London, UK, 3 edition. 104, 105

Bentley, M. (1999). Volume of Antarctic ice at the Last Glacial Maximum, and its impact on global sea level change. *Journal of Quaternary Science*, 18(14):1569–1595. 58

Bentley, M. (2010). The Antarctic paleo record and its role in improving predictions of future Antarctic Ice Sheet change. *Journal of Quaternary Science*, 25(1):5–18. 2, 59

Bentley, M., Fogwill, C., Kubik, P., and Sugden, D. (2006). Geomorphological evidence and cosmogenic 10Be/26Al exposure ages for the Last Glacial Maximum and deglaciation of the Antarctic Peninsula Ice Sheet. *Geological Society of America Bulletin*, 118(9):1149–1159. 128

Bierman, P. and Turner, J. (1995). 10Be and 26Al evidence for exceptionally low rates of Australian bedrock erosion and the likely existence of Pre-Pleistocene landscapes. *Quaternary Research*, 44(3):378–382. 42

Bindschadler, R. (2006). The environment and evolution of the West Antarctic ice sheet: setting the stage. *Philosophical transactions. Series A, Mathematical, physical, and engineering sciences*, 364(1844):1583–605. 53

Bo, S., Siegert, M., Mudd, S., Sugden, D., Fujita, S., Xiangbin, C., Yunyun, J., Xueyuan, T., and Yuansheng, L. (2009). The Gamburtsev mountains and the origin and early evolution of the Antarctic Ice Sheet. *Nature*, 459(7247):690–3. 51

Bockheim, J. (2010). Soil preservation and ventifact recycling from dry-based glaciers in Antarctica. *Antarctic Science*, 22(04):409–417. 33, 37, 107, 110, 113, 115, 135

Bockheim, J., Prentice, M., and McLeod, M. (2008). Distribution of glacial deposits, soils, and permafrost in Taylor Valley, Antarctica. *Arctic, Antarctic and Alpine Research*, 40(2):279–286. 113

Bockheim, J. and Wilson, S. (1979). Pedology of the Darwin Glacier area. *Antarctic Journal of the United States*, 14(October 1978):58–59. 153

Bockheim, J., Wilson, S., Denton, G., Andersen, B., and Stuiver, M. (1989). Late Quaternary ice-surface fluctuations of Hatherton Glacier, Transantarctic Mountains. *Quaternary Research*, 31(2):229–254. iii, 3, 5, 7, 47, 66, 67, 70, 71, 72, 81, 82, 85, 97, 102, 106, 107, 108, 109, 110, 111, 112, 113, 114, 115, 116, 117, 118, 119, 120, 121, 123, 126, 127, 128, 129, 130, 132, 133, 134, 135, 136, 139, 140, 141, 142, 143, 151, 153, 154, 155, 161, 163, 164, 183, 184, 192, 193, 194, 195, 196, 197, 199, 202, 203, 207, 208, 209, 210, 211, 221, 230, 238, 239, 251, 256, 257

Boggs, S. (2006). *Principles of sedimentology and stratigraphy*. Pearson Prentice Hall, Upper Saddle River, NJ, USA, 4th edition. 105

Böhm, G., Ocakouglu, N., Picotti, S., and De Santis, L. (2009). West Antarctic Ice Sheet evolution: New insights from a seismic tomographic 3D depth model in the Eastern Ross Sea (Antarctica). *Marine Geology*, 266(1):109–128. 54

Bormann, J., Surpless, B., Caffee, M., and Wesnousky, S. (2012). Holocene earthquakes and late-Pleistocene slip-rate estimates on the Wassuk Range fault zone, Nevada. *Bulletin of the Seismological Society of America*, 102(4):1884–1891. 12

Briner, J. (2009). Moraine pebbles and boulders yield indistinguishable 10Be ages: A case study from Colorado, USA. *Quaternary Geochronology*, 4(4):299–305. 46

Briner, J., Kaufman, D., Manley, W., Finkel, R., and Caffee, M. (2005). Cosmogenic exposure dating of late-Pleistocene moraine stabilization in Alaska. *Geological Society of America Bulletin*, 117(7):1108. 37

Briner, J., Lifton, N., Miller, G., Refsnider, K., Anderson, R., and Finkel, R. (2012). Using in situ cosmogenic 10Be, 14C, and 26Al to decipher the history of polythermal ice sheets on Baffin Island, Arctic Canada. *Quaternary Geochronology*, pages 1–10. 21

Bromley, G., Hall, B., Stone, J., and Conway, H. (2012). Late-Pleistocene evolution of Scott Glacier, southern Transantarctic Mountains: implications for the Antarctic contribution to deglacial sea level. *Journal of Quaternary Science*, 50:1–13. 66, 70, 71, 74, 82, 210

Bromley, G., Hall, B., Stone, J., Conway, H., and Todd, C. (2010). Late-Cenozoic deposits at Reedy Glacier, Transantarctic Mountains: implications for former thickness of the West Antarctic Ice Sheet. *Journal of Quaternary Science*, 29(3-4):384–398. 4, 5, 42, 70, 74, 80, 81, 202, 204, 206

Brook, E., Brown, E., Kurz, M., Ackert, R., Raisbeck, G., and Yiou, F. (1995a). Constraints on age, erosion, and uplift of Neogene glacial deposits in the Transantarctic Mountains determined from in situ cosmogenic 10Be and 26Al. *Geology*, 23(12):1063–1066. 41

Brook, E. and Kurz, M. (1993). Surface exposure chronology using in situ 3He in Antarctic quartz sandstone boulders. *Quaternary Research*, 39:1–10. 74, 78

Brook, E., Kurz, M., and Ackert, R. (1993). Chronology of Taylor Glacier advances in Arena Valley, Antarctica, using in situ cosmogenic 3He and 10Be. *Quaternary Research*, 39:11–23. 120

Brook, E., Kurz, M., Ackert, R., Raisbeck, G., and Yiou, F. (1995b). Cosmogenic nuclide exposure ages and glacial history of late-Quaternary Ross Sea drift in McMurdo Sound, Antarctica. *Earth and Planetary Science Letters*, 131(1-2):41–56. 41, 74, 75

Brook, E., White, J., Schilla, A., Bender, M., Barnett, B., Severinghaus, J., Taylor, K., Alley, R., and Steig, E. (2005). Timing of millennial-scale climate change at Siple Dome, West Antarctica, during the last glacial period. *Journal of Quaternary Science*, 24(12-13):1333–1343. 64

Brown, E., Bourles, D., Colin, F., Raisbeck, G., Yiou, F., and Desgarceaux, S. (1995). Evidence for muon-induced production of 10Be in near-surface rocks from the Congo. *Geophysical Research Letters*, 22(6):703–706. 22, 28

Brown, E., Edmond, J., Raisbeck, G., Yiou, F., Kurz, M., and Brook, E. (1991). Examination of surface exposure ages of Antarctic moraines using in situ produced 10Be and 26Al. *Geochimica et Cosmochimica Acta*, 55(8):2269–2283. 21, 78

Brunt, K., Fricker, H., Padman, L., Scambos, T., and O'Neel, S. (2010). Mapping the grounding zone of the Ross Ice Shelf, Antarctica, using ICESat laser altimetry. *Annals of Glaciology*, 51(55):71–79. 60

Budel, B., Schulz, B., Reichenberger, H., Bicker, F., and Green, T. G. (2009). Cryptoendolithic cyanobacteria from calcite marble rock ridges, Taylor Valley, Antarctica. *Algological Studies*, 129(1):61–69. 36

Butler, E. (1999). Process environments on modern and raised beaches in McMurdo Sound, Antarctica. *Marine Geology*, 162(1):105–120. 66

Carlson, A. and Winsor, K. (2012). Northern Hemisphere ice-sheet responses to past climate warming. *Nature Geoscience*, 5(9):607–613. 1, 55

Cary, S., McDonald, I., Barrett, J., and Cowan, D. (2010). On the rocks: the microbiology of Antarctic Dry Valley soils. *Nature Reviews Microbiology*, 8:129–138. 92

Child, D., Elliott, G., Mifsud, C., Smith, A., and Fink, D. (2000). Sample processing for earth science studies at ANTARES. *Nuclear Instruments and Methods in Physics Research Section B: Beam Interactions with Materials and Atoms*, 172(1-4):856–860. 13, 45

Clark, D., Bierman, P., and Larsen, P. (1995). Improving in situ cosmogenic chronometers. *Quaternary Research*, 44(3):366–376. 21

Clark, P. (1982). The Derrick Peak, Antarctica, iron meteorites. *Meteoritics*, 17(3):129–134. 122

Cockburn, H., Seidl, M., and Summerfield, M. (1999). Quantifying denudation rates on inselbergs in the central Namib Desert using in situâĂŞproduced cosmogenic 10Be and 26Al. *Geology*, 27(5):399–402. 42

Codilean, A. (2006). Calculation of the cosmogenic nuclide production topographic shielding scaling factor for large areas using DEMs. *Earth Surface Processes and Landforms*, 794:785–794. 30

Conway, H., Hall, B., Denton, G., Gades, A., and Waddington, E. (1999). Past and future grounding-line retreat of the West Antarctic Ice Sheet. *Science*, 286(5438):280–283. 66, 67, 68, 70, 108, 184, 218, 219

Corbett, L., Young, N., Bierman, P., Briner, J., Neumann, T., Rood, D., and Graly, J. (2011). Paired bedrock and boulder 10Be concentrations resulting from early Holocene ice retreat near Jakobshavn Isfjord, western Greenland. *Journal of Quaternary Science*, 30(13-14):1739–1749. 47

Craig, H. and Poreda, R. J. (1986). Cosmogenic 3He in terrestrial rocks: The summit lavas of Maui. *Proceedings of the National Academy of Sciences*, 83(7):1970–1974. 9

Cuffey, K., Conway, H., Gades, A., Hallet, B., Lorrain, R., Severinghaus, J., Steig, E., Vaughn, B., and White, J. (2000). Entrainment at cold glacier beds. *Geology*, 28(4):351–354. 103

Dalziel, I. and Lawver, L. (2001). The lithospheric setting of the West Antarctic Ice Sheet. In Bindschadler, R., editor, *The West Antarctic Ice Sheet: Behaviour and environment.*, pages 29–44. American Geophysical Union., Washington, DC, 77 edition. 52

Davis, P., Briner, J., Coulthard, R., Finkel, R., and Miller, G. (2006). Preservation of Arctic landscapes overridden by cold-based ice sheets. *Quaternary Research*, 65(1):156–163. 106

Davis, R. and Schaeffer, O. (1955). Chlorine-36 in nature. *Annals of the New York Academy of Sciences*, 62(5):107–121. 9

De Santis, L., Prato, S., Brancolini, G., Lovo, M., and Torelli, L. (1999). The Eastern Ross Sea continental shelf during the Cenozoic: Implications for the West Antarctic Ice Sheet development. *Global and Planetary Change*, 23:173–196. 50, 54

DeConto, R. and Pollard, D. (2003). Rapid Cenozoic glaciation of Antarctica induced by declining atmospheric CO2. *Nature*, 421(6920):245–9. 2, 49, 50, 51, 87

DeConto, R., Pollard, D., and Kowalewski, D. (2012). Modeling Antarctic ice sheet and climate variations during marine isotope stage 31. *Global and Planetary Change*, In Press. 60

Delmas, M., Gunnell, Y., Braucher, R., Calvet, M., and Bourles, D. (2008). Exposure age chronology of the last glaciation in the eastern Pyrenees. *Quaternary Research*, 69(2):231–241. 47

Denton, G. (1979). Glacial history of the Byrd-Darwin Glacier area, Transantarctic Mountains. *Antarctic Journal of the United States*, 14(5):57–58. 5, 85, 87, 108, 121

Denton, G., Andersen, B., and Conway, H. (1986a). Late quaternary surface fluctuations of Beardmore Glacier, Antarctica. *Antarctic journal of the United States*, 21(5):90–92. 59, 121

Denton, G., Anderson, R., Toggweiler, J., Edwards, R., Schaefer, J., and Putnam, A. (2010). The last glacial termination. *Science*, 328(5986):1652–6. 55

Denton, G., Armstrong, R., and Stuiver, M. (1970). Late Cenozoic glaciation in Antarctica: the record in the McMurdo Sound region. *Antarctic journal of the United States*, 5(1):15–21. 121

Denton, G., Bockheim, J., Wilson, S., Leide, J. E., and Andersen, B. (1989a). Late Quaternary ice-surface fluctuations of Beardmore Glacier, Transantarctic Mountains. *Quaternary Research*, 31(2):183–209. 3, 66, 70, 71, 82, 120, 121, 161, 184

Denton, G., Bockheim, J., Wilson, S., and Schuluchter, C. (1986b). Late Cenozoic history of Rennick Glacier and Talos Dome, northern Victoria Land, Antarctica. In *Volume 46: Geological investigations in northern Victoria land*, pages 339—-375. American Geophysical Union. 121

Denton, G., Bockheim, J., Wilson, S., and Stuiver, M. (1989b). Late Wisconsin and early Holocene glacial history, inner Ross embayment, Antarctica. *Quaternary Research*, 31(2):151–182. 72, 117, 121

Denton, G., Borns, H., GrosvalâĂŹs, M., Stuiver, M., and Nichols, R. (1975). Glacial history of the Ross Sea. *Antarctic journal of the United States*, 10(4):160–164. 121

Denton, G. and Hughes, T. (2000). Reconstruction of the Ross Ice Drainage System, Antarctica, at the Last Glacial Maximum. *Geografiska Annaler, Series A: Physical Geography*, 82(2-3):143–166. 64, 66, 72

Denton, G. and Hughes, T. (2002). Reconstructing the Antarctic Ice Sheet at the Last Glacial Maximum. *Journal of Quaternary Science*, 21(1-3):193–202. 2, 58, 59, 64, 72, 73, 77, 81, 85, 112, 136, 184, 210, 211

Denton, G. and Marchant, D. (2000). The geologic basis for a reconstruction of a grounded ice sheet in McMurdo Sound, Antarctica, at the Last Glacial Maximum. *Geografiska Annaler, Series A: Physical Geography*, 82(2-3):167–211. 2, 4, 49, 65, 66, 112, 120, 210, 211

Denton, G., Prentice, M., and Burckle, L. (1991). Cainozoic history of the Antarctic Ice Sheet. In Tingey, R., editor, *Geology of Antarctica*, pages 365–433. Oxford University Press, New York, NY ,USA. 58, 59

Denton, G. and Sugden, D. (2005). Meltwater Features That Suggest Miocene Ice-Sheet Overriding of the Transantarctic Mountains in Victoria Land, Antarctica. *Geografiska Annaler, Series A: Physical Geography*, 87(1):67–85. 125

Desilets, D., Zreda, M., and Prabu, T. (2006). Extended scaling factors for in situ cosmogenic nuclides: New measurements at low latitudes. *Earth and Planetary Science Letters*, 246(3):265–276. 23, 26

Di Nicola, L., Baroni, C., Strasky, S., Salvatore, M., Schlüchter, C., Akçar, N., Kubik, P., and Wieler, R. (2012). Multiple cosmogenic nuclides document the stability of the East Antarctic Ice Sheet in northern Victoria Land since the Late Miocene (5âĂŞ7 Ma). *Journal of Quaternary Science*, 57:85–94. 4, 41, 43

Di Nicola, L., Strasky, S., Schlüchter, C., Salvatore, M., Akçar, N., Kubik, P., Christl, M., Kasper, H., Wieler, R., and Baroni, C. (2009). Multiple cosmogenic nuclides document complex Pleistocene exposure history of glacial drifts in Terra Nova Bay (northern Victoria Land, Antarctica). *Quaternary Research*, 71(1):83–92. 74, 79, 106

Diehl, R., Halloin, H., Kretschmer, K., Lichti, G., Schönfelder, V., Strong, A., von Kienlin, A., Wang, W., Jean, P., Knödlseder, J., Roques, J., Weidenspointner, G., Schanne, S., Hartmann, D., Winkler, C., and Wunderer, C. (2006). Radioactive 26Al from massive stars in the Galaxy. *Nature*, 439(7072):45–7. 10

Domack, E., Jacobson, E., Shipp, S., and Anderson, J. (1999). Late PleistoceneâĂŞHolocene retreat of the West Antarctic Ice Sheet: Part 2 Sedimentologic and stratigraphic signature. *Geological Society of America Bulletin*, 111(April 2009):1517–1536. 67

Doran, P., Priscu, J., Lyons, W., Walsh, J., Fountain, A., McKnight, D., Moorhead, D., Virginia, R., Wall, D., Clow, G., Fritsen, C., McKay, C., and Parsons, A. (2002). Antarctic climate cooling and terrestrial ecosystem response. *Nature*, 415(6871):517–20. 92

Dorman, L. I., Valdes-Galicia, J. F., and Dorman, I. (1999). Numerical simulation and analytical description of solar neutron transport in the EarthâĂŹs atmosphere. *Journal of Geophysical Research*, 104:22417–22426. 10

Dunai, T. (2000). Scaling factors for production rates of in situ produced cosmogenic nuclides: a critical reevaluation. *Earth and Planetary Science Letters*, 176(1):157–169. 23

Dunai, T. (2001). Influence of secular variation of the geomagnetic field on production rates of in situ produced cosmogenic nuclides. *Earth and Planetary Science Letters*, 193(1):197–212. 23, 26, 27, 41

Dunai, T. (2010). *Cosmogenic nuclides: principles, concepts and applications in the earth surface sciences*. Cambridge University Press, Cambridge, UK., first edition. 11, 23

Dunne, J., Elmore, D., and Muzikar, P. (1999). Scaling factors for the rates of production of cosmogenic nuclides for geometric shielding and attenuation at depth on sloped surfaces. *Geomorphology*, 27(1):3–11. 29, 31

Elliott, C. (2006). *Physical rock weathering along the Victoria Land coast , Antarctica.* PhD thesis, University of Canterbury. 95, 96

Exon, N., Kennett, J., and Malone, M. (2004). *The Cenozoic Southern Ocean: Tectonics, sedimentation and climate change Between Australia and Antarctica*. American Geophysical Union. 50

Fabel, D., Fink, D., Fredin, O., Harbor, J., Land, M., and Stroeven, A. (2006). Exposure ages from relict lateral moraines overridden by the Fennoscandian ice sheet. *Quaternary Research*, 65(1):136–146. 33

Fairbanks, R. (1989). A 17,000 year glacio-eustatic sea level record: influence of glacial melting rates on Younger Dryas event and deep ocean circulation. *Nature*, 342:637–642. 1

Faure, G. and Mensing, T. (2011). *The Transantarctic Mountains*. Springer Netherlands, Dordrecht. 2, 162

Federico, L., Capponi, G., and Crispini, L. (2006). The Ross orogeny of the transantarctic mountains: a northern Victoria Land perspective. *International Journal of Earth Sciences*, 95(5):759–770. 89

Fink, D. and Smith, A. (2007). An inter-comparison of 10Be and 26Al AMS reference standards and the 10Be half-life. *Nuclear Instruments and Methods in Physics Research Section B: Beam Interactions with Materials and Atoms*, 259(1):600–609. 22

Fitzgerald, P. (1992). The Transantarctic Mountains of southern Victoria Land: The application of apatite ĭňĄssion track analysis to a rift. *Tectonics*, 11(3):634–662. 87

Fitzgerald, P. (2002). Landscape evolution of the Antarctic plate since the breakup of Gondwana, with an emphasis on the West Antarctic Rift System and the Transantarctic Mountains. *Royal Society of New Zealand Bulletin*, 35:453–469. 51, 88, 89

Fitzsimons, S. (2003). Ice-marginal terrestrial landsystems: polar continental glacier margins. In Evans, J., editor, *Glacial Landsystems*, pages 89–110. Arnold, London. 106

Fleming, K., Johnston, P., Zwartz, D., Yokoyama, Y., Lambeck, K., and Chappell, J. (1998). Refining the eustatic sea-level curve since the Last Glacial Maximum using far- and intermediate-field sites. *Earth and Planetary Science Letters*, 163(1-4):327–342. 55

Fogwill, C., Bentley, M., Sugden, D., a.R. Kerr, and Kubik, P. (2004). Cosmogenic nuclides 10Be and 26Al imply limited Antarctic Ice Sheet thickening and low erosion in the Shackleton Range for >1 m.y. *Geology*, 32(3):265. 43

Fogwill, C., Hein, A., Bentley, M., and Sugden, D. (2012). Do blue-ice moraines in the Heritage Range show the West Antarctic ice sheet survived the last interglacial? *Palaeogeography, Palaeoclimatology, Palaeoecology*, 335-336:61–70. 22

Fogwill, C. and Kubik, P. (2005). A glacial stage spanning the Antarctic cold reversal in Torres Del Paine (51S), Chile, based on preliminary cosmogenic exposure ages. *Geografiska Annaler, Series A: Physical Geography*, 87(2):403–408. 32

Fountain, A., Nylen, T., Monaghan, A., Basagic, H., and Bromwich, D. (2009). Snow in the McMurdo Dry Valleys , Antarctica. *International Journal of Climatology*. 37, 39, 92

Frankel, K., Brantley, K., Dolan, J., Finkel, R., Klinger, R., Knott, J., Machette, M., Owen, L., Phillips, F., Slate, J., and Wernicke, B. (2007). Cosmogenic 10Be and 36Cl geochronology of offset alluvial fans along the northern Death Valley fault zone: Implications for transient strain in the eastern California shear zone. *Journal of Geophysical Research*, 112(B6). 42

French, H. and Guglielmin, M. (2000). Cryogenic weathering of granite, northern Victoria Land, Antarctica. *Permafrost and Periglacial Processes*, 314(July):305–314. 98, 99

Frohlich, K. and Lubert, J. (1973). About the possibility to measure erosion rates of surface rocks using the natural radionuclides 41Ca and 39Ar. *Zeitschrift fur Geomorphologie*, 19:550. 9

Fujioka, T. (2012). Dune-field chronology in the Simpson Desert, revealed by cosmogenic nuclide and luminescence dating. *Quaternary International*, 279:153. 12

Golledge, N. R., Fogwill, C., Mackintosh, A., and Buckley, K. M. (2012). Dynamics of the last glacial maximum Antarctic Ice Sheet and its response to ocean forcing. *Proceedings of the National Academy of Sciences*, 109(40):16052–16056. 2, 55, 58, 59, 60, 66, 72, 213

Golledge, N. R. and Levy, R. (2011). Geometry and dynamics of an East Antarctic Ice Sheet outlet glacier, under past and present climates. *Journal of Geophysical Research*, 116(F3):F03025. 3, 70, 103, 136, 189, 191, 217

Gore, D., Rhodes, E., Augustinus, P., Leishman, M., Colhoun, E., and Rees-Jones, J. (2001). Bunger Hills, East Antarctica: Ice free at the Last Glacial Maximum. *Geology*, 29(12):1103–1106. 151

Gosse, J. (2011). Terrestrial cosmogenic nuclide techniques for assessing exposure history of surfaces and sediments in active tectonic regions. In Busby, C. and Azor, A., editors, *Tectonics of Sedimentary Basins: Recent Advances*. Wiley, Chicester, UK. 12

Gosse, J. and Phillips, F. (2001). Terrestrial in situ cosmogenic nuclides: theory and application. *Journal of Quaternary Science*, 20(14):1475–1560. 10, 11, 16, 21, 38, 42, 43, 44, 95

Goudie, A., editor (1994). *The encyclopedic dictionary of physical geography.* Blackwell, Oxford, 2nd edition. 95

Granger, D. and Muzikar, P. (2001). Dating sediment burial with in situ-produced cosmogenic nuclides: theory, techniques, and limitations. *Earth and Planetary Science Letters*, 188(1-2):269–281. 12, 44

Greenwood, S., Gyllencreutz, R., Jakobsson, M., and Anderson, J. (2012). Ice-flow switching and East/West Antarctic Ice Sheet roles in glaciation of the western Ross Sea. *Geological Society of America Bulletin*, 124(11-12):1736–1749. 64, 66

Grindley, G. and Laird, M. (1969). Geology of the Shackleton coast. *Antarctic Map Folio Series Folio 12, XIV.* 88, 89, 153, 154, 157

Grosse, A. (1934). An unknown radioactivity. *Journal of the American Chemical Society*, 56(1):1922–1924. 9

Guglielmin, M., Cannone, N., Strini, A., and Lewkowicz, A. G. (2005). Biotic and abiotic processes on granite weathering landforms in a cryotic environment , northern Victoria Land , Antarctica. *Permafrost and Periglacial Processes*, 85(June 2004):69–85. 98, 99

Guglielmin, M., Worland, M., Convey, P., and Cannone, N. (2011). Schmidt hammer studies in the maritime Antarctic: Application to dating Holocene deglaciation and estimating the effects of macrolichens on rock weathering. *Geomorphology.* 36

Guyodo, Y. and Valet, J. (1999). Global changes in intensity of the EarthâĂŹs magnetic field during the past 800 kyr. *Nature*, 399:249–252. 25, 26, 27

Hall, B. (2004). Holocene relative sea-level history of the southern Victoria Land Coast, Antarctica. *Global and Planetary Change*, 42(1-4):241–263. 41, 66, 96, 98

Hall, B. and Denton, G. (2000). Radiocarbon chronology of Ross Sea drift, eastern Taylor Valley, Antarctica: Evidence for a grounded ice sheet in the Ross Sea at the Last Glacial Maximum. *Geografiska Annaler, Series A: Physical Geography*, 82(2-3):305–336. 56, 64, 66, 72

Hall, B., Denton, G., Stone, J., and Conway, H. (2013). History of the grounded ice sheet in the Ross Sea sector of Antarctica during the Last Glacial Maximum and the last termination. *Geological Society, London, Special Publications*, 381. 66, 67, 68, 184

Hall, B., Hendy, C., and Denton, G. (2006). Lake-ice conveyor deposits : Geomorphology , sedimentology , and importance in reconstructing the glacial history of the Dry Valleys. *Geomorphology*, 75:143 – 156. 39

Hall, K., Guglielmin, M., and Strini, A. (2008). Weathering of granite in Antarctica : I . Light penetration into rock and implications for rock weathering and endolithic communities. *Earth Surface Processes and Landforms*, 307:295–307. 98

Hall, K., Thorn, C., Matsuoka, N., and Prick, A. (2002). Weathering in cold regions: some thoughts and perspectives. *Progress in Physical Geography*, 26(4):577–603. 36, 95

Hammer, O. and Harper, D. (2008). *Paleontological data analysis.* Wiley. 177

Haskell, T. R., Orombelli, G., and Prebble, W. (1964). Basement and sedimentary geology of the Darwin Glacier area. In ADIE, J. R., editor, *SCAR - IUGS. Symposium of Antarctic Geology.*, Cape Town, South Africa. 88, 90, 91, 125, 153

Hearty, P., Kindler, P., Cheng, H., and Edwards, R. (1999). A +20 m middle Pleistocene sea-level highstand (Bermuda and the Bahamas) due to partial collapse of Antarctic ice. *Geology*, 27(4):375–378. 61

Heimann, A., Fleming, T., Elliot, D., and Foland, K. (1994). A short interval of Jurassic continental flood basalt volcanism in Antarctica as demonstrated by 40Ar / 39Ar geochronology. *Earth and Planetary Science Letters*, 121:19–41. 91

Hein, A., Fogwill, C., Sugden, D., and Xu, S. (2011). Glacial/interglacial ice-stream stability in the Weddell Sea embayment, Antarctica. *Earth and Planetary Science Letters*, 307(1):211–221. 136

Hein, A., Fogwill, C., Sugden, D., and Xu, S. (2013). Geological scatter of cosmogenic-nuclide exposure ages in the Shackleton Range, Antarctica: implications for glacial history. *Quaternary Geochronology.* 177, 178, 180

Hendy, C. (2000). Late Quaternary lakes in the McMurdo Sound region of Antarctica. *Geografiska Annaler, Series A: Physical Geography*, 82A(2-3):411–432. 39

Heroy, D. and Anderson, J. (2005). Ice-sheet extent of the Antarctic Peninsula region during the Last Glacial Maximum (LGM)âĂŤInsights from glacial geomorphology. *Geological Society of America Bulletin*, 117(11):1497. 58

Heyman, J., Stroeven, A., Harbor, J., and Caffee, M. (2011). Too young or too old: Evaluating cosmogenic exposure dating based on an analysis of compiled boulder exposure ages. *Earth and Planetary Science Letters*, 302(1-2):71–80. 33, 34, 35, 36

Hodgson, D., Bentley, M., Schnabel, C., Cziferszky, A., Fretwell, P., Convey, P., and Xu, S. (2012). Glacial geomorphology and cosmogenic 10Be and 26Al exposure ages in the northern Dufek Massif, Weddell Sea embayment, Antarctica. *Antarctic Science*, 24(04):377–394. 5, 43

Hooke, R. (2005). *Principles of glacier mechanics.* Cambridge University Press, New York, NY ,USA, 2nd edition. 58

Howard-Williams, C., Hawes, I., and Gordon, S. (2010). The environmental basis of ecosystem variability in Antarctica : research in the Latitudinal Gradient Project. *Antarctic Science*, 22(6):591–602. 85

Hubbard, A., Lawson, W., Anderson, B., Hubbard, B., and Blatter, H. (2004). Evidence for subglacial ponding across Taylor Glacier, Dry Valleys, Antarctica. *Annals of Glaciology*, 39(1):79–84. 103

Hughes, T. and Fastook, J. (1981). Byrd Glacier: 1978-1979 field results. *Antarctic Journal of the United States*, 16(5):86–89. 85, 100

Humbert, A., Greve, R., and Hutter, K. (2005). Parameter sensitivity studies for the ice flow of the Ross Ice Shelf, Antarctica. *Journal of Geophysical Research - Earth Surface*, 110(F4). 100

Huybrechts, P. (1990). Antarctic Ice Sheet during the last glacial- interglacial cycle: a three-dimensional experiment. *Annals of Glaciology*, 14:115–119. 58

Huybrechts, P. (2002). Sea-level changes at the LGM from ice-dynamic reconstructions of the Greenland and Antarctic ice sheets during the glacial cycles. *Journal of Quaternary Science*, 21(1-3):203–231. 2, 58, 73, 81, 184, 210

Ingólfsson, O. (2004). Quaternary glacial and climate history of Antarctica. *Developments in Quaternary Science*, 2(Part C):3–43. 49

IPCC (2007). *Working Group I Contribution to the IPCC Fourth Assessment Report Climate Change 2007: the Physical Science Basis*. Cambridge University Press, Cambridge, UK. 2, 49, 52

Ishimaru, S. and Yoshikawa, K. (2000). The weathering of granodiorite porphyry in the Theil Mountains, inland Antarctica. Geografiska Annaler. *Geografiska Annaler, Series A: Physical Geography*, 82A(1):45–57. 96

Ivins, E. and James, T. (2005). Antarctic glacial isostatic adjustment: a new assessment. *Antarctic Science*, 17(04):541. 41

Ivy-ochs, S., Schlüchter, C., Kubik, P., Dittrich-hannen, B., and Beer, J. (1995). Minimum 10Be exposure ages of early Pliocene for the Table Mountain plateau and the Sirius Group at Mount Fleming ,. *Geology*. 43

James, T. and Ivins, E. (1998). Predictions of Antarctic crustal motions driven by present-day ice sheet evolution and by isostatic memory of the Last Glacial Maximum. *Journal of Geophysical Research*, 103(B3):4993–5017. 41

Jennings, J. (1968). Tafoni. In Fairbridge, R., editor, *The Encyclopedia of Geomorphology*. Reinhold, New York. 98

Johnson, J. and Staiger, J. (2007). Modeling long-term stability of the Ferrar Glacier, East Antarctica: Implications for interpreting cosmogenic nuclide inheritance. *Journal of Geophysical Research*, 112(F3):1–14. 70, 189, 190, 191

Jolliffe, I. (2005). Principal component analysis. In *Encyclopedia of Statistics in Behavioral Science*. John Wiley & Sons. 177

Joughin, I. and Alley, R. (2011). Stability of the West Antarctic ice sheet in a warming world. *Nature Geoscience*, 4(8):506–513. 54

Jouzel, J., Masson-Delmotte, V., Cattani, O., Dreyfus, G., Falourd, S., Hoffmann, G., Minster, B., Nouet, J., Barnola, J., Chappellaz, J., Fischer, H., Gallet, J., Johnsen, S., Leuenberger, M., Loulergue, L., Luethi, D., Oerter, H., Parrenin, F., Raisbeck, G., Raynaud, D., Schilt, A., Schwander, J., Selmo, E., Souchez, R., Spahni, R., Stauffer, B., Steffensen, J., Stenni, B., Stocker, T., Tison, J., Werner, M., and Wolff, E. (2007). Orbital and millennial Antarctic climate variability over the past 800,000 years. *Science*, 317(5839):793–6. 55, 61, 62, 63

Joy, K., Fink, D., Storey, B., and Atkins, C. (2014). A 2 million year glacial chronology of the Hatherton Glacier, Antarctica and implications for the size of the East Antarctic Ice Sheet at the Last Glacial Maximum. *Journal of Quaternary Science*, 83:46–57. 7

Jull, A., Burr, G., and Hodgins, G. (2012). Radiocarbon dating, reservoir effects, and calibration. *Quaternary International*. 117

Kamp, P. and Lowe, D. (1982). Geology and terrestrial age of the Derrick Peak meteorite occurrence, Antarctica. *Meteoritics*, 17(3):119–127. 85, 121, 122, 123, 200

Kavanaugh, J. and Cuffey, K. (2009). Dynamics and mass balance of Taylor Glacier, Antarctica: 2. Force balance and longitudinal coupling. *Journal of Geophysical Research: Earth Surface*, 114(F4):n/a—-n/a. 191

Kavanaugh, J., Cuffey, K., Morse, D., Conway, H., and Rignot, E. (2009). Dynamics and mass balance of Taylor Glacier, Antarctica: 1. Geometry and surface velocities. *Journal of Geophysical Research: Earth Surface*, 114(F4):n/a—-n/a. 191

Kennedy, A. (1993). Water as a limiting factor in the Antarctic terrestrial environments: A Biogeographic synthesis. *Arctic and Alpine Research*, 25(4):308–315. 120

Keys, J. (1980). Air temperature, wind, precipitation and atmospheric humidity in the McMurdo Region, Victoria, Antarctica. Technical report, Victoria University of Wellington, Wellington, New Zealand. 37

Kiernan, K., Gore, D., Fink, D., White, D., McConnell, A., and Sigurdsson, I. (2009). Deglaciation and weathering of Larsemann Hills, East Antarctica. *Antarctic Science*, 21(04):373. 98

Kirkbride, M., Bradshaw, M., and Harmsen, F. (1991). Further finds of the Derrick Peak meteorite, transantarctic mountains, and implications for terrestrial age. *Meteoritics*, 26(3):213–216. 85, 121, 122, 123, 200

Klein, J., Giegengack, R., Middleton, R., Sharma, P., Underwood, J., and Weeks, R. (1986). Revealing histories of exposure using in situ produced 26Al and 10Be in Libyan desert glass. *Radiocarbon*, 28(2A):547–555. 9

Kleman, J. (2007). Subglacial processes and the geomorphological impact of cold-based ice sheets. *Geophysical Research Abstracts*, 9:6999. 106

Knight, J. (2008). The environmental significance of ventifacts: A critical review. *Earth-Science Reviews*, 86(1-4):89–105. 115

Korschinek, G., Bergmaier, A., Faestermann, T., Gerstmann, U., Knie, K., Rugel, G., Wallner, A., Dillmann, I., Dollinger, G., and von Gostomski, C. (2010). A new value for the half-life of 10Be by Heavy-ion elastic recoil detection and liquid scintillation counting. *Nuclear Instruments and Methods in Physics Research Section B: Beam Interactions with Materials and Atoms*, 268(2):187–191. 13

Kruetzmann, N., Rack, W., McDonald, A., and George, S. (2011). Snow accumulation and compaction derived from GPR data near Ross Island ,Antarctica. *The Cryosphere*, 5:391–404. 37

Kubik, P., Ivy-Ochs, S., Masarik, J., Frank, M., and Schlüchter, C. (1998). Be and Al production rates deduced from an instantaneous event within the dendro-calibration curve, the landslide of Kofels, Otz Valley, Austria. *Earth and Planetary Science Letters*, 161(1-4):231–241. 23

Kubik, P. and Reuther, A. (2007). Attenuation of cosmogenic 10Be production in the first 20cm below a rock surface. *Nuclear Instruments and Methods in Physics Research Section B: Beam Interactions with Materials and Atoms*, 259(1):616–624. 38

Kurz, M. (1986). Cosmogenic helium in a terrestrial igneous rock. *Nature*, 320:435–439. 9

Lal, D. (1991). Cosmic ray labeling of erosion surfaces: in situ nuclide production rates and erosion models. *Earth and Planetary Science Letters*, 104:424–439. 14, 18, 23, 24, 25, 26, 27, 41

Lal, D. and Arnold, J. (1985). Tracing quartz through the environment. *Journal of Earth System Science*, 94(1):1–5. 16

Lal, D. and Peters, B. (1967). Cosmic ray produced radioactivity on Earth. In Flugg, S., editor, *Handbook of Physics*, pages 551–612. Springer, Berlin. 11

Lambeck, K. (2000). Global ice volumes at the Last Glacial Maximum and early Late glacial. *Earth and Planetary Science Letters*, 181(4):513–527. 57

Lambeck, K., Purcell, A., Johnston, P., Nakada, M., and Yokoyama, Y. (2003). Water-load definition in the glacio-hydro-isostatic sealevel equation. *Journal of Quaternary Science*, 22:309–318. 57

Lawver, L., Gahagan, L., and Coffin, M. (1992). The development of paleoseaways around Antarctica. *Antarctic research series*, 56:7–30. 88

LeMasurier, W. and Rex, D. (1983). Rates of uplift and the scale of ice level instabilities recorded by volcanic rocks in Marie Byrd Land, West Antarctica. In Oliver, R., James, P., and Jago, J., editors, *Antarctic Earth Science*, pages 663–670. Cambridge University Press, New York. 54

Lenaerts, J., van den Broeke, M., Déry, S., van Meijgaard, E., van de Berg, W., Palm, S., and Sanz Rodrigo, J. (2012). Modeling drifting snow in Antarctica with a regional climate model: 1. Methods and model evaluation. *Journal of Geophysical Research*, 117(D5):1–17. 37

Lewis, A., Marchant, D., Ashworth, A., Hemming, S., and Machlus, M. (2007). Major middle Miocene global climate change: Evidence from East Antarctica and the Transantarctic Mountains. *Geological Society of America Bulletin*, 119(11):1449–1461. 125

Li, Y., Fabel, D., Stroeven, A., and Harbor, J. (2008). Unraveling complex exposure-burial histories of bedrock surfaces under ice sheets by integrating cosmogenic nuclide concentrations with climate proxy records. *Geomorphology*, 99(1-4):139–149. 20

Libby, W., Anderson, E., and Arnold, J. (1949). Age determination by radiocarbon content : Assay of natural radiocarbon. *Science*, 109(2827):227–228. 9

Licht, K. and Andrews, J. (2002). The 14 C record of late-Pleistocene ice advance and retreat in the central Ross Sea, Antarctica. *Arctic, Antarctic and Alpine Research*, 34(3):324–333. 58

Lide, D. (1999). *CRC handbook of chemistry and physics: a ready-reference book of chemical and physical data*. CRC Press. Bacco Raton, Florida, 79th edition. 24, 26

Lifton, N., Bieber, J., Clem, J., Duldig, M., Evenson, P., Humble, J., and Pyle, R. (2005). Addressing solar modulation and long-term uncertainties in scaling secondary cosmic rays for in situ cosmogenic nuclide applications. *Earth and Planetary Science Letters*, 239(1):140–161. 23, 26

Lifton, N., Smart, D. F., and Shea, M. A. (2008). Scaling time-integrated in situ cosmogenic nuclide production rates using a continuous geomagnetic model. *Earth and Planetary Science Letters*, 268(1):190–201. 23

Lilly, K. (2008). *Three million years of East Antarctic Ice Sheet history from in situ cosmogenic nuclides in the Lambert-Amery Basin*. Phd, Australian National University. 5, 56, 57

Lilly, K., Fink, D., Fabel, D., and Lambeck, K. (2010). Pleistocene dynamics of the interior East Antarctic Ice Sheet. *Geology*, 38(8):703–706. 22, 73, 136, 174, 185

Lisiecki, L. and Raymo, M. (2005). A Pliocene-Pleistocene stack of 57 globally distributed benthic δ 18 O records. *Paleoceanography*, 20(1):1–17. 1, 60, 62, 63

Lloyd Davies, M., Atkins, C., van der Meer, J., Barrett, P., and Hicock, S. (2009). Evidence for cold-based glacial activity in the Allan Hills, Antarctica. *Journal of Quaternary Science*, 28(27-28):3124–3137. 103, 135

Lowell, T. (1995). The application of radiocarbon age estimates to the dating of glacial sequences: An example from the Miami sublobe, Ohio, U.S.A. *Journal of Quaternary Science*, 14(1):85–99. 132

Lythe, M. and Vaughan, D. (2001). BEDMAP- A new ice thickness and subglacial topographic model of Antarctica. *Journal of Geophysical Research*, 106(B6):11335–11351. 49, 51, 53, 58

MacAyeal, D. (1992). Irregular oscillations of the West Antarctic Ice Sheet. *Nature*, 359(6390):29–32. 54

Mackintosh, A., Golledge, N. R., Domack, E., Dunbar, R., Leventer, A., White, D., Pollard, D., DeConto, R., Fink, D., Zwartz, D., Gore, D., and Lavoie, C. (2011). Retreat of the East Antarctic Ice Sheet during the last glacial termination. *Nature Geoscience*, 4(3):195–202. 2, 55, 58, 59, 102, 136, 210, 213, 214, 215

Mackintosh, A., White, D., Fink, D., Gore, D., Pickard, J., and Fanning, P. (2007). Exposure ages from mountain dipsticks in Mac. Robertson Land, East Antarctica, indicate little change in ice-sheet thickness since the Last Glacial Maximum. *Geology*, 35(6):551–554. 5, 35, 56, 73

Magalhaes, C., Stevens, M., Cary, S., Ball, B., Storey, B., Wall, D., Türk, R., and Ruprecht, U. (2012). At limits of life: Multidisciplinary insights reveal environmental constraints on biotic diversity in continental Antarctica. *PLoS ONE*, 7(9):e44578. 85

Malvin, D., Wang, D., and Wasson, J. (1984). Chemical classification of iron meteorites-X . Multielement studies of 43 irons , resolution of group IIIE from IIIAB , and evaluation of Cu as a taxonomic parameter. *Geochimica et Cosmochimica Acta*, 48(4):785–804. 122

Marchant, D., Denton, G., Bockheim, J., Wilson, S., and Kerr, A. (1994). Quaternary changes in level of the upper Taylor Glacier , Antarctica : Implications for paleoclimate and East Antarctic Ice Sheet dynamics. *Boreas*, 23(23):29–43. 66, 70

Marchant, D. and Head, J. (2007). Antarctic dry valleys: Microclimate zonation, variable geomorphic processes, and implications for assessing climate change on Mars. *Icarus*, 192(1):187–222. 92, 99

Marti, K. and Craig, H. (1987). Cosmic-ray-produced neon and helium in the summit lavas of Maui. *Nature*, 325:335–337. 9

Masarik, J. and Beer, J. (2009). An updated simulation of particle fluxes and cosmogenic nuclide production in the Earth's atmosphere. *Journal of Geophysical Research*, 114(D11):D11103. 12

Masarik, J. and Reedy, R. C. (1996). Monte Carlo simulation of in-situ produced cosmogenic nuclides. *Radiocarbon*, 38:163–164. 10

Masson-Delmotte, V. (2000). Holocene climate variability in Antarctica based on 11 ice-core isotopic records. *Quaternary Research*, 54(3):348–358. 211, 217, 218, 219

Matmon, A., Stock, G., Granger, D., and Howard, K. (2012). Dating of Pliocene Colorado River sediments: Implications for cosmogenic burial dating and the evolution of the lower Colorado River. *Geological Society of America Bulletin*, 124(3-4):626–640. 12

Matsuoka, N. (1995). Rock weathering processes and landform development in the Sør Rondane Mountains, Antarctica. *Geomorphology*, 12(4):323–339. 98

Matsuoka, N., Moriwaki, K., and Hirakawa, K. (1996). Field experiments on physical weathering and wind erosion in an Antarctic cold desert. *Earth Surface Processes and Landforms*, 21(8):687–699. 96

Matsuoka, N. and Murton, J. (2008). Frost weathering : Recent advances and future directions. *Permafrost and Periglacial Processes*, 210(October 2007):195–210. 96

Matsuoka, N., Thomachot, C., Oguchi, C., Hatta, T., Abe, M., and Matsuzaki, H. (2006). Quaternary bedrock erosion and landscape evolution in the Sør Rondane Mountains, East Antarctica: Reevaluating rates and processes. *Geomorphology*, 81(3-4):408–420. 43, 98

Mayewski, P. (1982). Upper Rennick Glacier Ice Mass fluctuation Study. *Antarctic Journal of the United States*, 17(5):51. 121

Mayewski, P., Goldthwait, R., and Coates, D. (2013). *Glacial events in the Transantarctic Mountains: a record of the East Antarctic Ice Sheet*. American Geophysical Union, Washington, DC. 121

McCormac, F., Hogg, A., Blackwell, P., Buck, C., Higham, T., and Reimer, P. (2004). SHCAL04 Southern Hemisphere calibration, 0âĂŞ11.0 cal kyr BP. *Radiocarbon*, 46(3):1087–1092. 117

McKay, R., Dunbar, G., Naish, T., Barrett, P., Carter, L., and Harper, M. (2008). Retreat history of the Ross Ice Sheet (Shelf) since the Last Glacial Maximum from deep-basin sediment cores around Ross Island. *Palaeogeography, Palaeoclimatology, Palaeoecology*, 260(1-2):245–261. 64

McKay, R., Naish, T., Powell, R., Barrett, P., Scherer, R., Talarico, F., Kyle, P., Monien, D., Kuhn, G., Jackolski, C., and Williams, T. (2012). Pleistocene variability of Antarctic Ice Sheet extent in the Ross Embayment. *Journal of Quaternary Science*, 34:91–112. 61, 62, 63, 64, 67

Mercer, J. (1968). Glacial geology of the Reedy Glacier area, Antarctica. *Geological Society of America Bulletin*, 79(4):471–486. 52, 80, 121, 209

Mercer, J. (1972). *Some observations on the glacial geology of the Beardmore Glacier area*. Ohio State University, Institute of Polar Studies. 121

Mifsud, C., Fujioka, T., and Fink, D. (2012). Extraction and purification of quartz in rock using hot phosphoric acid for in situ cosmogenic exposure dating. *Nuclear Instruments and Methods in Physics Research Section B: Beam Interactions with Materials and Atoms*, 294:203–207. 13

Mix, A., Bard, E., and Schneider, R. (2001). Environmental processes of the ice age: land, oceans, glaciers (EPILOG). *Journal of Quaternary Science*, 20(4):627–657. 54

Monnin, E., Steig, E., Siegenthaler, U., Kawamura, K., Schwander, J., Stauffer, B., Stocker, T., Morse, D., Baroni, C., and Bellier, B. (2004). Evidence for substantial accumulation rate variability in Antarctica during the Holocene, through synchronization of CO2 in the Taylor Dome, Dome C and DML ice cores. *Earth and Planetary Science Letters*, 224(1-2):45–54. 64

Morgan, V., Delmotte, M., van Ommen, T., Jouzel, J., Chappellaz, J., Woon, S., Masson-Delmotte, V., and Raynaud, D. (2002). Relative timing of deglacial climate events in Antarctica and Greenland. *Science*, 297(5588):1862–4. 64

Moriwaki, K., Hirakawa, K., Hayashi, M., and Iwata, S. (1992a). Late Cenozoic glacial history in the Sør-Rondane Mountains, East Antarctica. *Recent Progress in Antarctic Earth Science.*, pages 661–667. 135

Moriwaki, K., Yoshida, Y., and Harwood, D. (1992b). Cenozoic glacial history of Antarctica. A correlative synthesis. In Yoshida, Y., Kaminuma, K., and Shiraishi, K., editors, *Recent Progress in Antarctic Earth Science.*, pages 773–780. Terra Scientific Publishing, Toyko. 72, 108, 120, 121

Morrison, A. and Reay, A. (2004). Geochemistry of Ferrar Dolerite sills and dykes at Terra Cotta Mountain, south Victoria Land, Antarctica. *Antarctic Science*, 7(01):73–85. 91

Mudelsee, M. and Schulz, M. (1997). The mid-Pleistocene climate transition: onset of 100 ka cycle lags ice volume build-up by 280 ka. *Earth and Planetary Science Letters*, 151(1-2):117–123. 1

Mukhopadhyay, S., Ackert, R., Pope, A. E., Pollard, D., and DeConto, R. (2012). Miocene to recent ice elevation variations from the interior of the West Antarctic Ice Sheet: Constraints from geologic observations, cosmogenic nuclides and ice sheet modeling. *Earth and Planetary Science Letters*, 337-338:243–251. 43, 98

Naish, T., Powell, R., Levy, R., Wilson, G., Scherer, R., Talarico, F., Krissek, L., Niessen, F., Pompilio, M., Wilson, T., Carter, L., DeConto, R., Huybers, P., McKelvey, B., Pollard, D., Ross, J., Winter, D., Barrett, P., Browne, G., Cody, R., Cowan, E., Crampton, J., Dunbar, G., Dunbar, N., Florindo, F., Gebhardt, C., Graham, I., Hannah, M., Hansaraj, D., Harwood, D., Helling, D., Henrys, S., Hinnov, L., Kuhn, G., Kyle, P., Läufer, A., Maffioli, P., Magens, D., Mandernack, K., McIntosh, W., Millan, C., Morin, R., Ohneiser, C., Paulsen, T., Persico, D., Raine, I., Reed, J., Riesselman, C., Sagnotti, L., Schmitt, D., Sjunneskog, C., Strong, P., Taviani, M., Vogel, S., Wilch, T., and Williams, T. (2009). Obliquity-paced Pliocene West Antarctic Ice Sheet oscillations. *Nature*, 458(7236):322–8. 52, 61

Naish, T., Woolfe, K., Barrett, P., and Wilson, G. (2001). Orbitally induced oscillations in the East Antarctic Ice Sheet at the OligoceneâĂŞMiocene boundary. *Nature*, 413:719–723. 51

Nakada, M. (2000). Late Pleistocene and Holocene melting history of the Antarctic Ice Sheet derived from sea-level variations. *Marine Geology*, 167(1-2):85–103. 58, 59

Nakada, M. and Lambeck, K. (1988). The melting history of the late Pleistocene Antarctic Ice Sheet. *Nature*, 333(6168):36–40. 58, 59

Nishiizumi, K., Caffee, M., Finkel, R., Brimhall, G., and Mote, T. (2005). Remnants of a fossil alluvial fan landscape of Miocene age in the Atacama Desert of northern Chile using cosmogenic nuclide exposure age dating. *Earth and Planetary Science Letters*, 237(3-4):499–507. 42

Nishiizumi, K., Elmore, D., and Kubik, P. (1989). Update on terrestrial ages of Antarctic meteorites. *Earth and Planetary Science Letters*, 93(3-4):299–313. 21, 22, 30, 123, 200

Nishiizumi, K., Imamura, M., Caffee, M., Southon, J., Finkel, R., and Mcaninch, J. (2007). Absolute calibration of 10Be AMS standards. *Nuclear Instruments and Methods in Physics Research Section B: Beam Interactions with Materials and Atoms*, 258(2):403–413. 22

Nishiizumi, K., Klein, J., Middleton, R., and Arnold, J. (1987a). Long-lived cosmogenic nuclides in the Derrick Peak and Lazarev iron meteorites. *Abstracts of the Lunar and Planetary Science Conference*, 18:724. 9, 123

Nishiizumi, K., Klein, J., Middleton, R., and Craig, H. (1987b). In situ produced 10Be and 26Al in olivine from Maui. *Eos, Trans. Am. Geophys.* 9

Nishiizumi, K., Kohl, C., Arnold, J., and Klein, J. (1991). Cosmic ray produced 10Be and 26Al in Antarctic rocks: exposure and erosion history. *Earth and Planetary Science Letters*, 104:440–454. 13, 18

Nishiizumi, K., Lal, D., Klein, J., Middleton, R., and Arnold, J. (1986). Production of 10Be and 26Al by cosmic rays in terrestrial quartz in situ and implications for erosion rates. *Nature*, 319:134–136. 9

Nong, G., Najjar, R., Seidov, D., and Peterson, W. (2000). Simulation of ocean temperature change due to the opening of Drake Passage. *Geophysical Research Letters*, 27(17):2689–2692. 50

Oberholzer, P., Baroni, C., Schaefer, J., Orombelli, G., Ivy-ochs, S., Kubik, P., Baur, H., and Wieler, R. (2003). Limited Pliocene/Pleistocene glaciation in Deep Freeze Range, northern Victoria Land, Antarctica, derived from in situ cosmogenic nuclides. *Antarctic Science*, 15(4):493–502. 43

Orombelli, G., Baroni, C., and Denton, G. (1990). Late Cenozoic glacial history of the Terra Nova Bay. *Terra*, 13. 67

Orombelli, G., Baroni, C., and Denton, G. (1991). Late Cenozoic glacial history of the Terra Nova Bay region, northern Victoria Land. *Geogr. Fis. Dinam. Quat*, 13(1990):139–163. 79

Pallàs, R., Rodés, A., Braucher, R., Carcaillet, J., Ortuño, M., Bordonau, J., Bourles, D., Vilaplana, J., Masana, E., and Santanach, P. (2006). Late Pleistocene and Holocene glaciation in the Pyrenees: a critical review and new evidence from 10Be exposure ages, south-central Pyrenees. *Journal of Quaternary Science*, 25(21-22):2937–2963. 47

Peltier, W. (2004). Global glacial isostasy and the surface of the ice-age earth: The ICE-5G (VM2) Model and GRACE. *Annual Review of Earth and Planetary Sciences*, 32(1):111–149. 55

Petit, J., Jouzel, J., Raynaud, D., Barkov, N., Barnola, J., Basile, I., Bender, M., Chappellaz, J., Davisk, M., Delaygue, G., Delmotte, M., Kotlyakov, V., Legrand, M., Lipenkov, V., Lorius, C., Pepin, L., Ritz, C., Saltzmank, E., and Stievenard, M. (1999). Climate and atmospheric history of the past 420,000 years from the Vostok ice core, Antarctica. *Nature*, 399:429–436. 1, 61, 62, 63, 212

Philippon, G., Ramstein, G., Charbit, S., Kageyama, M., Ritz, C., and Dumas, C. (2006). Evolution of the Antarctic Ice Sheet throughout the last deglaciation: A study with a new coupled climateâĂŤnorth and south hemisphere ice sheet model. *Earth and Planetary Science Letters*, 248(3-4):750–758. 58

Phillips, F., Leavy, B., Jannik, N., Elmore, D., Kubik, P., Dorn, R., and Roddy, D. (1986). The accumulation of cosmogenic chlorine-36 in rocks: A method for surface exposure dating. *Science*, 231(4733):41–43. 9

Phillips, F., Zreda, M., Gosse, J., Klein, J., Evenson, E., Hall, R., Chadwick, O., and Sharma, P. (1997). Cosmogenic 36Cl and 10Be ages of Quaternary glacial and fluvial deposits of the Wind River Range, Wyoming. *Geological Society of America Bulletin*, 109(11):1453–1463. 16

Pollard, D. and DeConto, R. (2009). Modelling West Antarctic Ice Sheet growth and collapse through the past five million years. *Nature,* 458(7236):329–32. 52, 54, 58, 59, 61, 62, 63, 67, 77, 102, 216

Prantzos, N. (1993). Radioactive 26Al from massive stars: Production and distribution in the galaxu. *The Astophysical Journal*, 405(2):55–58. 10

Prentice, M., Bockheim, J., Wilson, S., Burckle, L., Hodell, D., Schlüchter, C., and Kellogg, D. (1993). Late Neogene Antarctic glacial history: Evidence from central Wright Valley. *Antarctic research series*, 60:207–250. 105

Putkonen, J. and Swanson, T. (2003). Accuracy of cosmogenic ages for moraines. *Quaternary Research*, 59(2):255–261. 44

Putnam, A., Schaefer, J., Barrell, D., Vandergoes, M., Denton, G., Kaplan, M., Finkel, R., Schwartz, R., Goehring, B., and Kelley, S. (2010). In situ cosmogenic 10Be production-rate calibration from the Southern Alps, New Zealand. *Quaternary Geochronology*, 5(4):392–409. 22, 32

Radok, U., Allison, I., and Wendler, G. (1996). Atmospheric surface pressure over the interior of Antarctica. *Antarctic Science*, 8(2):209–217. 24

Raymo, M., Lisiecki, L., and Nisancioglu, K. (2006). Plio-Pleistocene ice volume, Antarctic climate, and the global δ18O record. *Science*, 313(July):492–495. 60

Reimer, P., Baillie, M., Bard, E., Bayliss, A., Beck, J., Blackwell, P., Ramsey, C., Buck, C., Burr, G., Edwards, R., Friedrich, M., Grootes, P., Guilderson, T., Hajdas, I., Heaton, T., Hogg, A., Hughen, K., Kaiser, K., Kromer, B., McCormac, F., Manning, S., Reimer, R. W., Richards, D., Southon, J., Talamo, S., Turney, C., van der Plicht, J., and Weyhenmeyer, C. (2009). IntCal09 and Marine09 radiocarbon age calibration curves, 0âĂŞ50,000 years cal BP. *Radiocarbon*, 51(4):1111–1150. 72, 117

Rhodes, R., Bertler, N., Baker, J., Steen-Larsen, H., Sneed, S., Morgenstern, U., and Johnsen, S. (2012). Little Ice Age climate and oceanic conditions of the Ross Sea, Antarctica from a coastal ice core record. *Climate of the Past*, 8(4):1223–1238. 64

Riger-Kusk, M. (2011). Ice dynamics of the Darwin-Hatherton glacial system , Transantarctic Mountains , Antarctica. *Unpublished PhD thesis. University of Canterbury, Christchurch, New Zealand.* 70, 100, 101, 102, 103, 106, 156, 184, 189, 208, 211, 215, 218, 221

Rignot, E., Bamber, J., van den Broeke, M., Davis, C., Li, Y., van de Berg, W., and van Meijgaard, E. (2008). Recent Antarctic ice mass loss from radar interferometry and regional climate modelling. *Nature Geoscience*, 1(2):106–110. 100

Rignot, E., Mouginot, J., and Scheuchl, B. (2011). Ice flow of the Antarctic Ice Sheet. *Science*, 333(6048):1427–30. 52

Ritz, C., Rommelaere, V., and Dumas, C. (2001). Modeling the evolution of Antarctic Ice Sheet over the last 420, 000 years- Implications for altitude changes in the Vostok region. *Journal of Geophysical Research. D. . . .*, 106. 58, 210

Rohling, E., Grant, K., Hemleben, C., Siddall, M., Hoogakker, B., Bolshaw, M., and Kucera, M. (2008). High rates of sea-level rise during the last interglacial period. *Nature Geoscience*, 1(1):38–42. 216

Rossi, B. (1952). *High energy particles.* Prentice-Hall, New York, NY ,USA. 28

Rutt, I., Hagdorn, M., Hulton, N., and Payne, A. (2009). The Glimmer community ice sheet model. *Journal of Geophysical Research: Earth Surface*, 114. 59

Saito, F. and Abe-Ouchi, A. (2010). Modelled response of the volume and thickness of the Antarctic Ice Sheet to the advance of the grounded area. *Annals of Glaciology*, 51(55):41–48. 58

Schaefer, J. (1999). Cosmogenic noble gas studies in the oldest landscape on earth: surface exposure ages of the Dry Valleys, Antarctica. *Earth and Planetary Science Letters*, 167(3-4):215–226. 43

Scher, H. and Martin, E. (2006). Timing and climatic consequences of the opening of Drake Passage. *Science*, 312:428–430. 50

Scherer, R., Aldahan, A., Tulaczyk, S., Possnert, G., Engelhardt, H., and Kamb, B. (1998). Pleistocene collapse of the West Antarctic Ice Sheet. *Science*, 281(5373):82–85. 61

Schildgen, T., Phillips, W., and Purves, R. (2005). Simulation of snow shielding corrections for cosmogenic nuclide surface exposure studies. *Geomorphology*, 64(1-2):67–85. 38

Shackleton, N. (1987). Oxygen isotopes, ice volume and sea level. *Journal of Quaternary Science*, 6(3):183–190. 55

Shipp, S. and Domack, E. (1999). Late Pleistocene - Holocene retreat of the West Antarctic Ice Sheet system in the Ross Sea : Part 1 âĂŤ Geophysical results. *Geological Society of America Bulletin*, 111(10):1517–1536. 58, 64, 67

Shreve, R. (1984). Glacier sliding at subfreezing temperatures. *Journal of Glaciology*, 30(106):341–347. 103

Shulmeister, J., Fink, D., and Augustinus, P. (2005). A cosmogenic nuclide chronology of the last glacial transition in North-West Nelson, New ZealandâĂŤnew insights in Southern Hemisphere climate forcing during the last deglaciation. *Earth and Planetary Science Letters*, 233(3-4):455–466. 23, 32, 128

Siegert, M., Woodward, J., and Royston-Bishop, G. (2012). Antarctic Subglacial Lakes. In Bengtsson, L., Herschy, R., and Fairbridge, R., editors, *Encyclopedia of Lakes and Reservoirs*, pages 37–39. Springer Berlin Heidelberg. 52

Simpson, A. and Cooper, A. (2002). Geochemistry of the Darwin Glacier region granitoids, southern Victoria Land. *Antarctic Science*, 14(4):425–426. 90

Simpson, J. (1983). Elemental and isotopic composition of the galactic cosmic rays. *Annual Review of Nuclear and Particle Science*, 33(1):323–382. 10

Staiger, J., Marchant, D., Schaefer, J., Oberholzer, P., Johnson, J., Lewis, A., and Swanger, K. (2006). Plio-Pleistocene history of Ferrar Glacier, Antarctica: Implications for climate and ice sheet stability. *Earth and Planetary Science Letters*, 243(3-4):489–503. 36, 74, 78, 79, 189

Stauffer, B., Wolff, E., and Barnes, P. (2004). The EPICA deep ice cores: first results and perspectives. *Annals of Glaciology*, 39(1):93–100. 64

Steig, E., Morse, D., Waddington, E., Stuiver, M., Grootes, P., Mayewski, P., Twickler, M., and Whitlow, S. (2000). Wisconsian and Holocene climate history From an ice core at Taylor Dome , Western Ross Embayment, Antarctica. *Geografiska Annaler, Series A: Physical Geography*, 82A(2&3):213–235. 211, 217, 219

Stenni, B., Buiron, D., Frezzotti, M., Albani, S., Barbante, C., Bard, E., Baroni, C., Baroni, M., Baumgartner, M., Bonazza, M., Capron, E., Castellano, E., Chappellaz, J., Delmonte, B., Falourd, S., Genoni, L., Iacumin, P., Jouzel, J., Kipfstuhl, S., Landais, a., Lemieux-Dudon, B., Maggi, V., Masson-Delmotte, V., Mazzola, C., Minster, B., Montagnat, M., Mulvaney, R., Narcisi, B., Oerter, H., Parrenin, F., Petit, J., Ritz, C., Scarchilli, C., Schilt, a., Schüpbach, S., Schwander, J., Selmo, E., Severi, M., Stocker, T., and Udisti, R. (2010). Expression of the bipolar see-saw in Antarctic climate records during the last deglaciation. *Nature Geoscience*, 4(1):46–49. 134

Stern, T., Baxter, A., and Barrett, P. (2005). Isostatic rebound due to glacial erosion in the Transantarctic Mountains. *Geology*, 33(3):221–224. 42

Stone, J. (1999). A consistent Be10 production rate in quartz - muons and altitude scaling. In *AMS-8 Proceedings Abstract Volume, Vienna, Austria*. 22

Stone, J. (2000). Air pressure and cosmogenic isotope production. *Journal of Geophysical Research*, 105(1):753–759. 13, 22, 23, 24, 25, 26, 27, 28, 29, 41, 232, 242, 243, 253, 260, 261

Stone, J., Balco, G., Sugden, D., Caffee, M., Sass, L., Cowdery, S., and Siddoway, C. (2003). Holocene deglaciation of Marie Byrd Land, West Antarctica. *Science*, 299(5603):99–102. 5, 35, 46, 74, 76, 77, 132, 206

Storey, B., Fink, D., Hood, D., Joy, K., Shulmeister, J., Riger-Kusk, M., and Stevens, M. (2010). Cosmogenic nuclide exposure age constraints on the glacial history of the Lake Wellman area, Darwin Mountains, Antarctica. *Antarctic Science*, 22(06):603–618. 4, 7, 103, 108, 110, 120, 148

Strasky, S., Di Nicola, L., Baroni, C., Salvatore, M., Baur, H., Kubik, P., Schlüchter, C., and Wieler, R. (2009). Surface exposure ages imply multiple low-amplitude Pleistocene variations in East Antarctic Ice Sheet, Ricker Hills, Victoria Land. *Antarctic Science*, 21(01):59–69. 4, 41, 43, 74, 79, 106

Strini, A., Guglielmin, M., and Hall, K. (2008). Tafoni development in a cryotic environment: an example from northern Victoria Land, Antarctica. *Earth Surface Processes and Landforms*, 1519(December 2007):1502–1519. 98

Stroeven, A. (2002). A relict landscape in the centre of Fennoscandian glaciation: cosmogenic radionuclide evidence of tors preserved through multiple glacial cycles. *Geomorphology*, 44(1-2):145–154. 33

Stroeven, A., Fabel, D., Harbor, J., Fink, D., Caffee, M., and Dahlgren, T. (2011). Importance of sampling across an assemblage of glacial landforms for interpreting cosmogenic ages of deglaciation. *Quaternary Research*, 76(1):148–156. 33

Stuiver, M., Denton, G., Hughes, T., and Fastook, J. (1981). History of the marine ice sheet in West Antarctic during the last glaciation, a working hypothesis. In Denton, G. and Hughes, T., editors, *The last great ice sheets*, pages 319–436. Wiley, New York, NY ,USA. 59, 75, 121

Sugden, D., Balco, G., Cowdery, S., Stone, J., and Sassiii, L. (2005). Selective glacial erosion and weathering zones in the coastal mountains of Marie Byrd Land, Antarctica. *Geomorphology*, 67(3-4):317–334. 106

Sugden, D., Bentley, M., and O Cofaigh, C. (2006). Geological and geomorphological insights into Antarctic Ice Sheet evolution. *Philosophical transactions. Series A, Mathematical, physical, and engineering sciences*, 364(1844):1607–25. 116, 120

Sugden, D., Denton, G., and Marchant, R. (1995). Evolution of the Dry Valleys , Transantarctic Mountains : Tectonic implications. *Journal of Geophysical Research - Earth Surface*, 100(B6):9949–9967. 41, 107

Sugden, D., Summerfield, M., Denton, G., Wilch, T., McIntosh, W., Marchant, D., and Rutford, R. (1999). Landscape development in the Royal Society Range , southern Victoria Land , Antarctica : stability since the mid-Miocene. *Geomorphology*, 28:181–200. 41, 107

Summerfield, M. (1999). Long-term rates of denudation in the Dry Valleys, Transantarctic Mountains, southern Victoria Land, Antarctica based on in-situ-produced cosmogenic 21Ne. *Geomorphology*, 27(1-2):113–129. 43, 44, 98

Thomas, R. and Bentley, C. (1978). A model for Holocene retreat of the West Antarctic Ice Sheet. *Quaternary Research*, 10(2):150–170. 64

Thomas, R., Scheuchl, B., Frederick, E., Harpold, R., Martin, C., and Rignot, E. (2013). Continued slowing of the Ross Ice Shelf and thickening of West Antarctic ice streams. *Journal of Glaciology*, 59(217):838–844. 51

Todd, C., Stone, J., Conway, H., Hall, B., and Bromley, G. (2010). Late Quaternary evolution of Reedy Glacier, Antarctica. *Journal of Quaternary Science*, 29(11-12):1328–1341. 4, 5, 41, 67, 70, 73, 74, 80, 81, 82, 135, 184, 202, 206, 209, 210, 213, 217, 218, 219

Tuniz, C., Bird, J., Fink, D., and Herzog, H. (1998). *Accelerator mass spectrometry: Ultrasensitive analysis for global science*. CRC Press. Bacco Raton, Florida, Boca Raton, Florida, USA, 1 edition. 9, 33

Turkington, A. and Phillips, J. (2004). Cavernous weathering, dynamical instability and self-organization. *Earth Surface Processes and Landforms*, 29(6):665–675. 98

Tushingham, A. and Peltier, W. (1991). ICE-3G: a new global model of late Pleistocene deglaciation based upon geophysical predictions of postglacial relative sealevel. *Journal of Geophysical Research*, 96:4497–4523. 58

Una Alvarez, E. (2008). Description and nomenclature of the tafoni features (cavernous rock forms). Research approaches in granite terrains. *Xeolóxico de Laxe Coruña*, 33:65–82. 99

Vaughan, D. and Arthern, R. (2007). Climate Change: why is it hard to predict the future of ice sheets? *Science*, 315(5818):1503–1504. 60

Verleyen, E., Hodgson, D., Sabbe, K., Cremer, H., Emslie, S., Gibson, J., Hall, B., Imura, S., Kudoh, S., Marshall, G., McMinn, A., Melles, M., Newman, L., Roberts, D., Roberts, S., Singh, S., Sterken, M., Tavernier, I., Verkulich, S., de Vyver, E., Van Nieuwenhuyze, W., Wagner, B., and Vyverman, W. (2011). Post-glacial regional climate variability along the East Antarctic coastal marginâĂŤEvidence from shallow marine and coastal terrestrial records. *Earth-Science Reviews*, 104(4):199–212. 117, 211, 217, 219

Waller, R., Murton, J., and Kristensen, L. (2012). Glacier–permafrost interactions: Processes, products and glaciological implications. *Sedimentary Geology*. 106

Webster-Brown, J., Gall, M., Gibson, J., Wood, S., and Hawes, I. (2010). The biogeochemistry of meltwater habitats in the Darwin Glacier region (80ÂřS), Victoria Land, Antarctica. *Antarctic Science*, 22(06):646–661. 159

White, D., Bennike, O., Berg, S., Harley, S., Fink, D., Kiernan, K., McConnell, A., and Wagner, B. (2009). Geomorphology and glacial history of Rauer Group, East Antarctica. *Quaternary Research*, 72(1):80–90. 43, 98

White, D., Fink, D., and Gore, D. (2010). Cosmogenic nuclide evidence for enhanced sensitivity of an East Antarctic ice stream to change during the last deglaciation. *Geology*, 39(1):23–26. 21, 22, 56

White, D., Fülöp, R., Bishop, P., Mackintosh, A., and Cook, G. (2011). Can in-situ cosmogenic 14C be used to assess the influence of clast recycling on exposure dating of ice retreat in Antarctica? *Quaternary Geochronology*, 6(3-4):289–294. 16

Whitehouse, P., Bentley, M., and Le Brocq, A. (2012). A deglacial model for Antarctica: geological constraints and glaciological modelling as a basis for a new model of Antarctic glacial isostatic adjustment. *Journal of Quaternary Science*, 32:1–24. 58, 59, 66, 210

Wilch, T., Denton, G., Lux, D., and McIntosh, W. (1993). Limited Pliocene glacier extent and surface uplift in middle Taylor Valley, Ant arctica. *Geografiska Annaler, Series A: Physical Geography*, 75a:331–351. 41

Wilch, T. and McIntosh, W. (2000). Eocene and Oligocene volcanism at Mount Petras, Marie Byrd Land: implications for middle Cenozoic ice sheet reconstructions in West Antarctica. *Antarctic Science*, 12(4):477–491. 54

Wilson, D., Pollard, D., DeConto, R., Jamieson, S., and Luyendyk, B. (2013). Initiation of the West Antarctic Ice Sheet and estimates of total Antarctic ice volume in the earliest Oligocene. *Geophysical Research Letters*, 40(16):4305–4309. 54

Woolfe, K. (1993). Devonian depositional environments in the Darwin Mountains: Marine or non-marine? *Antarctic Science*, 5(02). 91

Wright, A., White, D., Gore, D., and Siegert, M. (2008). Antarctica at the Last Glacial Maximum, Deglaciation and the Holocene. *Developments in Earth and Environmental Sciences*, 8(08):531–570. 52

Yamane, M., Yokoyama, Y., Miura, H., Maemoku, H., Iwasaki, S., and Matsuzaki, H. (2011). The last deglacial history of Lützow-Holm Bay, East Antarctica. *Journal of Quaternary Science*, 26(1):3–6. 22

Yokoyama, Y., Lambeck, K., De Deckker, P., Johnston, P., and Fifield, K. (2000). Timing of the Last Glacial Maximum from observed sea-level minima. *Nature*, 406(6797):713–6. 55, 56, 57

Zachos, J., Pagani, M., Sloan, L., Thomas, E., and Billups, K. (2001). Trends, rhythms, and aberrations in global climate 65 Ma to present. *Science*, 292(5517):686–93. 49, 60

Zawar-Reza, P., George, S., Storey, B., and Lawson, W. (2010). Summertime boundary layer winds over the DarwinâĂŞHatherton glacial system, Antarctica: observed features and numerical analysis. *Antarctic Science*, 22(06):619–632. 85, 93